

Conference Proceedings, Published Version

**Ricci, Sophie (Hg.)**

## **Proceedings of the XXVIth TELEMAT-MASCARET User Conference, 15th to 17th October 2019, Toulouse**

Zur Verfügung gestellt in Kooperation mit/Provided in Cooperation with:  
**TELEMAT-MASCARET Core Group**

---

Verfügbar unter/Available at: <https://hdl.handle.net/20.500.11970/107362>

Vorgeschlagene Zitierweise/Suggested citation:

Ricci, Sophie (Hg.) (2019): Proceedings of the XXVIth TELEMAT-MASCARET User Conference, 15th to 17th October 2019, Toulouse. Toulouse: CNRS/CERFACS.

### **Standardnutzungsbedingungen/Terms of Use:**

Die Dokumente in HENRY stehen unter der Creative Commons Lizenz CC BY 4.0, sofern keine abweichenden Nutzungsbedingungen getroffen wurden. Damit ist sowohl die kommerzielle Nutzung als auch das Teilen, die Weiterbearbeitung und Speicherung erlaubt. Das Verwenden und das Bearbeiten stehen unter der Bedingung der Namensnennung. Im Einzelfall kann eine restriktivere Lizenz gelten; dann gelten abweichend von den obigen Nutzungsbedingungen die in der dort genannten Lizenz gewährten Nutzungsrechte.

Documents in HENRY are made available under the Creative Commons License CC BY 4.0, if no other license is applicable. Under CC BY 4.0 commercial use and sharing, remixing, transforming, and building upon the material of the work is permitted. In some cases a different, more restrictive license may apply; if applicable the terms of the restrictive license will be binding.

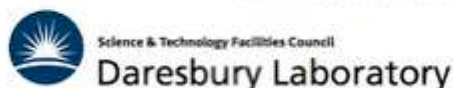


CENTRE EUROPÉEN DE RECHERCHE ET DE FORMATION AVANCÉE EN CALCUL SCIENTIFIQUE

# Proceedings of the **XXVI<sup>th</sup> TELEMAC-MASCARET User Conference**

**15 to 17 October 2019,  
Toulouse, France**

Organised by Sophie Ricci, CECI CERFACS/CNRS UMR5318



## Session 1 - River and urban floods, flood forecasting and management

Comparison of different vegetation models using TELEMAC-2D

*R. Kopmann, F. Folke, G. Dalledonne, M. Attieh*

[https://zenodo.org/record/3611486#.XiH\\_QOtCd-U](https://zenodo.org/record/3611486#.XiH_QOtCd-U) ----- 1

Durance River modelling for environment and safety management

*T. Viard, M. Duclercq*

<https://zenodo.org/deposit/3611613> ----- 9

Numerical investigation of non-cohesive fluvial dike breaching induced by flow overtopping

*L. Kheloui, R. Ata, K. El Kadi Abderrezzak* ----- 15

Flooding dynamics within an Amazonian floodplain: water circulation patterns and inundation duration

*S. Pinel, M.-P. Bonnet, J. S. Da Silva, T. Catry, F. Seyler*

<https://zenodo.org/deposit/3611590> ----- 16

Numerical modelling of flash flood event in steep river using Telemac2D and Sisyphe

*M. Pavlicek, O. Bruland*

<https://zenodo.org/record/3611582#.XxbRzRFCTAg> ----- 25

## Session 2 - River and urban floods, flood forecasting and management

A flood forecasting model on river Oise with the plugin mascaret

*P. Chasse, C. Chabridier, D. Duval, C. Sourdiaux*

<https://zenodo.org/record/3611529#.XiIMHOtCd-U> ----- 32

Floods risk management based on 2D TELEMAC computations: an example with Swiss hazard maps

*R. Salvisberg, T. Marti, S. Arrigo Meier, M. Petar*

<https://zenodo.org/deposit/361159> ----- 38

Application of the TELEMAC-3D to simulate flooding and hydrodynamics patterns of southern Brazilian wetlands

*J. Costi, A. Forster, W. C. Marques, J. Arigony-Neto, R de F. Duarte*

<https://zenodo.org/record/3611534#.XiINzutCd-U> ----- 47

Open TELEMAC as a decision making tool in developing countries. Case of flash floods and boundary demarcation in Colombia

*J. Escobar-Vargas, C. Fuentes-Cabrejo* ----- 53

### Session 3 - River, estuaries, maritime, coastal sediment processes

Numerical modelling of released dredged sediment dispersion from Pandop harbour (New Caledonia) <i>J. Baills, J. Dugor, D. Rihouey</i> <a href="https://zenodo.org/record/3611509#.XiIEutCd-U">https://zenodo.org/record/3611509#.XiIEutCd-U</a>	54
Calibration and validation strategy for 2D hydrodynamic modelling: application to morphodynamics of a gravel bed river with suspended sediments <i>C. Bel, M. Jodeau, P. Tassi, N. Claude, H. Haddad</i> <a href="https://zenodo.org/deposit/3611515">https://zenodo.org/deposit/3611515</a>	60
TEL2TOM: coupling TELEMAC2D and TOMAWAC on arbitrary meshes <i>A. Breugem, E. Fonias, L. Wang, A. Bolle, G. Kolokythas, B De Maerschalck</i> <a href="https://zenodo.org/record/3611518#.XiIXetCd-U">https://zenodo.org/record/3611518#.XiIXetCd-U</a>	66
Density stratification and turbulent mixing in a salt-wedge estuary: The Adour river <i>S. Defontaine, D. Sous, P. Maron, D. Morichon</i>	75
A preliminary study of tide propagation and sediment dynamics in a macrotidal estuary influenced by the presence of a tidal power station <i>R. Rtimi, A. Sottolichio, P. Tassi</i>	76
Benchmark of hydro-sedimentary 1D codes : HEC-RAS, COURLIS and ADIS-TS <i>E. Lalinde, V. Dugué, T. Frétau, M. Sécher, E. Valette, J.-B. Faure, B. Camenen</i> <a href="https://zenodo.org/deposit/3611552">https://zenodo.org/deposit/3611552</a>	77
2D and 3D numerical modelling of the flow and sediment transport in shallow reservoirs: application to a real case <i>N. Claude, M. Sécher, J. Deng, E. Valette, M. Duclercq</i> <a href="https://zenodo.org/record/3611531#.XiIM6etCd-U">https://zenodo.org/record/3611531#.XiIM6etCd-U</a>	85
A Sand Transport Model for the Scheldt Estuary: The 3D Scaldis Sand Model <i>S. Smolders, Y. Plancke, Q. Bi, J. Vanlede, G. Kolokythas</i> <a href="https://zenodo.org/deposit/3611598">https://zenodo.org/deposit/3611598</a>	91

### Session 4 - Data assimilation, optimization, risks and uncertainties

Sensitivity Analysis of the Mascaret model on the Odet River <i>A.-L. Tiberi-Wadier, N. Goutal, S. Ricci, P. Sergent, C. Monteil</i> <a href="https://zenodo.org/record/3611478#.XiH21-tCejQ">https://zenodo.org/record/3611478#.XiH21-tCejQ</a>	99
--	----



The impact of observation densification in an Ensemble Kalman Filter <i>I. Mirouze, S. Ricci, N. Goutal</i> <a href="https://zenodo.org/record/3549572#.XiH_V-tCd-U">https://zenodo.org/record/3549572#.XiH_V-tCd-U</a>	107
Mixture of polynomial chaos expansions for uncertainty propagation <i>S. El Garroussi, S. Ricci, M. De Lozzo, N. Goutal, D. Lucor</i>	115
A Metamodel of the Telemac Errors <i>F. Zaoui, C. Goeury, Y. Audouin</i> <a href="https://zenodo.org/deposit/3611615">https://zenodo.org/deposit/3611615</a>	116
Telemac optimisation with OpenTURNS <i>T. Oudart, O. Bertrand</i> <a href="https://zenodo.org/deposit/3611578">https://zenodo.org/deposit/3611578</a>	123
 <b>Session 5 - Numerical methods, code coupling and high performance computing</b>	
Using TELEMAC-2D for Hydrodynamic Modelling of Rainfall-Runoff <i>K. Broich, T. Pflugbeil, M. Disse, H. Nguyen</i> <a href="https://zenodo.org/record/3611524#.XiILYOtCd-U">https://zenodo.org/record/3611524#.XiILYOtCd-U</a>	124
New Python3 module for TELEMAC-MASCARET dedicated post-treatment: Postel <i>Y. Audouin, Y. Audouin, J. Fontaine, T. Fouquet, C. Goeury, A. Leroy, C.-T. Pham, F. Souillé, F. Taccone, M.-P. Daou, L. Duron, M. Sécher</i> <a href="https://zenodo.org/record/3611502#.XiIAe-tCd-U">https://zenodo.org/record/3611502#.XiIAe-tCd-U</a>	131
Blue Kenue enhancements from 2014 to 2019 <i>A. Barton</i> <a href="https://zenodo.org/deposit/3611511">https://zenodo.org/deposit/3611511</a>	138
Open channel model using a coupled MASCARET-MATLAB Model <i>M. Breysse</i> <a href="https://zenodo.org/record/3611522#.XiIJLutCd-U">https://zenodo.org/record/3611522#.XiIJLutCd-U</a>	146
Tatooine Mesher: Anisotropic interpolation from 1D cross-section and 2D river mesher <i>L. Duron, F.-X. Cierco, K. Saad</i> <a href="https://zenodo.org/record/3611546#.XiIRGOtCd-U">https://zenodo.org/record/3611546#.XiIRGOtCd-U</a>	150

Porting TELEMAC-MASCARET to OPENPOWER and experimenting GPU offloading to accelerate the TOMAWAC module <i>J. Grasset, S. Longshaw, C. Moulinec, D. Emerson, Y. Audouin, P. Tassi</i> <a href="https://zenodo.org/record/3611548#.XiIR4etCd-U">https://zenodo.org/record/3611548#.XiIR4etCd-U</a> _ _ _ _ _	158
An Efficient Implementation of Parallelization in the Domain Decomposition of TELEMAC <i>D. Nguyen, T. Liepert, M. Reisenbüchler, K. Kaveh, M. D. Bui, P. Rutschmann</i> _ _ _ _ _	164
Large-scale high-resolution urban flood modeling in the cloud using TELEMAC <i>F. Saleh, V. Rodriguez, V. Ramaswamy</i> _ _ _ _ _	165
 <b>Session 6 - River, estuaries, maritime, coastal sediment processes</b>	
Introducing GAIA, the brand new sediment transport module of the TELEMAC-MASCARET system <i>P. Tassi Contributors to Gaia in alphabetical order: Y. Audouin, T. Benson, M. Delinares, J. Fontaine, B. Glander, N. Huybrechts, R. Kopmann, A. Leroy, S. Pavan, C.-T. Pham, F. Taccone, R. Walter</i> <a href="https://zenodo.org/deposit/3611600">https://zenodo.org/deposit/3611600</a> _ _ _ _ _	166
Method to integrate a simplified erosion channel during flood in reservoir simulation with Telemac <i>E. Valette, M. Sécher, Y. Audouin, J. Fontaine, C. Goeury</i> <a href="https://zenodo.org/deposit/3611611">https://zenodo.org/deposit/3611611</a> _ _ _ _ _	174
Development of a hydro-morphodynamic Model for Sediment Management in the Rosenheim Reservoir <i>D. Aguirre, M. Duc Bui, S. Giehl, M. Reisenbüchler, P. Rutschmann</i> <a href="https://zenodo.org/record/3611498#.XiH_IutCd-U">https://zenodo.org/record/3611498#.XiH_IutCd-U</a> _ _ _ _ _	178
Numerical Modelling of Local Scour Around Cylindrical Piers Including Secondary Flows Effects <i>L. Duran-Santana, J. Escobar</i> <a href="https://zenodo.org/deposit/3611540#">https://zenodo.org/deposit/3611540#</a> _ _ _ _ _	186
Sediment modelling for Poole and Christchurch Bay <i>M. Knaapen</i> <a href="https://zenodo.org/deposit/3611550">https://zenodo.org/deposit/3611550</a> _ _ _ _ _	193
Ship-current interactions with TELEMAC <i>J. Parisi, M. Turnbull, A. Cooper, J. Clarke</i> <a href="https://zenodo.org/record/3611580#.XiIcYutCd-U">https://zenodo.org/record/3611580#.XiIcYutCd-U</a> _ _ _ _ _	201

## Session 7 A - River, estuaries, maritime, coastal sediment processes

Computation of 3D coastal hydrodynamics through the vortex force formalism implemented by coupling TOMAWAC and TELEMAC-3D

*M. J. Teles, T. Fouquet, A. Pires-Silva*

<https://zenodo.org/deposit/3611606> \_\_\_\_\_ 208

Impact of the initial sediment condition on the numerical modelling of bedload transport

*M. Utz*

<https://zenodo.org/deposit/3611609> \_\_\_\_\_ 214

Application of TELEMAC2D for water levels assessment in the Laita estuary, France

*N. Chini, P. Timmerman, R. Delmas*

\_\_\_\_\_ 220

## Session 7 B - Water quality, biodiversity, ecology and environmental pollution

Three-dimensional hydrodynamic modelling in a bay of the Lake Mälaren to assess environmental impacts from a cooling and heating power plant production

*P.-L. Ligier, N. Okumura*

<https://zenodo.org/deposit/3611558> \_\_\_\_\_ 221

Numerical modelling of bacteriologic impacts in the Laita estuary (France)

*J. Dugor, J. Dugor, J. Baills, D. Rihouey*

<https://zenodo.org/record/3611538#.XiIQQ-tCd-U> \_\_\_\_\_ 230

Telemac3D for aquatic ecological modelling: calibration of the coupled ecological library AED2

*F. Piccioni (LEESU Ecole des Ponts ParisTech, AgroParisTech, UPEC), B. Vinçon-Leite, M.H. Le, B. J. Le-maire, C. Casenave, Y. Hoang, M. Jodeau, C.-T. Pham, J. Vidal, N. Goutal*

\_\_\_\_\_ 236

Thermal Stratification in Small Lakes with Telemac3D: Showase “Lake Monsterloch”

*U. Merkel*

<https://zenodo.org/deposit/3611576> \_\_\_\_\_ 237

Developing and validating a Telemac3D model for E. coli and norovirus dispersal through aquaculture systems

*J. Bacon, S. Kershaw*

\_\_\_\_\_ 244

## Session 8 - Waves, tidal renewable and hydro power energy assessment

Internal boundary conditions for Telemac

*C. Dorfmann* ----- 245

Visualising uncertainties in coastal flooding

*J. Maskell*

<https://zenodo.org/deposit/3611562> ----- 246

# Comparison of different vegetation models using TELEMAC-2D

Frederik Folke, Rebekka Kopmann,  
Guilherme Dalledonne

Dept. of Hydraulic Engineering  
Federal Waterways Engineering and Research Institute  
(BAW)  
Karlsruhe, Germany  
frederik.folke@baw.de

Mohamad Attieh

Institute for Water and River Basin Management  
Karlsruhe Institute of Technology (KIT)  
Karlsruhe, Germany

**Abstract**— Riparian vegetation on German federal waterways is of growing importance. The occurrence of vegetation significantly increases the hydraulic resistance. In most cases classical friction formulations in depth-averaged models fail to model the effect of vegetation. For skin friction and form roughness the hydraulic resistance decreases with increasing water depth. In contrast, the hydraulic resistance increases with depth for non-submerged vegetation. It is highly important to capture the vegetation effects on the flow field adequately by special friction formulations. The only vegetation formulation in the current TELEMAC-2D version (v8p0r2) is from Lindner [1] and Pasche and Rouvé [2], evaluated for rigid non-submerged cylinders.

In a previous study [3] the approaches of Järvelä [4] and Baptist et al. [5] were recommended to model the hydraulic resistance of bushes, shrubs and trees. Within the current study these approaches are investigated using a 1D-flume model and an existent model of the river Rhine and compared to the current approach in TELEMAC-2D.

The predicted friction values of both new approaches are in good agreement with data from a flume experiment. The current approach in TELEMAC-2D shows only reasonable results using a constant drag coefficient but still has significant deviations from the experimental data. For a certain discharge, the measured water levels in the main channel of the 11 km long Rhine model can be captured equally well independently from vegetation approach used. The need for a two-layer vegetation approach is highlighted. The results show that the current vegetation formulation in TELEMAC-2D should be improved and additional vegetation models are needed.

## I. INTRODUCTION

Riparian vegetation on German federal waterways is of growing importance. To satisfy the requirements of the EU Water Framework Directive the connection and restoration of branches covered by riparian vegetation and technical-biological bank protection measures are focus of several ongoing projects. The occurrence of vegetation significantly increases the hydraulic resistance. In most cases classical friction formulations in depth-averaged models, such as the Chézy, fail to model the effect of vegetation. Furthermore, the vertical velocity profile changes and the logarithmic velocity distribution over the whole water column is not valid anymore, so that also the law of Nikuradse cannot be applied.

For grain roughness and form roughness the hydraulic resistance decreases with increasing water depth – but in the case of non-submerged vegetation the hydraulic resistance increases with water depth. In regard to river engineering it is highly important to capture the vegetation effects on the flow field adequately by special friction formulations. The only vegetation formulation in the current TELEMAC-2D version (v8p0r2) is from Lindner [1] and Pasche and Rouvé [2] (hereafter referred to as Lindner approach), evaluated for rigid non-submerged cylinders.

In recent decades many new approaches to model the effect of vegetation have been developed. Their scope ranges from very flexible sea grass through bushes to rigid tree stumps. In a previous study [3] the authors investigated the suitability of five different vegetation models with regard to large scale applications at German federal waterways. The approaches of [4] and [5] (hereafter referred to as Järvelä approach and Baptist approach) were both recommended to model the hydraulic resistance of bushes, shrubs and trees. Additionally, the study highlighted the suitability of the leaf area index to account for vegetation density term in large-scale applications, which is not discussed further herein.

An overview of the vegetation models is given and their implementation into TELEMAC-2D is presented. The implementation is done in such a way that it can easily be extended to additional vegetation models including a flexible number of input parameters. Within this study, the existing Lindner approach and the two recommended approaches are investigated using a 1D-flume model and an existing model of the river Rhine. Recommendations for further TELEMAC-2D versions are provided in the discussion.

## II. MODELLING VEGETATION USING TELEMAC-2D

To consider the additional resistance caused by vegetation the principle of linear superposition is used. Thus, the total friction  $\lambda$  is the sum of the bed roughness coefficient  $\lambda'$  and the vegetation form resistance per unit surface  $\lambda''$ :

$$\lambda = \lambda' + \lambda''. \quad (1)$$

In TELEMAC-2D different friction laws for the bed roughness are available (keyword: LAW OF BOTTOM FRICTION). For the combination with vegetation the law of

Nikuradse is recommended, as it is independent of the water level. When vegetation exists, the vegetation friction coefficient is usually much higher and therefore decisive for the total friction. To model vegetation friction different approaches are used within this study and are described below. Further information can be found in [3].

#### A. Vegetation models

Based on the vegetation density [6] analytically derived a formula to describe the resistance induced by vegetation. Simplifying the vegetation as rigid cylinders the friction of non-submerged vegetation (flow depth  $h$ , smaller than plant height  $h_p$ ) can be expressed as

$$\lambda'' = 4C_D \cdot \frac{Dh}{\Delta^2}, \quad (2)$$

with the drag coefficient  $C_D$ , the diameter  $D$ , and the spacing between the plant  $\Delta$ . Equation (2) is the basis for most of the existing vegetation models.

1) *Lindner approach*: [1] adopted the Petryk and Bosmajian formula and enhanced the approach by quantifying the drag coefficient  $C_D$  at the reach scale. He assumed that the drag coefficient is dependent on the drag coefficient of a single cylinder, the resistance due to narrowing effects of the adjacent cylinders, and the resistance due to gravity wave [2]. The vegetation model of the Lindner approach is already available in TELEMAC-2D (v8p0r2). The drag coefficient is determined iteratively based on the flow velocity, the flow depth and the vegetation parameters diameter and spacing between the vegetation elements (not shown here).

2) *Järvelä approach*: [4] developed an approach for flexible non-submerged ( $h < h_p$ ) and just submerged ( $h \approx h_p$ ) vegetation.

$$\lambda'' = \begin{cases} 4C_{D\chi} \left( \frac{u_m}{u_\chi} \right)^\chi LAI \cdot \frac{h}{h_p} & \text{for } h < h_p \\ 4C_{D\chi} \left( \frac{u_m}{u_\chi} \right)^\chi LAI & \text{for } h \approx h_p \end{cases} \quad (4)$$

Proposing the foliage as the main contributor to vegetation resistance, the vegetation parameter leaf-area index ( $LAI$ ) is used to account for the vegetation density. In case of non-submerged vegetation a linear distribution of the  $LAI$  is assumed in vertical direction. To account for the streamlining effect due to the flexibility of the plants, the exponent  $\chi$ , based on the empirical concept of [7], and the corresponding reference velocity  $U_\chi$  are used. The Järvelä approach is only valid for flow velocities larger than the used reference velocity. It is assumed that plant deformation occurs only for velocities larger than the reference velocity. Therefore, a limit for the velocity ratio to values greater than or equal one is introduced.

3) *Baptist approach*: Both models above mentioned are only valid in case of non-submerged flow conditions. [5] introduced a two-layer approach to model both non-submerged and submerged vegetation. Using the

simplification of rigid cylinders, the vegetation friction coefficient is defined as

$$\lambda'' = \begin{cases} 4C_D \cdot \frac{Dh}{\Delta^2} & \text{for } h \leq h_p \\ 4 \cdot \left( \frac{1}{\sqrt{C_D \frac{Dh_p}{\Delta^2}}} + \frac{1}{\sqrt{2\kappa}} \ln \frac{h}{h_p} \right)^{-2} & \text{for } h > h_p \end{cases} \quad (5)$$

with the von Kármán constant  $\kappa$ .

For species with no well-defined plant diameter, the rigid cylinder approaches are not appropriate. In this case, [3] recommended using the relation between the vegetation density parameters of rigid cylinders (diameter and spacing) to the  $LAI$  by [8].

$$\frac{D}{\Delta^2} = \frac{1}{2} \cdot \frac{LAI}{h_p}. \quad (6)$$

This relation was used in the current study to compare the individual models.

#### B. Implementation

In the TELEMAC-2D release (v8p0r2) the effect of vegetation can be modelled by the Lindner approach using the keyword NON-SUBMERGED VEGETATION FRICTION. In the new implementation this is changed to VEGETATION FRICTION since some of the new models are valid for both non-submerged and submerged vegetation. To use the vegetation friction models, the logical keyword FRICTION DATA has to be activated, in order to define individual bottom friction laws and vegetation models by area. Furthermore, two additional files are needed: the zones file (a list of nodes and corresponding friction IDs) and the friction data file (a table which defines the friction laws and its parameters for each friction ID). In Tab. 1 all needed keywords for vegetation friction are summarised. In the friction data file the setting of the bottom friction and the vegetation friction have to be defined as described below.

TABLE 1: KEYWORDS FOR VEGETATION FRICTION (TELEMAC-2D)

FRICTION DATA	=	YES
VEGETATION FRICTION (old keyword: NON-SUBMERGED VEGETATION FRICTION)	=	YES
ZONES FILE (not needed if FRIC-ID is defined in geometry file)	=	'list.bfr'
FRICTION DATA FILE	=	'friction.tbl'

Taking into account more than one vegetation approach the friction table had to be enhanced. For each friction ID a specific vegetation friction law can be specified in the new implementation. In the adjacent columns the corresponding vegetation parameters have to be set (cf. Tab. 2). The maximum number of vegetation parameters is set to 15. As described above, the vegetation friction is added to the bottom friction by linear superposition. Just like in the current version of TELEMAC-2D, the user can choose

between eight different bottom friction laws (cf. Telemac2D User Manual). In this study only the bottom friction law of Nikuradse (keyword NIKU) is used.

TABLE 2: FRICTION DATA FILE EXAMPLE (NEW: GREY COLUMNS, COMMENT LINES START WITH \*)

Friction ID	Bottom friction law	Parameter for bottom friction	Vegetation friction law	Parameter 1 for vegetation friction	Parameter 2 for vegetation friction	Parameter x for vegetation friction
*				D	$\Delta$	
1	NIKU	0.1	LIND	0.05	2.0	
*				$C_D$	mD	hp
2	NIKU	0.05	BAPT	1.0	0.0025	2.0

[9] implemented seven new vegetation approaches into TELEMAC-2D. All available approaches in the new implementation and the corresponding keywords and number of needed vegetation parameters are listed in Tab. 3. To make a simple addition and an easy modification possible, each vegetation approach is implemented in its own subroutine. From the new approaches only [4] and [5] are used in this paper. For further information see [3] and [9].

TABLE 3: KEYWORDS FOR VEGETATION FRICTION (TELEMAC-2D)

Vegetation approach	Keyword	Number of parameters
no vegetation	NULL	-
Linder [1] and Pasche and Rouvé [2]	LIND	2
Järvelä [4]	JAER	5
Whittaker at al. [10]	WHIT	6
Baptist et al. [5]	BAPT	3
Huthoff [11]	HUTH	4
Van Velzen et al. [12]	VANV	3
Luhar and Nepf [13]	LUNE	4
Västilä and Järvelä [14]	VAST	8

To simplify, an additional modification was done to remove the zones file. The friction IDs can now be read from the variable “FRIC-ID” in the geometry file. With this procedure the program code is optimized and the friction handling is less prone to errors.

### III. NUMERICAL INVESTIGATION

In this study the recommended vegetation approaches [3] of Baptist and Järvelä were compared to the vegetation approach of Lindner, which is currently the only one available in TELEMAC-2D (v8p0r2). A numerical model of a vegetation flume experiment [15] was setup and the numerical results were compared to the measurements. This enabled the calculation of the vegetation friction coefficients to be validated. In addition, the differences between the different vegetation approaches were highlighted by simulating an 11 km long stretch of the River Rhine.

#### A. 1D flume model

A 1D-flume model was used to investigate the prediction accuracy of the individual vegetation approaches with TELEMAC-2D. The laboratory experiments [15] were performed using a 32 m long flume with a rough bed ( $k_s \approx 3$  mm) and smooth sidewalls. Artificial plants with an undeflected height of 0.23 m were used to model the vegetation elements. The vegetation characteristics were similar to that of natural poplar. The setups of the experiments were chosen to achieve just-submerged flow conditions. Two different vegetation configurations (inline: L and staggered: S) and three different plant spacings (0.15 m, 0.20 m and 0.30 m), resulting in 6 data sets of measurements, were simulated. Detailed information can be found in [3] and [9]. In the current study the approaches of Lindner with and without the iterative calculation of the drag coefficient are compared to the Järvelä and Baptist approaches. To derive the vegetation parameters for the rigid approaches, the relation given in (6) was used. The vegetation parameters are summarized in Tab. 4. The vegetation parameters were chosen analogue to [3].

TABLE 4: USED PARAMETERS FOR THE VEGETATION LAWS

Arr.	$\Delta$	$h_p$	LAI	$C_{D\chi}$	$U_\chi$	$\chi$
	[m]	[m]	[-]	[-]	[m/s]	[-]
Inline (L)	0.30 0.20 0.15	0.23	0.437 0.984 1.748	0.34	0.13	-0.73
Staggered (S)	0.30 0.20 0.15	0.23	0.437 0.984 1.748	0.50	0.11	-0.74

Initially, the friction coefficients calculated by the TELEMAC-2D approach were validated by measurements. In Fig. 1 the predicted friction coefficients of the Lindner approach compared to the measured ones are shown. Using default settings the implemented Lindner approach estimates friction values which are too high (cf. Fig. 1, left). Use of a constant value of  $C_D$  of 1.0 produces much improved results (cf. Fig. 1, right). It seems that the iterative method for the estimation of  $C_D$  fails in this example. In both cases the predicted friction coefficient shows a high sensitivity to the spacing which cannot be observed in the measurements from [15].

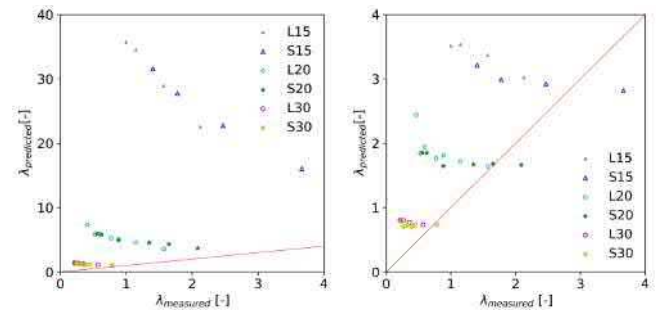


Figure 1: Comparison of predicted and measured friction coefficients of the vegetation approach in the official Telemac-2D release (left: iterative estimation of  $C_D$ ; right:  $C_D=1.0$ ) with two different vegetation configurations (inline: L and staggered: S) and three different plant spacing (0.15 m, 0.20 m and 0.30 m)



The predicted friction values by the Järvelä and the Baptist approaches are in good agreement with the measurements for all configurations (cf. Fig. 2). For the Baptist approach a  $C_D$  of 1.0 was set. It should be noted that the vegetation parameter for the Järvelä approach (cf. Tab. 4) were directly derived from the present experimental data.

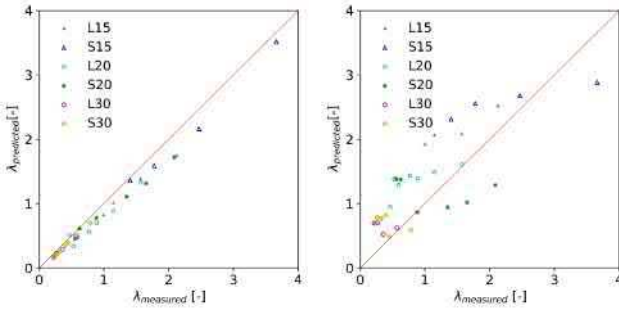


Figure 2: Comparison of predicted and measured friction coefficients of Järvelä (left) and Baptist (right) with two different vegetation configurations (inline: L and staggered: S) and three different plant spacing (0.15 m, 0.20 m and 0.30 m)

For further investigations both new implemented vegetation approaches are promising. The Järvelä approach considers the effect of flexibility but is only valid for non-submerged conditions. In case of submerged vegetation a two-layer approach should be chosen like the Baptist approach.

#### B. Rhine model

In the study of [16] an 11 km long section of the lower Rhine River (Rhine-km 738.5 – 749.5) near Düsseldorf (Germany) was used for a comparison between the different vegetation models. Fig. 3 gives an overview of the model boundaries and its topography. The main flow direction is from south to north. The flow field is affected by strong bends and, at higher discharges, by vegetation on the floodplains.

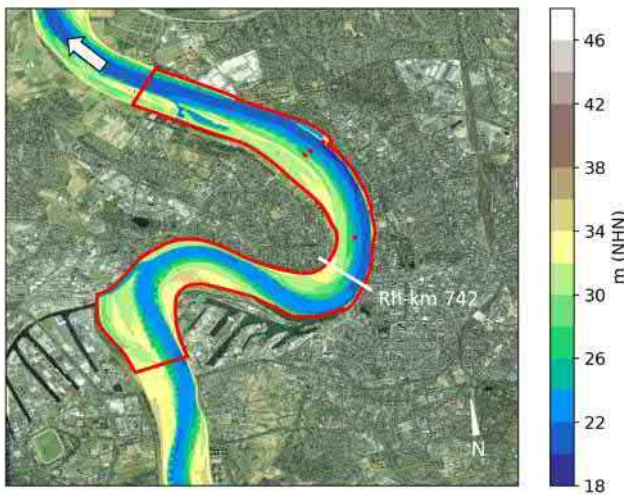


Figure 3: Lower Rhine river topography and numerical model boundaries (red polygon) nearby Düsseldorf. ([16], Copyright © 2019 Esri and its licensors)

To keep the model simple, four friction zones for groynes ( $k_s=0.30$  m), floodplains ( $k_s=0.10$  m), banks ( $k_s=0.08$  m) and river bed ( $k_s=0.07$  m) are distinguished (Fig. 4). To model the influence of the vegetation on the floodplains the same approaches was used as in the 1D-flume model. In this study a constant high water discharge of  $7870 \text{ m}^3/\text{s}$  ( $> \text{HQ}_5$ ) was chosen. In this study the floodplains are assumed to be fully covered by vegetation, regardless of the real situation.

As a reference, the model was calibrated against measured water levels in the main channel using the Lindner approach. A plant diameter of 10 cm was chosen. The distance between the plants was calibrated to 2 m resulting in water level deviations less than  $\pm 5$  cm between numerical predictions and the measured values. Fig. 5 shows that at the chosen discharge large parts of the floodplains are inundated with water depths up to 5 m. Water depths lower than 10 cm only occur on the floodplain on the first inner bend and on the northern left-sided floodplain (marked grey).

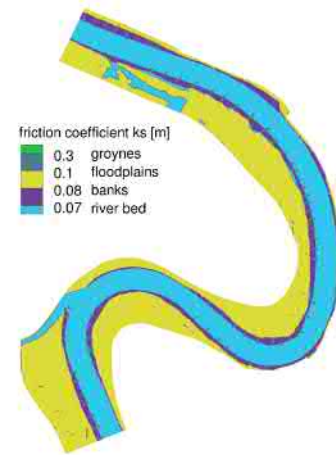


Figure 4: Friction zones

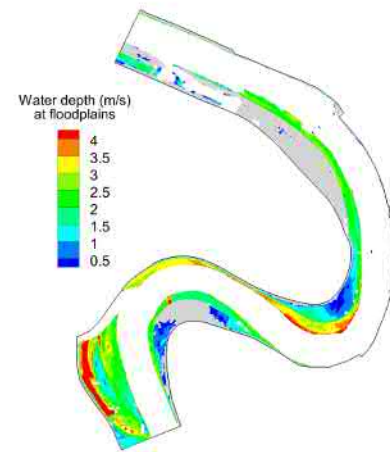


Figure 5: Water depths on the floodplains at a discharge of  $7870 \text{ m}^3/\text{s}$  (grey areas: water depths lower than 0.1 m) simulated with Lindner.



The scalar velocities at a discharge of 7870 m<sup>3</sup>/s are shown in Fig. 6. On most parts of the floodplains the velocities are small, except for the floodplain located at the second inner bend (Rhine-km 742 – 744). In this part velocities up to 2 m/s occur.

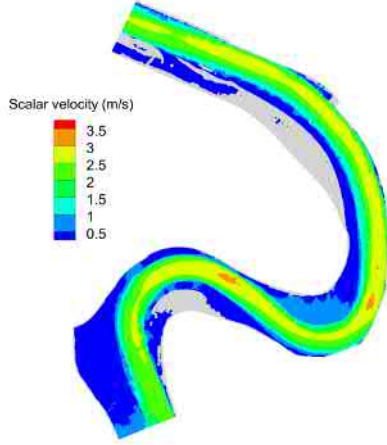


Figure 6: Scalar velocity at a discharge of 7870 m<sup>3</sup>/s (grey areas: water depths lower than 0.1 m) simulated with Lindner.

To investigate the influence and the behaviour of the other vegetation approaches, the same vegetation density was used. The plant height was set to 4.0 m resulting in non-submerged flow conditions on most parts of the floodplains. The  $LAI$  was derived by the relation in (6). For Baptist  $c_D$  was set to 1.0 and for Järvelä  $c_{D\chi}$  was set to 0.5 as recommended in the literature. Furthermore, the approach of Lindner was modified using a constant value for  $C_D$ , also set to 1.0. The vegetation was assumed as rigid ( $\chi=0$ ). The vegetation parameters are summarized in Tab. 5.

TABLE 5: USED PARAMETERS FOR THE VEGETATION LAWS

Vegetation approach	$C_D$ ( $C_{D\chi}$ ) [-]	$D$ [m]	$\Delta$ [m]	$h_p$ [m]	$LAI$ [-]	$U_\chi$ [m/s]	$\chi$ [-]
Lindner	-	0.1	2	-	-	-	-
Linder, $C_D=const.$	1.0	0.1	2	-	-	-	-
Baptist	1.0	0.1	2	4	-	-	-
Baptist	1.0	0.1	2	2	-	-	-
Järvelä (rigid)	(0.5)	-	-	4	0.2	-	0
Järvelä (flexible)	(0.5)	-	-	4	0.2	0.1	-0.9

In Fig. 7 the differences between the predicted water levels  $H$  and the measured values are presented. All approaches show very similar results. Only close to the inlet very small deviations occur. In case of non-submerged rigid vegetation the approaches of Baptist and Järvelä behave the same as the Lindner approach with a constant  $C_D$  value. Due to the chosen plant height, resulting in mainly non-submerged conditions and the assumption of rigid plants only

these small deviations between the approaches are observed in this case study.

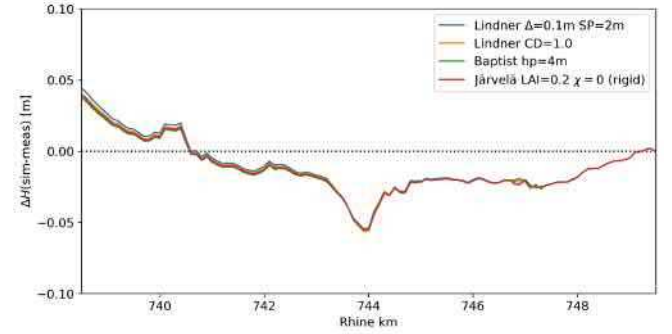


Figure 7: Differences between simulated and measured water levels in the main channel for the different vegetation laws with mostly non-submerged conditions and without flexibility

The  $C_D$ -estimator of Lindner depends on the specified vegetation parameters (diameter  $D$  and spacing  $\Delta$ ) and on the occurring flow conditions defined by the water depth and the scalar velocity. In Fig. 8 the predicted  $C_D$  values by Lindner in the study are presented. The values show a high sensitivity to the flow depth with an asymptotic behaviour and no clear trend depending on the scalar velocity. For water depth higher than 1 m a drag coefficient of about one is predicted. Therefore, only small deviations between the original Lindner approach and the one with a constant drag coefficient occur.

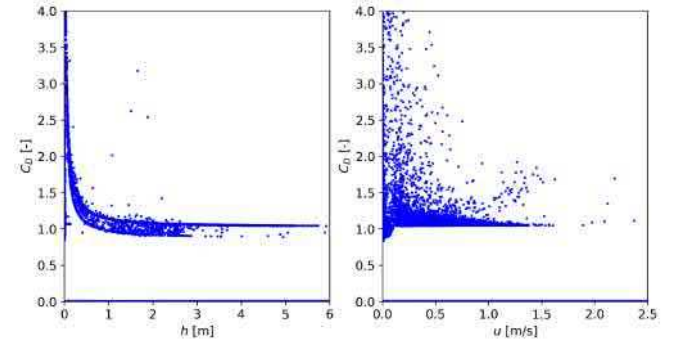


Figure 8: Drag coefficient predicted by Lindner approach depending on the water depth (left) and on the scalar velocity (right)

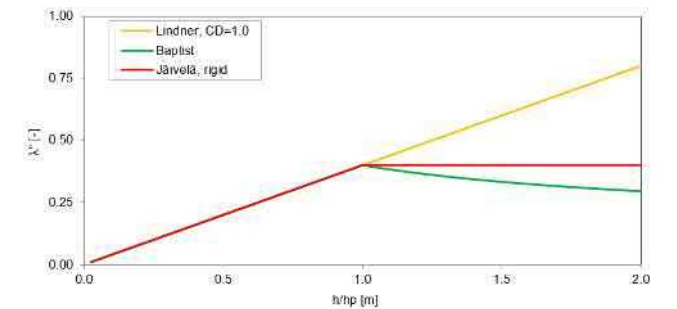


Figure 9: Vegetation friction coefficient as a function of relative submergence

In Fig. 9 the vegetation friction coefficients of the three approaches with a constant drag coefficient are shown for this case as a function of relative submergence. If the water level is lower than the plant height, no difference between the three approaches can be found. In case of shallow submergence, the assumption of a constant value of Järvelä might be acceptable. For deeper submerged vegetation, only the two-layer approach predicts reasonable results.

To investigate the influence of the vegetation height, the plant height was reduced to  $h_p=2$  m. Only the approach of Baptist is used in this case since it is the only two-layer approach. Fig. 10 shows the friction coefficients for both plant heights. For flow depths larger than 2 m large differences occur, since the vegetation is submerged in one case and non-submerged in the other one. At a flow depth of 6 m the vegetation friction is still more than twice as high for the case of the  $h_p=4$  m.

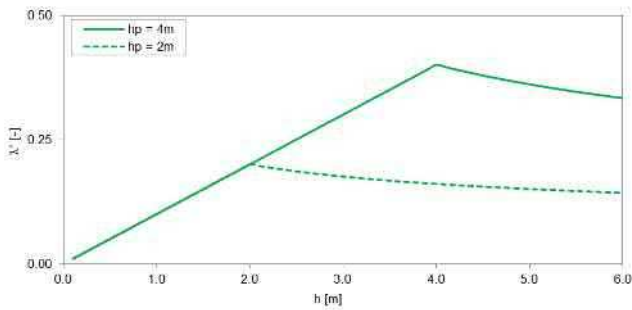


Figure 10: Vegetation friction coefficient of Baptist for  $h_p=4$  m (solid line) and  $h_p=2$  m (dashed line) depending on the water depth

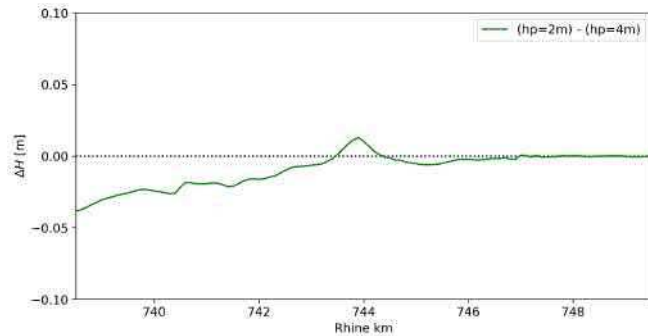


Figure 11: Differences between simulated water levels of mostly submerged ( $h_p=2$  m) and mostly non-submerged ( $h_p=4$  m) vegetation in the main channel for the Baptist approach.

The influence on the water level of the reduced vegetation friction due to the smaller plant height in the Baptist approach can be seen in Fig. 11. As described above, the vegetation friction is reduced for water levels higher than 2 m. As expected, water levels are decreased. Only at Rhine-km 744 an increase of the water level in the main channel can be observed. The reason for this is explained below.

The influence of flexibility is investigated using the approach of Järvelä. For this, a Vogel coefficient of  $\chi=-0.9$  and a reference velocity of  $U_\chi=0.1$  m/s was used. In Fig. 12

the friction coefficient as a function of scalar velocity is shown. In case of flexible vegetation, the friction coefficient is decreasing with increasing velocities. At a scalar velocity of  $u=0.5$  m/s the friction is reduced by 77%, and at  $u=1.0$  m/s by 87% compared to rigid vegetation. For velocities lower than the reference velocity the friction coefficient is set to a constant.

The plant bending and the so-called streamlining effect of flexible plants reduce the induced drag force. According to the reduced plant height, this results also in lower water levels as shown in Fig. 13. Like in the previous case, the low water levels at Rhine-km 744 are diminishing when flexible vegetation is considered.

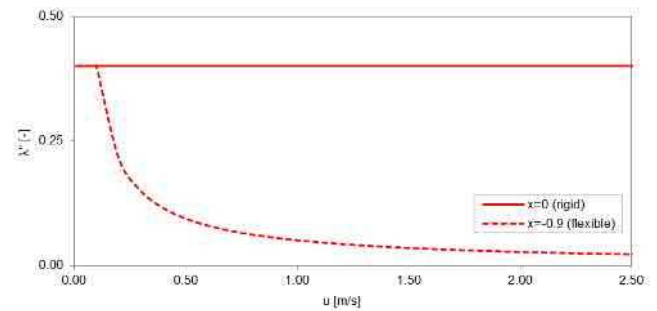


Figure 12: Vegetation friction coefficient of Järvelä for rigid ( $\chi=0$ , solid line) and flexible ( $\chi=-0.9$ , dashed line) plants depending on the scalar velocity

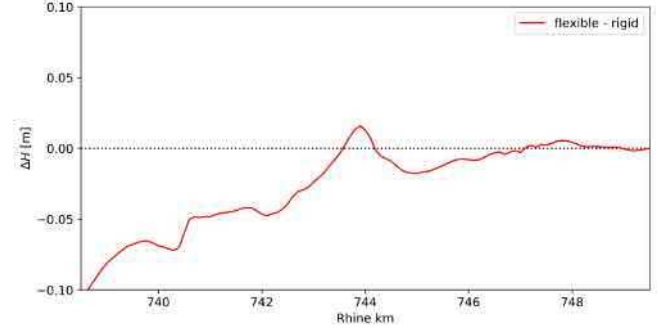


Figure 13: Differences between simulated water levels in the main channel for the Järvelä approach with and without considering flexibility.

Considering submerged conditions with Baptist approach or flexible plants with Järvelä approach lead to reduced vegetation friction. In Figs. 14 and 15 the resulting increase of the scalar velocity at the floodplains and a small decrease in the main channel at the second bend are visible. Due to the chosen parameters the influence of flexibility is larger than the influence of the submergence. Therefore the scale in the figures differs. But the qualitative behaviour in both cases is the same. Noticeable is the redistribution of the discharge at the second bend (Rhine-km 744). As mentioned above, reduced friction at the floodplains is leading to higher velocities at the floodplains resulting in a redistribution of the specific discharge. The higher velocities also accelerate the flow field over the banks and groynes adjacent to the floodplains. Furthermore, higher crossflows occur in the sharp bend. Both phenomena are leading to higher flow

resistance resulting in locally higher water levels (see Figs. 11 and 13).

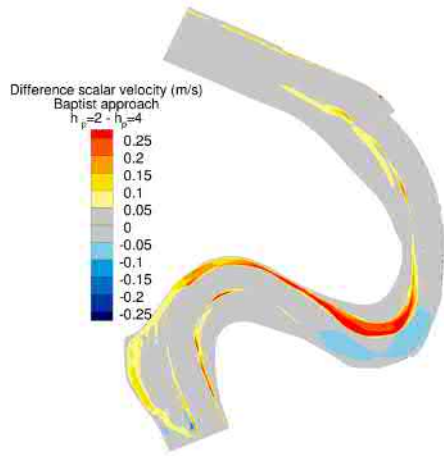


Figure 14: Scalar velocities differences between mostly submerged ( $h_p=2$  m) and mostly non-submerged ( $h_p=4$  m) conditions considered by Baptist approach.

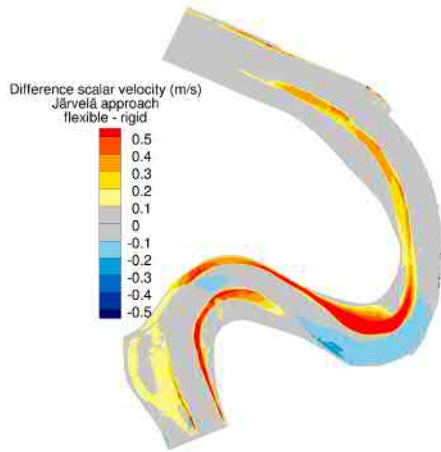


Figure 15: Scalar velocities differences between flexible and rigid condition considered by Järvelä approach.

In Tab. 6 the computing times at 40 processors of the BAW cluster (CPU Intel(R) Xeon(R) Gold 6138, 2x20 cores per node) for the different vegetation approaches are summarised. The iteration of the  $C_D$  value in the Lindner formulation takes a lot of computing time. In typical BAW models including sediment transport 20% of the overall computing time is dedicated to the  $C_D$  iteration. The results are very similar using a constant  $C_D$  value (see Fig. 7). Therefore a constant  $C_D$  value is more reasonable as default option in TELEMAC-2D.

Vegetation approach	computing time	
	[min:s]	[%]
no vegetation	1:11	-
Lindner	4:44	400
Linder, $C_D=\text{const.}$	1:18	110
Baptist	1:25	120
Järvelä	1:20	113

#### IV. RESULTS AND DISCUSSIONS

Currently only one vegetation approach is available in the official TELEMAC-2D release (v8p0r2). This vegetation approach was developed for rigid non-submerged vegetation and simplifies the vegetation as single, equally spaced cylinders. One peculiarity of the approach is the determination of the drag coefficient. Firstly, vegetation like trees or bushes is simplified into cylinders. The drag coefficient is afterwards computed using a complex iterative method considering different effects of the interaction of a group of cylinders. From the authors' point of view, this iterative method to determine the drag coefficient should only be applied if the shape of the vegetation is cylindrical and both diameter and spacing are well known. Moreover, this determination is only valid for regularly arranged non-submerged smooth cylinders.

[9] implemented seven new vegetation approaches into TELEMAC-2D. Within this study two of the new approaches were investigated and compared to the current approach. In accordance to the new approaches, a constant drag coefficient was used for the implemented approach additionally.

Based on comparison between the results of a 1D-flume model and experimental data with flexible just-submerged vegetation, this study shows the limitations of the current approach (Lindner) in TELEMAC-2D and the advantages of alternative methods. Both the predicted friction coefficients of the Järvelä approach, developed for flexible non-submerged vegetation, and of the Baptist approach, agree well with the measured data from [15].

The application "Rhine model" shows the influence of relative submergence and flexibility. Although it is possible to fit the water levels within the fairway to measured values with all approaches, local effects cannot be reproduced. Furthermore, extrapolation to other water levels is difficult with the current approach, as the vegetation friction coefficient increases linearly with increasing water levels, which is not physical in case of submerged vegetation. Moreover, the strong influence of canopy flexibility is shown. It should be noted that not all natural vegetation show such high flexibility as used in this study. Therefore, the relevance of considering the flexibility has to be estimated in each individual case.

The advantages of the iterative predictor of the drag coefficient of the current approach could not be observed in the present study. For the 1D-flume model the method does not reveal reasonable results. In the case of the application example, the differences from the method of using a constant

TABLE 6: COMPUTING TIMES FOR DIFFERENT VEGETATION FORMULAS

drag coefficient are negligible. Regarding the computational costs, the iterative method needs nearly four times longer than the other ones. Using a constant  $C_D$  value the results are very similar. Therefore, a constant  $C_D$  value should be the default option in TELEMAC-2D for the Lindner approach.

The present study has shown the need for new vegetation approaches in river modelling. In particular, a two-layer approach should be available in the standard version since in real case applications both non-submerged and submerged vegetation occur. This also should be set as default option for vegetated flow.

The new vegetation models require additional input data, as the plant height or flexibility parameters. This requirement places new demands on the field data collection on floodplains. The quality of the input parameters directly determines the effectiveness of the applied vegetation model.

#### ACKNOWLEDGEMENT

The authors would like to thank the LWI, TU Braunschweig, especially Jochen Aberle and Stephan Niewerth for providing the data for the numerical investigations and their unhesitating answers to questions.

#### REFERENCES

- [1] K. Lindner, "Der Strömungswiderstand von Pflanzenbeständen", Braunschweig, 1982
- [2] E. Pasche, G. Rouvé, "Overbank flow with vegetatively roughened flood plains", *J. of Hydr. Eng.*, 111(9), 1985
- [3] F. Folke, M. Attieh, R. Kopmann, "In search of friction laws for vegetated flow within 2D large-scale applications", E-proceedings of the 38<sup>th</sup> IAHR World Congress, Panama City, Panama, 2019.
- [4] J. Järvelä, "Determination of flow resistance caused by non-submerged woody vegetation", *Int. J. of River Basin Manag.*, 2:1, 61-70, 2004
- [5] M.J. Baptist, V. Babovic, J. Rodríguez Uthurburu, M. Keijzer, R.E. Uittenbogaard, A. Mynett, A. Verwey, "On inducing equations for vegetation resistance", *J. of Hydr. Res.*, 45:4, 435-450, 2007
- [6] S. Petryk, G. Bosmajian, "Analysis of Flow through Vegetation", In: *Journal of the Hydraulics Division* 101, pp. 871-884, 1975
- [7] S. Vogel, "Drag and Reconfiguration of Broad Leaves in High Winds." *J. of Exp. Botany*, 40 (217), pp. 941-948, 1989.
- [8] J.J. Finnigan, "Turbulence in plant canopies", *Ann. Rev. Fluid Mech.*, 32(1), 519-571, 2000.
- [9] M. Attieh, "Modeling of vegetation in open channel flow using Telemac-2D", master thesis, Karlsruhe Institute of Technology, 2019.
- [10] P. Whittaker, C. Wilson, J. Aberle, "An improved Cauchy number approach for predicting the drag and reconfiguration of flexible vegetation". In: *Advances in Water Resources* 83. doi: 10.1016/j.advwatres.2015.05.005, 2015
- [11] F. Huthoff, D.C.M. Augustijn, S.J.M.H. Hulscher, "Analytical solution of the depth-averaged flow velocity in case of submerged rigid cylindrical vegetation", 2007, *Water Res. Res.*, 43.6, doi: 10.1029/2006WR005625.
- [12] E.H. Van Velzen, P. Jesse, P. Cornelissen, H. Coops, "Stromingsweerstand Vegetatie in Uiterwaarden", 2003.029. RIZA, Arnhem, 2003
- [13] M. Luhar, H. Nepf, "From the blade scale to the reach scale: A characterization of aquatic vegetative drag". In: *Advances in Water Resources* 51, pp. 305-316. doi: 10.1016/j.advwatres.2012.02.002, 2013
- [14] K. Västilä, J. Järvelä, "Modeling the flow resistance of woody vegetation using physically based properties of the foliage and stem", In: *Water Resources Research* 50.1, pp. 229-245. doi: 10.1002/2013WR013819, 2014
- [15] T. Schoneboom, J. Aberle, A. Dittrich, "Hydraulic resistance of vegetated flows: Contribution of bed shear stress and vegetative drag to total hydraulic resistance", *River Flow 2010*, Braunschweig, 8-10 September, 269-276, 2010.
- [16] G. Dalledone, R. Kopmann, T. Brudy-Zippelius, "Uncertainty analysis of floodplain friction in hydrodynamic models", *Hydrol. Earth Syst. Sci. Discuss.*, <https://doi.org/10.5194/hess-2019-159>, accepted, 2019.

# Durance River modelling for environment and safety management

Viard Thomas  
Hydraulic Engineering Center  
EDF  
La Motte Servolex, France  
Thomas.viard@edf.fr

Duclercq Marion  
Hydraulic Engineering Center  
EDF  
La Motte Servolex, France

**Abstract**— Durance River in South East of France is highly influenced by Serre-Ponçon and Sainte Croix dams. With those dams, regular floods no longer clear vegetation in Durance River bed. EDF manages those dams and has to clear vegetation to replace flood action to avoid worsening extreme floods. Authorities in charge of flood safety management ask EDF for an important clearing of vegetation, and authorities in charge of Environment ask EDF to preserve vegetation as much as possible. To reconcile those two opposite objectives, a prefectural decree was published asking EDF to preserve vegetation if it doesn't worsen water level in flood plain (increase between with and without vegetation of less than 5 cm in highly sensitive areas – urban areas – and less than 10 cm in moderately sensitive areas – agricultural areas). To answer that prefectural decree, EDF chooses to model Durance River from Serre-Ponçon dam to its confluence with Rhone River (204 km). 14 TELEMAC-2D models are or will be built to optimise the clearing of vegetation. Durance bed changes often, therefore those models and their calibration are updated regularly.

This article focuses on two models: “Bonpas Le Rhône”, just upstream of the confluence with the Rhône River, and “Brillanne”, a part of Durance between the confluence with the Bléone River and the confluence with the Verdon River. It details methodology for construction, updates, calibration and way of optimisation.

## I. INTRODUCTION

Construction of the Serre-Ponçon dam and Sainte Croix dam significantly modified flows downstream in the Durance River. EDF, as a manager of those dams, have to limit growth of vegetation in river bed to avoid increase of damages in flood plain in case of significant flood (until 100-year return flood).

On the other hand, vegetation in river bed represents a real environmental interest for fauna and flora (beavers, many kind of birds...).

Therefore Authorities ask EDF to reconcile two opposite objectives:

- To maintain a good level of safety against floods
- To limit environmental impact of vegetation clearing

Authorities published a prefectural decree asking EDF to model Durance River with and without bed vegetation to compare free surface elevation. That decree defines the following criterion: “An interesting environmental site can be preserved from vegetation clearing if the averaged increase of free surface

elevation is limited to 5 cm in highly sensitive areas and to 10 cm in moderately sensitive areas”.

## II. METHODOLOGY

### A. Vocabulary

The part of river bed where EDF has to limit growth of vegetation is called the “clearing” channel. The width of this clearing channel is defined by law since 1979. Its width varies from 60 m downstream Serre-Ponçon dam to 400 m just upstream confluence with Rhone River (Fig. 1). Exact localisation of this clearing channel is not defined by law, but it is supposed to be centred on the river axis, except locally (if a river bank is significantly higher than the other, clearing channel is deported on the lowest bank).

To evaluate the increase of free surface elevation, the reference case is a clearing channel without vegetation. It is called the reference channel.

The objective of EDF is to keep the maximum of interesting environmental sites while respecting the prefectural decree. The final channel, which is reaching EDF objectives, is called “optimised” channel.





Area	Surface	Length	Width
HD01	48 ha	11 km	60 m
HD02	45 ha	12 km	60 m
HD03	117 ha	14 km	100 m
HD04	87 ha	10,5 km	100 m
HD05	83 ha	12,5 km	100 m
MD01	45 ha	5,5 km	100 m
MD02	107 ha	7 km	200 m
MD03	137 ha	7 km	200 m
MD04	188 ha	9,5 km	200 m
MD05	141 ha	6,5 km	250 m
MD06	150 ha	6 km	250 m
MD07	89 ha	3,7 km	250 m
MD08	188 ha	7,5 km	250 m
BD01	172 ha	8 km	250 m
BD02	195 ha	8,5 km	250 m
BD03	58 ha	2,8 km	250 m
BD04	92 ha	4 km	250 m
BD05	282 ha	11,7 km	250 m
BD06	453 ha	15 km	350 m
BD07	414 ha	14,3 km	300 m
BD08	116 ha	4,3 km	300 m
BD09	396 ha	11,4 km	400 m
BD10	443 ha	11,2 km	400 m

Figure 1: Width of the clearing channel along Durance River (the "REF" of each sector is indicated on the above map)

### B. Model construction

14 TELEMAC-2D models are or will be built to optimise the clearing channel.

1) *Bathymetry/topography*: In 2016, a LIDAR was done for all the river bed topography from Serre-Ponçon dam to Rhone River (204 km) during low-water periods. For bathymetry, cross sections were also measured every 500m. During low water periods, water depths are in general less than 20 cm in Durance River, therefore LIDAR is main source used to build the River bed geometry of the TELEMAC model; cross section are used only for pools. Local bathymetry were done for dam reservoirs. For Flood plain topography, a LIDAR from French National Geographic Institute (IGN) is used. Finally, local topography information (from Syndicat Mixte d'Aménagement de la vallée de la Durance – SMAVD – organization in charge of flood mitigation on Durance River) is used to model flood protection structures.

2) *Mesh*: the average mesh size is 10 m in river bed, without constraint lines for easy update in the future. ; it is between 20 and 30 m in flood plain, except for flood protection structures. Thoses structures are modelled with 5 constraint lines (2 at the bottom, 3 at the crest) to avoid "numerical overtopping" (Fig. 2). The mesh size for the structures depends on their type : 10 m for weirs and bridges, 20 m for dykes, 40 m for roads and railways.

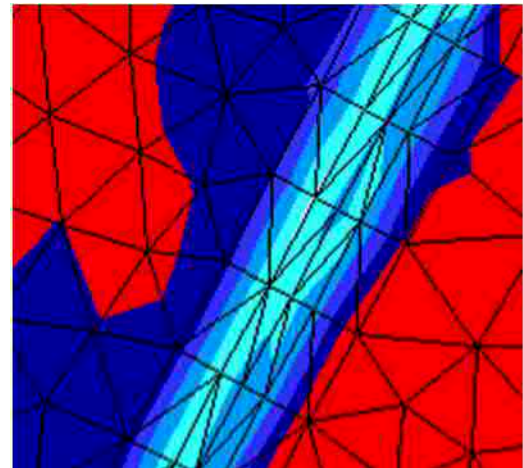


Figure 2: mesh for flood protection structures

3) *Boundary conditions*: hydrographs are imposed upstream. The shape of 1994 main flood is reused with homothety for maximal discharge. Rating curves are used downstream. Floods of return periods ranging between 30 and 100 year are studied.

4) *Strickler coefficient*: during model construction, the following Strickler coefficients are used:

- Reservoirs, lakes, pools :  $35 \text{ m}^{1/3}/\text{s}$
- River bed:  $30 \text{ m}^{1/3}/\text{s}$
- Fields, dykes and rockfill weirs:  $20 \text{ m}^{1/3}/\text{s}$
- Vegetation with low density:  $15 \text{ m}^{1/3}/\text{s}$
- Urban areas:  $10 \text{ m}^{1/3}/\text{s}$
- Vegetation with high density:  $8 \text{ m}^{1/3}/\text{s}$

### C. Model validation

To optimise the clearing channel, vegetated areas and cleared areas are modelled with different Strickler coefficients. Therefore the usual step of calibration of the model must rather be considered here as a validation step, since Strickler coefficients are changed for each simulation.

Models are validated jointly between EDF and SMAVD. SMAVD has a large experience of Durance River that helps EDF to interpret model results. Floods marks are completed with information from flood witnesses about specific flooded areas.

Air photographs were done simultaneously with the LIDAR done in March 2016 used for the bathymetry. Those photos are used to define the state of vegetation in clearing channel for validation step.

A significant flood ( $1650 \text{ m}^3/\text{s}$ ) occurred in November 2016 downstream to the confluence between Durance and Buech River. For models downstream to this confluence, that flood is used for validation. For models upstream to that confluence, only one flood occurred in the last 20 years. It was in 2008. Between 2008 and 2016 bathymetry and vegetation of Durance river bed have changed. Thus, validation is more complicated because of those evolutions.

#### D. Data for Model using

1) *Sensitive areas*: The prefectural decree gives criteria for sensitive areas (an averaged increase of 5 cm in highly sensitive and 10 cm in moderately sensitive areas). But that decree does not clearly define the sensitive areas nor the surface areas to average free surface elevation. Therefore, first step was to ask authorities for the definition of sensitive areas. Highly sensitive areas are urban areas (defined in flooding prevention maps or in Corine Land Cover [1] data base if flooding prevention maps does not exist). Moderately sensitive areas are agricultural areas, except meadows (surface areas are defined with Corine Land Cover data base).

2) *Environmental stakes*: before using a model, environmental inventory are done to localize vegetation with high environmental interests in the clearing channel. The optimised channel will try to take into account this inventory. Vegetation with low environmental interests (invasive plants...) will be cleared first.

3) *Studied floods*: Prefectural decree gives criteria regarding the increase of the free surface elevation “for the moderately sensitive areas overflowing flood, for the high sensitive areas overflowing flood and for dykes design flood”. In a model, there are a lot of sensitive areas and often a lot of dykes. Therefore, those 3 floods cannot be exactly defined. EDF chose to design the optimised channel on one flood – 30, 50 or 100 year return period – and then to validate that optimised channel with many floods with a return period ranging between 30 and 100 year (with a step of 100 m<sup>3</sup>/s).

#### E. Model using

From the validated model, the sensitive areas map and the environmental stakes, the final channel to be cleared can be optimised. This is usually done in 2 steps: one “manual” step to design the optimised channel with one flood and one “automatic” step to validate the optimised channel with many floods.

- *Manual step*: 30, 50 and 100 year return period floods are simulated with the reference channel (cleared channel – Strickler coefficient of 30 m<sup>1/3</sup>/s). The most relevant flood is chosen for optimisation (depending on observed overflowing between river bed and flood plain and flooding kinetic). Then the chosen flood is simulated with the actual state of vegetation (Strickler coefficient of 8 m<sup>1/3</sup>/s in areas with vegetation – vegetation is supposed to become mature – and 30 m<sup>1/3</sup>/s in areas without vegetation – those values are based on SMAVD experience feedback). The results of that simulation are compared to the results with the reference channel. If the criteria the from prefectural decree are met, channels with more vegetated zones are tested. On the contrary, if the criteria are not met, channels with less vegetated zones are tested following these principles :

- trying to keep vegetation upstream of highly sensitive areas to limit flooding downstream and where there are interesting environmental sites

- Vegetation is cleared downstream of highly sensitive areas and near connections between river bed and flood plain to lower water levels at those key points.

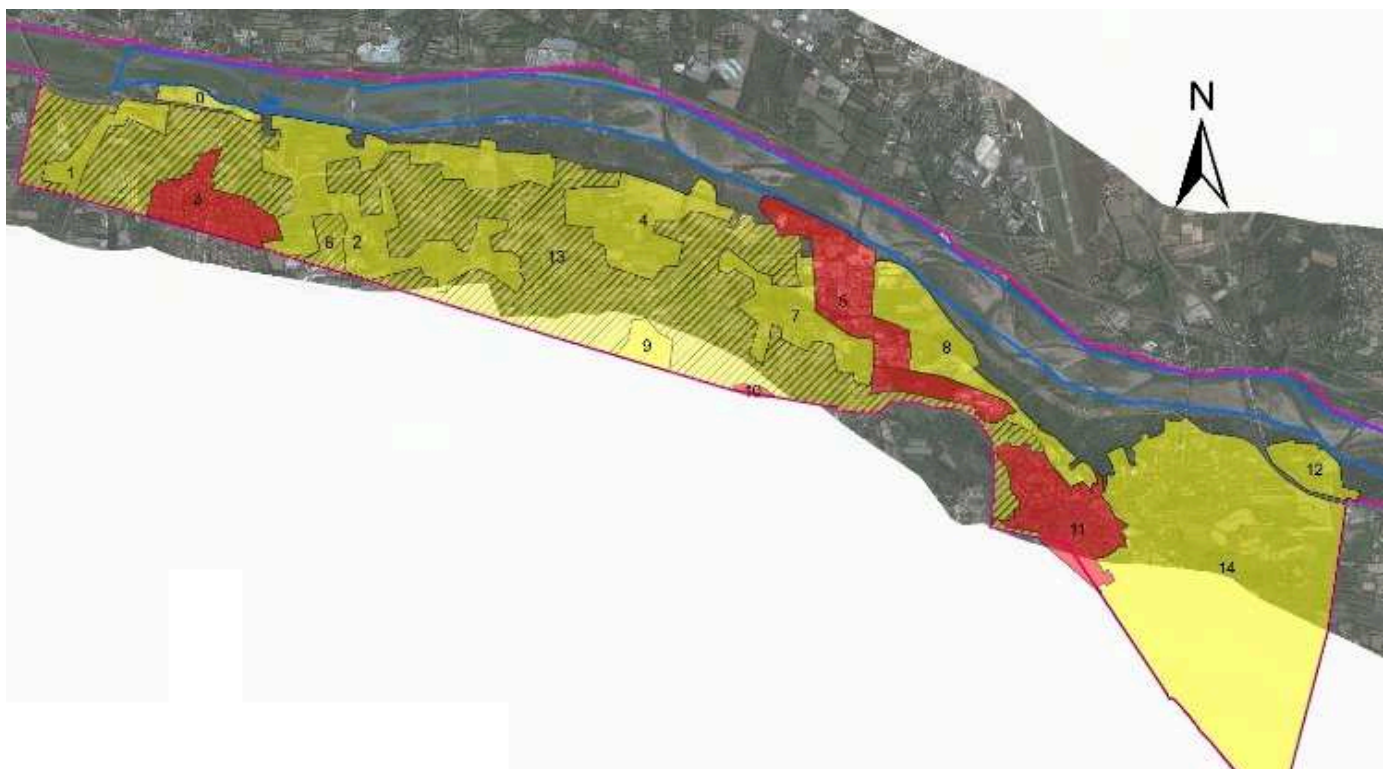


Figure 3: Bonpas Le Rhône model – sensitive areas map (highly sensitive in red and moderately sensitive in yellow)



Ultimately, vegetation is maximised with respect of the decree.

- *Automatic step:* Once an optimised channel is found for the chosen flood, this channel has to be validated for other floods. All floods with a return period ranging between 30 and 100 year with a step of 100 m<sup>3</sup>/s are simulated twice: with the optimised channel and with the reference channel. For each flood, the maximal water level with the optimised channel is compared to the water level with the reference channel. An averaged difference is computed in each sensitive area to validate the optimised channel for each flood. Few adjustments of the optimised channel can be necessary to meet the decree criteria for all floods.

### III. BONPAS LE RHÔNE MODEL

This methodology was first applied to define the optimised channel in the downstream part of Durance River. Model was built from Bonpas Dam to Rhône confluence (BD10 in Fig. 1). As Fig. 3 shows, floods mainly concern the left bank of Durance River and this bank is almost everywhere covered by sensitive areas.

The first simulations with a Strickler coefficient of 8 m<sup>1/3</sup>/s where vegetation is not cleared showed that no mature vegetation could be preserved to respect the criteria of the prefectural decree. Therefore, it was chosen to partially clear vegetation to find a compromise between total clearing and mature vegetation. The Strickler coefficient corresponding to partially cleared vegetation was calculated with Baptist formula [2]:

$$K = \frac{C_k}{R_h^{1/6}} \quad C_k = \sqrt{\frac{1}{C_b^2 + \frac{C_d m D H}{2g}}}$$

With H water depth, C<sub>k</sub> Chézy coefficient, C<sub>b</sub> Chézy coefficient of a cleared area, C<sub>d</sub> drag coefficient, m vegetation density, D averaged diameter of trees, and R<sub>h</sub> hydraulic radius. A Strickler coefficient of 19 m<sup>1/3</sup>/s was associated to partially cleared vegetation. With that coefficient, few interesting environmental sites could be kept.

After many simulations of the 100 year return period flood (5 000 m<sup>3</sup>/s), an optimised channel was found. The flood discharge for 30 year return period is 3 000 m<sup>3</sup>/s. Therefore 42 simulations, 21 simulations by 100 m<sup>3</sup>/s step for the optimised channel and as many simulations for the reference channel, were necessary to validate the final optimised channel (Fig. 4).

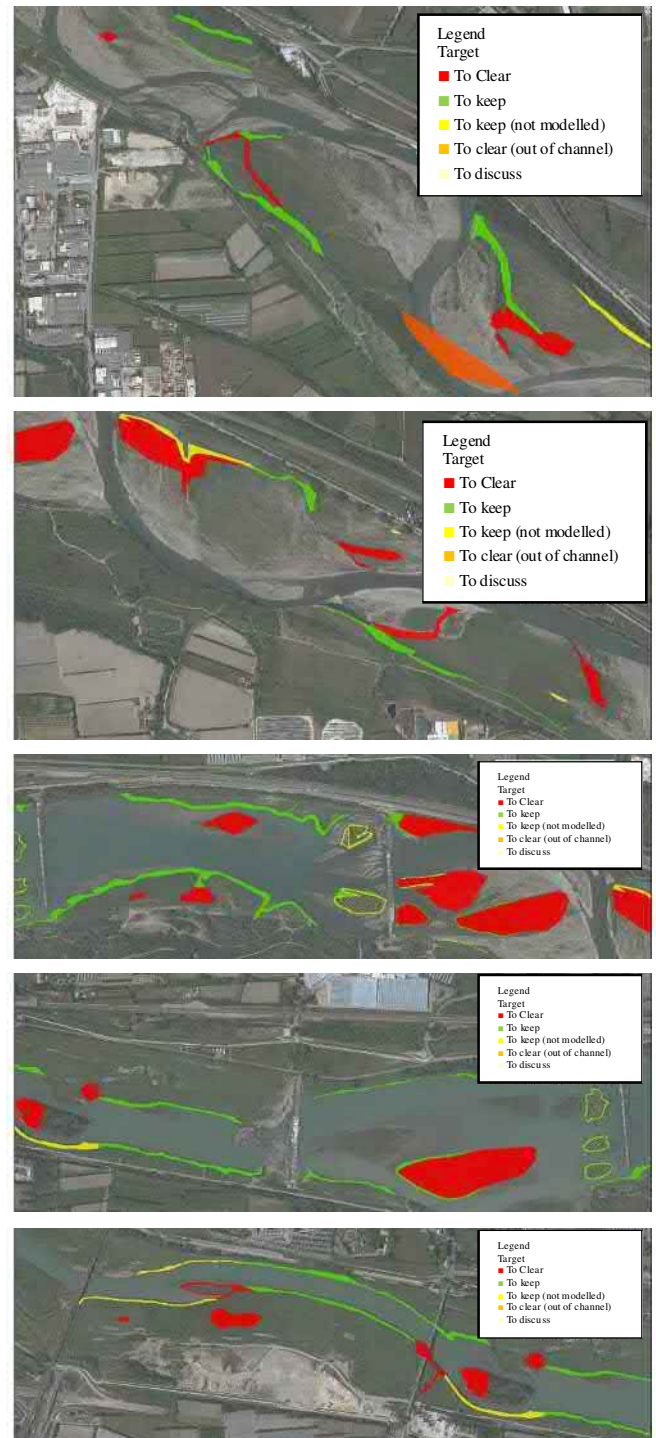


Figure 4: optimised channel for Bonpas Le Rhône model (red and orange: to clear, green and yellow: to partially clear)

### IV. BRILLANNE MODEL

The Brillanne model was the second model following the methodology explained above. This model corresponds to MD04 in Fig. 1. As Fig. 5 shows, floods mainly concern the left bank of Durance River and there is a lot of space between the river bed and the sensitive areas.



The clearing channel is 200m width in this model but the active river bed is larger. Contrary to Bonpas Le Rhône model, mature vegetation will not grow in all areas where EDF does not clear. Therefore, air photographs between 2000 and 2016 (around 8 photographs are available) were used to determine the exact active bed of Durance River. Then, averaged vegetation surfaces in that bed were estimated on each photograph and analysed regarding occurred floods and past clearing done by EDF to determine a state of vegetation without EDF clearing. This state of vegetation was assimilated to a Strickler coefficient of  $24 \text{ m}^{1/3}/\text{s}$  (with few simulations).

To optimise the clearing channel in Brillanne model, a Strickler coefficient of  $24 \text{ m}^{1/3}/\text{s}$  was used for the active river bed outside the clearing channel and for the non-cleared areas in the clearing channel.

Contrary to Bonpas Le Rhône model, thanks to floods naturally clearing vegetation in the active bed and because of less sensitive areas, many parts of the clearing channel can be preserved in the optimised channel.

The reference and the optimised channels are compared considering an averaged state of vegetation in the river bed outside the clearing channel. The real state of vegetation depends on recent floods. Therefore recent Air photographs are analysed before clearing works to evaluate the state of vegetation all over the river bed and to determine how to fit the optimised modelled channel.

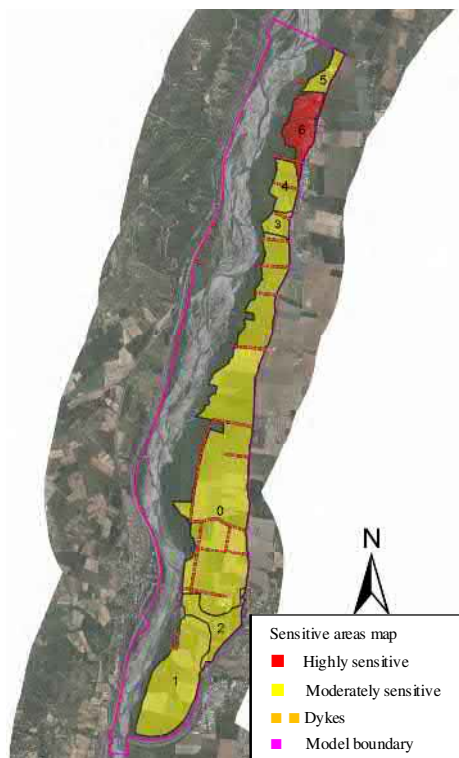


Figure 5: Brillanne model – sensitive areas map (highly sensitive in red and moderately sensitive in yellow)

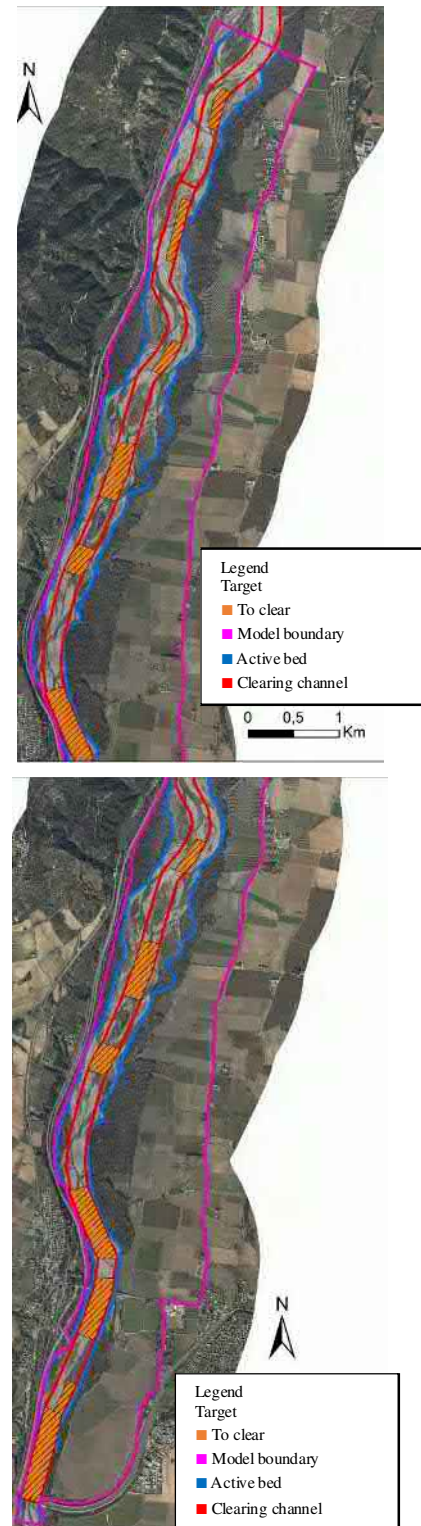


Figure 6: optimised channel for Brillanne model (orange: to clear)

## V. CONCLUSION

Since building of Serre-Ponçon and Sainte Croix dams in Durance river basin, EDF has to clear vegetation in the river bed to replace the natural effect of floods on vegetation. A prefectural decree was published to reconcile safety and

environmental management during clearing works. TELEMAT modelling is done by EDF to find an optimised clearing channel respecting that prefectural decree. The methodology was established with SMAVD and Authorities. This methodology was already successfully used for 2 models with few adjustment to local context.

#### ACKNOWLEDGEMENT

We would like to thank SMAVD for their experience feedback and knowledge on Durance river sharing.

#### REFERENCES

- [1] <https://www.data.gouv.fr/fr/datasets/corine-land-cover-occupation-des-sols-en-france/>
- [2] Baptist, M., V. Babovic, J. Rodríguez Uthurburu, M. Keijzer, R. Uittenbogaard, A. Mynett, and A. Verwey (2007), "On inducing equations for vegetation resistance", *Journal of Hydraulic Research*, 45(4), 435-450.

# Numerical investigation of non-cohesive fluvial dike breaching induced by flow overtopping

Lydia KHELOUI<sup>1,2</sup>, Riadh ATA<sup>1,2</sup>, Kamal EL KADI ABDERREZZAK<sup>1,2</sup>

<sup>1</sup>EDF R&D, National Laboratory for Hydraulics and Environment, Chatou, France

<sup>2</sup>Saint Venant Laboratory for Hydraulics, Chatou, France

[lydia-l.kheloui@edf.fr](mailto:lydia-l.kheloui@edf.fr), [Riadh.ata@edf.fr](mailto:Riadh.ata@edf.fr), [kamal.el-kadi-abderrezzak@edf.fr](mailto:kamal.el-kadi-abderrezzak@edf.fr)

Fluvial dike breaching is a great concern for Nuclear Power Plants' safety and areas surrounding rivers. Due to overtopping flows, river dikes considered as defense structures, can fail and lead to devastating inundations with dramatic human and economic losses. It is therefore of great importance, for flood risk management and prevention, to provide a reliable prediction of the breach expansion and outflow hydrograph. In this study, we investigate the use of two different numerical models to simulate breach growth in non-cohesive, homogeneous fluvial dikes with the open source TELEMAC-MASCARET suite of solvers. First, a two-dimensional (2D) depth-averaged morphodynamic model is discussed. Exner equation is used to update bed elevation and sediment transport rate is computed with an empirical formula. The model also incorporates a bank failure operator, a correction of the sediment transport magnitude and direction for the bed slope effect, and a correction of the bottom shear stress direction for the secondary current effect. In the second model, the hydrodynamic solver TELEMAC-2D is used with specific empirical formulas to determine the evolution of breach characteristics. Both approaches are employed to simulate laboratory flume experiments for which 3D evolving dike geometry and time series of breach outflow and water levels in the main channel were recorded.

**Proposed session:** *River and urban floods, flood forecasting and management*

**Key words:** Breach, fluvial dike, non-cohesive material, overtopping, numerical models.

**Speaker:** Lydia KHELOUI

# Flooding dynamics within an Amazonian floodplain: water circulation patterns and inundation duration

Sebastien Pinel<sup>1</sup>, Marie-Paule Bonnet<sup>2</sup>, Joecila S. Da Silva<sup>1</sup>, Thibault Catry<sup>2</sup>, Frederique Seyler<sup>2</sup>

<sup>1</sup> RHASA  
Amazon state University (UEA)  
Manaus, Brazil  
sebpinel@gmail.com; jsdsilva@uea.edu.br;

<sup>2</sup> UMR 228 Espace-DEV Research Institute for  
Development (IRD)  
Montpellier, France  
marie-paule.bonnet@ird.fr; thibault.catry@ird.fr

**Abstract**—Amazonian floodplains ensure fundamental hydro-ecological functions and support a high level of biodiversity. Transformation in the Amazon basin, land use changes, dam construction and climate variability, increasingly threaten these emblematic ecosystems. In view of supporting their conservation, it is important to monitor the spatiotemporal distribution of key variables such as flood extent, inundation duration, and water velocities that constrain species habitats. However, floodplains are scarcely surveyed, and hydrological information is commonly restricted to water level and discharge measured in the mainstream. As a solution, 2D-hydrodynamics modelling allows monitoring these threatened zones and getting new information such as water circulation. Flooding dynamics across a medium-size floodplain system (Janauacá Lake, 786 km<sup>2</sup>) along the Amazon/Solimões River over a 9-years period (2006–2015) is studied through integration of remote sensing and limited *in situ* data in hydrologic-hydrodynamic modelling based on Telemac-2D model. We firstly detail the methodological approach and the modelling assessment in terms of water level, flood extent and velocity. It correctly reproduces floodplain water level (Nash-Sutcliffe Efficiency=0.97) and flood extent (averaged Threat Score=62) and horizontal velocity (Nash-Sutcliffe Efficiency >0.68). The model's high accuracy varies along the hydrological year. Then, we focused on seasonal and inter-annual spatial variability of water circulation and inundation duration. We highlighted strong heterogeneities in water velocity magnitude between the different morphological domains of the floodplain, the highest velocities being encountered in the river-floodplain channel. In addition to topography, we emphasized the importance of the mainstream and the local runoff in controlling the water circulation, at least during part of the hydrological year. During the early rising period, local runoff constrains the river incursion across the floodplain, while the rates of mainstream rising/receding controls the flood duration. The comparison of several hydrological years highlights the interannual changes of these hydraulic controls and also the influence exerted by prior inundation conditions. While we observed only few changes in water velocity distribution among hydrological years, the inundation duration is highly variable. Extreme flood events may induce positive (up to 40 days) but also negative (up to -20 days) anomalies of inundation duration.

## I. INTRODUCTION

Wetlands and floodplains (FP) cover about 14% of the Amazon Basin. In the lowland Amazon, FPs roughly occupy 800,000 km<sup>2</sup> [1]. They trap substantial amounts of sediment [2]. High primary production in FPs partly supplies the

mainstream with labile organic matter [3] and regulates CO<sub>2</sub> or CH<sub>4</sub> emissions [4]. They are essential components regulating flow propagation [5]. They support fisheries yields [6] and host several endangered species [7]. In coming years, FPs will be increasingly threatened by in-river infrastructure [8]. Conjointly with climate change, these expected development trends seriously endanger Amazon FP ecosystems and biodiversity [9].

Large seasonal variations of water level and highly smooth topography generate complex inundation patterns. Water quality and habitats characteristics are tightly related with FP water circulation. Flood amplitude and water velocity across the FP drive the inundation extent and key-variables such as depth, habitat connectivity and hydroperiod that control suspended and dissolved material fates and species distribution and interactions [10]. As shown by local hydrological studies, in-waters originate from the mainstream and from local sources such as hyporheic water, local runoff and direct precipitation [11]. The mixing area between these water sources, its extent and location through the FP depend on water head distribution within the different ponds and significantly vary along the corridor and hydrological year.

Full 2D hydrodynamics models appear to be a good tool to study FP. However, they present the inconvenient to be time-consuming. The LISFLOOD-FP hybrid model [12] based on simplified propagation equations appears as a solution for modelling studies over Amazon FP. Based on this hybrid model or on simple flow routing schemes. Several modelling studies have focused on FP hydrology: at regional scale [13], medium scale [14], and local scale in the lowland Amazon [11]. These studies essentially focused on capturing flood extents (FE), water level, exchanged fluxes with the mainstream and stored water volume throughout HY. Only few studies involved a full 2D hydrodynamics model in the Amazon FPs that allow accurate velocity modelling. References [15,16] coupled a sedimentation module to a hydrodynamics model to study the planform dynamics of anabranching structures. Finally, in the Amazon, water circulation across the FP have been little investigated. References [17,18] presented the most comprehensive studies of water head distribution within a lowland Amazon FP but did not specifically address velocity patterns across the FP.

In this study, we combine *in situ* information, remote sensing and a hydrologic-hydrodynamic modelling to simulate

flooding dynamic in a medium-size Amazonian FP and investigate spatial velocity patterns and flood frequency. We firstly present i) the methodology and the necessary datasets; ii) the hydrologic-hydrodynamic model performance in reproducing water level, flood extent and velocity. Then we employed this model to i) exhibit spatial velocity patterns and flood frequency at seasonal scale, ii) examine the influence of extreme drought or flood events on velocity patterns and flood duration.

## II. STUDY ZONE

The study site is the Janauacá FP (3.200°S-3.250°S, 60.230°W-60.130°W, Amazon state, Brazil), a medium-size FP located on the right bank of the Amazon/Solimões River, 40 km upstream its junction with the Negro River. It is formed by the mixture of a várzea (the North-east part) and a ria-lake, a composition rather typical along this Amazon/Solimões River reach. The mainstream at this location generally exhibits a monomodal flood phase, rising regularly from November to June. The Amazon/Solimões River is commonly considered as a “white-water” river [19]. The Janauacá FP is composed of a lake with fringing wetlands and inundated forest, linked to the mainstream by a unique channel (Figure 1a-b). The FP and its local drainage basin extend over 786 km<sup>2</sup> (Pinel et al., 2015). Flood extent seasonally varies from 4% to 50% of the FP watershed, with water level variations between 10 m and 24 m. Like other Amazon FPs, flooding is ensured by several water sources: mainstream through channelized flow or overflow that is the main source but and local runoff, hyporheic water and direct rainfall. From late low water period to mid rising period, the channel acts as an inlet until overflow starts. The mainstream water quality highly contrasts with water quality of small tributaries that is closer to “black water” properties.

## III. MATERIAL AND METHODS

### A. Modelling approach and settings

The modelling approach relies on the coupling of two models: a hydrological model, which simulate runoff from the uplands, followed by a hydrodynamics model.

The hydrological model LUMP-FP, developed and applied to the study site [11], was used to produce runoff from the upland local watershed as boundary condition for the hydrodynamic model (Figure 1b). We used the same settings as [11] to generate daily runoff for the study period extending from 11/01/2006 to 12/31/2015.

The TELEMAC-MASCARET system is freely available at [www.opentelemac.org](http://www.opentelemac.org) and was designed for computational fluid dynamics [20]. We specifically used its two dimensional (2D) hydrodynamic module (TELEMAC-2D v7p3) that simulates free-surface flows in the two dimensions of horizontal space. For more details, readers are referred to the TELEMAC-2D user manual [21].

The modelled domain was limited to the pixels whose elevation was lower than 29 m, i.e. the domain that contains the floodable area (Figure 1b). The initial pixels water level condition was set to the RL1 value at the 11/01/2006, and velocity was assumed null in the whole domain. The hydrodynamic model requires boundary conditions: i) water flow boundary condition (inflow from the local basins); ii) water level boundary conditions (WLBC) (inflow from the mainstream) in which observed mainstream stage is imposed.

LUMP-FP model provided the total discharge from the uplands. Based on sub-catchment area ratio, we distributed the flow among the different streams draining the local watershed. Regarding WLBC, the combination of visual inspection of ALOS-1/PALSAR images and mainstream stage allowed

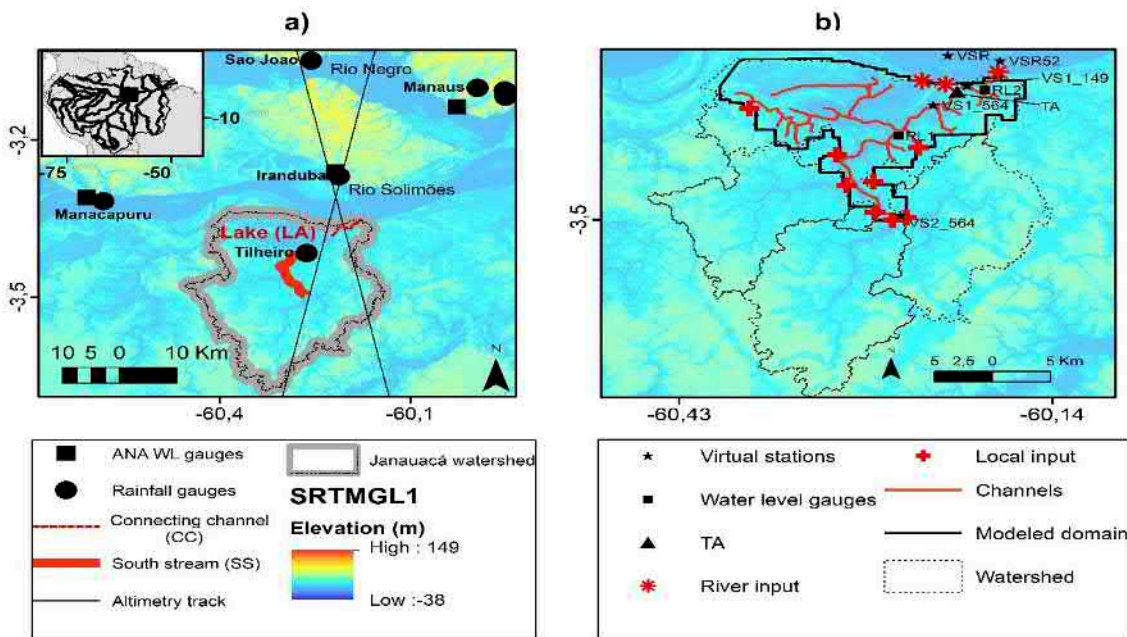


Figure 1. a) Study site with the locations of available water level and rainfall gauges, b) Model domain with background SRTMGL1 and boundaries location



determining the zones associated with overflow and corresponding water level thresholds. We identified: WLBC1 (water level boundary condition 1) underwater for a water level of 19.50 m at 49 km downstream Manacapuru, and WLBC2 underwater for a level of 20.00 m at 47 km downstream Manacapuru (Figure 1b). At these locations, we modified the levee elevations to match these elevation thresholds. At last, the junction between the mainstream and the connecting channel constitutes the third WLBC3. Water level at these three boundary conditions were linearly derived from the VSR gauge (VSR47, VSR49 and VSR52).

TELEMAC-2D model offers several options for calculation. Here, we chose the method of characteristics to simulate velocity advection and the propagation step is solved by the conjugate gradient method with a diagonal preconditioning which ensures numerical stability. We used a constant viscosity set to  $10^{-6} \text{ m}^2 \cdot \text{s}^{-1}$  and a constant water density set to  $996.1 \text{ kg} \cdot \text{m}^{-3}$  [22]. Bottom friction was based on the Manning coefficient map. We used the Blue Kenue software [23] to generate a mesh of 224 527 triangular elements with sides ranging from 23 m to 77 m. The model was run from 11/01/2006 to 12/31/2015 using a 30 s time-step on a multi-core cluster environment: the Altix-XE 340 cluster platform, located at LNCC (*Laboratório Nacional de Computação Científica*, Brazil).

### B. Calibration and validation assessment

As LUMP-FP model was fully validated for the study site [11], and as we used same settings and the same simulation period, further calibration and validation were not necessary for this model. However, we calibrated the hydrodynamic model (TELEMAC component) against water level measured at RL1 and RL2 from April 2007 (rising water) to January 2008 (low water) adjusting Manning coefficients by a trial-and-error method. The model was validated in terms of vertical, horizontal and velocity accuracy. The reference datasets for the vertical validation were water level measured at RL1, RL2, VS1\_564, VS2\_564, and VS1\_149. The horizontal validation consisted in comparing modelled and ALOS-1/PALSAR-deduced flood extents. Velocity accuracy was controlled against *in situ* measurements.

Several classical statistics served to appraise model vertical accuracy: the Pearson correlation coefficient, the RMSE (m), the Nash-Sutcliffe efficiency (NSE). The horizontal accuracy was assessed using the following skills scores: the Threat Score (TS) measures the model accuracy with a perfect score of 100; the bias index (BIAS) indicates the type of error (overestimation or underestimation). Those scores are determined using the following relations:  $TS = 100(a/(a+b+c))$ ;  $BIAS = 100(1-(a+b)/(a+c))$ ; where, *a* is the area that is both mapped and modelled as inundated, *b* is the inundated area modelled but not mapped, and *c* is the inundated area mapped but not modelled.

### C. Available datasets and consolidation towards modelling

#### Water level time series

Daily stages data from two gauges of the Brazilian national network, namely Manacapuru gauge (3.317°S, 60.583°W) and Iranduba gauge (3.268°S, 60.215°W) were retrieved from

the Brazilian water agency (ANA) website. Two additional gauges were installed in the Janauacá FP at “RL1” (3.424°S, 60.264°W) and “RL2” (3.368°S, 60.193°W) (Figure 1b). All the gauges were levelled by a high-precision bi-frequency Global Positioning System (GPS) unit.

We also used water level data from altimetry satellites: the ENVISAT/RA-2 altimeter operated by European Spatial Agency (2002-2010) and its follow-on French-Indian joint mission SARAL/ALtiKa altimeter in operation on the same orbit since 2013. Both furnish reliable measurements every 35 days [24]. We produced 7 virtual stations (VS) (Figure 1b): VS1\_564, VS2\_564, VS1\_149, VSR\_149 and VSR\_564 in the FP, and VSR\_564 and VSR\_149 in the mainstream. The two latter being close (1.6 km), we merged both into a unique station denoted VSR hereafter. We used a linear relationship between Manacapuru gauge and VSR water level to produce daily mainstream stages at VSR52 (located 52 km downstream from Manacapuru)

#### Rainfall and meteorological data

We used daily rainfall data from six gauges from the Brazilian national network, downloaded from the ANA website (Figure 1a). Averaged rainfall on the FP was obtained weighting each gauge data series by the Thiessen polygon area. The Brazilian national meteorological institute (INMET) provided hourly climatic data from the nearest meteorological station (Manacapuru, Brazil, Para state, 3.317°S, 60.583°W) through its website. We used the following meteorological parameters: insolation ( $\text{W} \cdot \text{m}^{-2}$ ), wind speed ( $\text{m} \cdot \text{s}^{-1}$ ), wind direction, air relative humidity (%), air temperature (°C) and pressure (hPa) useful for evapotranspiration computation in the hydrological modelling step.

#### Bottom friction map

We used the dual-season wetlands map of Amazon Basin [25] to define zones with same cover assumed to reflect friction properties in the FP. This product is available at the NASA Earth Observing System Data and Information System (EOSDIS) website. From this classification map, we retained 4 distinct classes: permanent water, shrubs, flooded forest and forest in spatial proportions of 44%, 14%, 21%, and 20%, respectively. The Manning coefficient attributed to each zone follows literature advises [26]: 0.02-0.04, 0.03-0.06, 0.05-0.15 and 0.1-0.2 for permanent water, shrubs, flooded forest, and forest, respectively. Adjusting the Manning coefficient is part of the hydrodynamic model calibration step.

#### Topography and bathymetry data

We used the topography dataset produced by [27] for the study area. This dataset was derived from SRTMGL1 (30 m-resolution) dataset. Combining *in situ* bathymetry and remotely sensed products, these authors removed the interferometric bias and the vegetation-induced bias. Then, they interpolated the unbiased elevations, the bathymetric data using the ANUDEM v5.3 algorithm [28] constrained by a drainage channel network. The produced topographic map presents a vertical accuracy of 1.7 m for a 30 m resolution [27]. Moreover, the method proposed by [27] ensures numerical stability of the mesh processing and the hydrodynamics model.

### *Flood extent from ALOS/PALSAR imagery*

Due to limitations in retrieving water under forest, product based on optical imagery were not adapted to this study. As an alternative, L-band Synthetic Aperture RADAR (SAR) permits this detection. We performed a thresholding classification based on ALOS-1/PALSAR images, available through the ALOS Kyoto & Carbon initiative at the Alaska Satellite Facility website. We retrieved 24 scenes covering the whole range of water level conditions to better capture the flood pulse dynamics.

### *Velocity data*

Averaged velocities of cross-sections were measured with an Acoustic Doppler Current Profiler (ADCP) (RDI instrument 1200 Hz) at the Terra Alta (TA) location (3.370°S, 60.214°W) and RL2 gauge location (Figure 1b). These two locations permitted measuring the channel discharges within a short distance from RL2 gauge. At last, the velocity dataset consisted of 30 measures collected during the 2006-2011 period.

### *Water circulation pattern analysis*

To examine seasonal velocity patterns, we partitioned both space and time. An hydrological year was subdivided into six hydrologic periods: i) late low water, ii) early rising water, iii) late rising water, iv) high water, v) falling water, vi) early low water. All hydrologic periods were defined from RL1 stages time-series.

Also, the FP was subdivided into three distinct domains: the lake area with fringing flooded forests and other wetlands (denoted LA, hereafter) from the south stream (denoted SS, hereafter) as suggested by these authors, and, we extended this partition to include the connecting channel (denoted CC, hereafter) (Figure 1a). By convention, positive velocities and slopes indicate water flowing from river to FP.

To examine spatial inundation frequency, for each mesh node and each hydrological year, we computed the inundation duration, i.e. the number of days during which a node is flooded. The inundation frequency map was deduced from the average of the duration of inundation of each node over each simulated hydrological year and reported to the length of the longest hydrological year over the study period.

The study period encompasses one extreme drought during 2009-2010 hydrological year and several extreme floods (2008-2009, 2011-2012 and 2014-2015 hydrological years). We computed the difference in inundation duration between the normal year and the extreme drought or flood hydrological years to build anomaly maps of inundation duration.

## IV. RESULTS

### *A. Model performance assessment*

#### *Water level*

It is noteworthy to mention that the hydrodynamic model was poorly sensitive to the choice of the Manning parameter: the averaged RMSE varied from 0.37 m to 0.41 m when exploring the whole range of Manning values. We finally selected the values giving the lowest RMSE: 0.032, 0.042,

0.14 and 0.18 s.m<sup>-2/3</sup> for permanent water, shrubs, flooded forest, and forest zones, respectively.

The simulated and observed water level are in good agreement at all gauges. Global RMSE, NSE and correlation coefficient at the fifth stations over the entire period were 0.32 m, 0.99 and 0.99, respectively. Comparing to the accuracy of the bathymetry (1.70 m) and the amplitude of the flood wave (11.05 m), the RMSE value remained low. The validation upon VS (RMSE, NSE and correlation coefficient of 0.30 m, 0.99 and 0.99, respectively) remained similar to the ones upon *in situ* gauges (RMSE, NSE and correlation coefficient of 0.38 m, 0.99, and 0.99, respectively). The vertical accuracy also has temporal variations. RMSE, NSE and correlation coefficient presented the lowest values at low water with scores of 0.48 m, 0.75, and 0.93, respectively. Best scores are obtained during rising water (RMSE, NSE and correlation coefficient of 0.17 m, 0.99 and 0.99, respectively).

### *Flood extent*

The overall horizontal accuracy TS was 62 (Table 1). The averaged positive BIAS (20) suggested a slight flood extent under-prediction by the model. Nevertheless, the discrepancies magnitude showed temporal variations depending on the FP stage. For water level > 15 m, i.e. during rising water, high water and early falling water, skills scores remained good (TS>58). Positive BIAS (22-38) render a slight model underestimation. Conversely, for water level <15 m, the skills scores testify for a model overestimation (negative BIAS) with a lower accuracy (TS<48). This analysis also evidences geomorphological controls that confine inundation and critical thresholds (12 m, 15 m and 21 m). Indeed, for very low water level, the inundation remains confined to the inner drainage channels and small ponds. Between 12 and 15 meters, the flood extent passes from 21% to 47% of the modelled domain, progressing essentially in the LA-domain. Above 21 m, most of the inner natural levees are below water and inundation expands almost the modelled domain.

Table 1. Results of horizontal accuracy for flood extent modelling

Water level	Comparison number	TS	BIAS
All	24	62	20
<12 m	1	24	-88
>12 m and <15 m	2	48	-19
>15 m and <21 m (rising water)	6	58	38
>15 m and <21 m (falling water)	4	65	22
>21 m	11	70	27

### *Velocity*

Computed and simulated CC-velocities are in satisfactory agreement. The model correctly simulates the variation amplitude, with velocities values, ranging from -101.3 cm.s<sup>-1</sup> to 56.7 cm.s<sup>-1</sup>. Over the whole simulated period, the correlation coefficient and NSE were superior to 0.83 and 0.68, respectively. The RMSE remained below 23.5 cm.s<sup>-1</sup>. The outflow peaks can vary between -24 % (2009-2010) to +28 % (2014-2015). Conversely, inflow peaks remain similar with little inter-annual variations (SD=4.8 cm.s<sup>-1</sup>).

## B. Patterns of water circulation and flood duration

### Seasonal patterns

The model simulated contrasted velocity magnitudes over the three domains, and high magnitude variation between hydrological periods (Figure 2). Regardless the hydrological period, the highest velocity magnitudes are encountered in CC-domain with values over  $5.0 \text{ cm.s}^{-1}$  at high water, and the lowest in LA-domain with a mean value inferior to  $1.7 \text{ cm.s}^{-1}$ . Velocity magnitudes exhibit little variations in SS-domain ( $0.8\text{--}1.7 \text{ cm.s}^{-1}$ ), while they range between  $5.1 \text{ cm.s}^{-1}$  during early low water ( $0.2 \text{ cm.s}^{-1}$  at late low water) and  $20.1 \text{ cm.s}^{-1}$  ( $6.2 \text{ cm.s}^{-1}$ ) during high water in CC-domain (LA-domain). In SS-domain, the velocity magnitude is maximum during the falling period.

The water circulation patterns are highly variable along the HY. Until early rising water, CC-domain acts as an inlet. From late rising water to falling water, water circulation in the three domains is organized toward the mainstream. At early low water, the river flows into the LA- and SS-domain. Between early low water and early rising water, the rise of the local runoff counterbalances the increase of rivers-to-FP discharge, limits the river incursion into SS-domain and spreads over LA-domains. The moving frontier position between mainstream water and water coming from the local drainage watershed is well-defined, around the mid-course of SS-domain. During late rising water and high water, overflow induces a significant velocity magnitude increase in the north-eastern part of LA-domain and in CC-domain, and also a circular water circulation. At falling water, flows are organized towards the mainstream in all domains.

Water circulation results in contrasted inundation frequency across the FP (Figure 3). On average over the studied period, SS and CC-domains and the inner-channels in the LA-domain remain inundated all year-round. Some ponds located in the north-west of LA-domain, but also some located in the CC-domain also remain flooded all year-round. Inundation frequency is reduced by 20% (about 2 months and a half) in the flat LA-embayment and small bays along SS-domain. The inundation duration of levees and creeks is less than 6 months while some topographical features remain free of water all year-round, leaving some wetlands disconnected a large part of the HY.

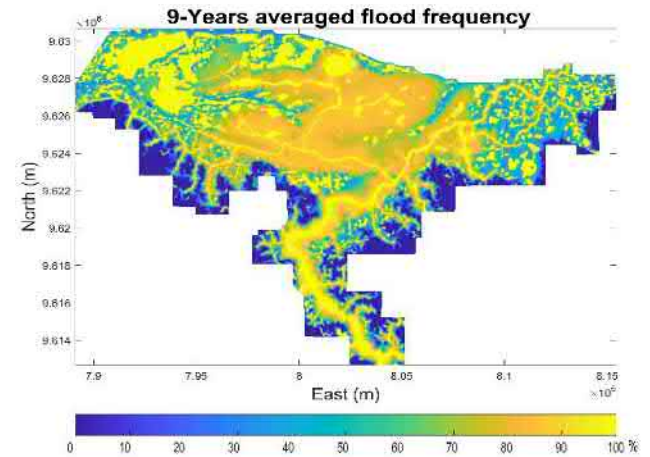


Figure 3. Nine-years averaged frequency flood map.

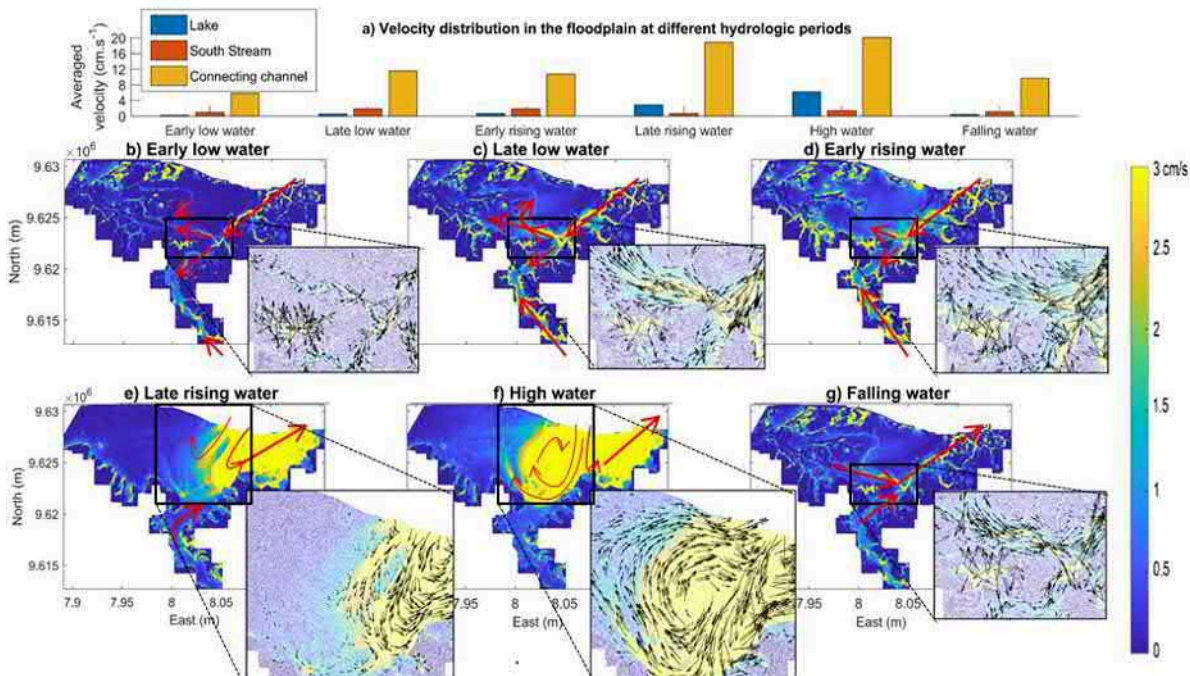


Figure 2. a) Average velocity distribution following the hydrologic period; b)-g) Velocity distribution in the FP at different hydrological periods with velocity magnitude in  $\text{cm.s}^{-1}$  set as background. The schematic red and black arrows indicate the direction of water circulation.



### Extreme events impact upon flood duration

Extreme events influence the inundation duration across the FP (Figure 4a-e). Compared to normal hydrological year, the inundation duration during the 2009-2010 drought was reduced by more than a month in a large region of the LA-domain and in the small creeks and bays along the SS-domain (Figure 4a-b). Interestingly, extreme floods impact varies as a function of the considered event. As expected, extreme floods cause an increase of the inundation duration for pixels located along the margins of the different domains (LA, CC, SS), that are not inundated or only immersed a couple of months during a normal HY. For pixels in the LA-domain, which are usually flooded more than half a hydrological year, the inundation duration may reduce up to 20 days (e.g. during 2011-2012 Figure 4d) or increase up to 50 days (e.g. during 2014-2015 Figure 4e). In addition, in the CC and the central part of the SS domains, the inundation duration increases between 10 and 20 days as a function of the HY.

## V. DISCUSSION

### A. Model reliability

#### Model performances

Over the whole study period, the simulated water level and flood extent were in good agreement with the observations. However, both vertical and horizontal assessment underlined a degradation of accuracy during low water, as reported in other studies about Amazonian FP hydrodynamics [e.g. 19]. This deterioration is likely due to an under-representation of the inner-drainage channels that organize the flooding and the falling period [14]. Besides, the quality of the observation datasets should slightly lower during low water: i) the RL1 and RL2 could have remained out of water ii) the probability of

mixed water-non water pixels increases. During high water, our analysis highlighted slight vertical and horizontal underestimation that we associate to little inaccuracies of bank elevations or locations for the WLBC, leading to slight overflow underestimation.

The model was able to simulate the CC-velocities variations. It also reproduces that the flow reversion in the channel and that overflow is the main water inflow pathway. However, the model delays the overflow onset of roughly 15 days, more likely because levee elevation is slightly overestimated. Levee overestimation also induces a slight overflow underestimation that is reflected in the computed velocities at high water.

### Limitations and recommendations

The analysis of the model performance evidenced the topographic controls. Hence, modellers should take into account both the accuracy and the resolution of input topography. Here, ALOS-1/PALSAR images allowed detecting several channels whose width remains inferior to the minimum mesh edge size (23 m). In addition, forested wetlands present pronounced microtopography (hummocks and hollows) that affect the local water velocity field. With a 23m-mesh resolution, the model does not capture such fine-scale topographic controls. However, these features were taken into account through the roughness coefficient that is adjusted during the model calibration.

This study highlighted the necessity of controlling the quality of the validation datasets. Indeed, both observed water level and flood extent suffer from degradation at low water preventing robust validation at that period. Besides, simulated velocity fields cannot be fully (spatially and temporally)

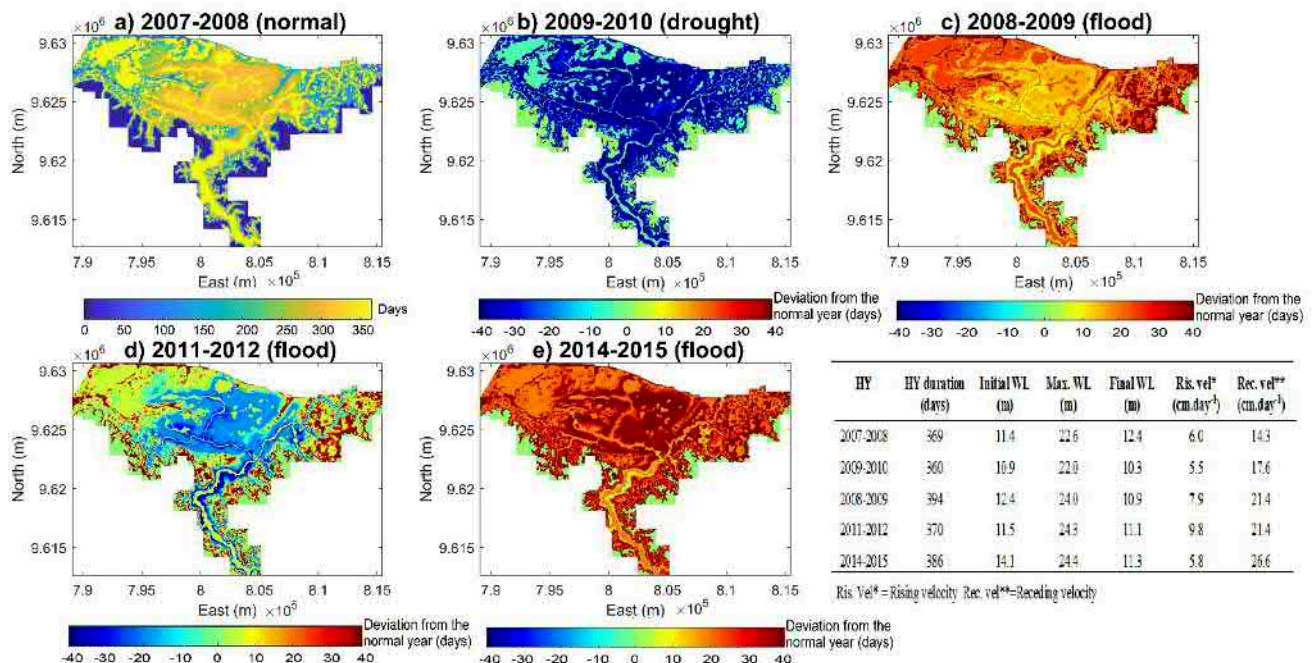


Figure 4. a) Spatial distribution of inundation duration for a hydrological normal year, deviations from the normal year, b) a drought hydrological year, c-e) flood extreme events.

The table indicates the hydrological year characteristics (duration, min. and max)

validated with observations. Nevertheless, velocities validation indicates that CC-velocities are correctly estimated giving confidence for the other FP domains.

The presented model could have been more sophisticated by including the evolution of bottom shear stress or the wind effect. Unfortunately, no data upon vegetation growth were available for this study. Regarding the wind effect, Amaral et al. (2018) showed in the same floodplain that sites with more wind exposure have different biogeochemical characteristics than wind protected areas. Even if both variables may have impact on our results, the topography data remain the primary source of model uncertainty.

Despite these limitations, the good agreement between observed and simulated data suggests the hydrological-2D-hydrodynamics modelling is sufficient to capture the flow in the floodplain. Finally, our modelling approach only required a limited *in situ* data (bathymetry and velocity observation). Hence, our methodological framework can be transferred to any floodplain in the world.

#### B. Water circulation pattern: seasonal and spatial distribution

The seasonal and spatial velocity magnitude evolution and the distribution of inundation duration reported in this study reveal the complexity of water circulation patterns as already reported in [29] at regional scale and in [17,18] for a larger Amazon FP system. The inundation extent, duration and velocity magnitude in the different domains of the FP are only partly controlled by topography. As expected, current CC-velocities magnitude is significantly higher where the flow is well constrained by levees. Velocity magnitudes are also greater in SS-domain than in LA-domain, but not during late rising water and high water when overflow occurs in the north-westward region of LA-domain (Figure 4a-d). Our results suggest the importance of hydraulic controls.

During the early rising period (water level <17 m), water slopes in CC are positive and in opposite direction than those in SS and in a higher magnitude ( $0.6 \text{ cm.km}^{-1}$  in CC against  $-6.82.10^{-4} \text{ cm.km}^{-1}$  in SS). The river incursion into the channel is limited by local runoff (maximum at this period) and spreads rather over the LA-domain. However, later in the rising period ( $17 < \text{water level} < 20 \text{ m}$ ), when local runoff already diminished, slopes equilibrate between these two domains allowing the river progression along SS. For water level higher than 20 m (high water and overflow period), there are no velocity magnitudes differences between rising and receding periods. This period also corresponds to maximum velocity in the LA-domain. At this period, flows have a circular pattern driven by topography and hydraulic controls exerted by SS-domain and the Amazon/Solimões River that act as hydraulic barriers. That the mainstream partly blocks the FP output is not surprising as such effect is already reported for Amazon River tributaries [30]. However, the role of local runoff upon river incursion is much less documented. Based on regional remote sensing analysis, [29] mentioned the role of FP water saturation prior to mainstream inundation as a main factor to explain the river incursion extent across the FP. During late high water and falling water, the main hydrodynamics driver

stays the Amazon/Solimões that keep on acting as a hydraulic barrier. The flood receding phase of the mainstream starts before ones of the Janaúacá FP. Consequently, it induces a strong gradient between FP water level and mainstream stages (computed CC-slope of  $-5.4 \text{ cm.km}^{-1}$ ). This hydraulic gradient may also be the main driver of SS-velocity during falling water. During this period, LA-domain loses its direct connection with the mainstream (the mainstream margins) and velocity falls back to moderate velocity ( $< 2 \text{ cm.s}^{-1}$ ). Our findings support Alsdorf et al. (2007) statement upon the difficulty to retrieve water circulation from FP topography only. They also confirm those obtained by Ji et al. (2019) on another Amazonian FP that highlighted a strong interplay between local rainfall/runoff and river rising/receding rate.

#### C. Extreme events impact upon flood inundation

Based on our findings for the 2009-2010 drought, the inundation duration is reduced, especially in the LA-domain where the topography is relatively flat. Conversely, the study period encompasses three important floods events (2008-2009, 2011-2012, and 2014-2015). The flood amplitude obviously controls the inundation extent and thus controls the inundation duration of pixels with bottom elevation above the “normal” maximum flood amplitude. On the other hand, changes in inundation duration for pixels that are “normally” flooded differ between flood events, especially in the LA-domain. These differences reflect FP saturation conditions prior to inundation (i.e. the initial FP water volume) and the strength of the hydraulic control exerted by the Amazon/Solimões River, which vary inter-annually. At the beginning of the 2014-2015 cycle, the minimum stage was roughly 2 meters above that of 2008-2009 and 2.5 m above that of 2011-2012. We appraised the strength of hydraulic control by the Amazon/Solimões River through rising and receding water rates for water level ranging between 14 and 20 m (Figure 4). The rising rate was the highest during the 2011-2012 hydrological year, and the smallest during 2014-2015 hydrological year. The receding rate was the highest during the 2014-2015 hydrological year and was equal during the 2008-2009 and 2011-2012 hydrological years. Thus, the difference of positive inundation duration anomaly observed between 2014-2015 and 2008-2009 hydrological years might be explained by the prior inundation condition in 2014-2015. The negative inundation duration anomaly during 2011-2012 hydrological year should result from higher rising water rate while receding water rate is comparable to 2008-2009 hydrological year.

## V. CONCLUSION

Based on a hydrologic-2D hydrodynamic modelling (LUMP-FP and Telemac-2D), we investigate flooding dynamics across a medium-size Amazonian floodplain system (786 km<sup>2</sup>, including the local catchment). The proposed approach integrates *in situ* data and remote sensing into a hydrologic-hydrodynamic model to simulate a 9-years period (2006-2015) that encompass floods and drought events. The model correctly reproduced water level, flood extent and velocity. However, its accuracy varies along the hydrological year. Indeed, misrepresentation of inner-channels and

imprecision in levee elevation slightly lower the accuracy of the model at low water period and high water, respectively.

The analysis of velocity spatiotemporal patterns highlights strong heterogeneities in water velocity magnitude between the different morphological domains of the floodplain. The river-floodplain connecting channel (CC-domain), where flow is well constrained by levees, presented the highest velocities, and the large embayment (LA-domain) in the northern-westward direction the lowest, except during high water. However, topography only partly controls the water circulation. Flows are also constrained by the interplay between mainstream and local runoff at least part of the hydrological year. Comparing several hydrological years highlights the interannual changes of these hydraulic controls in function of mainstream rising and receding rates, the local runoff and the influence exerted by prior inundation conditions.

Seasonally and spatially contrasted velocities across the FP imply spatially contrasted inundation duration. Drought essentially modifies SS-domain velocities, where higher values are encountered during the rising and late rising periods. It also reduces the velocity in the LA-domain during the high water, and consequently every mixing process in this area. The inundation duration is reduced, especially in the flat LA-domain. Flood events slightly affect the velocity magnitude at late rising water and high water (overbanking) and alter the duration of seasonal velocity patterns. While the flood amplitude controls the inundation extent, the rate of the rising/receding water in the mainstream and the prior inundation conditions control the inundation duration in the floodplain during flood events. Consequently, extreme flood amplitude does not necessary implies longer inundation duration. The latter results are also important while considering the potential impact of dams. Indeed, hundreds of spatially distributed dams across the Amazonian basin will not only affect the water level range in the dammed rivers but also the rising and receding rates of the associated rivers and far downstream with hardly foreseeable impacts.

The seasonal pattern of water circulation and inundation duration exhibits strong intra- and inter-annual variations. As these hydrodynamic features are key factors upon suspended solids transport, biogeochemical processes distribution, these parameters should be more cautiously taken into account in multi-disciplinary studies.

#### ACKNOWLEDGEMENT

Several international research programs supported this research: (CNES/TOSCA), (OSCA-Varz) CNPq-MCTI 400029/2015-4, INCT ODISSEIA (Grant n° 16- 2014 with funding from CNPq/CAPES/FAP-DF) and from the European Union Horizon 2020 Research and innovation program under the Marie Skłodowska - Curie grant agreement No. 691053 (H2020-MSCA-RISE-2015 ODYSSEA project).

#### REFERENCES

- [1] Hess, L.; Melack, J.M.; Affonso, A.G.; Barbosa, C.; Gastil-Buhl, M.; Novo, E.M.L.M. "Wetlands of the Lowland Amazon Basin: Extent, Vegetative Cover, and Dual-season Inundated Area as Mapped with JERS-1 Synthetic Aperture Radar". *Wetlands* **2015**, *35*, 745–756.
- [2] Fassoni-Andrade, A.C.; Paiva, R.C.D. de "Mapping spatial-temporal sediment dynamics of river-floodplains in the Amazon". *Remote Sens. Environ.* **2019**, *221*, 94–107.
- [3] Moreira-Turcq, P.; Bonnet, M.P.; Amouroux, D.; Bernardes, M.C.; Lagane, C.; Maurice-Bourgoin, L.; Perez, M.; Seyler, P. "Seasonal variability in concentration, composition, age, and fluxes of particulate organic carbon exchanged between the floodplain and Amazon River". *Global Biogeochem. Cycles* **2013**, *27*, 119–130.
- [4] Barbosa, P.M.; Farjalla, V.F.; Melack, J.M.; Amaral, J.H.F.; da Silva, J.S.; Forsberg, B.R. "High rates of methane oxidation in an Amazon floodplain lake". *Biogeochemistry* **2018**, 351–365.
- [5] Richey, J.E.; Mertes, L.; Dunne, T.; Victoria, R.L.; Forsberg, B.R.; Tancredi, A.C.F.N.S.; Oliveira, E.; Victoria, R.L.; Forsberg, B.R.; Tancredi, A.C.F.N.S. "Sources and routing of the Amazon River flood wave". *Global Biogeochem. Cycles* **1989**, *3*, 191–204.
- [6] Castello, L.; Hess, L.; Thapa, R.; McGrath, D.G.; Arantes, C.C.; Renó, V.F.; Isaac, V.J. "Fishery yields vary with land cover on the Amazon River floodplain". *Fish Fish.* **2018**, *19*, 431–440.
- [7] Da Silva, V.; Trujillo, F.; Martin, A.; Zerbini, A.N.; Crespo, E.; Aliaga-Rossel, E.; Reeves, R. 2018. *Inia geoffrensis*. "The IUCN Red List of Threatened Species 2018" e.T10831A50358152. In: 2018.
- [8] Anderson, E.P.; Jenkins, C.N.; Heilpern, S.; Maldonado-Ocampo, J.A.; Carvajal-Vallejos, F.M.; Encalada, A.C.; Rivadeneira, J.F.; Hidalgo, M.; Cañas, C.M.; Ortega, H.; et al. "Fragmentation of Andes-to-Amazon connectivity by hydropower dams". *Sci. Adv.* **2018**, *4*, 1–8.
- [9] Castello, L.; Macedo, M.N. Large-scale degradation of Amazonian freshwater ecosystems. *Glob. Chang. Biol.* **2016**, *22*, 990–1007.
- [10] Gurnell, A.; Petts, G. Hydrology and Ecology of River Systems. In *Treatise on Water Science*; 2010; Vol. 2, pp. 237–269 ISBN 9780444531933.
- [11] Bonnet, M.P.; Pinel, S.; Garnier, J.; Bois, J.; Bonaventura, G.; Seyler, P. "Amazonian floodplain water balance based on hydrologic and electrical conductivity data analyses and modelling". **2017**, 1–38.
- [12] Bates, P.; De Roo, a. P. "A simple raster-based model for flood inundation simulation". *J. Hydrol.* **2000**, *236*, 54–77.
- [13] Luo, X.; Li, H.Y.; Ruby Leung, L.; Tesfa, T.K.; Getirana, A.; Papa, F.; Hess, L. "Modeling surface water dynamics in the Amazon Basin using MOSART-Inundation v1.0: Impacts of geomorphological parameters and river flow representation". *Geosci. Model Dev.* **2017**, *10*, 1233–1259.
- [14] Wilson, M.D.; Bates, P.; Alsdorf, D.E.; Forsberg, B.R.; Horritt, M.S.; Melack, J.M.; Frappart, F.; Famiglietti, J. "Modeling large-scale inundation of Amazonian seasonally flooded wetlands". *Geophys. Res. Lett.* **2007**, *34*, L15404.
- [15] Frias, C.E.; Abad, J.D.; Mendoza, A.; Paredes, J.; Ortals, C.; Montoro, H. "Planform evolution of two anabranching structures in the Upper Peruvian Amazon River". *Water Resour. Res.* **2015**, *51*, 2742–2759.
- [16] Mendoza, A.; Abad, J.D.; Frias, C.E.; Ortals, C.; Paredes, J.; Montoro, H.; Vizcarra, J.; Simon, C.; Soto-Cortes, G. "Planform dynamics of the Iquitos anabranching structure in the Peruvian Upper Amazon River". *Earth Surf. Process. Landforms* **2016**, *41*, 961–970.
- [17] Rudorff, C.M.; Melack, J.M.; Bates, P. "Flooding dynamics on the lower Amazon floodplain: 2. Seasonal and interannual hydrological variability". *Water Resour. Res.* **2014**, *50*, 635–649.
- [18] Rudorff, C.M.; Melack, J.M.; Bates, P. "Flooding dynamics on the lower Amazon floodplain: 1. Hydraulic controls on water elevation, inundation extent, and river-floodplain discharge". *Water Resour. Res.* **2014**, *50*, 619–634.
- [19] Sioli, H. "The Amazon and its main afluentes: Hydrography,

- morphology of the river courses and river types". In *The Amazon Liminology and landscape ecology of a mighty tropical river and its basin*; 1984; pp. 127–165 ISBN 978-94-009-6544-7.
- [20] Hervouet, J.M. "TELEMAC modelling system: an overview". *Hydrol. Process.* **2000**, 14, 2209–2210.
- [21] Lang, P.; Desombre, J.; Ata, R. TELEMAC-2D Software Release 7.0 User Manual 2014, 1–115.
- [22] Trevethan, M.; Santos, R. V.; Ianniruberto, M.; Oliveira, M.; Martinelli, A.; Gualtieri, C. "Influence of tributary water chemistry on hydrodynamics and fish biogeography about the confluence of Negro and Solimões rivers", Brazil. *11<sup>o</sup> Simpósio Int. Eco-hidráulica (ISE 2016)* **2016**, 16.
- [23] Canadian Hydraulics "Centre Blue Kenue". Available online: <http://www.nrc-cnrc.gc.ca/eng/ibp/chc/software/kenue/bluekenue.html> (accessed on Sep 1, 2018).
- [24] Verron, J.; Sengenès, P.; Lambin, J.; Noubel, J.; Steunou, N.; Guillot, A.; Picot, N.; Coutin-Faye, S.; Sharma, J.R.; Gairola, R.M.; et al. "The SARAL/AltiKa Altimetry Satellite Mission". *Mar. Geod.* **2015**, 00–00.
- [25] Chapron, B.; McDonald, K.; Shimada, M.; Rosen, P. a.; Schroeder, R.; Hess, L. "Mapping Regional Inundation with Spaceborne L-Band SAR". *Remote Sens.* **2015**, 7, 5440–5470.
- [26] Arcement Jr, G.J.; Schneider, V.R. "Guide for Selecting Manning's Roughness Coefficients for Natural Channels and FloodPlains". *Tech. Report, Geol. Surv. Water-Supply, United States Gov. Print. Off. Washington, U.S.A* **1989**, 38.
- [27] Pinel, S.; Bonnet, M.P.; Santos, J.; Moreira, D.; Calmant, S.; Satge, F.; Seyler, F. "Correction of interferometric and vegetation biases in the SRTMGL1 spaceborne DEM with hydrological conditioning towards improved hydrodynamics modeling in the Amazon basin". *Remote Sens.* **2015**, 16108–16130.
- [28] Hutchinson, M.F. ANUDEM VERSION 5.3 USER GUIDE 2011.
- [29] Mertes, L. "Documentation and significance of the perirheic zone on inundated floodplains". *Water Resour. Res.* **1997**, 33, 1749.
- [30] Paiva, R.C.D.; Buarque, D.C.; Collischonn, W.; Bonnet, M.P.; Frappart, F.; Calmant, S.; Bulhões Mendes, C.A. "Large-scale hydrologic and hydrodynamic modeling of the Amazon River basin". *Water Resour. Res.* **2013**, 49, 1226–1243.

# Numerical modelling of flash flood event in steep river using Telemac 2D and Sisyphe

Michal Pavlíček and Oddbjørn Bruland

Department of Civil and Environmental Engineering  
Norwegian University of Science and Technology (NTNU)  
Trondheim, Norway  
michal.pavlicek@ntnu.no

**Abstract**— Extreme weather events, natural disasters as well as failure of climate change mitigation and adaptation are the risks with the highest likelihood of occurrence and largest global impact. Historically, the attention has been on floods in the larger, slow responding watercourses. Due to a changing climate, it is both expected and experienced more frequent and more extreme rainfalls, creating violent flash floods in small catchments. In steep rivers, this induces rapid changing discharges and large water forces resulting in erosion and rivers taking new courses, destroying communities and threatening livelihoods and lives. Municipalities are responsible for mapping the risks natural hazards induce. When it comes to the risks due to floods in steep rivers, there is still a lack of approach and methodologies to handle their analysis. For mapping of such an event, the identification of critical points where the water can find the way from the river channel due to erosion and sedimentation is important. Therefore, the methodology has to include sediment transport and bed evolution in the river channel and the inundation area of the flood.

In this study, the flooding of Utvik (western Norway) in July 2017 is reconstructed using TELEMAC – MASCARET numerical simulating software. The longitudinal slope of the river in Utvik is ca. from 3 to 17 %. A 2D numerical model of Utvik was built. The proposed solution consists of hydrodynamic simulation carried out in Telemac 2D and morphodynamic simulation (i.e. including bedload transport and bed evolution) using coupling of Telemac 2D and Sisyphe. Instabilities in bed evolution were observed in the river channel with steep longitudinal slope and steep river banks. To avoid the instabilities, non-erodible bed was set-up in the river channel in the final morphodynamic simulation. The results of the simulations were compared with the documentation of the flood event.

## I. INTRODUCTION

The extend and potential consequences of floods in large water courses are in most cases in Norway well mapped [1]. Here the flood risks are related to inundation which have been mapped using hydraulic routing of the floods of different return periods. The risks in small and steep catchment are not that well mapped. Flash floods in such catchments occur due to heavy rainfall and are characterized by fast process (i.e. flooding starts after 6 hours of rainfall) [2]. Therefore, the faster response and the forces due to high water velocities induces another risk dimension that is significantly more

challenging to handle. Municipalities in Norway deal with flash flood events caused by heavy rain [3], [4]. Therefore, there is an urgent need to develop methodologies to estimate the risk level and find mitigation measures also in these water courses.

Two-dimensional (2D) numerical simulations are nowadays an important tool for modelling and mapping floods in general. Most of these models consist of the resolution of Shallow Water Equations (SWE) [5]. There are several commercial, free ware and open source software, that could be used to carry out these simulations (e.g. MIKE, HEC-RAS, TELEMAC-MASCARET, Basement, etc.). In order to reconstruct flash flood events similar to the one that took place in Utvik (western Norway) in July 2017, it is important to simulate morphodynamically and to include the effect of erosion and deposition to the flood's study. Morphodynamic simulation consists of a hydrodynamic part as well as sediment transport and river's bed evolution [6]. Coarse sediment, boulders and rocks are located in the river bed and the slope of the river channel in Utvik is considered steep (ca. 3-17%).

There are some studies regarding hydrodynamic simulations of flash floods and flow in steep slopes using SWE. In [7], hydrological and hydraulic simulation of flash flood event in small ungauged steep catchment. Hydraulic simulation adequately reproduced the flood event. However, the domain is in the urban area without any sediment transport included.

Several configurations of 2D DIVAST model were tested on idealized valley with steep slope and on real flash flood event in [8]. The authors recommend to use shock-capturing schemes in the simulations of flow in the longitudinal slopes greater than 1%.

Dam [9] also performed 2D morphodynamic simulation of Utvik's flood event. FINEL2D model was used to carry out hydrodynamic and morphodynamic simulation. The results of bed evolution match well with the documentation of real flood even though notably finer sediment diameters than observed in the area were set-up in the model. Except this study, no application of any SWE model to flash flood in steep river similar to the one in Utvik has been found.



The goal of this study is to examine the critical points in the river channel during this recent flash flood. In this study, critical points are spots where water could find the way out from the river channel, which could be caused by erosion and deposition of sediments. A 2D numerical model of Utvik was built and the flood event was reconstructed. The proposed solution consists of hydrodynamic and morphodynamic simulation (i.e. including sediment transport and river's bed evolution). Results of the simulation were compared with documentation of the event [4], [10], [11].

TELEMAC – MASCARET (“Telemac” hereafter) was selected as a suitable tool to carry out the 2D morphodynamic simulations. However using of Telemac for simulations of sediment transport was validated against laboratory experiments and study cases with gentle slope [12]. Hence, the goal of this study is also to evaluate suitability of the model to simulation of flash flood in steep rivers (i.e. longitudinal slope greater than 3%).

## II. STUDY AREA

The study area is located in Utvik in Sogn og Fjordane (western Norway). On 24<sup>th</sup> July 2017, the most recent flash flood due to highly concentrated heavy rain took place in the municipality of Utvik. The research performed in this study is focused on Storelva river; the catchment of this river is displayed in dark blue color in Figure 1. Area of the catchment is ca. 25 km<sup>2</sup>.

As shown in Figure 2, the river made new flow paths due to a combination of rising water levels, water velocities, and the following erosion and bed evolution. During its channel migration, the large amount of wood and coarse sediment as well as rapid water flow, incremented by the steep downhill slope, triggered the breach of key connecting infrastructure (e.g. bridges and roads) and an increased consequent damage to neighboring property on the river's way to the fjord. Therefore, it is evident that a complementary morphodynamic simulation should be carried out in this case.



Figure 1 Storelva catchment in Utvik (Geonorge 2018), (NVE 2018a).



Figure 2. Aerial view of Utvik flood event from the fjord [4], with original river thalweg (blue line) and bridges.

## III. METHODS

### A. Data for numerical model

The data used to build the numerical models consist of: pre-flood event Digital Elevation Model (DEM) with grid size 0.5 m [11]; post-flood event DEM created in 2017 with grid size 0.25 m [11]; orthophoto map and geometry of buildings and roads [13]; flow hydrograph [10]; measurement of bridge opening dimensions (measured in the field by O. Bruland); photo and video documentation of flood event in Utvik (taken by O. Bruland); [4].

### B. Model description

Version v7p3 of Telemac was used to perform the simulations. BlueKenue, FUDAA, HEC-RAS, ParaView and QGIS were used for pre- and post- processing.

In particular, Telemac's 2D module was used to run 2D hydrodynamic simulations in the horizontal plane. The code solves Saint-Venant (shallow water) equations in non-conservative form. The result is the water depth and two velocity components in each point of the computational mesh. Finite element or finite volume method can be chosen as resolution method. In addition, the module includes the solution of flow through structures in the river channel (e.g. bridges, weirs, etc.). Further description of theory can be seen in [14] and [15].

Regarding the morphodynamic simulations (i.e. sediment transport and river's bed evolution; see further description in section D), Sisyph module was used. The morphodynamic simulation consists of i) hydrodynamic solution (see section C), ii) sediment transport (i.e. bedload and suspended load) and iii) river's bed evolution (see section D for the latter two). This software offers several formulas available for sediment transport and the module solves river's bed evolution with the sediment mass conservation equation (Exner equation). The module is applicable to either uniform/non-uniform, cohesive/non-cohesive sediments. Second currents and effect of bed's slope associated with the influence of gravity can be included. Also, vertical stratification of sediments and non-erodible river's bed is possible to set up in the model [6].

### C. Hydrodynamic simulation

Input data of the model are listed in the previous section (see section A). By discretization, the computational domain was divided into mesh elements in BlueKenue (see Figure 3), which uses triangular shapes for these. The mesh elements had a size of 20 m in the fjord, 2 m in the river channel and of 3 m in the rest of the domain. Buildings were set-up as holes in the mesh so there is no flow through them. Roads and river banks were set up as break lines in the mesh (i.e. the edges of mesh elements lie on the break lines). The mesh contains ca. 70,000 elements and 36,000 nodes.

Flow through bridges can be simulated by modification of the terrain (i.e. adding bridge abutments to DEM). But this way does not include overflowed bridges. When flow over the bridge deck is desired, the bridges are treated as couples of points with flow between them. The discharge through the bridge is a function of water level in the points [15], this option was used in the simulations. Mesh size was refined (i.e. 1.0 m, see Figure 3) in the inflow and outflow bridge points, in order to create representative cross sections around the bridges.

A flow hydrograph (Figure 4) of Utvik's flood event was assigned as the inflow open boundary condition. There is no continuous discharge measurement in Storelva in Utvik. The flow hydrograph is reconstructed based on observation carried out during the event and the maximum discharge is estimated based on posterior measurements of flood level over a dam crest [10]. 30 m long artificial reach of the channel with mild slope was created by modification of DEM downstream the inflow boundary condition to avoid supercritical flow on the boundary. Constant water surface elevation 0 m a.s.l. was attached to the outflow open boundary condition. The rest of the boundary is closed (wall). The result of a steady flow simulation with an inflow discharge of 0.5 m<sup>3</sup>/s was used as initial condition for subsequent unsteady simulations.

The domain was divided into polygons according to the type of surface, hence, different values of Manning roughness coefficient were assigned: 0.045 for the river channel and the fjord bed, 0.025 for the roads, and 0.100 for the rest of the domain.



Figure 3. Example of the mesh (cell size is 2 m in the river channel and 3 m in the rest of the domain). Buildings are cropped out of the mesh.

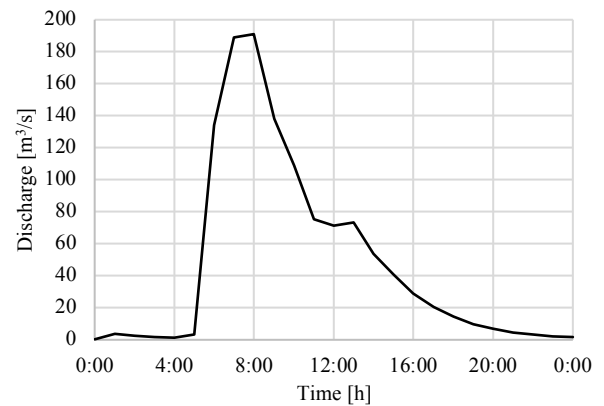


Figure 4. Flow hydrograph of Utvik's flood [10]

Time step was computed according to the value of Courant number ( $Cu = 1.0$ ). Duration of the simulation was 23 hours.

Finite elements and finite volumes methods were tested for resolution of the governing equations. It is possible to use HLLC (Harten Lax Leer-Contact) shock-capturing scheme within finite volumes method [16]. Eventually, finite elements method was used for all the simulations, due to the equivalent results of both methods and shorter execution time.

Constant viscosity turbulent model was assumed.

### D. Morphodynamic simulation

Once hydrodynamic simulation is fully developed, Telemac 2D could be coupled with Sisyphe to carry out the morphodynamic simulation. Sisyphe was fully coupled with Telemac 2D. For initial simulation set-up, mesh size 20 m in fjord and 1 m in the river channel and the rest of the domain was set-up. Uniform sediment diameter 0.01 m were assumed in the whole computational domain. Bedload transport was simulated using Meyer-Peter and Müller formula, no suspended load was taken into account. No solid discharge was attached to the inflow boundary condition. It was assumed an active layer thickness of sediment and the thickness of erodible layer 100 m (i.e. the layer of material that can be transported and eroded). The effect of the local bed slope on the magnitude and direction of bedload was modelled with Koch and Flokstra formula [6].

Instabilities in the bed evolution were observed in the reaches with the steepest slope and steep river banks. Figure 5 shows the example of the instabilities in results of the initial simulation. The example in Figure 5 is located in the river reach with longitudinal slope ca. 17 % and presented results of bed evolution are in the peak of the hydrograph (i.e. 8:00, Figure 4). Longitudinal profile of the river channel with the results from the initial simulation set-up can be seen in Figure 6. Cross sections of the river channel are presented in Figure 7, Figure 8 and Figure 9. Instabilities in the whole wide of the channel are observed in Figure 8 and also some in the riverbanks (Figure 7, Figure 9). In order to avoid the instabilities, several combinations of sediment parameters, bedload transport formulas, mesh size, active layer and erodible layer thickness, excluding bridge structures and



numerical set-up were tested to find out the best match with the flow paths observed during the flood event. However, no model configuration without appearance of the instabilities was found.

In order to simulate Utvik flood event, an assumption of non-erodible bed in the river channel and the fjord was accepted for the final simulation set-up. Mesh size was 20 m in the fjord, 2 m in the river channel and 3 m in the rest of the domain. The values of sediment diameters and an erodible layer in the rest of the domain were modified, unless the best match with the flow paths observed during the flood event was reached. In this final set-up, an erodible layer 2.5 m was assumed in the rest of the domain and sediment diameter in the inundation area was set up 0.5 mm. Otherwise the set-up was the same as in initial simulation. Tab. 1 presents the summary of the morphodynamic simulations.

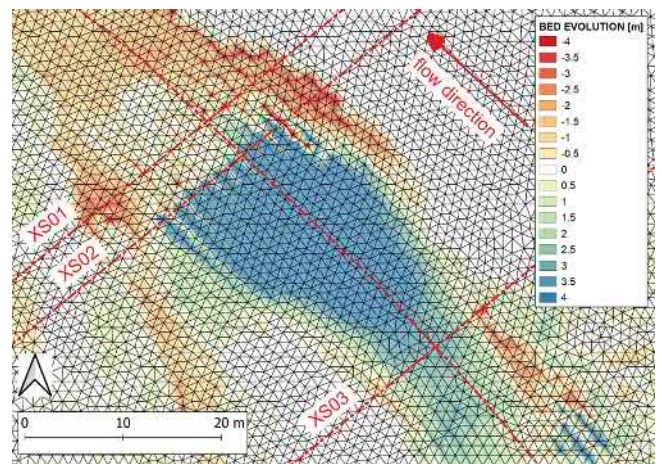


Figure 5. Results of morphodynamic simulation in Utvik. Displayed variable is bed evolution in the peak of the hydrograph (i.e. 8:00).

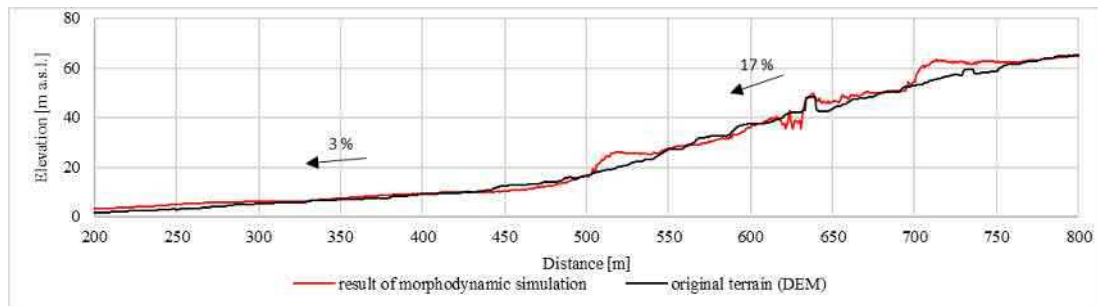


Figure 6. Longitudinal profile of the river channel. Black line represents the original river bed, red line represents river bed obtained from morphodynamic simulation with the initial set-up.

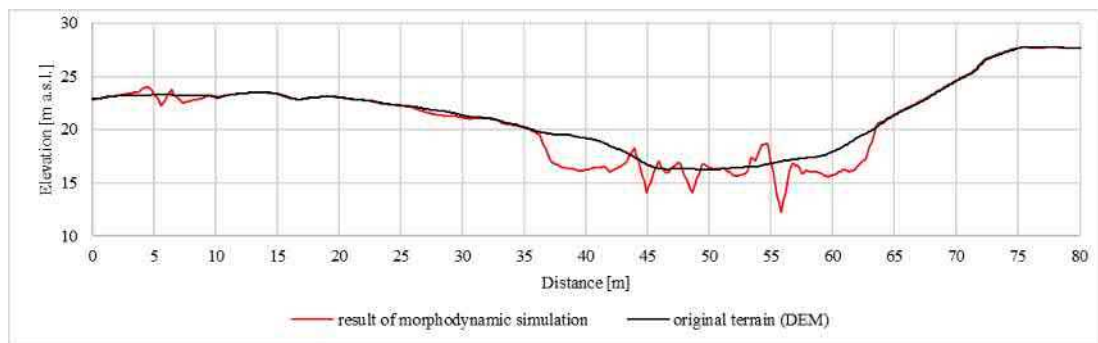


Figure 7. Cross-section XS01 of the river channel. Black line represents the original river bed, red line represents river bed obtained from morphodynamic simulation with the initial set-up.

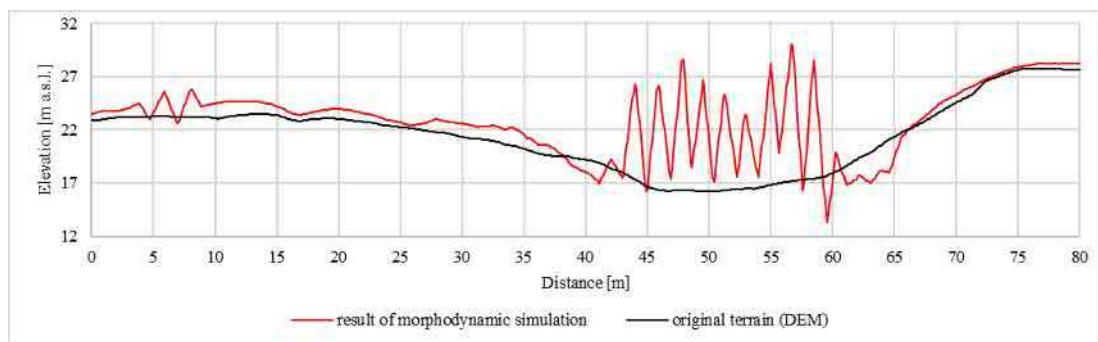


Figure 8 Cross-section XS02 of the river channel. Black line represents the original river bed, red line represents river bed obtained from morphodynamic simulation with the initial set-up.



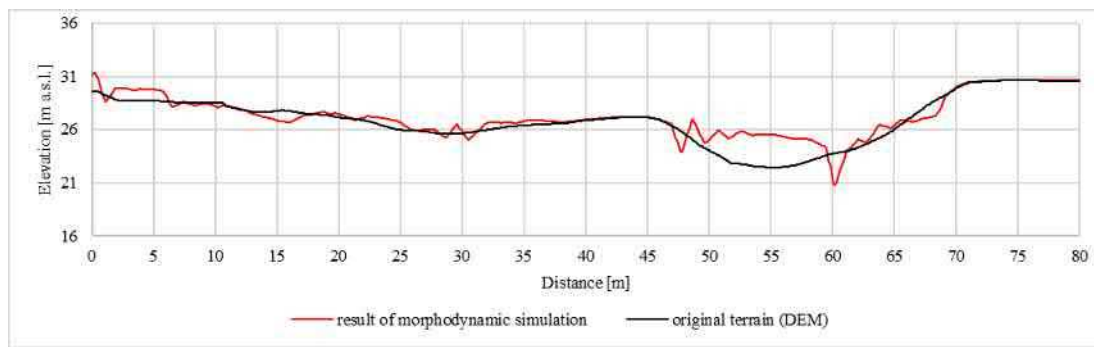


Figure 9. Cross-section XS03 of the river channel. Black line represents the original river bed, red line represents river bed obtained from morphodynamic simulation with the initial set-up

TABLE 1 SUMMARY OF THE MORPHODYNAMIC SIMULATIONS

		Initial morphodynamic simulation	Final morphodynamic simulation
Mesh size [m]	Fjord	20	20
	River channel	1	2
	Rest of the domain	1	3
Sediment diameter [mm]	Fjord	10	non-erodible
	River channel	10	non-erodible
	Rest of the domain	10	0.5
Active layer thickness and erodible layer [m]		100	2.5

#### IV. RESULTS AND DISCUSSION

Figure 10 shows results of hydrodynamic and the final morphodynamic simulations. Displayed variable is maximum water depth (m). Figure 11 represents results of maximum shear stress (Pa) from hydrodynamic simulation (left), results of the bed evolution (m) from morphodynamic simulation (center) and the bed evolution (m) obtained from pre and post flood event DEM [11] (right). In the figures, black dashed lines represent the original river channel; red circles represent the critical points and purple lines represent flow paths during flood event. The critical points and flow paths were identified

according to bed evolution obtained from pre and post flood event DEM [11] and photo and vide documentation of the flood [4]; (taken by O. Bruland).

There are not any available data for calibration the model in Utvik. The results were compared with the flow paths and bed evolution obtained from documentation of the flood event [4] and the post flood DEM (in 2017; [13]). From the results is clear that in the hydrodynamic simulation (Figure 10, left), the main flow path is located in the river channel and the other paths matches quite well with the paths from the real flood.

As for the final morphodynamic simulation (i.e. non-erodible bed in the river channel), results show that the water found new flow path on the left side of the bridge 02 (Figure 10, right), which is the most critical point in the domain. But the inundation area is similar as in the hydrodynamic simulation and the other critical points were not found according the results. From Figure 11 (center) is clear that the water found the new path from the river channel due to erosion of the road embankment. As can be seen in Figure 11 (left), the results of shear stress from hydrodynamic simulation are also suitable to find the critical point besides bridge 02 due to the high values of the shear stress in this area (i.e. erosion would be expected). Hence, there is not much of a difference between the results of hydrodynamic simulation and morphodynamic simulation with non-erodible bed in the river channel.

In both types of simulation, all bridges were overflowed. There were also no data for calibration a flow through the bridges opening.

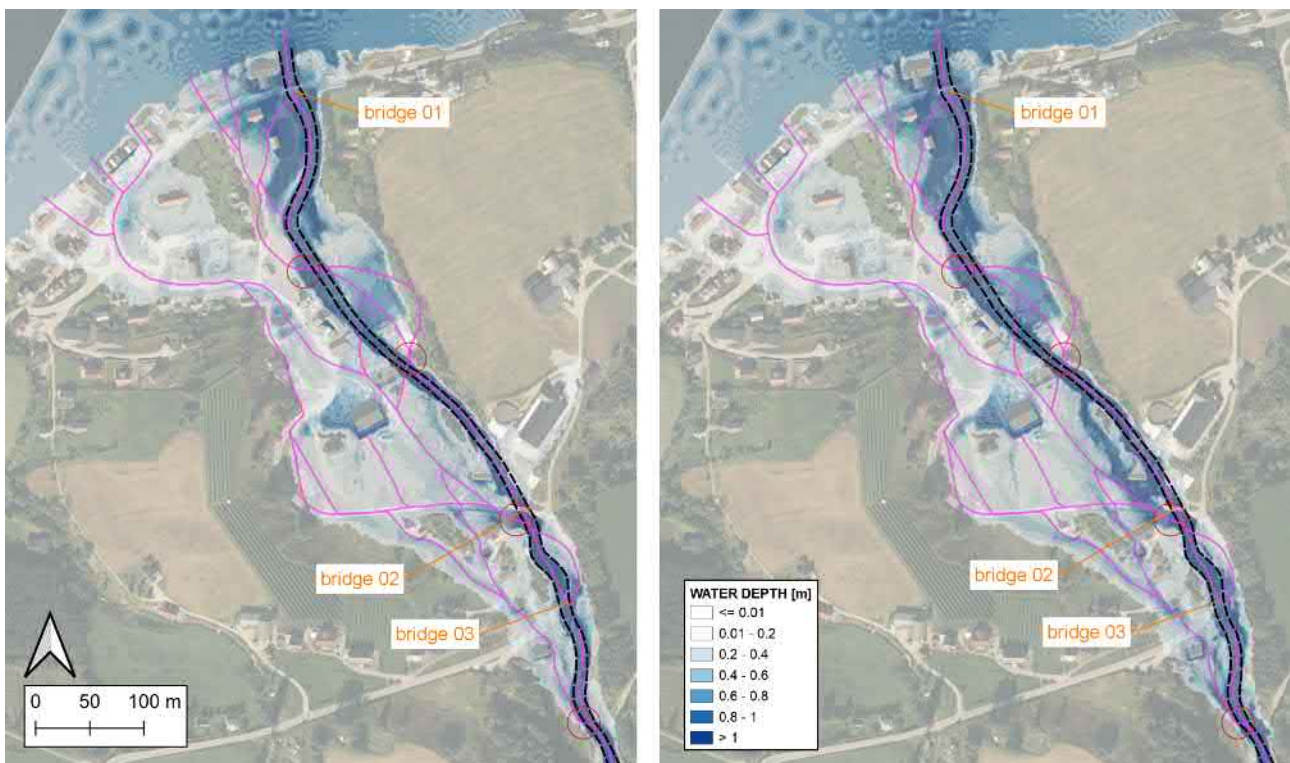


Figure 10. Results of hydrodynamic (left) and final morphodynamic (right) simulations in Utvik. Displayed variable is maximum water depth; black dashed line represents the original river channel; red circles represent the critical points; purple lines represent flow paths during flood event.

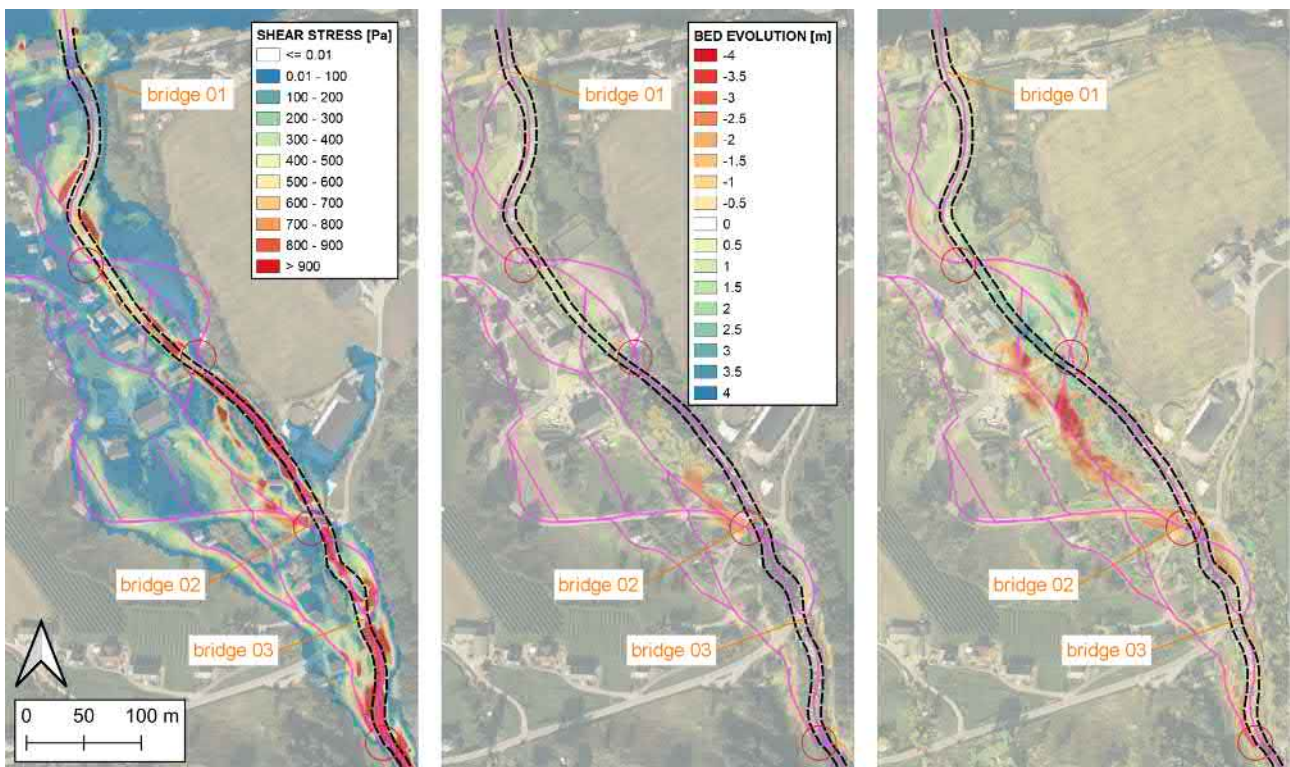


Figure 11. Results of hydrodynamic simulation in Utvik (left, maximum shear stress), final morphodynamic simulation (center, bed evolution in the end of simulation) and bed evolution measured after real flood event (right, bed evolution [11]); black dashed line represents the original river channel; red circles represent the critical points; purple lines represent flow paths during flood event

## V. CONCLUSIONS

Hydrodynamic and morphodynamic simulations were carried out in Utvik study area. Instabilities in the river bed evolution were observed in the morphodynamic simulations. Due to the instabilities, non-erodible bed in the river channel was assumed for final morphodynamic simulation.

The results presented in this paper showed that the hydrodynamic simulation could be used to determine the capacity of the river channel and finding the critical points due to the shear stress. However, it does not take into account the creation of the new flow paths due to erosion and deposition processes, so the critical points do not have to be clearly identified.

Regarding the morphodynamic simulation, the inundation area in both types of simulations is not much different. The results of the current morphodynamic simulation present a non-erodible bed, thus, a negligible volume of transported sediment in the river channel. So, the assumption of non-erodible river channel is a significant simplification and further research should be focused on improving the configuration of the model in order to find the suitable set-up for morphodynamic simulation in steep rivers. Therefore, the configuration should be tested and improved on the simpler cases with steep longitudinal slope covering an erodible bed in the river channel to investigate the source of the instabilities. Erosion and sedimentation processes are important to determine the critical points during flash floods, hence, the phenomena of bedload transport in steep terrains needs to be investigated further.

According to the results of both types of simulations, capacities of bridges openings are insufficiently dimensioned to deal with the peak discharge in the river's channel. The conclusion is that the capacity of bridges is an important parameter determining flash flood extent and it should be further investigated. Impact of clogged bridges due to debris (e.g. wood, sediment, man-made objects, etc.) could be investigated as well.

Further research will focus on numerical modeling of the phenomena. Both 2D and 3D numerical models will be tested in order to find suitable model for bedload transport in steep slopes. Therefore, simulations of laboratory experiments and cases with field measurements will be carried out for validation and adaptation/development of the numerical model. Initially Telemac and REEF3D (includes the solution of non-hydrostatic SWE) models will be tested.

Bedload transport formulas implemented in Telemac are developed for certain limitations regarding longitudinal slope and sediment diameter. Hence, further research will be also focused on implementation of bedload transport formula for steep rivers, e.g. Smart formula [17].

## REFERENCES

- [1] NVE, "Mapping (Kartlegging)," 2019. [Online]. Available: <https://www.nve.no/flaum-og-skred/kartlegging/>.
- [2] H. A. P. Hapuarachchi, Q. J. Wang, and T. C. Pagano, "A review of advances in flash flood forecasting," *Hydrological Processes*, vol. 25, no. 18, pp. 2771–2784, 2011.
- [3] VG, "Skjåk flooded and isolated (Skjåk oversvømt og isolert)," 2018. [Online]. Available: <https://www.vg.no/nyheter/innenriks/i/Kv4p1E/skjaak-oversvoemt-og-isolert>.
- [4] VG, "Per Inge Verlo's (58) house was in the middle of the flood (Per Inge Verlos (58) hus sto midt i flommen)," 2017. [Online]. Available: <https://www.vg.no/nyheter/innenriks/i/GVbeQ/per-inge-verlos-58-hus-sto-midt-i-flommen-helt-ufattelig>.
- [5] J. Teng, A. J. Jakeman, J. Vaze, B. F. W. Croke, D. Dutta, and S. Kim, "Flood inundation modelling: A review of methods, recent advances and uncertainty analysis," *Environmental Modelling and Software*, vol. 90, pp. 201–216, 2017.
- [6] P. Tassi, "Sisyphe UserManual Version v7p3," EDF, 2018.
- [7] F. Ciervo, M. N. Papa, V. Medina, and A. Bateman, "Simulation of flash floods in ungauged basins using post-event surveys and numerical modelling," *Journal of Flood Risk Management*, vol. 8, no. 4, pp. 343–355, Dec. 2015.
- [8] D. Kvočka, R. Ahmadian, and R. A. Falconer, "Flood inundation modelling of flash floods in steep river basins and catchments," *Water (Switzerland)*, vol. 9, no. 9, 2017.
- [9] G. Dam, "Simulating the flooding in Utvik on 24 July 2017 using a high-resolution 2D hydro- and morphological model," *Presentation at XXX Nordic Hydrological Conference 13–15 August 2018, Bergen, Norway*, 2018.
- [10] O. Bruland, "How extreme can specific runoff become in steep Norwegian catchments?," *unpublished*.
- [11] Kartverket, "Height data (Høydedata)," 2018. [Online]. Available: <https://hoydedata.no/>.
- [12] C. Villaret, J. M. Hervouet, R. Kopmann, U. Merkel, and A. G. Davies, "Morphodynamic modeling using the Telemac finite-element system," *Computers and Geosciences*, vol. 53, no. October 2017, pp. 105–113, 2013.
- [13] Geonorge, "Map Catalogue," 2018. [Online]. Available: <https://kartkatalog.geonorge.no/search>.
- [14] J. M. Hervouet, *Hydrodynamics of Free Surface Flows: Modelling with the finite element method*. John Wiley and Sons, 2007.
- [15] R. Ata, "Telemac2d User Manual v7p3," EDF, 2018.
- [16] R. Ata, "TELEMAC-2D new finite volume schemes for shallow water equations with source terms on 2D unstructured grids," *XIXth TELEMAC-MASCARET User Conference*, 2012.
- [17] G. M. Smart, "Sediment Transport Formula for Steep Channels," *Journal of Hydraulic Engineering*, vol. 110, no. 3, pp. 267–276, 1984.



# A flood forecasting model on river Oise with the plugin mascaret

*Patrick CHASSE*  
Cerema Eau Mer et Fleuves  
Margny lès Compiègne, France  
patrick.chasse@cerema.fr

Cédric CHABRIDIER, Delphine DUVAL, Charles  
SOURDIAUX  
Service de Prévision des Crues Oise-Aisne  
Compiègne, France  
cedric.chabridier@developpement-durable.gouv.fr  
delphine.duval@developpement-durable.gouv.fr  
charles.sourdiaux@developpement-durable.gouv.fr

**Abstract** — The flood forecasting service Oise-Aisne commissioned Cerema to adapt an existing model for flood forecasting under the plugin mascaret, because it is easier for them to control the data on the mascaret model. The chosen river is a branch of Oise located between Origny-Saint-Benoite upstream to Sempigny downstream. The distance between these two stations is around 85 kilometers.

## I. INTRODUCTION

On the rivers Oise and Aisne catchments, there are seven propagation sub-models used by the flood forecasting service for predicting flood connected with rain-flow models where necessary. One sub-model was chosen to the experiment of the transposition of the existing model to a new model under the Mascaret plugin. All the available data were used to construct the model, calibrate and verify its validity. One of the most difficult tasks was to geolocate the cross sections and to integrate the bathymetry with the topography extracted from the digital terrain model. Finally we have succeeded in developing a propagation model that responds quite well to the observed data in situ.

The figure 1 hereunder shows the general map of the model location.

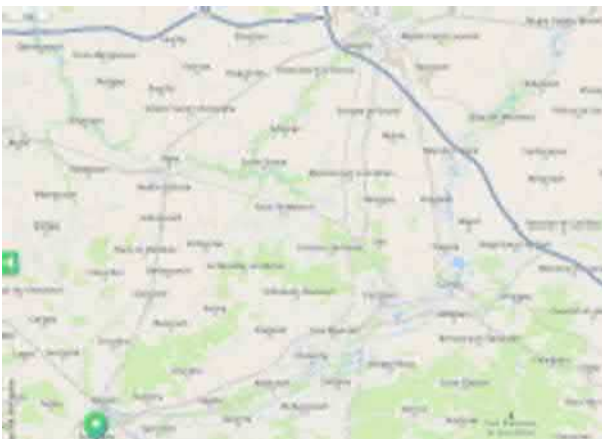


Figure 1 – General map of the model location

## II. DATA AVAILABLE FOR THE PROJECT

### A. Bathymetry

We had on one side the traces of the georeferenced profiles and on the other the bathymetric points with the name of the profiles and the location of the profiles with their name in a pdf file. With this information, we managed to fill in the georeferenced bathymetric points table of the Mascaret plugin to connect to the cross profiles table.

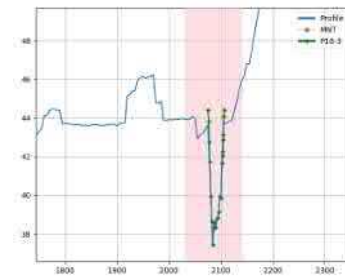


Figure 2 – Bathymetric points in green

### B. Topography

The Oise-Aisne flood forecasting service has made available the digital terrain model available on the study area at a distance of 1 meter.

From these data we were able to extract the topographic points of the flood plain for each of the cross sections constituting the model.

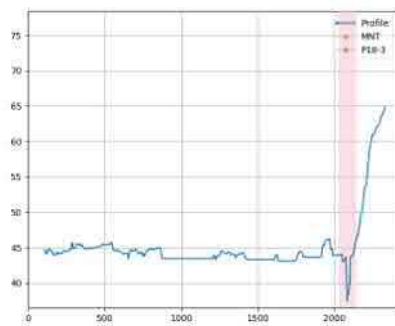


Figure 3 – Final profile in blue

With the topographic and bathymetric points of each cross section, we were able to build the final profile that is shown in Figure 3 above. The part in pink corresponds to the minor bed of the river.

### C. Hydrology

In the study area, we have three hydrometric stations on the Oise river (Origny-Sainte-Benoite, Condren and Sempigny) and three hydrometric stations on tributaries (Serre, Ailette and Verse).

We have data for several floods : 1993, 1995, 2011, 2003, 2011, 2013 and 2016.

We have calibrated the model on the 2011 flood, which has the advantage of presenting fairly simple characteristics, then we will check the calibration on the more complex floods of 1993 and 1995. Finally we exploited the model on the other floods to test its reaction.

One of the main difficulties of this hydrological component is to estimate the diffuse inputs, because the flows of the tributaries do not always cover the inflows of flows observed at Sempigny.

### D. Hydraulic

We do not have a lot of hydraulic data, like flood markers, to calibrate or validate the model. However, we have water level data recorded at the Origny-Sainte-Benoite, Condren and Sempigny stations. This makes it possible to compare the calculated limnigraphs or hydrographs with those observed at the stations.

The figure 4.1 hereunder gives an example of these comparisons at Sempigny station for Mascaret model.

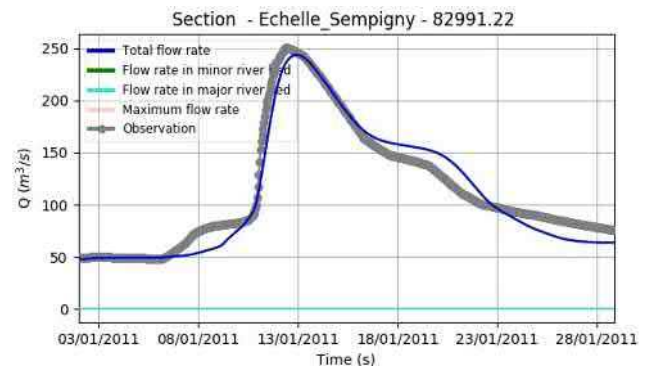


Figure 4.1 – Comparison of discharges at Sempigny station for Mascaret model (flood 2011)

The figure 4.2 hereunder gives an example of these comparisons at Sempigny station for previous model.

### Oise à Sempigny, janvier 2011

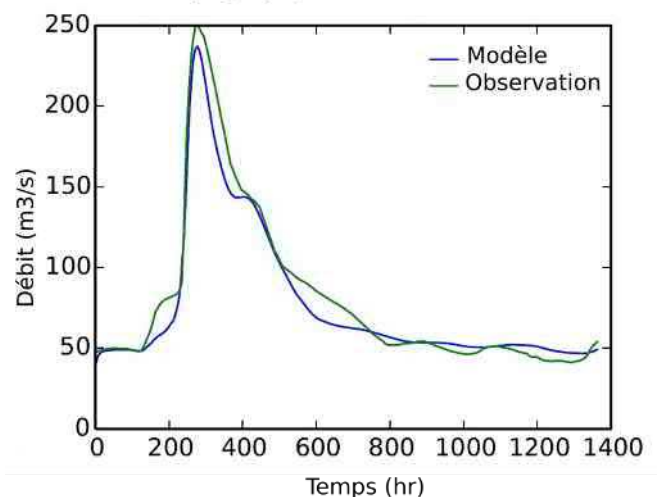


Figure 4.2 – Comparison of discharges at Sempigny station for previous model (flood 2011)

## III. PRESENTATION OF THE MODEL

As indicated above, the model extends from Origny-Sainte-Benoite upstream to Sempigny downstream, about 85 km in length. In the upstream part, about 30 kilometers, the river Oise is separated into two branches by the Sambre canal. The two branches then meet at the Fère town to form a single reach.

Between the upstream and the town of la Fère, there is a connection between the two reaches of the river Oise, with a structure consisting of 7 pipes that pass under the Sambre canal (see photo in Figure 5).





Figure 5 – Hydraulic structure under the Sambre canal

The final model consists of 175 cross sections, a basin and two links to represent the connection between the two branches of the river Oise mentioned above.

The model was calibrated on the flood of 2011 which has the advantage of being a simple flood with a single peak.

The result of the calibration leads to Strickler coefficients similar to those retained by the Hydratec consultant, namely 18 for the minor bed and 8 for the floodplain.

In addition, it was necessary to add diffuse inputs, in addition to tributary flows, to obtain a flow rate comparable to that observed at Sempigny. The equivalent of the hydrograph of the Serre river for the 2011 flood has been added in linear form.

Tributary flows are derived from the nearest hydrometric stations at the confluence.

At the upstream boundary condition, there are two branches of the river Oise at Origny-Sainte-Benoite, where we inject 2/3 of the flow on the right ranch and 1/3 of the flow on the left branch. The imposed flows at the boundary conditions are deduced of the observed hydrographs at the Origny-Sainte-Benoite station.

At the downstream boundary condition, we impose the Sempigny rating curve, deduced from measurements and gauges made at the hydrometric station (see figure 6 hereunder).

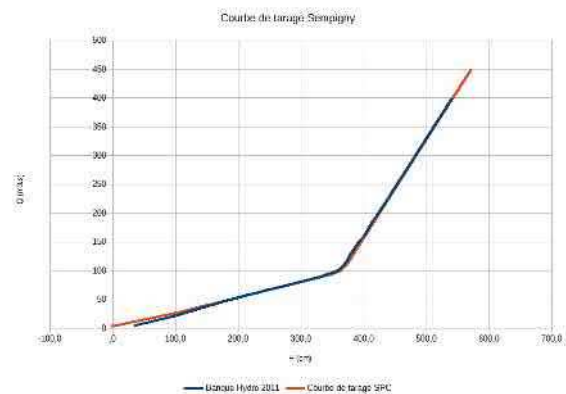


Figure 6 - Rating curve at Sempigny station

The results of the 2011 flood at Origny-Sainte-Benoite, Condren and Sempigny stations are shown in Figures 7, 8 and 9 below (these are calculated and observed water level results).

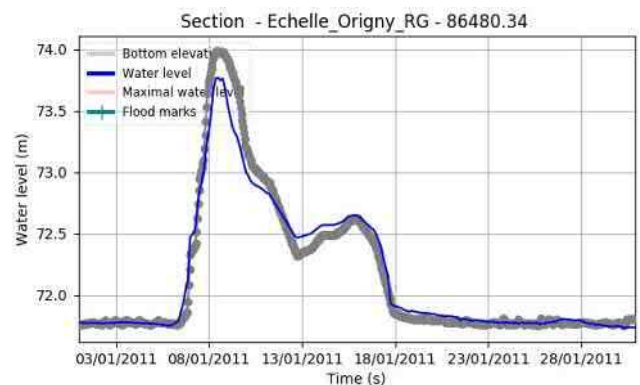


Figure 7 – 2011 flood – Results at Origny-Sainte-Benoite (left branch)

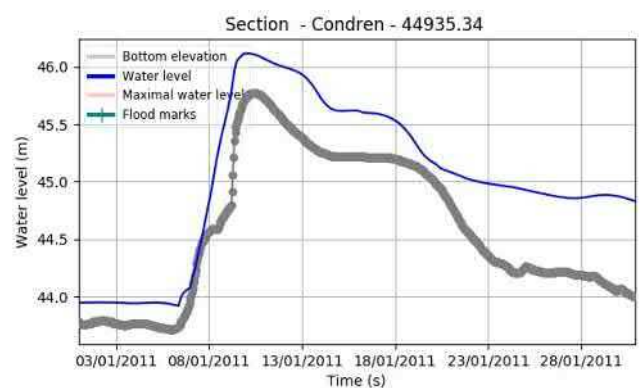


Figure 8 - 2011 flood – Results at Condren

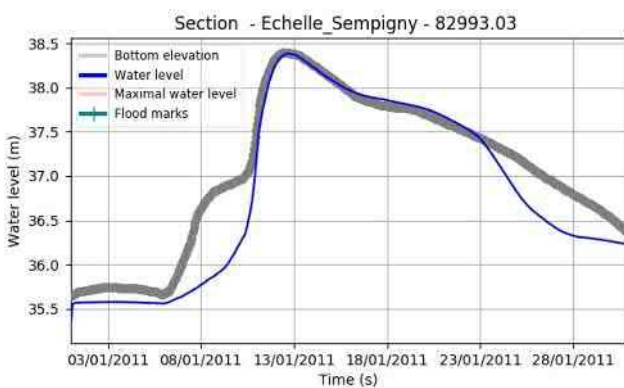


Figure 9 - 2011 flood – Result at Sempigny

The results for the 2011 flood are quite good, even if they are not perfect. The predictions at Origny-Sainte-Benoite station are very closed to the observed water levels, that confirm the discharge ratio used between the right and left branches. The predictions at Condren station are not so good, they are overestimated which can be due to the diffuse discharges injected in the upstream branch. Finally, the predictions at Sempigny station are quite good, specially for the peak water level.

#### IV. ASSESSMENT OF CALIBRATION

We used the floods of 1993 and 1995 to evaluate the quality of the rigging of the model. The highest flood recorded in recent years is that of 1993. It is for this flood that we will present the results obtained with the propagation model.

The maximum flow recorded at the Origny-Sainte-Benoite station is 272 m<sup>3</sup>/s on December 21, 1993 at 15:00.

The figure 10 hereunder shows the flow discharge registered at Origny-Sainte-Benoite station.

The flood of 1993 is more complex than those of 2011 because there are high discharges during about 20 days before the peak of discharge.

This hydrograph was imposed at the upstream boundary condition, with the same ratio as 2011 flood between the right and left branches.

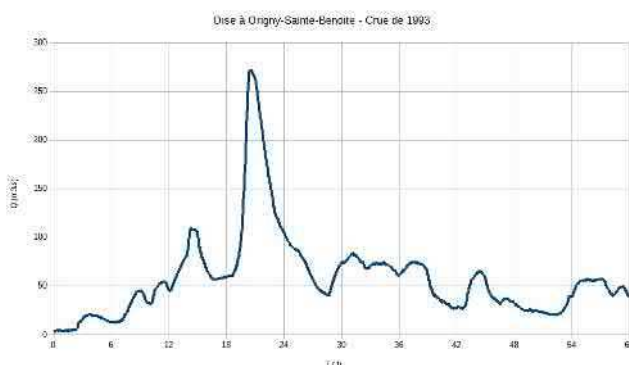


Figure 10 – Flow discharge at Origny-Sainte-Benoite station during the 1993 flood

The downstream boundary condition is always the rating curve at the Sempigny station. The tributary flows are taken into account and the intermediate inputs have this time been limited to 40% of the Serre river hydrograph.

The results obtained at the Sempigny station for the discharge and the water level are shown respectively on figures 11 and 12 hereunder.

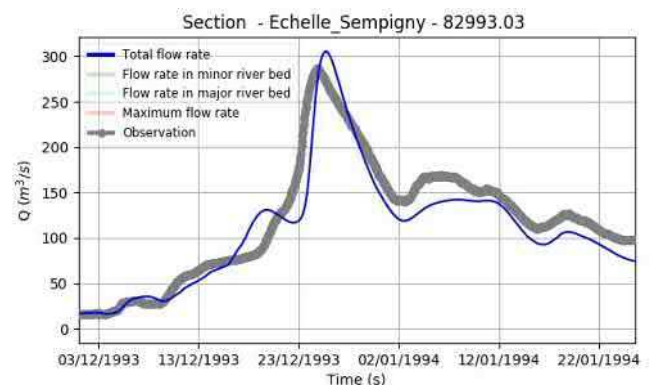


Figure 11 – 1993 flood – Results at Sempigny station for discharge

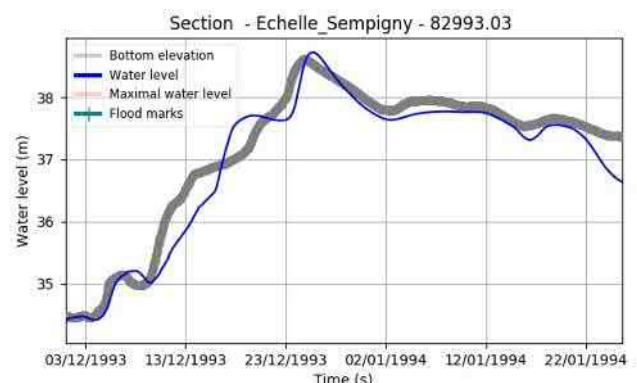


Figure 12 – 1993 flood – Results at Sempigny station for water level

The results are quite good even if they are not perfect. So the propagation model can be considered as validated, but the remained difficulties is to calibrate the intermediate discharges.

## V. IMPLEMENTATION OF THE MODEL ON RECENT FLOODS

The most recent flood of medium importance is that of February 2016. The maximum flow in Origny-Sainte-Benoite would be 87 m<sup>3</sup>/s. As we will see in the analysis of the results, it seems that the flows recorded at Origny-Sainte-Benoite are over-estimated except for the peak of discharge.

The boundary conditions imposed for the calculation are the same as for the previous floods, namely the hydrograph of the 2016 flood in Origny-Sainte-Benoite, with the distribution 1/3 in the right branch and 2/3 in the left branch, and the rating curve at Sempigny. The flows of the tributaries are taken into account in the form of hydrographs, but there are no additional diffuse intermediate discharges.

The results obtained at the Sempigny station for the discharge and the water level are shown respectively on figures 13 and 14 hereunder.

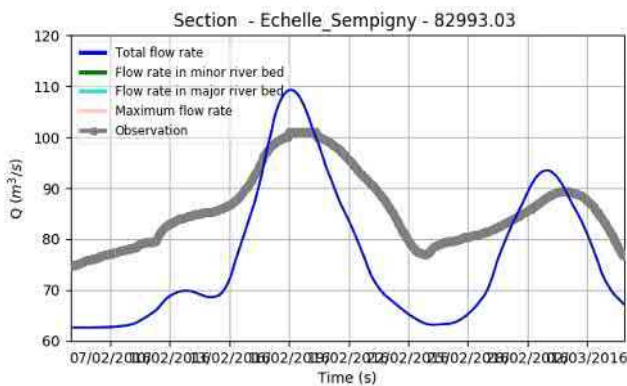


Figure 13 – 2016 flood – Results at Sempigny station for discharge

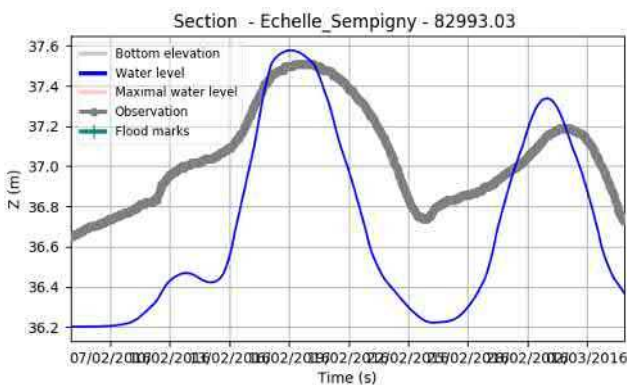


Figure 14 – 2016 flood – Results at Sempigny station for water level

Peak flows and water levels are fairly well represented, however there is an underestimation of the calculated flow or overestimation of the observed flow for the rest of the hydrograph at Sempigny. Taking into account intermediate inputs could improve this situation, but the result would be degraded for peaks.

The results obtained at the Condren station for the discharge and the water level are shown respectively on figures 15 and 16 hereunder.

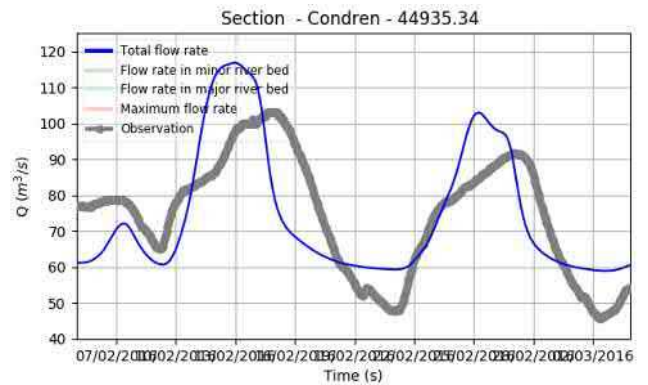


Figure 15 – 2016 flood – Results at Condren station for discharge

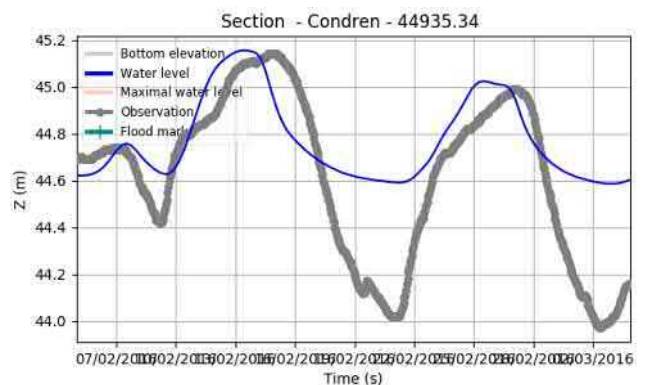


Figure 16 – 2016 flood – Results at Condren station for water level

The results obtained at the Condren station are not too bad. However, there is an overestimate of the water level of 60 cm between the two flood peaks which is relatively large. This can come from the model, but also from the measuring station.

The results obtained at the Origny-Sainte-Benoite station for the water level in the left branch are shown on figure 17 hereunder.

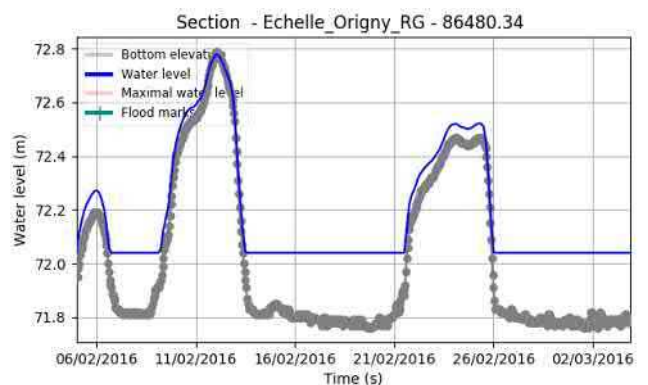


Figure 17 – 2016 flood – Results at Origny-Sainte-Benoite station for water level

The water levels calculated in Origny-Sainte-Benoite are rather good. However, there is a difference of 1 m during low flow, which is normal, because there is a weir of 1 m height

downstream of the station, which is lying during the floods, while it is not in the calculation.

## VI. CONCLUSION

The construction of the propagation model on the Oise river between Origny-Sainte-Benoite and Sempigny made it possible to test the Mascaret plugin under Qgis. It was also an opportunity to contribute to the debug of several modules with the consultant Artélia.

The final result allows the flood forecasting service to have an operational flood forecasting model, all of whose data is accessible and can be corrected or modified.

The model is not perfect, but its behavior on observed floods, even those like 2016 that were not used for calibration or validation, is rather satisfactory.

## ACKNOWLEDGEMENT

We first thank the Oise-Aisne flood forecasting service, which allowed us to do this work and provided us with its data.

We also thank the consultant Artélia for his responsiveness in the debugging of the plugin.

## REFERENCES

- [1] Artélia Eau et Environnement, "Plugin Qgis pour Mascaret – Guide utilisateur", Janvier 2019
- [2] Schapi, "Guide utilisateur Mascaret + plugin Qgis", E. Le Pape, Avril 2019
- [3] Cerema, "Documentation utilisateur – Les casiers dans le plugin Mascaret", P. Bagot, Juin 2019



# Flood risk management based on 2D TELEMAC computations: an example with Swiss hazard maps

Roman Salvisberg, Thomas Marti, Sabrina Arrigo-Meier, Mattia Petar

Niederer + Pozzi Umwelt AG  
CH-8730 Uznach, Switzerland  
roman.salvisberg@nipo.ch

**Abstract**— A case study in Switzerland is considered, where hazard/flood maps are established as part of the planning of flood protection measures. Due to the commune's location within a flat plain divided by a railway dike, it could be shown that the settlements and infrastructures are much more endangered by floods than originally thought. Using the theme "land cover" of the digital cadastral survey, a digital terrain model (DTM) and bathymetry data, break lines were generated to build a triangular mesh. Culverts, tubes, and bridges are an important element of hazard mapping, as they can alter or create new flow paths not only as common bottlenecks in the channel (overflow), but also outside in flooded settlement areas where pedestrian/road underpasses and tunnels are present. However, the modelling of culverts and tubes has revealed that they are no longer suitable from a certain size of the channel, as the flow passes by the point which defines the culvert. Thus, several workarounds were tested to improve the reliability of the culverts/tubes. Recorded floods have shown that buildings are not necessarily an impermeable obstacle for the flowing water. An approach was developed to consider buildings as floodable as well as impermeable, as it could be observed that larger building complexes may be traversed by floods and alter the flow paths in this way. If these aspects are taken into account, an informative hazard map may be established.

## I. INTRODUCTION

Switzerland is regularly affected by natural hazards, especially floods (Fig. 1). The impacts of climate change are expected to lead to an increased danger where more frequent and intensive flooding can be expected in winter and spring. The risk of flooding will also increase in areas that have so far been spared from such floods. To enable an adequate response to natural hazards, their posed danger must be identified. Key elements are inundation maps, which indicate the threatened settlements and infrastructures, the extent of the associated flooding danger and the probability of hazard occurrence. The extent of the danger is derived from the intensity of the inundation and the associated probability (return period). Our hydraulic engineering company is active throughout Switzerland in the field of hazard/inundation mapping, using 2D TELEMAC.



Fig. 1: Flood overflow from and discharge under a road bridge [1]

The natural hazard protection is based on the principles of integrated risk management, aiming at an optimal combination of different protective measures and reducing existing risks to an acceptable level. The risk results from the possible extent of damage and the associated probability of occurrence. The risk resulting from inundation has increased in recent decades. The main reason for this is the greater potential for damage resulting from the growth of the population, the expansion of settlement areas into threatened regions and the increase in value of public infrastructures. Two important questions arise in the context of planning flood protection measures:

- How much can the risk be reduced (impact of the project)?
- What is the ratio of the risk reduction achieved to the costs caused by the measures (economic efficiency)?

To answer these questions, a hazard map for the initial state and a possible project state with protective measures must be elaborated. The hazard map documentation consists of a hazard map, a flow velocity map  $u$ , a flow depth map  $h$  and an intensity map ( $\max(h; u \cdot h)$ ) for specific return periods 30, 100, 300 and 1000 years.

Depending on the region, Switzerland has a very diverse and dense river network with a density of up to  $2.9 \text{ km/km}^2$  (on a scale of 1:25'000) [2]. Both, small mountain streams and larger rivers or currents have to be investigated. Using a concrete project example, we will show the procedures of hazard mapping for a particular river in Switzerland, with emphasis on the application of 2D TELEMAC.



## II. METHODS AND MATERIALS

Fig. 2 shows the schematic procedure and materials used for hazard mapping.

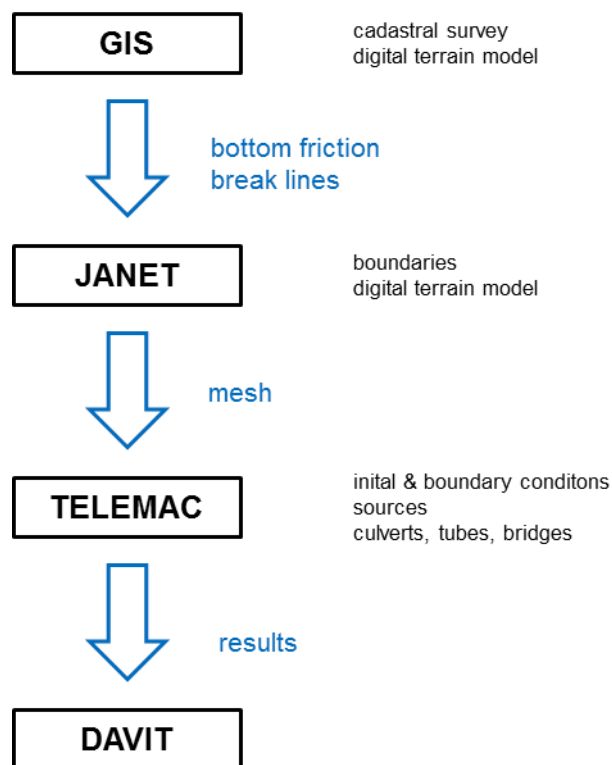


Fig. 2: Procedure with software and materials used for hazard mapping

### A. Mesh

The topography of the mesh is based on a Digital Terrain Model (DTM), usually captured with Airborne Laser Scanning. The resolution of the DTM grid typically ranges between 0.25 and 2 meters. It is crucial that the Laser Scanning takes place in the leafless vegetation period to ensure the DTM covers the earth surface without shrubs and trees (especially next to water bodies). The DTM may be enhanced with bathymetry data to include important low transverse structures of the channel bed, such as sills (Fig. 3).

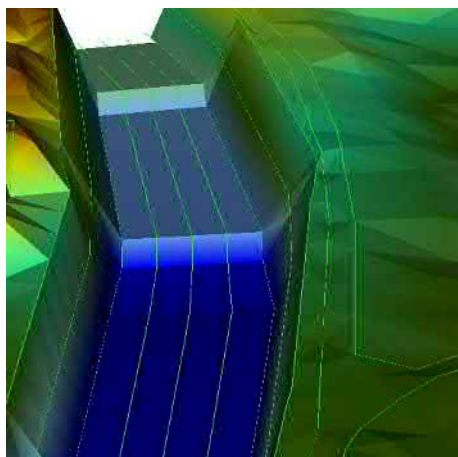


Fig. 3: River bathymetry data, showing the river bed with sills

The break lines are extracted from the land cover data of the digital cadastral surveying using a python-based script in GIS. The cadastral survey is a national product, providing data relating to landownership divided into eleven themes (Fig. 4). The theme “land cover” data contains accurate data on ground cover, such as buildings, roads, bodies of water, forest, etc.

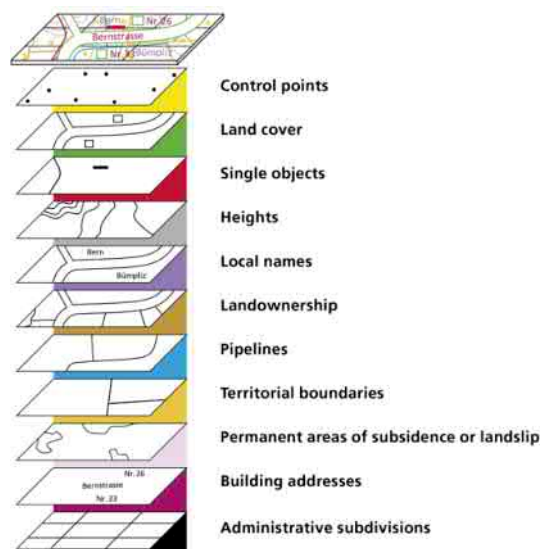


Fig. 4: The eleven information levels of the cadastral survey [3]

The break lines are used to define streams, ridges, shorelines of lakes, building footprints, dams (e.g. of rivers or railways) and other locations of abrupt surface change and/or a change in the land cover (smooth vs. rough). Normally, the extracted break lines have to be generalized to reduce the vertex count in lines that were captured in too much detail by the survey, such as traffic hubs or walls. Walls represent a vertical fault with more than one z-value at a given x-y-location, which cannot be stored in the mesh when using 2D TELEMAT (Fig. 5).

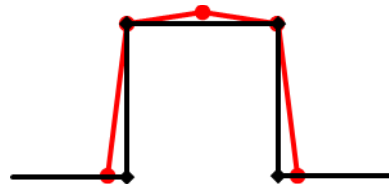


Fig. 5: An example for a wall (cross-section): captured by the survey (black) and adapted for the implementation in 2D TELEMAT (red)

Instead, it is possible to represent a nearly vertical wall with two parallel break lines: one containing surface z-values at the top of the wall, and a second with z-values at the bottom. Usually, an additional break line is added in-between the top break lines with z-values slightly higher than the top break lines. This in-between break line prevents water from overtopping when the water surface reaches (but does not exceed) the upper edge of a protective wall (e.g. next to a river).

The mesh is generated based on the break lines and the DTM using JANET by smile consult GmbH.

### B. Roughness

The bottom friction zones are extracted from the land cover data and categorised accordingly to its roughness. The following seven roughness zones are usually defined:

ROUGHNESS ZONES

Nr.	Roughness table	
	Specification of land cover	Roughness value
1	River bed	27 m <sup>1/3</sup> /s
2	River embankment	25-30 m <sup>1/3</sup> /s
3	Forest	15 m <sup>1/3</sup> /s
4	Humus (meadow, pasture, etc.)	25 m <sup>1/3</sup> /s
5	Paved areas (e.g. streets)	35 m <sup>1/3</sup> /s
6	Buildings*	0-1 m <sup>1/3</sup> /s
7	Non-vegetated areas	20 m <sup>1/3</sup> /s

\* Only footprints of buildings.

Tab. 1: The seven roughness zones, extracted from the land cover data

Fig. 6 shows an example of how the roughness zones are defined according to the land cover data in Tab. 1.



Fig. 6: The roughness zones categorised according to the land cover (above) and the corresponding Orthophoto (below) (Orthophoto: [4])

### C. Initial and boundary conditions

Boundary conditions are defined for the inflow at the inlet and the outflow at the basin outlet of the investigated river, and if necessary, at the basin outlet of eventual flood corridors outside of the main channel. Around the boundary points, pools are created with a bottom height lower than the rest of the domain (to avoid dry boundaries).

A computation is performed, where a constant elevation is initialized at the boundaries. Next, the pools are filled up to the corresponding pool's top edge in this computation. As a result, the entire domain is dry but the pools are wetted. This computation is later on continued with prescribed flow rates at the inlet and prescribed elevation(s) at the outlet(s) for simulating the floods.

The prescribed elevation at the basin outlet is constant in time and sometimes defined by a receiving watercourse or by a lake. The prescribed flow rates at the inlet are variable in time and are prescribed by hydrographs. In some cases, the hydrographs can be derived from the measurement data of past flood events. Usually, as no gauging station is present at the point of interest, synthetically generated hydrographs are used. These are based on the characteristics of the catchment area and the amount of precipitation.

### D. Water sources (Tributaries)

Water sources are placed at junctions where the river is joined by lateral tributaries increasing its discharge. The hazard maps of the tributaries are elaborated separately. The discharge of the tributaries is time-dependent and prescribed by hydrographs. A first computation is performed without any input at the junctions (only input at the inlet of the domain) and its results are used to identify the travel time of the flood peak along the river between the junctions. Based on this information, the hydrographs of the tributaries are adapted in order to achieve a flood with peaks converging.

### E. Culverts, Tubes, and Bridges

In most cases, culverts, tubes, and bridges constitute weak points of the river and as a result of their bottleneck effect, may lead to overflow and altered or even new flow paths, especially within settlement areas. For this reason, the behaviour of these structures must be taken into account in flood modelling to produce a meaningful hazard map:

- Identification of weak points / bottlenecks such as culverts and bridges by means of a general plan, an Orthophoto and use of Google Street View.
- Surveying the geometry of the weak points (length, width, height, total cross-sectional area, constriction, slope, bank heights, material and /or roughness) and assessing the probability of clogging at the weak points by driftwood, debris or other material.
- Definition of the weak points; information about culvert/tube characteristics is stored in the CULVERT DATA FILE.
- The culverts and tubes are then calibrated. By conducting several simulations and adjusting the

characteristics of culverts and tubes (cross-sectional area, losses), the flows computed by 2D TELEMATC are checked and matched with the capacity calculated in a one-dimensional steady flow model (e.g. HEC-RAS).

If driftwood is mobilised in the upper reaches of a forest-covered catchment area, this can lead to partial or complete clogging at weak points downstream. The proportion of clogging of the cross-section depends on the flow velocities and the type and quantity of driftwood. Thus, the cross-section area of the culverts or tubes is reduced by the percentage clogged. For both cases, a simulation is conducted without consideration of floating solids (pure water, primary process) and one with floating solids and possible clogging (secondary process).

In addition to culverts and bridges, pedestrian or road underpasses and tunnels can also play an important role. Underpasses and tunnels can change the flow paths of an inundation and flood areas where flooding is not expected at first glance. They must therefore also be taken into account and defined as culverts or tubes.

#### F. Model Parameters

The computations are run with TELEMATC v7p1 on Linux Ubuntu Mate (16.04.01) with 80 processors on five servers. The Time step is an important parameter: it should be as long as possible (to keep the computation time short), and as short as necessary to meet the CFL criterion (usually determined by the shortest element in the grid where small structures such as walls have to be represented).

Since we have experienced unstable flow directions next to the channels and water emerging and disappearing in flat plains next to the channels in several simulations for various projects, different parameter sets were tested within the scope of this project case. Tab. 5 (at the end of the paper) lists all the parameter sets tested.

### III. PROJECT CASE

#### A. Project Area

The project area consists of one main river and several tributaries in a commune with two separated settlement areas, one in the south and one in the north. The project area is divided into two parts by an important railway-line on a dike: a western part with settlements and infrastructures, a natural eastern part (Fig. 7). The capacity of the culvert through the railway dike is a limiting factor. Various events have confirmed that there is a flood protection deficit.



Fig. 7: Orthophoto showing the settlement areas, the main river (flow direction from left to right) and the railway-line on a dike (black line) (Orthophoto: [5])

#### B. Modelling & Challenges

1) *Tributaries (Water sources)*: The peak flow data for the investigated river at the different junctions of the tributaries are shown in Tab. 2 (for the return period 100 years).

#### HYDROLOGY

Location	Peak discharge in River	$\Delta$ peak discharge at junction	Catchment Area
	$m^3/s$	$m^3/s$	$km^2$
Inflow (0)	17	-	4.3
Junction 1	18	1	4.5
Junction 2	25	7	7.9
Junction 3	26	1	8.3
Junction 4	28	2	9.5
Junction 5	29	1	9.7
Junction 6	31	2	10.0

Tab. 2: Peak discharges in the river at the different junctions for the return period 100 years

The discharge increases by more than 50% along the river by the tributaries. The aim is to determine the hazard posed by the river for the return periods 30, 100, 300 and 1'000 (extreme flood); both with and without taking into account the risk of clogging at selected culverts/tubes. The hazard maps of the tributaries were elaborated separately. Other hazard processes such as surface runoff are not taken into account.

The discharge of the river was supplied by an inflow boundary. On the other hand, there are six lateral tributaries



along the river, which were taken into account through sources at the junctions. At each junction, the peak discharge and a corresponding hydrograph were defined for the (increasing) catchment area. Building the difference of the hydrographs between the junctions  $x$  and  $x-1$  ( $x = 1-6$ ), the hydrograph for the junction  $x$  is obtained. The hydrographs of these sources were adjusted in timing to make the runoffs along the river superimpose, peaking in the values listed in Tab. 2.

For this purpose a computation with sources switched off was carried out. Based on the acquired propagation time of the flood peak between the junctions, the hydrographs of the sources were temporally shifted to adequately reflect the propagation of the flood event.

2) *Culverts, Tubes, and Bridges*: The model contains 18 culverts, some of which have a capacity of  $2 \text{ m}^3/\text{s}$ . However, the focus is on the culvert at the railway dike (Fig. 8), which is the key point in the system, as it divides the project area in two due to its elevated position relative to the flat plain. The modelling has shown that the culvert has a very limited capacity of  $6 \text{ m}^3/\text{s}$  (Fig. 9) and cannot discharge the  $30 \text{ m}^3/\text{s}$  design flood through the dam.



Fig. 8: Culvert through the railway dike [6]

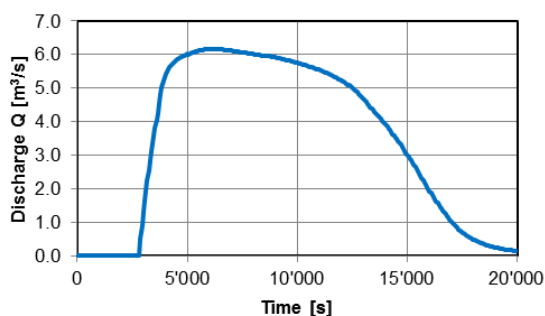


Fig. 9: Time-series of discharge through the culvert during the simulation

Problems have occurred with the modelling of larger culverts/tubes in a wider channel bed because they are only described as couples of points in the grid between which flow may occur (as a function of the respective water level at these points). It has been established that in wider channels the major part of the discharge does not flow to the receiving point of the culvert but flows past it and leads to overflow, although the capacity of the culvert would actually still be

sufficient. Since the modelling of the culverts did not lead to the desired results, further workarounds had to be found: (1) the coupling points of the culverts were lowered, (2) multiple parallel culverts were used, and finally (3) no culverts were used but open channels with built-in bottlenecks to reproduce the cross-sectional area of the culverts.

- The coupling points of the culverts were lowered to change the flow field by aligning the streamlines to the receiving point of the culvert. However, the flow field was only marginally improved with this measure.
- Several parallel culverts were defined, which have the same cumulative capacity as the actual culvert. The intention was to distribute the runoff to multiple receiving points to prevent it from over-flowing. However, counter-current flow and general instabilities have occurred at the downstream points of certain culverts, which have falsified the results.
- No culverts were used but open channels with built-in bottlenecks to simulate the cross-sectional area of the culverts. However, the modification of the open channel to replicate a culvert is very time-consuming and error-prone. In the case of longer culverts, the problem arises that the water that has been spilled out upstream of the culvert can flow back along the route of the culvert, even though the culvert would actually be underground.

3) *Roughness*: Determining the roughness based on the land cover data is a simple and reliable method. It opens up the possibility of carrying out computations with different roughness values for specific land covers.

4) *Consideration of buildings*: The buildings are primarily modelled as impenetrable obstacles. However, analyses of past flood events have shown that buildings are not always an impenetrable obstacle to runoff and in certain cases can be crossed by floods. Particularly in larger buildings, different flow paths occur depending on whether they were modelled as impenetrable or crossable obstacles.

For this reason, usually two computations for the roughness values of buildings are performed:

- Strickler =  $0 \text{ m}^{1/3}/\text{s}$ , to model the buildings as impermeable obstacles in the grid, and
- Strickler =  $1 \text{ m}^{1/3}/\text{s}$ , to model the buildings as permeable/traversable for floods

Industrial complexes constitute a special case as some buildings may have openings, e.g. in the form of a stock hall. Such a complex can be traversed using the second method, which may have the effect of slowing down the flood wave and possibly reducing the peak discharge.

If buildings in a sink are flooded, (1) the damming at the building shell can be determined using the first method and (2) the traversing flow through the buildings, as soon as the openings no longer withstand the water pressure and break, can be determined using the second method (Fig. 10).

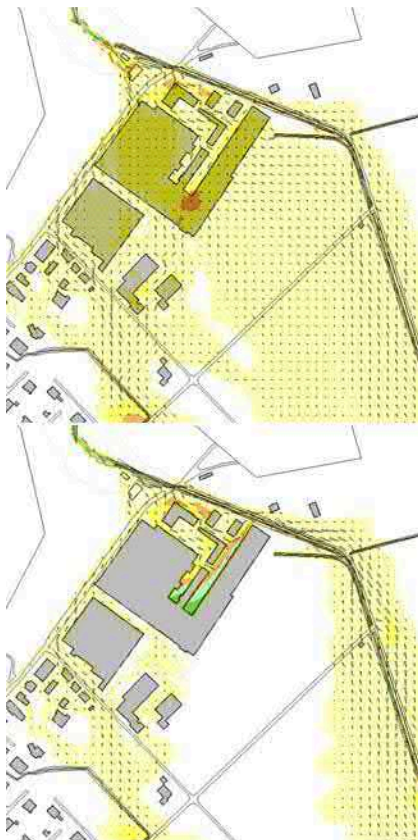


Fig. 10: Complex modelled as impermeable obstacle, Strickler  $0 \text{ m}^{1/3}/\text{s}$  (above) and as permeable, Strickler  $1 \text{ m}^{1/3}/\text{s}$  (below) (Background: [5])

**Calibration and Verification:** By adjusting the parameters (Strickler), the calculated water levels of an observed flood event are checked and matched to the gauging measurements recorded. Tab. 3 shows the measured and the calculated values for water depth and discharge of another project case/river with a gauging station.

MEASUREMENTS VERSUS CALCULATIONS

Variable	Measured at gauging station	Calculated 2D TELEMAC
Water level [MASL]	404.83	404.72 (water depth = 3.6 m)
Discharge [ $\text{m}^3/\text{s}$ ]	110 $\pm$ 10*	115

\* The discharge at the gauging station is derived from measured water level and known stage-discharge curve. This derivation is associated with a certain uncertainty in the high water range, as the stage-discharge curves are usually extrapolated.

Tab. 3: Measured/observed values at gauge vs. calculated values

Our models typically present important topographic gradients, tidal flats and steep banks. The objective is to find a parameter set which presents...

- reasonable water lines in flat ( $\sim 1\%$ ) channels, steep ( $\sim 10\%$ ) channels and in the flood plain
- reasonable flood propagation in the flood plain, no water disappearing in the flood plain
- no flow direction artefacts in the channel producing erroneous discharge to the plain (unrealistic flow

directions going upwards the embankment resulting in a discharge from the channel to the plain, even though the water level is way below terrain)

Different parameter sets were tested (Tab. 5 at the end of the paper) based on the recommendations from the user manual [7] and posted in the forum ([www.opentelemac.org](http://www.opentelemac.org)). The recommendation with tidal flat are TYPE OF ADVECTION = 1;5;14 or 14;5;14. Based on this, two runs different keywords mentioned in the recommendations were modified singularly and the results evaluated. The meaning of the keywords can be found in the TELEMAC-2D reference manual [8]. The results are presented in Tab. 4. It has emerged that the parameter set T14 is best suited for our field of application. It consists of a TYPE OF ADVECTION = 1;5;14 and a TREATMENT OF NEGATIVE DEPTHS = 1.

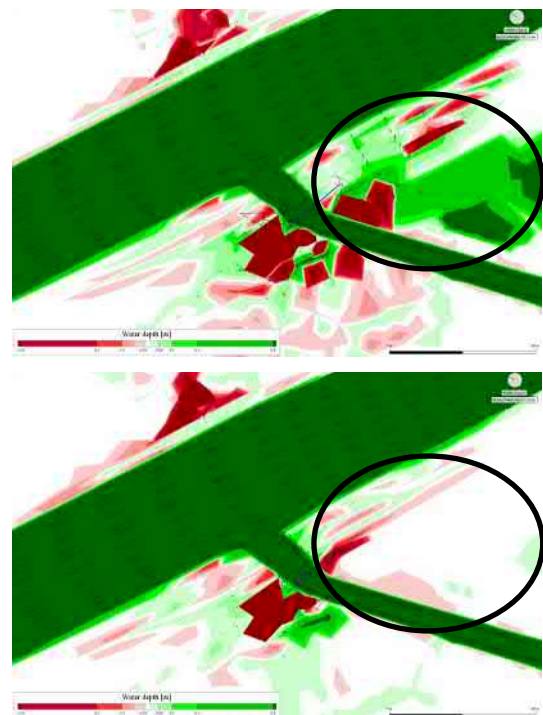


Fig. 11: Water depth in the main channel and the tributary of another project case to illustrate the positive water depth = green and the negative depth = red. The results yielded with parameter sets T10 (above) and parameter set T11 (below).

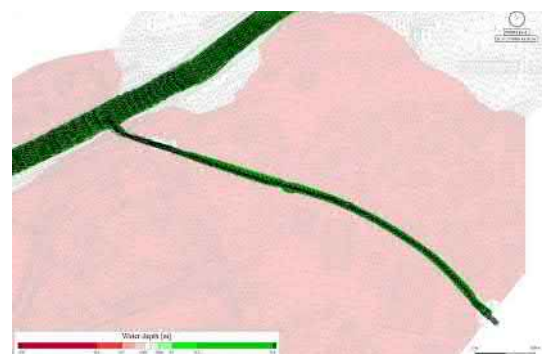


Fig. 12: Water depth of another project case to illustrate the positive water depth = green and the negative depth = pink propagating over the plain.



## RESULTS

Test	Modifications of keywords to T1	Courant number	Computation rate	Total volume lost	Water line	Artefacts because of steep banks	Conclusions
		-	-	m <sup>3</sup> /s			
<b>T1</b>		1.96	0.09	-0.31	Smooth	Local erroneous discharge to the plain because of artefacts in the flow direction	Strong oscillation of the water line, computation rate is poor as well as the water balance in comparison with T1. Rejected solution because of quality of the results and performance.
<b>T2</b>	TYPE OF ADVECTION = 14;5;14 NUMBER OF SUB-ITERATIONS FOR NON-LINEARITIES=10 instead of 1	1.41	0.74	-16.2	Strong oscillations	Similar to T1, little more discharge to the plain	Rejected solution because of quality of the results.
<b>T3</b>	Based on T2, DISCRETIZATION IN SPACE to 11;11 instead of 12;11 and TREATMENT OF NEGATIVE DEPTHS = 2 instead of 0	0.38	0.09	0.00	Similar to T1	more artefact around the steep banks as T1	Shows similar results and performances as T2, but with a better water balance. Rejected solution because of quality of the results and performance.
<b>T4</b>	Based on T3, NUMBER OF SUB-ITERATIONS FOR NON-LINEARITIES=10 instead of 1.	0.38	0.74	0.00	Similar to T2	more artefact around the steep banks as T1, even as T3	Shows similar results of the water lines as T2 but with a performance equal to T1 and a good water balance. Rejected solution because of quality of the results.
<b>T5</b>	TYPE OF ADVECTION = 14;5	0.38	0.09	0.00	Similar to T2	Similar to T3	-
<b>T6</b>	TREATMENT OF THE LINEAR SYSTEM = 1 instead of 2	-	-	-	-	Could not be run	Shows erroneous water line at the confluence, a poor courant number and a poor water balance. Rejected solution because of quality of the results.
<b>T7</b>	DISCRETIZATION IN SPACE = 11;11 instead of 12;11	2.31	0.06	-6.97	Oscillations and high level in comparison to the other runs	Very important number of erroneous discharge. Even building (400 m higher than the plain) are flooded	-
<b>T8</b>	OPTION FOR DIFFUSION OF VELOCITIES= 2 instead of the default value 1	-	-	-	-	Could not be run	Shows similar water lines and computation rate as T1, slightly better courant number as T1 but poorer water balance. Rejected solution because of quality of the water balance
<b>T9</b>	MASS-LUMPING ON H and MASS-LUMPING ON VELOCITY = 0 instead of 1	1.66	0.09	7.25	Similar to T1	Similar to T1	Shows strong artefacts at the confluence. Rejected solution because of quality of the results.
<b>T10</b>	FREE SURFACE GRADIENT COMPATIBILITY = 1 instead of 0.9	1.91	0.09	-0.35	Smooth and lower level in comparison to the other runs	Instabilities at the water mouth between large main river and tributary. (Fig. 11).	Shows similar results as T1 with better courant number. The water balance is slightly inferior. The performance is equal. Rejected because other combination shows better results
<b>T11</b>	FREE SURFACE GRADIENT COMPATIBILITY = 0.8 instead of 0.9	0.39	0.09	-0.87	Similar to T1	Similar to T1.	Shows similar results as T1 with a poor water balance. (Fig. 11).
<b>T12</b>	SOLVER = 7 instead of 1	1.96	0.10	-3.45	Similar to T1	Similar to T1	Shows strong artefacts at the confluence. Rejected solution because of quality of the results.
<b>T13</b>	OPTION FOR THE TREATMENT OF TIDAL FLATS = 3 instead of 1	0.38	0.09	0.10	Smooth and higher level in comparison to the other runs	Instabilities at the water mouth between large main river and tributary	Shows a smooth water line. In the steep channel the water line is high but comprehensible. In the flat channel the difference is no so important. No erroneous discharges along steep banks are observed. But desired flood propagation in the plain could be underestimated.
<b>T14</b>	TREATMENT OF NEGATIVE DEPTHS = 1 instead of 0	0.38	0.08	-0.85	Smooth and higher level in comparison to the other runs, even than T13	No artefacts, important development of negative depth in the entire plain.	Fig. 12

Tab. 4: Results of tested parameter set

### C. Results of modelling the Project Case

1) *Initial state:* So far, it has been assumed that the uncultivated area to the right of the railway dike would be flooded and that the settlement areas in the northeast of the commune would not or only to a small extent be affected by flooding. However, the new simulations have shown that the culvert through the railway dike has a limited capacity to  $6 \text{ m}^3/\text{s}$  as a result of which the design flood of  $30 \text{ m}^3/\text{s}$  cannot be discharged to the other side of the dike. The inundation maps show that the majority of the flooding is on the left side of the railway dike and that the northern settlement area is considerably more endangered than originally thought (Fig. 13).

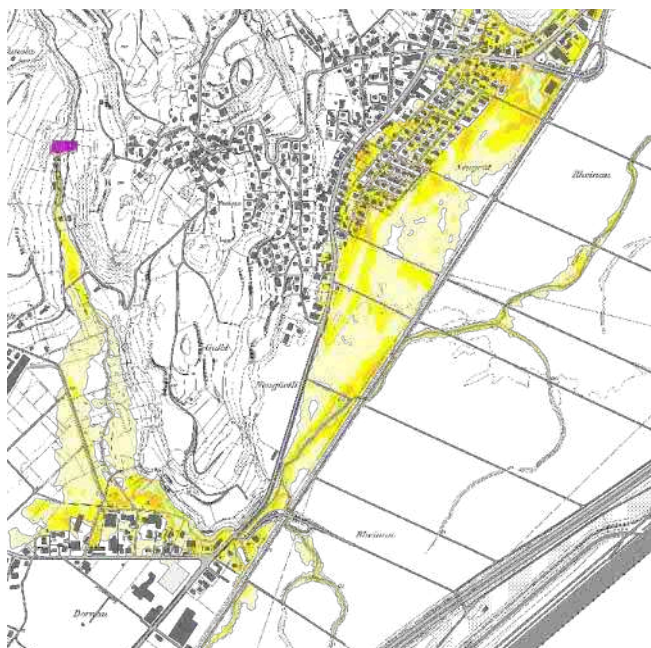


Fig. 13: Inundation map (return period 100 years) (Background: [5])

2) *Project state:* On the right side of the railway dike would be enough space for a natural retention area, but it is difficult to conduct the discharge to the other side of the dike because (1) the slope is extremely flat and leads to a significant backwater effect, and (2) the capacity of the culvert is not sufficient. The expansion of the railway culvert including the downstream channel to a capacity of  $30 \text{ m}^3/\text{s}$  is technically complex and economically unfavourable considering the large span required below the railway dike. The flood area on the left must therefore be limited to a man-made retention basin to be able to protect the settlement areas in the north from flooding.

### IV. CONCLUSIONS

With the described methods for hazard/flood mapping by using 2D TELEMAC good results can be achieved. It allows an efficient delimitation of hazard areas under consideration of different aspects such as culverts, buildings, etc. This is essential for large-scale assessments with many origins of danger.

Nevertheless, the modelling of larger culverts or tubes has revealed a number of problems: (1) The culvert or tube geometry cannot be reproduced adequately and some simplification is required, (2) the definition of the culverts with the node numbers is not optimal, because an adaptation of the model grid after verification of the results in the field requires the adaptation of the CULVERT/TUBE DATA FILE, and (3) the calibration of the culvert is time-consuming and error-prone. The tested workarounds did not really improve the situation. It might be advisable to model the larger culverts or bridges as modified weirs that are considered as linear singularities across the channel (in contrast to the culverts or tubes, which are defined as punctual singularity).

To improve the quality of the results and to reduce the effort for the analyses, the Python scripts and workflows used are constantly being further developed. An important aspect is to adjust the mesh resolution to the size of the channels, which reduces numerical problems such as negative water depths and the occurrence or disappearance of water. However, the problem can be observed in small channels with steep slopes or walls in particular. For these cases, no solution could be found so far so that a time-consuming review of the results is still necessary.

### REFERENCES

- [1] Tiefbauamt Stadt Schaffhausen
- [2] Bundesamt für Umwelt BAFU (2019, August 31). Auswertungen zum Gewässernetz. Retrieved from URL <https://www.bafu.admin.ch/bafu/de/home/themen/wasser/zustand/karten/gewaessernetz-der-schweiz.html>
- [3] Cadastre.ch (2019, August 31). Information levels & data. Retrieved from URL <https://www.cadastre.ch/en/av/result/layer.html>
- [4] Abteilung Geoinformation, Kanton Schwyz
- [5] Amt für Raumentwicklung und Geoinformationen, Kanton St. Gallen
- [6] Naturgefahrenanalyse, Kanton St. Gallen
- [7] User manual Telemac-2D Software, release 7.0, 12/2014
- [8] Reference manual Telemac-2D Software, release 6.2 07/2013

## COMPUTATION PARAMETERS

Runs	Computation parameters												
	Type of Advection	SUPG Option	Number of sub-iterations for non-linearity	Discretization in space	Option for Diffusion of Velocities	Mass-Lumping on $H$	Mass-Lumping on Velocity	Treatment of the linear system	TIDAL FLATS	Free surface gradient compatibility	Solver	Option for treatment of tidal flats	Treatment of negative depths
T1	1;5;14		1	12;11		1	1	2	YES	0.9	1	1	0
T2	14;5;14		10	12;11		1	1	2	YES	0.9	1	1	0
T3	14;5;14	0;0;0*	1	11;11		1	1	2	YES	0.9	1	1	2
T4	14;5;14	0;0;0	10	11;11		1	1	2	YES	0.9	1	1	2
T5	14;5	0;0;0	1	11;11		1	1	2	YES	0.9	1	1	0
T6	1;5;14		1	12;11		1	1	1	YES	0.9	1	1	0
T7	1;5;14		1	11;11		1	1	2	YES	0.9	1	1	0
T8	1;5;14		1	12;11	2	1	1	2	YES	0.9	1	1	0
T9	1;5;14		1	12;11		0	0	2	YES	0.9	1	1	0
T10	1;5;14		1	12;11		1	1	2	YES	1	1	1	0
T11	1;5;14		1	12;11		1	1	2	YES	0.8	1	1	0
T12	1;5;14		1	12;11		1	1	2	YES	0.9	7	1	0
T13	1;5;14		1	12;11		1	1	2	YES	0.9	1	3	0
T14	1;5;14		1	12;11		1	1	2	YES	0.9	1	1	1

\* With adaption to the recommendation 2;0 (User manual) run breaks off.

Tab. 5: Computation parameters: if no value is specified, default values were used. The recommendations in the User Manual and the TELEMAT-forum were regarded. Equations for all sets: SAINT-VENANT EF. THRESHOLD FOR NEGATIVE DEPTHS = default values

# Application of the TELEMAC-3D to simulate flooding and hydrodynamic patterns of Southern Brazilian wetlands

Juliana Costi, Aldair Forster, Wiliam C. Marques

Instituto de Matemática, Estatística e Física  
Universidade Federal do Rio Grande  
Rio Grande, Brazil  
ju.costi@gmail.com

Raquel de F. Duarte, Jorge Arigony-Neto

Instituto de Oceanografia  
Universidade Federal do Rio Grande  
Rio Grande, Brazil

**Abstract**—Wetlands are highly productive systems that provide valuable ecosystem services. In the extreme south of Brazil, extensive wetlands are protected areas with global importance recognized by the RAMSAR convention ([www.ramsar.org](http://www.ramsar.org)). The Mirim – São Gonçalo system is comprised by a shallow coastal lagoon (Mirim lagoon) that receives the discharge of three main tributaries at its southern region, and drains towards the Patos Lagoon estuary through a 78 km long channel (São Gonçalo Channel), at its northern tip. The system lies on a wide coastal plain with flat topography and very low permeability, favouring the occurrence of extensive wetlands surrounding the permanent water bodies. The system is the main source of water for agricultural irrigation and urban supply. The establishment of a binational (Brazil – Uruguay) waterway is under discussion, though very few studies have addressed the circulation of the lagoon and the channel, and their impacts on the wetlands. In this study, we ran a one-year simulation using the TELEMAC-3D to investigate the hydrodynamics of the Mirim – São Gonçalo system, to understand how the permanent water bodies hydrodynamics can affect the flooding patterns of wetlands. We validate the model results using European Remote Sensing 2 mission (ERS-2) derived flood maps of seven different dates, and water level time series measured in two different locations. The average agreement between the simulated flood extent and the ERS-2-derived flood maps was 65%. Regarding water level, the average error was -0.6 m and the correlation coefficient was 0.61. The prevailing winds from the northeast over the lagoon imply that, normally, higher water levels occur in the south of the lagoon. However, the wetlands that fringe the northern sector of the lagoon show average water levels higher than those observed for the southern wetlands. This may be explained by the choked configuration of the lagoon at its northern sector. Once the prevailing current is northwards, the constriction of the connection between the lagoon and the channel causes a damming effect, resulting in further overflow towards the fringing wetlands. On the other hand, the highest standard deviation of the free surface elevation was found for the southern wetlands, which is related to the effects of the passage of cold fronts. These atmospheric systems cause the inversion of the prevailing northeast wind toward the southwest and, consequently, the direction of the barotropic gradient and the prevailing current. Thereafter, the flooding patterns observed for the wetlands that fringe the Mirim lagoon are not directly associated to the water level in the

lagoon, but to the circulation forced by the wind and to the geomorphology of the region. Such patterns are in agreement with the velocity fields observed for the Mirim lagoon, which are more variable in the southern sector, whereas in the northern region it is consistently directed towards the wetlands.

## I. INTRODUCTION

The conservation of wetlands is highly relevant for maintaining the multiple ecosystem services that they provide. Understanding the physical processes acting on wetlands and their variability is primary for their correct management and sustainable development. In the extreme South of Brazil, extensive wetlands surround the largest lagoon complex of Latin America, formed by the Mirim (ML) and Patos lagoons connected by the São Gonçalo channel (SGC). Even though they are legally protected areas, agricultural, urban and industrial activities constantly pressure the natural system.

This bi-national (Brazil – Uruguay) hydrological system has enormous environmental and socio-economic importance. Surrounding the lagoon and the channel, highly productive wetlands shelter a rich biodiversity [1]. Moreover, wetlands have a part in the carbon biochemical cycle, being the largest source of methane for the atmosphere [2,3]. The establishment of a bi-national waterway is under discussion, which will require dredging operations and impose further risks for the environmental safety. Though, wetlands of the extreme South of Brazil have been the subject of a limited number of studies.

In the present study, we employed the TELEMAC-3D model to investigate the flooding patterns and hydrodynamics of the wetlands that surround the Mirim lagoon and the São Gonçalo channel during the year 2000. We focus the analysis on the identification of spatial variations of wetlands that can be related to the hydrodynamics of the water bodies that they fringe. By applying the TELEMAC-3D, the representation of the hydrodynamics was improved compared to TELEMAC-2D, with an additional computational cost that was considered worth for the objective of this study.

### A. Study Area

The southern Brazilian coast, located between 29.5°S and 32°S, comprises a large coastal plain shaped by recent sea level fluctuations led by glacial-eustatic adjustments. The system developed and evolved after successive marine regressions and transgressions during the Quaternary, resulting in the sequential deposition of four barrier-lagoon depositional systems [4].

The coastal plain is formed by typical barrier-lagoon deposits, which explains its flat, micro-topographical terrain, and the occurrence of several lakes and lagoons. The lagoon complex formed by the Mirim and Patos lagoon, both connected by the 78 km long São Gonçalo channel (Fig. 1), is the largest lagoon complex of Latin America. These water bodies are fringed by extensive wetlands and floodplains that are often flooded.

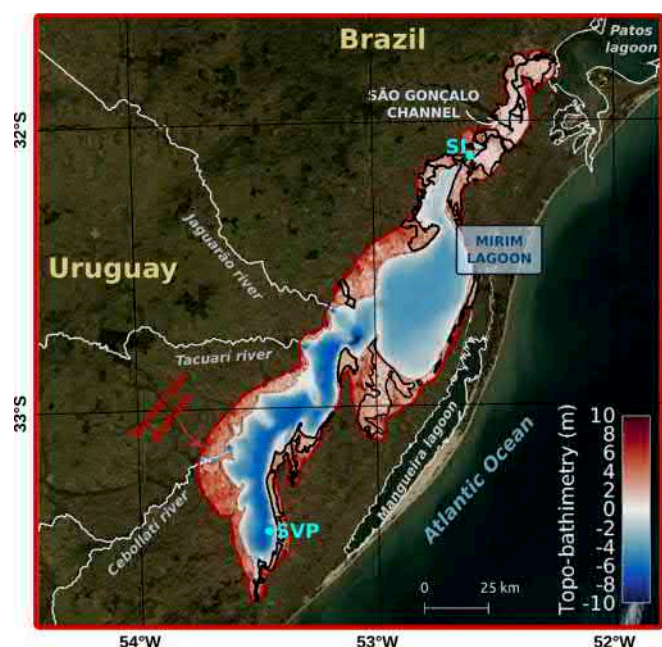


Figure 1: Map showing the location of the Mirim Lagoon, the São Gonçalo channel and their surrounding wetlands (black polygons). The red polygon corresponds to the numerical domain, and the cyan dots show the location of the Santa Izabel (SI) and Santa Vitoria Port (SVP) gauge stations.

The Mirim lagoon is a shallow transboundary coastal lagoon, with maximum depths reaching 12 m and covering an area of approximately 3,749 km<sup>2</sup>. Its catchment basin drains a large area, with abundant and well-distributed precipitation over the year [5], and includes Brazilian and Uruguayan rivers. The main tributaries are the Jaguarão, Tacuari and Cebollati rivers.

The Mirim lagoon does not have a direct connection with the ocean, but is connected with the estuary of the Patos lagoon. Though, a sluice gate built near the São Gonçalo channel's mouth prevents the inflow of brackish towards the ML. Its major axis has an azimuth of 43°, which is nearly the orientation of the prevailing winds. The system works as a water reservoir, supplying water for human consumption,

agricultural production and industrial processes. Large inputs of fresh, nutrient-rich waters are exported towards the estuarine region and, subsequently, to the coastal sea.

The prevailing winds are from Northeast over the year. During the passage of cold fronts and extra tropical cyclones, winds are from the Southern quadrant. The wind strongly influences the lagoon hydrodynamics in the synoptic time scale, and river discharge dominates the water level variability from annual to intra-seasonal time scales [6].

### II. METHODS

We ran a simulation using the TELEMAC-3D model covering the period starting on 1 January 2000, until 31 December 2000. This is the first year when discharge data of the main Mirim lagoon tributaries is available.

A numerical grid with 63,401 nodes was constructed using the Blue Kenue software. Bathymetry data of the water bodies was obtained from navigation charts, provided by the Brazilian Navy. Elevation data of the surrounding areas was extracted from the TANDEM-X digital elevation model [7]. The bottom friction was set to Manning's coefficient of 0.035 inside the ML and the SGC and to 0.05 in the flooding areas, in accordance with the values estimated by [8] for muddy to silty bottoms and grasslands.

We activated the treatment of tidal flats, using the default option (equations solved everywhere with correction on tidal flats). We considered constant viscosity for horizontal and vertical turbulence with coefficients of  $10^{-6}$ . Density law was set to density as function of temperature. The implication value for depth and velocity was set to 1. The advection schemes for velocities and advection of tracers was set to 14 (N-scheme for tidal flats).

The superficial conditions were forced using ERA-interim reanalysis data interpolated for each node of the mesh. We used time series of the *u* and *v* components of wind velocity, atmospheric pressure at the surface and air temperature at 2 m above surface obtained each 6 hours. Air temperature is taken into account through direct programming in the BORD3D subroutine, allowing representing the heat exchanges between water and atmosphere. Fig. 2 represents the average time series of the superficial conditions and the total discharge of the tributaries during the simulation period. As the initial conditions were not known, we ran a warm-up simulation of 1 year using an average time series of river discharge calculate from measurements carried out over 5 years (2000 – 2004) to force the liquid boundaries, and atmospheric data corresponding to the year 1999.

The computational domain was defined considering the topography of the region, with four open liquid boundaries: the Jaguarão, Tacuari, and Cebollati rivers and the mouth of the São Gonçalo channel. The liquid boundaries are forced with discharge data measured in gauge stations placed in the



three most important tributaries and water level measurements carried out near the SGC mouth. The Brazilian National Water Agency distributes these data through its website (<http://hidroweb.ana.gov.br>).

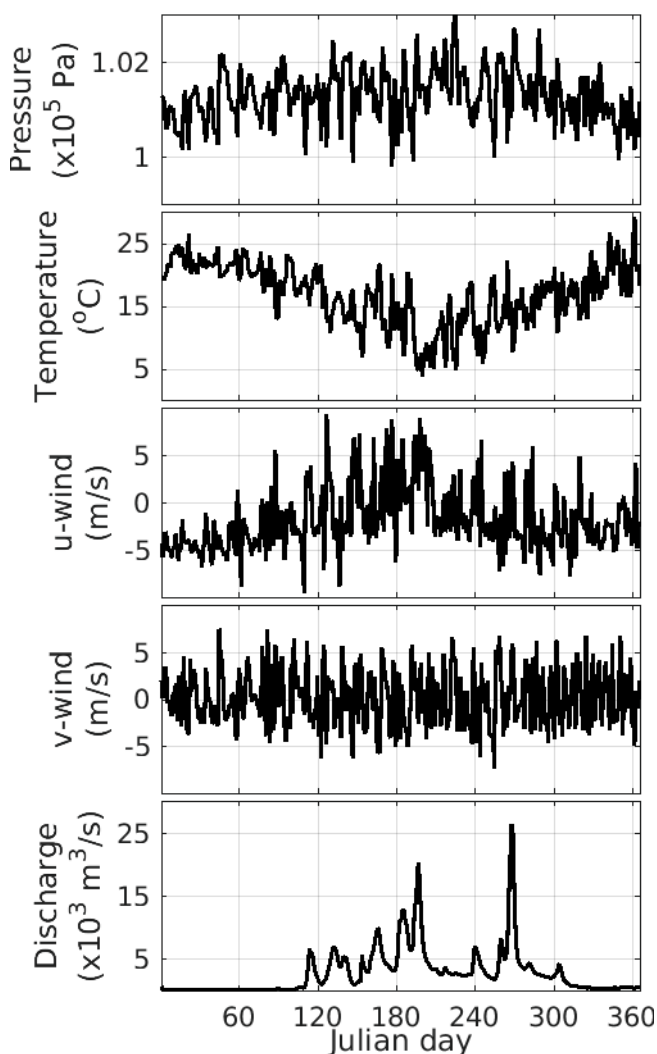


Figure 2: Time series of the average surface boundary conditions considered in the present study, and total discharge of the three main tributaries of the Mirim lagoon (Jaguarão, Tacuari and Cebollati rivers).

To validate the model results, we used water level time series measured at two different gauge stations and flood extents derived from ERS-2 imagery covering the São Gonçalo channel wetlands. The Santa Vitória gauge station is located at the south of the lagoon, and the Santa Izabel gauge station is located in the São Gonçalo Channel, near its connection with the lagoon (Fig. 1). The measurements are performed in a daily basis by the Mirim Lagoon Agency (<https://wp.ufpel.edu.br/alm/agencia/>).

A dataset of ERS-2 imagery from 7 different dates was used to derive flood extent maps and validate the modelled flood extent. The ERS-2 derived flooding extents were

obtained using a threshold method, developed specifically for the study area, based on the image histogram analysis and the visual inspection of the ERS-2 [9] imagery in combination with a LANDSAT ETM+ image [10]. The pixels located on the floodplain with backscattering values lower than -8 dB and higher than -12 dB are classified as wet, while those presenting backscattering values smaller than -12 dB are classified as flooded [10].

The calibration, geometric correction and speckle-filtering were performed using the SNAP software. The water bodies were masked out, and the pixels were then classified as flooded and not flooded using the regional algorithm, developed specifically for the study area.

Considering the hydrodynamics of the study area, we subdivided the wetlands in three larger groups: wetlands that surround the São Gonçalo Channel, the northern Mirim lagoon (north of Jaguarão river), and the southern Mirim lagoon (south of Jaguarão river). This division of the lagoon was based on the study of [6], which showed that water levels are, in average, higher in the southern region due to the action of the prevailing winds. Moreover, the lagoon width abruptly increases at the Jaguarão river latitude, whereas the tributaries discharge at the southern sector.

### III. RESULTS AND DISCUSSION

To investigate the hydrodynamic behaviour of the Mirim Lagoon, the São Gonçalo channel and their adjacent wetlands, we performed a one-year simulation using the TELEMAC-3D model. Considering the morphological and hydrodynamic characteristics of the study area, the wetlands were divided in three sectors. The São Gonçalo channel group comprises the wetlands that fringe the channel, whereas the North and South groups comprise the wetlands that fringe the northern and southern sectors of the Mirim lagoon, respectively. The Jaguarão river was considered the limit between North and South sectors, i.e., wetlands fringing the Mirim lagoon and located north (south) of the Jaguarão river were grouped in the North (South) sector.

Figure 3 presents a comparison of the water level time series measured at Santa Izabel (3.a) and Santa Vitória Port (3.b) gauge stations, and the ERS2-derived flooded area (3.c), against the modelled results. The simulated water level presented an average error of -0.6 m and the correlation coefficient between the simulated and measured data was 0.61. The largest discrepancies occur concomitantly with the two most pronounced discharge peaks, when the model overestimated the water level.

The flooded area simulated with TELEMAC-3D showed a general good agreement with the ERS2-derived, except for the first image, when TELEMAC-3D largely underestimated the flooded area. This may be explained by the uncertainties involved in the beginning of the simulation period, as the initial conditions were unknown. The spatial average agreement between modelled and ERS2 flooded area was 65%.

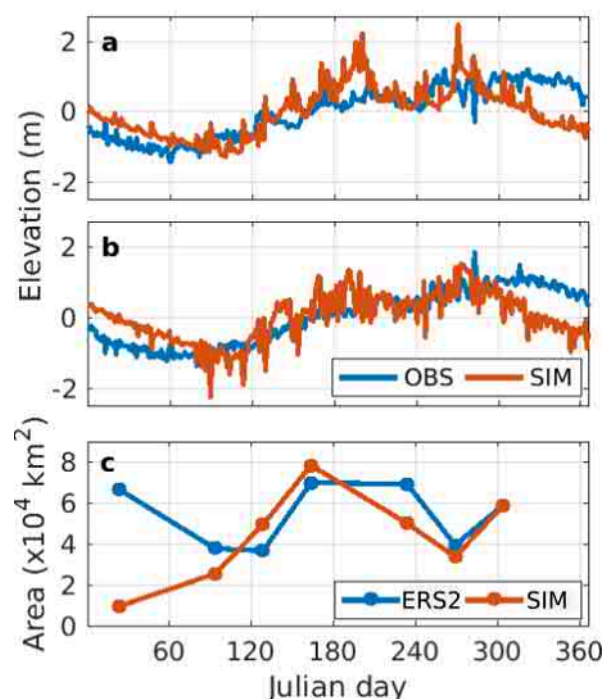


Figure 3: Blue (red) lines indicate observed (simulated) water levels in a) Santa Izabel and b) Santa Vitória Port gauge stations. The c panel present the flooded area as estimated by ERS2-derived mapping (blue line) and TELEMAC-3D (red line).

In comparison with the flooding area simulated by [6] using the TELEMAC-2D model, TELEMAC-3D provided a better estimative of the flooding temporal behaviour. The TELEMAC-2D failed in represent the decrease of the flooded area after the peak near the middle of the year, whereas TELEMAC-3D provided results that better approximate to those observed by the ERS2 data. Despite the higher computational costs for running three-dimensional hydrodynamic simulations, the improved representation of the physical processes may justify their employment, especially for regions where field measured data is poor and/or scarce, representing considerable sources of error. The computational time for running a 1-year simulation with TELEMAC-3D was about 5 times larger than for running the TELEMAC-2D (1 day with an Intel core i7 processor of 8 cores).

The water depth time series for each sector is represented in Fig. 4 a (wetlands) and Fig 4 b (permanent water bodies). The overall variability of the water depth time series present patterns similar to those observed for the water bodies. The seasonal variability is associated to higher discharges during the autumn and winter, which causes the most pronounced variations in water levels. The higher frequency oscillations are associated to the hydrodynamic response of the system to the incident wind direction.

The prevailing wind direction in the study area is from Northeast, which implies in higher water levels at the

southern Mirim lagoon during most of the time. The establishment of a wind-induced barotropic gradient northward, allied to the tributaries discharge, induces a prevailing northward current. However, the passage of atmospheric systems such as cold fronts and cyclones causes the inversion of the wind direction to Southwest. These synoptic events are more frequent during the winter and spring, and cause temporary inversions of the prevailing current to southwards. Considering this behaviour, it would be expected that wetlands surrounding the southern Mirim lagoon would show higher water levels compared to those fringing the northern sector of the lagoon. Nevertheless, the opposite is observed, and further higher depths are found at the SGC wetlands.

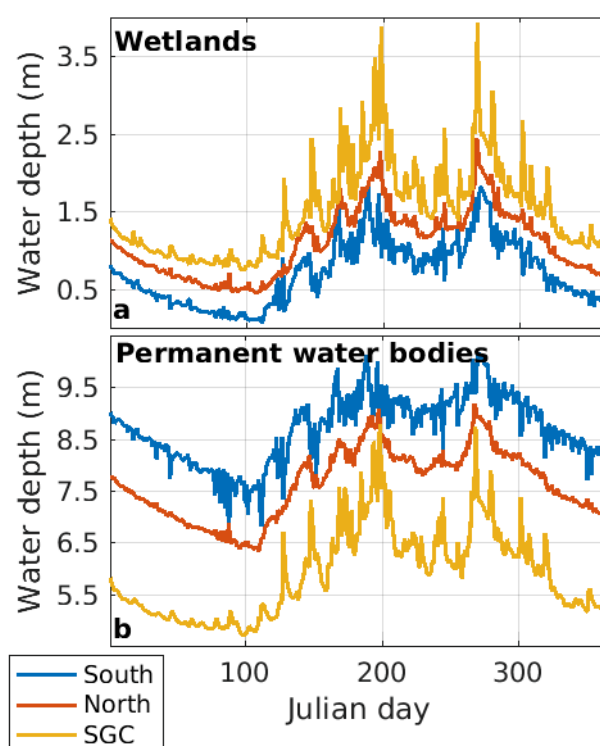


Figure 4: Time series of the water depth simulated by TELEMAC at the South, North and SGC wetlands (a) and water bodies (b).

The difference among the SGC and Mirim lagoon wetlands water depth may be explained by the terrain elevation. The SGC wetlands average elevation is 1.6 m, whereas either southern and northern Mirim lagoon wetlands is 2.9 m. On the other hand, the difference among North and South cannot be explained by the terrain topography, as both wetlands groups have nearly the same average elevation.

By analysing the time series of currents velocity at the wetlands (Fig. 5) we observed that the zonal (u) component of the southern group is considerably more variable, and present more pronounced negative values compared to the north. Once the southern wetlands are located to the east of

the lagoon, the circulation favours the water to flow back towards the lagoon, decreasing the storage of water in the wetlands. The fact that the southern sector of Mirim lagoon presents slightly higher depths may also contribute to less water being stored in the wetlands.

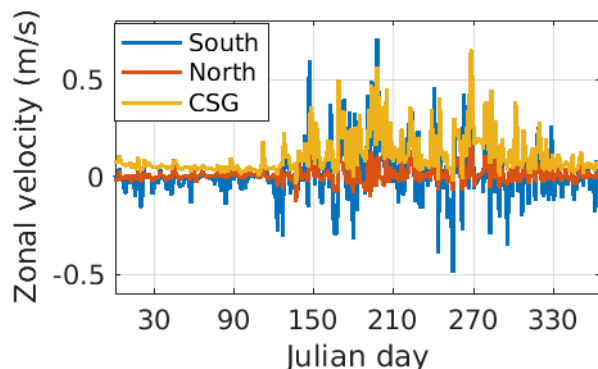


Figure 5: Time series of the average zonal (u) velocity of each wetland group.

[11] simulated the behaviour of lagrangian drifters to investigate the water residence time of Mirim lagoon. The authors observed less drifters being transported to the wetlands in the southern Mirim lagoon in comparison to the northern region. Nevertheless, higher residence times are observed in the south as a result of the dynamic circulation barrier imposed by the Cebollati river discharge.

The northern sector of the Mirim lagoon, on the other hand, presents a physical circulation barrier imposed by its choked connection with the São Gonçalo Channel. Allied to the shallower depths, it may explain the larger water levels simulated on northern wetlands compared to the south. Once the water flows preferably towards north, larger amounts of water are being exported to the wetlands at the northern Mirim lagoon, despite the normally higher water levels observed in the south.

The average water depth of the wetlands is represented in Fig 6 for each season of the year 2000. All wetlands present minimum water depth in summer, increasing in autumn and reaching the maximum in winter, and decreasing again in spring. This general pattern follows the tributaries discharge behaviour, which is the dominant factor determining the wetlands flooding. However, it is worth noting that the highest discharge peak occurred in the spring, which did not determine higher levels in the wetlands compared to winter.

#### IV. CONCLUSIONS AND OUTLOOKS

In the present paper, we analysed the results of a one year hydrodynamic simulation of the Mirim-São Gonçalo complex. The temporal variability of the wetlands water depth is dominated by the river discharge, but spatial differences are associated to the hydrodynamics of the lagoon and the terrain elevation.

Our results showed that the zonal (u) component of the current velocity is different for the North and South Mirim lagoon wetlands. The wind action is responsible for imposing an average setup in the southern part of the Mirim lagoon, though the wetlands of this sector present lower water levels, which may be explained by larger zonal velocities directed toward the lagoon during the winter.

To better address the relationship between the hydrodynamics the water bodies and their fringing wetlands, it is important to perform simulations covering longer periods of time. River discharge and winds are the main factors controlling the hydrodynamic temporal variability in the study region, and both are largely influenced by climate teleconnections such as the El Nino – Southern Oscillation and the Southern Annual Mode. The investigation of such lower frequency variability requires longer-term simulations.

Future studies are being designed to include the Patos lagoon and its surrounding wetlands in the numerical domain, including salt marshes. Additionally, it will allow the representation of a transient connection of the São Gonçalo channel wetlands with the Patos lagoon, which is not considered in the present study.

#### ACKNOWLEDGEMENTS

The authors acknowledge the support of the Coordenação de Aperfeiçoamento de Pessoal de Nível Superior (CAPES) for the Post-Doctoral fellowships and the Conselho Nacional de Desenvolvimento Científico e Tecnológico (CNPq) under contract 304227/2016-1. Further acknowledgements go to the Brazilian Navy for providing detailed bathymetric data for the coastal area; the Brazilian National Water Agency and ERA-Interim reanalysis project for supplying the validation and boundary conditions data sets, respectively; the Open Telemac-Mascaret Consortium for freely distribution of the TELEMAC system making viable this research, the Deutsches Zentrum für Luft- und Raumfahrt for the TADEM-X digital elevation model, to the Supercomputing Center of the Federal University of Rio Grande do Sul (CESUP-UFRGS) and the National Laboratory of Scientific Computing (LNCC), where most of the computational work was carried out. Although some data were taken from governmental databases, this paper is not necessarily representative of the views of the government.

#### REFERENCES

- [1] Asmus, M. L. (1998). A Planície Costeira e a Lagoa dos Patos. In U. Seeliger, C. Odebrecht, & J. P. Castelo (Eds.), *Os ecossistemas costeiro e marinho do extremo sul do Brasil* (pp. 9–12). Ecossentia.
- [2] Wang, Z., Zeng, D., & Patrick Jr, W. H. (1996). Methane emissions from natural wetlands. *Environmental Monitoring and Assessment*, 42, 143–161.
- [3] Meng, L., Roulet, N., Zhuang, Q., Christensen, T. R., & Frohking, S. (2016). Focus on the impact of climate change on wetland ecosystems and carbon dynamics. *Environmental Research Letters*, 11, 1–4.

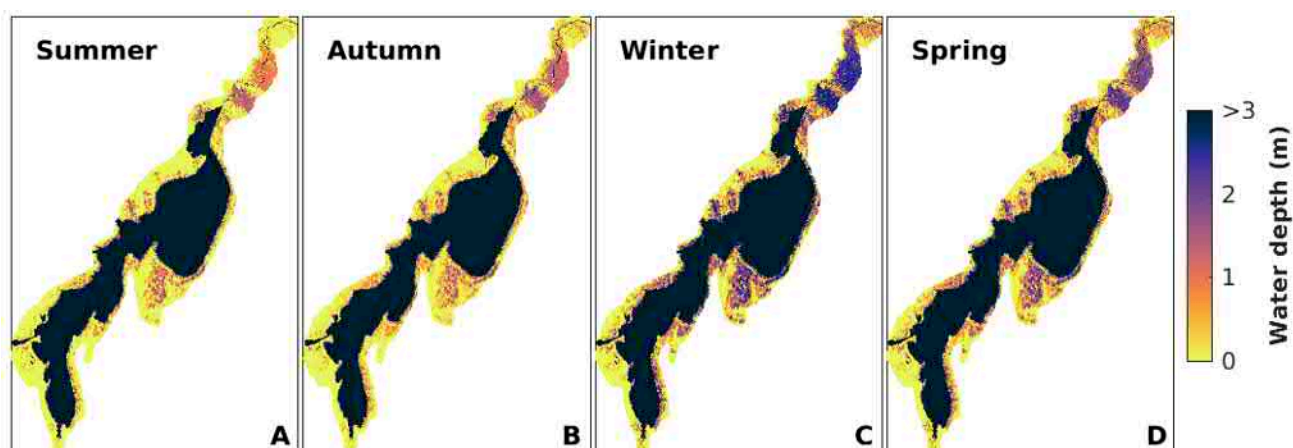


Figure 6: Seasonal average of water depths for the year 2000.

- [4] Tomazelli, L. J., Dillenburg, S. R., & Villwock, J. A. (2000). Late Quaternary Geological History of Rio Grande do Sul Coastal Plain, Southern Brazil. *Revista Brasileira de Geociências*, 30(3), 474–476.G.
- [5] Maier, E. L. B., Costi, J., Barreira, S., & Simões, J. C. (2016). Precipitation in South America: climatic means and variability patterns from 1979 to 2008 (Precipitação na América do Sul: médias climáticas e padrões de variabilidade de 1979 a 2008). *Revista Brasileira de Geografia Física*, 09(01), 32–46.
- [6] Costi, J., Marques, W. C., Paula Kirinus, E. de, Freitas Duarte, R. de, & Arigony-Neto, J. (2018). Water level variability of the Mirim - São Gonçalo system, a large, subtropical, semi-enclosed coastal complex. *Advances in Water Resources*, 117(May), 75–86
- [7] DLR, August 2019. TanDEM-X science service system. <https://tandemx-science.dlr.de>.
- [8] Medeiros, S. C., & Hagen, S. C. (2013). Review of wetting and drying algorithms for numerical tidal flow models. *International Journal for Numerical Methods in Fluids*, 71(4), 473–487.
- [9] G. Duchossois, P. Martin, “ERS-1 and ERS-2 Tandem Operations,” *ESA Bulletin*, No. 83, August 1995, pp. 54-60.
- [10] Duarte, R. F. (2013). Monitoramento das áreas úmidas e inundadas adjacentes ao Canal São Gonçalo com uma série de imagens ERS-1/2 SAR e Envisat ASAR adquiridas entre 1992 e 2007 (Universidade Federal do Rio Grande).
- [11] da Silva, D. V., Oleinik, P. H., Costi, J., de Paula Kirinus, E., & Marques, W. C. (2019). Residence time patterns of Mirim Lagoon (Brazil) derived from two-dimensional hydrodynamic simulations. *Environmental Earth Sciences*, 78(5), 163.

# Open TELEMAC as a decision making tool in developing countries. Case of flash floods and boundary demarcation in Colombia

Jorge Escobar-Vargas<sup>1</sup>, Carlos Fuentes-Cabrejo<sup>2</sup>

<sup>1</sup> Instituto Javeriano del Agua, Pontificia Universidad Javeriana

<sup>2</sup> Carrera 7 # 40 – 62, Bogotá, Colombia.

[jorge-escobar@javeriana.edu.co](mailto:jorge-escobar@javeriana.edu.co)

**Abstract:** In this work, we present the recent improvements of using Open TELEMAC as a decision making tool for regional planning in Colombia. Two specific cases are presented: a first one where the modeling suite was used for the development of an early warning system for debris flows and flash floods, and a second one for boundary demarcation over periodically flooded territories. For both cases, a detailed explanation of the numerical set up, and limitations of the information needed to build the models is described. In the same way, the adaptations and modifications done to the source code, in terms of added source terms to the mass and momentum equations, are presented. The latter, in order to represent in a more detailed way the observed dynamics of the flows. Results of the first case showed that OpenTELEMAC is a versatile tool to compute, in a detailed way, the flow path, the force imposed by the fluid to the structures, and the deposition patterns in the municipality affected by the debris flow. For the second case was found that for flat regions, with terrain slopes smaller to 2%, precision in altimetry data is required to obtain plausible results. On the other side, OpenTELEMAC was found to be suited to represent the hydrodynamics of shallow lagoons (ciénagas), and the connections between them and the river who supply the water to the ecosystem. Preliminary results of an exercise where OpenTELEMAC is being use for the representation of surface water/ground water interaction in flat regions are presented as well. The work finishes with a discussion on the way this type of tools can be used in rural areas of a developing country, where there is not enough technical capacity to manage this type of technology.

**Proposed session:** *River and urban floods, flood forecasting and management*

**Key words:** Flash Floods, land demarcation, numerical modeling, regional planning, developing countries

**Speaker:** Jorge Escobar-Vargas



# Numerical modelling of released dredged sediment dispersion from Pandop harbour (New Caledonia)

Julien Baills, Jérémy Dugor, Didier Rihouey  
CASAGEC Ingénierie  
Anglet, France  
baills@casagec.fr  
dugor@casagec.fr  
rihouey@casagec.fr

**Abstract**— The Pandop harbour is located in the New Caledonia North-West lagoon. This site is subject to sedimentation processes requiring dredging operations in order to maintain its activities. The present work aims to evaluate the released sediment impact on outside coral reef.

The first step of this work consists in evaluating oceanic-climatic conditions impacting the study site, i.e. tide, global circulations, waves, wind and upwelling phenomena. Offshore wave conditions were analysed from WW3 numerical model over a 23 years period. The tide is taken into account using the TPXO database (Egbert et al., 2002). The offshore general currents around New Caledonia are studied from results of Mercator model (Brasseur et al., 2005) at different depths over a 10 years period. Circulations along the west coast of New Caledonia show a seasonal variability in terms of intensity and direction (weaker currents during austral winter). These circulations are used to force the TELEMAC3D model.

The mesh covers the North-West part of New Caledonia and is refined in the lagoon, on the coral barrier and around the disposal zone. The vertical mesh is only composed of 10 planes (fixed and sigma planes) to limit computation time and is refined in the upper part of the water column. The numerical model is calibrated and validated with tide gauge measurements from SHOM and ADCP campaign. Friction coefficients are assigned depending on the bottom type especially on the coral reef.

To model the sediment disposal, a simplistic but realistic solution was used following the bibliography (KBR (2002), Alzieu (2000), Boutin (2000)). Indeed, in order to represent the sediment resuspension during the fall, sediments are injected in the water column at different depths and especially at the pycnocline. The results allowed to define a disposal zone that gives the best compromise between a relatively close disposal area and a low impact on the coral reef. Moreover, the cumulative impact of successive disposals is studied with long-term simulations. Finally, the currents around the disposal zone are relatively low and thus sediment transport is limited.

## I. INTRODUCTION

### A. General context and goals of the study

The Pandop harbour is subject to sedimentation processes requiring dredging operations in order to maintain its activities. The dredge project consists of about 114 000 m<sup>3</sup> of sediments to be dredged to reach a bathymetry of -4,50 m Chart Datum in the harbour. A solution for the dredged sediments consists in dumping them in the sea.

A modelling work is needed in order to:

- Characterize the oceanic-climatic conditions impacting the study site.
- Evaluate the released dredged sediment dispersion in order to define a disposal zone that gives the best compromise between a relatively close disposal area and a low impact on the coral reef.
- Study the cumulative impact of successive disposals by means of long-term simulations.

A three-dimensional hydrosedimentary model has been developed to represent the different processes impacting the study site. Two specific modules have been created or modified to force the model with global circulations and to represent the sediment disposal.

### B. Geographic situation

The Pandop harbour is located in the Northern Province of New Caledonia at the tip of Koumac. In order to dump the dredged sediment, the barges have to cross the lagoon for about 11,5 km to the Koumac inlet. The bathymetry decreases quickly from 15m in the lagoon to 1000m of depth at 3 km of the Koumac inlet. In front of the Koumac inlet, the barrier reef represents a 9 km diameter bay with two inlets: the Koumac inlet and the Deverd inlet.



Fig. 1 Study site (North-West of New Caledonia)

## II. OCEANO-CLIMATIC CONDITIONS

### A. General climate

The New Caledonia climate is characterized by two main seasons:

- The hot season characterized by the passage of depressions and tropical cyclones and a wind regime from South-East to East (south-east trade wind).
- The cool season characterized by wind from East-South-East sector but also cold fronts accompanied by abundant rainfall and West sector winds that can blow in storm (shots from West).

The tide is semi-diurnal and the maximum tidal range is about 1,67m at the Pandop harbour.

### B. Wind climate

The wind climate around the study site was studied thanks to two years measurements at the Duroc inlet done during the Koniambo project in 2001 and 2002.

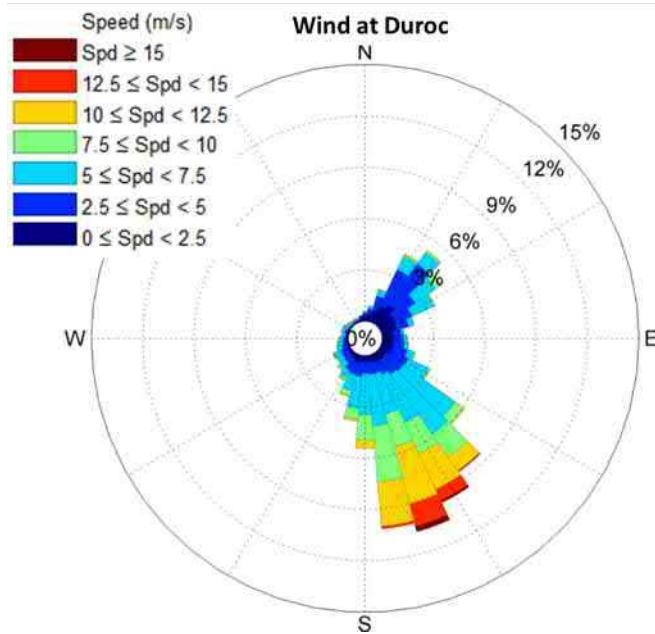


Fig. 2 Wind rose at the Duroc inlet.

The mean velocity is about 5,73 m/s and the wind originates mostly from South-East. Indeed, the strongest winds come from South and South-East.

The wind velocities measured are below 5,5 m/s during 26% of the time and below 10,5 m/s during 79% of the time.

During the cool season, westerly sea breezes can be observed.

### C. General wave conditions

Offshore wave conditions were studied from a WW3 numerical model from IFREMER over a 28 years period from 1990 to 2018. The wind forcing comes from ECMWF (European Centre for Medium-Range Weather Forecasts) model.

The Mean wave conditions can be summarized as follow:

- Waves preferentially originate from South-East (135°N) to South-South-West (210°N).
- The significant wave height is lower than 1,5m for 23% of the time, lower than 2m for 55% of the time and lower than 3m for 92% of the time.
- Sea states below 3.0 m usually have peak periods of the order of 9 to 14 s. More rarely, some sea states can reach significant heights of more than 6m and long periods up to 20s.

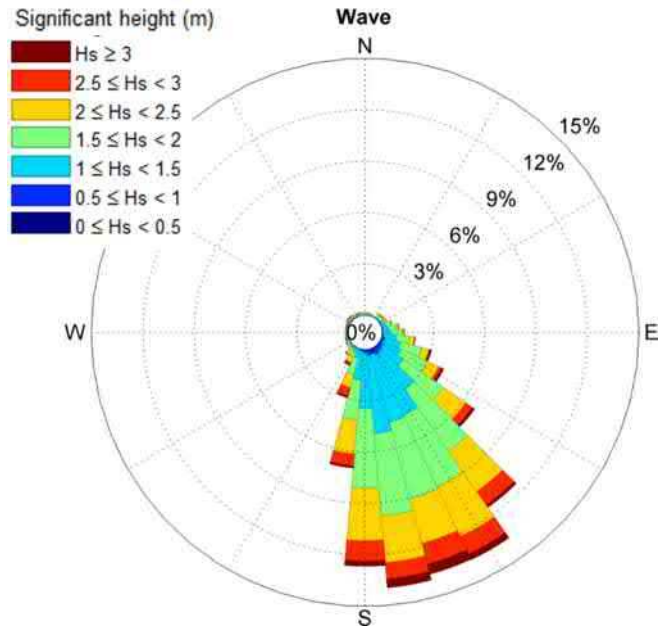


Fig. 3 Wave rose from the WW3 model.

### D. Offshore general current

The global circulations around New Caledonia are complex and difficult to characterize ([1],[2],[3]). Current circulations have been extracted from the Mercator ([4]) model over a 10 years period (2007-2016). Moreover, these velocities are recuperated for several depths (surface, 100m, 400m and 1000m).

The velocities are studied for a point located off the Koumac inlet. The global currents are mostly parallel to the coast.

With these data, velocity roses (Fig 4) have been constructed for the different depths and seasons and thus analysed.

These figures show a strong seasonal variability.

Indeed, during the hot season (from November to April), currents are mainly directed towards South-East with intensities of about 0,15 to 0,5 m/s at the surface. Moreover, current directions are homogeneous in the water column and velocities are lower near the bottom.

However, during the cool season (from May to October), currents are still directed towards South-East but with lower

velocities of about 0,05 to 0,3 m/s. Otherwise, opposite currents toward North-West can be observed under the pycnocline.

Moreover, global velocities of about 1 m/s can be observed during cyclonic events.

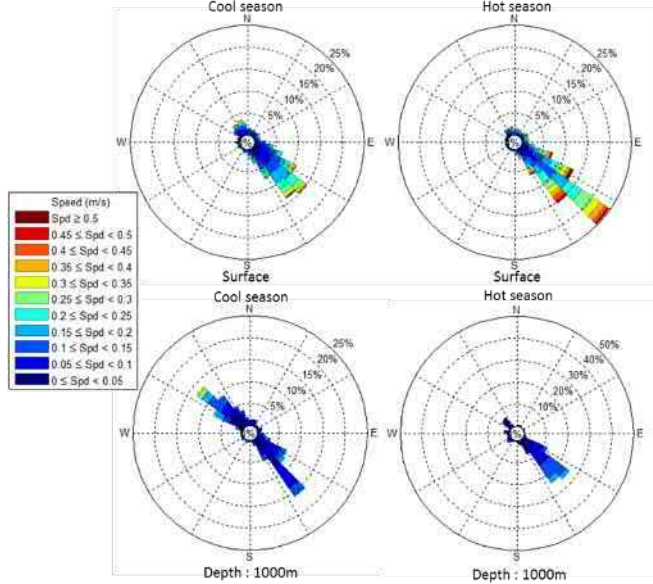


Fig. 4 Velocity roses off the lagoon from Mercator model

### III. NUMERICAL MODEL DESCRIPTION

#### A. Mesh and forcings

The Telemac software using Finite Element Method was used to model the three-dimensional hydrodynamic processes and the dredged sediment dispersion. The 2D mesh covers the North-West part of New Caledonia (about 100km from North to South), it is refined in the lagoon, on the coral barrier and around the disposal zone and is composed of about 41 200 nodes. The mesh size is about 1000m off the lagoon to 500m in the lagoon and 100m at the reef. The mesh size is minimal around the disposal zone (mesh size of about 50m).

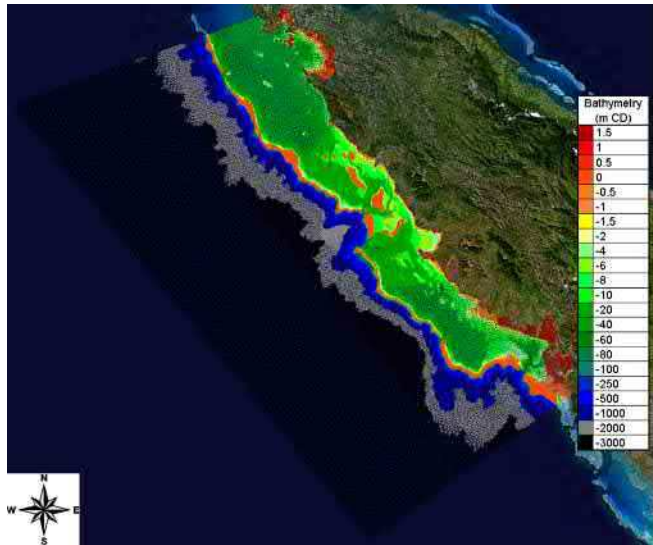


Fig. 5 Mesh and bathymetry

The vertical mesh is only composed of 10 planes (fixed and sigma planes) due to computation time and it is refined in the upper part of the water column.

Different bathymetric data were used to generate the digital depth model:

- GEBCO (General bathymetric Chart of the Oceans) 2014 30 arc-second grid for the offshore part.
- ZONECO bathymetry (Zone économique de Nouvelle-Calédonie) for the lagoon part of the model.
- Digitalisation of SHOM maps for the missing part of the lagoon.

The reef bathymetry is imposed to +0,3 m Chart Datum.

The model is forced on its oceanic boundaries by the global oceanic tide model TPXO ([5]). The tide model gives water depth and velocities at the ocean limit allowing to have a good reproduction of the tidal phenomenon.

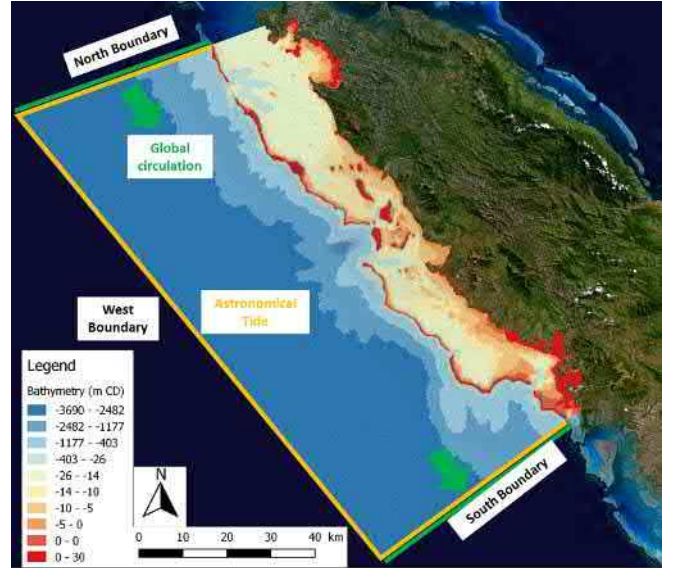


Fig. 6 Forcing scheme

To impose velocity profiles related to the Mercator model at the boundaries, a specific module has been developed. The velocities are imposed to the different boundaries at the different layers. The wind is imposed with a time series and is considered constant in space. The k-epsilon turbulence model ([6]) is used for this study.

The friction is computed with the Manning law and the friction coefficients are assigned depending on the bottom type (sand, mud, reef). The coefficients values given according to the Koniambo project ([7]) are the following:

- 0,02  $m^{-1/3}s$  for the ocean,
- 0,024  $m^{-1/3}s$  for the sandy part of the lagoon,
- 0,035  $m^{-1/3}s$  for the muddy part of the lagoon,
- 0,083  $m^{-1/3}s$  for the reef.



### B. Calibration and validation

The model is firstly calibrated in terms of water levels comparing with the SHOM predictions at the Paagoumène harbour located at the north part of the model. The comparison is done for two weeks (one in May 2015 and one in August 2015). The water levels are well reproduced by the model with a bias of about 1-2cm (cf. Fig 7).

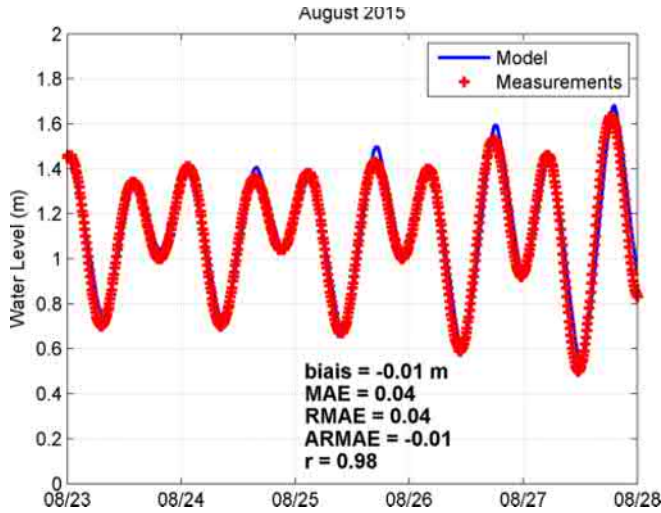


Fig. 7 Comparison of water levels modelled and measured at Paagoumène

The 3D model is then validated in terms of currents with aDcp measurements (measurement campaign of the Koniombo project at the Duroc inlet cf. Fig 8). The comparison between the measured and modelled velocities also shows good results with correct statistical indices (bias of about 7 cm/s).

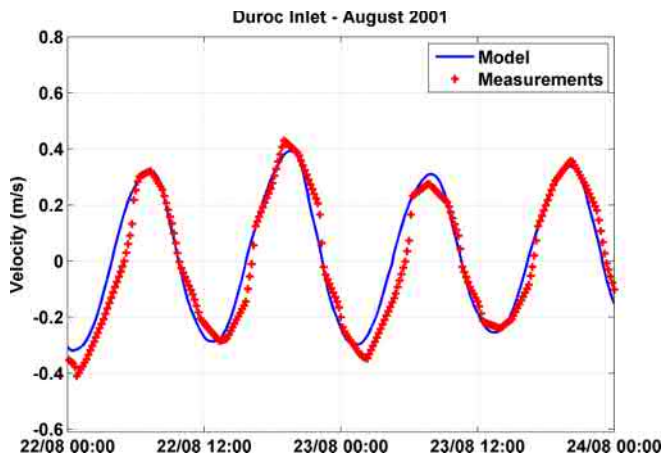


Fig. 8 Comparison of modelled and measured velocities at the Duroc inlet during the campaign of August 2001

These differences can be explained by the bad bathymetric resolution of this part of the mesh due to the lack of data.

## IV. MODELLING STRATEGY AND RESULTS

### A. Hypothesis

To model the sediment disposal, a simplistic but realistic solution was used following the bibliography ([7], [8], [9]). Indeed, in order to represent the sediment resuspension during the fall, sediments are injected in the water column at different depths and especially at the pycnocline.

Depending on the current velocities, 5% for calm conditions and 10% for agitated conditions of the dumped sediments are injected at the surface and also at the pycnocline (layer of density change). The convective descent of the majority of the dumped sediment is not represented in the model.

Grain size measurements show that the sediment dumped are mostly mud (grain size inferior to  $63 \mu\text{m}$ ). Due to the sediment size, the fall velocity is estimated with the Stokes formula to be about  $0,1 \text{ mm/s}$  (neglecting flocculation effects). To only observe the dumping impact, no sediments are considered at the bottom at the beginning of the simulation. The critical shear stress for deposition and erosion were adapted linked to the state of art.

The impact threshold for the reef is considered regarding to the state of art ([3], [10]). Indeed, the reef is considered as impacted for sediment concentrations higher than  $10 \text{ mg/l}$  (for depth less than  $100\text{m}$ ).

Concerning the position of the dumping site, similar constraints of the Koniombo project are taken into account i.e. the zone must be located at more than  $3,5 \text{ km}$  of the reef and for depth higher than  $1000\text{m}$ . Therefore, two disposal zones were defined at  $4,5 \text{ km}$  and  $6,5 \text{ km}$  of the coral reef. Due to the number of dredges, their capacities and the position of the disposal zone, the dumping occurred about every 3 hours and are considered to last 5 minutes. Therefore,  $0,16 \text{ m}^3$  of sediment are injected at each time step.

Three scenarii defined with the analysis of the oceanoclimatic conditions were modelled on fifteen days:

- Scenario 1 - Calm conditions: weak wind ( $1 - 5 \text{ m/s}$ ), low sea state ( $0,5 \text{ m}$ ) from South and general current of  $0,2 \text{ m/s}$  from North-West to South-East.
- Scenario 2 - Agitated conditions of the cool season: waves of  $1,8\text{m}$  from South, wind time series of trade wind and westerly sea breezes and no general circulation.
- Scenario 3 - Agitated conditions of the hot season: waves of  $1,8\text{m}$  from South, strong south-east trade wind and a general current of  $0,4 \text{ m/s}$  from North-West to South-East.

### B. Results

In order to respect the Courant condition, a time step of 5 seconds had been chosen. With a sixteen-core computer, simulations of fifteen days had a computation time of about twenty-four hours.

The different simulations show that the currents around the disposal zone are relatively low ( $< 0.3 \text{ m/s}$ ). The strongest currents are observed at the inlets of the lagoon with velocities of about  $0,8 \text{ m/s}$  especially during the flood and the ebb tide.

A gyre can be observed around the dumping zone generated by the global circulation impacting the bay and the two inlets. The velocities of the gyre are linked to the global circulation.



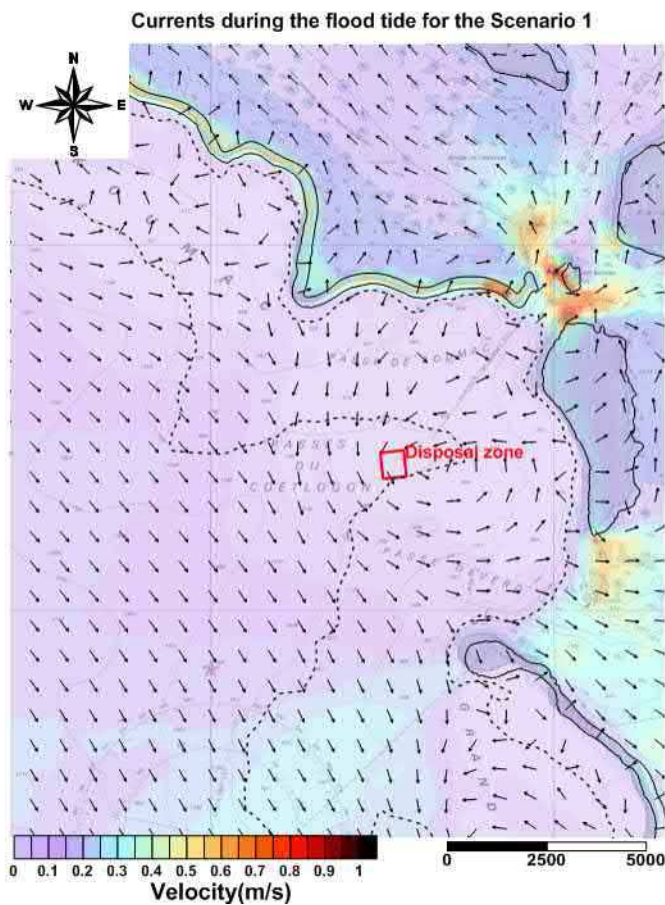


Fig. 9 Map of current during the flood tide for the scenario 1 conditions. The red square shows the position of the disposal zone.

Indeed, due to the low velocities, sediment transport is limited, the sediments fall in the water column and stay close to the disposal site (cf. Fig. 10 and Fig. 11). After a dumping, the sediment concentration in the disposal zone decreases quickly.

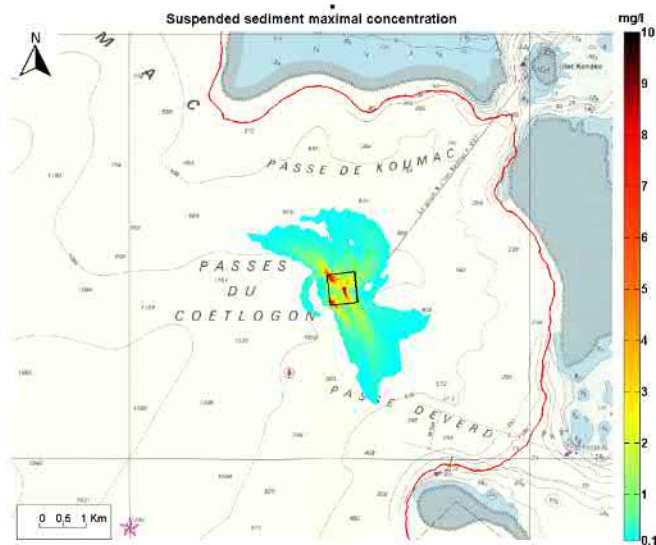


Fig. 10 Map of maximal sediment concentration for the scenario 1. The red line is the isobath -100m Chart Datum. The black square shows the disposal site position.

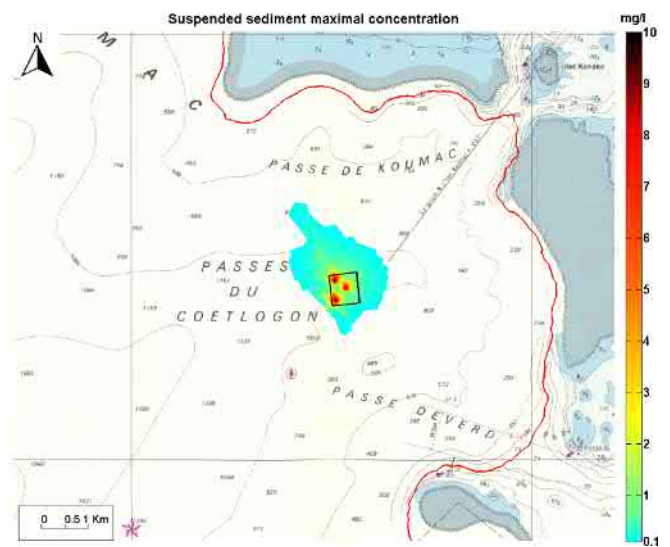


Fig. 11 Map of maximal sediment concentration for the scenario 3. The red line is the isobath -100m Chart Datum. The black square shows the disposal site position.

The maximal sediment concentration modelled are about 15-20 mg/l in the disposal zone and less than 5 mg/l out of the dumping zone. The influence of wind or wave is limited due to the depths around the disposal zone. However, the sediment plume for the scenario 3 is mostly propagated to the North-North-West due to South-South-East winds.

The simulations show that the reef should not be impacted for the different modelled conditions. The sediment concentrations are relatively low near the reef. The scenario 3 for agitated conditions of the hot season is the worst one with concentrations at the reef of about 0,13 mg/l. The maximal concentration at the reef for the calm scenario is about 0,075 mg/l and 0,02 mg/l for the cool season simulation. These simulations show that the concentrations observed at the reef are one hundred times lower than those who could impact the reef.

A second disposal site has also been studied at 6,5 km of the reef. The site is more sensible to the global current. Indeed, this site is located out of the gyre. Therefore, the reef is less impacted by the dumping. For the scenario 3, the maximal sediment concentration at the reef is about 0,085 mg/l which is twice as low as for the closest site.

Long term simulations of one month has also been carried out to observe the cumulative impact of successive disposals. This work showed that the cumulative impact of successive dumpings is negligible. The dumping impacts are temporary and punctual.

## V. CONCLUSION

The Pandop harbour requires dredging operations to maintain its activities due to important sedimentation processes. The aim of this study is to evaluate the impact of the dumped sediment dispersion especially on the coral reef.

For this purpose, a 3D hydrosedimentary model has been developed to reproduce the different hydrodynamic processes on the North-West part of New Caledonia. Some specific modules

have been added or modified to represent the dumping in the model and to impose velocities profiles at the different boundaries.

Thanks to this work, the dispersion of released dredged sediment has been modelled for different oceano-climatic conditions to estimate their impact on the reef. The studied disposal site is located in a "bay" where a gyre can be observed. The site configuration leads to low currents resulting in limited sediment transport. For the different modelled oceano-climatic conditions, the suspended sediment concentrations at the reef caused by the dumping are relatively low and do not impact the coral reef.

Moreover, the cumulative impact of successive disposals is limited and negligible especially on the reef.

A second disposal site has also been studied leading to a diminution of the impact but a cost rise (rise of the distance with the harbour and need of a supplementary dredge to keep the same work rate).

#### REFERENCES

- [1] S.Cravatte, E. Kestenare, G. Eldin, A. Ganachaud, J. Lefèvre, F. Marin, C. Menkes and J. Aucan, "Regional circulation around New Caledonia from two decades of observations," *Journal of Marine Systems*, vol. 148 pp. 249–271, 2015.
- [2] C. Hénin, J. M. Guillermin and L. Chabert, "Circulation superficielle autour de la Nouvelle-Calédonie," in *Océanographie Tropicale*, pp. 113-126, 1984.
- [3] NSR, "Koniombo Project, Physical Marine Investigations," NSR Environmental Consultants, 2002, unpublished.
- [4] P. Brasseur, P. Bahurel, L. Bertino, F. Birol, J. M. Brankart, N. Ferry, S. Losa, E. Remy, J. Schröter, S. Skachko, C. E. Testut, B. Tranchant, P. J. Van Leeuwen and J. Verron, "Data assimilation in operational ocean forecasting systems: The Mercator and Mersea developments", *Q.J.R. Met. Soc.*, Vol. 613, C, pp 3561-3582(22).
- [5] G. D. Egbert and S. Y. Erofeeva, "Efficient inverse modelling of barotropic ocean tides". *Journal of Atmospheric and Oceanic Technology*, Vol. 19, pp 183-204, 2002.
- [6] B. E. Launder and D.B. Spalding, "Lectures in Mathematical models of Turbulence", Academic Press, 1972.
- [7] KBR, "Koniombo Port Project," Dredge spoil disposal report, 2002.
- [8] C. Alzieu, "Dragages et environnement marin. Etat des connaissances," Editions Ifremer, 225 p. 2000.
- [9] R. Boutin, "Dragage et rejets en mer. Les produits de type vase", Presses de l'ENPC, 307p. 2000.
- [10] P. L. A. Erftmeijer, B. Riegl, B. W. Hoeksema and P. T. Todd, "Environmental impacts of dredging and other sediment disturbances on corals: A review," *Marine Pollution Bulletin*, vol. 64. Pp 1737-1765. 2012.

# Calibration and validation strategy for 2D hydrodynamic modelling: application to morphodynamics of a gravel-bed river with suspended sediments

Coraline Bel (1), Magali Jodeau (1, 2), Pablo Tassi (1,2)  
(1): Saint-Venant Hydraulics Laboratory (LHSV)  
ENPC, Cerema, EDF R&D  
Chatou, France  
coraline.bel@enpc.fr

Nicolas Claude (2), Hanna Haddad (2)  
(2): National Hydraulics and Environment Laboratory  
(LNHE)  
EDF R&D  
Chatou, France

**Abstract**—This work aims at presenting an example of application of the APIs for the step of hydrodynamic model calibration and validation in the case of an ongoing study. The study site is a gravel bed river where the fine sediment dynamics is a main concern of the river management.

## I. INTRODUCTION

Nowadays, many mountain and piedmont regulated rivers present steady vegetated alternate bar systems as a consequence of the anthropogenic modifications – embankment, hydroelectric facilities, gravel extraction, land use change, etc. – that, over the last two centuries, have impacted the hydrologic regime and the sediment supply [1]. During high flow events, massive deposits of fine sediment occur on gravel bars, leading to bar elevation, riparian vegetation growth and consequently to bar stabilization (Fig. 1). This results in river ecological quality degradation and increased flooding risk. To optimize gravel-bed river management strategies aiming at preventing bar colonization by plants, a better understanding of the involved processes is necessary. In particular, improving our knowledge of cohesive sediment dynamics (storage and re-suspension) on gravel bars during varying hydrologic events (natural flood and reservoir flushing) is important. The purpose of our study is to investigate hydro-morphodynamic processes at the scale of a few kilometers long reach, by means of flow and sediment transport simulations performed using the modules TELEMAC-2D and GAIA [2] (previously SISYPHE) of the TELEMAC-MASCARET suite of solvers. The implemented two-dimensional (2D) model accounts for bedload and suspended load transport processes of cohesive and non-cohesive sediments.

The study site is the Combe-de-Savoie reach of the Isère River (France). A field campaign performed in 2018 during a reservoir flushing event showed that both bedload and mixed (cohesive and non-cohesive) suspended sediment transport play a critical role on the morphological evolution of the riverbed. In this study case, accounting for bedload transport processes is important to capture significant bathymetric changes, while modelling suspended load transport is

necessary to reproduce distribution and thickness of fine sediment deposits, for both sands and cohesive sediments.

Before examining the effects of different environmental forcing (e.g., water and sediment supplies, etc.) on bed evolution to propose new management strategies, the numerical model must be calibrated and validated. This is done in two consecutive steps, according to the different physical processes: (i) the calibration and validation of the hydrodynamics, and (ii) the calibration and validation of the sediment transport and morphodynamics. Here, we will focus on the former step.

The calibration and validation procedure of the hydrodynamic model is supported by high-quality water surface elevation and flow velocity measurements. This proceeding aims to detail the strategy adopted for the optimal and efficient parametrization of the hydrodynamic model. For this purpose, the APIs (Application Programming Interface) developed for the automatic model calibration using data assimilation algorithm [3], [4] are used.



Figure 1. Example of fine deposit and vegetation establishment on gravel bar. Frériverie gravel bar, June 2018.



## II. STUDY CASE

### A. Study site

The Isère River is an Alpine regulated gravel-bed river located in South-Eastern France. Its flood regime is pluvio-nival and impacted by hydroelectric structures. The study reach is located downstream the Aigueblanche reservoir dam, in the Fréterive area at Combe-de-Savoie, southwest of Albertville (Fig. 2). It is about 100-m wide between dikes, and extends over 3 km up to upstream of the Arc-Isère confluence. The bed slope is 0.0016 m/m. The  $D_{50}$  is approx. 24 mm, 180  $\mu$ m, and 50  $\mu$ m for coarse, non-cohesive (2-0.063 mm) and cohesive (<0.063 mm) sediments respectively. In this area, the flow discharges for 2 and 10-year floods are 209 m<sup>3</sup>/s and 345 m<sup>3</sup>/s, respectively. The average suspended sediment concentration (SSC) is less than 1 g/l but can reach up to about 10 g/l during major floods.

In winter 2017, this area was the subject to restoration works which consisted in removing fine sediment and vegetation, and in remodelling a part of the bared gravel bars.

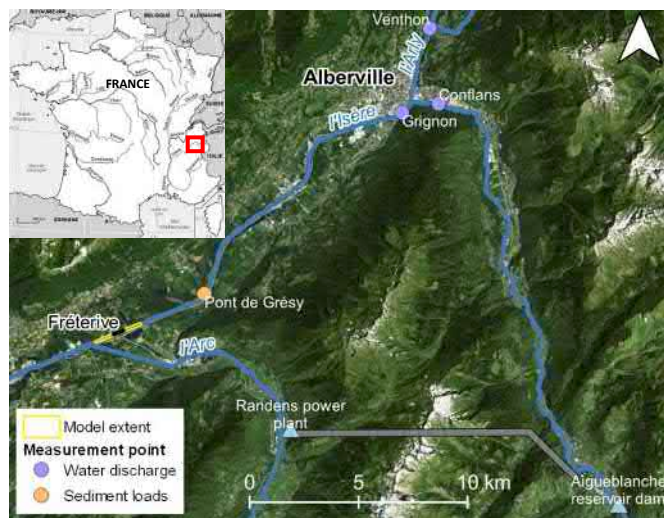


Figure 2. Study site map and extent of the model: Isère River at Combe-de-Savoie.

### B. Field data

In 2018, time series of water discharge, suspended sediment concentration (both cohesive sediment and sand) were reconstructed upstream the study reach, at Pont-de-Grésy, with a 1-h time step from January 1 to September 28 (Figs. 2 and 3). Similarly, bedload fluxes (estimated with a hydrophone [5]) were reconstructed from March 21 to June 7. During the same period, free surface elevation was also recorded using four piezometers distributed along a part of the study reach, in the area of Fréterive (Fig. 7).

From May 6 to 11 2018, a comprehensive field campaign was conducted during the reservoir flushing of the Aigueblanche dam (Fig. 2). During the flushing event, point measurements of current velocities (aDcp – Fig. 7), of fine sediment settling velocities (SCAF measurements on SSC samples at Pont-de-Grésy [6], [7]), of bedload fluxes and of grain size of the transported fraction (Helley-Smith samples

at Pont-de-Grésy, etc.) were performed. In addition, pre- and post-event measurements were achieved, in particular on the Fréterive gravel bar, including aerial photographs, topobathymetry (Fig. 5), flow velocities (LSPIV [8] – Figs. 4 and 7), gravel-bar material characterisation (measurements of grain size by mass on cryogenic coring, and by Wolman pebble count technic on bars – Fig. 6), fine-sediment deposit

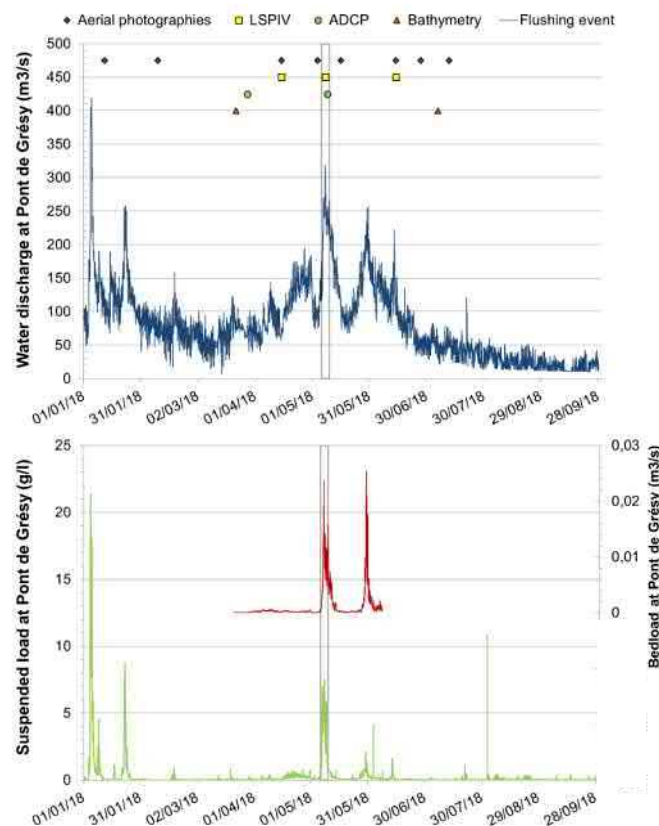


Figure 3. Dates of the surveys, time series of water discharge (blue), suspended load (green) and bedload (red) recorded at Combe-de-Savoie.

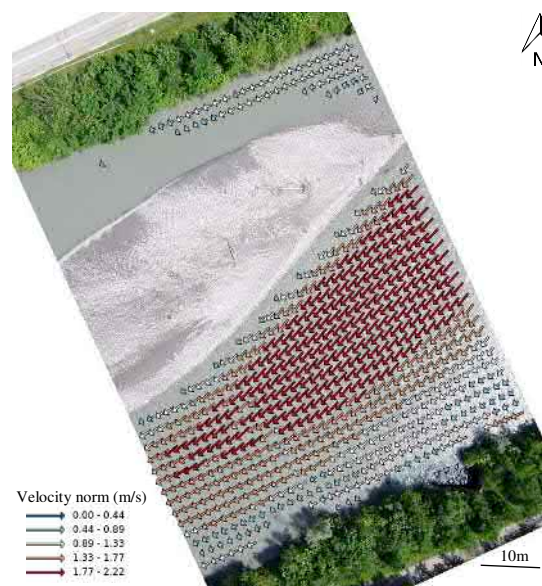


Figure 4. Extract of velocities field obtained by LSPIV on June 14, 2018.



characterisation, geomorphic observations and vegetation monitoring.

All these measurements are used either as model input, as prior knowledge of model parameters, or again as comparison elements for the calibration and validation stages.

Before going further in the numerical model, few elements of analysis of the measurements may be introduced. The comparison of the bathymetric surveys before and after the flushing event shows significant changes (Fig. 5). It emphasises the importance of anticipating the bed modification while adjusting the hydrodynamic parameters in the former step of modelling. It also brings out the key role played by bedload transport which must be represented in the morphodynamic modelling. The grain size measurements, by mass or by counting, at the surface of gravel bars (Fig. 6) are consistent and highlights the strong heterogeneity present in

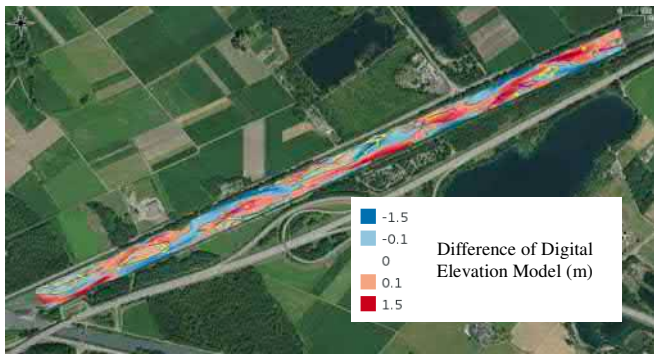


Figure 5. Bathymetric evolution from March to July 2018. The limits of flooded areas before (04/05/2018) and after (16/05/2018) the flushing event are marked with the yellow and blue lines.

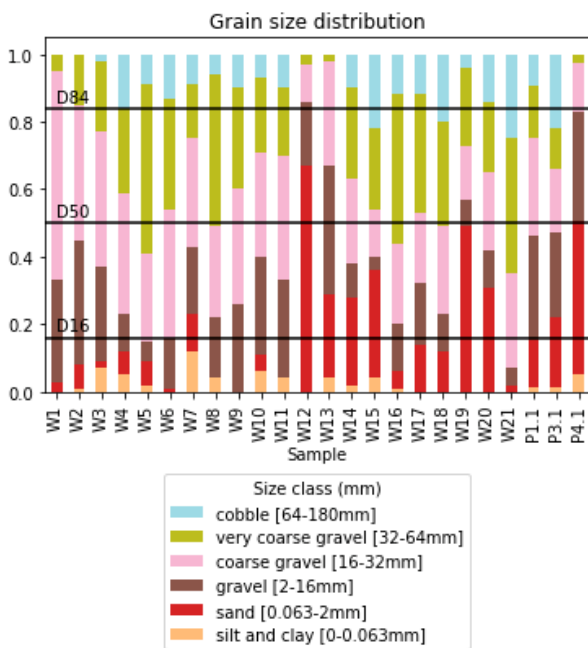


Figure 6. Grain size distribution at bar surface. Wx: Wolman pebble count on bars; Px.1: mass grain size on 0-20cm layer of cryogenic cores.

field environment (Fig. 1). Even so, the  $D_{50}$  may be represented by coarse gravel. Otherwise, we can notice the important proportion of cohesive sediments and sand, and so the necessity of properly representing the suspended load in the morphodynamic modelling.

### III. NUMERICAL MODEL

#### A. Mesh and boundary conditions

The computational domain extent starts downstream Pont-de-Gresy and stops upstream the confluence with the Arc River so that the confluence with Arc is not modelled. The flow regime is subcritical and there is no flow change. The upstream boundary condition is a prescribed flow rate based on the Pont-de-Grésy records. The downstream boundary condition is a prescribed elevation that is function of the discharge, on the basis of a stage-discharge relationship established at the level of the fourth piezometer. Two different friction areas are defined to separate the main stream from the vegetated banks. No friction area is dedicated to the bars (tidal flats) although the friction coefficient may differ from the main stream because of logjam and young vegetation (Fig. 1). This choice is made because the limits of these areas may evolve due to bed modification (Fig. 5) and so fixing these areas could generate a modelling artefact during the morphodynamic simulation.

The model consists of an unstructured mesh discretized with 117,557 triangular elements (approximately 60,000 nodes) with a 2-m resolution (Fig. 6). A mesh convergence analysis was performed based on several mesh refinements, ranging from 8 to 0.5-m resolution using the STBTTEL module.

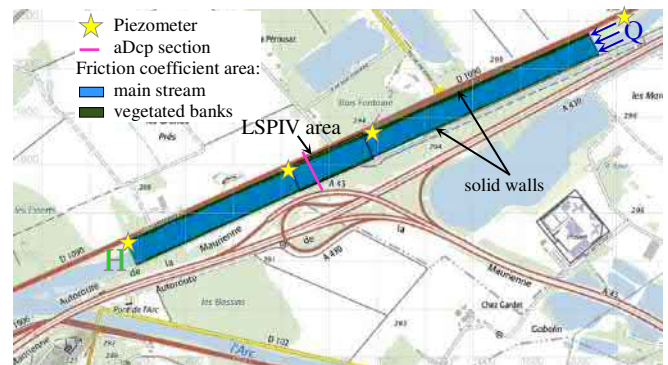


Figure 7. Mesh and boundary conditions of the hydrodynamic model. Piezometer position. LSPIV area and aDcp section.

#### B. Equations and parameters to calibrated

In this study, flow, sediment transport and bed evolution are simulated by coupling the modules TELEMAC-2D and GAIA so as to solve, at each time step, (i) the hydrodynamics with fixed bottom [9], then (ii) the morphodynamics [10]. In this section, we focus on the hydrodynamic modelling.

Hereafter, the unknowns, the variables requiring a closure model and the calibration parameters are noted in red, in blue and in green respectively.

TELEMAC-2D solves the non-conservative shallow-water equations (1) and requires one closure model for friction and one closure model for turbulence.

$$\begin{cases} \partial_t h + \mathbf{u} \cdot \mathbf{grad}(h) + h \operatorname{div}(\mathbf{u}) = 0 \\ \partial_t \mathbf{u} + \mathbf{u} \cdot \mathbf{grad}(\mathbf{u}) = -g \partial_x z_s + F_x^f + \frac{1}{h} \operatorname{div}(h \mathbf{v}_t \mathbf{grad}(\mathbf{u})) \\ \partial_t \mathbf{v} + \mathbf{u} \cdot \mathbf{grad}(\mathbf{v}) = -g \partial_y z_s + F_y^f + \frac{1}{h} \operatorname{div}(h \mathbf{v}_t \mathbf{grad}(\mathbf{v})) \end{cases} \quad (1)$$

with  $h$  (m) the water level,  $u, v$  (m/s) the horizontal velocity components,  $z_s = z_b + h$  (m) the free surface elevation,  $z_b$  (m) the bottom elevation,  $g$  (m/s<sup>2</sup>) the gravity acceleration,  $t$  (s) the time, and  $x, y$  (m) the horizontal space coordinates.

$(F_x^f, F_y^f) = f(\mathbf{u}, h, k_s)$  (m/s<sup>2</sup>) are the friction source terms (2) which depend on  $k_s$  (m), the roughness height to be calibrated, associated to the chosen closure relationship (e.g. Nikuradse law [11] for considering the low water depths face with grain size when tidal flats occurred (3)).

$$\begin{cases} (F_x^f, F_y^f) = g \frac{u|\mathbf{u}|}{h C^2} \\ C^2 = \frac{2g}{C_F} \end{cases} \quad (2)$$

$$C = \frac{\sqrt{g}}{\kappa} \ln\left(\frac{12h}{k_s}\right) \quad (3)$$

where  $\kappa$  is the Von Kármán constant (0.4 for clear water), and  $C_F = f(k_s)$  is the resulting friction coefficient.

$\nu_t$  (m<sup>2</sup>/s) is the diffusion coefficient which includes both the effects of molecular viscosity and of turbulence; it can be set to a constant value (in such a case it has to be calibrated), or depends on a closure model for turbulence (e.g.  $\nu_t = f(k, \varepsilon)$  with  $k$  and  $\varepsilon$ , the turbulent kinetic energy and the turbulent dissipation respectively, two news unknowns that bring in addition two transport equations to solve).

#### IV. APIS : OPTIMIZATION BASED ON DATA ASSIMILATION

The APIs of TELEMAC-MASCARET SYSTEM (Fortan) make possible to have control on a simulation while running a case. Thus, some parameters (e.g. friction coefficient) can be manipulated during the simulation. The Python module TelApY gives access to the Fortan APIs and can be coupled in particular with other Python libraries dedicated to optimization [3].

In our study case, we focus on the automatic calibration based on a data assimilation algorithm of the ADAO library (<https://pypi.org/project/adao/>). The goal is to estimate the optimal parameters of the model by minimizing a cost function (4).

$$\begin{cases} J(X) = J_b + J_o \\ J_b = \frac{1}{2} (X - X_b)^T B^{-1} (X - X_b) \\ J_o = \frac{1}{2} (Y - H(X))^T R^{-1} (Y - H(X)) \end{cases} \quad (4)$$

where  $J(X)$  is the cost function – known as the variational data assimilation cost function 3D-VAR [12] –  $J_b$  and  $J_o$  are

the background and observation components respectively;  $X$  is the vector of the parameters to be estimated;  $X_b$  represents the prior knowledge of  $X$ ;  $Y$  is the observation vector and  $H(X)$  is the result of the hydraulic solver that correspond to the observation vector;  $B$  and  $R$  are the background and observation error covariance matrices respectively. The resolution of the minimization problem is based on a gradient descent method, so-called constrained Broyden Fletcher Goldfarb Shanno Quasi-Newton method (c-BFGS-QN) [4]. The partial derivatives of hydraulic solver  $H(X)$  are approximated by a classical finite difference method.

#### V. CALIBRATION AND VALIDATION STRATEGY

In this stage, we are interested only in the calibration of the hydrodynamic modelling. The simulations run with a fixed bottom, without tracer. Two parameters have to be calibrated: (i) the roughness height – flow resistance – that appears in the Nikuradse closure relationship; (ii) the diffusion coefficient – effective eddy viscosity – which depends on the chosen turbulence model. We start by the roughness height because, here, it plays a major role in comparison with the diffusion coefficient.

##### A. Calibration of the roughness height

First, we assume that there is no turbulence, with a constant viscosity model and a velocity diffusion coefficient set in first approximation. Its value differs from the molecular viscosity of water (10<sup>-6</sup> m<sup>2</sup>/s) because it also includes the effects of turbulent viscosity. The value of the effective eddy viscosity was estimated with the turbulent boundary layer theory, whose the depth-mean value (5) was considered as a proper order of magnitude in shallow regime [13].

$$\nu_t \approx \kappa \sqrt{C_F} UH / 6 \quad (5)$$

The simulations are performed at steady flow condition that corresponds to the date of the bathymetric survey before the flushing event (Fig. 3, Tab. 1).

Date	22/03/2018
<i>bathymetry before the flushing event</i>	
Q (m <sup>3</sup> /s)	67
Downstream free surface elevation (m)	287.91
$k_s$ (m) / equivalent $K_{Strickler}$ (m <sup>1/3</sup> /s) <i>main stream</i>	0.07 [0.01-0.1] / 40 [38-56]
$k_s$ (m) / equivalent $K_{Strickler}$ (m <sup>1/3</sup> /s) <i>vegetated area</i>	25 [1-35] / 15 [14-26]
$\nu_t$ (m <sup>2</sup> /s)	0.008

Table 1. Value of the hydraulic boundary conditions and of the prior knowledge of the parameters to calibrate.

For that stage, we use the APIs detailed in section IV. The vector of parameters to estimate  $X$  is of length two and corresponds to the roughness heights of the main stream area and of the vegetated bank area ( $X$  could have included in addition the diffusion coefficient). The prior knowledge of  $X$ , named  $X_b$ , is estimated from the varying surface grain size measurements ( $\sim 3D_{50}$  or again  $D_{90}$  – Fig. 6) for the main stream, and from an approximation valid for the vegetated area (height of the highest trees of the ripisylve, as willows or

poplars). One can notice that the bathymetric surveys are carried out at low flow, and as a consequence, the vegetated banks are unlikely to be flooded and the roughness height of the vegetated area would have little effect on the simulation. Finally, the observation vector  $Y$  corresponds to the free surface level records at the location of the 2 piezometers upstream and downstream the Fr  rerie gravel bar for that date (Fig. 7).

An example of simulation result is shown on Fig. 8.

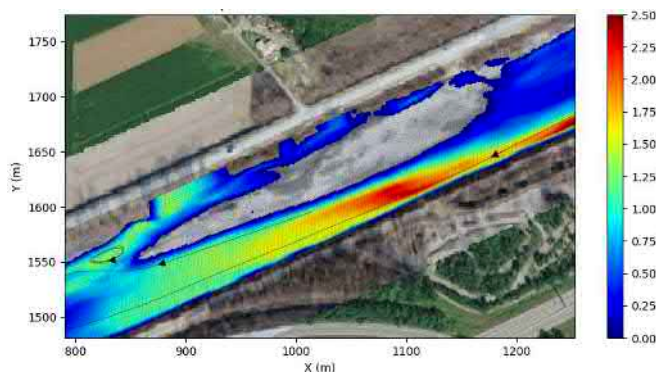


Figure 8. Preliminary result of hydrodynamic simulation. Water depth (m) and streamlines in the interest area (22/03/2018,  $Q=67\text{ m}^3/\text{s}$ ). The nodes where the water depth is below  $0.05\text{ m}$  are masked. Aerial photography (09/02/2018,  $Q=71\text{ m}^3/\text{s}$ ).

### B. Validation

In order to validate the calibration of the roughness height, a new simulation is performed with unsteady flow conditions corresponding to the flushing event and the bathymetry before the flushing event. The free surface level records at the location of the piezometers are compared to the hydraulic solver results. Differences can be expected during the period of intense bedload transport, where the bottom changes.

A second validation stage consists in performing new simulations with the bathymetry surveyed after the flushing event and the steady flow conditions corresponding to the dates of aerial photography surveys. The aim is to ensure that the flooded surfaces are correctly reproduced by the model.

### C. Choice of the turbulence model

Once the roughness heights calibrated and validated, the objective is to choose the best turbulence model and so diffusion coefficient to reproduce the size and the location of the recirculation zones using the velocities fields assessed by aDcp and LSPIV.

To do so, new simulations are performed with the post-flushing bathymetry and the steady flow conditions corresponding to the dates of the aDcp and LSPIV surveys (Fig. 3). Varying diffusion coefficient parameters are tested with the constant viscosity model. In addition, the other friction models implemented in TELEMAC-2D are tested ( $k$ - $\epsilon$ , mixing length, Smagorinski).

## VI. CONCLUSION AND PERSPECTIVES

The calibration and validation of the 2D hydrodynamic model only involves two parameters related to the flow resistance and the eddy viscosity. The calculation requires measurements of bathymetry, water discharge and downstream free surface elevation, while the calibration and validation may be based on free surface elevation and current velocities. In addition, the grain size characterization is useful to have a first approximation of the friction coefficient, and so of the diffusion coefficient. The objective is to adjust these physical parameters until the comparison with the data is as accurate as possible. This can be time consuming and subjective, so automatic calibration through the APIs is as well as relevant that it allows the consideration of many measurements while assessing simultaneously several parameters.

In the next stage, considering in addition the morphodynamic processes, with bedload, suspended sand, and cohesive suspended load strongly increases the number of parameters to estimate, as well as the data required. These information - sediment load and grain size for each class of sediment considered, settling velocities, erosion rate, critical shear stresses etc. - come with uncertainties that we must also consider. Considering the complexity of morphodynamic modelling (bed evolution, the numerous involved processes and their interactions), it is important to proceed step by step. The APIs and in particular data assimilation but also uncertainty quantification open new perspectives towards a better modelling.

### ACKNOWLEDGEMENT

This work is part of the ANR Project DEAR (Deposition and Erosion in Alpine Rivers) and of the Project Cigale2 (EDF R&D). The authors would like to thank all the teams that carried out the field measurements and in particular the colleagues of EDF CIH and EDF DTG. We are also grateful for the precious help of C. Goeury and Y. Audouin in the use of the APIs.

### REFERENCES

- [1] A. J. Serlet, A. M. Gurnell, G. Zolezzi, G. Wharton, P. Belleudy, and C. Jourdain, 'Biomorphodynamics of alternate bars in a channelized, regulated river: an integrated historical and modelling analysis', *Earth Surface Processes and Landforms*, vol. 43, no. 9, pp. 1739–1756, Jul. 2018.
- [2] Y. Audouin, T. Benson, M. De Linares, J. Fontaine, B. Glander, N. Huybrechts, R. Kopmann, A. Leroy, S. Pavan, C.-T. Pham, F. Taccone, P. Tassi, and R. Walther, 'Introducing GAIA, the brand new sediment transport module of the TELEMAC-MASCARET system', presented at the XXVI<sup>th</sup> TELEMAC - MASCARET Technical User Conference, Toulouse, France, 2019.
- [3] Y. Audouin, C. Goeury, F. Zaoui, R. Ata, S. El Idrissi Essebtey, A. Torossian, and D. Rouge, 'Interoperability application of TELEMAC-MASCARET System', presented at the XXII<sup>th</sup> TELEMAC - MASCARET Technical User Conference, Graz University of Technology, Austria, 2017.
- [4] C. Goeury, A. Pon  ot, J. P. Argaud, F. Zaoui, R. Ata, and Y. Audouin, 'Optimal calibration of TELEMAC - 2D models based on a data assimilation algorithm', presented at the XXII<sup>th</sup> TELEMAC - MASCARET Technical User Conference, Graz University of Technology, Austria, 2017.

- [5] T. Geay, S. Zanker, A. Hauet, C. Misset, and A. Recking, 'An estimate of bedload discharge in rivers with passive acoustic measurements: Towards a generalized calibration curve?', *E3S Web of Conferences*, vol. 40, p. 04009, 2018.
- [6] V. Wendling, N. Gratiot, C. Legout, I. G. Droppo, C. Coulaud, and B. Mercier, 'Using an optical settling column to assess suspension characteristics within the free, flocculation, and hindered settling regimes', *Journal of Soils and Sediments*, vol. 15, no. 9, pp. 1991–2003, Sep. 2015.
- [7] C. Legout, I. G. Droppo, J. Coutaz, C. Bel, and M. Jodeau, 'Assessment of erosion and settling properties of fine sediments stored in cobble bed rivers: the Arc and Isère alpine rivers before and after reservoir flushing', *Earth Surface Processes and Landforms*, vol. 43, no. 6, pp. 1295–1309, 2018.
- [8] J. Le Coz, M. Jodeau, A. Hauet, B. Marchand, and R. Le Boursicaud, 'Image-based velocity and discharge measurements in field and laboratory river engineering studies using the free FUDAA-LSPIV software', in *Proceedings of the International Conference on Fluvial Hydraulics*, Lausanne, Switzerland, 2014.
- [9] J. Hervouet, *Hydrodynamics of Free Surface Flows: Modelling with the finite element method*. 2007.
- [10] C. Villaret, J.-M. Hervouet, R. Kopmann, U. Merkel, and A. G. Davies, 'Morphodynamic modeling using the Telemac finite-element system', *Computers & Geosciences*, vol. 53, pp. 105–113, Apr. 2013.
- [11] J. Nikuradse, 'Laws of flow in rough pipes', Washington: National Advisory Committee for Aeronautics, 1950.
- [12] J.-P. Argaud, 'User Documentation, in the SALOME 7.5 platform, of the ADAO module for Data Assimilation and Optimization'. EDF R&D report, 2016.
- [13] C. A. Vionnet, P. A. Tassi, and J. P. Martin Vide, 'Estimates of flow resistance and eddy viscosity coefficients for 2D modelling on vegetated floodplains', *Hydrological Processes*, vol. 18, no. 15, pp. 2907–2926, Oct. 2004.



# TEL2TOM: coupling TELEMAC2D and TOMAWAC on arbitrary meshes

WA Breugem<sup>1</sup>, E Fonias<sup>1,2</sup>, L Wang<sup>1,2</sup>, A Bolle<sup>1</sup>

<sup>1</sup>International Marine and Dredging Consultants  
Antwerp, Belgium  
[abr@imdc.be](mailto:abr@imdc.be)

G Kolokythas<sup>2</sup>, B De Maerschalck<sup>2</sup>

<sup>2</sup>Flanders Hydraulics Research  
Antwerp, Belgium

**Abstract**—In this paper, a novel approach is presented to perform coupled simulations of TELEMAC2D and TOMAWAC. In this approach different meshes are considered: a dense mesh for TELEMAC2D in order to manage fast and accurate resolution of the flow and a much coarser for TOMAWAC in order to increase the computational speed of the wave model. The communication of flow variables is implemented by means of linear interpolation. Two applications are presented utilizing the TEL2TOM functionality: the existing littoral test case from the TELEMAC2D test bank, and a real world application in the Belgian coastal zone.

## I. INTRODUCTION

Currently, TELEMAC and TOMAWAC use the same computational meshes for performing coupled simulations of waves and currents. However, it would be advantageous to be able to use different meshes in TELEMAC and TOMAWAC. Then it would be possible to use a different spatial resolution in each model, which could lead to a substantial speed up in case a coarser mesh is used in TOMAWAC than in TELEMAC. Additionally it would be possible to use domains with different spatial extents. This could for example be used to exclude bays or rivers from TOMAWAC, where little wave action is expected. Another use would be to use a larger domain for TOMAWAC than for TELEMAC, in order to have a smoothly varying wave field at the boundary of the TELEMAC domain, which is beneficial when performing simulations of wave-current interaction. Because of the preceding examples, a very flexible coupling method is needed, that permits the use of interpolation as well as extrapolation. Moreover, in order to have fast calculation times, the coupling should be fully parallel and have little computational overhead.

The objective of the present paper is to present flexible model coupling framework developed within TELEMAC, which is applied to coupling TELEMAC2D and TOMAWAC on arbitrary grids. Further it is the objective to show examples of the application of this framework in a simplified and a real world test case.

## II. DESCRIPTION OF THE CODE DEVELOPMENT

### *Model coupling framework*

Presently, already some module coupling frameworks exist such as MCT [1] or OASIS, which served as inspiration

for the present code development. However, it was chosen to use a custom module coupler, specially designed for TELEMAC, rather than a general purpose model coupler. In this way maximum advantage of TELEMAC could be taken, while minimizing the changes needed to the code.

The coupling module consists of a main `mod_couple_mod.F` whose objectives are to exchange data in parallel between two models, which may have different meshes as well as different domain compositions (though both are using the same number of processors). The module is intended to be as flexible as possible, allowing the communication of a varying number of variables between both models. Also, the module is designed to allow interpolation and extrapolation of variables in a flexible way, based on weight factors and matching node numbers specified by the user in the geometry files of each coupled model. In this way different interpolation methods can easily be defined. For example:

- Nearest neighbour interpolation can be defined, by using a single node number of the closest node, with a weight factor of one. This type of interpolation can also be used for extrapolation (for data on nodes outside of the mesh).
- Bilinear interpolation (on a triangular mesh), can be obtained using the three nodes of a triangle in the mesh of the sender with the weights for the three points determined according to the distance of the node to the three other nodes.
- Other forms of interpolation (e.g. inverse distance interpolation or conservative interpolation) can be used using a larger number of nodes from which information is received.

It was chosen to let the user provide the information about interpolation and extrapolation in order to allow maximum flexibility. Many optimized routines are available, for example Python or Matlab, to determine these coefficients efficiently during preprocessing.

The general methodology of the coupling is as follows:

- In a model receiving information, the following information is defined for each node of the mesh:

- Global node number(s) in the sending model from which information is received at a point. The number of nodes from which information is received can be varied, but is constant for all the points in the mesh. Hence one can specify for example to use information from three nodes (e.g. for linear interpolation) when sending information from TELEMAC to TOMAWAC, but only use information from one node (for nearest neighbour interpolation), when sending information from TOMAWAC to TELEMAC. However in this example, each node in TOMAWAC needs to receive information from three different nodes in TOMAWAC. In case one wants to use information from less nodes for some specific locations (e.g. to mix nearest neighbour and linear interpolation), one has to specify some dummy node numbers, in combination with a weighting factor (described below) of zero. In case a node does not receive any information from the sending model, the number of the node from which information is received is set to zero. In that case, a default value (typically zero) is applied on the received information.
- There are weighting factors specifying the weight applied to a variable on the sending process in order to determining the interpolated variable on the receiving process. This weight is specified on each node of the sending process that are used to determine the value on the receiving process. The sum of these weights should be one.
- The node numbers from which information is received and their corresponding weights is used to determine the parallel communication pattern between the two models.
- At each coupling period step, information is exchanged in parallel between the two models. In order to interpolate, the weighting factors are used

The module consists of the following subroutines:

INIT\_COUPLE: initialisation of the coupling module, which allocates memory for the data structures used in the coupling.

ADD\_SENDER: Every model that sends information to another module calls this routine once, in order to let the coupler know that it will send information to another model. In this routine, some memory allocations are done, and the

list of global node numbers from the sender is sent to all processes of the receiving model.

ADD\_RECEIVER: Every model that receives information will call this module once. First the list of global node numbers is received from the sending model. Then, the node numbers of the sending model from which information is expected are read from the geometry file (in a separate subroutine READ\_RECV). Also the weighting factors related to these are read. The list of node numbers from which information is expected, in combination with the received global node numbers of the sending model are used to determine how to communicate data from the sender to the receiver by making lists of data to send, and data to receive, i.e. a mapping between the sender and the receiver. The lists of node numbers from which information is expected, is communicated to the right processor of the sender model.

SEND\_COUPLE: this routine is called by the sender at every coupling period time step. This routine sends the necessary variables to the correct process of the receiver, using the mapping defined in ADD\_RECEIVER.

RECEIVE\_COUPLE: this routine is called by the receiver at every coupling period time step. It receives the data sent by SEND\_COUPLE, and performs the interpolation using the stored weighting factors.

END\_COUPLE: Deallocation of the memory used for the coupling.

#### *Application for coupling TELEMAC and TOMAWAC*

The implementation is made in the cookiecuttershark branch, which is based on TELEMAC v7p2r1. In order to apply the coupling module for coupling TELEMAC and TOMAWAC, the following modifications of the code are made:

- Two new variables are added (type bief\_obj; object of objects), namely TEL2TOM and TOM2TEL. Through POINT\_TELEMAC2D and POINT\_TOMAWAC, the subroutine ADDBLO is called to set pointers to the coupled variables. The number of variables being communicated is stored in the new variables NVARTOM2TEL and NVARTEL2TOM.
- The variables that can currently be communicated are:
  - Water depth, U velocity and V velocity (from TELEMAC to TOMAWAC)
  - Significant wave height, Peak period, Wave radiation forces (in x and y directions), Wind velocity (in x and y directions), orbital wave velocity and mean wave direction (from TOMAWAC to TELEMAC).
- The variables that are communicated (for example water depth), need to be defined

separately in both TELEMAC and TOMAWAC, as they are on different meshes.

- Each model (TELEMAC and TOMAWAC) have already dedicated variables to define the mesh (defined respectively in `declarations_telemac2d.f` and `declarations_tomawac.f`). Nevertheless both variables are used in the subroutine `homere_telemac2d.f`, and hence it was necessary to define in the latter an alias for the TOMAWAC mesh. Moreover, there is one variable related to the mesh in parallel, which is not in the variable `MESH`, but in the variable `NPTIR`. Therefore, it is necessary to update this variable by calling the subroutine `GET_MESH_NPTIR` in the subroutines `WAC` and `TELEMAC2D`.

Note also that `PARTEL` splits up each geometry file separately by default. Hence no changes to `PARTEL` or the `PYTHON` scripts were necessary for the coupling of TELEMAC and TOMAWAC with different meshes. Also `GRETEL` correctly merges the meshes in case different meshes are used. Hence changes to `GRETEL` were also not needed.

- Some function calls to the coupling routines need to be made. The routines `ADD_SENDER` and `ADD_RECEIVER` are called twice in `HOMERE_TELEMAC2D`, once for sending information from TELEMAC to TOMAWAC and once for sending information from TOMAWAC to TELEMAC. The functions `SEND_COUPLE` and `RECEIVE_COUPLE` are used to exchange data between the modules during the initialisation and at every coupling period time step.
- Finally, some default values were needed in the initialisation (for example the radiation forces were set to zero in the initialisation).

### Limitations

Presently there are some limitations, when using the coupling:

- The coupling currently only works in parallel (using more than one processor for each coupled model). This stems from the fact that in the present implementation, the global node numbering (in the variable `MESH%KNOLG`) is used to determine the communication between the two processes. This variable does not exist for one processor. In principle, this limitation can be overcome quite easily.
- The number of processors needs to be the same for each coupled model, as there is currently. This limitation stems from the fact that

TELEMAC2D and TOMAWAC use the same variable `NCSIZE` to specify the number of processors that is used.

- No special treatment of dry nodes is currently implemented.
- No special interpolation method is used for interpolating wave directions, which may give inaccurate results for a wave direction close to 0 degrees. In principle this limitation could be easily resolved by sending the sine and cosine of the wave direction, rather than the wave direction, which can be interpolated without any problem. The wave direction can then
- The coupling is currently only implemented between TELEMAC2D and TOMAWAC, not yet between TELEMAC3D and TOMAWAC. In principle, this extension to TELEMAC3D is straight forward, especially when the exchange is limited to two-dimensional variables (as it is the case in TELEMAC v7p2). In that case, the changes that need to be made are limited to a number of function calls to the coupling routines within TOMAWAC-3D, and the definition of some separate variables in TELEMAC3D for the coupling. The flexibility of the coupling module, also allows three-dimensional information to be sent, for example by specifying each vertical layer as a separate two-dimensional variable, defined as a pointer to a part of a three-dimensional variable.

## III. TEST CASES

### Schematic test (*Littoral*)

In order to test the TEL2TOM functionality, an existing TELEMAC test (*littoral*) was executed. In this test case, the three-way coupling between TELEMAC2D, TOMAWAC and SISYPHE is tested. The test case describes a beach with a slope of 1:5, on which waves (significant wave height 1.0 m, peak period 8.0 s, wave direction 30°) propagate toward the coast. The waves generate a longshore current in the breaker zone, which on its turn induces sediment transport (calculated using the equation of Bijker). On the lateral boundaries of the TELEMAC model, a custom FORTRAN code is used to calculate the lateral velocity from the radiation stresses calculated in TOMAWAC. Note that in principle, it would have been possible to use the Neumann boundary conditions developed by [2] to calculate the velocity at the boundary, but it was chosen to keep the test case as close as possible to the original one. For the test case, two different setups were tested (Figure III-1):

- Settings comparable to the original test case setup (further referred to as *fine*). The same mesh is used for TELEMAC2D as for TOMAWAC. In order to have a fully developed wave profile at the lateral boundaries the wave

spectra at the centreline of the model are applied to the lateral boundaries using a custom boundary condition. The settings for TEL2TOM were defined such that data was directly applied at each node (without any interpolation).

- A setup with different meshes (further referred to as *coarse*). The mesh for TELEMAC2D and SISYPHE was kept the same as in the original test case. However, the mesh for TOMAWAC was coarsened by a factor 2. Further, the TOMAWAC domain was extended laterally to make sure that a correctly developed wave profile forms at the lateral boundary of the TELEMAC model (Figure III-1). On the lateral boundaries, a wave height of 1.0 m was applied.. Hence the custom FORTRAN code for transferring wave conditions from the centre to the boundary was not used any longer. The weighting factors were set such that linear interpolation was used to exchange information between the two meshes. . The extrapolation used on the extended TOMAWAC domain, outside TELEMAC2D mesh, was the nearest neighbour method.

Each case was run on two parallel processors (the minimum number of processors to use in TEL2TOM).

The results from the first case in TELEMAC v7p2 (using TEL2TOM), not shown, and from the original test case in TELEMAC v7p3 are similar. Nevertheless some small changes existed in the spin-up period, because of changes in the application of the boundary conditions in TOMAWAC between v7p2 and v7p3.

Results of the wave height, velocity profile and free surface elevation on a profile perpendicular to the beach in the centre of the domain, using TEL2TOM with the same and with different meshes, are shown in Figure III-2 to Figure III-4. In general the results are very similar. The wave height has the same maximum in both cases, but the profile is slightly different around the breaker zone, due to the differences in mesh resolution between TOMAWAC and TELEMAC2D. This leads to a wave driven current, with a slightly broader profile (but the same peak velocity) as in the case with the same meshes. The current profile is slightly broader in the case with the coarse TOMAWAC mesh, with a slight change of the location of the peak. This is presumably, because the force due to radiation stresses is very non-linear, but is interpolated using linear interpolation, such that the force profile is slightly different between the two cases. Also the calculated wave setup is very similar between the two models. With respect to the calculation time, the coarse case with two different meshes is about two times faster than the original case.

Hence this test case shows that, using TEL2TOM, similar results can be obtained with the same or different meshes, but that substantial calculation time (as well as storage space for output) can be saved. Also this test case shows that using extrapolation of water depths and velocities outside the

TELEMAC2D domain, a more flexible modelling approach is possible, which can be for example advantageous in determining boundary conditions for TOMAWAC on the boundary of a TELEMAC domain.

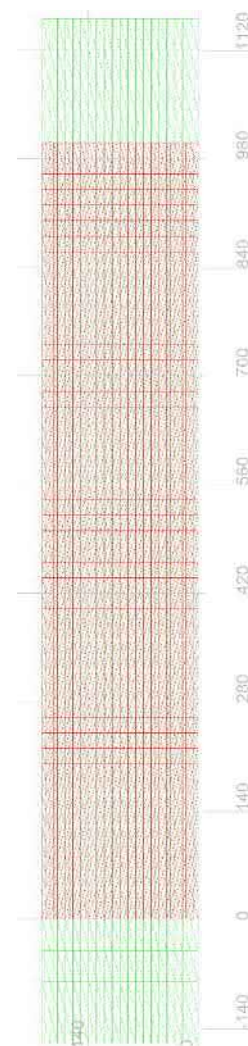


Figure III-1 Mesh for TELEMAC2D and SISYPHE (red) and TOMAWAC (green) for the "littoral" test case.



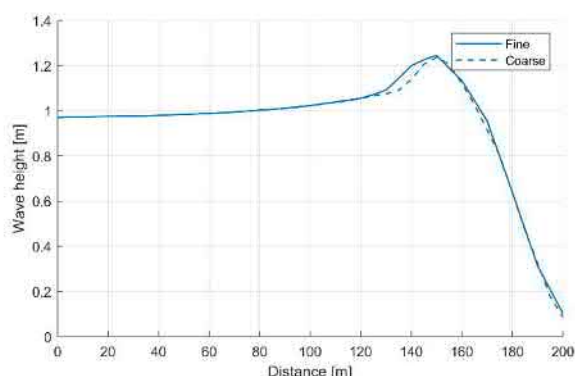


Figure III-2 Calculated significant wave height on a transect perpendicular to the beach for the fine and the coarse model.

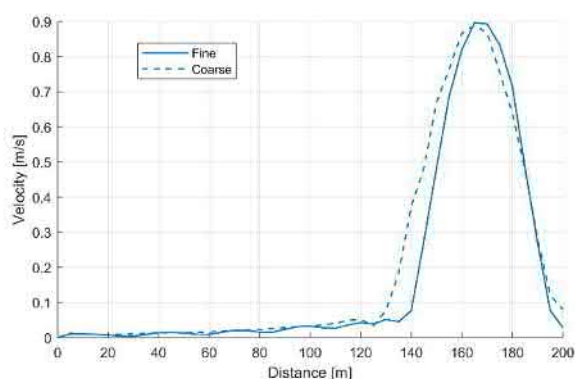


Figure III-3 Calculated velocity profile on a transect perpendicular to the beach for the fine and the coarse model.

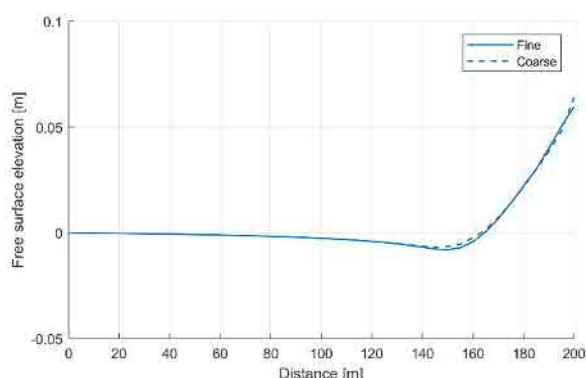


Figure III-4 Calculated free surface elevation on a transect perpendicular to the beach for the fine and the coarse model.

#### *Real case (Belgian coast)*

The TEL2TOM functionality has also been implemented within the Scaldis-Coast model for simulating tidal flow, wave flow and sediment transport within the Belgian coast. The computational meshes for TELEMAC2D and TOMAWAC are presented in Figure III-6. In this application, both TELEMAC2D and TOMAWAC have the same offshore

boundary, but, within the TOMAWAC domain, the inner ports, the Eastern Scheldt and Western Scheldt regions have been excluded in order to reduce number of elements in the mesh. Furthermore, the minimum resolution of TOMAWAC is substantially coarser (using elements of 50 m resolution) than the resolution of the TELEMAC2D mesh in the coastal zone (using elements of 25 m). This resulted in the reduction of the number of nodes for TOMAWAC down to 137,752 from the initial number of 258,390 (46.6% reduction). Linear interpolation is used for exchanging information between TELEMAC2D and TOMAWAC.

The coupled model simulated a period of 8 days starting from 16 Nov 2015 and the wave boundary conditions came from Westhinder station (code name WHIDW1, Figure III-5). The model results are compared with the dataset collected at stationary measurement points in the Broersbank project ([3]).

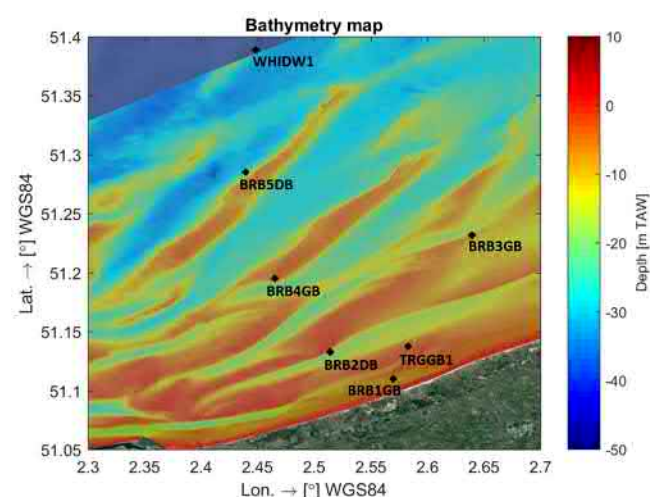


Figure III-5: Locations of the field measurement stations of the Broersbank project (Komijani *et al.* [3]).

The TEL2TOM model results are given in Figure III-7 and Figure III-8 in terms of significant wave height and mean period, respectively. The results demonstrate a very good agreement with the observations (and comparable to results obtained using the same mesh for TELEMAC2D and TOMAWAC, not shown). However, the simulation time is reduced significantly, more or less by a factor 2.

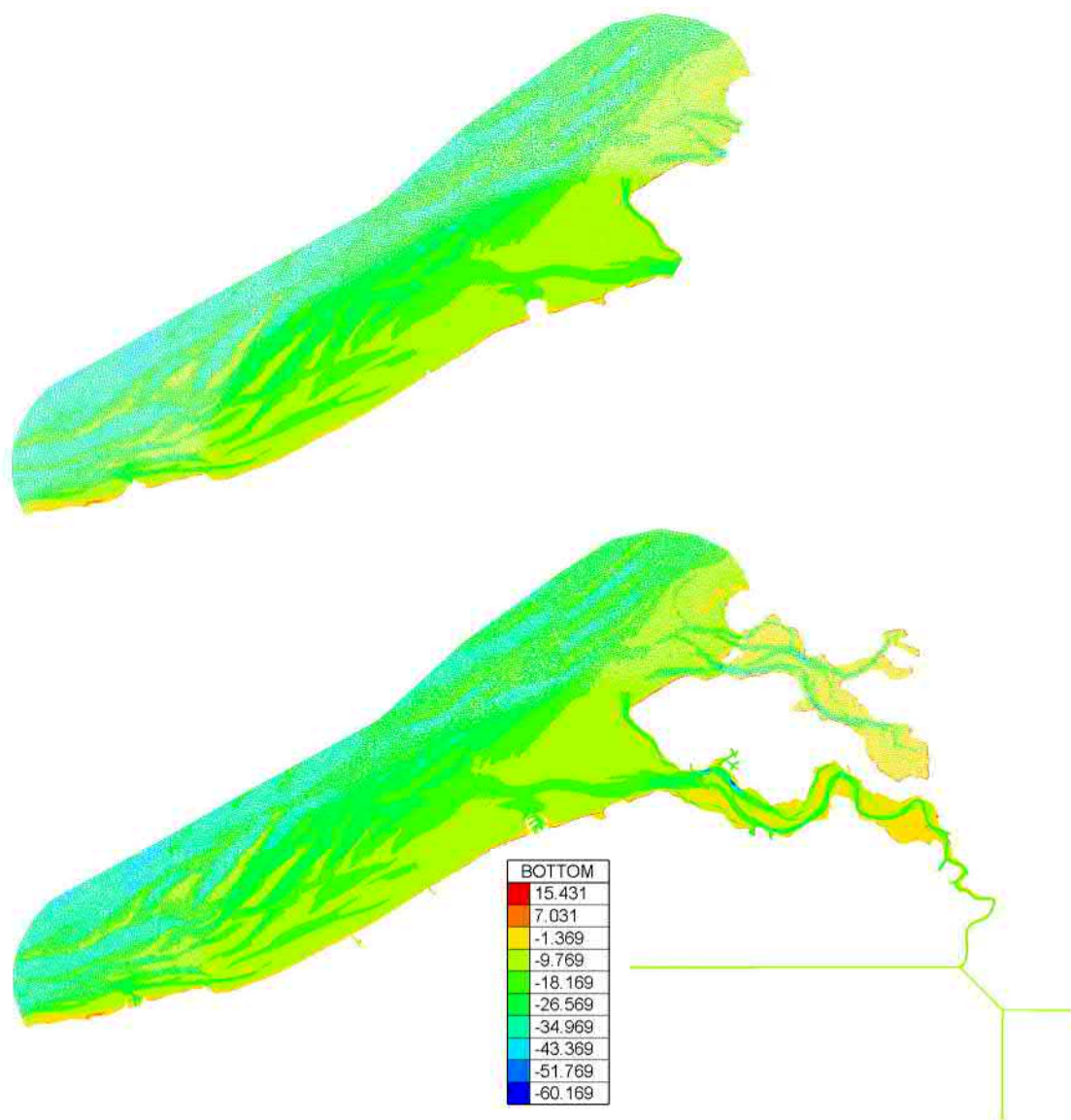


Figure III-6: Computational domains and meshes for TOMAWAC (upper figure) and TELEMAC2D (lower figure) for the TEL2TOM simulation of the Scaldis-Coast model.

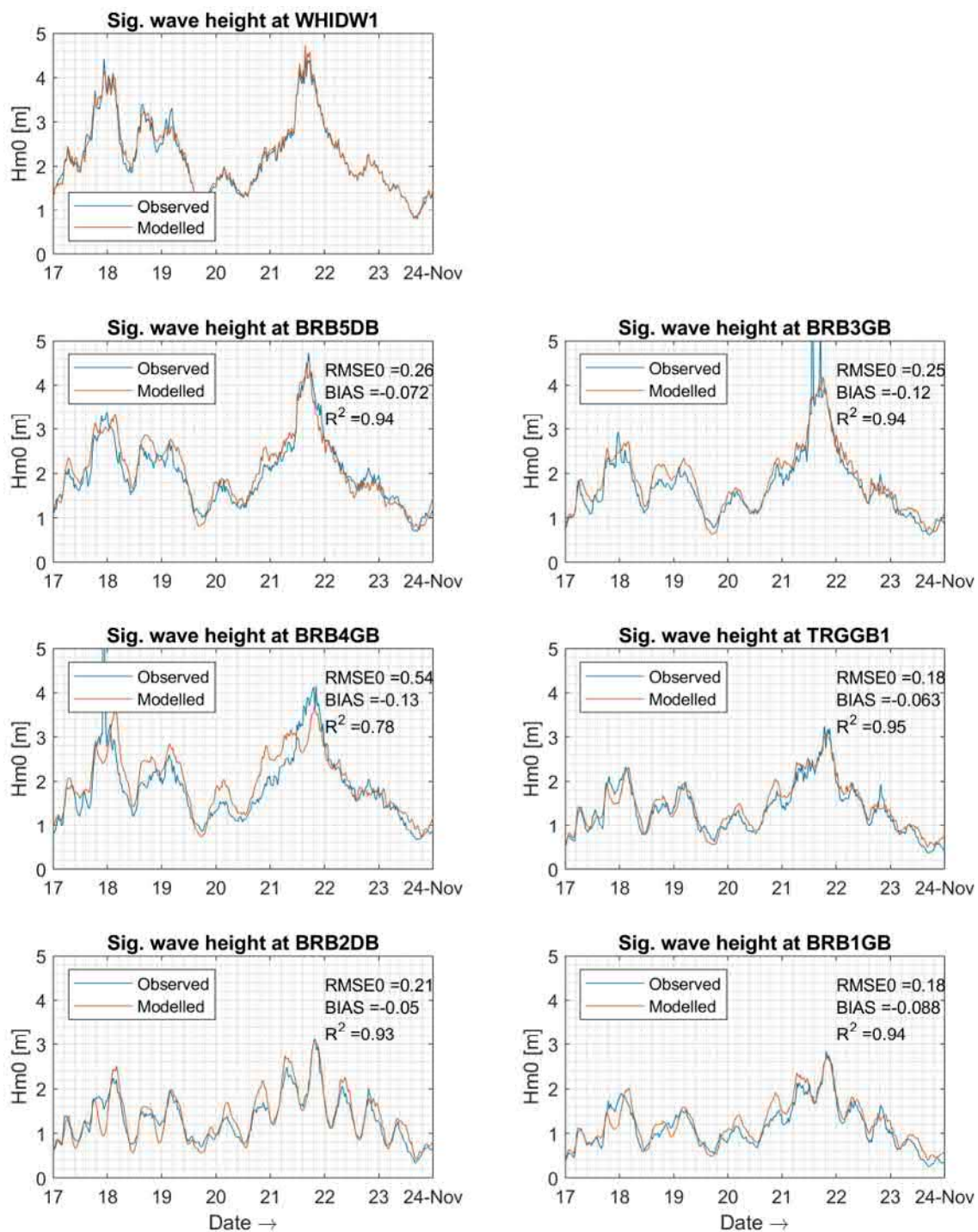


Figure III-7: Comparison of significant wave height between the observed data and modelled results at measurement stations, for a coupled TELEMAC2D-TOMAWAC case using TEL2TOM with a coarser TOMAWAC mesh.



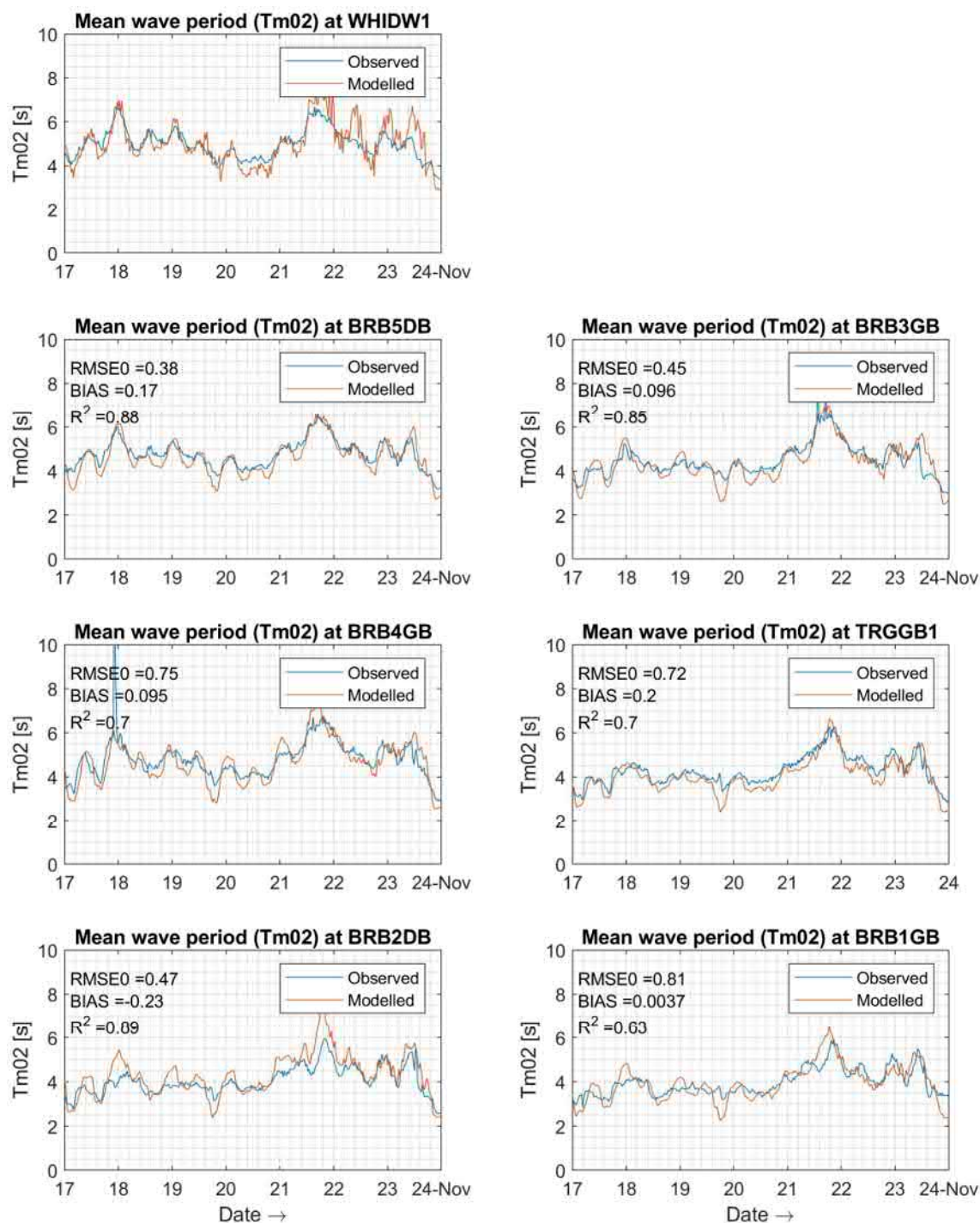


Figure III-8: Comparison of mean wave period between the observed data and modelled results at measurement stations, for coupled a TELEMAC2D-TOMAWAC case using TEL2TOM with a coarser TOMAWAC mesh.



## IV. USER MANUAL

In order to use different meshes on TELEMAC2D and TOMAWAC coupling the following should be done:

- 1.) Generate separate GEOMETRY FILES for TELEMAC2D and TOMAWAC (with a different mesh). Add these on each respective .cas model file.
- 2.) Add to the TOMAWAC GEOMETRY file the following variables:
  - a. TEL2TOM01: This variable contains, for each node in the TOMAWAC mesh, the number of the first node in TELEMAC from which TOMAWAC receives information. In case the node does not need to receive information, set this number to zero.
  - b. TEL2TOMWTS01. The weight factor applied to the information received from the node specified in TEL2TOM01.
  - c. Optionally add information from additional nodes in variables TEL2TOM02 to TEL2TOMNN, where NN is the number of nodes from which information is received.
  - d. For each of these additional variables TEL2TOM02 to TEL2TOMNN add the corresponding weights TEL2TOMWTS02 to TEL2TOMWTSNN. For each receiving node, the sum of the weights of the sending nodes must be equal to one.

An example of the above procedure is shown in Figure IV-1, for a simple mesh consisting of one TOMAWAC element and two TELEM2D elements. .

- 3.) Add to the TELEMAC2D GEOMETRY file the following variables:
  - a. TOM2TEL01 to TOM2TELNN: for each node in TELEMAC mesh, it has the node number in TOMAWAC from which TELEMAC receives information. It works in a similar way as explained above for TEL2TOM..
  - b. TOM2TELWTS01 to TOM2TELWTSNN: the corresponding weights to send information from TOMAWAC to TELEMAC.
- 4.) Specify the keyword PARALLEL PROCESSORS in TELEMAC and TOMAWAC .cas files. Use the same number of processors in both models. The minimum number of processors that can be used is currently 2.

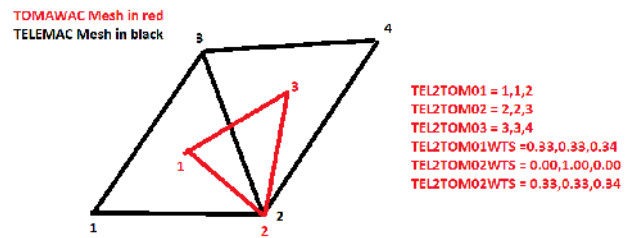


Figure IV-1 Example showing the numbering convention for linear interpolation on a simple mesh when sending information from TELEMAC to TOMAWAC. The TOMAWAC mesh is shown in red, the TELEMAC mesh in black. Linear interpolation is used, using three nodes in TELEMAC to get information for one node in TOMAWAC. The variables added to the TOMAWAC are shown in red for each different node. In this example, node 1 in TOMAWAC received information from nodes 1, 2 and 3 of TELEMAC. The weights are each approximately 0.33 (as the TOMAWAC node is in the centre of the TELEMAC node). Node 2 in TOMAWAC also receives information from nodes 1, 2 and 3 of TELEMAC. However, because this node coincides with node 2 in TELEMAC, the weight for this node is 1.0, whereas the weight for information coming from the other nodes is 0.0.

## V. SUMMARY AND CONCLUSIONS

In this paper, the TEL2TOM functionality has been presented. Through this novel approach, TELEMAT and TOMAWAC meshes and domains can be different. The TEL2TOM has been firstly applied in a schematic case through the Littoral tutorial and then in a real application within the Belgian coast using the Scaldis-Coast model for tidal flow and waves. The use of TEL2TOM resulted in significant computational speed-up (to a factor of 2) while showing similar accuracy against field measurements for waves in the Belgian coast.

## REFERENCES

- [1] Larson, Jay, Robert Jacob, and Everest Ong. "The model coupling toolkit: a new Fortran90 toolkit for building multiphysics parallel coupled models." *The International Journal of High Performance Computing Applications* 19.3 (2005): 277-292.
- [2] Breugem, Alexander, Efstratios Fonias, Li Wang, Annelies Bolle, Gerassimos Kolokythas, and Bart De Maerschalck. "Neumann (Water Level Gradient) Boundaries in TELEMAC 2D and Their Application to Wave-Current Interaction," 111–16. Norwich, United Kingdom, 2018. <https://doi.org/10.14465/2018.tucxxv.nrw>.
- [3] H. Komijani, H. Ortega and Q. Zhang, "Opstellen van een hydrodynamische modellen suite TELEMAC-TOMAWAC voor de Broersbank: Leuven", 2016

# Density stratification and turbulent mixing in a salt-wedge estuary : The Adour river .

S. Defontaine<sup>1</sup>, D.Sous<sup>2,3</sup>, P. Maron<sup>2</sup>, D. Morichon<sup>2</sup>

<sup>1</sup>CNRS / Univ. Pau & Pays Adour/ E2S UPPA, Laboratoire de Mathématiques et de leurs Applications de Pau - Fédération MIRA, UMR5142 64000, Pau, France

<sup>2</sup>Univ. Pau & Pays Adour / E2S UPPA, Laboratoire des Sciences de l'Ingénieur Appliquées à la Mécanique et au Génie Electrique (SIAME) - MIRA, EA4581, 64600, Anglet, France

<sup>3</sup>Université de Toulon, Aix Marseille Université, CNRS, IRD, Mediterranean Institute of Oceanography (MIO), La Garde, France

## Abstract:

Estuaries are complex transfer areas of water masses and suspended particulate matters (SPM).. From a physical point of view, estuaries are exchange areas between fresh brackish continental water and salty marine waters, mainly driven by river run-off, tides and wind forcing. Density gradients generated by the continental waters inter-playing with marine waters, and interactions between tides and estuarine morphology have been shown to be the major mechanisms governing the estuarine dynamics. The vertical density stratification, which results from the competition between density gradient and velocity/bottom shear, plays a major role in the transfer and mixing of water masses and the transport of dissolved and particulate matters. Its precise reproduction is therefore one of the cornerstones of estuarine numerical modeling.

The present study has been specifically designed to provide a detailed insight on hydrodynamics in a man-engineered channel-shape estuary, subjected to strong tidal and fluvial forcing, with few intertidal area and small watershed; as very few is known about such estuaries. The selected field site is the Adour river estuary, located at the bottom of the Bay of Biscay. It is a highly developed estuary with several kilometres of its downstream part completely channelised in order to secure the Bayonne harbour operations. This specific morphology is reinforced by a man-engineered reduction of the section at the last reach, in order to ease the expulsion of water and sediment. The Adour estuary morphology combined with the competition between the tide and the river flow result in a time-dependent salt-wedge estuary.

A numerical model has been developed based on the open source code TELEMAC-3D to investigate the interaction between light continental waters and heavy salty marine waters, focusing on the salt-wedge intrusion inside the estuary. A major issue of our numerical study is to reproduce the striking variability of the Adour lower estuary in terms of hydrological regimes, ranging from salt-wedge to partially mixed regimes depending on tidal and discharge conditions. These features are strongly related to the variations of turbulent properties and salinity structure, with higher turbulent mixing when stratification is minimal. The model is tested against a series of field campaigns performed inside the lower estuary between September 2017 and September 2018, to cover contrasted conditions of river discharge and tidal range. Velocity profilers and high frequency point current-meters were moored, at two different stations inside the estuary, during one month. The correct representation of density stratification processes by the numerical model remains, as expected, a challenging issue. The choice of the turbulence model is of the foremost importance for a good representation of the interaction between water masses. A comparison between constant viscosity, mixing length with damping function and k-epsilon turbulence models will be discussed within the physical framework provided by field measurements.

**Proposed session:** *River, estuaries, maritime, coastal sediment processes*

**Key words:** TELEMAC3D, stratification, turbulence, salt-wedge estuary

**Speaker:** S. Defontaine

# A preliminary study of tide propagation and sediment dynamics in a macrotidal estuary influenced by the presence of a tidal power station

R. RTIMI<sup>1,2</sup>, A. SOTTOLICHIO<sup>1</sup>, P. TASSI<sup>2</sup>

<sup>1</sup>University of Bordeaux, EPOC UMR5805, Pessac, France

<sup>2</sup>EDF R&D – LHSV, Chatou, France

Email: [rajae.rtimi@edf.fr](mailto:rajae.rtimi@edf.fr)

**Abstract:** Estuaries are complex ecosystems hosting intense biogeochemical processes and habitat diversity, where many industrial, commercial and recreational activities develop. Located on the Brittany coast of northern France, the Rance estuary is a relatively small steep-sided *ria*, with a maximum spring tidal range of 13.5 m at the mouth and an average fluvial discharge of  $7 \text{ m}^3/\text{s}$  [Bonnot-Courtois *et al.* (2002)]. Taking advantage of this macrotidal regime, the first and largest operational tidal power station in the world was built at the estuary mouth and is operating since the 1960s [Pelc and Fujita (2002)]. The estuarine area extends over a length of approximately 20 km between the tidal power station in the north and the Châtelier lock in the south (Figure 1). The morphology of this *ria* is remarkably complex. Its layout is a function of the geology and rocks resistance that composes the valley (Figure 1). The estuary presents low suspended sediment concentration, with average values below  $10 \text{ mg/l}$ . However, an estuarine turbidity maximum is observed located in the vicinity of the Châtelier lock (Figure 1), showing seasonal upstream downstream fluctuations following the saline intrusion, and reaching concentrations in the range of  $[100\text{-}300] \text{ mg/l}$ , as observed in 1991, during a low tide period [Bonnot-Courtois *et al.* (2002)]. Despite a well-known drastic effect of the plant on the damping of estuarine water levels, little attention has been given to the propagation of the tidal wave along the estuary. Moreover, net siltation has been reported by several observations, but there is no quantitative assessment of the plant role on sediment dynamics along the estuary.

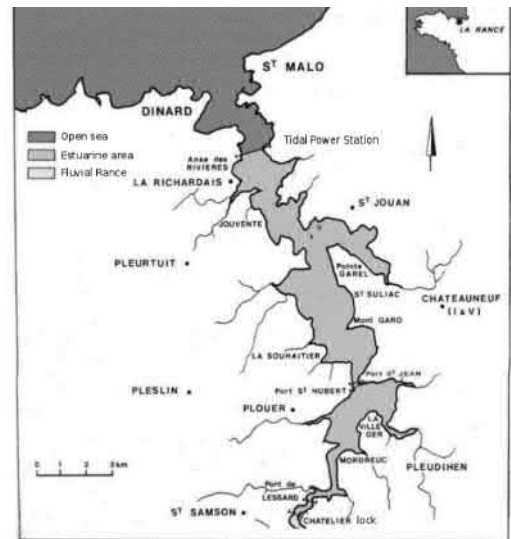


Figure 1: The Rance estuary (adapted from [Bonnot-Courtois *et al.* (2002)])

In this study we analyze for the first time tidal wave patterns and sediment dynamics in this particular man-engineered system. A preliminary numerical model, based on a 2D depth-averaged approach was implemented to predict the tide propagation and tidal flows in the estuary, accounting for the presence of the tidal power station in present-day conditions. The models used the bathymetry of 2018 and real tides were imposed at the estuary mouth, downstream and upstream the tidal power plant. The model was validated by comparison with existing data in the estuary, available at two stations. The effect of the power plant is analyzed by comparing the present-day tidal wave with theoretical water levels expected in the absence of the power-plant damping. Then, a simple parameterization of the physical variables is used to simulate suspended sediment transport and in particular estuarine turbidity maximum, observed near the freshwater/saltwater interface in the upstream area. First results are analyzed and discussed to highlight the role of the tidal power station on the transformation of the tidal wave along the estuary and its impact on the fine sediment concentration and turbidity maximum.

**Proposed session:** River, estuaries, maritime, coastal sediment processes

**Key words:** estuary, tidal power plant, tidal distortion, sediments dynamic, estuarine turbidity maximum

**Speaker:** RTIMI Rajae

## References:

- Bonnot-Courtois, C., Caline, B., L'Homer, A., & Le Vot, M. (2002). *La baie du Mont-Saint-Michel et l'estuaire de la Rance*. 26.
- Pelc, R. & Fujitas, R. M. (2002). *Renewable energy from the ocean. Marine Policy*, 26(6):471 – 479.

# Benchmark of hydro-sedimentary 1D codes: HEC-RAS, COURLIS and ADIS-TS

Emilio Corrales Lalinde<sup>1</sup>, Violaine Dugué<sup>1</sup>, Thierry Frétau<sup>1</sup>, Matthieu Sécher<sup>2</sup>, Eric Valette<sup>2</sup>, Jean-Baptiste Faure<sup>3</sup>,  
Benoît Camenen<sup>3</sup>

<sup>1</sup> Compagnie Nationale du Rhône (CNR)  
69316 69004 Lyon Cedex 04  
France

<sup>2</sup> Electricité de France (EDF) – Centre d'Ingénierie  
Hydraulique (CIH)  
73370 La Motte Servolex  
France

<sup>3</sup> Irstea – UR RiverLy  
Centre de Lyon-Villeurbanne  
69100 Villeurbanne  
France

**Abstract** — The objective of this work is to discuss the performance of three different 1-D hydro-sedimentary numerical codes: (i) HEC-RAS (Corps of Engineers of the US Army), (ii) TELEMAT-MASCARET/COURLIS (EDF) and (iii) MAGE/ADIS-TS (Irstea). These numerical codes are commonly used in France in engineering or research projects. Their hydrodynamic module is based on similar equations (1D Shallow Water Equations). However, the sedimentary modules often differ in the description and modelling of parameters such as bed shear stress representation, grain size distribution, or bed evolution and involve different input data. The three numerical codes were used to simulate the 2016 dam flushing operation on the French Upper Rhône River, which is characterised by three different phases: (i) sediment deposition, (ii) erosion and (iii) propagation. The calibration of the hydro-sedimentary models was performed using Suspended Particle Matter (SPM) loads (from calibrated turbidity records), particle-size measurements and bathymetric data. Sensitivity analysis was performed for the most relevant parameters of each software (critical bed shear stress, median grain size, etc.). The main criterions of the benchmark are the user experience, the ability to reproduce observations and the time calculation.

## I. INTRODUCTION

Suspended Particulate Matter (SPM) transport through engineered rivers is of primary concern for security and operational purposes. Indeed, sediment deposition in dam reservoirs can increase the water level and endanger surrounding habited areas, and it affects the hydro-electric production by reducing the reservoir capacity. Several desiltation technics exist to reduce deposition in a long-term perspective but they need to be carefully managed in order to limit downstream ecological impacts [10]. To develop efficient sediment management and control strategies, river managers need relevant field data and practical numerical tools.

Combined with field and laboratory measurements, numerical modelling of transport, deposition and erosion of SPM is commonly used in engineering studies. Nowadays,

different numerical codes (1D, 2D and 3D) exist to represent those phenomena; however, the choice of the model dimension is conditioned by the objective of the study, the user's need and the available resources. This is represented by the temporal and spatial scales and the degree of simplification.

Each kind of model has its strengths and weaknesses: (i) 1D hydro-sedimentary numerical codes are relevant to simulate long-term events on a long river network with small time steps [8]. They help to improve the understanding of hydro-sedimentary processes in the river and they can be used in some cases to predict long-term bed evolution [12]. (ii) 2D hydro-sedimentary numerical models are mainly used to simulate both short and medium terms events on a specific river reach in order to evaluate the sediment behaviour in vertical and horizontal axis and the local bed evolution [16]. (iii) 3D hydro-sedimentary numerical models are appropriate to represent the local and/or punctual (small scale) morphological phenomenon like sediment effects around hydraulics structures such as intakes, controls structures, transitions, bridge piles, etc.

The present study arises from the need of the Compagnie Nationale du Rhône (CNR) to find a numerical modelling tool able to represent the dynamics of suspended sediments and bed evolution during a dam flushing operation event on the French Upper Rhône River. In accordance with the industrial needs of the company, this tool must be reliable, robust and user-friendly, for both internal and external projects. Due to the complex phenomenon involved, its numerical simulation requires an important amount of field data, before, during and after the event; nevertheless, the acquisition of the data is expensive, especially bathymetric profiles and measurements of the bed sediment grain size distribution. The length of the studied reach (about 30 km) and the lack of data (cross-section every 200 m in average) are the main reasons leading to the choice of a 1D modelling.



The aim of this paper is (i) to present a short description of the of the case used for the benchmark, which is a dam flushing event in the Upper Rhône River in 2016, (ii) to present the numerical codes used for the project, (iii) to describe the construction of the models and finally, (iv) to illustrate and discuss the obtained results with each numerical code and the performance of the code.

## II. THE 2016 UPPER RHÔNE DAM FLUSHING EVENT

Every 3 years, between end of May and beginning of June, to prevent flood hazards, regulatory sediment flushing are carried out to reduce the volume of sediments in the Verbois reservoir. These sediment flushing involve the sediment flushing of downstream dam reservoirs, including Genissiat and Seyssel (see Figure 1a).

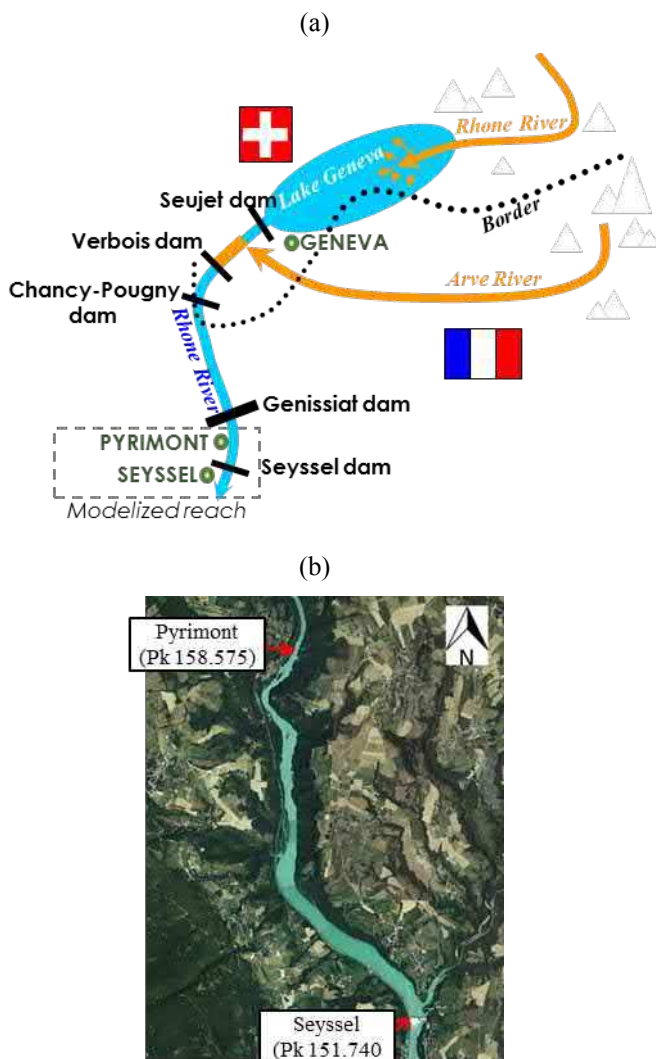


Figure 1: (a) Schematic overview of the upper Rhone River situation and (b) Modelized reach from Pymont station to Seyssel hydro-electric power scheme (Source: Géoportail, 2018).

This kind of events is controlled on the Upper French Rhône River. For example, the suspended sediment concentrations released from the Génissiat reservoir (upstream Pymont station, Figure 1b) have not to exceed 5

g/l on average over the entire operation, 10 g/l on average over any 6 hour period, and 15 g/l over any 30 minutes period. [11]. Based on the above, the numerical simulation becomes relevant in order to “predict” the evolution of SPM concentration during the flushing event.

The modelled area is a reach of the French Upper Rhône river from Pymont monitoring station (downstream Génissiat dam) onto Seyssel hydro-electric power scheme, whose length is about 6.8 Km (Figure 1b). This reach is characterized by 1D flow; there are not natural or anthropic (structures) singularities.

The flushing event selected for this benchmark, which took place between May 20<sup>th</sup>, 2016 and May 30<sup>th</sup>, 2016, presents at Seyssel, three characteristic phases: (i) deposition, (ii) erosion and (iii) propagation (Figure 2b). Several measurements (discharge, water level and SPM concentration) were undertaken during the event both upstream (Pymont) and downstream (Seyssel) (Figure 2).

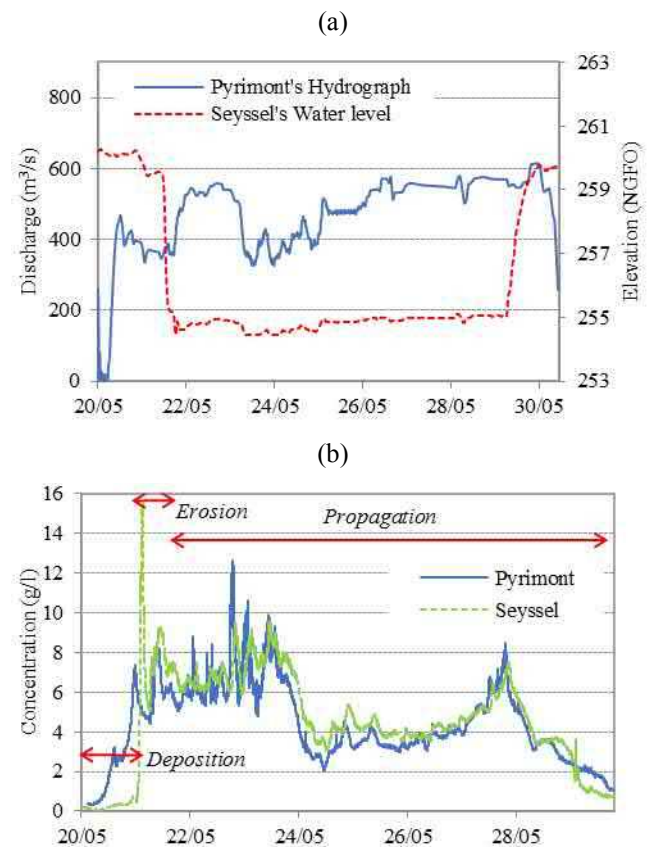


Figure 2: field measurements at Pymont and Seyssel stations during the flushing event of 2016. (a): Water Discharge at Pymont and water level at Seyssel station; (b) SPM concentrations.

## III. SELECTION OF THE NUMERICAL CODES

Several hydro-sedimentary numerical codes are available. Among them, some are commercial or shareware and others are freeware. According to the industrial needs, the CNR decided to evaluate the capabilities of three different 1-D hydro-sedimentary numerical codes, commonly used in France in engineering or research projects, in order to know

the advantage and disadvantage of each one: (i) HEC-RAS (Corps of Engineers of the US Army) a software used worldwide, (ii) TELEMAT-MASCARET/COURLIS (EDF) and (iii) MAGE/ADISTS (Irstea); both EDF and Irstea are French institutions working together with CNR to develop this project.

For the three numerical codes, the hydrodynamic module is based on similar equations (1D Barré de Saint-Venant equations). However, the sedimentary modules often differ in the description and modelling of parameters such as bed evolution, bed shear stress representation or grain size distribution and involve different input data.

#### A. HEC-RAS V5.0.3

HEC-RAS (Version 5.0.3, Hydrologic Engineering Centers - River Analysis System) allows to perform the 1D and 2D hydraulic simulations and its integrated sedimentary module makes it possible to perform simulations of both bed load and suspended sediment transport and represent the bed evolution (quasi-unsteady flow and unsteady flow). [14][15]

HEC-RAS has several functions and parameters included in sedimentary module. The user, based on its expertise, has to choose the appropriate functions and values in order to obtain physical and coherent results. The most relevant parameters are:

- Thickness of the bed sedimentary layer: Only one sedimentary layer with different depths along the reach can be modelled.
- Critical shear threshold: as HEC-RAS uses the equations of Krone (1962) [6] and Partheniades (1965) [9] to represent deposition and erosion for cohesive sediments, it is necessary to define a value for the critical shear stress (in Pa), which is used for erosion and deposition for particle erosion. There is also a second shear stress thresholds  $\tau_m$  ( $\tau_m > \tau_c$ ) implemented in HEC-RAS for mass wasting erosion. The slopes of the erosion rate curve for each type of erosion (in N/m<sup>2</sup> hr) must be defined [15].
- Bed grain size distribution (GSD): HEC-RAS allows defining the particle size-distribution (in mm).
- Inlet SPM concentration: as for bed gradation, HEC-RAS allows defining the particle size-distribution and also the concentration, in tons per day.
- Settling velocity method ( $w_s$ ): the user has to choose between Van Rijn, Ruby, Toffaleti, Report 12 and Dietrich.
- Sorting method: 3 options are available, Thomas (Ex5), Active Layer and Copeland (Ex7).
- Transport function: there is a set of several semi-empirical sediment transport formulas. The user has to select one of them (Ackers & White, Engelund & Hansen, Laursen (Copeland), Meyer Peter & Muller, Toffaleti, MPM-Toffaleti, Yang, and Wilcock & Crowe) according to the characteristic of the case to model.

- The user must select between quasi-unsteady flow and unsteady flow to carry out a sediment transport simulation.

#### B. COURLIS - MASCARET

COURLIS is a one-dimensional hydro-sedimentary code, developed by EDF (Électricité de France). In its suspension module, by solving advection-diffusion equation (Eq. 1), it can model transport, deposition and erosion of fine sediments (sands and silts), as well as the bed evolution. It can be used to model flows in rivers or in reservoirs when the flows can be considered as 1D. The code is weakly coupling with the hydraulic module MASCARET, also developed by EDF. [1][12].

$$\frac{\partial A \cdot C}{\partial t} + \frac{\partial Q \cdot C}{\partial x} = \frac{\partial}{\partial x} \left( k \cdot A \cdot \frac{\partial C}{\partial x} \right) + E - D \quad (1)$$

The most relevant parameters to perform sediment's transport simulation are:

- Number of sedimentary layers: COURLIS can use up to 5 layers with different thickness.
- Critical constraints for erosion and deposition: as COURLIS uses the equations Krone (1962) [6] and Partheniades (1965) [9] to represent the deposition (Eq. 2) and the erosion (Eq. 3), of cohesive sediments, respectively, it is necessary to provide a critical threshold for both erosion and deposition (in Pa) and the Partheniades coefficient (in kg/m<sup>2</sup>/s).\*

$$D = w_s C \left( 1 - \frac{\tau}{\tau_{cd}} \right) \quad (2)$$

where,  $\tau$  is the local shear stress (Pa),  $\tau_{cd}$  is the deposition critical shear stress (Pa), and  $w_s$  is the settling velocity (m/s).

$$E = M \left( \frac{\tau}{\tau_{ce}} - 1 \right) \quad (3)$$

where,  $\tau$  is the local shear stress (Pa),  $\tau_{ce}$  is the erosion critical shear stress (Pa) (or slope of the erosion rate curve), and  $M$  is the erosion rate coefficient (kg.m<sup>-2</sup>.s<sup>-1</sup>).

- The settling velocity value ( $w_s$ ) in (m/s): this parameter is adapted according to the sediment grain size (correlation between the settling velocity and the particle diameter).
- The value of the estimated skin Strickler roughness coefficient ( $K_p$ ): one value for each sedimentary layer (m<sup>1/3</sup>/s).
- Inlet SPM concentration: COURLIS uses only one sediment class and the concentration should be defined in g/l for each time step.
- The boundary sections of the reach: the first and the last section of the simulation domain are "fixed profiles" and do not evolve along the simulation; for that reason, it is important to define the study area in between those profiles.

### C. ADISTS - MAGE

ADISTS is a sedimentary module weakly coupled with the hydraulic module Mage, both codes developed by Irstea. ADISTS has been first developed to simulate the transport of pollutants in a hydrographic network; it was then adapted to simulate the transport of suspended sediments [2][3][4][5]. ADISTS solves the advection-dispersion equation (Eq. 1) using a simplified version of the source terms:

$$(E - D) = a_{PD} \cdot (C_{eq} - C)w_s \quad (4)$$

where  $a_{pd}$  is a calibration coefficient,  $C$  the concentration (kg/m<sup>3</sup> or g/L) and  $C_{eq}$  the equilibrium concentration:

$$C_{eq} = C_o \left( \frac{\tau}{\tau_{cr}} - 1 \right) \quad (5)$$

where,  $C_o$  (g/l) is a calibration coefficient,  $\tau$  effective bed shear stress (Pa)  $\tau_{cr}$  critical bed shear stress (Pa).

The most relevant parameters to compute sediment's transport simulation are:

- Thickness of the sedimentary layer: there may be one layer per sediment type and its thickness may vary along the reach but must be constant for each cross section.
- Number of sediment types: ADISTS can work with several classes of sediments.
- Characteristics of each class of sediments: defined by several parameters such as average diameter  $d_{50}$  (in m), porosity of the deposit, density, and the calibration parameters to solve the advection-dispersion equation [3].
- Inlet sediments load: the concentration of upstream sediments (in g/l) should be defined for each type of sediment.

### IV. CONSTRUCTION OF THE MODELS

Three models (one per numerical code) were built to reproduce the flushing event of 2016. Due to some differences between the input parameters of each software, the models were carefully built in order to be homogeneous and consistent.

The bathymetry of the reach was represented by 73 cross-sections with a regular interval of 100 m. The downstream cross-sections, near Seyssel dam, are closer.

The time steps for the simulations were selected for each numerical code as follow: (i) 10 s for HEC-RAS, (ii) 1 s for COURLIS and (iii) 60 s for ADIS-TS.

The simulations were initially performed with only one sediment class with a  $d_{50} = 20 \mu\text{m}$ . This diameter corresponds to the most often observed sediment in the French Upper Rhone River [13][7][2]. This sediment diameter was used for the inlet SPM concentration as well as for the characteristics of the bed. The sediment's characteristics were defined according to the parameters of each software and adapted in order to find more accurate results.

Based on estimation of the stocked volume of sediments, three different bed configurations (distribution of sediment's deposit along the reach) were defined: (i) 0 m<sup>3</sup> stocked along the reach, (ii) 3 sectors of thickness, 0 m – 1 m – 3 m, and (iii) 2 sectors of thickness, 0 m – 3 m (Figure 3). They are useful to identify the influence of the stocked sediments before the flushing event, on the SPM concentration signal registered during the event.

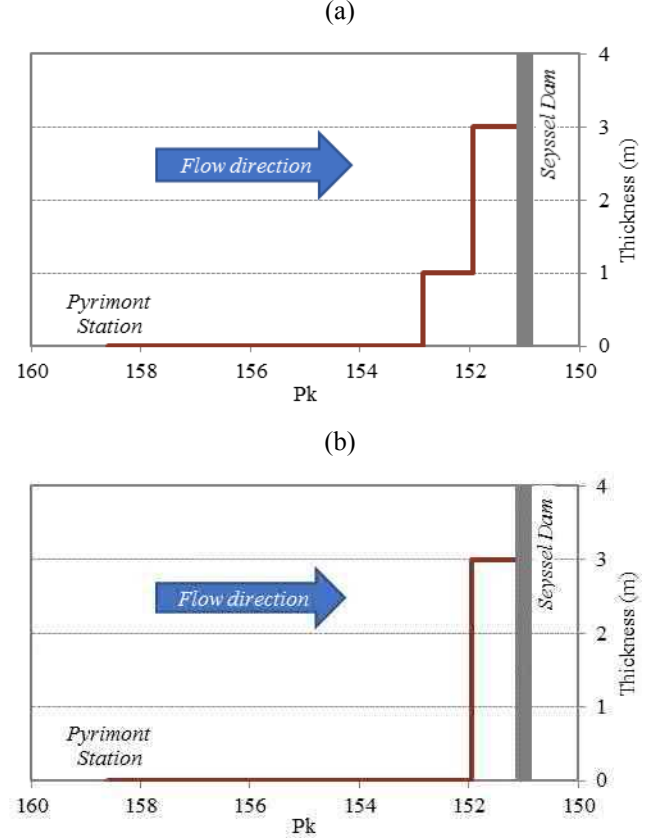


Figure 3: Thickness of the sediment layer in the river bed. (a) Configuration 0 m – 1 m – 3 m and (b) Configuration 0 m – 3 m.

### V. RESULTS

#### A. Hydraulic

The three hydrodynamic models were calibrated and validated along the whole river reach using water elevation longitudinal profiles and discharge measurements.

In general, the hydraulic performance is the same for the three software. However, a little deviation exists in the first section of the reach (between Pyrimont (Pk 158.575) and section Pk 158.00) where the flow regime is supercritical (Figure 4).



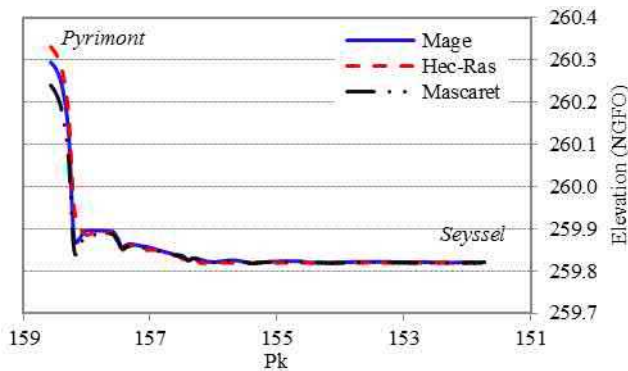


Figure 4: Water elevation longitudinal profile at the end of simulation

### B. Hydro-sedimentary calibration and sensitivity analysis

Calibration of the hydro-sedimentary models was performed using SPM loads from calibrated turbidity records, particle-size measurements and bathymetric data.

Sensitivity analysis was performed for the most relevant parameters (critical bed shear stress,  $d_{50}$  of particles and volume of sediments stocked before the event) keeping up the same hydraulics characteristics and inlet SPM concentration.

The results clearly show the numerical codes' sensitivity to parameter calibration, which have a strong influence on deposition and erosion phenomena. Among many results, the figures below were selected to show the impact of the parameters mentioned above on the sedimentary results during the 3 phases of the simulated event (deposition, erosion and propagation).

Figure 5 shows the influence of the stored volume of sediment in the river bed on the concentration signal during the erosion phase (between May 21<sup>st</sup> and May 22<sup>nd</sup>, 2016). The bigger the amount of stored sediments, the longest is the erosion phase.

Figure 6 shows the influence of the sediment GSD on the deposition phase (between May 20<sup>th</sup> and May 21<sup>st</sup>, 2016); the settling velocity is linked to the diameter and in consequence the behaviour of the models during the deposition period is affected. The bigger the diameter, the fastest the sediments settled.

Figure 7 shows that the critical bed shear thresholds have strong influence on the motion to start the erosion phase and therefore on the peak representation.

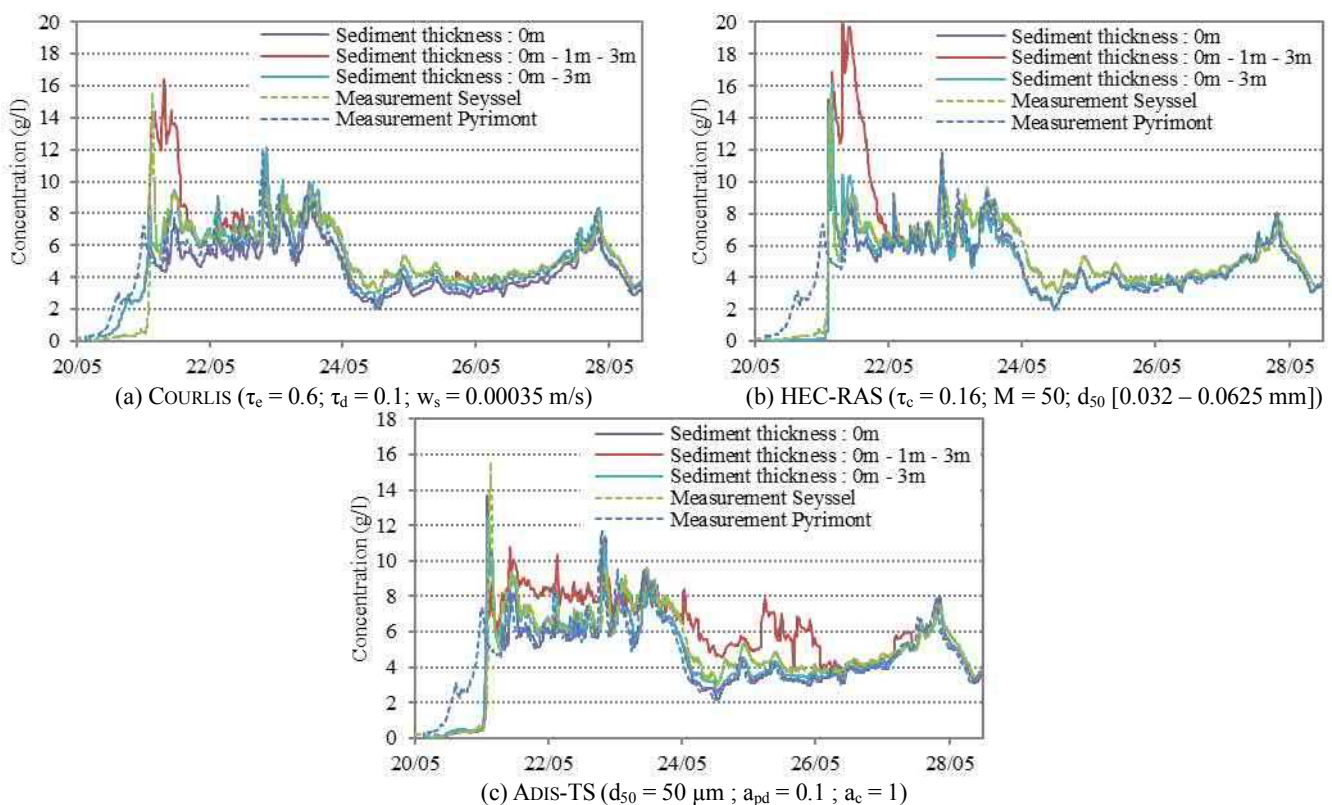


Figure 5: Sensitivity analysis of stored sediments volume.



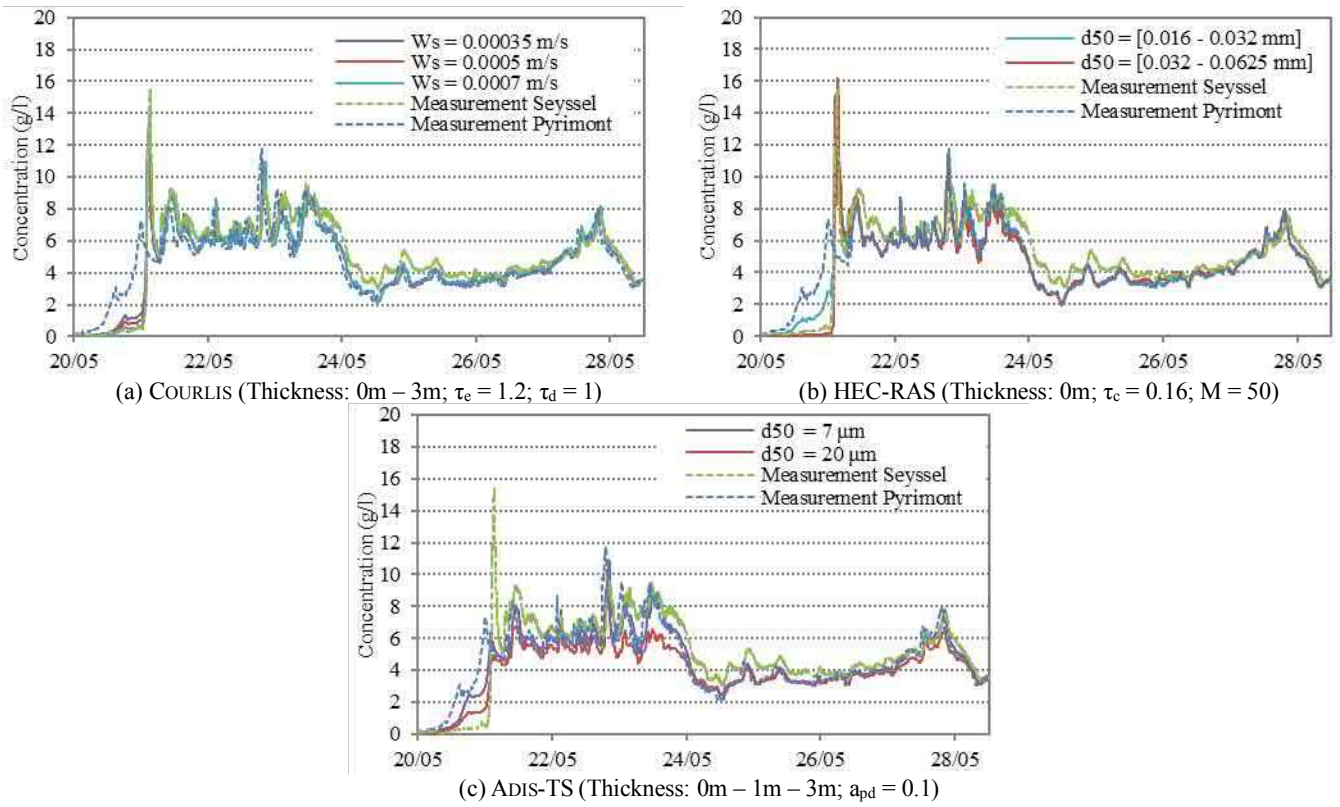


Figure 6: Sensitivity analysis of sediments size

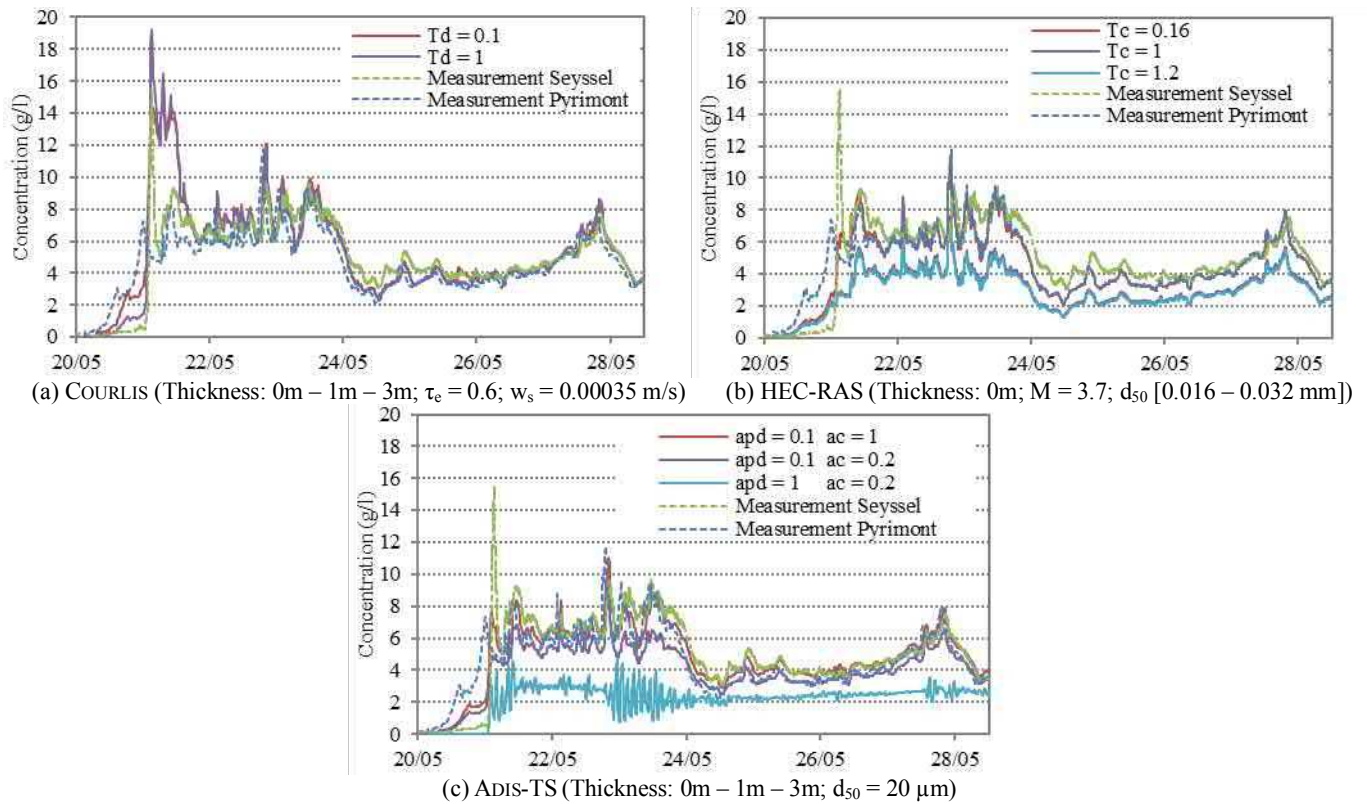


Figure 7: Sensitivity analysis of shear thresholds

### C. Discussion

Once the sensitivity analysis and the calibration were done, the most accurate results of each software were compared.

The results show that the three numerical codes have the same hydraulic performance. For sedimentary simulations, it is possible to well represent the phenomena of deposition, erosion and propagation with the 3 of them (Figure 8).

However, it was necessary to adjust the values of the different parameters to properly calibrate the results at Seyssel (Table 1 shows the different parameters according to the software). It should be noted that equations are not exactly the same for each code, which explains why best results are not obtained for the same parameter calibration depending on the code used.

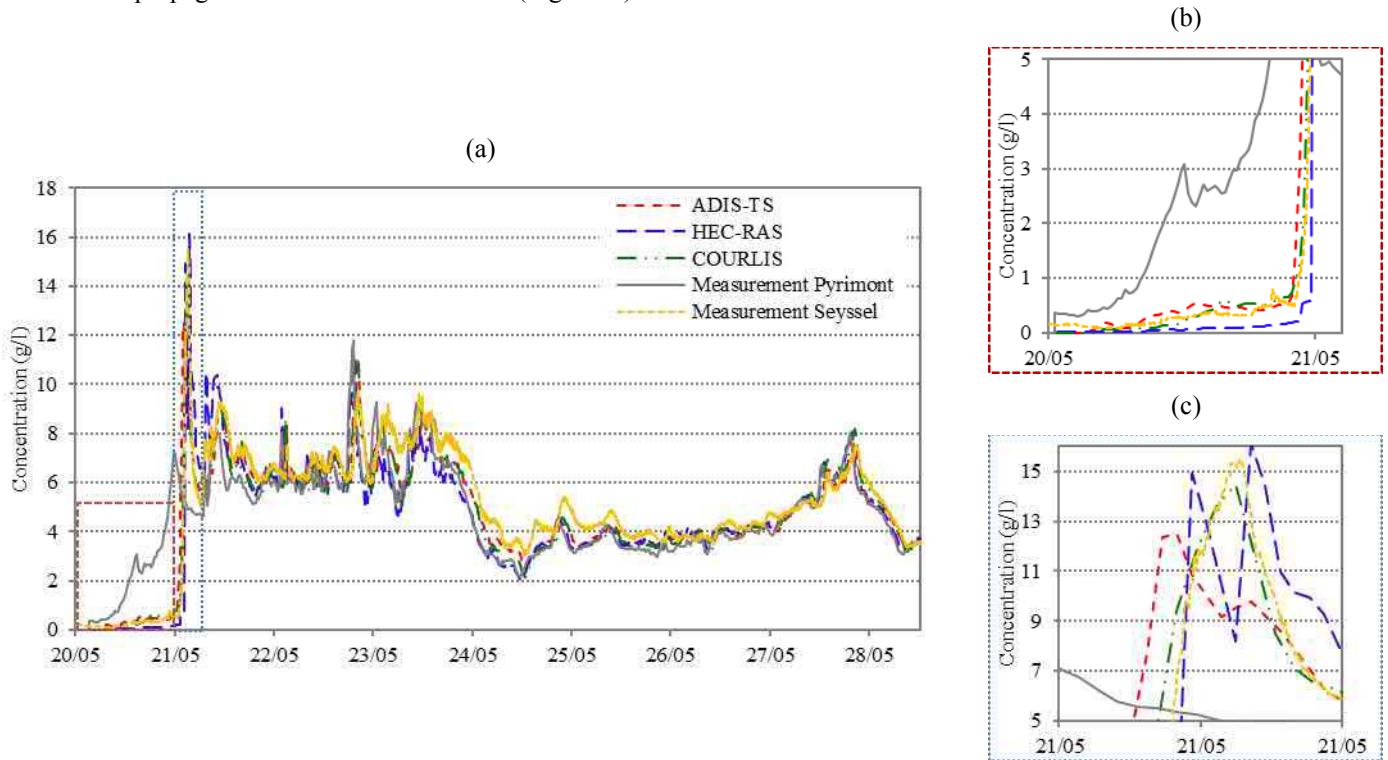


Figure 8: Comparison of SPM concentrations simulated with the 3 software. (a) Complete flushing event, 2016. (b) Zoom in, Deposition phase. (c) Zoom in, Erosion phase

Table 1: Setting parameters for the three models

HEC-RAS	COURLIS	ADISTS
<ul style="list-style-type: none"> <li>- Critical shear stress (<math>\tau_c</math>) = 0.16 Pa</li> <li>- Erosion rate (<math>M</math>) = 50 N/m<sup>2</sup> hr</li> <li>- Diameter (<math>d_{50}</math>) = 32 <math>\mu</math>m – 62.5 <math>\mu</math>m</li> <li>- Bottom configuration = 0m et 3m.</li> </ul>	<ul style="list-style-type: none"> <li>- Critical erosion shear stress (<math>\tau_{ce}</math>) = 1.2 Pa</li> <li>- Critical deposition shear stress (<math>\tau_{cd}</math>) = 1 Pa</li> <li>- Settling velocity (<math>w_s</math>) <math>d_{50}</math>] = <math>7 \times 10^{-4}</math> m/s [27 <math>\mu</math>m]</li> <li>- Bottom configuration = 0m et 3m.</li> </ul>	<ul style="list-style-type: none"> <li>- APD = 0.1</li> <li>- Diameter (<math>d_{50}</math>) = 50 <math>\mu</math>m</li> <li>- Bottom configuration = 0m et 3m.</li> </ul>

Figure 8 clearly demonstrates that the overall performance of the three numerical codes is good; as soon as they are properly calibrated following recommendations prescribed for each code. Nevertheless, some differences have been noticed between the models. First; although the deposit is well presented, the concentrations are slightly different, probably due to the critical shear parameters. Second, even though the erosion phase has been represented

with the three codes, the general shape and the width of the peak are not the same. Those differences could stem from the critical bed shear stress thresholds. Finally, the fluctuations along the propagation phase are well represented and the dissimilarities with the measured signal are mostly the same at the same time step.

## VI. CONCLUSION

### A. Benchmark conclusions and recommendations

The three numerical codes used in this study (HEC-RAS, ADISTS and COURLIS) are able to accurately reproduce water discharge and level measurements during a dam flushing event on the Upper-Rhône River. The modelled suspended sediment transport time series agree acceptably well with field measurements. However, in the deposition and erosion phases, some differences have been noticed between the models. Those differences are potentially due to the selected bed shear stress threshold. The three codes are sensitive to calibration parameters. Indeed, if the modelling of a single hydro-sedimentary event in a river reach can be accurately performed with any of these numerical codes, the simulation of another event (even in the same river reach) using identical calibration parameters may lead to significant errors. There is a strong need to provide recommendations (based on field, lab, and simulation experience to know the possible order of magnitude of each value) to better characterize these physical-based parameters.

The aim of this study was to identify a numerical tool able to well reproduce a flushing event; despite the lacks and difficulties identifies to perform this type of simulations, the objective has been achieved. Although, it is necessary to provide parameter recommendations in order to better replicate a past event, and for further studies, to make predictions of sediments behaviour during a flushing event knowing the initial variables as stored volume of sediments, granular sizes, discharge, etc. Those predictions will be very useful for operational actors.

### B. Conclusions for COURLIS

In terms of computational time, Courlis was the longest among the three numerical codes tested. The average simulation time on this case were: 60 s for HEC-RAS, 1050 s for COURLIS and 180 s for ADISTS. It is mainly due to the chosen time steps (10s for HEC-RAS, 1s for COURLIS and 60s for ADISTS). This small time step for COURLIS was forced by the imperativeness with the version used during this benchmark to run the calculation with the supercritical kernel of MASCARET (with an explicit time numerical scheme).

With the implementation of COURLIS in the TELEMAC-MASCARET trunk, the MASCARET version will be the last and should allow more flexibility for the kernel. It will be also possible to use the unsteady subcritical kernel (named "REZO") and even, the Steady kernel (named "SARAP"). These abilities should improve a lot the computational time.

Otherwise, comparison with ADISTS and HEC-RAS was interesting about their approach on shear stress thresholds. Unlike COURLIS, these codes forced user to have only one thresholds for deposition and erosion. HEC-RAS allows also another mode of erosion, with mass wasting erosion.

Finally, this benchmark highlighted some limitations of COURLIS suspension like the ability of model GSD, the lack of classical settling velocities laws proposed to users or, the impossibility to have multiple reaches (only punctual tributaries on the main reach for now).

## VII. REFERENCES

- [1] EDF. (2014). "Code COURLIS 5.2 Note de principe-validation-utilisation", (In French). France.
- [2] Guertault, L. (2015). Evaluation of the hydro-sedimentary processes of an elongated dam reservoir: Application to the Génissiat reservoir located on the Upper Rhône River, (In French). Claude Bernard University, Lyon 1, PhD thesis.
- [3] Guertault, L.; Camenen, B.; Peteuil, C.; Paquier, A. & Faure, J.-B. (2016). One dimensional modelling of suspended sediment dynamics in elongated dam reservoirs. *Journal of Hydraulic Engineering*, 142, 1-9.
- [4] Faure, J.B. (2018). User documentation of ADIS-TS, (In French). Techreport Irstea.
- [5] Faure, J.B. (2018). Development documentation of ADIS-TS, (In French). Techreport Irstea.
- [6] Krone, R. B. (1962). Flume studies of the transport of sediment in estuarial shoaling processes: final report. University of California, Hydraulic Eng. Lab. and Sanitary Eng. Res. Lab.
- [7] Launay, M. (2014) "Flux de contaminants particuliers dans un grand cours d'eau anthropisé : dynamique des PCB et du mercure transportés par les matières en suspension du Rhône, du Léman à la Méditerranée", (in French). Claude Bernard University, Lyon.
- [8] Nguyen, V. T., & Yun, N. (2016). Numerical Investigation of Sediment Transport and Bed morphology on a Stretch of Nakdong River. *12<sup>th</sup> International Conference on Hydroinformatics*, HIC 2016, pp. 550-556.
- [9] Partheniades, E. (1965). Erosion and deposition of cohesive soils. *Journal of Hydraulic Division*, 91, 105-139.
- [10] Peteuil, C., Fruchart, F., Abadie, F., Reynaud, S., Camenen, B., & Guertault, L. (2013). Sustainable management of sediment fluxes in reservoir by environmental friendly flushing: The case study of the Genissiat Dam on the upper Rhone River (France). *Advances in River Sediment Research*, Taylor & Francis Group, London. pp. 1147-1156.
- [11] Peteuil, C. (2018). Sustainable management of sediments fluxes in the Rhône river cascade. *Hydrolink*, 4, 112-114.
- [12] Sécher, M., Ung, P., Valette, E., Jodeau, M., & Goutal, N. (2018). COURLIS: a 1D suspension and bedload code. *Proc. River Flow 2018, 9<sup>th</sup> International Conference on Fluvial Hydraulics*, Lyon.
- [13] Thomas, B. (2017). "Modélisation des processus hydro-sédimentaires du Haut-Rhône", (In French). Master. Thesis, INP Toulouse ENSEEIHT, DIGP - ERE. Lyon: CNR.
- [14] US Army Corps of Engineers. Hydrologic Engineering Center. (2016). HEC-RAS River Analysis System. Hydraulic Reference Manual. Version 5.0. USA
- [15] US Army Corps of Engineers. Hydrologic Engineering Center. (2016). HEC-RAS River Analysis System. User's manual. Version 5.0. USA
- [16] Zhang, W., Xu, Y., Wang, Y., & Peng, H. (2014). "Modeling Sediment Transport and River Bed Evolution in River System". *Journal of Clean Energy Technologies*, 2, 175-179

# 2D and 3D numerical modelling of the flow and sediment transport in shallow reservoirs: application to a real case

Nicolas Claude<sup>1</sup>, Matthieu Secher<sup>2</sup>, Jujian Deng<sup>2</sup>, Eric Valette<sup>2</sup>, Marion Duclercq<sup>2</sup>

<sup>2</sup>EDF CIH

La Motte Servolex, France

<sup>1</sup>National Hydraulics and Environment Laboratory (LNHE)

EDF R&D

Chatou, France.

nicolas-n.claude@edf.fr

**Abstract**— A hydro-sedimentary numerical study is performed on a real shallow reservoir to evaluate the ability of both Telemac-2D/Sisyphe and Telemac-3D/Sedi3D to reproduce the flow structure and sediment transfer in these infrastructures. Both 2D and 3D models are able to capture correctly the global behaviour of the hydrodynamic and sediment transport processes at the reservoir scale. However, models exhibit some difficulties to predict accurately the local evolution of sediment dynamic. Overall, results of the 2 models present few discrepancies. The 3D modelling improves slightly the results due to the structure mainly bi-dimensional of hydro-sedimentary mechanisms generated in this shallow reservoir with the boundary conditions simulated here.

## I. INTRODUCTION

Shallow reservoirs are common hydraulic structures usually used as water storage reservoirs, as sedimentation tanks as well as in aquaculture [1]. Complex flow develops in these structures involving large-scale horizontal coherent structures responsible for momentum transfers. Interactions between reservoir dimensions, hydraulic boundary conditions [2] and sediment load [3] control the flow structure which exhibit different patterns (Figure 1). Therefore, flow fields can present large recirculation zones organized either in symmetric configurations (S0 and S1) or in asymmetric patterns with one (A1 and A2) or multiples reattachment points (A3) [2, 4, 5]. In other configurations, flows can also show a channel-like pattern (CH-L) [4, 5] or a meandering jet (M) [6]. These flow characteristics influence significantly the transport, deposition and erosion of contaminants and sediments inside reservoirs through complex processes [3, 7, 8]. In turn, sediment deposition and bed evolution can modify flow structure by retroaction [9].

Due to these complex mechanisms, modelling of flow and sediment transport in shallow reservoirs remains a great challenge and an important task to provide operational tools sufficiently accurate for improving design and management of these infrastructures [10]. For these purpose, a hydro-sedimentary numerical study is performed on a real shallow reservoir. The objective is to evaluate the ability of Telemac-

2D/Sisyphe and Telemac-3D/Sedi3D to reproduce the flow structure and sediment transfer in a real basin.

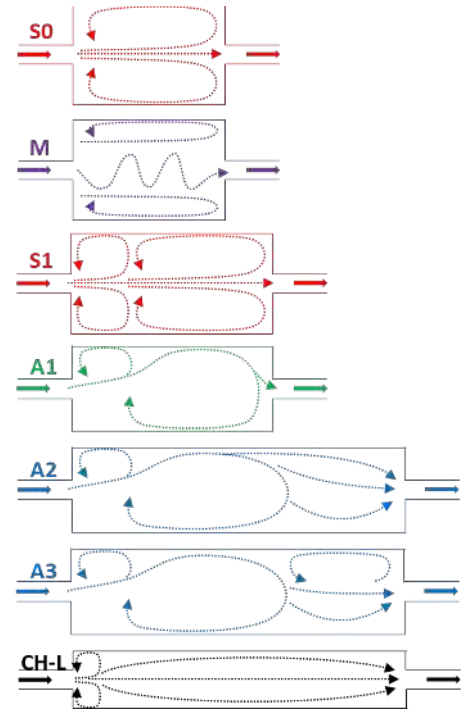


Figure 1: Flow patterns observed in shallow reservoirs.

## II. MATERIALS AND METHODS

### A. Study site

The studied shallow reservoir is located in the French Alps and belongs to Arc-Isère hydropower structures (Figure 2). The basin is 1,400 m long and 450 m wide (Figure 3). Water depth ranges between [0-14] m. Bed topography presents a sinuous channels that delimit 3 large deposits and connect the basin inlet to the outlet (Figure 3). Transported particles have a mean grain size of 20  $\mu\text{m}$  and are considered as cohesive.



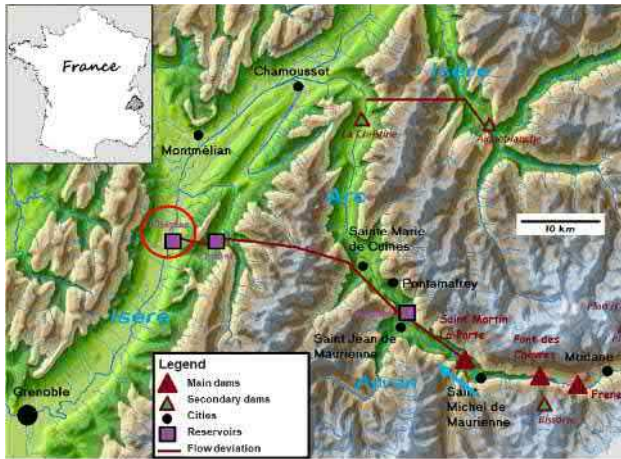


Figure 2: Location of the study site



Figure 3: Location of ADCP cross-sections (red lines) and sediment concentration measurements (black points).

### B. Field measurements

A large field campaign involving ADCP (Acoustic Doppler Current Profiler) measurements on 7 cross-sections and sediment concentration gauging on 6 locations was performed during 2 weeks in June 2018 in order to characterize the 3D flow structure as well as the spatial and

temporal distribution of sediments in the basin. Devices for sediment concentration gauging are located roughly at 1 m deep. Flow discharges ( $Q$ ) and water levels monitored during the field campaign are presented on Figure 4. ADCP data were acquired during the 1<sup>st</sup> week at flow discharges approximatively equals to  $98 \text{ m}^3/\text{s}$  (see black points on Figure 4). Sediment concentrations were recorded continuously during the 2<sup>nd</sup> week.

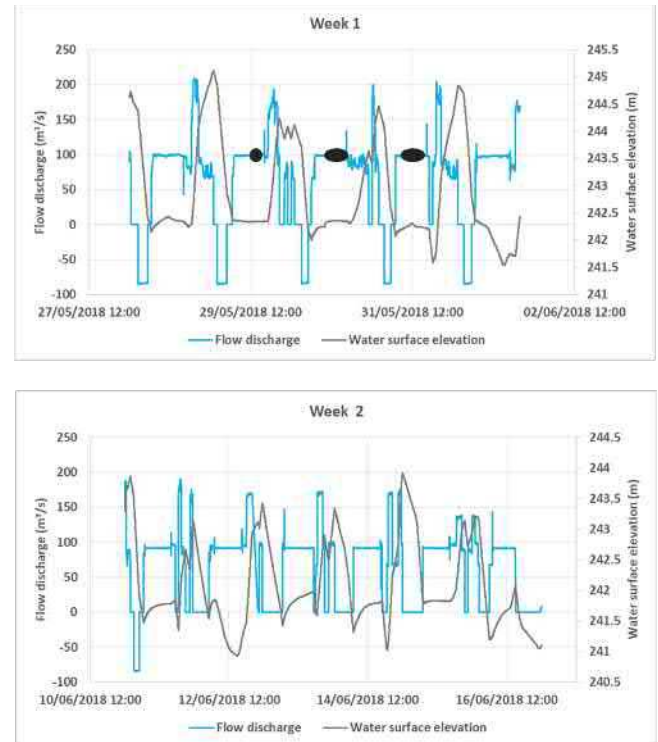


Figure 4: Hydraulic boundary conditions during field measurements.

### C. Models set-up

Coupling of Telemac-2D/Sisyphe and Telemac-3D/Sedi3D are used for the bi and tri-dimensional modelling, respectively. The 2 models are based on unstructured meshes of approximatively 160,000 nodes leading to an element mean size of 2 m. The 3D model is composed of 5 layers uniformly distributed on the vertical. Flow discharge and water surface elevation are imposed on the upstream (basin inlet) and downstream (outlet) boundary conditions, respectively. The end of the tunnel from which water enters in the basin is represented as an island. Numerical schemes ERIA and LIPS are used in the 2D and 3D model, respectively [11, 12].

Calibrated bed roughness is equal to a Manning–Strickler coefficient of  $55 \text{ m}^{1/3}/\text{s}$  in the 2D model and to a Nikuradse coefficient of  $3 \times 10^{-5} \text{ m}$  in the 3D model. Turbulence is modelled with a constant eddy viscosity both in the 2D model ( $1 \times 10^{-4} \text{ m}^2/\text{s}$ ) and in the 3D model for the horizontal plan ( $1 \times 10^{-5} \text{ m}^2/\text{s}$ ). Turbulence on the vertical plan is computed in the 3D case with a mixing length model (constant base eddy viscosity =  $1 \times 10^{-4} \text{ m}^2/\text{s}$ ).

Dynamic of cohesive sediments is modelled in both models from calibrated laws for settling velocities. According to these laws, settling velocity varies with sediment concentration (Figure 5). Critical shear stress for deposition and erosion as well as Partheniades coefficient have constant values equals to 2.5 N/m<sup>2</sup>, 5 N/m<sup>2</sup> and 0.01 kg/m<sup>2</sup>/s, respectively, in the 2 models.

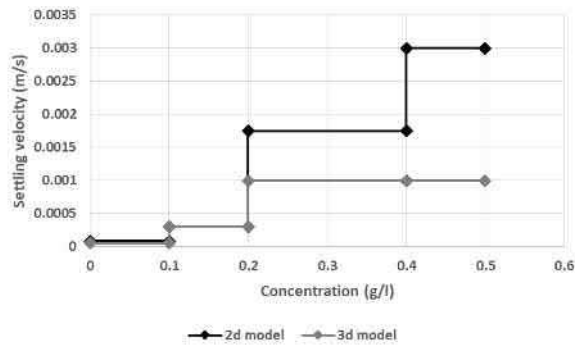


Figure 5: Evolution of settling velocity as a function of sediment concentration in the 2D and 3D models.

### III. RESULTS

#### A. Horizontal flow structure

Velocities observed at  $Q \sim 98 \text{ m}^3/\text{s}$  from ADCP measurements (Figure 6) indicate that the flow structure in the studied shallow reservoir presents an asymmetric pattern with 2 large recirculation zones similar to pattern A2 illustrated on Figure 1. Recirculation cells are located in the north and middle parts of the reservoir. A main current flows along the west bank in the middle part of the basin and crosses the downstream deposition to join the reservoir outlet.

Results of hydrodynamic simulations performed with the 2 models show a flow field with the same spatial layout (Figure 7). Both models are able to reproduce correctly and qualitatively the flow structure observed in the shallow reservoir.

#### B. Flow velocity

Comparison of observations and simulation results along ADCP cross-sections confirms that spatial distribution of flow velocities is effectively well modelled (Figure 8 and Figure 9). Indeed, computed velocities are generally included in the uncertainty range of measurements (equal to standard deviation of observations along cross-section). Therefore, the hydraulic models reproduce quantitatively the reservoir hydrodynamic. Results of the 2 models are equivalent even though the 2D model tends to more underestimate velocity magnitudes than the 3D model.

Vertical distribution of velocities only shows a small flow stratification (Figure 9) which explains the weak differences between the 2 models.

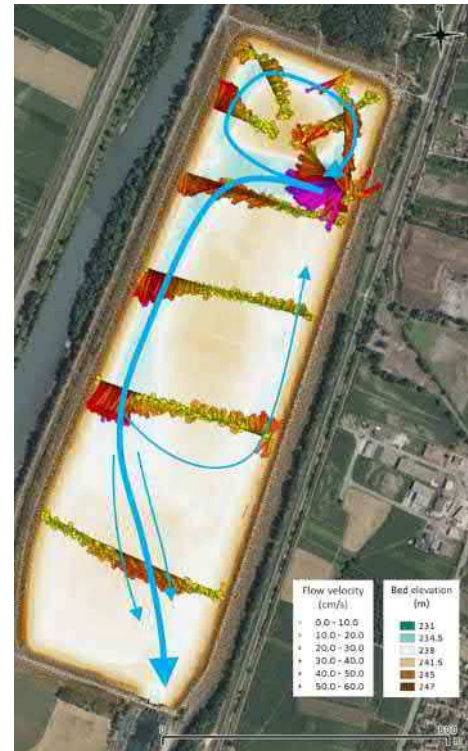


Figure 6: Flow structure observed from ADCP measurements.

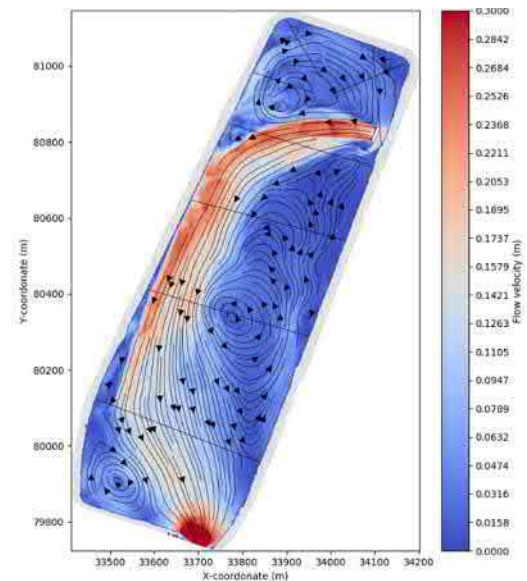


Figure 7: Example of flow structure obtain with the 3D model at  $Q = 98.24 \text{ m}^3/\text{s}$ .

#### C. Sediment concentration

Observations of backscatter signals from ADCP (which constitute a proxy of sediment concentrations) and concentrations computed from the 3D model indicates that the sediment distribution along the water column is slightly less uniform than for velocities (**Erreur ! Source du renvoi introuvable.**).

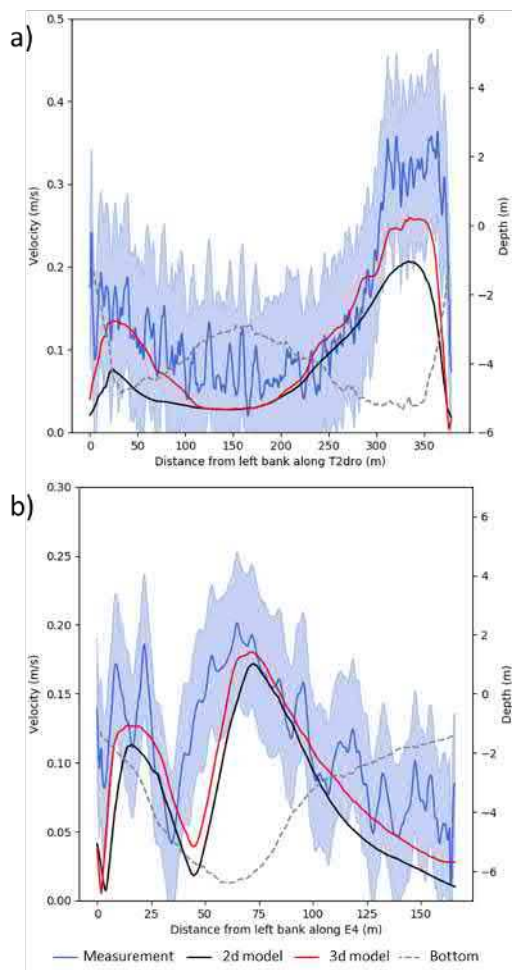


Figure 8: Comparison of depth-averaged flow velocities measured and simulated at cross-sections a) T2dro and b) E4 (see Figure 3 for cross-section locations). Measurement uncertainty is delimited by blue areas and corresponds to standard deviation of observations along cross-section.

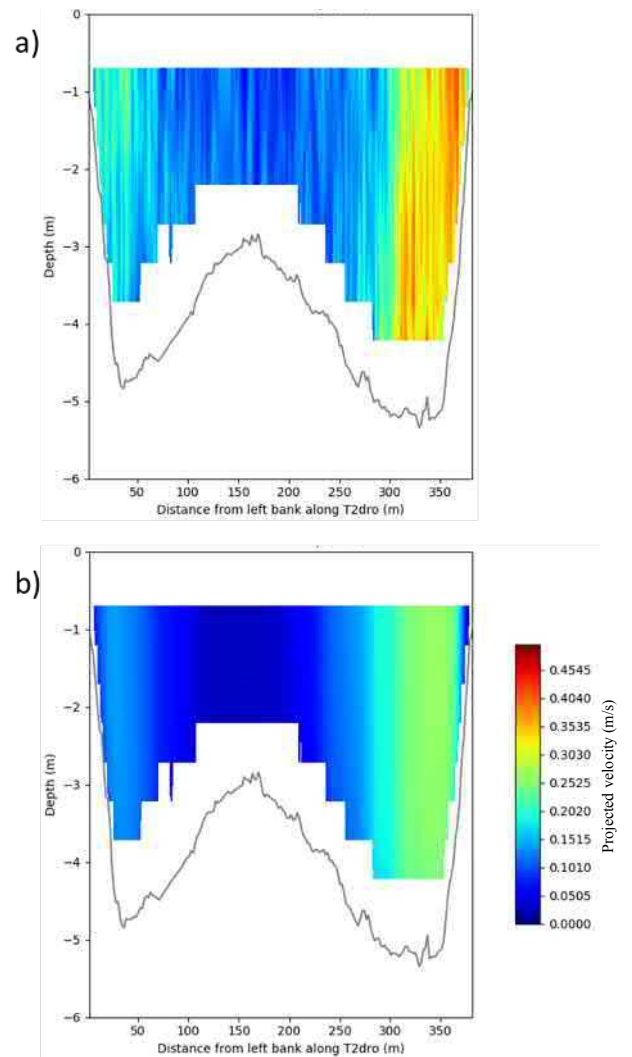


Figure 9: Comparison of flow velocities a) measured and b) simulated at cross-sections T2dro (see Figure 3 for cross-section locations).

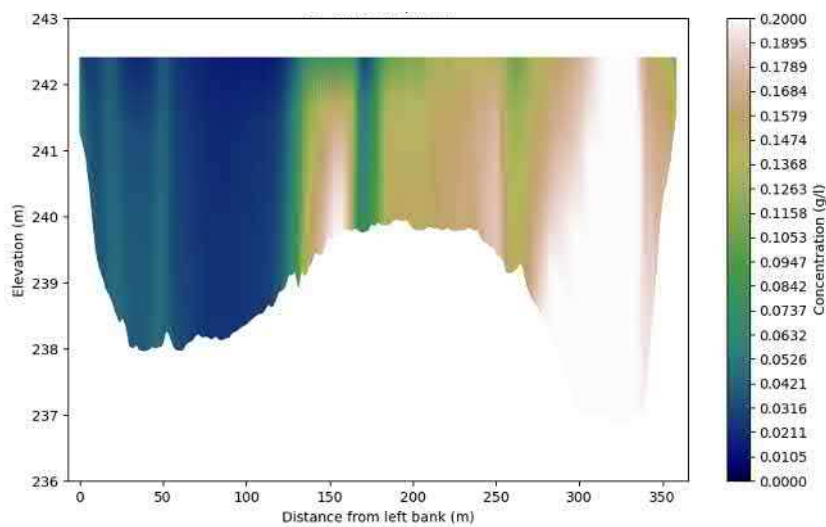
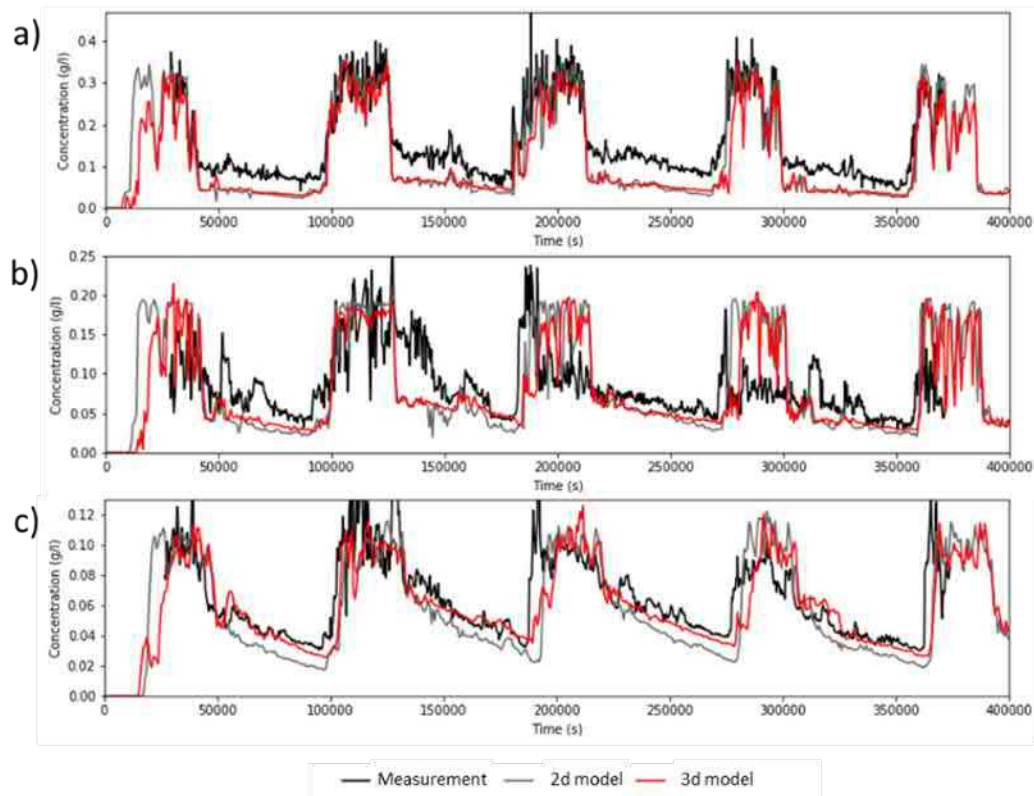


Figure 10: Sediment concentration at cross-section T3 (see Figure 3 for cross-section location).





3

Figure 11: Comparison of temporal sediment concentration at locations a) P3, b) P5 and c) outlet (see Figure 3 for measurement locations).

Figure 11 presents temporal evolution of sediment concentration recorded along the main current. Sediment fluxes show large variations associated to hydraulic condition fluctuations (Figure 4). Concentrations decrease from upstream (location P3, see Figure 3) to downstream (outlet, see Figure 3) which indicates that particle transport and deposition constitute the main sedimentary processes.

Sediment suspension load is relatively well predicted by the 2 models in the upstream part of the main current (location P3, see Figure 3 and Figure 11a) during high concentration periods. At the opposite, computations give underestimation of the suspension load in this area at low concentrations. Downstream, at location P5 in the middle part of the main current (Figure 3), concentrations are correctly modelled until 130,000s (Figure 11b). Then, fluxes are first underestimated and finally significantly overestimated during the high concentration periods encountered throughout the last 200,000s of the simulation. At the basin outlet, temporal evolution of sediment concentrations is well reproduced even if the 2D model tends to underestimate fluxes during low concentration periods (Figure 11c).

Analysis of sediment concentrations indicates that the global behaviour of the sediment dynamic (transport and deposition) is correctly captured at the reservoir scale. However, both models show some difficulties to predict accurately the local evolution of sediment transport.

#### IV. CONCLUSIONS

A hydro-sedimentary numerical study is performed on a real shallow reservoir to evaluate the ability of Telemac-2D/Sisyphe and Telemac-3D/Sedi3D to reproduce the flow structure and sediment transfer in these infrastructures.

The studied shallow reservoir is located in the French Alps and belongs to Arc-Isère hydropower structures. The basin is 1,400 m long and 450 m wide. Water depth ranges between [0-14] m. A large field campaign involving ADCP measurements and sediment concentration gauging was performed in order to characterise the 3D flow structure as well as the spatial and temporal distribution of sediments in the basin. Transported particles have a mean grain size of 20  $\mu\text{m}$  and are considered as cohesive.

Comparison between measurements and simulation results shows that the 2D and 3D models are able to reproduce quite well the flow structure and velocity magnitude observed in the shallow reservoir. The 2 models capture correctly the global behaviour of the sedimentary processes (mainly characterized by transport and deposition of particles) at the reservoir scale but exhibit some difficulties to predict accurately the local evolution of sediment transport.

Overall, results of the 2 models present few discrepancies and 3D modelling only brings a slight improvement in this study case. This result is explained by the bi-dimensional behaviour of hydraulic and sediment transport mechanisms in



a shallow reservoir such as the studied reservoir and with the boundary conditions encountered during measurements.

#### V. REFERENCES

- [1] Ferrara, V., Erpicum, S., Archambeau, P., Piroton, M., and Dewals, B. (2018). Flow field in shallow reservoir with varying inlet and outlet position. *Journal of Hydraulic Research*, 56(5), 689-696.
- [2] Dufresne, M., Dewals, B. J., Erpicum, S., Archambeau, P., & Piroton, M. (2010). Classification of flow patterns in rectangular shallow reservoirs. *Journal of Hydraulic Research*, 48(2), 197-204.
- [3] Camnasio, E., Erpicum, S., Orsi, E., Piroton, M., Schleiss, A. J., & Dewals, B. (2013). Coupling between flow and sediment deposition in rectangular shallow reservoirs. *Journal of Hydraulic Research*, 51(5), 535-547.
- [4] Camnasio, E., Orsi, E., and Schleiss, A. J. (2011). Experimental study of velocity fields in rectangular shallow reservoirs. *Journal of Hydraulic Research*, 49(3), 352-358.
- [5] Kantoush, S. A. (2008). Experimental study on the influence of the geometry of shallow reservoirs on flow patterns and sedimentation by suspended sediments. EPFL, Lausanne, Switzerland, PhD thesis 4048.
- [6] Peltier, Y., Erpicum, S., Archambeau, P., Piroton, M., and Dewals, B. (2014). Experimental investigation of meandering jets in shallow reservoirs. *Environmental Fluid Mechanics*, 14(3), 699-710.
- [7] Sloff, C. J., Jagers, H. R. A., and Kitamura, Y. (2004). Study on the channel development in a wide reservoir. *Proc. River Flow, Napoli*, 811-819.
- [8] Dufresne, M., Dewals, B. J., Erpicum, S., Archambeau, P., and Piroton, M. (2010). Experimental investigation of flow pattern and sediment deposition in rectangular shallow reservoirs. *International Journal of Sediment Research*, 25(3), 258-270.
- [9] Kantoush, S. A., Sumi, T., and Schleiss, A. (2010). Geometry effect on flow and sediment deposition patterns in shallow basins. *Annual Journal of Hydraulic Engineering, JSCE*, 54, 133-138.
- [10] Zahabi, H., Torabi, M., Alamatian, E., Bahraei, M., and Goodarzi, M. (2018). Effects of geometry and hydraulic characteristics of shallow reservoirs on sediment entrapment. *Water*, 10(12), 1725.
- [11] Hervouet, J-M. (August 2017). Residual distribution advection schemes in Telemac. Project-Team CADAMOM, INRIA. Research Report n°9087.
- [12] Hervouet, J-M., (2016). Latest news on distributive advection schemes and dry zones: the ERIA schemes. *Proceedings of the XXIII<sup>rd</sup> TELEMAC-MASCARET User Conference*, 201-208.

# A Sand Transport Model for the Scheldt Estuary: The 3D Scaldis Sand Model

Sven Smolders, Yves Plancke, Qilong Bi, Joris Vanlede, Gerasimos Kolokythas

Department of Mobility and Public Works, Flemish Government

Flanders Hydraulics Research

Antwerp, Belgium

[sven.smolders@mow.vlaanderen.be](mailto:sven.smolders@mow.vlaanderen.be)

**Abstract**—A sand transport model for the Scheldt estuary, located in the Netherlands and Belgium, based on the hydrodynamic 3D Scaldis model is presented in this paper. The objective is to model only non-cohesive sediment transport. The model is validated using field measurements performed with a Delft bottle at different locations along the estuary. Asymmetry of the cross sectionally averaged flow velocity is used to understand the results of the sand model in terms of net sand transport direction.

## I. INTRODUCTION

In Western Europe the implementation of the Seine-Scheldt connection will improve the European waterway network in order to meet the growing demands of modern logistics in a more effective manner [1]. This will result in increased shipping traffic between France and Flanders (Belgium) and the Flemish Government will improve the navigability of the upper part of the Scheldt estuary in order to allow class Va ships to pass. At the moment, the upstream part of the Upper Sea Scheldt (Figure 1) is a Class IV fairway (ships up to 85 m long and 9.5 m wide) and forms a bottleneck in the European network.

Therefore, an integrated plan is being developed, in which navigability, safety and nature are the key elements. The questions that are to be answered within this integrated plan pertain to the measures that need to be taken to upgrade the Upper Sea Scheldt to a Class Va fairway suitable for ships up to 2250 tons (ships up to 110 m long and 11.4 m wide and 3.5 m draught), taking into account the other functions of the estuary, like safety, nature and recreation.

The outcome of a feasibility study was that with relatively small measures a balance between cost and benefit can be found, but allowing navigability up to Class Va while increasing safety for ships of class IV and lower. The integrated plan aims at further developing the conclusions from this feasibility study towards Class Va shipping. It is of the utmost importance that the design of this enlargement leads to a multifunctional Scheldt estuary with assets for navigability, guarantees for protection against flooding and a sustainable natural system.

In the framework of the study “Integrated Plan Upper Sea Scheldt”, a set of models are improved or developed by the different project partners. The output of one model can be input for another and as such a model train is used to evaluate the effects of different alternatives (specified morphology of the

Scheldt river in a specific state and at a specific time) under different scenarios (a range of boundary conditions that take into account the climate change, sea level rise, increasing or decreasing tidal amplitude, high or low discharge).

Flanders Hydraulics Research developed a 3D high resolution model for hydrodynamics in the tidal Scheldt estuary, called Scaldis [2,3]. The hydrodynamic model was extended with a model for both cohesive [5] as non-cohesive [6] sediment transport. The University of Antwerp (UA) improves their 1D ecosystems model for primary production in the Scheldt estuary [7]. The Research Institute for Nature and Forest (INBO) builds ecotope and physiotope maps and models benthos, birds and migratory fish (twait shad) for the different alternatives.

This paper focusses on the setup and parameter sensitivity of the non-cohesive or sand transport model. The sand transport model will be described in detail and the results for the 2013 reference state of the model will be discussed.

## II. THE SCHELDT ESTUARY

The Scheldt estuary is situated in Western Europe in the Netherlands and Belgium (Figure 1). The part of the estuary from the mouth till the Dutch/Belgian border (located at 67 km from the mouth, measured along the thalweg) is called Western Scheldt and is characterized by different ebb and flood channels surrounding large intertidal sand and mud flats. The part further upstream from the border till Ghent (located at 170 km from the mouth) is called Sea Scheldt and is characterized by a single channel bordered by much smaller intertidal flats and marshes. The part upstream from the tributary Rupel is called the Upper Sea Scheldt as shown in Figure 1.

The estuary mouth near Vlissingen (km 2) is approximately 5 km wide and flood enters twice a day with an average flood volume of 1.04 Gm<sup>3</sup> [8]. The funnel shape of the estuary amplifies the tidal range, for mean spring and neap tides respectively, from 4.46 m and 2.97 m at the mouth to 5.93 m and 4.49 m near Hemiksem (km 104) (Figure 1). Further upstream friction dampens the tidal wave, which has still a mean tidal range of 2.24 m and 1.84 m for spring and neap tides respectively near Merelbeke (km 170), where the tide is stopped by a weir-lock construction. The total discharge of the Scheldt and tributaries (on average 120 m<sup>3</sup>/s) is very small compared to the tidal volume [9].

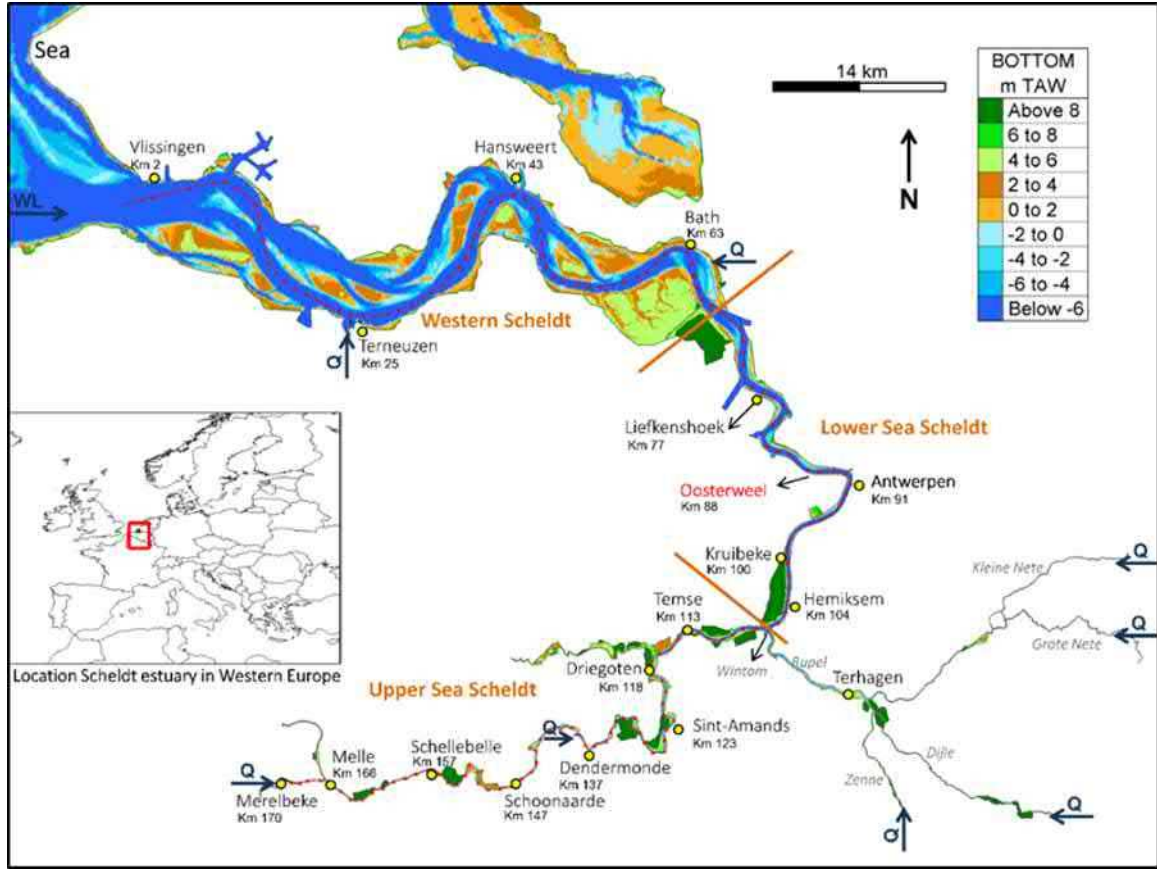


Figure 1 Introduction to the Scheldt estuary. Distances are measured from the estuary mouth

### III. TELEMAC-3D HYDRODYNAMIC MODEL: SCALDIS 3D

The hydrodynamic model, called Scaldis, is a TELEMAC-3D model. The model domain contains the full Scheldt estuary as it is shown in Figure 1 and also includes the Belgian coastal zone, extended to France in the South and The Netherlands in the north. The tributaries are included as far as the tidal influence reaches. Figure 1 shows a Q where eight daily averaged upstream discharges enters the model domain. Water level time series are imposed on the sea boundary. The mesh resolution increases from 500 meters in the coastal zone to 120 meters in the Western Scheldt, to 60 meters in the Sea Scheldt further increasing upstream towards 5 meters at the upstream boundaries. The horizontal grid contains 459,692 nodes. In the vertical there are five layers following a sigma transformation (0, 0.12, 0.30, 0.60 and 1). The bathymetry is interpolated from multi-beam measurements and Lidar data. Wind is assumed to be incorporated into the water level boundary downstream and is not taken into account further. The model was calibrated using a spatial varying Manning bottom friction coefficient. The friction coefficient varies from  $0.026 \text{ s/m}^{1/3}$  in the downstream part and decreases to  $0.014 \text{ s/m}^{1/3}$  in the upstream river part. Salinity is present as an active tracer and density effects are taken into account. The mixing length model of Nezu and Nakagawa is used for the vertical turbulence modelling. The horizontal turbulence model is the Smagorinski model.

Tidal flats are present and equations are solved and corrected on tidal flats. Coriolis is taken into account. This model was calibrated using measured water levels, flow velocities and discharges over ADCP transects, and point measured flow velocities [3].

### IV. SAND TRANSPORT MODEL: SCALDIS SAND

SISYPHE is coupled with TELEMAC-3D. No parameter changes were done in the hydrodynamic model. The coupling with the hydrodynamics is done every time step. Based on experience in previous projects and on a sensitivity study that is not shown here, the Engelund and Hansen (1967) total sand transport equation was chosen. This formula is derived for river flow [10]. The formula given by Engelund and Hansen estimates the total transport  $\vec{Q}_0$  in the direction of the flow velocity  $\vec{v}$ :

$$|\vec{Q}_0| = \frac{0.05\alpha|v|^5}{\sqrt{g}s^2C^3d_{50}} \quad (1)$$

where  $|\vec{Q}_0|$  is the magnitude of the total sand transport rate;  $\alpha$  is a calibration coefficient (order 1);  $|v| = \sqrt{u^2 + v^2}$  is the magnitude of the flow velocity [m/s] with  $u$  and  $v$  the flow velocity along the x and y axis;  $s = (\rho_s - \rho)/\rho$  is the relative density with  $\rho_s$  and  $\rho$  the sediment and water density, respectively [-];  $C$  is the Chézy friction coefficient [ $\text{m}^{1/2}/\text{s}$ ]; and  $d_{50}$  is the

median grain size [m]. Furthermore, to account for the bed slope effects, the correction method of Flokstra and Koch [11] is available in SISYPHE (keyword: FORMULA FOR DEVIATION = 1) and multiplies the above equation by a factor:

$$|\vec{Q}| = |\vec{Q}_0| \left(1 - \beta \frac{\partial z_b}{\partial s}\right) \quad (2)$$

where  $\beta$  is a bed slope coefficient (keyword: BETA = 1.3);  $s$  is the coordinate in the flow direction and  $z_b$  is the bed level. This formula is implemented in SISYPHE in the subroutine bedload\_engel.f. The formula is implemented as follows:

$$\Phi_b = C_{engel} \sqrt{(C_1 \times TOB)^5 / \max(CF, 1.E - 6)} \quad (3)$$

with

$$C_{engel} = 0.1 \sqrt{s \times g \times d^3} \quad (4)$$

and

$$C_1 = \frac{1}{(s \times \rho \times g \times d)} \quad (5)$$

and

$$CF = \frac{2n^2 g}{h^{1/3}} \quad (6)$$

and

$$TOB = 0.5 \times \rho \times CF \times |v|^2 \quad (7)$$

where  $\Phi_b$  is the dimensionless current induced sediment transport rate;  $TOB$  is the bed shear stress [Pa];  $CF$  is the quadratic friction coefficient;  $g$  is the gravitational acceleration constant [m/s<sup>2</sup>];  $d$  is the sediment grain size [m];  $n$  is the Manning friction coefficient [s/m<sup>1/3</sup>];  $h$  is the water depth [m]; and  $\rho$  is the water density [kg/m<sup>3</sup>].  $CF$  can have a different formula depending on the type of friction coefficient that was chosen in the model. For Scaldis a Manning bottom friction coefficient was chosen and the corresponding formula for  $CF$  is given here (equation 6).

Suspended load transport is not activated in SISYPHE because the Engelund and Hansen transport equation is a total load equation. The morphological factor is set to 1. The sediment grain size is equal to 150  $\mu$ m. Only a single sediment fraction is taken into account over the entire model domain. There is an unlimited amount of sediment available in the model (= 100 m of sediment layer thickness). The simulation will run for 15 days (a full spring-neap tidal cycle) and graphical output is written to a results file every half hour. the time step is four seconds. No sediment will enter the model domain through the boundaries. Sediment can leave the domain freely. To prevent the model from resulting into unwanted erosion at the inflow boundaries, a fixed bed elevation (zero evolution) was defined in the boundary conditions file (.cli). This can be achieved by

assigning LIEBOR=5 for the inflow nodes (8th column in .cli file).

The hydrodynamic model has two days to spin up. After these two days the model is started again from the last time step of the spin up simulation and the sediment module SISYPHE is coupled. A uniform sediment layer is available throughout the entire model domain.

In the hydrodynamic model a Manning bottom friction coefficient was spatially varied to calibrate the water levels and flow velocities in the model (Figure 2). By default the sediment module uses the bottom friction coefficient of the hydrodynamic module to calculate the bed shear stresses to estimate sediment motion. But during calibration of the hydrodynamic model the variation in bottom friction coefficient is used to compensate also for non-physical properties of the model, like numerical diffusion. Taking these values of the bottom friction coefficient would not be correct for sediment transport. Therefore a fixed value for the Manning bottom friction coefficient was used for the entire model domain for the sediment transport module. In the subroutine coefro\_sisyphe.f a fixed value for the bottom friction coefficient was introduced. The Manning coefficient was set to 0.02 m/s<sup>1/3</sup>. In the subroutine tob\_sisyphe.f changes were made to make sure the fixed bottom friction coefficient was used in the calculations of the bed shear stress.

The difference in sand transport between using a fixed Manning value for the entire model domain or using the Manning coefficient spatially varying from the hydrodynamic model is part of the sensitivity analysis that follows.

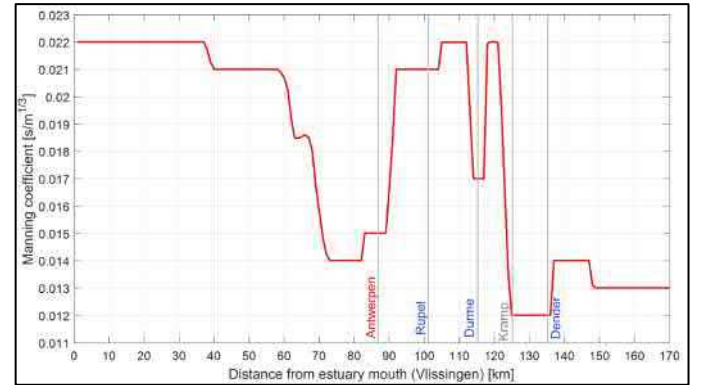


Figure 2 - Manning bottom roughness coefficient of Scaldis 3D 2013 along the estuary axis.

The sediment module calculates a certain sand transport and the related bottom changes. By default these bottom changes are updated in the bottom file of the hydrodynamic model every time step. As the focus of the sand transport model is on sand transport and not on morphology. Therefore the update of the bottom in the hydrodynamic model is switched off in the code. The mass balance and bottom changes are still recorded in the sediment module and are given as output, but the sand transport is always calculated based on the hydrodynamics with a fixed initial bathymetry.



## V. MODEL VALIDATION

### Delft bottle measurements

A simulation of 15 days with TELEMAC-3D coupled with SISYPHE was run. The downstream boundary is a forced water level combined with X and Y velocity components. A 15 day simulation makes sure a complete spring-neap tidal cycle is simulated. The upstream boundaries (8) have a constant discharge imposed. This is 23, 34.7, 11.1, 15.92, 34.6, 8.3, 10.4, 35, 0 m<sup>3</sup>/s for the Terneuzen, Merelbeke, Dender, Zenne, Dijle, Grote Nete, Kleine Nete and Bath discharge boundary respectively (Figure 1). The bathymetry of 2013 is used [3]. Model validation was done using Delft bottle (Figure 3) sand transport measurements of 13 hour (= full ebb and flood cycle) measurements campaigns at different locations along the Sea Scheldt [12]. Different measurements at different heights in the water column were used to estimate the total transport over the entire water column [12]. From the 15 day simulation a tide was chosen that came closest to the tide during the 13 hour measurement campaign at the specific location. The sand transport rate close to the location of the point measurement was extracted from the model and plotted together with the measured values for total sand transport. Good measurement results are available for six locations along the Sea Scheldt: Oosterweel, Kruikebe, Driegoten, Dendermonde, Schoonaarde, and Schellebelle (locations indicated in Figure 1).



Figure 3 – Delft bottle on frame to measure sand transport just above the bottom.

The comparison between modelled and measured sand transport for these locations is given in Figure 4 to Figure 9. Time in the x-axis is expressed relative to low water. Throughout the Sea Scheldt there is a low but longer sand transport during the ebb flow and a high but short peak during the flood flow. All locations except Driegoten gave a very good agreement between model and measurement for sand transport.

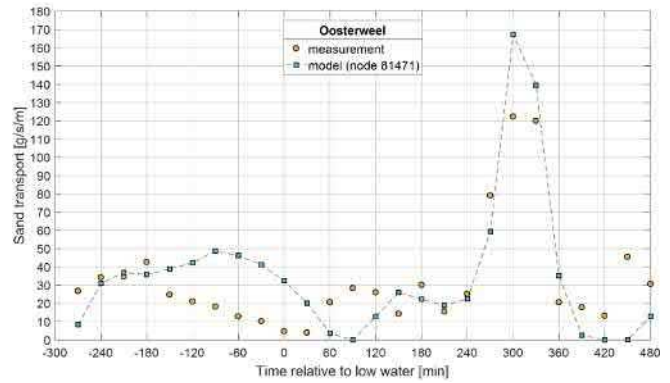


Figure 4 – Modelled and measured sand transport at Oosterweel (km 88)

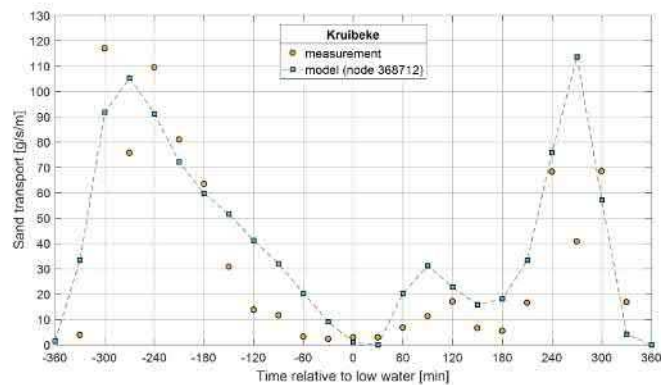


Figure 5 – Modelled and measured sand transport at Kruikebe (km 100)

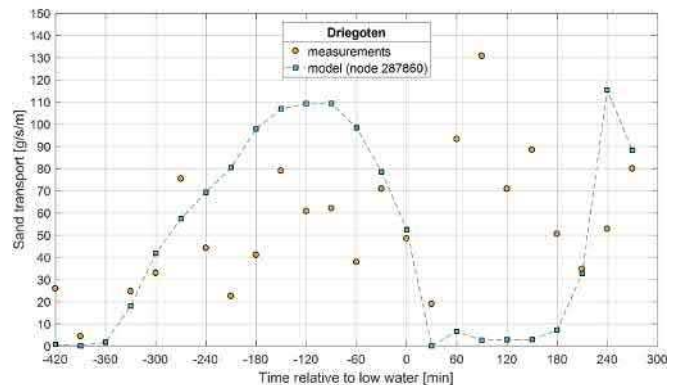


Figure 6 – Modelled and measured sand transport at Driegoten (km 118)

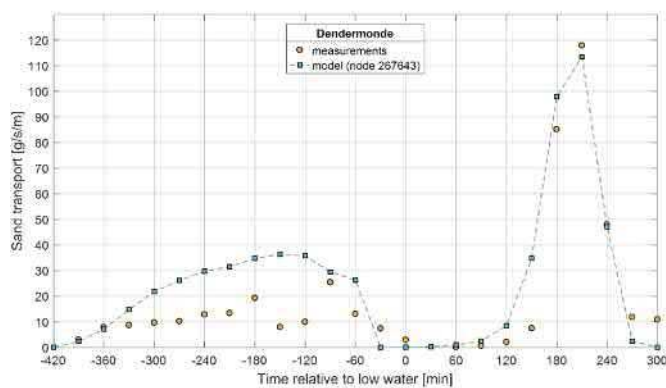


Figure 7 – Modelled and measured sand transport at Dendermonde (137)

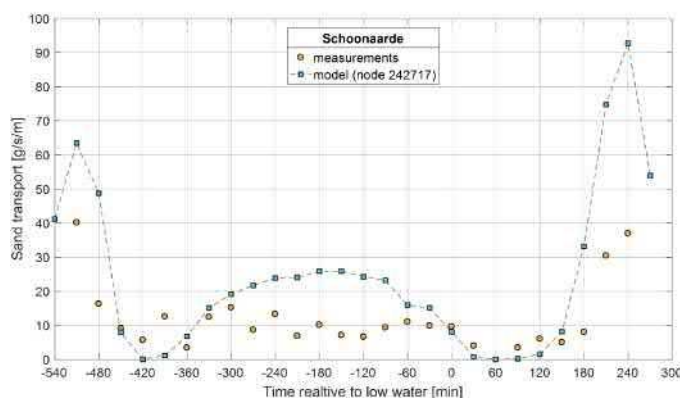


Figure 8 – Modelled and measured sand transport at Schoonaarde (km 147)

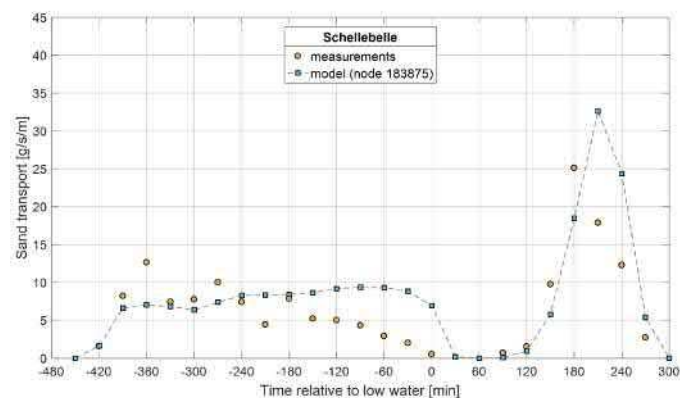


Figure 9 – Modelled and measured sand transport at Schellebelle (km 157)

### Computed transport rates

In [13] sand transport rates over transects in the Sea Scheldt were calculated based on the difference in bathymetry data from 2001 and 2010, lithological information of the bottom and

data of the dredging and disposal works. These transport rates are compared to the model results and this is shown in Figure 11. The model results are scaled up from a net transport over a spring-neap tidal cycle (15 days) to a net transport over a period of 1 year. The calculated sand transport from [13] is scaled down from a transport over ten years to a transport number of one year and was then adjusted to take a bed porosity of 0.5 into account. For the Upper Sea Scheldt the model shows a very good agreement with the calculated sand transport, both in magnitude as in transport direction. The model tends to underestimate the sand transport a little, mainly in the Lower Sea Scheldt. For the tidal arm to Gentbrugge (box 19 in Figure 11), the model gives a net import, although very small, and the calculated sand transport gives a value 200 times larger. In the sand transport model the Durme (tributary, location shown in Figure 11) is importing sand like the calculated transport. The value given by the model is much smaller than the calculated import. For the Lower Sea Scheldt the model results give mainly ebb dominated sand transport, whereas the calculated transports are directed upstream. Transport rates are in the same order of magnitude, except for the three transects closest to the border (most downstream); there the model results are much smaller than the calculated results. Larger scale changes to the estuary like dredging and dumping and de-embankments are not included in a short model run, but it is unclear if this might give the difference seen in the sand transport numbers and directions in the Lower Sea Scheldt. In [14] a sand transport model (Delft3D) is used for the Scheldt estuary and on the Dutch/Belgian border the transport directions show also a net downstream transport direction.

### VI. SAND TRANSPORT OVER TRANSECTS

The net sand transport over transects can be calculated for different type of tides: neap and spring tide or averaged over a spring/neap tidal cycle tide. Figure 10 shows that for an averaged spring/neap tidal cycle the sand transport in the Western Scheldt is directed upstream (negative value). Around the Dutch-Belgian border the direction of the transport changes to downstream. The sand transport increases a lot between km 90 and 100 in downstream direction with some peaks with upstream transport in between. In the Upper Sea Scheldt the transport direction is usually downstream with one exception around km 147 (around Schoonaarde). The transport rates during a neap or spring tide behave differently and are also plotted in Figure 10. Over most transects the transport rate increase during spring tide and decreases during neap tide, but in the Upper Sea Scheldt starting from km 132 the opposite trend is seen (Figure 10). Sometimes the net transport direction changes when going from a neap tide to a spring tide, like around km 100-115 (Figure 10).

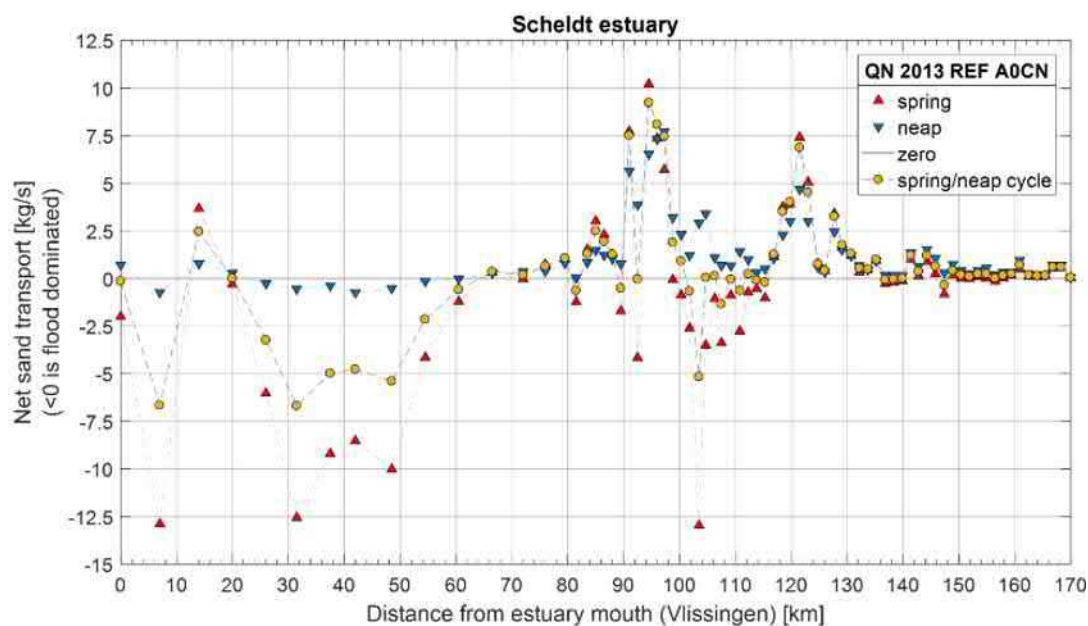


Figure 10 – Net sand transport over different cross sections along the Scheldt estuary calculated and plotted for a neap and spring tide, and averaged over a spring/neap tidal cycle. A positive value means transport in downstream direction.

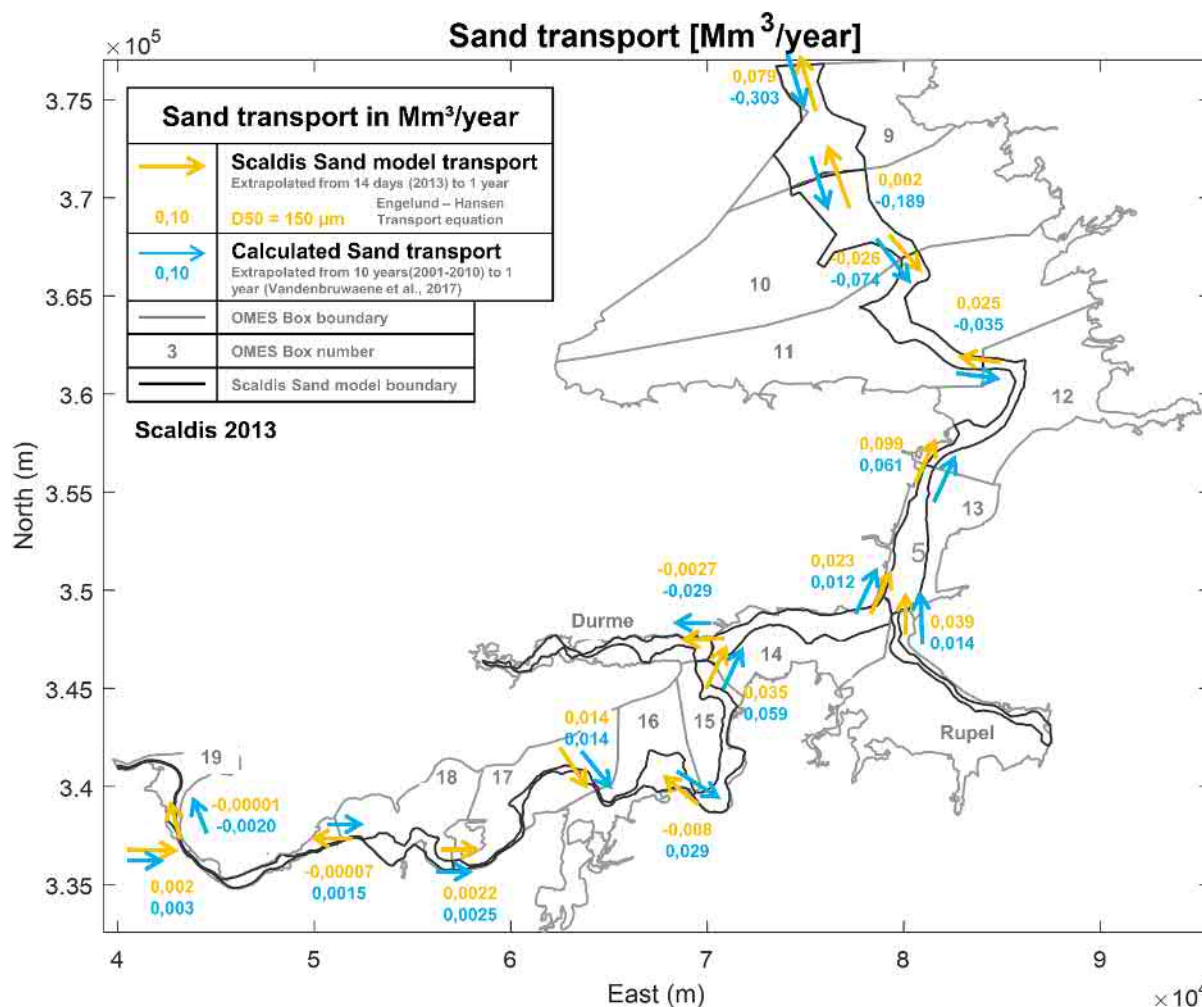


Figure 11 – Sand transport between different parts of the estuary. Model results are compared with calculated sand transport.



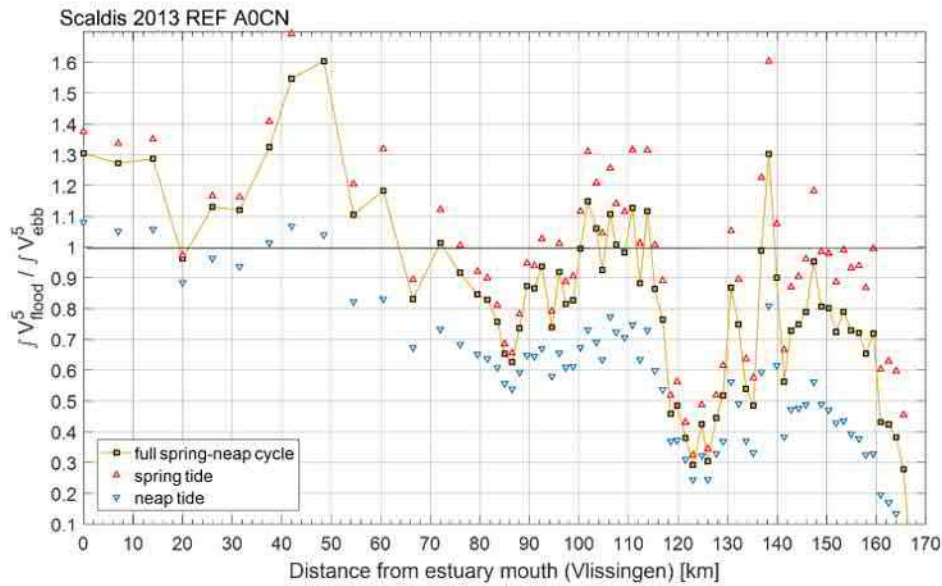


Figure 12 – Asymmetry between flood and ebb over time integrated cross sectional averaged flow velocity to the power five

## VII. FLOW VELOCITY ASYMMETRY

The flow velocity is the largest driving force behind the Engelund and Hansen equation (see equation 1). Since there is no threshold for this velocity for incipient motion, an integration of both flood and ebb cross sectional averaged flow velocity to the power five can give more insight in why the net sand transport is going in up- or downstream direction. The asymmetry between the integrated cross sectional averaged flood and ebb velocity to the power five is shown in Figure 12. The asymmetry is shown for an integration over a full spring-neap tidal cycle and for an integration over two spring (to take diurnal inequality into account) and two neap tides separately. When the asymmetry is larger than 1 it means that the flow velocity to the power five is larger in the upstream direction and is thus flood dominated. If the asymmetry is smaller than 1 it is ebb dominated. Since cross sectional averaged flow velocities are used, the spatial variation along the transect is lost. Figure 12 shows that for the Western Scheldt the asymmetry is mostly larger than 1, which coincides with the upstream direction of the transport found in Figure 10. At approximately the Dutch-Belgian border (km 65) the asymmetry drops below 1, changing the direction of the transport to downstream. Between km 100 and 115 the transport direction changed again from downstream to upstream and this is also seen in Figure 12 where the asymmetry rises again above 1. In the Upper Sea Scheldt the asymmetry is mostly below 1 and the transport direction is ebb dominated. One peak in asymmetry above 1 can be seen around km 138 and this coincides with a reduced transport in the ebb direction, but the net sand transport does not change entirely to the upstream direction. The spring and neap tide markers show that asymmetry can change a lot between these two extremes in tides and can also change the dominance from ebb to flood or vice versa.

## VIII. MASS BALANCE

The sand transport over the different transects along the Scheldt estuary was calculated for a full spring-neap tidal cycle. A mass balance is calculated for each polygon formed by a downstream and upstream transect. This sand mass balance is shown in Figure 13. This figure shows the areas in the Upper Sea Scheldt that are accumulating sand (in red) and other areas that are eroding and thus losing sand (in blue).

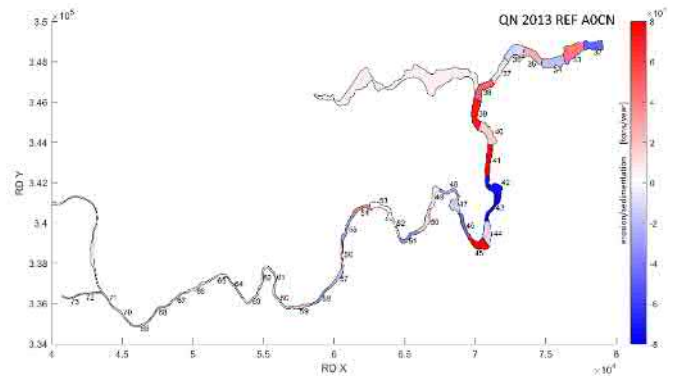


Figure 13 - A sand mass balance calculated after a full spring-neap tidal cycle and extrapolated to one year based on calculated transports over transects for run 2013 REF A0CN.

## IX. SENSITIVITY: CONSTANT MANNING COEFFICIENT CORRECT?

The spatial varying Manning coefficient from the hydrodynamic model is the result of a calibration exercise. This coefficient takes also non-physical processes, like numerical diffusion, into account. Because of this, we think it is better to use a constant Manning bottom roughness coefficient for the sediment module SISYPHE separately. According to equations 6 and 7, the larger the Manning coefficient, the larger the



calculated bed shear stress will be. So the locations in the model domain where the constant Manning coefficient of  $0.02 \text{ m/s}^{1/3}$  is larger than the coefficient given in the hydrodynamic module, will have larger sand transport rates and vice versa. This is shown in Figure 14 where the results of a simulation with a fixed Manning coefficient (equal to  $0.02 \text{ m/s}^{1/3}$ ) over the entire domain and the results of a run where SISYPHE uses the Manning coefficient of the hydrodynamic model (spatially varying as seen in Figure 2). The Manning coefficient in the hydrodynamic model is lower than the constant value given for the sediment module for the region between km 70 and km 90 and upstream of km 123. The differences can be big and even result in a difference in net transport direction. This also means that choosing a different constant Manning coefficient could change the net transport magnitude and direction. Furthermore when comparing a sand transport model in TELEMAC and SISYPHE with a sand transport model in a less diffusive code (and thus with higher Manning coefficient values in the hydrodynamics and sediments) such as Delft3D, the latter will show higher sand transport rates. For a Manning coefficient varying from  $0.012 \text{ m/s}^{1/3}$  to  $0.022 \text{ m/s}^{1/3}$  the transport rate can be 10 times higher!

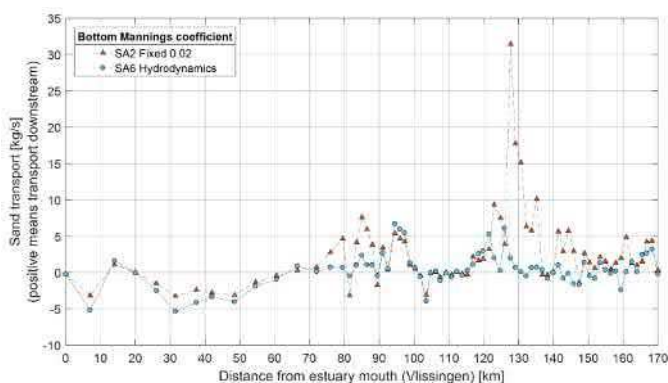


Figure 14 - Effect of choice of Manning coefficient on net sand transport over different transects along the Scheldt estuary. A positive net transport is transport in the downstream direction. A negative net transport is transport in the upstream direction.

## X. CONCLUSIONS

This paper describes a new sand transport model for the Scheldt estuary. The Engelund and Hansen total load equation was chosen as transport equation. The hydrodynamic data was delivered by the 3D Scaldis model. When the model results are compared to point measurements for total sand transport most locations show a very good agreement.

Comparing model results with calculated net sand transport rates based on the difference of bathymetry measurements between 2001 and 2010 showed that the model reproduces the sand transport rate and directions in the Upper Sea Scheldt well. Conversely, the model underestimates the transport rate in the Lower Sea Scheldt and finds opposite directions of transport close to the Dutch/Belgian border.

Transport rates over transects are shown for the entire estuary and most of the transport rates and directions can be explained by the integration over time of the cross sectional averaged flow velocity to the power five (as it is used in the Engelund and Hansen equation).

Finally, the sensitivity of the sand transport rate results to the choice of Manning bottom roughness coefficient are shown. Specific measurements are necessary to confirm the use of a different Manning coefficient in the sediment model compared to the coefficient in the hydrodynamic model.

## REFERENCES

- [1] Bour, N. (2008) Seine-Nord Europe Canal: central segment of the Seine-Scheldt waterway link. On Course: PIANC magazine 132: 5-12.
- [2] Smolders, S.; Maximova, T.; Vanlede, J.; Teles, M.J. (2014). Implementation of controlled reduced tide and flooding areas in the TELEMAC 3D model of the Scheldt Estuary, in: Bertrand, O. et al. (Ed.) (2014). Proceedings of the 21st TELEMAC-MASCARET User Conference, 15th-17th October 2014, Grenoble – France. pp. 111-118
- [3] Smolders, S.; Maximova, T.; Vanlede, J.; Plancke, Y.; Verwaest, T.; Mostaert, F. (2016). Integraal plan Boven-Zeeschelde: Subreport 1. SCALDIS: a 3D Hydrodynamic model for the Scheldt Estuary. Version 5.0. WL Rapporten, 13\_131. Flanders Hydraulics Research: Antwerp. XXVIII, 246 + 228 p. bijl. pp.
- [4] Smolders, S., Bi, Q., Maximova, T., & Vanlede, J. (2018). Modelling Cohesive Sediments in the Scheldt Estuary (Belgium) with SEDI-3D. In Proceedings of the XXVth TELEMAC-MASCARET User Conference, 9th to 11th October 2018, Norwich (pp. 53-60).
- [5] Smolders, S.; Maximova, T.; Vanlede, J.; Plancke, Y.; Verwaest, T.; Mostaert, F. (2016). Integraal Plan Boven-Zeeschelde: Subreport 1 – SCALDIS: a 3D Hydrodynamic Model for the Scheldt Estuary. Version 5.0. WL Rapporten, 13\_131. Flanders Hydraulics Research: Antwerp, Belgium.
- [6] Smolders, S.; Plancke, Y.; Vanlede, J.; Mostaert, F. (2019). Integraal Plan Boven-Zeeschelde: Sub report 10 – Scaldis Sand: a sand transport model for the Scheldt estuary. Version 4.0. FHR Reports, 13\_131\_10. Flanders Hydraulics Research: Antwerp.
- [7] Van Engeland T., T.J.S. Cox, K. Buis, S. Van Damme, P. Meire (2018). 1D Ecosystem model of the Schelde estuary: model calibration and validation. Report 018-R217.
- [8] Baeyens, W., van Eck, B., Lambert, C., Wollast, R., and Goeyens, L. General description of the Scheldt estuary. *Hydrobiologia* 34:83-107, 1998.
- [9] Meire, P., Ysebaert, T., Van Damme, S., Van den Bergh, E., Maris, T., and Struyf, E., (2005). The Scheldt estuary: a description of a changing ecosystem. *Hydrobiologia* 540:1-11, 2005.
- [10] Engelund, F. and Hansen, E., (1967). A Monograph on Sediment Transport in Alluvial Streams. Teknisk Forlag, Copenhagen, Denmark.
- [11] Flokstra, C.; Koch, F. (1981). Numerical aspects of bed level predictions for alluvial river bends. Delft Hydraulics Laboratory. Netherlands, Publication 258
- [12] Plancke, Y.; Smolders, S.; Mostaert, F. (2018). Sedimenttransport in het Schelde-estuarium: deelrapport 1. Bepalen van het aandeel zandtransport uit metingen met de Delftse fles. Versie 3.0. WL Rapporten, 16\_001\_1. Waterbouwkundig Laboratorium: Antwerpen. VI, 13 + 22 p. bijl. pp
- [13] Vandenbruwaene, W.; Levy, Y.; Plancke, Y.; Vanlede, J.; Verwaest, T.; Mostaert, F. (2017). Integraal plan Boven-Zeeschelde: Deelrapport 8 – Sedimentbalans Zeeschelde, Rupel en Durme. Versie 4.0. WL Rapporten, 13\_131\_8. Waterbouwkundig Laboratorium: Antwerpen.
- [14] Coen, L.; Plancke, Y.; De Maerschalck, B.; Mostaert, F. (2018). Agenda voor de Toekomst Morfologie Mesoschaal: Deelrapport 13 – Scenario's morfologisch beheer. Versie 4.0. WL Rapporten, 14\_024\_13. Waterbouwkundig Laboratorium: Antwerpen.

# Sensitivity Analysis of the Mascaret model on the Odet River

Anne-Laure Tiberi-Wadier\*, Nicole Goutal<sup>†</sup>, Sophie Ricci<sup>‡</sup>, Philippe Sergent<sup>§</sup> and Céline Monteil<sup>¶</sup>

\*Cerema Eau, Mer et Fleuves, Plouzané, France, Anne-Laure.Tiberi-Wadier@cerema.fr

<sup>†</sup>EDF R&D et Laboratoire d'Hydraulique Saint-Venant, Chatou, France, nicole.goutal@edf.fr

<sup>‡</sup>CECI, UMR5318, CNRS/CERFACS, Toulouse, France, ricci@cerfacs.com

<sup>§</sup>Cerema Eau, Mer et Fleuves, Margny-Les-compiègne, France, Philippe.Sergent@cerema.fr

<sup>¶</sup>EDF R&D, Chatou, France

**Abstract**—A Global Sensitivity Analysis (GSA) is carried out on the Mascaret model of the Odet river (France, Brittany) to identify and rank the major sources of uncertainty at observing stations on the network for the simulated water level, considering the upstream and downstream boundary conditions and the area distributed friction coefficients values. Upstream, ensemble hydrologic forcings are forecasted with the rainfall-runoff distributed model MORDOR-TS, using uncertain hydrologic model parameters drawn from uniform distributions. The downstream maritime boundary condition is perturbed taking into account the temporal correlation of the errors in storm surge. The Sobol' indices are computed at Kervir, Moulin-Vert and Justice stations given hypothesis on the statistical distribution of the aleatory variables.

The study focuses on the 23 to the 26 December 2013 event. GSA highlights that the simulated water level at the three stations is mainly controlled by the immediate downstream friction coefficient when the boundary conditions are not perturbed. The flood plain friction coefficients only become important around the peak of the event. However, when the boundary conditions are also taken into account, they become predominant for the simulated water level and the value of the friction coefficients has less influence.

## I. INTRODUCTION

SCHAPI and SPC (i.e. flood forecasting services) use day-to-day deterministic hydrologic and hydraulic models forced by precipitation forecasts. Input and parameters to these models are uncertain, thus limiting the reliability of a deterministic discharge forecast. An ensemble approach should be thus favoured. The cascade of uncertainty in a chained ensemble framework is being investigated on the Odet catchment, in the North-West of France in Brittany.

The hydrodynamics of the river is simulated with the 1D solver MASCARET. This model is used daily by the SCP VCB (Vilaine et Côtières Bretons) for flood forecasting in the city of Quimper. However, the geometry of the model has been modified here for a better numerical stability and a new calibration has been done. The model used in this study is thus not exactly the operational model. Ensemble hydrologic forcings are forecasted with the rainfall-runoff distributed model MORDOR-TS, using uncertain hydrologic model parameters drawn from uniform distributions.

A Global Sensitivity Analysis (GSA) on the hydraulic model is carried out in order to identify and rank the major sources of uncertainties in water level, considering uncertainties in the

upstream and downstream boundary conditions and the area distributed friction parameters values ( $K_s$ ).

The article is organized as follows. Section II presents the catchment study and the areas represented by the hydrologic and hydraulic models. Section III presents the data sets used in the study. Section IV describes the calibration of the MORDOR-TS model, and the construction of the Hydrologic Ensemble Forecasts (HEF). Section V is devoted to the calibration of the Mascaret model. The GSA is presented in section VI, and the associated results are given in section VII. Conclusion and perspectives are finally given in section VIII.

## II. PRESENTATION OF THE STUDY AREA

The Odet river is a coastal river located in Western Brittany. It flows through the city of Quimper, then South to the sea (Fig 1). Astronomical tide ranges between 1.40 m and 5.55 m at the mouth at Plaisance. The Odet catchment area is 720 km<sup>2</sup>, for a total length of about 60 km for the Odet river. The Jet and Steir rivers are two tributaries of the Odet river.



Fig. 1: The rivers Odet, Steir and Jet with the location of the hydrologic stations.

### A. Hydrologic modeling

The MORDOR-TS rainfall-runoff model provides hydrologic streamflows on each of the three upstream subcatchments



Fig. 2: Parts of the rivers covered by the Mascaret model.

which exutories are named Tréodet, Kerjean and Ty Planche (Fig 1). Table I summarizes the characteristics of the upstream subcatchments.

#### B. Hydraulic modeling

Mascaret is a 1D model based on Saint-Venant equations. The Mascaret model covers the downstream part of the catchment and focuses on urban areas as shown on Figure 2. It aims at forecasting the water level at three observing stations Kervir, Justice (river Odet) and Moulin Vert (river Steir), represented in red in figure 2. The upstream and downstream stations of the hydraulic model are represented in green. The length of the reaches are about 23 km, 6 km, and 6 km respectively for the Odet, Jet and Steir rivers.

TABLE I: Characteristics of the sub-catchments Tréodet, Kerjean, Ty Planche and the whole catchment.

Sub-catchment	Tréodet	Kerjean	Ty Planche
Elevation of the source (IGN69)	175 m	200 m	100 m
Total length of the river (km)	37	21	23
Catchment area (km <sup>2</sup> )	205	107	179
Mean streamflow (m <sup>3</sup> /s)	4.8	2.27	3.79
10-years flows (m <sup>3</sup> /s)	55	19	39
50-years flows (m <sup>3</sup> /s)	75	25	53
Max flow 12-2000 (m <sup>3</sup> /s)	110	46.6	81
Max flow 12-2013 (m <sup>3</sup> /s)	91.5	17.6	42.7
Mean rainfall (mm/year)	743	672	671

### III. DATA SET

The following data sets are used in the study. They all are available from January 2007 to January 2017:

- Spatially distributed observed rainfall and surface temperature data are used as input to the hydrologic model. They respectively come from ANTILOPE (Champeaux et al., 2009) and SAFRAN (Vidal et al., 2010) reanalysis and are available at hourly time step.
- Continuous streamflow measurements come from the French national archive (Banque hydro, <http://www.hydro.eaufrance.fr>) and are available at the three upstream observing stations (Tréodet, Kerjean, Ty-Planche) at hourly time step. The data are used for hydrologic and hydraulic models calibration.
- Continuous water level measurements provided by the SPC VCB are available at three observing stations on the river (Kervir, Moulin-Vert, Justice) and at the downstream boundary of the model (Plaisance) with a time step of 6 minutes. These data are both used for the calibration of the hydraulic model and the determination of the storm surge for the perturbation of the maritime boundary condition when performing the GSA (see VI-B3).

### IV. MORDOR-TS HYDROLOGIC MODEL

#### A. Description and calibration

MORDOR-TS (Garçon, 1996; Garavaglia et al., 2017; Rouhier et al., 2017) is a spatialized and continuous conceptual rainfall-runoff hydrologic model. It has 10 parameters calibrated with respect to a multi-objective function using the caRamel genetic algorithm (Le Moine et al., 2015; Monteil et al., 2019). The calibration of the hydrologic parameters is achieved over a 10-year period from 01/01/2007 to 05/31/2017, after a spin-up period of one year.

Three scores are gathered in the multi-objective function: (i) Nash over the entire time series, (ii) Nash over the inter-annual daily regime and (iii) Nash over the empirical cumulative distribution. Table II shows the Nash values after calibration on these three hydrologic signatures.

Catchment	Tréodet	Kerjean	Ty Planche
Nash hourly runoff	0.94	0.95	0.94
Nash daily regime	0.99	0.99	0.99
Nash cumulative distribution	0.99	0.995	0.996

TABLE II: Nash after calibration of MORDOR-TS parameters.

#### B. Hydrologic Ensemble Forecasts (HEF)

An Hydrologic Ensemble Forecast (HEF) system is setup by perturbing the value of the parameters of MORDOR-TS. A GSA on discharge computed with the MORDOR-TS model has shown that only 8 over the 10 calibrated parameters control the simulated runoff. The Probability Density Functions (PDF) of these 8 uncertain variables are supposed to be uniform  $U[V_{min}, V_{max}]$ . For each parameter,  $V_{min}$  and  $V_{max}$  are determined by the realization of a set of calibrations of the MORDOR-TS model over 2 years periods. The ensemble is created with a Halton sequence of 99 members.



## V. MASCARET MODEL

The hydraulic model consists in 172 geometrical cross-sections for a total length of 35 km. The resolution of the computational mesh varies between 5 m and 10 m. The vertical discretization of cross sections is 10 cm. After calibration, 12 different zones of friction coefficients are retained (Figure 3). Strickler coefficients are set to values ranging between  $15 \text{ m}^{1/3}\text{s}^{-1}$  and  $37 \text{ m}^{1/3}\text{s}^{-1}$  in the riverbed, and between  $1 \text{ m}^{1/3}\text{s}^{-1}$  and  $34 \text{ m}^{1/3}\text{s}^{-1}$  in the flood plains. The very low value of  $1 \text{ m}^{1/3}\text{s}^{-1}$  compensates for an incomplete knowledge of the topography/bathymetry and for the presence of a bend in the river geometry.

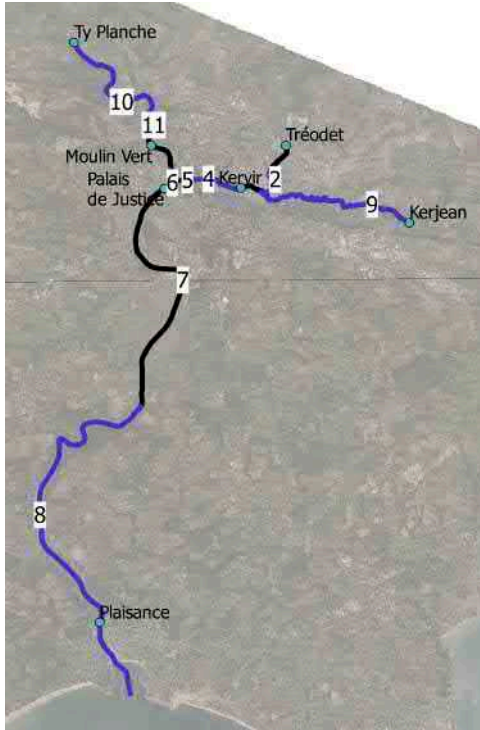


Fig. 3: 12 zones of friction coefficients.

### A. Calibration methodology

The hydraulic numerical model was calibrated comparing the simulated water levels over November 1st, 2013 - February 28th, 2014 to observed water level. This winter was characterized by numerous flood events and storm surges. The model was then assessed over November 1st, 2012 - February 28th, 2013. This winter had less storms than the winter used for the calibration.

The cost function is a combination of the RMSE over the whole time series and the RMSE calculated on the value of simulated peaks during extreme events (1):

$$f_C = 0.8 * RMSE_{TimeSeries} + 0.2 * RMSE_{peaks} \quad (1)$$

Figure 4 shows the measured water level at Kervir, Moulin Vert and Justice during the calibration winter. For Kervir and

Moulin-Vert, a set of 11 events represented in red are used for the calculation of  $RMSE_{peaks}$  in Equation (1). At Justice, the water level is dominated by tide effects, even during river floods. For this location, all the high tide peaks are considered for the calculation  $RMSE_{peaks}$ . The calculation of  $RMSE_{peaks}$  in Equation (1) is thus made on 11 peaks for Kervir and Moulin-Vert, and on about 200 peaks of high tide for Justice.

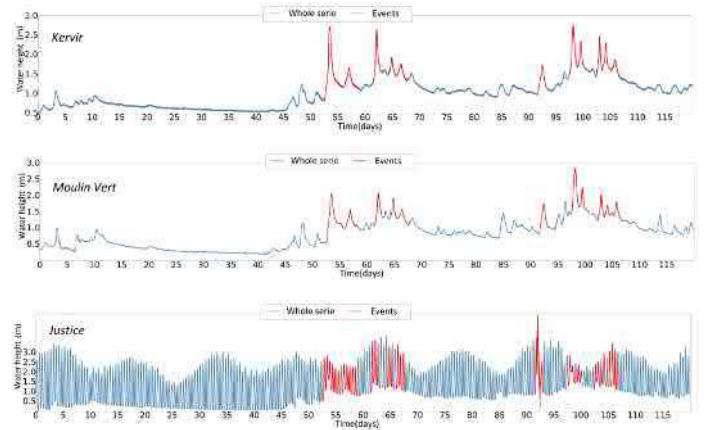


Fig. 4: Measured water level at Kervir, Moulin Vert and Justice from November 1st, 2013 to February 28th, 2014. Flood and storm surge events are represented in red.

### B. Results

Table III shows the results of the calculation of the RMSE for the whole time series during the calibration and the validation winters (respectively denoted “CAL” in black and “VAL” in blue in the table). The green, yellow and orange vigilances correspond to water level classes used for operational forecasting by the SPC VCB. These results show that the performance of the model during the calibration and the validation periods are similar. The model is thus relatively robust.

TABLE III: RMSE (cm) during calibration and validation.

Water height class	Period	Kervir	Moulin-Vert	Justice
All water heights	CAL	2.9	4.8	6.0
	VAL	2.4	4.5	5.3
Green vigilance	CAL	2.6	4.3	6.2
	VAL	2.3	4.4	5.5
Yellow vigilance	CAL	6.0	7.2	5.7
	VAL	6.3	7.2	5.0
Orange vigilance	CAL	3.8	15.46	no data
	VAL	no data	no data	no data

Table IV represents the value of the peaks of the 11 events of the calibration winter and the associated simulated error for Kervir and Moulin-Vert. The value of the peaks are relatively well simulated by the model.



TABLE IV: Value of the peaks of water level for the 11 events of the calibration winter and associated simulated error - Stations Kervir and Moulin-Vert.

Event	Measured water height at Kervir (m)	Error (cm)	Measured water height at Moulin-Vert (m)	Error (cm)
Dec 2013 - 1	2.72	-4.8	2.07	-1.9
Dec 2013 - 2	1.66	6.7	1.58	8.9
Jan 2014 - 1	2.67	-3.1	2.09	-3.4
Jan 2014 - 2	1.94	3.3	1.93	4.5
Jan 2014 - 3	1.78	3.7	1.58	6.8
Jan 2014 - 4	1.74	-0.6	1.76	6.2
Feb 2014 - 1	2.76	-6.7	2.85	3.2
Feb 2014 - 2	2.35	-0.5	2.26	-5.7
Feb 2014 - 3	2.48	7.1	2.06	0.6
Feb 2014 - 4	2.31	4.6	1.71	5.6
Feb 2014 - 5	1.88	1.3	1.81	2.3

Figure 5 represents the difference between measured and simulated water level for each high tide during the calibration period at Justice. The water level measurement at the moment of the peaks is also represented. A positive value for the peak error corresponds to an overestimation of the model relative to measurements.

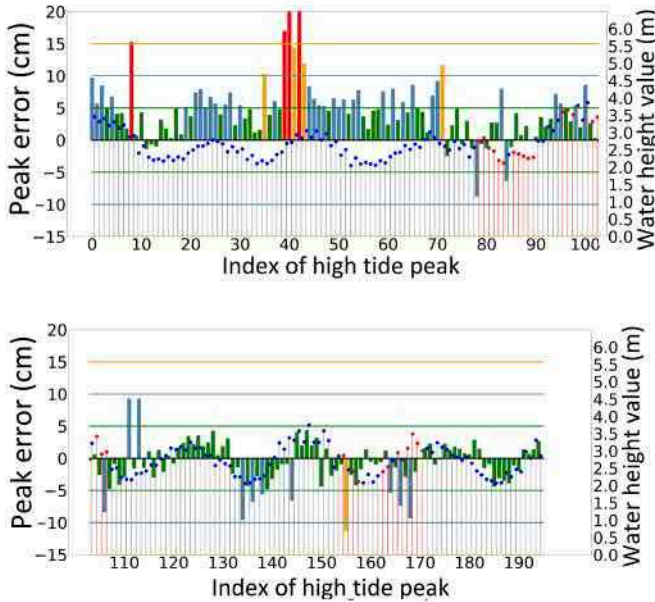


Fig. 5: Peaks errors and associated water level for high tide during 2013-2014 winter - Station Justice.

On this figure, errors are color-coded:

- green corresponds to a difference of less than 5 cm
- blue corresponds to a difference between 5 and 10 cm
- orange corresponds to a difference between 10 and 15 cm
- red corresponds to a difference of more than 15 cm

Figure 5 shows that most of simulated peaks are less than 5 cm of the measures. For only 4 high tides, the model calculates a value with an error more than 15 cm.

## VI. GLOBAL SENSITIVITY ANALYSIS (GSA)

### A. Variance decomposition and Sobol' indices

Sobol' indices apportion the variance of the output  $Y = f(X)$  with  $X = (X_1, X_2, \dots, X_k)$ , to the variation of different inputs  $(X_1, \dots, X_k)$  on their uncertainty domain. With the assumption that the variance of  $Y$  is finite and the input variables are independent, the Hoeffding decomposition (Hoeffding, 1948) provides the relation:

$$V(Y) = \sum_i V_i + \sum_i \sum_{j>i} V_{i,j} + \dots + V_{1,2,3,\dots,K} \quad (2)$$

where

- $V_i$  is the elementary contribution of  $X_i$  to  $V(Y)$ ,
- $V_{i,j}$  is the contribution due to interactions between  $X_i$  et  $X_j$  to  $V(Y)$ ,
- ...
- $V_{1,2,\dots,k}$  is the contribution due to interaction between all inputs to  $V(Y)$ .

Dividing Eq. 2 by  $V(Y)$  leads to :

$$\sum_i S_i + \sum_i \sum_{j>i} S_{i,j} + \dots + S_{1,2,3,\dots,K} = 1 \quad (3)$$

In (3),  $S_i$  is the first order Sobol index which represents the normalized elementary contribution of  $X_i$  to  $V(Y)$ . The total Sobol index representing all contributions related to  $X_i$  is defined by:

$$ST_i = S_i + \sum_{i \neq j} S_{i,j} + \dots + S_{1,2,3,\dots,K} \quad (4)$$

If they are no interaction between the input parameters,  $\sum_i S_i = 1$ . In the following, since there are very few interaction between the input parameters, only the first order Sobol' indices will be shown.

### B. Uncertainty space for GSA

In order to carry out a GSA on the Mascaret model, we consider three types of uncertain inputs:

- the minor and flood plain friction coefficients for the 12 different zones of the model ( $K_{s_i}$  and  $K_{s_{iM}}$ ), represented on figure 3;
- the three hydrologic upstream time series at Tréodet, Kerjean and Ty-Planche (Q);
- the maritime boundary time series (CLMAR).

The quantity of interest  $Y$  is the measured water level at a forecast station at a specific time. The GSA is thus applied over time at Kervir, Moulin-Vert and Justice. Scalar uncertain variables are described by their Probability Density Function (PDF) which characteristics are described thereafter.

1) *Friction coefficients*: The PDFs of friction coefficients are supposed to be uniform. The distribution is centered on the calibrated value with a width of 5 on each side. The values are described in table V.

TABLE V: Distribution of the Strickler coefficients for the GSA

Zone	$K_{smin}$ minor	$K_{smax}$ minor	$K_{smin}$ flood plain	$K_{smax}$ flood plain
1	25	35	15	25
2	15	25	5	15
3	10	20	5	15
4	33	43	8.5	18.5
5	13	17	5	15
6	31.5	41.5	29	39
7	32	42	20	30
8	20.5	30.5	1	10
9	15	25	5	15
10	15	25	5	15
11	27.5	37.5	1	10
12	17.5	22.5	5	15

2) *Hydrologic input*: The HEF described in section IV-B provides 99 members of hydrologic time series. The uncertainty in the hydrologic input is thus represented by an index drawn uniform between 1 and 99.

3) *Maritime boundary condition*: The water height at the downstream maritime boundary condition is time-dependent. The sampling procedure must thus preserve the temporal correlation of errors.

The time varying perturbation is applied on the storm surge  $s$ . The perturbation is supposed to be a Gaussian Process with a Gaussian covariance function  $C$ . The correlation length is arbitrary set to 6 hours, which is the duration of a half tide. The amplitude of the covariance function  $C$  is chosen in order to set the median standard deviation of the perturbed storm surge to about 18 cm, which is approximatively the median standard deviation of the measured tide surge.  $s$  is written as a Karhunen-Loève decomposition as the truncated form of  $n_p$  orthogonal functions where the mode coefficients  $\epsilon_i$  are independent standard normal variables:

$$s(t) = \sum_{i=0}^{n_p} \sqrt{\lambda_i} \phi_i(t) \epsilon_i. \quad (5)$$

$\lambda_i$  and  $\phi_i$  are respectively the eigenvalues and the eigenfunctions of the covariance function, i.e. solutions of the Fredholm equation:

$$\int C(t_1, t_2) \phi_i(t_2) dt_2 = \lambda_i \phi_i(t_1). \quad (6)$$

A set of 99 perturbed storm surge time series are generated with a sampling of  $\epsilon_i$ . The uncertainty in the maritime boundary condition input is thus represented by an index drawn uniform between 1 and 99.

4) *Comparison of the standard deviation of upstream and downstream perturbations*: Figure 6 represents the standard deviation of the upstream and downstream perturbations. On this figure, upstream streamflows have been converted into water level by their rating curve. It should be noted that the magnitude of the imposed perturbations are of the same order for the four boundary conditions.

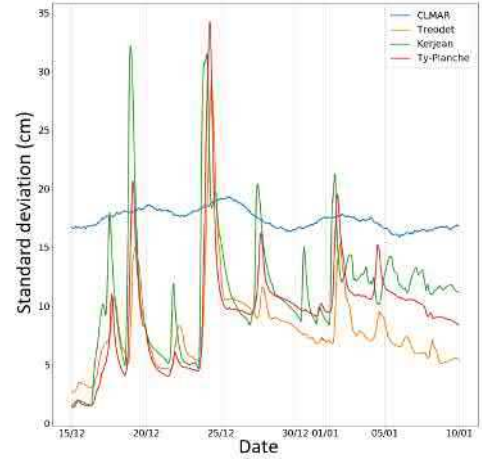


Fig. 6: Standard deviation of the upstream and downstream perturbations (cm)

## VII. RESULTS AND DISCUSSION

A GSA is carried out for four different configurations:

- Configuration 1: the values of the minor friction coefficients of the 12 zones are perturbed. The aim of this study is to determine the impact of the spatially distributed minor friction coefficients. The Sobol' indices are computed with 20800 perturbed simulations.
- Configuration 2: only the 6 zones which mainly control the simulated water level at the three stations are considered. These zones are determined thanks to the previous study (configuration 1). The minor and flood plain friction coefficients are now perturbed. The aim of this study is to determine the impact of flood plain friction coefficients. The Sobol' indices are calculated with 20800 perturbed simulations.
- Configuration 3: the same 6 zones as in configuration 2 are considered, but again only with a perturbation of minor friction coefficients. In addition, the hydrologic inputs and the maritime boundary condition are also taken into account. The aim of this study is to determine the impact of the forcings against the friction coefficients. The Sobol' indices are computed with 30600 perturbed simulations.
- Configuration 4: the same 6 zones as in configuration 2 and 3 are considered with a perturbation of both minor and flood plain friction coefficients. The hydrologic inputs and the maritime boundary condition are also taken into account. The aim of this study is to determine the impact of the forcings against the minor and flood plain friction coefficients. The Sobol' indices are computed with 48000 perturbed simulations.

For each configuration, the value of the friction coefficients are perturbed according to the ranges described in table V. The results are achieved for the event from the 23 to the 26 December

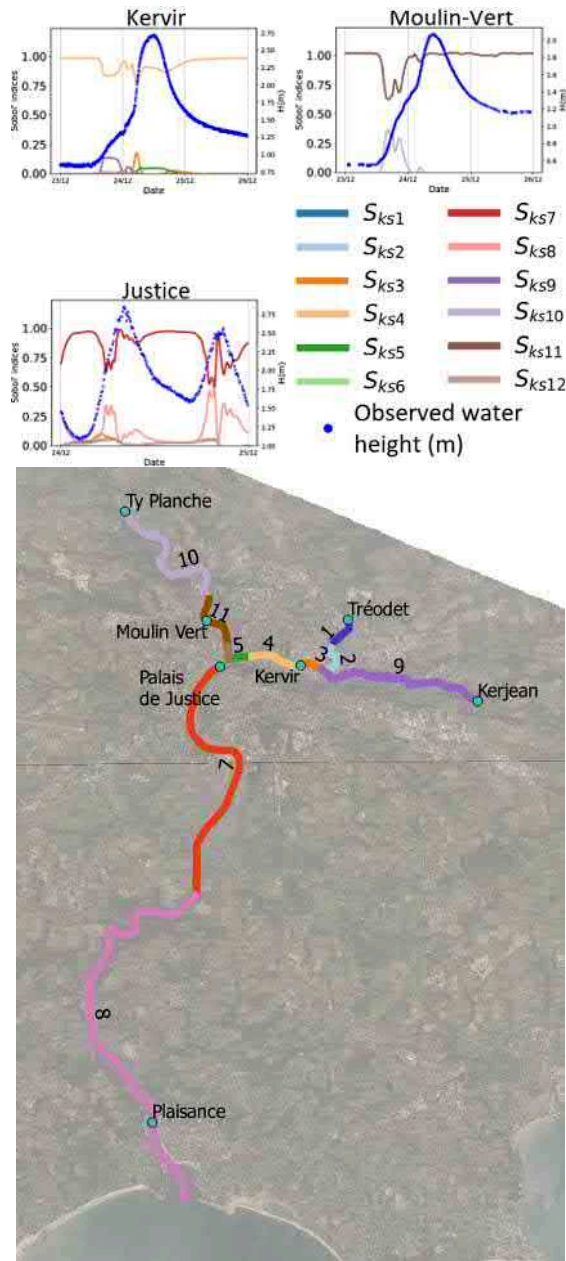


Fig. 7: Configuration 1: Sobol' indices time series and associated zones for the event from the 23 to the 26 December, 2013

2013. The computation of Sobol' indices is realized thanks to the python modules OpenTURNS (<http://openturns.org/>) and Batman (Roy et al., 2018).

#### A. Configuration 1: impact of spatially distributed minor friction coefficients

Figure 7 shows the Sobol' indices time series during the event. These graphics highlight that for Kervir and Moulin-Vert, the simulated water level is mainly controlled by the downstream Strickler friction coefficient:  $K_{s4}$  for Kervir and  $K_{s11}$  for Moulin-Vert. To a lesser extent, the upstream Strick-

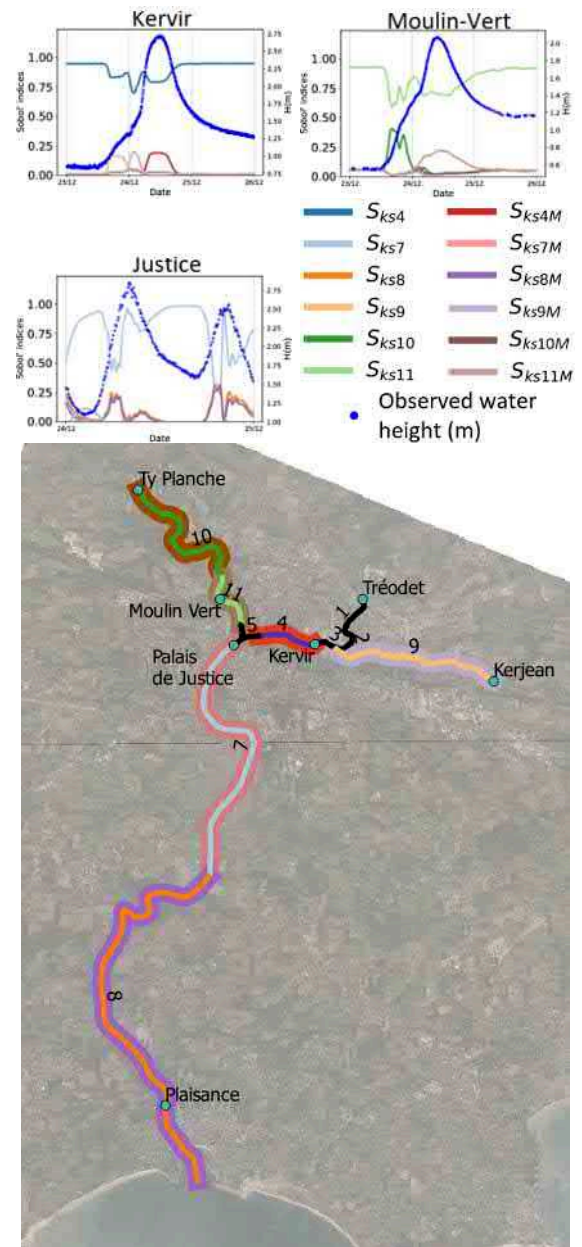


Fig. 8: Configuration 2: Sobol' indices time series and associated zones for the event from the 23 to the 26 December, 2013

ler friction coefficient slightly controls the simulated water level during the beginning of the flood and the end of the receding water level:  $K_{s9}$  for Kervir and  $K_{s10}$  for Moulin-Vert.

The behavior is different at Justice: the simulated water level is mainly controlled by the just downstream Strickler friction coefficient  $K_{s7}$ . But it is also cyclically controlled by  $K_{s8}$  according the tide level, the zone 8 being situated immediately downstream the zone 7. The value of the upstream Strickler friction coefficients have no impact on the simulated level at Justice.



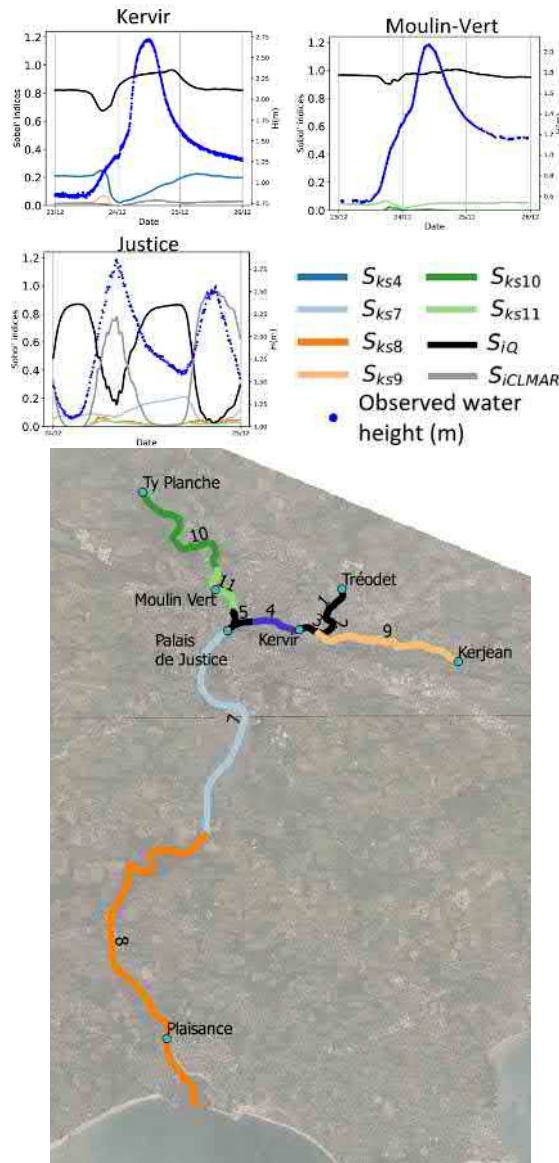


Fig. 9: Configuration 3: Sobol' indices time series and associated zones for the event from the 23 to the 26 December, 2013

### B. Configuration 2: impact of flood plain friction coefficients

In this second study, we consider the minor and flood plain friction coefficients of the 6 zones which mainly control the simulated water level at the three stations: zones 4, 7, 8, 9, 10 and 11. Figure 8 shows the Sobol' indices time series during the event.

At Kervir, the water level is still controlled by the value of the minor Strickler coefficient of the downstream zone  $K_{s4}$ . Simultaneously with the peak of water level, the value of the flood plain Strickler coefficient  $K_{s4M}$  increases in importance. This corresponds to the moment when the floodplain is activated. The upstream zone 9 maintains a little influence at the beginning of the event, firstly with the minor coefficient  $K_{s9}$ , and then with the flood plain coefficient  $K_{s9M}$ .

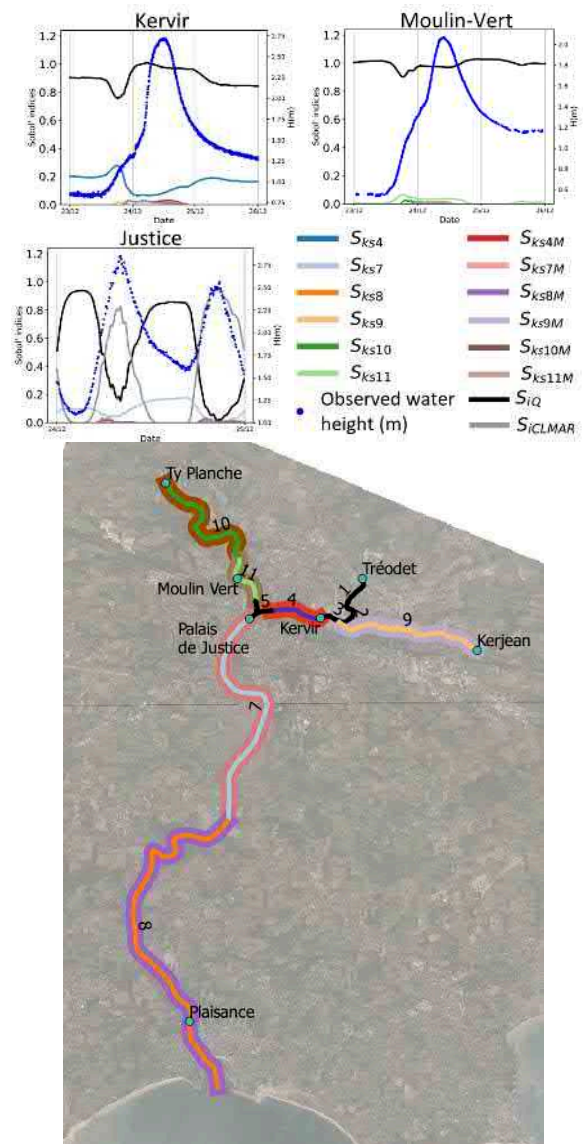


Fig. 10: Configuration 4: Sobol' indices time series and associated zones for the event from the 23 to the 26 December, 2013

Moulin-Vert shows similar characteristics, with a main control by  $K_{s11}$  minor, and  $K_{s11M}$  activated around the peak of the event. At the beginning of the event, the minor upstream coefficient  $K_{s10}$  has some influence.

At Justice, the same trend as the previous study (configuration 1) is found regarding the minor coefficient  $K_{s7}$ . However, the flood plain is not activated here since the Sobol index of  $K_{s7M}$  is insignificant. This result is consistent with the sections geometry in this zone. Both minor and flood plain coefficients of the zone 8 are important when the water level is rising. The zone 8 corresponds to an estuary zone. The flood plain considered in the model is in fact activated at each tide cycle when the tide rises.



### C. Configuration 3: impact of forcings against minor friction coefficients

In this third study, we consider the same 6 zones as in configuration 2 where friction coefficients mainly control the simulated water level at the three stations: zones 4, 7, 8, 9, 10 and 11. Only the minor friction coefficients are considered. In addition, we also take into account the hydrologic inputs and the maritime boundary condition. Figure 9 shows the Sobol' indices time series for the three forecast stations during the event.

At Kervir and Moulin-Vert, it is overall the choice of the hydrologic scenario which determines the simulated water level. It should be noted that at Moulin-Vert, the downstream friction coefficient has almost no influence. This trend is a little less marked during other events.

At Justice, the influence of the minor Strickler coefficient  $K_{s8}$  remains significant, yet the water level is largely dominated by the choice of the hydrologic and the maritime boundary condition scenarios. When the levels are high, the maritime boundary condition is for a large part responsible for the simulated water level, and on the contrary, when the levels are low, the hydrologic scenario mainly controls the simulated water level.

### D. Configuration 4: impact of forcings against minor and flood plain friction coefficients

In this last study, we consider the minor and flood plain coefficients of the 6 zones where friction coefficients mainly control the simulated water level at the three stations: zones 4, 7, 8, 9, 10 and 11. The hydrologic inputs and the maritime boundary condition are also taken into account. Figure 10 shows the Sobol' indices time series for the three forecast stations during the event.

This graphs highlight that the flood plain friction coefficients are not very influent, since the Sobol' indices time series are almost identical to those of the configuration 3. However, we note a slight influence of the flood plain coefficient  $K_{s11}$  at Moulin-Vert during other events (not shown here).

## VIII. CONCLUSION

The Mascaret model of the Odet river, daily used by the SPC VCB for flood forecasting, was studied through a Global Sensitivity Analysis (GSA). It provides Sobol' indices that rank the uncertainty sources. GSA shows that if the boundary conditions are not perturbed, the simulated water level at the stations are mainly controlled by the immediate downstream friction coefficient. The flood plains are activated around the peak of the events and then the flood plain Strickler friction coefficients become important. GSA also shows that if perturbed, the boundary conditions are decisive for the simulated water level.

In further work, the results of the GSA study will be used for the realization of Hydraulic Ensemble Forecasts, and for correcting the simulation chain by data assimilation.

## IX. ACKNOWLEDGEMENTS

The authors would like to thank the French national service for flood forecasting (SCHAPI) for supporting this study. They also would like to thank EDF-DTG for the fourniture of the MORDOR-TS hydrologic model and Fabrice Zaoui (EDF R&D) for the interfacing python module pymordor. The authors also acknowledge the Pôle de Calcul et de Données Marines (PCDM) for providing DATARMOR storage and computational resources. URL: <http://www.ifremer.fr/pcdm>.

## REFERENCES

- Champeaux, J.L., Dupuy, P., Laurantin, O., Soulan, I., Tabary, P., Soubeyroux, J.M., 2009. Les mesures de précipitations et l'estimation des lames d'eau à Météo-France : état de l'art et perspectives. *La Houille Blanche*, 28–34doi:10.1051/lhb/2009052.
- Garavaglia, F., Le Lay, M., Gottardi, F., Garçon, R., Gailhard, J., Paquet, E., Mathevet, T., 2017. Impact of model structure on flow simulation and hydrological realism: from a lumped to a semi-distributed approach. *Hydrology and Earth System Sciences* 21, 3937–3952. doi:10.5194/hess-21-3937-2017.
- Garçon, R., 1996. Prévision opérationnelle des apports de la Durance à Serre-Ponçon à l'aide du modèle MORDOR. Bilan de l'année 1994-1995. *La Houille Blanche*, 71–76doi:10.1051/lhb/1996056.
- Hoeffding, W., 1948. A Class of Statistics with Asymptotically Normal Distribution. *The Annals of Mathematical Statistics* 19, 293–325. doi:10.1214/aoms/1177730196.
- Le Moine, N., Hendrickx, F., Gailhard, J., Garçon, R., Gottardi, F., 2015. Hydrologically Aided Interpolation of Daily Precipitation and Temperature Fields in a Mesoscale Alpine Catchment. *Journal of Hydrometeorology* 16, 2595–2618. doi:10.1175/JHM-D-14-0162.1.
- Monteil, C., Zaoui, F., Le Moine, N., Hendrickx, F., 2019. Technical note: the caRamel R package for Automatic Calibration by Evolutionary Multi Objective Algorithm. *Hydrology and Earth System Sciences Discussions* 2019, 1–16. doi:10.5194/hess-2019-259.
- Rouhier, L., Le Lay, M., Garavaglia, F., Le Moine, N., Hendrickx, F., Monteil, C., Ribstein, P., 2017. Impact of mesoscale spatial variability of climatic inputs and parameters on the hydrological response. *Journal of Hydrology* 553, 13–25. doi:10.1016/j.jhydrol.2017.07.037.
- Roy, P., Ricci, S., Dupuis, R., Campet, R., Jouhaud, J.C., Fournier, C., 2018. BATMAN: Statistical analysis for expensive computer codes made easy. *The Journal of Open Source Software* 3, 493. doi:10.21105/joss.00493.
- Vidal, J.P., Martin, E., Franchistéguy, L., Baillon, M., Soubeyroux, J.M., 2010. A 50-year high-resolution atmospheric reanalysis over France with the Safran system. *International Journal of Climatology* 30, 1627–1644. doi:10.1002/joc.2003.

# The impact of observation spatial and temporal densification in an ensemble Kalman Filter

Isabelle Mirouze, Sophie Ricci

CECI CERFACS / CNRS UMR 5318  
Toulouse, France  
isabelle.mirouze@cerfacs.fr

Nicole Goutal

LNHE-EDF, -LHSV  
Chatou, France

**Abstract**—To reduce uncertainties in a modelled system, data assimilation strongly relies on the availability of observations, and its performance depends directly on the spatial density, the frequency, and the quality of these observations. Yet, rivers are rather poorly observed. The SWOT (Surface Water and Ocean Topography) mission, to be launched in 2021, is expected to provide global water level observations at a high-resolution coverage for rivers down to 50-meter wide.

In order to highlight the merits of these future observations, we compare the performance of an Ensemble Kalman Filter on a 50-kilometre reach of the Garonne (South of France) when only hourly water height gauge measurements are available in the middle of the reach, and when complementary SWOT-like observations are available. A 10-kilometre spatial average with frequencies of 3 and 1 days are tested in the framework of twin experiments. Results show that assimilating the SWOT-like observations allows the ensemble size to be reduced without losing accuracy. With a better correction of the friction coefficients and the upstream discharge, the water height systematic bias is cancelled out and the root mean square error is decreased, *i.e.* the deviation to the reference is reduced. The beneficial impact of the SWOT-like observations holds in the 12 first hours of the forecast.

## I. INTRODUCTION

Data assimilation aims to reduce the uncertainties in a modelled system by correcting the initial conditions, the boundary conditions and the parameters of this system. Among the different schemes available, the Ensemble Kalman Filter (EnKF; [1]) has the advantage of not requiring any adjoint model. Moreover, the background error covariance matrix being calculated using the ensemble, the analysis benefits from its flow-dependency. Like any Monte Carlo-based methods however, it requires a large number of members to estimate the background error covariance matrix accurately enough, which increases its cost.

Data assimilation also strongly relies on the availability of observations, and its performance depends directly on the spatial density, the frequency, and the quality of these observations. Yet, rivers are rather poorly observed. Observations come mainly from limnometric *in situ* stations, which provide water height measurements and, for few of them, discharge measurements. However, the network

coverage is not global, and not necessarily sustained, as shown in Fig. 1. In some regions, data can be difficult to access due to political instabilities, or financial fees. Even in countries such as USA, Canada, France or UK who are maintaining a sustainable network, entire sections of rivers are not watched on.

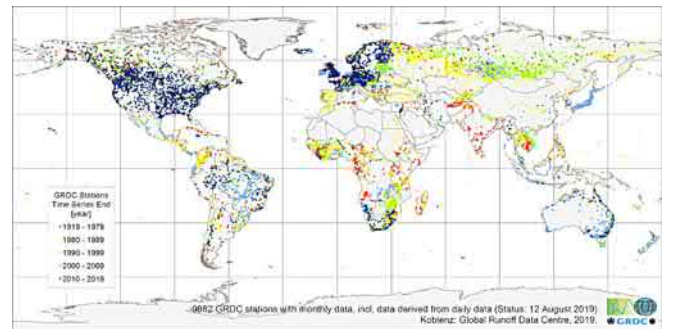


Fig. 1: Global Runoff Data Centre<sup>2</sup> stations with monthly data, status on 12 August 2019. Time series end between 1919 and 1979 (red), 1980 and 1989 (yellow), 1990 and 1999 (green), 2000 and 2009 (light blue), 2010 and 2019 (dark blue).

Nadir altimeters on board satellites such as Jason-2 can also provide water level measurements, but they have an incomplete and low-resolution spatial coverage that make them adapted for major rivers only. The SWOT (Surface Water and Ocean Topography) mission<sup>1</sup> of CNES (Centre National d'Etudes Spatiales) and NASA (National Aeronautics and Space Administration), to be launched in 2021, is expected to provide water level measurements with a global and high-resolution spatial coverage, decreasing thus the width of potentially observed rivers down to 50 meters. The temporal revisit will be of 21 days, with a 4-day insight on catchments at our latitudes. The accuracy of the water level measurements, will depend on the product delivered. For example, for 10-kilometre reach average observations, the accuracy is expected to be 10 cm.

1: <https://swot.cnes.fr/en/mission-1>, <https://swot.jpl.nasa.gov/mission.htm>

2: [https://www.bafg.de/GRDC/EN/Home/homepage\\_node.html](https://www.bafg.de/GRDC/EN/Home/homepage_node.html)



Fig. 2: The 50-kilometer reach of the Garonne, from Tonneins to La Réole. Credit: A. Besnard and N. Goutal, simHydro, 2010.

In this paper, we study the impact on the reanalyses and forecasts of densifying the observation network in space and time, using SWOT-like observations in twin experiments. To do so, we use the Smurf (System for Modelling with Uncertainty Reduction, and Forecasting; [2]) framework, an open source modular system developed in Python at Cerfacs for running and cycling data assimilation systems. The focus of the study is a 50-kilometer reach of the Garonne, from Tonneins to La Réole, modelled with the 1D hydrodynamics solver Mascaret [3].

The paper is organised as follows: section 2 provides information on the framework and the configuration used, whilst section 3 describes the experiments and their results; finally, section 4 summarises the study and gives some conclusions.

## II. FRAMEWORK AND CONFIGURATION

### A. The numerical model Mascaret

Mascaret is a Fortran code that solves the Saint-Venant equations with a finite difference scheme, in order to simulate one-dimensional free surface hydraulic systems. For our configuration, the equations are solved with a time step of 30 minutes and a spatial resolution of about 100 m (463 nodes).

The study focusses on a 50-kilometer reach of the Garonne, from Tonneins to La Réole as shown in Fig. 2. The Strickler coefficient  $K_s$  is uniformly defined over three areas, from Tonneins to Mas d'Agenais (zone 1), from Mas d'Agenais to Marmande (zone 2), and from Marmande to La

Réole (zone 3). The upstream boundary condition is prescribed with a discharge time series  $Q_{up}(t)$  at Tonneins created on purpose to represent a sequence of high and low flows (Fig. 3). The downstream boundary condition is a rating curve at La Réole.

### B. The Ensemble Kalman Filter

The stochastic version of the EnKF is used to correct the three Strickler coefficients and the time-varying upstream discharge. The idea is to construct an ensemble of corrected simulations of size  $N$  whose mean represents the best estimate of the hydraulic state of the river. The ensemble is constructed by generating perturbations with Batman-OT (Bayesian Analysis Tool for Modelling and uncertainAinty quaNtification – Open Turns; [4]). For the Strickler coefficients ( $K_{s1}$ ,  $K_{s2}$ ,  $K_{s3}$ ), scalar perturbations are drawn from a uniform law centred on the analysis mean with a range of  $\pm 5 \text{ m}^{1/3}\text{s}^{-1}$ . The upstream discharge time series  $Q_{up}(t)$  is perturbed by a Gaussian process applied to a reference time series. A principal component analysis is performed on a sample of 10000 processes with chosen features. In this study we chose a Matérn function with a smoothness parameter  $\eta = 0.5$  (exponential) and length scale of 1 day. A truncation is then applied according to a chosen threshold to keep a determined number of modes (3 in this study). To generate a sample of perturbations for  $Q_{up}(t)$ , the truncated principal components transformation is sampled from a centred normal distribution with a chosen standard deviation, before being applied to the weights. To minimise the cost of the analysis calculation, we chose to control the components of the transformation ( $c_1$ ,  $c_2$ ,  $c_3$ ) rather than the time series itself, which leads to a control vector

$$\mathbf{x} = (K_{s1}, K_{s2}, K_{s3}, c_1, c_2, c_3)^T. \quad (1)$$

A 50-day simulation is carried out over the sliding windows of 3 hours (assimilation cycle) every hour, with a 24-hour forecast launch at the end of each window as shown on Fig. 4. For example, a first assimilation cycle is conducted from  $T_0$  to  $T_3$  with a forecast from  $T_3$  to  $T_{27}$ , then a second cycle is performed from  $T_1$  to  $T_4$  with a forecast from  $T_4$  to  $T_{28}$ , and so on. The sliding windows imply that the same observations are used within different assimilation cycles. For each cycle, the assessment of the system is performed with respect to the end of the windows. For example, the date  $T_4$  with lead time 0h and 1h is picked into the second assimilation cycle and first forecast, respectively. At the start of the simulation, all members of the ensemble have the same hydraulic state. The members will diverge however due to the differences between their control vectors (1). Note that the perturbations are generated at the start of each assimilation cycle to avoid the ensemble to collapse (no inflation used). For the upstream discharge a common time series is kept to which perturbations are added for each member.

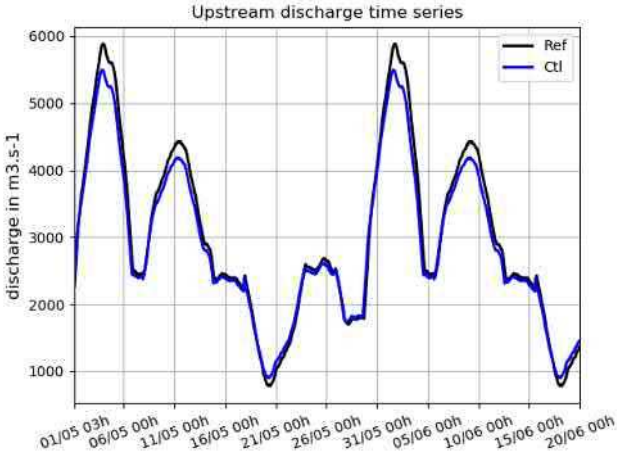


Fig. 3: Reference (black line) and perturbed (blue line) upstream discharge at Tonneins.

During the assimilation cycle an analysis  $\mathbf{x}^a$  for each member  $i = 1, \dots, N$  is firstly calculated

$$\mathbf{x}_i^a = \mathbf{x}_i^b + \mathbf{K} (\mathbf{y}_i^o - \mathbf{y}_i^b), \quad (2)$$

where  $\mathbf{x}^b$  is the background control vector and  $\mathbf{y}^b = \mathbf{H}\mathbf{x}^b$  its counterpart in the observation space.  $\mathbf{H}$  is the observation operator that maps the control vector space onto the observation space. In our case,  $\mathbf{H}$  is constituted of the model Mascaret providing the water height at the time and possibly interpolated location of the observation. The observation vector  $\mathbf{y}^o$  gathers all observations available within the window. This vector is then perturbed for each member according to a normal distribution with zero mean and the prescribed observation error covariance matrix  $\mathbf{R}$ . We have considered here a diagonal matrix (no correlation between observation errors). In (2) the correction (increment) to the background control vector is defined by the misfit between the observations and the background control vector counterpart (innovation) weighted by the Kalman gain

$$\mathbf{K} = \mathbf{B}\mathbf{H}^T (\mathbf{H}\mathbf{B}\mathbf{H}^T + \mathbf{R})^{-1},$$

where

$$\mathbf{B}\mathbf{H}^T = E[(\mathbf{x}^b - E[\mathbf{x}^b])(\mathbf{y}^b - E[\mathbf{y}^b])^T], \quad (3)$$

$$\mathbf{H}\mathbf{B}\mathbf{H}^T = E[(\mathbf{y}^b - E[\mathbf{y}^b])(\mathbf{y}^b - E[\mathbf{y}^b])^T], \quad (4)$$

are estimated from the ensemble.  $E[.]$  is the expectation operator.

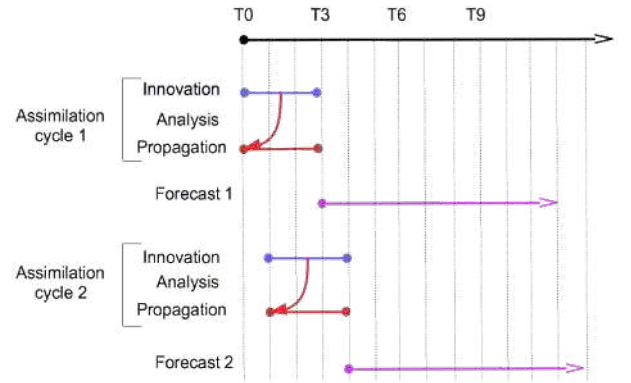


Fig. 4: Cycling of the simulation with 3-hourly sliding windows.

The corrected Strickler coefficients are taken into account and the uniform law used to generate the associated perturbations is re-centred about their analysis mean. The analysed principal components of each member are used to generate an analysed perturbation for the upstream discharge time series  $Q_{up}(t)$  that is taken into account. The common time series is corrected by the mean of these perturbations. The ensemble members are then propagated again from the start of the same window, before a 24-hour forecast is launched. During the forecast, the last upstream discharge of the assimilation cycle is persisted, assuming no upstream discharge forecast is available.

### C. The observations

The observations used in this study are synthetic, generated from the reference run of the twin experiments (see section III) with a perturbation drawn from a centred normal distribution with standard deviation of 10 cm. A first set of hourly water height at node 221 is defined to represent the *in situ* station of Marmande. The SWOT-like observations are simulated as if they were coming from limnimetric stations at nodes 47, 142, 236, 334, 423, representing a distance between stations of about 10 km. Two sets of data have been generated: one with daily observations, and one with observations every 3 days. The error standard deviation of 10 cm corresponds to the requirement of the SWOT mission for a 10-kilometre reach average. Preliminary tests with shorter spatial average (and appropriate error standard deviation, e.g. 20 cm for a 5-kilometre reach average) were conducted and showed that improvements in the root mean square (rms) error with respect



to the reference run were more linked to the frequency of the observations rather than the spatial average. Therefore, we chose to limit this study to a 10-kilometre reach average.

#### D. The Smurf framework

The experiments of this study have been carried out using Smurf<sup>3</sup>, an open source code developed in Python. It is used to run and cycle data assimilation systems in a modular way. Smurf is organised around three super classes for the numerical models, the data assimilation schemes and the observation instruments. Any new item can be easily plugged in by defining a child class that will override as many methods as necessary.

A specific python class has been developed for Mascaret in order for Smurf to set parameters, to launch the simulation and to retrieve variable values at specific times, through Application Programming Interfaces (API). A class *Gauge* has also been implemented to handle the observations coming from limnimetric stations. It manages the observation files and some basic checking such as the observation time with respect to the assimilation cycle currently processed. The EnKF used in this study is part of Smurf and available for any systems.

The possibility of integrating the ensemble members simultaneously in parallel (innovation calculation, analysis propagation, and forecast) has been used in this study, reducing significantly the elapsed time for the assimilation experiments.

### III. RESULTS OF TWIN EXPERIMENTS

Twin experiments have been conducted to assess the impact of densifying the observation network over time, in the prospect of the SWOT mission.

#### A. Experiments

The Reference experiment (Ref) is a deterministic simulation without data assimilation. The Strickler coefficients are set to  $K_{S1} = 40$ ,  $K_{S2} = 32$  and  $K_{S3} = 33$ , and the upstream discharge time series  $Q_{up}(t)$  is the originally designed one (Fig. 3, black line). This experiment is considered as the “truth” and is used to generate observations with a noise corresponding to the error standard deviation defined (10 cm).

The Control experiment (Ctl) is also a deterministic simulation without data assimilation. However, it respects the cycling of 3-hourly sliding windows in order to launch 24-hour forecasts (with persisted upstream discharge) at the end of each window. Although the initial hydraulic state is the same as Ref, the Strickler coefficients are set to  $K_{S1} = 30$ ,  $K_{S2} = 40$  and  $K_{S3} = 40$ , and the original upstream discharge time series  $Q_{up}(t)$  is perturbed to simulate some inaccuracies (Fig. 3, blue line). This experiment is considered as the one to improve towards Ref.

Different experiments with data assimilation have been carried out. They are all run with the same configuration as Ctl for the Strickler coefficients and the upstream discharge, but will diverge from it due to the corrections brought sequentially

by the assimilation. A first experiment (Ais) assimilates only the hourly in situ data at Marmande. The second and third experiments (A3d and A1d) assimilate SWOT-like observations every 3 and 1 days, respectively. The two last experiments (Ais3d and Ais1d) assimilate both the hourly in situ data at Marmande and the SWOT-like observations every 3 and 1 days, respectively.

Each simulation is run during 52 days. The first two days are considered as a spinup to allow for the hydraulic state to stabilise with respect to the initial conditions and parameters. As a consequence, Ref and Ctl (and hence the assimilation runs) will diverge slightly. Therefore, the period of assessment goes for 50 days, from the hypothetical dates of 1<sup>st</sup> May to 20<sup>th</sup> June.

#### B. Size of the ensemble

The choice of the ensemble size for an EnKF algorithm is crucial. Too small, it will lead to inaccurate covariance estimates and hence a poor performance, although techniques such as localisation are available to address this issue (e.g. [5]). Too big, it will lead to unaffordable costs. The experiment Ais assimilating only *in situ* observations at Marmande is representative of what can currently be done. Therefore, it was run with 50 (Ais) and 100 (Ais100) members, in order to assess the impact of the covariance estimate accuracy.

As expected, both experiments are well constraining the water height at Marmande. Whereas the water height stays close to Ctl for both runs at La Réole, a large difference can be seen upstream at Mas d’Agenais. With 50 members only (Fig. 5), the water height drifts slowly from Ctl, reaching a difference with Ref greater than 3 meters at the end of the period. With 100 members (Fig. 6), there is no obvious drift. This drift is due to incorrect analyses for the Strickler coefficients  $K_{S1}$  and  $K_{S2}$  as shown in Fig. 10 and Fig. 11 (brown line), respectively. This issue is a consequence of spurious correlations in the estimate of the covariances (3) and (4). Because Ais100 uses twice the number of members, the estimates are more accurate and these spurious correlations, though still existing, are smaller and hence, less detrimental. Nevertheless, evidence of a drift for Ais100 might have been spotted on a longer simulation period. Note that the upstream discharge time series is less sensitive to the problem, thanks to the fact that the correction is not done directly, but on hyperparameters. Fig. 9 shows the evolution of the global rms of the water height error with respect to Ref for Ctl and the ensemble means of Ais and Ais100. After a month, the rms for Ais is higher than for Ctl, whilst Ais100 stays below. The degradation in the rms for Ais is mainly due to a bias increase. Spatially, this bad performance of Ais is restricted to the first and second zones (Fig. 7), i.e. upstream of the observation location.

The choice is made to run the other assimilation experiments with 50 members only, since we expect the densification of the observation network to better constrain the problem.

#### C. Performance of the data assimilation

The performance of the data assimilation is assessed by comparing the mean and the rms of the water height difference

3: <https://gitlab.com/cerfacs/Smurf>

between the ensemble mean of each experiment with the reference (Ref). These diagnostics are performed by summing over time (Fig. 7 and Fig. 8), over location (Fig. 9), or both (Fig. 13, Fig. 14 and table hereafter). The global performance is summarised in the following table, with a focus at Marmande. As expected, the error is significantly reduced when data assimilation is used (except for Ais), although the performance is not spatially homogeneous (Fig. 7).

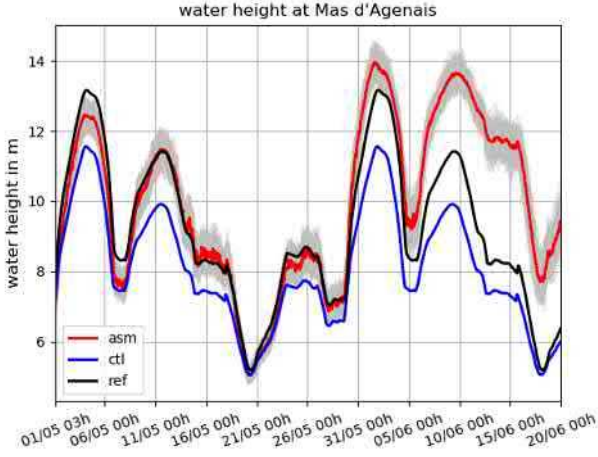


Fig. 5: Water height at Mas d'Agenais for Ref (black line), Ctl (blue line), and Ais (grey lines for the members, red line for the ensemble mean).

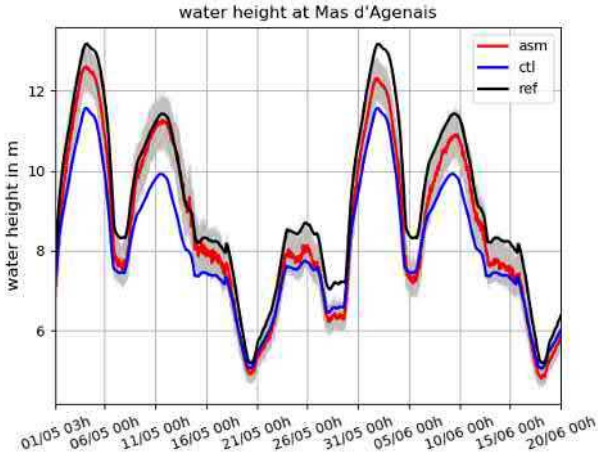


Fig. 6: Water height at Mas d'Agenais for Ref (black line), Ctl (blue line), and Ais100 (grey lines for the members, red line for the ensemble mean).

#### D. Performance of the data assimilation

The performance of the data assimilation is assessed by comparing the mean and the rms of the water height difference between the ensemble mean of each experiment with the reference Ref. These diagnostics are performed by summing over time (Fig. 7 and Fig. 8), over location (Fig. 9), or both (Fig. 13, Fig. 14 and table 1). The global performance is summarised in the following table, with a focus at Marmande. As expected, the error is significantly reduced when data assimilation is used (except for Ais), although the performance is not spatially homogeneous (Fig. 7).

TABLE 1: MEAN AND RMS ERROR WITH RESPECT TO REF FOR WATER HEIGHT

Experiment	Global (mm)		Marmande (mm)	
	Mean	Rms	Mean	Rms
Ctl	-696	854	-844	904
Ais100	-161	312	0	69
Ais	337	907	9	70
A3d	-104	363	-119	373
Ais3d	8	418	5	73
A1d	-29	199	-16	200
Ais1d	-16	157	2	69

In the first zone the rms error for Ctl is small close to Tonneins (45 cm) but increases rapidly (up to more than 1 m) due to the erroneous Strickler coefficient. In zones 2 and 3 the rms stays high although decreasing slowly. Near La Réole, the rms decreases again (35 cm) constraint by the rating curve. The large rms is mainly due to a systematic bias (Fig. 8). Between Tonneins and Marmande, the assimilation manages to reduce the rms for all experiments, except for Ais as mentioned in the previous section. We note nevertheless a slight increase in the rms for Ais3d, but this is mainly coming from the 10 first days of the period, the assimilation struggling a bit to adjust to occasional observations as shown in Fig. 9.

At Marmande, the significant bias of Ctl is almost cancelled out by the assimilation, reducing significantly the rms. This is especially true for the experiments assimilating hourly data at Marmande. For the latter, the constant Strickler coefficient of the third zone and the water height spatial correlations allow for the correction to hold downstream until a few kilometres before La Réole, where the rating curve takes precedence.

Assimilating only SWOT-like data (A3d and A1d) shows a good behaviour at all locations, with a rms about 40 cm and 20 cm depending on the observation frequency (3 days or 1 day, respectively). However, downstream of Marmande these experiments are not as successful as the experiments assimilating hourly observations at Marmande which show a rms smaller than 10 cm. It is interesting to note that all the experiments assimilating SWOT-like observations perform better than Ais100 upstream of Marmande, although their ensemble is twice smaller. The mean error in particular, is almost cancelled out. Fig. 9 shows that the assimilation struggles especially when there are rapid changes in the flow, as shown by the upstream discharge time series on Fig. 3.

The control vector (1) describes the variables that are corrected by the assimilation. The principal components of the transformation ( $c1$ ,  $c2$ ,  $c3$ ) do not have a “truth” value since they generate a perturbation, and cannot hence be compared to a reference, unlike the upstream discharge time series  $Qup(t)$  itself. The time series for each assimilation experiments are not sufficiently well corrected for their analysis mean to reach the reference values (not shown). In particular, the high flows are still underestimated by a few hundreds of m<sup>3</sup>s<sup>-1</sup>. The analysis mean of the Strickler coefficients  $KS_1$ ,  $KS_2$  and  $KS_3$  can be compared directly to the “truth” values of the Ref experiment. Fig. 10, Fig. 11 and Fig. 12 show the evolution of their analysis mean. The patterns for A3d and A1d are similar to Ais3d and Ais1d, respectively, and are therefore not shown.

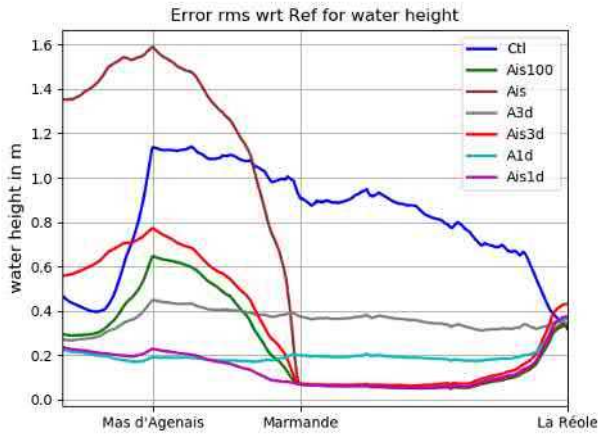


Fig. 7: Global rms of the water height error with respect to Ref depending on the location for Ctl and the ensemble mean of all experiments.

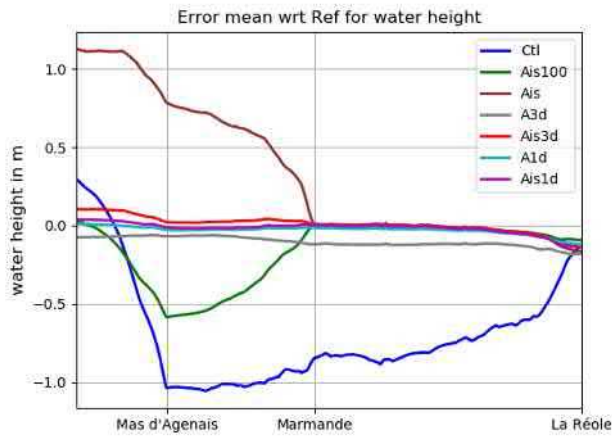


Fig. 8: Global mean of the water height error with respect to Ref depending on the location for Ctl and the ensemble mean of all experiments.

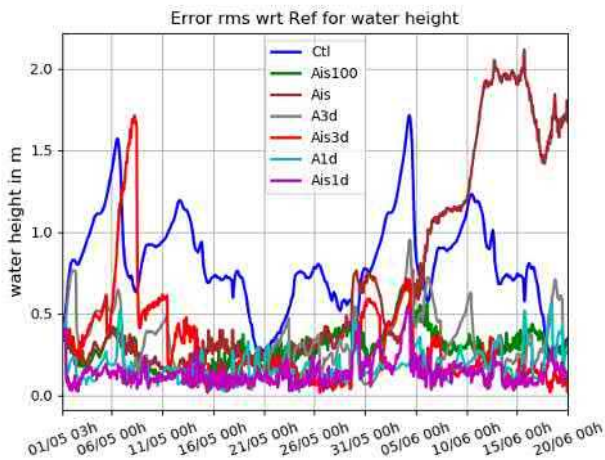


Fig. 9: Evolution of the global water height rms error with respect to Ref for Ctl and the ensemble mean of the assimilation experiments.

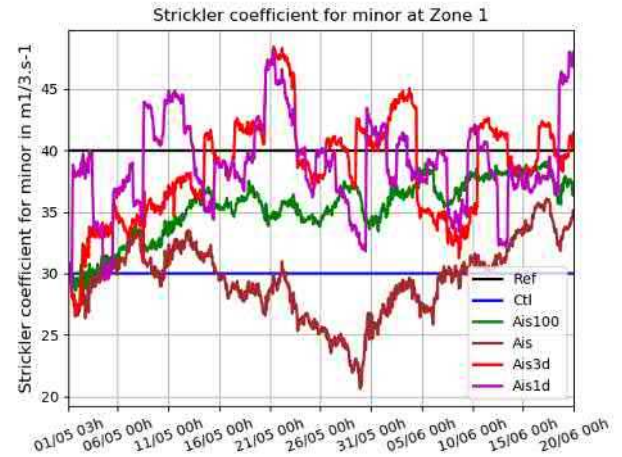


Fig. 10: Evolution of the analysis mean for  $K_{s1}$  in Ais100 (green line), Ais (brown line), Ais3d (red line) and Ais1d (pink line). The “truth” and erroneous values are shown by the black and blue lines, respectively.

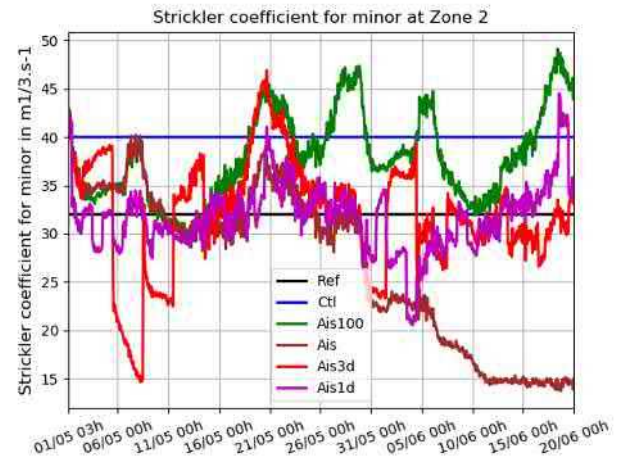


Fig. 11: Evolution of the analysis mean for  $K_{s2}$  in Ais100 (green line), Ais (brown line), Ais3d (red line) and Ais1d (pink line). The “truth” and erroneous values are shown by the black and blue lines, respectively.

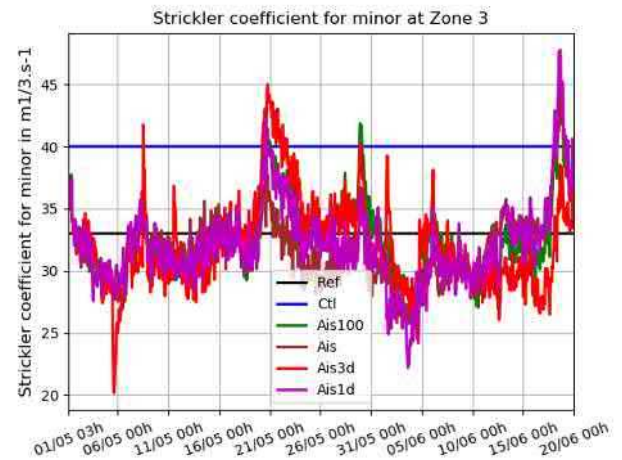


Fig. 12: Evolution of the analysis mean for  $K_{s3}$  in Ais100 (green line), Ais (brown line), Ais3d (red line) and Ais1d (pink line). The “truth” and erroneous values are shown by the black and blue lines, respectively.



Whilst the assimilation manages to correct  $K_{S3}$  towards its reference value for all experiments, it clearly struggles to do so for  $K_{S1}$  and  $K_{S2}$  when only hourly *in situ* data at Marmande are available. The SWOT-like observations have a clear positive impact on the analysis. The more frequent the observations, the better the impact is, accelerating the convergence for  $K_{S1}$  and reducing the amplitude of the oscillations for  $K_{S2}$ . It is worth mentioning that even if the upstream discharge time series and the Strickler coefficients are not exactly to their “truth” value, the water height at the location of frequent observations (Marmande in particular) is still close to the values of Ref. This is due to the well-known issue of equifinality [6].

#### E. Forecasts

At the end of each 3-hourly assimilation window, a 24-hour forecast is launched for each member of the ensemble, with the Strickler coefficients corrected during the assimilation cycle. The upstream discharge value at the end of the assimilation cycle is persisted during the forecast.

Fig. 13 and Fig. 14 show the global water height rms and mean error, respectively, with respect to Ref, for Ctl and all the assimilation experiments at hourly lead times (ensemble mean). For Ctl, the rms is about 85 cm during 12 hours, and starts then increasing reaching 1.1 m at the end of the forecast. If most of the error comes from a bias in the first half of the forecast, this bias increases only slightly in the second half. For the reasons exposed in section III-B, assimilating only *in situ* data at Marmande with 50 members, gives a higher rms than Ctl. During the first 12 hours, the other experiments benefit from the performance of their own assimilation cycle and hence have a smaller rms (and mean) than Ctl. Their respective performance are similar in the second half of the forecast, with a rms increasing faster than Ctl. After 24 hours, their rms is still about 20 cm smaller than Ctl. Extrapolating the data, we can estimate that the assimilation would lose its impact on the forecast after a lead time of about 30 to 32 hours. Note that the mean for all experiments is quite stable.

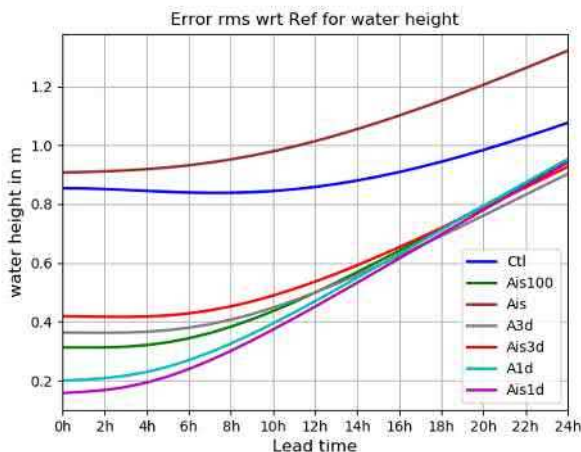


Fig. 13: Global water height rms error with respect to Ref for the ensemble mean of the assimilation experiments.

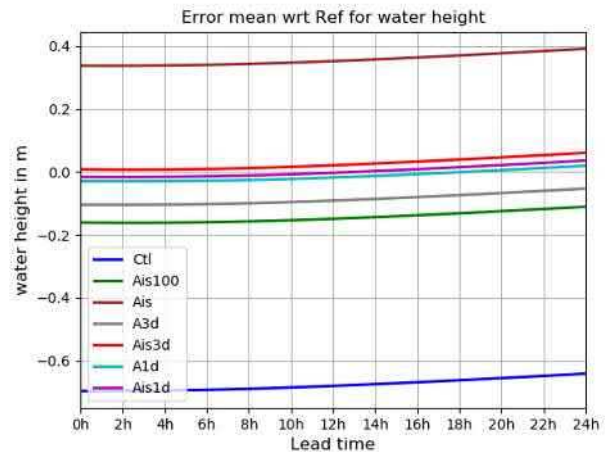


Fig. 14: Global water height mean error with respect to Ref for the ensemble mean of the assimilation experiments.

#### IV. CONCLUSION

We have studied the potential impact of the observation spatial and temporal densification on a data assimilation system using an EnKF, in terms of accuracy of reanalysis and forecast. On a 50-kilometre reach of the Garonne, we compared the assimilation of hourly *in situ* observation water height at Marmande to the assimilation of SWOT-like water height observations every 10 kilometres with a frequency of 3 and 1 days in the framework of twin experiments.

Having observations distributed regularly along the reach allows a smaller ensemble to have the same performance in terms of rms as a specified one. The decrease in ensemble size depends on the frequency of these regular observations. It is unlikely that SWOT observations will be available at a higher frequency than daily. Therefore, hourly data from limnometric stations will still be useful to reduce the rms error at their locations and downstream of them.

Assimilating SWOT-like observations constrains better the system and the Strickler coefficients are hence rather well corrected, whereas assimilating *in situ* data only manages to correct the Strickler coefficient of the third zone. We did not see any improvement on the upstream discharge time series however, probably because of the equifinality issue and the correction method. Nevertheless, this better set of parameters cancels out the systematic bias existing upstream of the limnometric station. The positive impact of the SWOT-like observations holds during the first 12 hours of the forecast.

The SWOT mission scheduled for a launch in late 2021 will allow us to have observations of water level regularly distributed in space for rivers down to 50-metre wide. This will be an opportunity to improve the reanalyses and forecasts of our hydraulic systems.

#### ACKNOWLEDGEMENT

This study has been carried out within the Discharge proposal of the SWOT – TOSCA (Terre solide, Océan, Surfaces Continentales et Atmosphère) program of CNES.



The authors are grateful to Matthias De Lozzo who coded the API used by Smurf to manage Mascaret.

#### REFERENCES

- [1] G. Evensen, “Sequential data assimilation with a nonlinear quasi-geostrophic model using Monte Carlo methods to forecast error statistics”, *J. Geophys. Res.*, 1994, vol. 94, pp. 10143–10162.
- [2] I. Mirouze and S. Ricci, “Smurf: System for Modelling with Uncertainty Reduction, and Forecasting”, unpublished.
- [3] N. Goutal and F. Maurel, “A finite volume solver for 1D shallow water equations applied to an actual river”, *Int. J. Numer. Math. Fluids*, 2002, vol. 38, pp. 1–19.
- [4] P. T. Roy, S. Ricci, R. Dupuis, R. Campet, J.C. Jouhaud, C. Fournier, “BATMAN : Statistical analysis for expensive computer codes made easy”, *Journal of Open Source Software*, 2018, vol. 3(21), 493.
- [5] P. R. Oke, P. Sakov, S. P. Corney, “Impacts of localisation in the EnKF and EnOI: experiments with a small model”, *Ocean Dyn.*, 2007, vo. 57, pp. 32–45
- [6] G. Aronica, B. Hankin, K. Beven, “Uncertainty and equifinality in calibrating distributed roughness coefficients in flood propagation model with limited data”, *Adv. Water Resour.*, 1998, vol. 22, pp. 349–365.

# Mixture of polynomial chaos expansions for uncertainty propagation

Siham El Garroussi<sup>1</sup>, Sophie Ricci<sup>1</sup>, Matthias De Lozzo<sup>2</sup>, Nicole Goutal<sup>3</sup>, Didier Lucor<sup>4</sup>

<sup>1</sup> CECI, CERFACS/CNRS, 42 Av Gaspard Coriolis 31057, Toulouse, Cedex 1

<sup>2</sup> IRT Saint Exupéry, CS34436, 3 Rue Tarfaya, 31400 Toulouse

<sup>3</sup> EDF, LNHE, 6 quai Watier, 78400 Chatou

<sup>4</sup> LIMSI, Campus Universitaire bâtiment 507, Rue John Von Neumann, 91400 Orsay

E-mail : [siham.elgarroussi@cerfacs.fr](mailto:siham.elgarroussi@cerfacs.fr)

**Abstract:** Reliability analysis and other probabilistic techniques are becoming increasingly important tools in hydraulic modeling and decision making. Hydraulic variables, such as roughness coefficient and discharge, common to many hydraulic-engineering problems, are known to contain considerable uncertainty. Knowledge of the type and magnitude of this uncertainty is crucial for a meaningful interpretation of the hydraulic model results. Probabilistic uncertainty quantification framework aims to define the uncertain inputs in terms of random variables, to propagate these stochastic uncertainties through the numerical model and to quantify their impact on the simulated quantity of interest. Here, the latter is the water level field discretized upon an unstructured finite element mesh over the Garonne River (South-West France) between Tonneins and La Réole simulated with the numerical solver Telemac-2D.

Monte Carlo sampling is the most standard method used to propagate uncertainty through dynamical models. Although universal, the approach is rather greedy and its use in conjunction with finite element models, like Telemac-2D, is limited due to computational cost constraints. In moderate dimensions, surrogate modeling allows to overcome this issue. For instance, polynomial chaos expansion (PCE) approximation has proven powerful in a wide range of applications for emulating responses of computational models with random input, quantifying the output uncertainty and conveniently providing sensitivity indices. However, PCEs may experience some convergence difficulties when applied to problems related to unsteadiness, stochastic discontinuities, long-term integration, and large perturbation.

In this context, we propose a mixture of experts as a surrogate model, which is based on the divide-and-conquer principle. This non-intrusive method uses multiple PCE models as local experts to approximate the numerical solver on different parts of the input space. This parametric space partitioning is automated by means of machine learning techniques. These various PCE models are tested using shallow-water simulations data for unsteady flow regime in order to assess the efficiency and the convergence of the proposed approach. Our results show that the proposed mixture of experts approach is efficient for this unsteady flow problem related to discontinuities induced by random inputs together with environmental terrain properties.

**Proposed session:** *Data assimilation, Optimization, Risks and Uncertainties*

**Key words:** Discontinuities, Machine learning methods, Telemac-2D, Surrogate model, Unsteady flow regime

**Speaker:** Siham El Garroussi

# A Metamodel of the Telemac Errors

Fabrice Zaoui<sup>1</sup>, Cédric Gœury<sup>1</sup>, Yoann Audouin<sup>1</sup>

<sup>1</sup> EDF R&D – National Laboratory for Hydraulics and Environment (LNHE)  
6 quai Wattier, 78401 Chatou, France  
E-mail : [fabrice.zaoui@edf.fr](mailto:fabrice.zaoui@edf.fr)

**Abstract**— A Telemac study is a computationally intensive application for the real cases and in the context of quantifying or optimizing uncertainties, the running times can be too long. This paper is an example of an approximation of the Telemac results by a more abstract but significantly faster model. It shows how a metamodel can be easily built with low computational costs, and how it can help to understand and improve some global results of Telemac.

## I. INTRODUCTION

Many sources of uncertainty lie in the real-world problems. Telemac as any model (i.e. approximation of reality) is error prone since uncertainties appear in the initial or boundary conditions, the system parameters, the modelling simplification or the numerical calculations themselves. Therefore, it is difficult to say with confidence if the design of a Telemac model has met all the requirements to be optimal. Calibration consists of tuning the model parameters so that the results are in better agreement with a set of observations. This phase is crucial before any further study can be conducted by avoiding a meaningless analysis or prediction based on false or too inaccurate results. This paper presents a statistical calibration of a Telemac 2D model (Gironde Estuary in France) with the learning of Telemac errors by a metamodel (i.e. a model of the simulation errors) to make the best use of limited observations data over a short time period. The metamodel here is a simplified version of Telemac behaving the same for all the locations where observation points are available. If the metamodel is correct, it will be able to compute as Telemac would do but with a highly reduced computational cost.

While doing an analysis of the simulation errors it is shown how a metamodel (or surrogate, i.e. methods like Kriging, Polynomial Chaos, Neural Networks, etc.) can be designed with a low number of calls to Telemac. The minimal number of calculations to have a good approximation can be empirically defined [1][2][3] by:

$$N_{calls} \cong 10 \times N_{parameters}$$

The strength of the metamodel is highlighted with the reduction of the modelling discrepancy between the simulation and the observations by considering different errors globally or locally depending on the goal(s) to achieve, see Fig. 1. For instance, a multi-objective calibration can be quickly conducted with a metamodel even when the optimizer is a meta-heuristic requiring many runs like a NSGA-II based algorithm [4]. The optimal solution obtained after many calls

to the metamodel is systematically validated by checking its expected performance with a last call to Telemac.

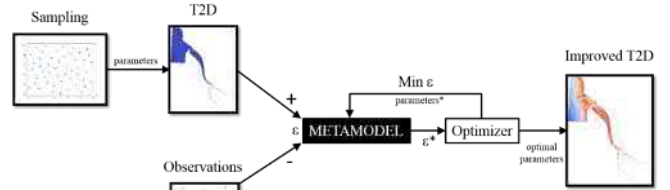


Figure 1. Workflow of the metamodel use

## II. FORWARD MODEL

Telemac 2D is used to solve the shallow waters equations on the real case of the Gironde Estuary in southwestern France, see Fig. 2. This estuary is important because of its large size involving many economic and environmental considerations.

Several Telemac studies of the estuary have been carried out for the last decade mainly concerning the hydrodynamic [5][6] and morphodynamic [7][8][9]. In these studies, the importance of the calibration phase is systematically emphasized to achieve operational performance. Are concerned the Telemac computation time and robustness but also the accuracy of the water levels for tide forecasts.

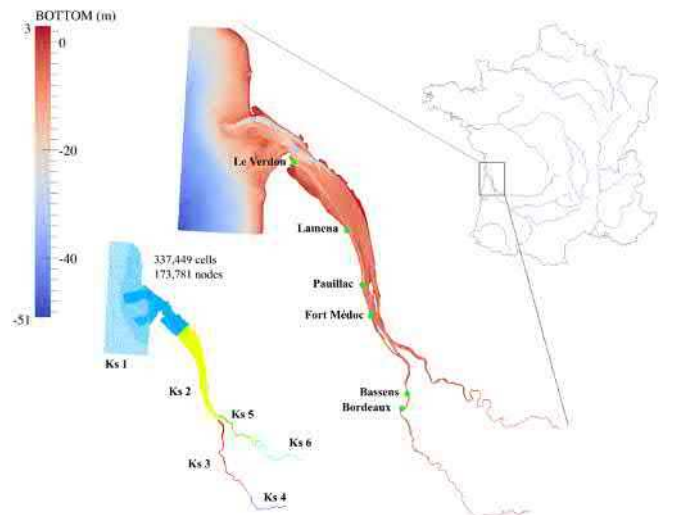


Figure 2. Gironde estuary with Telemac. Location of observation stations, bathymetry, friction zones and mesh size

The Gironde is a navigable estuary formed from the junction of rivers Dordogne and Garonne just downstream of the center of Bordeaux city, it is the largest estuary in western Europe. The hydraulic model used in this work covers approximately 195 km between the fluvial upstream and the marine boundary conditions downstream representing an area of around 635 km<sup>2</sup>. The mesh of 173,781 nodes varies with cell lengths of 40 m within the areas of interest (navigation channel) to 750 m offshore (western and northern sectors of the model). This model has been built by CEREMA in the framework of the Gironde XL project [10].

The boundary condition along with the marine border of the model has been set up using depth-averaged velocities and water levels coming from the dataset of Legos numerical model TUGO (46 harmonic constants). Surge data, describing the difference between the tidal signal and the observed water level, is taken into account using results from the Hycom2D model of SHOM [11]. Surface wind data is also considered for simulating flows under windy conditions.

The period of interest concerns two days of August 2015 with six stations providing water levels every minute [6]. The time step for Telemac is 10 seconds and the ratio between the simulated and execution times is about 120 on 56 Intel Xeon cores @ 2.4 GHz.

The calibration will aim to decrease water level differences between Telemac and the observation stations by optimizing some Root Mean Squared Errors over the two-day period:

$$J_s(x) = \sqrt{\frac{1}{N_t} \sum_{i=1}^{N_t} (T_i^s(x) - O_i^s)^2} \quad (1)$$

$\forall s \text{ in } (1..N_s)$

where:

- $N_s$  is the number of stations;
- $N_t$  is the number of time steps;
- $J_s$  is the RMSE for station  $s$ ;
- $x$  is a vector of physical parameters;
- $T$  is the water level computed by Telemac;
- $O$  is the corresponding observation.

If  $J_s(x)$  is minimized for a certain value of  $x = x_{opt}$ , the Telemac model is assumed to be well calibrated for the station  $s$  on average over two days. Finding  $x_{opt}$  implies the use of a specific algorithm with many trials and calls to Telemac to define an optimality path. These repeated model evaluations put a heavy workload on CPUs, and it makes more sense to replace  $J_s(x)$  by an estimate  $\hat{J}_s(x)$  with the help of a metamodel to be less resource intensive, see Fig. 1.

Therefore, the problem can be written as a bound constrained optimization:

$$\begin{aligned} & \text{minimize } \hat{J}_s(x) \cong J_s(x) \\ & \text{subject to } x_{lb} \leq x \leq x_{ub} \end{aligned} \quad (2)$$

where the vector  $x$  is made of three tidal parameters ( $\alpha, \beta, \gamma$ ) and six friction coefficients  $K_{Si}$  for  $i$  in (1..6), see Fig. 2, with bound constraints on the values of variables.

#### A. Tidal parameters

Tidal characteristics are imposed using a database of harmonic constituents to force the open boundary conditions. For each harmonic constituent, the water depth  $h$  and horizontal components of velocity  $u$  and  $v$  are calculated, at point  $M$  and time  $t$  by:

$$\begin{cases} F(M, t) = \sum_i F_i(M, t) \\ F_i(M, t) = f_i(t) A_{F_i}(M) \cos\left(\frac{2\pi t}{T_i} - \phi_{F_i}(M) + \varphi_i^0 + w_i(t)\right) \end{cases} \quad (3)$$

where  $F$  is either the water level (referenced to mean sea level)  $z_s$  or one of the horizontal components of velocity  $u$  or  $v$ ,  $i$  refers to the considered constituent,  $T_i$  is the period of the constituent,  $A_{F_i}$  is the amplitude of the water level or one of the horizontal components of velocity,  $\phi_{F_i}$  is the phase,  $f_i(t)$  and  $w_i(t)$  are nodal factors and  $\varphi_i^0$  is the phase at the original time of the simulation.

The water level and velocities of each constituent are then summed to obtain the water depths and velocities for the open boundary conditions:

$$\begin{cases} h = \alpha \sum_i z_{s_i} - z_f + z_{mean} + \gamma \\ u = \beta \sum_i u_i \\ v = \beta \sum_i v_i \end{cases} \quad (4)$$

where  $z_f$  is the bottom elevation and  $z_{mean}$  the mean reference level. In (4), the multiplier coefficients of the tidal range and velocity, respectively  $\alpha$  and  $\beta$ , at boundary locations and the sea level correction  $\gamma$  are the coordinates of  $x$  in (1) corresponding to tidal parameters.

Upper and lower bounds ( $x_{lb}, x_{ub}$ ) for the tidal parameters are [6]:

TABLE 1: BOUNDS FOR TIDAL PARAMETERS

Parameter	Lower bound $x_{lb}$	Upper bound $x_{ub}$
$\alpha$	0.8	1.2
$\beta$	0.8	1.2
$\gamma$	0.35	0.54

#### B. Friction coefficients

Friction terms come into the momentum equation of the shallow system are treated in a semi-implicit form in Telemac 2D. The bed friction in  $X$  and  $Y$  directions can be written as a function of the Strickler coefficient  $K_s$ :

$$\begin{aligned} F_x &= \frac{u\sqrt{u^2 + v^2}}{K_s^2 h^{4/3}} \\ F_y &= \frac{v\sqrt{u^2 + v^2}}{K_s^2 h^{4/3}} \end{aligned} \quad (5)$$



where  $h$  is the water depth and  $(u, v)$  the velocity components. Bounds for the friction coefficients are [6]:

TABLE 2: BOUNDS FOR FRICTION COEFFICIENTS

Parameter	Lower bound $x_{lb}$	Upper bound $x_{ub}$
$K_{S1}$	30	46
$K_{S2}$	64	96
$K_{S3}$	80	100
$K_{S4}$	20	30
$K_{S5}$	64	96
$K_{S6}$	36	54

### III. METAMODELLING

This part explains how to pass from  $J_s(x)$  to  $\hat{J}_s(x)$  in (2) by a training of the Telemac errors on the water levels given the space defined in Table 1 and 2.

#### A. Definition

A metamodel is a CPU time inexpensive mathematical function that can replace a more complex model by approximation. Indeed, many simulation codes have become accurate for complex problems in physics as with 3D modelling. On the other hand, the simulation times have not necessarily decreased, and this makes some engineering studies difficult if they require for example an uncertainty quantification, a sensitivity analysis or optimization that rely on these models. A way out of this difficulty is to build a metamodel [12] with a limited number of simulations, i.e. a low number of outputs from the original model.

Metamodels can be based on different methods like support vector machines, regression trees, proper orthogonal decomposition, neural networks, polynomial chaos, kriging and so on. Recent examples of metamodels with the Telemac-Mascaret system use the polynomial chaos [13][14][15] or Gaussian Process [15][16] for a steady state hydraulics.

#### B. Design

A design of experiments is the first step to build a metamodel. It is used to sample the space of input parameters. In this way, the space filling design has been developed to address the issues of numerical simulation. This approach tries to best distribute a minimal number of samples in the input parameter space in order to capture the non-linear behaviour of output parameters.

One of the most used design of experiments is the method called Latin Hypercube Sampling (LHS). This method generates well-distributed and non-redundant samples. It also addresses a wide variety of problems in terms of size of the input and output parameter spaces [17].

Fig. 3 shows two designs of experiments for a simple case with 50 points. The first design on the left is based on a random sampling while the second on the right is based on LHS. Input parameters space is better explored with LHS. For the case of the Gironde estuary, the LHS is built with 90 points as the length of  $x$  is 9. This is a minimal size according to [1][2][3].

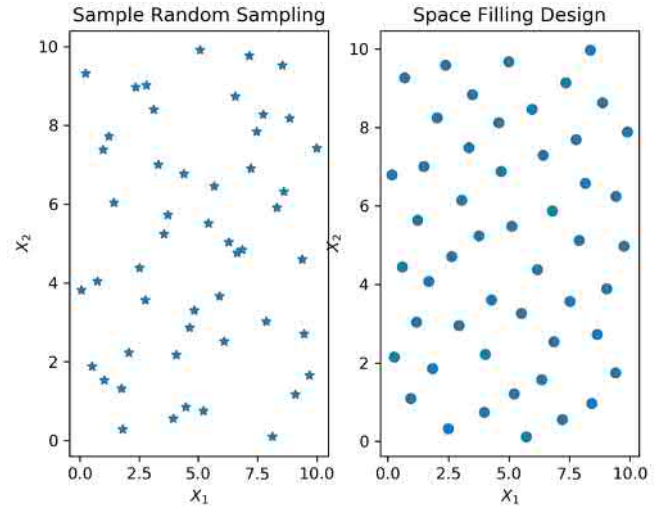


Figure 3. Comparison of two designs of experiments

#### C. Kriging Example

Kriging is method of geostatistics, a family of techniques building response surfaces from a limited number of samples and estimating values at unknown locations. This method is named in honor of engineer D. G. Krige [18] by G. Matheron [19] who formalized the approach a few years later.

The method approximates the deterministic function  $y$  by  $\hat{y}$  as the sum of a trend and a stationary stochastic process:

$$\hat{y} = \sum_{i=1}^k \lambda_i g_i(x) + Z(x) \quad (6)$$

$$\text{cov}[Z(x_i), Z(x_j)] = \sigma^2 R(x_i, x_j)$$

where:

- the trend  $\sum_{i=1}^k \lambda_i g_i(x)$  can be seen as a regression model with  $\lambda$  the regression parameter vector and  $g_i$  the basis functions;
- $Z(x)$  is a realization of a stochastic process with zero mean and spatial covariance function;
- $\sigma^2$  is the process variance;
- $R$  is a correlation function;
- $k$  is the number of samples from LHS ( $k = 90$ ).

#### D. Validation

An out-of-sample testing is used to validate the Kriging for assessing how the metamodel performs for unknown data. Ten points are added for testing the metamodel. Looking at the mean error over the six stations, the metamodel interpolates the test data with a mean squared error of  $2.22 \cdot 10^{-5} \text{ m}^2$  and a coefficient of determination  $R^2$  of 0.996. Thus, the quality of the metamodel as estimator is considered satisfactory.

### IV. APPLICATIONS

Paragraph § A is a distribution analysis of the errors in (1) after propagating the LHS design with Telemac. The paragraphs § B and § C are two applications of the metamodel that require many function evaluations  $\hat{J}_s(x)$ .

It should be noted here that the time required for the construction or use of Kriging is not significant compared to the calculation time of a Telemac run. Thus, the repeated metamodel evaluations are not an issue.

#### A. Error Analysis

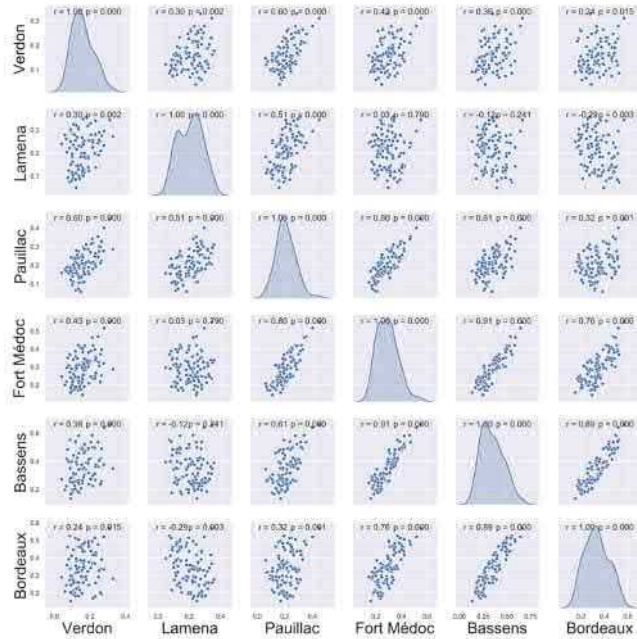


Figure 4. Scatter plot matrix of  $J(x)$  for the LHS

Fig. 4 plots the distribution of RMSE in (1) after propagating the LHS. For each station, the distribution looks like a Gaussian and two parts can be clearly identified depending on the geographical location and the distance from the sea, see Fig. 2. The errors on the Fort Médoc, Bassens and Bordeaux stations have a similar behaviour and clearly different from other stations closer to the sea.

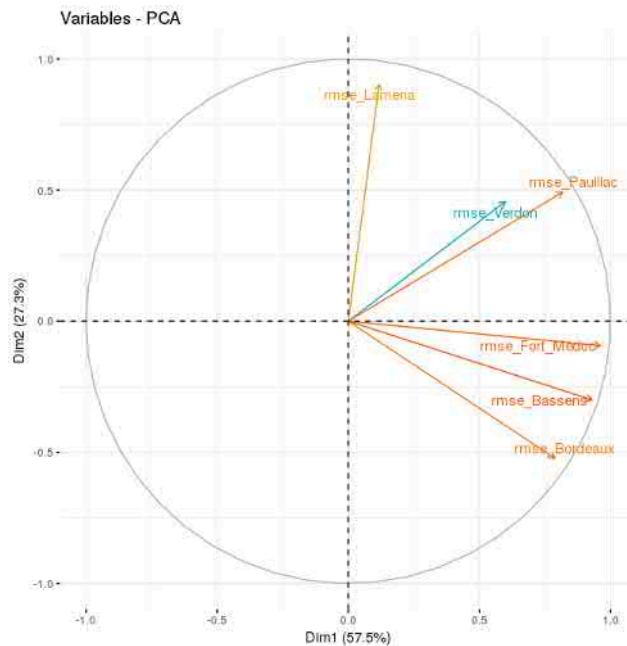


Figure 5. PCA correlation circle of  $J(x)$  for the LHS

A Principal Component Analysis (PCA) is a method of data mining that consists of reducing the dimensionality of the problem to extract information. It is a projection method into a smaller space that decreases the number of variables. A graphical diagnostic is possible on the reduced dimensions. Fig. 5 is a diagnostic example with the correlation circle of PCA for the two first dimensions (i.e. the most significant ones, 85% of the variance is explained here). Contributions to the dimensions differ according to the position of the stations. The group consisting of Fort Médoc, Bassens and Bordeaux is confirmed. The errors in this group do not have the same behaviour as the other stations. In particular, the behaviour of the Lamena station errors is orthogonal to that of Fort Médoc, which makes the global approaches less relevant.

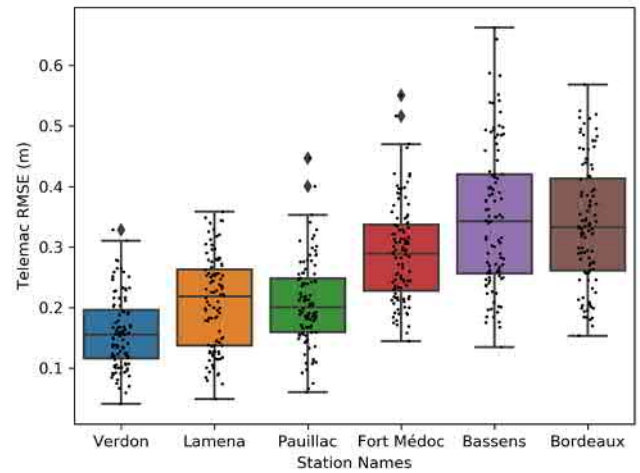


Figure 6. Box plot of  $J(x)$  for the LHS

Fig. 6 shows the distribution of RMSE in (1) with quantiles. Errors are larger on average for the most inland stations. It should be noted that in this study only tidal and friction parameters are considered. The influence of the hydrological forcing of the two upstream rivers Garonne and Dordogne is not studied. This one can have an influence at least locally [5].

#### B. Sensitivity Analysis

A global sensitivity analysis is carried out with a variance decomposition using the Sobol' indices [20]. The analysis makes it possible to rank in order of importance the sources of uncertainty on the output  $\hat{f}_s(x)$  of the metamodel.

The first order Sobol' index of variable  $x_i$  (i.e. linear effect of  $x_i$  on  $\hat{f}_s$ ) is:

$$S_i = \frac{\mathbb{V}_i}{\text{Var}(\hat{f}_s)} \quad (7)$$

$$\text{with } \mathbb{V}_i = \text{Var}[\mathbb{E}(\hat{f}_s | x_i)]$$

The second order Sobol' index of two variables  $x_i$  and  $x_j$  (i.e. cross influence on  $\hat{f}_s$ ) is:

$$S_{ij} = \frac{\mathbb{V}_{ij}}{\text{Var}(\hat{f}_s)} \quad (8)$$

$$\text{with } \mathbb{V}_{ij} = \text{Var}[\mathbb{E}(\hat{f}_s | x_i x_j)] - \mathbb{V}_i - \mathbb{V}_j$$

And the total Sobol' index of variable  $x_i$  (linear and non-linear effects on  $\hat{f}_s$ ) is:

$$S_{Ti} = S_i + \sum_j S_{ij} + \sum_{j < k} S_{ijk} + \dots = 1 - S_{\sim i} \quad (9)$$

The computation of Sobol' indices is often done with a numerical integration based on Monte Carlo method. This method is inexpensive here because the metamodel is extremely fast.

Sobol' indices are computed on the variance of the mean value RMSE over all the stations  $\hat{f}(x)$ :

$$\hat{f}(x) = \frac{1}{N_s} \sum_{s=1}^{N_s} \hat{f}_s(x) \quad (10)$$

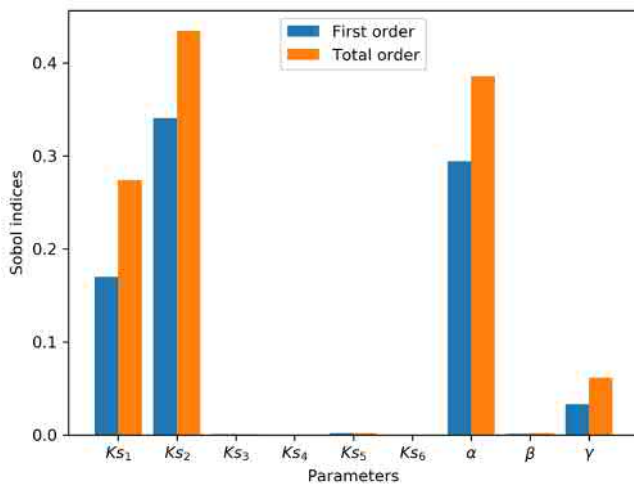


Figure 7. Sobol' indices (total and first order) of  $x$  on  $\hat{f}(x)$

According to Figure 7, only 4 of the 9 parameters are significant. The other parameters could have been ignored (i.e. fixed) because on average they have no influence on the water level errors.

This result is in perfect agreement with the transient computation of Sobol' indices as mentioned in [6].

### C. Optimization

Sensitivity analysis, calibration, design, reliability assessment and other studies require many function evaluations. In this section, several calibration examples using metamodel and optimization are presented.

The first example is the minimization of  $\hat{f}(x)$  in (10). This is done with two different optimization algorithms, a metaheuristic (PSO [6]) and a gradient based method (Newop, available in the sources of the Telemac-Mascaret system). Newop requires less function evaluations than PSO to converge but its final result can depend on the initial guess.

Fig. 8 shows the convergence of PSO and Newop with the values of  $\hat{f}(x)$  minimized. Both algorithms give exactly the same optimal result after convergence: 0.1259 m. This result is an average value of all the stations.

To see if the metamodel is reliable enough, the corresponding optimal solution for  $x$  has been checked directly with Telemac. That one gives: 0.1265 m. The difference is 0.5%, less than 1 mm which is remarkable and confirms the good construction of the metamodel.

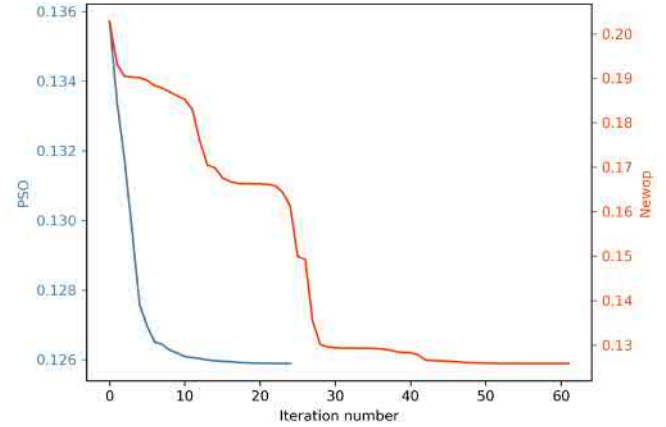


Figure 8. Convergence of the optimization algorithms

The result of this optimization for one period of a tidal wave is illustrated in Fig. 9. It corresponds to the worst result at Bordeaux station with an error value greater than 17.5 cm on two days.

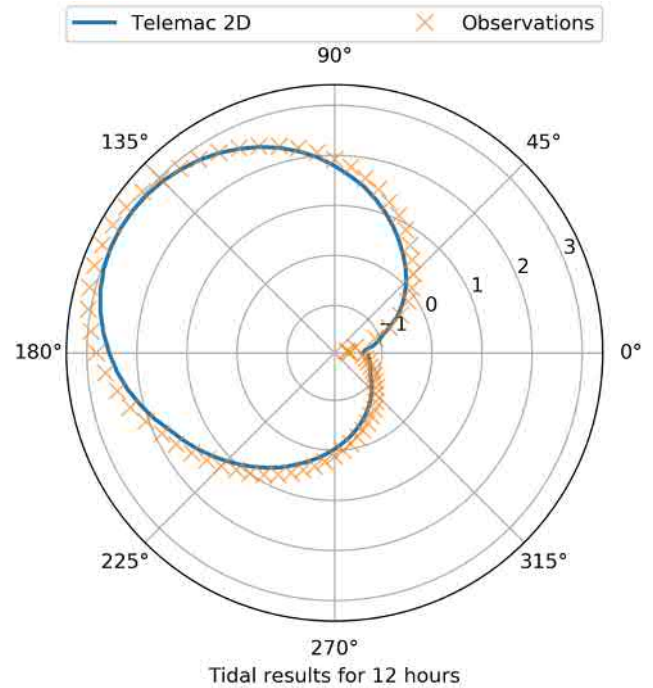


Figure 9. Tidal wave at Bordeaux after calibration (average goal)

Instead of looking for an average goal for all the stations, it might be interesting to calibrate each station individually, that is, to minimize  $\hat{f}_s(x)$  in (2) instead of  $\hat{f}(x)$  in (10).

In Fig. 10 improvements per station are indicated in comparison of the previous optimization. For each station there is a different optimal solution for  $x$  (tidal and friction parameters) that minimizes the RMSE on a two-day period.

As might be expected, the optimization of a particular station is locally more interesting than the shared solution by all the stations.

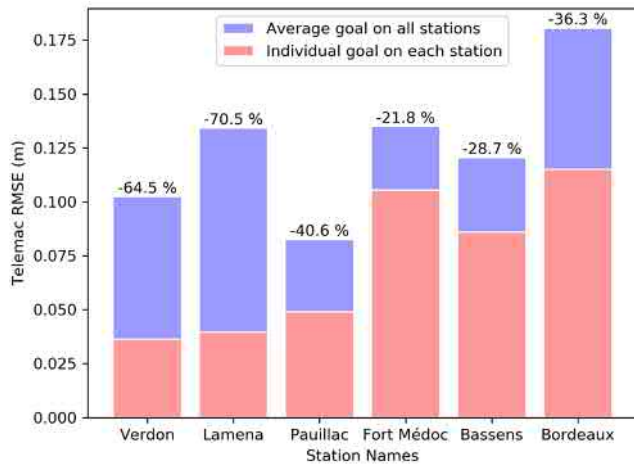


Figure 10. Improvement with an individual goal

One can also think of another mono-objective like minimizing the standard deviation if the model must have the same performance whatever the station or minimizing the maximum error which is a non-differentiable problem but treatable with PSO as shown in Fig. 11.

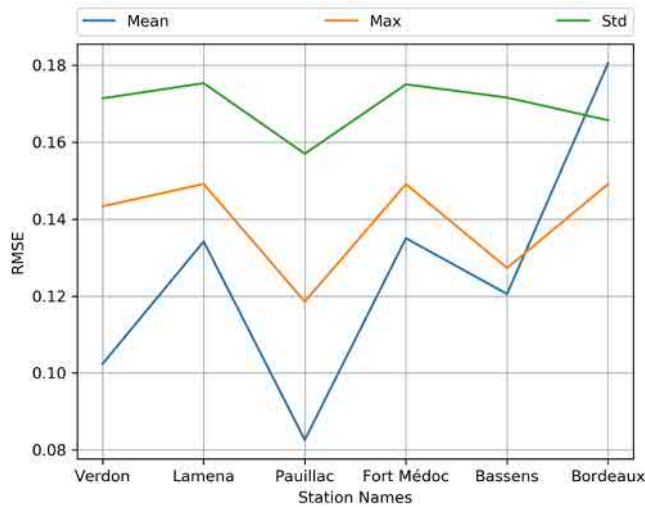


Figure 11. Minimizing  $\hat{f}_s(x)$  for three different objectives

RMSE for Fort Médéc and Lamena stations are orthogonal, see Fig. 5. Tackling the minimization of these two errors in the same mono-objective problem is risky because minimizing one is in conflict with the other. It is better to deal with two separated objectives simultaneously; it is the role of the multi-objective optimization. If the problem is nontrivial, it will find a number of nondominated solutions defining a Pareto front. This frontier is a trade-off between objectives.

The multi-objective evolutionary algorithms are dedicated to find a set of Pareto optimal solutions. This family of algorithms requires a high number of function evaluations to converge but thanks to the metamodeling this drawback is no more an issue. One of the most used algorithms is NSGA-II [4]. The solutions of a Pareto front with NSGA-II for the

simultaneous minimization of RMSE for Fort Médéc and Lamena stations is presented in Fig. 12.

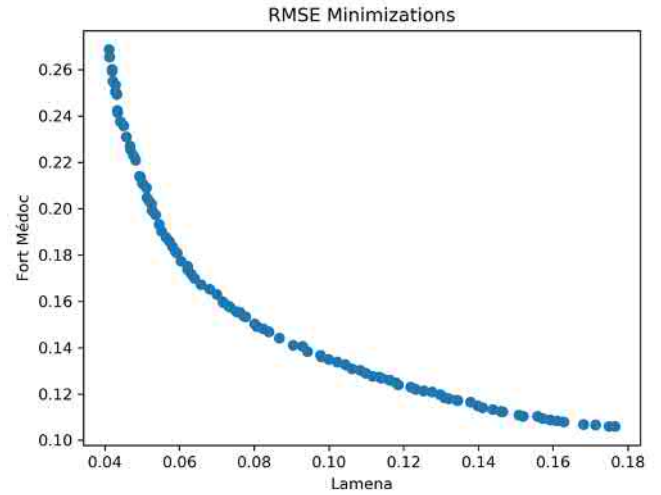


Figure 12. Pareto front of a two-objective minimization

With a multi-objective approach, it is easy to confirm that the objectives in Fig. 11 are conflicting. Indeed, if a two-objective minimization is launched with the pair (Max, Mean) or (Std, Mean), the result is again a Pareto front as illustrated in Fig. 13.

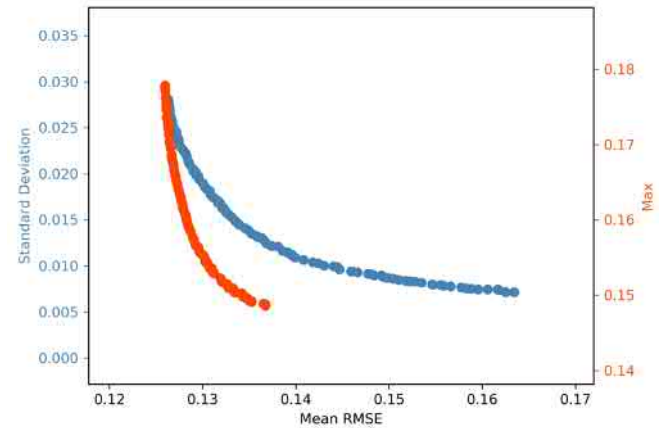


Figure 13. Pareto fronts of 2 two-objective minimizations

It is still possible to calibrate a model by supporting several objectives simultaneously, the number of objectives to be achieved may be greater than two. Other criteria than the RMSE could have been chosen, such as the bias or the Nash coefficient to evaluate the model efficiency. Following this idea, a new optimization with three objectives is carried out with always the metamodel based on the Kriging to evaluate the criteria. The results are shown in Fig. 14.

$$BIAS = \frac{1}{N_t} \sum_{i=1}^{N_t} T_i^s(x) - \frac{1}{N_t} \sum_{i=1}^{N_t} O_i^s \quad (11)$$

$$NASH = 1 - \frac{\sum_{i=1}^{N_t} (T_i^s(x) - O_i^s)^2}{\sum_{i=1}^{N_t} (T_i^s(x) - \bar{O}^s)^2}$$

$$\forall s \text{ in } (1..N_s)$$



From Fig. 14 it is clear that Nash values are not significative because they are all close to value 1. The bias is always positive with a value around 3 cm. Bias and RMSE may conflict with the lowest error values.

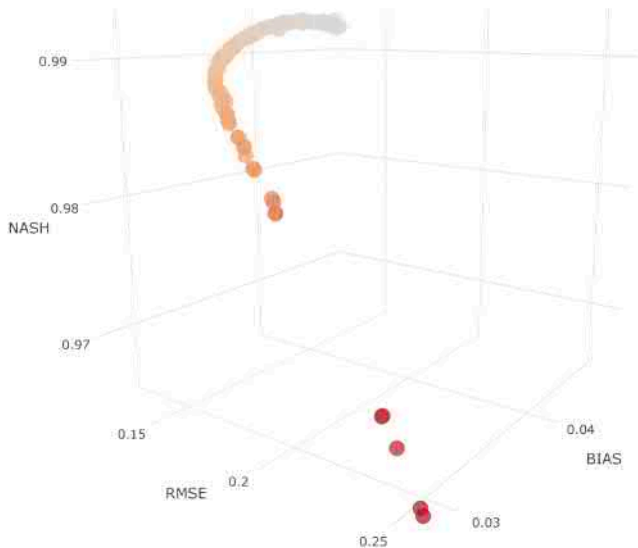


Figure 14. Pareto front of a three-objective minimization

## V. CONCLUSION

The purpose of this article is to introduce practitioners of the Telemac system to the construction of a metamodel. A metamodel is explained on the example of an approximation of Telemac errors compared to observations on a real case. The metamodel is then used for various applications concerning the analysis and the sensitivity of the errors as well as the calibration by minimization of these same errors.

A perspective of this work is to assess the validity period of a metamodel. Indeed, the behaviour of the physics can slightly change over time and it may be necessary to update the metamodel. This can be important for the implementation of data assimilation techniques.

## ACKNOWLEDGEMENT

The authors gratefully acknowledge the open source community and especially that of the [OpenTURNS](#) (An Open source initiative for the Treatment of Uncertainties, Risks'N Statistics).

## REFERENCES

- [1] D. R. Jones, M. Schonlau and W. J. Welch, "Efficient Global Optimization of Expensive Black-Box Functions", *Journal of Global Optimization*, vol. 13, pp. 455-492, 1998
- [2] A. Marrel, B. Iooss, B. Laurent, O. Roustant, "Calculations of Sobol indices for the Gaussian process metamodel", *Reliability Engineering and System Safety*, 94, pp. 742-751, Elsevier, 2009
- [3] J. L. Loepky, J. Sacks, W.J. Welch, "Choosing the sample size of a computer experiment: A practical guide", *Technometrics*, 51, pp. 366-376, 2009
- [4] K. Deb, A. Pratap, S. Agarwal, T. Meyarivan, "A fast and elitist multiobjective genetic algorithm: NSGA-II", *IEEE Transactions on Evolutionary Computation*, vol. 6 (2), pp. 182-197, 2002
- [5] V. Laborie, N. Goutal, S. Ricci, M. De Lozzo, P. Sergent, "Uncertainty Quantification for the Gironde Estuary Hydrodynamics with TELEM2D", *Advances in Hydroinformatics*, Springer, pp. 205-219, 2018
- [6] C. Gœury, F. Zaoui, Y. Audouin, P. Prodanovic, J. Fontaine, P. Tassi, R. Ata, "Finding Good Solutions to Telemac Optimization Problems with a Metaheuristic", 25<sup>th</sup> Telemac-Mascaret User Conference, Norwich, England, pp. 159-167, October 2018
- [7] C. Villaret, N. Huybrechts, L. A. Van, "Large Scale Morphodynamic Modeling of the Gironde Estuary", 18<sup>th</sup> Telemac-Mascaret User Conference, Chatou, France, pp. 117-123, October 2018
- [8] C. Villaret, N. Huybrechts, A. G. Davies, "A Large Case Morphodynamic Process-based Model of the Gironde Estuary", *Jubilee Conference Proceedings, NCK-Days*, pp. 69-76, 2012
- [9] N. Huybrechts, C. Villaret, F. Lyard, "Optimized Predictive Two-Dimensional Hydrodynamic Model of the Gironde Estuary in France", *Journal of Waterway, Port, Coastal, and Ocean Engineering*, vol. 138(4), pp. 312-322, 2012
- [10] F. Klein, A. Fort, A. Sottolichio, A. Beudin, G. Mattarolo, C. Gœury, A. Ponçot, J.-P. Argaud, S. Orseau, P. Tassi, N. Huybrechts, S. Cai, H. Smaoui, R. Gasset, Y. Nedelec, V. Laborie, R. Leroux, S. Barthelemy, M. Ali, S. Kaidi, "Gironde XL : an example of how estuarine scientific research can improve dredging and navigation operations in ports", VII Congreso Nacional de la ATPYC, 4<sup>th</sup> Mediterranean Days, Sevilla, Spain, 2018
- [11] E. P. Chassignet, H. E. Hurlburt, O. M. Smedstad, G. R. Halliwell, P. J. Hogan, A. J. Wallcraft, R. Baraille, R. Bleck, "The HYCOM (Hybrid Coordinate Ocean Model) Data Assimilative System", *Journal of Marine Systems*, vol. 65(1-4), pp. 60-83, 2007
- [12] J. Kleijnen, R. Sargent, "A Methodology for Fitting and Validating Metamodels in Simulation", *European Journal of Operational Research*, vol. 20, pp. 14-29, 2000
- [13] N. Goutal, C. Gœury, R. Ata, S. Ricci, N. El Mocyad, M. Rochoux, H. Oubanas, I. Gejadze, P.-O. Malaterre, "Uncertainty Quantification for River Flow Simulation Applied to a Real Test Case: the Garonne Valley", *SimHydro 2017: Choosing the right model in applied hydraulics*, Sophia Antipolis, 14-16 June 2017
- [14] N. El Mocyad, S. Ricci, N. Goutal, M. Rochoux, S. Boyaval, C. Gœury, D. Lucor, O. Thual, "Polynomial Surrogates for Open-Channel Flows in Random Steady State", *Environmental Modeling & Assessment*, vol. 23(3), pp. 309-331, June 2018
- [15] P. Roy, N. El Mocyad, S. Ricci, J.-C. Jouhaud, N. Goutal, M. De Lozzo, M. Rochoux, "Comparison of Polynomial Chaos and Gaussian Process surrogates for uncertainty quantification and correlation estimation of spatially distributed open-channel steady flows", *Stochastic Environmental Research and Risk Assessment*, vol. 32(6), pp. 1723-1741, April 2017
- [16] S. El Garroussi, M. De Lozzo, S. Ricci, D. Lucor, N. Goutal, C. Gœury, S. Boyaval, "Uncertainty Quantification in a Two-Dimensional River Hydraulic Model", *UNCECOMP 2019, 3<sup>rd</sup> ECOCOMAS Thematic Conference on Uncertainty Quantification in Computational Sciences and Engineering*, Crete, Greece, 24-26 June 2019
- [17] F. A. C. Viana, "Things you wanted to know about the Latin Hypercube Design and were afraid to ask", 10<sup>th</sup> World Congress on Structural and Multidisciplinary Optimization, Orlando, Florida, USA, pp. 1-9, 2013
- [18] D. G. Krige, "A statistical approach to some mine valuation problems on the Witwatersrand", *Journal of the Chemical, Metallurgical and Mining Society of South Africa*, vol. 52, pp. 119-139, 1951
- [19] G. Matheron, "Principles of Geostatistics", *Economic Geology*, vol. 58(8), pp. 1246-1266, 1963
- [20] I. M. Sobol, "Sensitivity estimates for nonlinear mathematical models", *Mathematical Modelling and Computational Experiment*, vol. 1, pp. 407-414, 1993

# Telemac optimisation with OpenTURNS

Thibault OUDART<sup>1</sup>, Olivier BERTRAND<sup>1</sup>

<sup>1</sup> ARTELIA Eau et Environnement  
6 rue de Lorraine  
38130 Echirolles, France

Thibault.OUDART@arteliagroup.com

**Abstract:** The Kasai River, affluent of Congo River, is one of the main transport axes for the Democratic Republic of the Congo. Many areas are clear of obstacle and are suitable for navigation but some channels like the Kandolo one are more difficult to cross. Due to its length of more than 2°153 km, it is difficult to achieve an accurate bathymetric survey over its entire length and in particular between small islands and in the vegetation zones. It is then proposed to complete the lack of bathymetric data in the Kandolo pass by using optimisation and by coupling Telemac with OpenTURNS.

This application require first to construct a model using available bathymetric data and create patches zones in the area where bathymetric data is not available, mainly in the small passes between the two mains arms. On each of these areas, a bathymetric mesh gradient coefficient is built and will be used multiply by an optimisation parameter to modify the bathymetry for each simulation run. A score is then calculate for each run by comparing the flows rates measured in situ on different profiles to the model results. Between each run, OpenTURNS is used to determine a new optimisation parameter per area based on the previous score obtained.

Project financed by the European Development Fund.



*Left : Kandolo pass with navigation roads in blue and flows rates measurement in red*

*Right : Area with bathymetric data (island are also cover with a Lidar)*

**Proposed session:** *Data assimilation, optimization, risks and uncertainties*

**Key words:** Optimization, sensibility, uncertainty, Kasai, Telemac 3D, OpenTURNS

**Speaker:** Thibault Oudart

# Using TELEMAC-2D for Hydrodynamic Modeling of Rainfall-Runoff

Karl Broich, Thomas Pflugbeil, Markus Disse  
Chair of Hydrology and River Basin Management Munich  
Technical University of Munich TUM  
Munich, Germany  
karl.broich@tum.de

Hai Nguyen  
Leibniz-Supercomputing Centre LRZ  
Garching, Germany

**Abstract**—TELEMAC-2D is a well known and established hydrodynamic model solving the shallow water equations. Since 2013, the SCS-CN-method has been implemented in TELEMAC-2D. With this supplement, the runoff generation is linked to overland flow and TELEMAC-2D could be extended to a Hydrodynamic Rainfall-Runoff Model (HRRM). Thus the most important requisites are fulfilled to simulate heavy rainfall and flash flood events. However, changes to the code were necessary concerning spatially distributed rainfall, time-dependent roughness and, the wet/dry boundary. The quality of the resulting method is demonstrated using the flash flood event in the district Rottal-Inn in Bavaria on June 1<sup>st</sup> in 2016. In the first step, the simulation is calibrated using a gauging station in the catchment Simbach a. Inn. After this, validation follows by applying the same methodology to the adjacent catchment Triftern. The results gained in both catchments showed good agreement with the event data. Using the new spacial rainfall module and changing the wet/dry boundary worked properly. A HPC-Scaling test showed a good scalability with the introduced methods. Therefore, the enhanced TELEMAC-2D model proved to be an accurate, efficient and versatile tool for the simulation of flash floods.

## I. INTRODUCTION

The cooperation project ‚Hinweiskarte Oberflächenabfluss und Sturzflut‘ (Indicator Map for Surface Runoff and Flash Floods) abbreviated HiOS is funded by the Bavarian State Ministry of the Environment and Consumer Protection (StMUV) and supervised by the Bavarian Environment Agency. The goals of HiOS are:

- Development of a method to evaluate and classify the risk due to surface runoff and flash floods using a GIS application.
- Refined study on 80 towns and municipalities in Bavaria using coupled hydrological and hydrodynamic simulations.
- Generation of a surface runoff and flash flood indicator map for Bavaria indicating different hazard zones for each of the more than 2000 Bavarian municipalities.

During the first project phase, four hydrodynamic models were tested to explore, which models are suitable for flash flood simulation. Although basic tests showed similar results for all four models, TELEMAC-2D has advantages due to its open-source license (adaptability) and code parallelization (high performance). Furthermore, the capability of TELEMAC-2D to include rainfall using a hydrological method had been a critical assessment criterion.

This paper reports recent developments in hydrodynamic rainfall-runoff modeling using TELEMAC-2D.

## II. IMPLEMENTATION

### A. Spatially distributed rainfall

The Soil Conservation Service Curve Number method (SCS-CN) [1] is a widely used calculation method to derive effective rainfall formation based on precipitation and area-specific runoff factors. The Curve Number (CN value) represents the respective input parameter, which can be easily determined by land use, soil group and, antecedent moisture conditions. A comprehensive dataset of the hydrological soil group (A, B, C and D) is available for Bavaria. The SCS unit hydrograph model, often used in combination with the CN values to simulate runoff concentration, is substituted by hydrodynamic simulation in this study. The same applies to the routing process. The SCS-CN method has been implemented in TELEMAC-2D in 2013 [2][3]. However, this implementation does not support spatially distributed rainfall. Because this feature is essential for the analysis of flash floods caused by convective rainfall events, an enhancement of the code was necessary.

We used rainfall radar data to match the spatial distribution of rainfall. The data is read by the new subroutine radarmap.f as x-y-P-pointset per time level  $t$ , where  $x$  and  $y$  are coordinates in [m] and  $P$  is the accumulated rainfall in [mm] for the actual time range  $dt$ . The parameter  $np$  is the number of following lines with x-y-P-pointsets until the next sections of t-dt-np-dataset occurs. The example in Table I demonstrates the data structure, Figure 1 represents the result for a 100 x 100 m domain.

TABLE I. DATA STRUCTURE READ BY THE SUBROUTINE RADARMAP.F FOR SPATIAL RAINFALL.

1	# Radar data
2	# comment line marked by #
3	# Row <t,dt,np>; t, dt in [s]; np in [-]
4	# Block with np-rows containing <x,y,P>; x,y in [m] ; P in [mm]
5	0. 300. 4
6	25. 25. 1.
7	75. 25. 2.
8	25. 75. 3.
9	75. 75. 4.
10	300. 300. 4
11	25. 25. 1.
12	75. 25. 2.
13	25. 75. 3.
14	75. 75. 4.

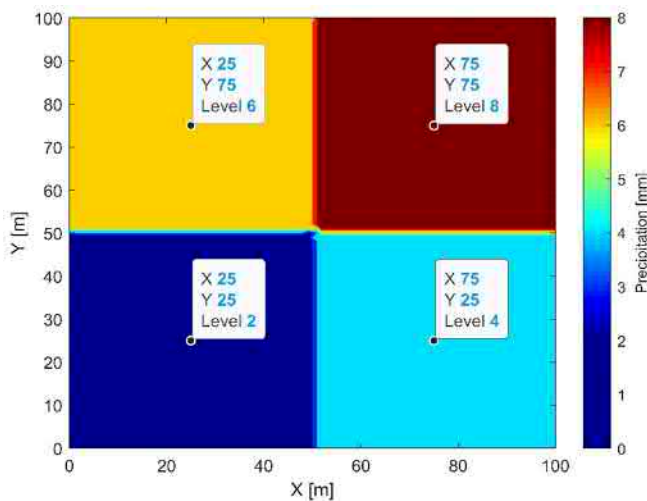


Figure 1. Accumulated precipitation [mm] after 600 s simulation time for the spatial rainfall example given in Table I.

The rainfall data is mapped to the computational mesh using the nearest neighbour interpolation method. Due to design problems, this calculation is repeated after each time step  $dt$ . A more efficient implementation could accelerate the computation.

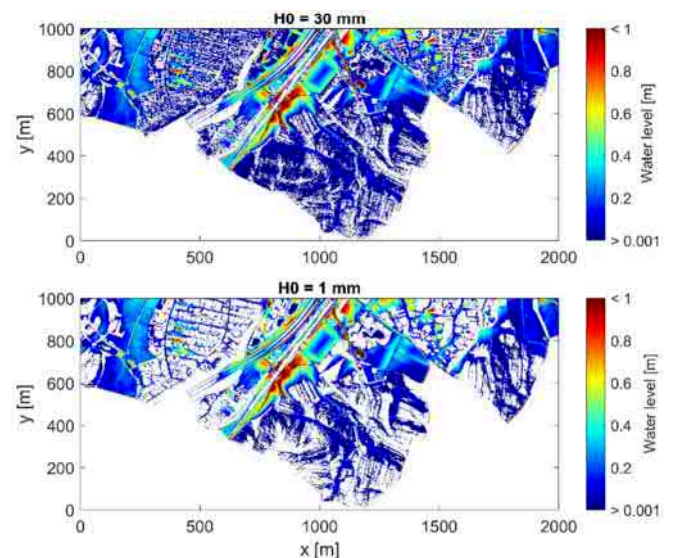
The name of the radar data file can be specified in the cas-file using the keyword FORMATTED DATA FILE 1. The list of subroutines changed is given in Table II.

TABLE II. LIST OF SUBROUTINES CHANGED.

	Subroutine	Description
1	declarations_telemac2d.f	Declarations
2	condin.f	Initial condition
3	runoff_scs_cn.f	Rainfall-runoff
4	nomvar_telemac2d.f	Name declaration
5	radarmap.f (New)	Reads rainfall radar data
6	fasp.f	Nearest neighbour interpolation

### B. Wet/dry boundary

Although the SCS-CN-method, at first sight, operated correctly, a deeper analysis revealed inaccuracies related to the wet/dry strategy of TELEMAC-2D. For water depth lower than 3 cm a change to viscous flow seems to happen. A thin water layer of about 1 to 3 cm remained temporary on the plane ground when using the FE-solver. Such a relatively thick water layer is not applicable for rainfall-runoff simulation, because the total amount of rainfall often is within the range of millimeters. The FV-solver in comparison simulated a plausible sheet flow but doubled the computational effort due to the explicit Courant criterion. Consulting the source code, the hard-coded parameter  $H0$  in fricti.f was found. This "Hidden Parameter"  $H0$  has a significant influence on the propagation of overland flow caused by rainfall for the FE-scheme. Figure 2 shows a comparison of max. water depths for  $H0 = 3$  cm (standard) and  $H0 = 1$  mm for flooding caused by heavy rainfall using the FE-model. The inundated area for  $H0 = 3$  cm is significantly larger than for  $H0 = 1$  mm. The solution of the FE-solver with  $H0 = 1$  mm is much closer to the FV-results. All results gained with  $H0 = 1$  mm are reasonable and the simulation runs smoothly without delay. Side effects in using a smaller  $H0$  were not observed. For the simulations in chapter III Calibration and Validation the FE-solver was applied with  $H0 = 1$  mm.

Figure 2. Inundated town area for calculation with TELEMAC-2D v7p3r1  $H0 = 30$  mm (Standard) and  $H0 = 1$  mm, cut-off = 1 mm.

### C. New roughness approaches

The Strickler roughness approach is widely used in shallow water equation simulations. However, its validity is not proven for flash flood simulations yet. For the hydrodynamic modeling of surface-runoff the proper representation of sheet flow is important. Otherwise, deviations in wave propagation time and water depth can be expected throughout the computational domain. Different alternatives to the Strickler roughness are already implemented in TELEMAC-2D. However, formulae



respecting both the influence of bottom structure and vegetation are not supported. This gap shall be filled implementing and analyzing new roughness formulae.

The scientific goal of this analysis is to find out, whether the Manning/Strickler law is appropriate for flash flood modeling or new approaches offer a better solution in terms of accuracy and efficiency.

The following three new roughness approaches were implemented [10]:

- Lawrence [5]
- Machiels [6]
- DWA [7]

The existing Lindner [8] roughness approach in TELEMAC-2D is used in a modified version from the Bundesanstalt für Wasserbau BAW (communication R. Kopmann).

Initial test-runs showed feasible results, but also the need for adaption. The observed computational effort for the new time-dependent roughness increased drastically due to the higher complexity of the new approaches.

### III. CALIBRATION AND VALIDATION

The extreme flash flood event on May 31<sup>st</sup> and June 1<sup>st</sup>, 2016 near Simbach a. Inn, Bavaria, is well documented [11]. The catchment of Simbach a. Inn has a size of 45.9 km<sup>2</sup>. The area of the adjacent catchment Triftern is 90.1 km<sup>2</sup> [11]. The basic digital elevation model DEM has a resolution of 1 m x 1 m. The standard look-up-table, which links the Strickler roughness values to the land usage, is given. As input for rainfall, radar data product RADOLAN YW by DWD [4] is available in 5 min temporal and 1 km<sup>2</sup> spatial resolution (see Figure 3 and Figure 4).

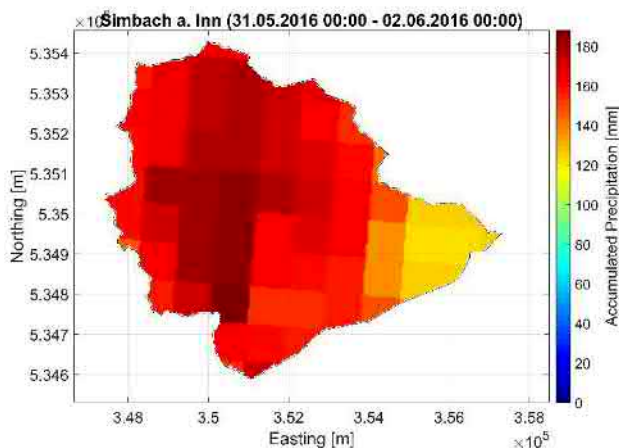


Figure 3. Accumulated precipitation from RADOLAN-YW Data for the heavy rainfall event in Simbach a. Inn in 2016. This data is used in TELEMAC-2D with the spacial rainfall module.

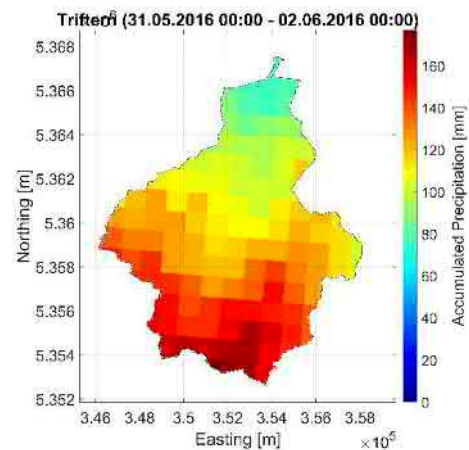


Figure 4. Accumulated precipitation from RADOLAN-YW Data for the heavy rainfall event in Triftern in 2016. This data is used in TELEMAC-2D with the spacial rainfall module.

All necessary data are available in good quality. Furthermore, both relevant catchments in Simbach a. Inn and Triftern are controlled by gauging stations (Figure 5). This situation that two adjacent catchments have reliable gauging stations and are hit by the same convective rainfall event is special. It offers the opportunity to calibrate the simulation method on one catchment and validate the procedure at the second catchment.

Here the data is first prepared for Simbach a. Inn. The optimal setup with respect to the reconstructed discharge at the gauging station Simbach a. Inn was chosen for calibration. The reconstructed discharge curve was taken from Hübl [11]. He derived the discharge upstream of the dam-break location fitting the result of a hydrological model to observed values. For better comparison with this result, the effect of a dam-break was not taken into consideration (Figure 6). It turned out, that the standard values for Strickler-roughness and CN - Values could be applied without changes. The steep slope correction SSC has some relevant impact on the results [2]. The initial abstraction ratio is set to 0.05 (default value 0.2) [2].

Afterward, the validation for the Triftern catchment can be tested following the same procedure for setting up the data and the same steering parameters for running the simulation.

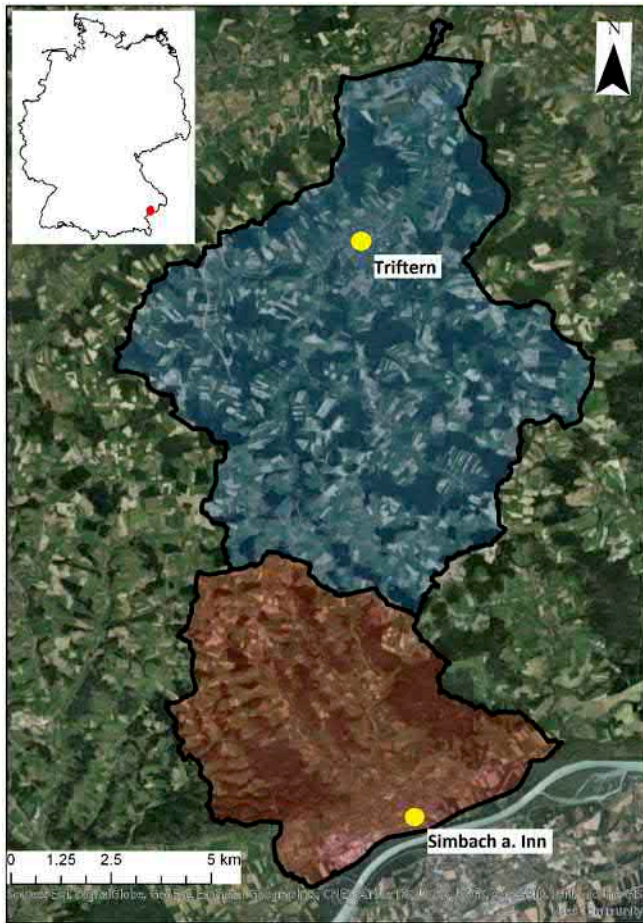


Figure 5. Catchments of Simbach a. Inn and Triftern (yellow point marks the location of gauging station).

The data were prepared and analyzed by Wencker [9]. Both simulations were run on an HPC cluster system with a spatial and temporal resolution of 5 m resp. 1 s.

The results for the calibration are represented in Figure 6, Figure 7 and Table III.

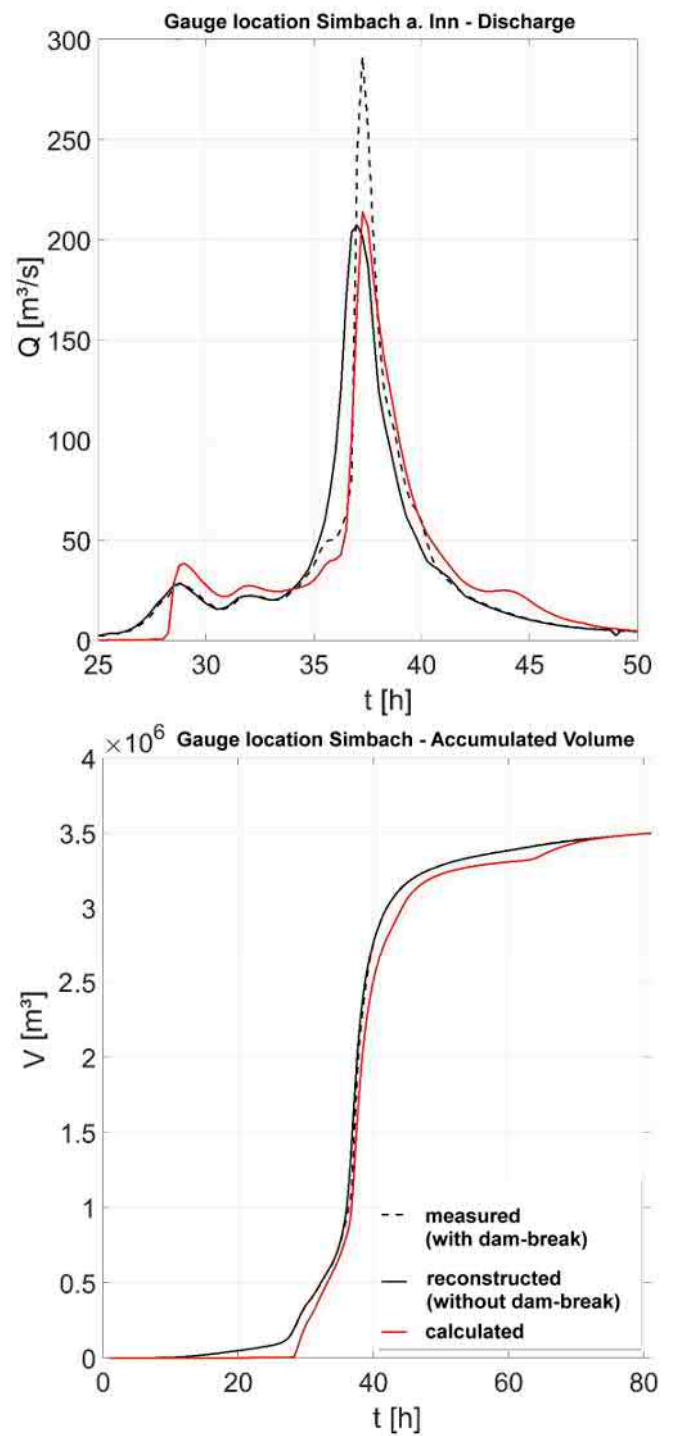


Figure 6. Calibration Simbach a. Inn, Comparison of calculated vs. reconstructed discharge (a) and accumulated volume (b), starting time 31.5.2016 0:00 UTC.

TABLE III. CALIBRATION SIMBACH A. INN, COMPARISON OF CALCULATED VS. RE-CONSTRUCTED DISCHARGE AND ACCUMULATED VOLUME.

	Reconstructed	Calculated	Deviation
Peak	207.3 m <sup>3</sup> /s	213.9 m <sup>3</sup> /s	+ 3.2 %
Time to Peak	37 h	37.25 h	+ 15 min
Final Volume	3.5*10 <sup>6</sup> m <sup>3</sup>	3.49*10 <sup>6</sup> m <sup>3</sup>	- 0.03 %

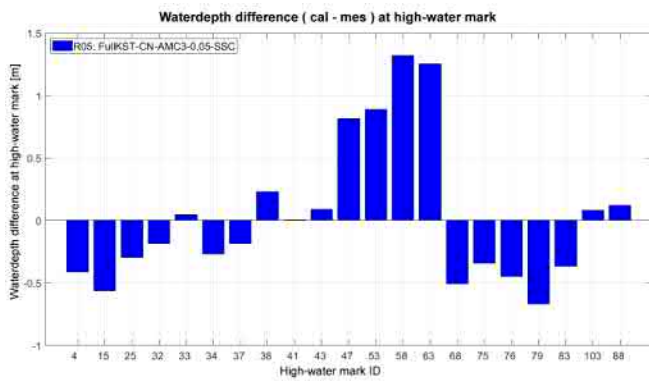


Figure 7. Calibration Simbach a. Inn, Difference of calculated and observed water depth at high water marks.

The deviation of measured and calculated discharge for the Simbach a. Inn calibration test case is below 5 % for peak discharge and well below 1 % for the accumulated volume. The deviations of observed and calculated water depth have much larger scatter (Figure 7). The simulation mostly underestimated the water levels by 20 – 70 cm. Within some polder area, an overestimation of more than 1 m occurred which is partly caused by insufficient information on outlets or pumps.

The procedure and the parameters gained by calibration in Simbach a. Inn is partially validated in Triftern. The characteristic of the discharge curve in Figure 8 is reproduced well. The deviation of the two maximum peaks is in the same magnitude as in the Simbach test case (Table IV). The deviation of accumulated volume again is almost zero. The accuracy of the water depths in comparison to high water marks is even better (Figure 9). This might be caused by the more mildly sloped terrain in Triftern.

TABLE IV. VALIDATION TRIFTERN, COMPARISON OF CALCULATED VS. MEASURED DISCHARGE AND ACCUMULATED VOLUME

	Measured	Calculated	Deviation
Peak 1	120.3 m <sup>3</sup> /s	121.8 m <sup>3</sup> /s	+ 1.3 %
Peak 2	125.5 m <sup>3</sup> /s	133.2 m <sup>3</sup> /s	+ 6.1 %
Time to Peak 1	36 h	35.25 h	- 45 min
Time to Peak 2	37.75 h	38.25 h	+ 30 min
Final Volume	4.93*10 <sup>6</sup> m <sup>3</sup>	4.93*10 <sup>6</sup> m <sup>3</sup>	- 0.02 %

Generally, high water marks tend to overestimate the real mean water elevation. Nevertheless the observed water level in Triftern and Simbach a. Inn is clearly underestimated by the simulation. The new roughness approaches described in Chap. IIC might help to improve the quality of simulated water depth.

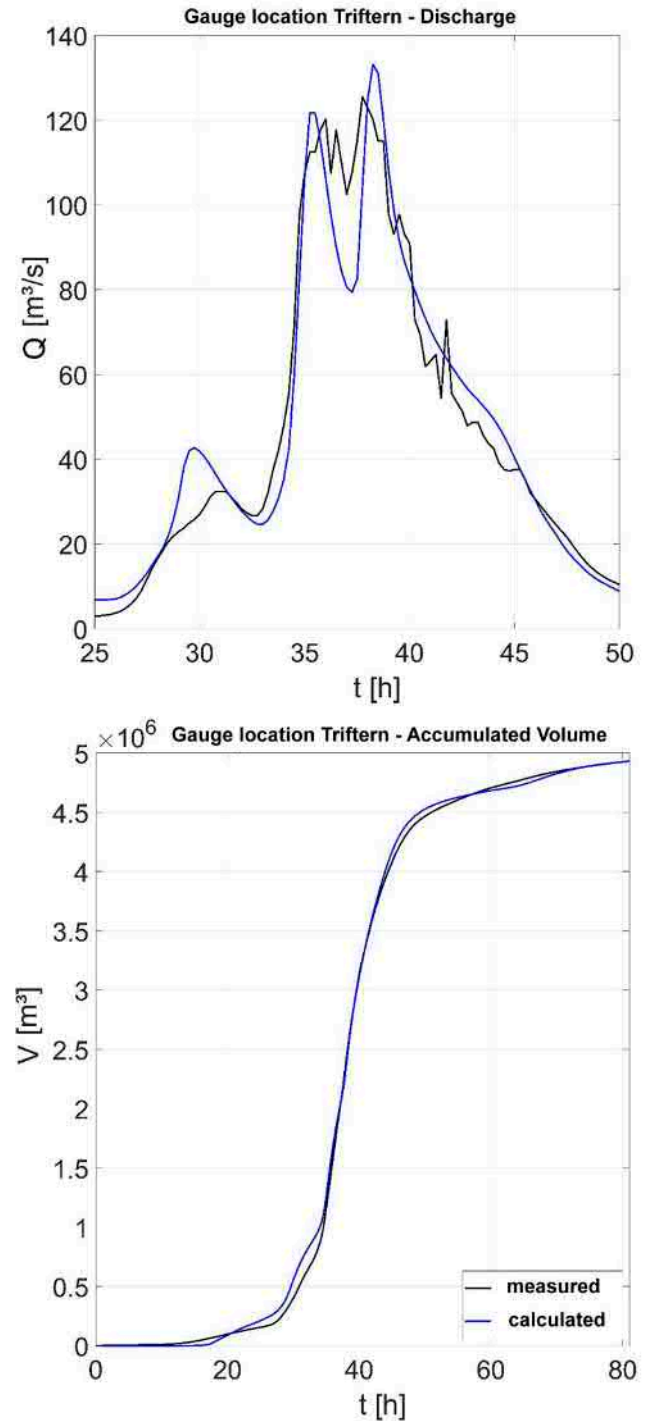


Figure 8. Validation Triftern, Comparison of calculated vs. measured discharge (a) and accumulated volume (b), starting time 31.5.2016 0:00 UTC.

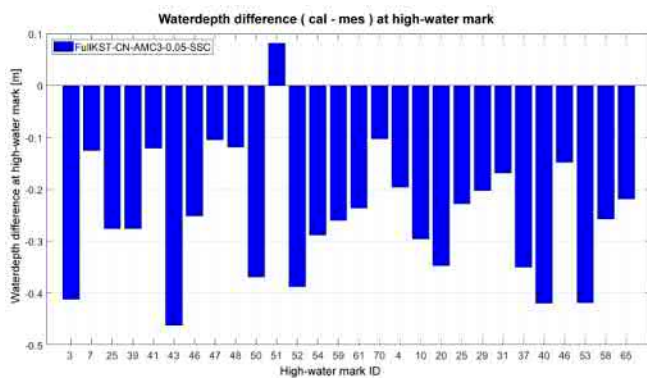


Figure 9. Validation of Triftern, Difference of calculated and observed water depth at high watermarks.

#### IV. HPC-SCALING TEST

Strong-scaling tests were carried out on the HPC cluster at LRZ. TELEMAC-2D v7p3r1 with extensions for spatially distributed rainfall was compiled using the Intel-MPI-Compiler 2017. TELEMAC-2D is configured for usage on the LRZ-SLURM load-leveler. The template for this configuration file was kindly provided by TU Wien.

The test case Simbach a. Inn described in the previous chapter was simulated using 2, 4, 8, 16 and 32 nodes, each node containing 28 cores. The wall time for the reference 1-node-run  $t_1$  and the parallel runs with more nodes  $t_N$  were recorded and the speed-up =  $t_N / t_1$  plotted against the number of nodes (Figure 10).

The program has very good HPC-performance. The speed-up is almost linear and even above the ideal line. This unusual behavior probably is caused by a different cache mode for the 1-node reference calculation. All the other simulations occupied less memory (because of the smaller sub-catchment for each core) and therefore could run inside the fast low-level cache. Simulations were repeated three times for 2, 4, 8, 16 and 32 nodes. The variation of the three identical sets is relatively small besides two calculations plotted in red. This difference probably is caused by the changing load of the HPC-system.

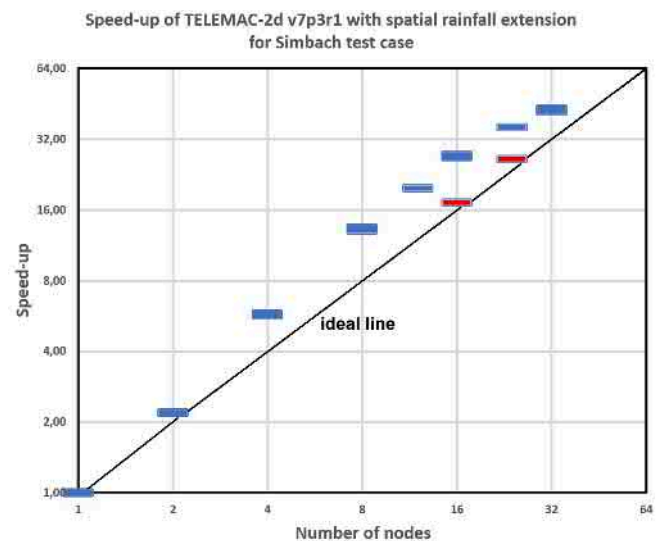


Figure 10. Strong scaling, speed-up Telemac-2D for Simbach-test case. Every node contains 28 cores. Outliers highlighted in red.

#### V. SUMMARY AND CONCLUSION

A general procedure for the simulation of flash floods using the TELEMAC-2D-FE-solver with an enhanced rainfall module extension was developed and validated. A good agreement of simulated and observed discharges was achieved for the study areas Simbach a. Inn and Triftern. Improvements concerning the accuracy of the simulated water depths for flash floods are still needed. Therefore different new roughness approaches are implemented. The hidden parameter  $H_0$  in subroutine `fricti.f` has to be reduced for all rainfall-runoff simulations using the FE-solver. The HPC-performance is good, but memory-bound weak-scaling still has to be tested.

In the next step, the derived method will be applied to 14 sites in Bavaria which experienced a flash flood. At each of these sites, discharge measurements are available for a more robust evaluation of the modeling setup.

#### ACKNOWLEDGMENT

The cooperation project HiOS analyses surface runoff and flash floods in various aspects. HiOS started in 2017 and will last until 2020. It consists of three teams working on GIS, hydrologic and hydrodynamic modeling. Technical University of Munich TUM, Ludwig-Maximilians-Universität LMU and the Leibniz-Supercomputing Centre LRZ are partners in this project. HiOS is funded by the Bavarian State Ministry of the Environment and Consumer Protection (StMUV) and supervised by the Bavarian Environment Agency.

#### REFERENCES

- [1] SCS, "National engineering handbook", Section 4: Hydrology, Soil Conservation Service SCS, USDA, Washington, D.C., 2004.
- [2] P.-L. Ligier, "Implementation of a rainfall-runoff model in TELEMAC-2D", Proceedings of the XXIIIrd TELEMAC\_MASCARET User Conference, 11.-13. October 2016, Paris, France.
- [3] R. Ata, "Telemac2d user manual. Version 7.2", April 2017, Paris.



- [4] DWD, „RADOLAN/RADVOR - Hoch aufgelöste Niederschlagsanalyse und -vorhersage auf der Basis quantitativer Radar- und Ombrometerdaten für grenzüberschreitende Fluss-Einzugsgebiete von Deutschland im Echtzeitbetrieb - Beschreibung des Kompositformats - Version 2.4.5“, Deutscher Wetterdienst DWD, Mai 2019.
- [5] D. S. L. Lawrence, “Macroscale surface roughness and frictional resistance in overland flow”, *Earth surface processes and landforms*, Vol 22, 365–382, 1997.
- [6] O. Machiels, S. Erpicum, P. Archambeau, B. Dewals Benjamin, M. Pirotton, “Bottom friction formulations for free surface flow modeling”, 8th NCTAM Congress, Brussels, 2009.
- [7] DWA, „Merkblatt DWA-M 524“, Gelbdruck, Hydraulische Berechnung von Fließgewässern mit Vegetation, Mai 2018.
- [8] K. Lindner, „Der Strömungswiderstand von Pflanzenbeständen“, *Mitteilungen Heft 75*, 1982, Leichweiß-Institut für Wasserbau, Technische Universität Braunschweig.
- [9] N. Wencker, „Validierung des Verfahrens anhand der Fallstudien Simbach a. Inn und Triftern – NA-Modellierung mit dem hydraulischen Simulationsprogramm TELEMAC-2D“, Master thesis, Juni 2019, TU München.
- [10] M. Deubler, „Untersuchung des Fließwiderstands bei kleinen Fließtiefen – Sturzflutmodellierung mit dem hydrodynamischen Simulations-programm TELEMAC-2D“, Master thesis, to be published in 2019, TU München.
- [11] Hübl J et al., „Ereignisdokumentation und Ereignisanalyse 2016 Rottal-Inn“, IAN Report 180, Band 1+2; Institut für Alpine Naturgefahren, Universität für Bodenkultur, März 2017, Wien.

# A new Python3 module for TELEMAC-MASCARET dedicated to post-treatment: Postel

Audouin Y., Fontaine J., Fouquet T., Goeury C.,  
Leroy A., Pham C.-T., Souillé F. and Taccone F.  
Laboratoire National d'Hydraulique et Environnement,  
EDF R&D, Chatou France  
[yoann.audouin@edf.fr](mailto:yoann.audouin@edf.fr)

Daou M.-P.  
Artelia Eau & Environnement  
Echirolles France

Duron L.  
Compagnie Nationale du Rhône  
Lyon France

Sécher M.  
Centre d'Ingénierie Hydraulique EDF  
La Motte Servolex France

**Abstract** — This paper describes the work started during the April 2019 Coding Week. The goal was to write a Python module to perform dedicated TELEMAC-MASCARET post-treatments using NumPy, SciPy, Matplotlib. The aim was to have a fully documented, validated and easy to use toolkit. Also it should make it possible for users to easily add their own modifications to the plots. The documentation was done using Jupyter notebooks which serve as documentation, validation and examples. The module can process to 2D/1D extractions from a 3D/2D mesh file, extraction from a TELEMAC listing, extraction from a shape file, plot of vectors and streamlines, plot with masked dry zones, plot over a background image (that can be extracted from a WMS flux), post-treatment for MASCARET files, spectrum specific plots, computation of fluxes, volumes, wet sections and statistics calculation, interpolation on a regular grid.

## I. INTRODUCTION

TELEMAC-MASCARET is a suite of scientific codes developed as interconnected modules entirely written in Fortran. Surrounding TELEMAC-MASCARET and also distributed as open source codes, an ensemble of pre- and post-processing scripts entirely written in Python have been developed over the last 5 years ([10], [11] and [12]). In fact, Python is a portable, dynamic, extensible, free language, which allows (without imposing) a modular approach and object oriented programming. Python has been developed since 1989 by Guido van Rossum and many volunteer contributors. In addition of the benefits of this programming language, Python offers a large amounts of interoperable libraries enabling to facilitate post-processing tasks on 2D or 3D TELEMAC-MASCARET computation results.

In order to gather all those tools and give them a place to flourish, a new Python [8] module “POStreatment TELeMac” (Postel) is created in the TELEMAC-MASCARET system [7]. It was developed only in Python 3 as Python will be retired by the end of the year. This module will be available in TELEMAC-MASCARET 8.1.

This module is developed with the guidelines below in mind:

- A user friendly list of classes and functions.
- Well documented and with examples.
- Easily customizable (you should be able to do it the way you want).

To match those guidelines the first thing done is to split this development in two parts “Data” and “Plot”.

The “Data” part contains all the functions around extracting and manipulating data. It can be to extract 1D, 2D data from a file, interpolate data along a polyline or compute fluxes for example. This part mainly uses NumPy [2] and SciPy [1] libraries.

The “Plot” part contains all the functions to plot graphs. It contains 1D, 2D and 3D plotting functions and allows plotting mesh, vectors, scalar map and contours for instance. This part is mainly based on the Matplotlib [3] library. This part can both take as input data extracted with the “Data” part or custom data.

To provide a useful documentation and proper examples, Python Notebooks are used [4].

First, this paper gives a brief explanation of the internal structure of the module and a layout of a code using it. Then, a more thorough description of the “Data” part of the module is given. Finally we will show some of the graphs we can do with the “Plot” part.

## II. STRUCTURE

This part presents the organisation of the code sources of the module. Then, a post-treatment example using the Postel module gives a framework of its use. The access to the notebook documentation is finally introduced.

### A. Module structure

The scripts of the module are located in the same folder as all the other TELEMAC-MASCARET scripts (\$HOMETEL/scripts/python3), where \$HOMETEL is the path to your installation of TELEMAC-MASCARET. The developments for this module are grouped in two folders: *postel* for “Plot” part and *data\_manip* for “Data” part. The Figure 1 shows the content of those folders.

Not all of the content of *data\_manip* will be described here but notebooks can be found for most of them.

All the scripts follow the PEP 8 [5] coding convention (we used Pylint [6] to check that convention).

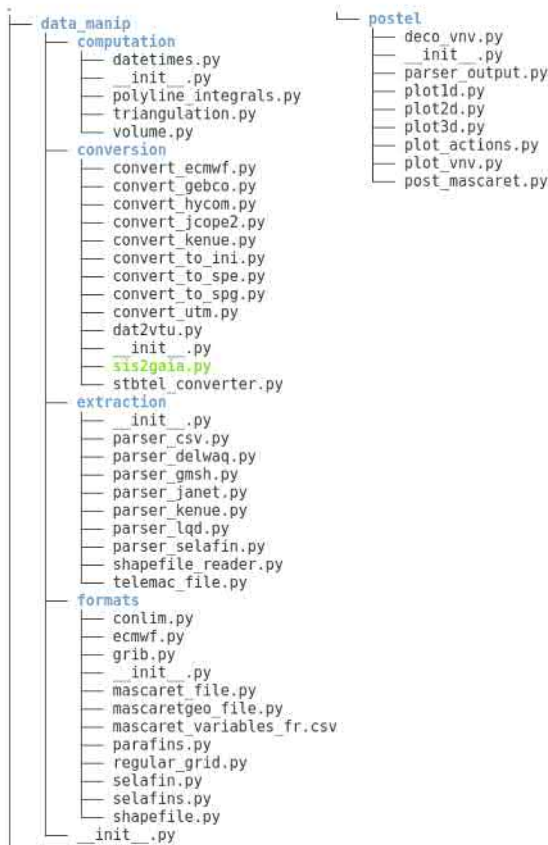


Figure 1: Tree of the content of data\_manip and postel

## B. Code structure

Figure 2 is a template of what a post-treatment code using Postel looks like.



Figure 2: Examples of code using Postel

Where:

- Part A: imports the different Python modules needed.

- Part B: extracts or computes the data. This is the “Data” part.
- Part C: initialises the Matplotlib figures.
- Part D: adds plots to the figures and sets its parameters.
- Part E: displays or saves the figure.

Parts C, D, E represent the “Plot” part.

Most of the examples you will see below follow that structure.

## C. Notebooks

The Jupyter Notebooks are a mixed between a “IPython” [9] session and a website. This gives you a platform in which you can write a Python code and execute it. This leads to an interactive documentation where you can easily modify the code to match your own data.

This is used for documentation, examples and validation of the module. To start exploring the notebooks, run the following command:

```
jupyter-notebook $HOMETEL/notebooks/index.ipynb
```

This notebook will be your guide into the world of not only Postel but also all the Python scripts orbiting TELEMAT-MASCARET. It is an index of all the functionalities you have access to and a link to a notebook for all of them.

To display them you will need to install jupyter (<https://jupyter.org/>) follow the instructions on their website.

## III. DATA MANIPULATION

This part will give an overview of the functionalities of data extraction and computation functions of the Postel module.

### A. How to extract data from files

The data extraction part allows us to obtain different types of information from a mesh or a TELEMAT result file (whether in med or selafin format). The class *TelemacFile* contains several parameters and methods designed for this purpose. The properties *meshx* and *meshy* give the coordinates of each node of the mesh, while the method *get\_timeseries\_on\_nodes* extracts a time series of variables from the graphical outputs on a given node or point defined by its coordinates. It is also possible to retrieve the spatialized value of a variable at a given frame with the method *get\_data\_value*. This spatial extraction can also be interpolated on a regular grid with the method *interpolate\_on\_grid*, which permits to compare two results on different meshes using the *field\_diff\_on\_grid* method. Finally, the method *get\_liq\_bnd\_info* provides information on the location of boundaries, their type, as well as the table of correspondences between the global node number and the boundary condition number.

When the results come from a TELEMAT-3D simulation, it is possible to use them in several ways thanks

to the module. It is possible to extract horizontal sections, either following a plane of the three-dimensional mesh with the `get_data_on_horizontal_plane` method, or having a fixed elevation with the `get_data_on_horizontal_slice` method. It is also possible to extract the data on a vertical section with fixed coordinates using the `get_data_on_vertical_plane` method, and to perform a time series of the value of a variable in the entire water column at a given point in the horizontal plane with `get_timeseries_on_vertical_segment`.

In addition to the extraction of data from a result file, Postel offers the possibility of reading into the listing outputs to retrieve certain information thanks to the class `OutputFileData`. This gives, among other things, the possibility to know the time profile of the simulation (which physical time corresponds to which iteration) with the method `get_time_profile`, the name of the study with the method `get_name_of_study`, or the mass fluxes at the boundaries and the mass-balance data with the method `get_value_history_output`. The user can also customize his query by giving a word to find in the listing so that the code returns information on the corresponding line using the method `get_user_defined_output`.

It is also possible to read shapefiles and extract polylines or polygons with the `shapefile_reader` class, but also to read and write information in csv format based on `savetxt` function of NumPy.

### B. How to compute data from extractions

After the extraction of the data from the result files, the Postel module provides various functionalities to calculate the values of interest associated with the hydraulic variables.

For a given polygonal chain, it is indeed possible to compute the wet area with the function `wet_area_2d` after a TELEMAC-2D result file extraction of the water depth. The `flux_2d` function can be used to compute the flux of a scalar through this chain. By additionally extracting the velocity components in both directions, it is also possible to calculate the flow rate through this polygonal chain using the `flux_2d` function. This same function is also able to calculate solid discharge if the corresponding variables are previously extracted from a SISYPHE result file.

The function `volume_calculation` allows the integration of a variable extracted from a TELEMAC result file over the entire domain. It can be used, for example, to calculate the total volume of water in a domain by taking as an input, the extraction of water depths in the results file and the information of coordinates and triangulation of the mesh from `TelemacFile`. This can also be applied to erosion/deposit volume computation, if the evolution variable of the SISYPHE results file is extracted.

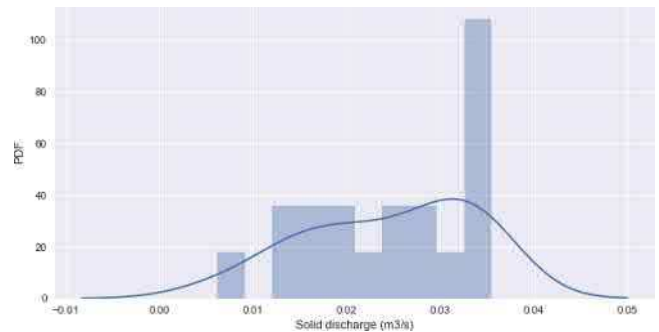


Figure 3: Probability Density Function of the solid discharge

Statistical information from your data can be simply computed using the Python module Pandas have a look at the notebook *statistic* for a more detailed explanation. Figure 3 shows the result of the said notebook.

### C. How to post-treat MASCARET files

The first step for MASCARET file post-treatment is to be able to extract the data. There are two main classes to allow this:

- The class `MascaretGeoFile` allows reading and writing geometry files.
- The class `MascaretFile` allows reading different types of a MASCARET result file (whether in Rubens or Ophthya formats).

These classes contain several attributes and functions designed for post-treatment tasks.

Let us begin with the class `MascaretGeoFile`, the `summary` method gives the reaches and associated sections in a text format. These two items describe geometry in MASCARET. In this class, the `reaches` attribute stores the object list of reaches and each reach contain multiple Section objects.

The class `Reach` contains methods to get the pk with `get_section_pk_list` method, to get the index list of section in reach object with `get_section_id_list` method, in addition to get of the section index of geometry from previously index with `get_section_idx` method.

The class `Section` contains mainly geometric attributes which are:

- `axis`: x, y coordinates of hydraulic axis.
- `x, y, z`: 1D-arrays for coordinates *x y z respectively*.
- `distances`: 1D-array with cumulative distance from first point along the section.
- `nb_points`: number of points.
- `limits`: a dict with the position and name of all limits.

Note in class `MascaretGeoFile` that the `save` method allows us to write a geometry file after having modified the object attributes.

The `MascaretFile` is based on the same principle with the attribute `reaches` containing its associated sections (but in this case the geometry is not set because the result file do not provide it). This class contains the post-treatment



methods for results files. The *summary* method gives variables and number of temporal frame in addition to the information provided by the corresponding method in class *MascaretGeoFile*. The *get\_position\_var* method returns the variable index from the variable name given. The values along a reach for one time step are extracted with *get\_values\_at\_reach* method for the variable index and reach index. Furthermore the *get\_series* method allows us to get the temporal values at a given section.

Then, the step after data extraction is to be able to draw them in a graphic. For this, the same 1D plots function is used than TELEMAC (to see IV.A).

Another post-treatment step is writing results for specific variables or specific time steps with *write\_optfile* method. Finally there is also *export\_as\_lig* method allowing continuation of computation with the creation of LIDOP file from a given time step.

The different examples can be found in the notebook *example\_mascaret*.

#### IV. PLOT

This part will give examples of the different visualization tools available in Postel ranging from simple 1D plots to more complex 2D plots with multiple layers and 3D plots.

##### D. How to do 1D plots

From data extracted from TELEMAC result file, 1D plot can be done with abscissa and ordinate data. This can either be timeseries or plot along polygonal chain or any other data. Several plot examples are given in the *example\_plot1d* notebook as well as the corresponding extraction function. In Figure 4 and Figure 5 an example of plot of time series on points and plot along a polygonal chain are shown.

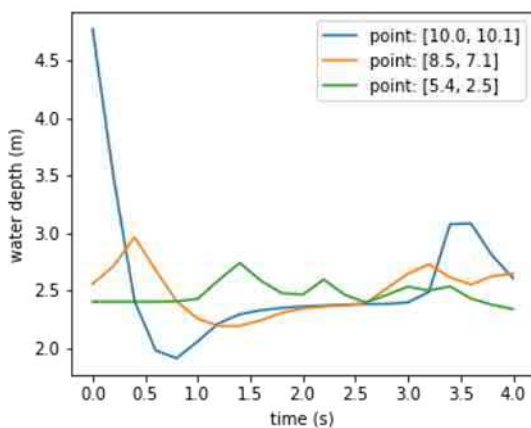


Figure 4: Example of 1d plot of time series on different points

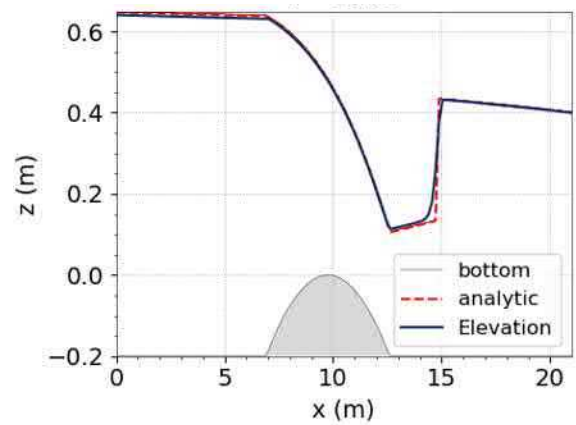


Figure 5: Example of 1d plot along a polyline

##### E. How to do 2D plots (x, y) plane view

In this section we mainly focus on the functions available in *postel/plot2d.py* which are described in detail in the *example\_plot2d* notebook.

The first function of 2D plots is *plot2d\_triangle\_mesh*. It allows the visualization of 2D mesh and takes as argument the triangulation contained in the TELEMAC result file, which is *tri*, a parameter of the *TelemacFile* class. At the same time, it can be useful to visualize boundary conditions types and numbers. It can be done with the *plot2d\_annotate\_bnd* and *plot2d\_annotate\_liq\_bnd* functions respectively. An example of 2D mesh plot with boundary annotations is shown on Figure 6.

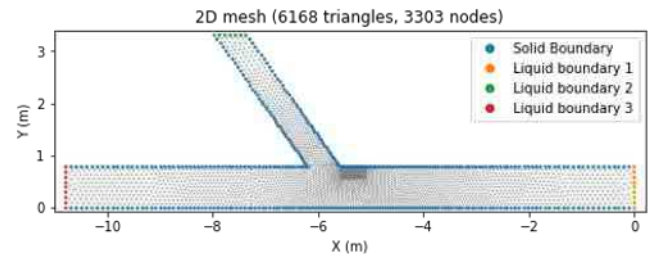


Figure 6: Example of mesh and boundary conditions plot with the confluence test case of TELEMAC-2D

To plot a scalar like water depth, elevation or velocity norm two functions are available in *plot2d*, *plot2d\_scalar\_map* and *plot2d\_scalar\_filled\_contour*. On Figure 7 and Figure 8 a scalar map and a scalar filled contours are shown with the mesh in the background. In addition, non-filled contours can also be plotted with the function *plot2d\_scalar\_contour*, as it is shown on figure 7. Note that these functions take as argument a mesh that can either be a triangulation or a regular grid and the scalar data extracted from that mesh. Colour bar can be customized via the *vmin*, *vmax* arguments for maximum and minimum values as well as *nv* for the number of ticks. In the case of contours, a list of values can be provided instead with the *levels* argument.

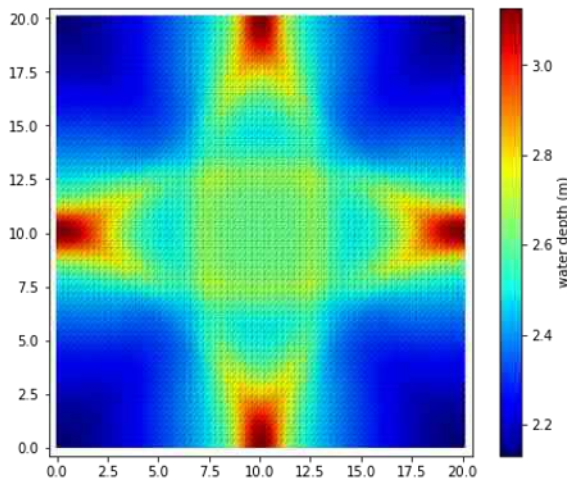


Figure 7: Example of scalar map plot with the gouteddo test case of TELEMAT-2D

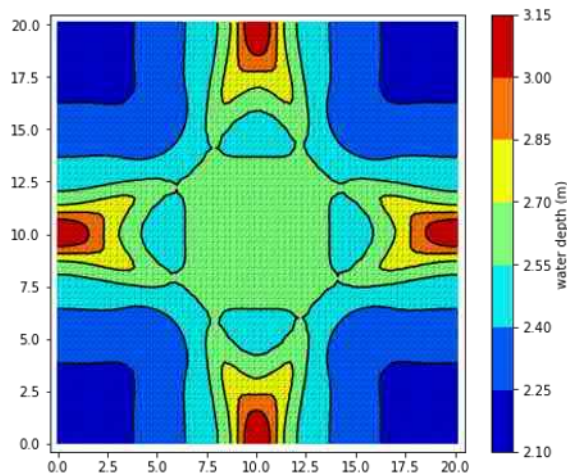


Figure 8: Example of scalar filled contours plot with the gouteddo test case of TELEMAT-2D

The last two functions in *plot2d* are *plot2d\_vectors* and *plot2d\_streamlines* and are used to visualize vectorial data like velocity, wind velocity or solid and liquid discharges. They take two scalars as inputs *data\_x* and *data\_y*, which correspond to *x* and *y* components of the vector. As for other 2D plots, *mesh* argument can either be a grid or a triangulation. But the user can also specify a grid resolution with the *grid\_resolution* argument to make the functions generate their own grid. This functionality is useful when the triangular mesh is too refined and lead to a large amount of vectors being plotted. Vectors size are adjustable with the *scale* argument as well as streamlines density with the *density* argument. Vectors and streamlines are coloured depending on their norm by default but can also be coloured uniformly with the *color* argument. An example of coloured vectors plot is shown on Figure 9.

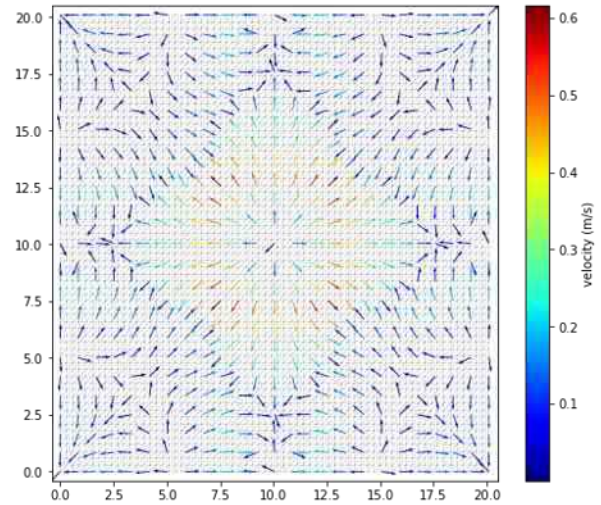


Figure 9: Example of vectors plot with the gouteddo test case of TELEMAT-2D

#### F. How to do 2D plots with *z* elevation as *y*-axis

TELEMAT-3D results can be visualized with 2D plots (*x*, *y*) presented previously if extraction is performed on a plane, defined at a fixed elevation or along a given computation plane. But 2D plots with elevation as *y*-axis could also be defined in combination with 2 possibilities for *x*-axis: curvilinear distance along a line or time.

The first example in Figure 10 displays velocity magnitude and shear velocity vectors in a user defined horizontal section. Although the vertical extraction (on the whole water column) is done along a straight line (*y*=10m), it could be performed along any arbitrary 2D polygonal chain.

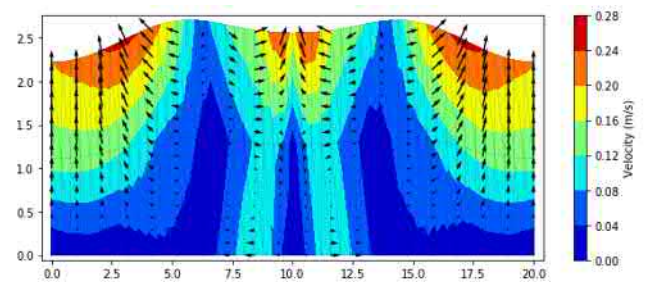


Figure 10: Example of 2D plot corresponding to a horizontal section (plane *y*=10m with gouteddo test case of TELEMAT-3D)

The alternative 2D plot with *z*-elevation is used to analyse the vertical distribution of a scalar over time. The Figure 11 presents vertical velocity distribution over time at the centre of the gouteddo domain (*x*=10m, *y*=10m).



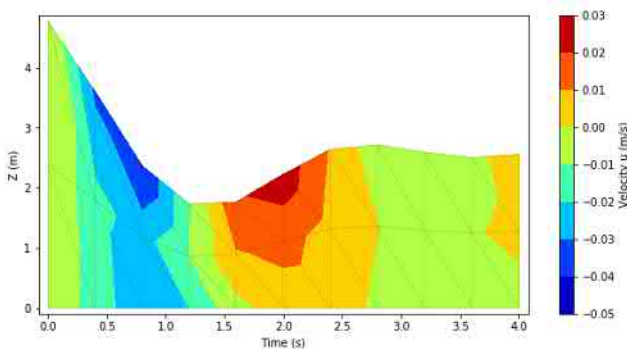


Figure 11: Example of a temporal 2D plot over the vertical with gouted test case of TELEMAC-3D

These 2D plots involving elevation are documented in the *3d\_extraction* notebook.

#### G. How to do fancy 2D plots

The logic behind Postel plotting functions is that it allows us to pile up multiple layers. For instance, we can have a scalar map on top of a mesh with vectors and streamlines above it. The amount of layers is not restricted but data overlapping is the main limitation. To overcome this problem, alpha of each layer can be adjusted and mesh triangles can be masked. Masking can be done with a customizable criterion with the *mask\_triangles* function. For example dry zones can be masked as on Figure 12. More details are presented in the notebook *example\_plot2d\_advanced*.

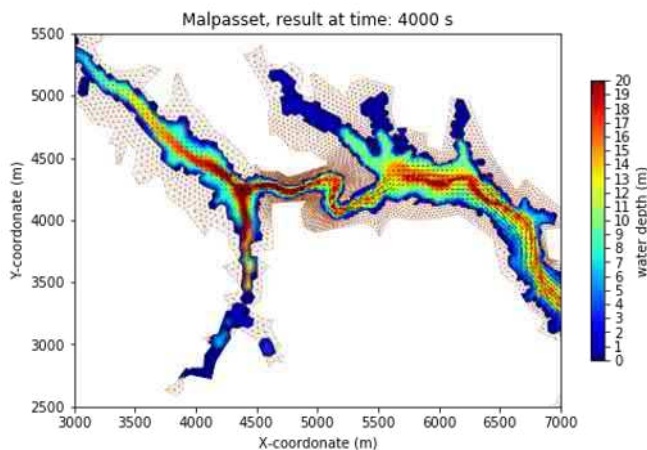


Figure 12: Example of advanced plotting with the Malpasset test case of TELEMAC-2D

In addition to basic 2D plots layers presented previously, images can also be added with the *plot2d\_image* function. Images can be background map as presented in the Figure 13. Plotting background map often requires to change the coordinate system of the mesh. This can be done with the *pyproj* Python package. Moreover background image can be taken directly from a web map service using the *owslib* package. An example of how to use those packages is presented in *example\_plot2d\_background\_map*.

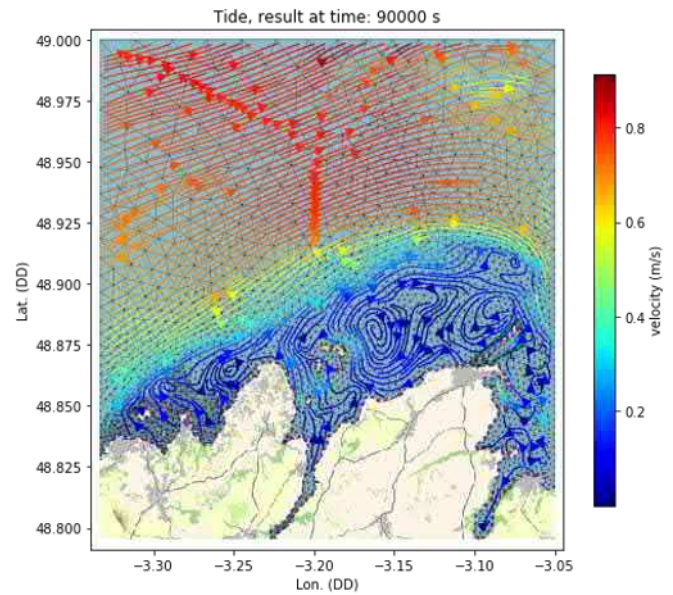


Figure 13: Example of background image plot with the tide test case of TELEMAC-2D

#### H. How to do 3d plots

3D plotting is limited in Python and only one function is available in Postel: *plot3d\_scalar\_map*. This allows us to visualize water depth as a 3D surface as presented in Figure 14.

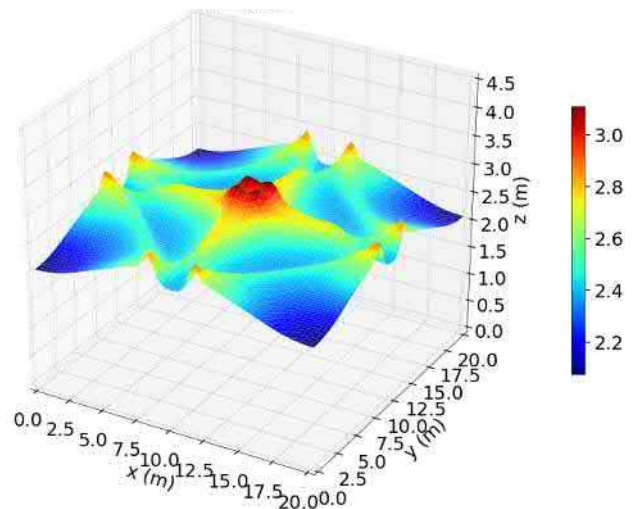


Figure 14: Example of 3D plot with the gouted test case of TELEMAC-2D

#### I. How to plot TOMAWAC spectrum files

Tomawac displays specific outputs, namely the spectrum, that need specific post-treatment. A user can specify several output locations over the domain, such that energy densities will be recorded for all discretised directions and frequencies. A couple of functions were added to get the spectrum graphic output. They are shown in the notebook *spectrum*.

First we added a method called `get_spectrum_name` in `TelemacFile` that gives you the name containing the spectrum associate to a point number given as a parameter. The function `get_list_spectrum_points` will give the list of points available in the file.

Figure 15 shows the integrated spectrum over the directions at a given point for a given record using `TelemacFile.get_spectrum`.

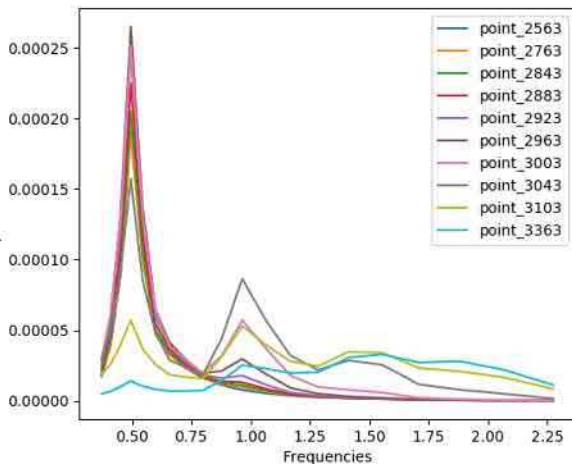


Figure 15: Plot of the TOMAWAC 1D spectrum for different output points

Using `TelemacFile.get_angular_dispersion` you can extract the energy integrated over the frequencies for a given point and record. The wave dispersion can be then observed. Figure 16:6 shows a polar projection example.

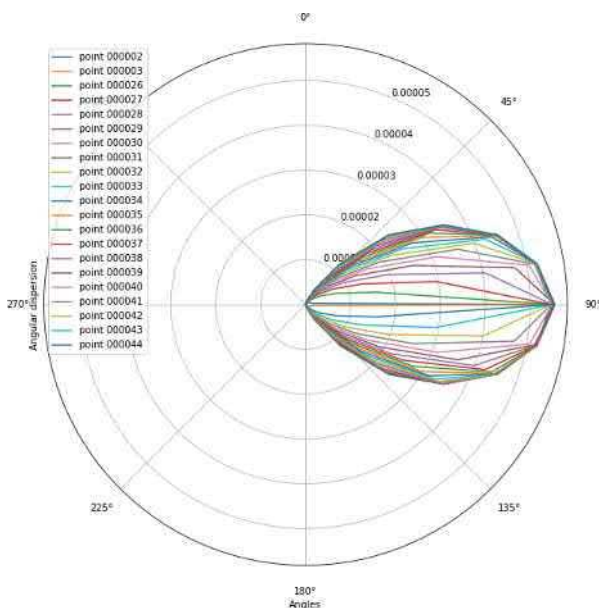


Figure 16: Plot of the energy density along wave directions of a TOMAWAC spectrum file for a list of points.

### J. One line simple plots

It is possible to do some of the plots describes before using a one line bash command. This means you will have less control over what you can modify but it is a good way to make simple “on the go” plots.

This script is called `plot.py`. Run it with the option `-h` to see how it works. You can also have a look at the notebook `plot`.

## V. CONCLUSION

We now have a nice Python module documented and easy to use. Containing all of the post-treatment we could do via the xml and more.

This will be available in the next release of TELEMAC-MASCARET (v8p1).

These scripts are bound to keep on evolving as they are used. Therefore contributions are more than welcome if you have scripts that could be integrated do not hesitate to contact the TELEMAC-MASCARET team.

## ACKNOWLEDGEMENTS

Thanks for all the hard work of the Coding Week team that made the creation of this module possible.

## REFERENCES

- [1] E. Jones, T. Oliphant, P. Peterson, et al. SciPy: Open Source Scientific Tools for Python, 2001-, <http://www.scipy.org/> [Online; accessed 2019-08-09].
- [2] T. E. Oliphant. A guide to NumPy, USA: Trelgol Publishing, (2006).
- [3] Hunter, J. D. Matplotlib: A 2D graphics environment, IEEE COMPUTER SOC Volume 9 Number 3 Pages 90-95 (2007)
- [4] T. Kluyver, B. Ragan-Kelley, et al. Jupyter Notebooks - a publishing format for reproducible computational workflows, ELPUB, 2016
- [5] G. van Rossum, B. Warsaw, N. Coghlan. PEP8 -- Style Guide for Python Code, <https://www.python.org/dev/peps/pep-0008>, 2001
- [6] Pylint, <https://www.pylint.org/>
- [7] J-M. Hervouet, “Hydrodynamics of Free Surface Flows”, Wiley, 2007, pp. 83–130.
- [8] G. van Rossum, Python tutorial, Technical Report CS-R9526, Centrum voor Wiskunde en Informatica (CWI), Amsterdam, May 1995.
- [9] F. Pérez, B. E. Granger, IPython: A System for Interactive Scientific Computing, Computing in Science and Engineering, vol. 9, no. 3, pp. 21-29, May/June 2007, doi:10.1109/MCSE.2007.53. URL: <https://ipython.org>
- [10] S. Bourban, J.-C. Parisi, A. Weisgerber, The TELEMAC’s automated management and continuous integration and validation system, Proceedings of the XXII Telemac User Conference, 2015, Daresbury (England).
- [11] P. Prodanovic, A practical toolkit for terrain free surface flow and wave modelling, 2017, PPUTILS user documentation.
- [12] L. Duron, Y. Wang, PyTelTools: Python scripts and GUI to automate Telemac post-processing tasks, 2017, Graz (Austria).

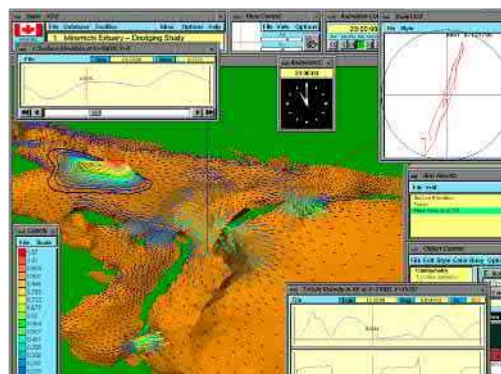


# Blue Kenue enhancements from 2014 to 2019

Alan J. Barton

Ocean, Coastal and River Engineering (NRC-OCRE)  
National Research Council Canada (NRC)  
Ottawa, Ontario, Canada  
alan.barton@nrc-cnrc.gc.ca

**Abstract**—Blue Kenue® has been under development for about 20 years, and provides a framework for pre-processing, post-processing and visualization of hydrodynamic model data. The National Research Council Canada makes this software freely available for use by the open TELEMAC-MASCARET user community and benefits significantly from the knowledge that the community shares. The paper will briefly describe some of the key changes to Blue Kenue that have been implemented over the last 5 years (such as how attributes are improving, how internal organization is changing and which new features have been added) and will provide some initial thoughts about potential future Blue Kenue enhancements (such as improved data analytics and additional modelling support for ice-hydrodynamics, microplastics and/or oil). The paper is intended to help be a starting point to identify needs and priorities for future development.



Blue Kenue's conceptual predecessor was named HYDA

## I. INTRODUCTION

This paper briefly describes Blue Kenue's origin, the new Blue Kenue development environment, some ways that the new environment is helping inform the development efforts, and a few yearly examples of Blue Kenue additions since 2014 to help understand where Blue Kenue is now. The paper concludes by describing three possible Blue Kenue future development directions.

## II. BLUE KENUE ORIGIN STORY

Originally conceived by the Canadian Hydraulics Centre (CHC) of the National Research Council Canada in 1991, HYDA was designed to provide a single consistent user interface and database for collection, preparation, and analysis of hydro-numerical model data. Through use of powerful 3D visualization HYDA was designed to provide a real time virtual environment for modellers regardless of simulation methodology. HYDA's solver neutral database architecture allowed for easy interchange of data between different models. In 1994 CHC (then known as IMD's Hydraulics Laboratory) entered into a collaborative agreement to commercialize and further the development of HYDA technology. The result of this collaboration was the commercial HYDA version 3.2. Then, in 1997, CHC stopped supporting HYDA development in favour of the technology underlying Blue Kenue.

## III. BLUE KENUE DEVELOPMENT ENVIRONMENT

Before 2014, Blue Kenue developers were using a version control system called *Microsoft Visual Source Safe*. In 2019, developers now rely on an online server called CHyMS; offering version control as one of its services.

### A. Canadian Hydrological Model Stewardship (CHyMS)

The original CHyMS server started to become operational in November 2011. In 2014, a major upgrade was performed that addressed a number of security related issues. The original CHyMS proposal can be found on CHyMS itself (in the Public Download Area). In essence, the proposal called for creation of a safe haven for Canadian hydrological models. A number of Canadian supporters were involved; including the Canadian Society for Hydrological Sciences. But how does CHyMS relate to Blue Kenue? Well, NRC also offers Green Kenue for free to the hydrological community. Therefore, Green Kenue developments and leading-edge installers were decided to be placed onto CHyMS for that community. And since the underlying technology behind Green Kenue overlaps with the underlying technology for Blue Kenue, both applications and the underlying technology made their way onto CHyMS. Therefore, CHyMS plays a key role in the development of Blue Kenue.

### B. What services does CHyMS offer in 2019?

CHyMS has a Frequently Asked Questions (FAQ) webpage that is, co-incidentally, frequently updated. When read sequentially the FAQ offers answers to a broad number of questions, including what services are currently offered. In 2019, CHyMS offers the Blue Kenue community the Public Download Area for sharing. This sharing space is where NRC places its alpha and beta versions of Blue Kenue, among other things.

CHyMS also hosts both private and more open projects. Each project has been created with specific people in mind. Each project has tickets, version control, reporting, Kanban, and email reminders (if configured). In addition to per project

information, cross-project reporting is offered to a person for those projects in which they have been granted access. Such reporting helps inform decision makers.

CHyMS is also a place for communities to come together; such as the Green Kenue Community and the pyEnSim Community. There is also a Blue Kenue Community on CHyMS, however, that mainly directs people to the OpenTelemac forum [2]. These CHyMS communities will expand depending on the specific community preferences.

#### C. How do Blue Kenue developers use CHyMS in 2019?

There are 4 main CHyMS services that Blue Kenue developers use: (i) CHyMS Public Download Area, (ii) CHyMS Project Hosting, (iii) CHyMS Gentle Reminder Email Service, and (iv) CHyMS Kanban.

The CHyMS Public Download Area is a web page on CHyMS that provides links to files such as: fact sheets, executables, data files, tutorials, presentations, and videos amongst other things. These freely shared items are created by NRC and by other people and organizations that are also willing to share.

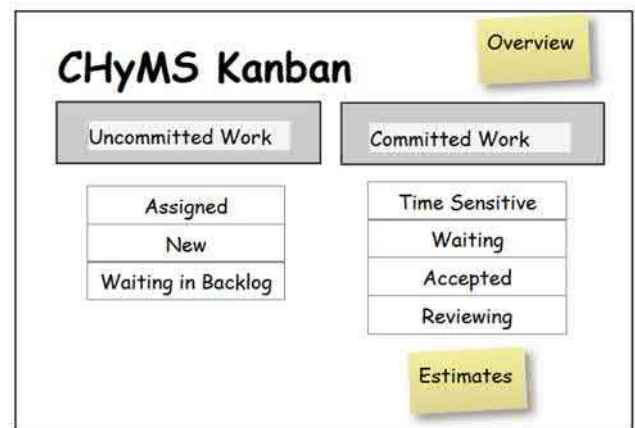
The CHyMS Project Hosting service offers a way for source code to be version controlled, tickets to be created, wiki pages to be shared, timelines to be viewed and other helpful things that most development projects might expect. One of the projects associated with Blue Kenue and hosted on CHyMS in 2019 is called “*EnSim Developer Stewardship Project*”. This project is a large internally funded NRC project with specific goals and deliverables. A more detailed description follows in the next section.

The CHyMS Gentle Reminder Email Service is performed once per week. Each Monday morning CHyMS will collect all time-sensitive tickets across all hosted projects and will group the tickets by owner. CHyMS will then sort each person’s owned tickets by due date and send the sorted time-sensitive information to the person. In this way, a person only receives one email for all time-sensitive tickets that they may have open. This helps to keep on top of work with a deadline.

The CHyMS Kanban is one way to visually represent a TODO list. This visual list typically comprises work, such as action items, bug fix descriptions, new features, etc. Each of these items is called a ticket. Such tickets may have comments such as status updates, attached files, images such as screen snapshots or links to other issues encountered. Each ticket also has attributes associated with it. These attributes can be customized. The CHyMS Kanban displays information about a few of the available ticket attributes and when a key attribute called “status” is changed, then the ticket automatically moves to another location in the Kanban. More details such as best practices for how to use the CHyMS Kanban are in the CHyMS FAQ.

#### IV. KNOWN WORK OVERVIEW

The EnSim Developer Stewardship Project is a large NRC-OCRE internally funded project that is primarily about refactoring the deepest part of Blue Kenue called EnSimCore. This part of Blue Kenue is a dynamic linked library (dll) that



The left (right) column shows tickets that have not been agreed (have been agreed) to be worked on. There are 8 locations for a ticket’s information to appear (the 8<sup>th</sup> is closed). A ticket appears in a location based on its state; such as “Accepted”. More details are available in the CHyMS FAQ [3].

is used by many other dlls and executables (exes) developed by NRC-OCRE. For example, both Blue Kenue and Green Kenue are executables that use the EnSimCore dll. The primary focus of the internal NRC-OCRE project is on: (i) improving attribute implementation, (ii) performing many code reviews to collect and describe potential errors, defects and faults, (iii) holding internal EnSim related discussions, and (iv) providing a small amount of time to fix a few external issues raised on the OpenTelemac forum. However, this internal project is not about building new features nor about addressing large amounts of technical debt left by other projects. Those things (and more) would be addressed under their own respective project(s).

Most of the known work is summarized (numerically) in the following table based on information stored on NRC’s CHyMS server. Ideally, each piece of known work is fully described in its own ticket such that there is a one-to-one mapping between known work and CHyMS tickets. It is also important that each ticket is as unambiguous as possible so that completed work means that an open ticket may be closed. A review of all 394 tickets was performed in order to classify each ticket into one of four work directions. The 2 columns “open” and “closed” count (at a high-level) the number of tickets that are either still to be performed (open – new,

BLUE KENUE (AND OTHERS) KNOWN-WORK SUMMARY

Work Direction	Counts for Tickets in Project on CHyMS [3]			
	Open (Residual)	Closed (Residual)	“Growth”	Calculated Strategy
Strategic (large)	85 (-17.5)	23 (8.0)	-25.5	2
New Feature (small)	22 (45.5)	12 (19.0)	26.5	3
Proactive Maintenance	113 (-45.5)	38 (-7.0)	-38.5	1
Reactive Maintenance	48 (19.5)	46 (-15.0)	34.5	4
<b>Total (394)</b>	<b>270</b>	<b>124</b>		

assigned, backlogged, accepted, waiting, under review) or completed (closed – fixed, duplicate, will not fix, etc).

For example, from the table we can see that 48 tickets are open in the reactive maintenance work direction. In other words, there are 48 (smallish) things that people have noticed about Blue Kenue (or its technological relatives) that would be good to fix and/or modify. There are a total of 270 possible open work items to consider during the decision process of asking the question “*What should be worked on now?*” and a further 124 work items have been completed that do not need to be considered. In addition, a residual has been computed and placed in parenthesis in the table. For the reactive maintenance work direction, the residual is 19.5, meaning that this work direction has about 20 fewer tickets than the average work direction (there are 4 work directions in the table). In other words, all tickets having the same weight implies that this work direction is performing well as compared to the other work directions. Carrying the analysis of the residuals further, since we do not (yet) have trend information, we can see that the difference between the open and closed residuals may provide a sense of how each work direction has grown under the assumption that a ticket may belong to any of the 4 work directions with equal probability. A quick calculation may then provide an answer to the aforementioned question; and in our case, following the logic to its conclusion means that we should focus on the proactive work direction in order to lower the work in that area.

The flaw in this type of numerical analysis (automated or not), of course, is that all tickets are not equal weight for users of Blue Kenue and some users place more importance on some things than other users; depending on which task they are working. Some types of observed faults should certainly be resolved much more quickly compared against others. And some types of new features should not wait forever to get implemented. All of this to posit that funding, available developer time, developer expertise and shared user needs all *jointly* play a large role in the future success of Blue Kenue. So, let’s all do our best to continue Blue Kenue’s success.

One measure of success for Blue Kenue is whether the installer is continuing to be downloaded. The following table shows the download counts in the last 5 years and more. From the table, it seems like 2018 was a very prolific year; however, there may be some data error due various internal changes [6].

BLUE KENUE DOWNLOAD COUNTS (GRAND TOTAL: 15,044)

	Pre-	2014	2015	2016	2017	2018	2019 <sup>a</sup>
[6] 32 bit	2537	352	273	303	197	159	87
[6] 64 bit	1868	1126	1196	1648	1524	2137	952
[3] 32 bit	-	-	-	5	30	53	8
[3] 64 bit	-	-	-	7	171	230	181
<b>Total</b>	<b>4405</b>	<b>1478</b>	<b>1469</b>	<b>1963</b>	<b>1922</b>	<b>2579</b>	<b>1228</b>

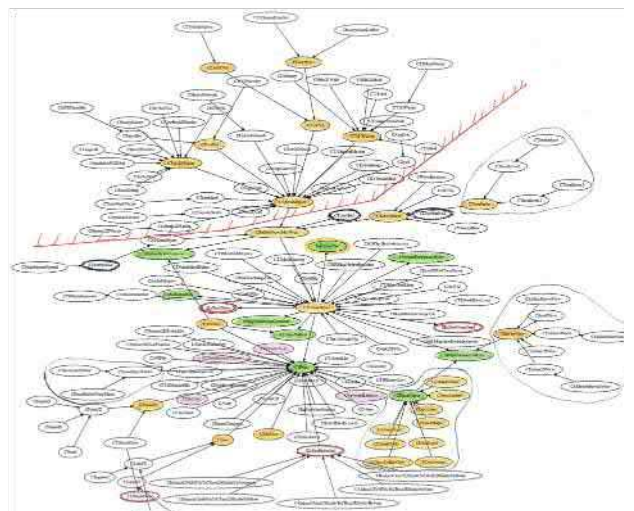
a. As of 16 August 2019

A more careful analysis would need to be carried out to improve the accuracy of that year’s 32 bit and 64 bit counts (top 2 rows values). In any case, the general trend, as would be expected, is that 32 bit versions of Blue Kenue are not being downloaded as often as their 64 bit counterparts. What is surprising, however, is the fact that the 32 bit versions are not zero; there are still a couple of hundred downloads.

## V. TECHNOLOGY OVERVIEW

Blue Kenue is built on top of a number of libraries; similar to Green Kenue, ECDE and others. The technology is mainly written in the C++ language (some parts are in Fortran and, exceptionally, pyEnSim allows the underlying technology to be exposed via the python language). This means that Blue Kenue needs to be fully compiled. Alternative language design approaches include, among others, interpreted languages, such as python, perl, or scripting languages such as bat, bash, bourne, etc., or interpret-compile hybrids, such as javascript. The underlying technology relies on the OpenGL library to provide all rendering functionality while application framework, menus, dialogs etc. are implemented via the Microsoft Foundation Class (MFC) library.

Creating an installer for Blue Kenue means that over 300,000 lines of code are selectively combined together in a meaningful way via a number of automatic and manual steps. Compilation means that one C++ source code file (\*.cpp) is used to create one object file (\*.o) and a set of object files are combined to make a static (\*.lib) or dynamic (\*.dll) library. Some object files and some of the static libraries are then linked together to make an executable (\*.exe). The dlls are loaded into memory only when they are used at runtime. In other words, for example, when a menu item in Blue Kenue is



Example demonstrating some of the complexity of the system (not intended to be read in detail). Blue Kenue’s C++ code is organized into classes (roughly 900). Each oval is one such class. Arrows go from one oval to another; signifying that one class is a child of another class. This figure shows only those parent/child relationships directly related to one very core class called *CEnSimObject*. In other words, this figure shows the connected component in which *CEnSimObject* belongs. Such a figure is helpful for developers learning the system architecture and for explanatory purposes.



used then the underlying implementing (if from a dll) means that the dll would be loaded into memory and then invoked. The executable for Blue Kenue uses about 8 static and 12 dynamic libraries. The installer (\*.msi) is then made by combining the executable, the appropriate dynamic link libraries, the documentation, the changelogs with a description of new features, fixed bugs, experimental features, etc., and any required data files, such as base maps, databases, configuration files, etc. The resulting installer is also manually edited after construction in order to allow installation within NRC's new, and stricter, security environment. The installer is then placed onto CHyMS in the Public Download Area for sharing.

## VI. BLUE KENUE EXAMPLES

Blue Kenue enhancements occur when a project funds development effort. One such project is called the EnSim Developer Stewardship Project and is hosted by CHyMS [3]. This NRC-OCRE internally funded project has almost 400 tickets in total; of which about 100 are related to completed work. The following subsections describe an assortment of the tickets that were created in each of the years succeeding 2014 until the year 2019 and for which the associated work is now (mid 2019) complete. CHyMS was instrumental in helping to determine these examples through the creation of a wiki page grouping tickets by year.

### A. Examples created in 2014 and now complete (9)

*Ticket #48 – AVI recording fails on 64 bit.* One comment on the ticket notes that the default encoder was Cinepak (that was not functioning properly) but that the other encoders do behave correctly. The fix was to generalize the existing code so that only those encoders that are installed on a user's machine (and for which Blue Kenue has implementations) will be presented within Blue Kenue for selection. This should stop situations where someone selects an encoder that they do not have installed and therefore for which they cannot record video. In other words, Blue Kenue has 4 implemented encoders and only a subset of those will be able to be selected from within the Recording tab of the 2D View properties. For example, on one development machine there are 7 unusable (by Blue Kenue) installed codecs and 3 usable (by Blue Kenue) installed codecs.

*Ticket #65 – Time series tools not respecting missing data.* In particular, computation of flow duration curves, cumulative sums, and integrals were reported to be not respecting the missing data value. Also of note, was the computation of distributions and performance statistics. The fix was to use a recently generalized *CAttributeSet* class which was used in many more places that described in this ticket. In other words, a lot of proactive maintenance was also involved in the resolution. The full and complete resolution touches many aspects of the 900 classes and is still a work in progress.

### B. Examples created 2015 and now complete (5)

*Ticket #78 – Cannot save points as (\*.pt2).* In other words, creating a new XYZ point set using Blue Kenue resulted in creation of a new object in the workspace that could not be directly saved as \*.pt2. During the investigation, it was determined that there is a work around; however, the addition

of functionality to directly save to a \*.pt2 file was added. A number of related issues were also identified; some of which were resolved.

*Ticket #82 – Add double precision SELAFIN file support.* A large effort was undertaken to add the required support. This included, among many other things, modifying display capabilities such as to add a “center of domain offset” and how the mouse interacts with it.

### C. Examples created 2016 and now complete (5)

*Ticket #103 – add “cell” drawing style to CRect2DScalar.* A developer working on another application relying on parts of Blue Kenue's underlying technology submitted a patch file to add a new small feature. The patch was applied, reviewed, approved and committed to CHyMS. Subsequent Blue Kenue releases have included the submitted patch with the new display capability. In other words, a new drawing style has been added to Blue Kenue.

### D. Examples created 2017 and now complete (4)

*Ticket #106 – invalid y location for time series extraction.* When extracting a time series at a point from a 2D spatial object (Rect 2D Scalar), the resulting metadata for the point's y location was incorrect. In addition, the same fix was made for 3D spatial object (Rect 3D Scalar) time series extraction.

*Ticket #114 – \*.ts1 not properly displayed in 1D view.* Blue Kenue version 3.3.4 did not display the Time Series Type I file correctly. However, Blue Kenue version 3.9.5-beta displayed the time series as expected. In the future, the reporter of this fault will check the most recent version of Blue Kenue and only report a fault if it has not been fixed. Of course, this assumes that a person is aware of where to find the most recent version (Available in the CHyMS Public Download Area [3]).

### E. Examples created 2018 and now complete (58)

The approval of a new NRC-OCRE internal project has allowed almost 10 times as many tickets to be created during 2018. The resolution of which may have also occurred during 2019 along with other tickets that had been created in previous years. A few of the 58 tickets created in 2018 include:

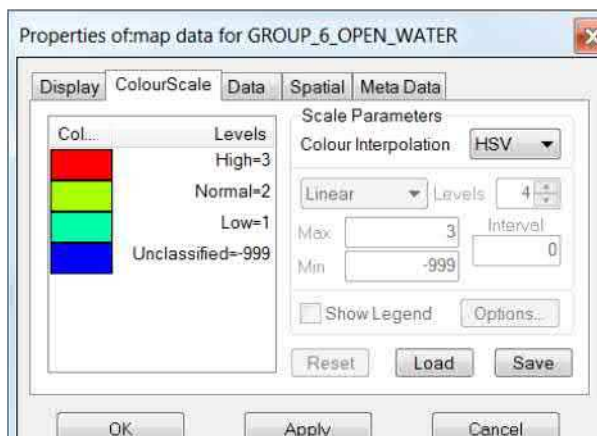
*Ticket #180 – Create AAttributeSet.* Pull out the attribute related functionality from the class hierarchy and localize it. The reason is to provide more consistency in dealing with multiple attributes; including robustness improvements and in the long term, easing introduction of attribute-related new functionality along with some performance gains due to localized memory. Historically, this ticket was motivated by observed faults in a different application that, upon inspection resulting in the EnSim Developer Stewardship project being proposed to and funded by NRC-OCRE. In addition, historically, Blue Kenue only had one attribute and over time multiple attributes were slowly added on an as-needed basis to the various data related classes. The work involved in this ticket was very detail oriented and involved reviewing hundreds of lines of C++ code located in tens to hundreds of classes depending on the specific aspect of the refactoring involved. As of mid-2019, the new *AAttributeSet* class has stabilized and the use of it by the subclasses in the hierarchy is a work in progress; with, perhaps, 80% to 90% coverage. Of



particular note is the use of 2 distinct types of attributes by one particular class in the hierarchy that will require a future change to this new class in order to support that functionality. For now, the specific customization is localized to the subclass and has become a TODO note for future consideration.

*Ticket #218 – pull current attribute information out of EnSimDrawableObject.* With the newly created *AAttributeSet* class, it became easier to localize current attribute selection information; further aiding developers and lowering future maintenance costs due to reducing the number of touch points required to understand how current attributes are maintained.

*Ticket #214 – pull \*m\_TimeAttribute out of CTableObject.* With the new *AAttributeSet* class implemented, it was fairly straightforward to remove the no-longer needed code from this class. For this work, a search of the 1,545 files revealed 32 possible locations that needed to be reviewed and adjusted appropriately.



The new colour scale showing both category and value.

*Ticket #197 – CColourScale should display “oneof” category and not value.* After improvements to multiple attributes a number of “ripple-effects” occurred; one of which was the incorrect display of a “oneof” value instead of its associated category.

*Ticket #236 – CColourScale dialog should display ABC=123 for “oneof” attributes.* After improvements to multiple attributes it also became much easier to add the new feature of displaying both the category and the associated value; making Blue Kenue slightly easier to use operationally.

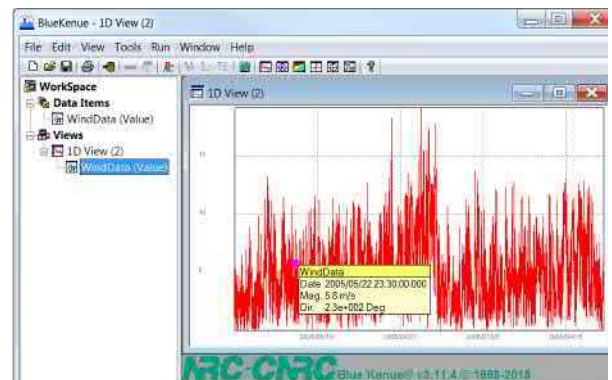
*Ticket #249 – default colour scale does not work for ATR\_INTEGER.* For example, if an integer attribute had values 1 to 6 then 10 intervals could not be created; causing a fault. This ticket resolved that issue.

*Ticket #186 – Modernize code that starts a thread.* This work is related to making the source code easier for developers to use and enhance with new features. Historically, the set of lines of code to start a thread were all copy and pasted including the associated switch statement on all possible return states. Now a new function at the root of the class hierarchy has been added in order to localize the functionality

in order to reduce future maintenance costs in terms of writing new code and also for easing understanding existing code by new developers.

*Ticket #209 – pull AEnSimWorkspaceObject out of CEnSimObject.* The work in this ticket will make it easier for developers to understand the coupling between the two aspects; now separated into two distinct classes. In the best case if the work was done well, a Blue Kenue user would not even know that something has changed with respect to how data objects interact with the work space. Further future enhancements in this area are planned.

*Ticket #210 – pull AEnSimContextMenu out of CEnSimObject, CDecoObject, CStationsTableView and CEnSimView.* Similar to #209, a Blue Kenue user would not be able to notice that this deep internal work had occurred. From a development point of view, this ticket removed redundant code in order to ease future maintenance and understanding.

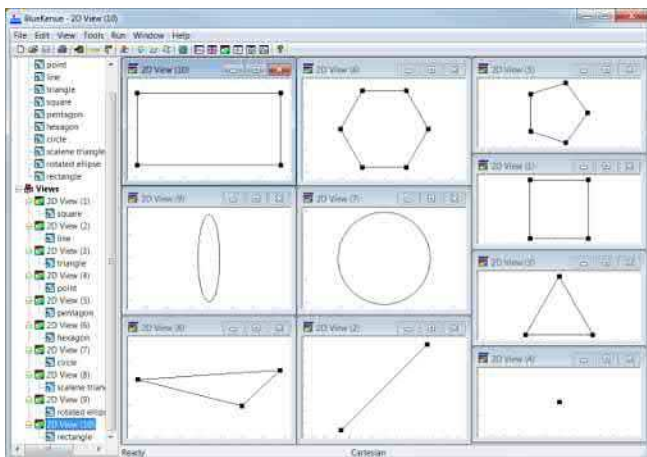


A popup for a point in a time series shown with values aligned

*Ticket #259 – popup does not align numbers.* When clicking on a point, line, cell, etc, the popup did not align the values in a column. This was resolved in multiple places.

*Ticket #263 – attribute properties should also display attribute type in properties dialogs.* 13 dialogs were modified in order to display each attribute’s type (e.g. double) and to display both the category value and index (e.g. ABC=123). See also #236.

*Ticket #275 – duplicated metadata is quietly overwritten.* Metadata handling improvements are slowly starting to be made now that multiple attribute improvements have stabilized. In this case, when the same metadata is used more than once in a data file then a warning is displayed and the ability to select which value to use is presented.

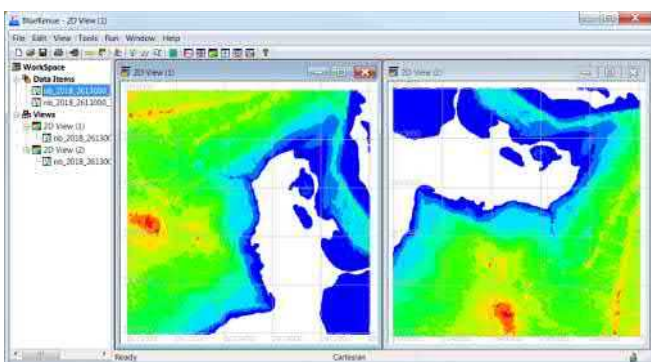


10 examples of creating simple new geometries in Blue Kenue  
(some are scaled and/or rotated) architecture

*Ticket #243 – Add new functionality to create circle and rectangle 2-d line sets.* The ticket's description proposed to add new functionality to be able to create a circle with a specified radius and origin. During review, the request was seen to be generalizable to points, lines, triangles, squares, pentagons, and, in general, scalable and rotatable n-gons (circles are n-gons with large n and ellipses are scaled circles).

#### F. Examples created in first half of 2019 and complete (12)

*Ticket #337 – display time in a consistent user readable string.* The time is presented in slightly differing ways throughout Blue Kenue. The work in the ticket was to find and resolve the differences. It was found that 34 different locations needed to become localized to one function; that was subsequently enhanced, thus propagating the enhancements to all 34 locations.



Swapping X and Y in an XYZ Point Set object (lat/lon vs. lon/lat)

*Ticket #408 – Swap attributes in an XYZ Point Set.* XYZ Files contain 3 columns of data. Different software applications create these files in different ways; some use space to delimit the columns, some use comma, some use semicolon etc. In addition, there may or may not exist a first line containing column names. Therefore, Blue Kenue has no way to determine if latitude (or longitude) will be in the first column (called X) or the second column (called Y). A new menu item was created (*Edit -> Point Set -> Swap X and Y*) to let the Blue Kenue user decide what should be done after an

XYZ file has been loaded into the Workspace and inspected within a 2D View. Note that Blue Kenue has many types of point set files; here we added functionality specifically for the XYZ Point Set object containing 1 frame of data. General Point Sets or Parcel Sets possibly containing multiple data frames may be considered in the future. Also note that Blue Kenue has its own native XYZ Point Set file format that differs from other XYZ formats due to the addition of a more detailed header section before the data section of the file.

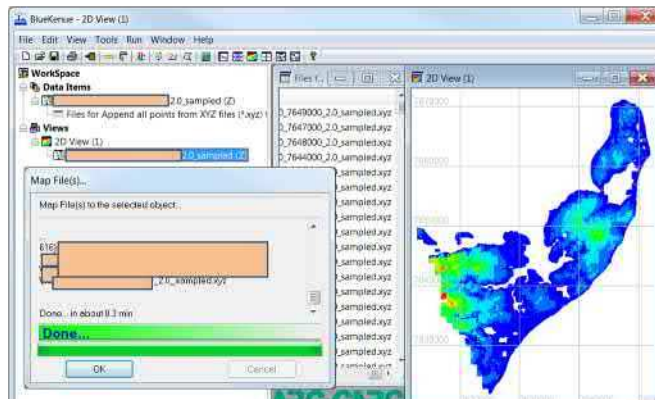
#### AVAILABLE BLUE KENUE REDUCTIONS FOR TOOLS -> MAP FILE(S)...

Selected Object in the Workspace	Available Reductions based on the Selected Object	File type that can be selected
Rect 2D Scalar	<ul style="list-style-type: none"> <li>Assign all DEMs</li> <li>Sum all Rect 2D Scalars</li> <li>Average all Rect 2D Scalars</li> <li>Sum all grib files</li> <li>Average all grib files</li> <li>More in Green Kenue</li> </ul>	<ul style="list-style-type: none"> <li>*.dem</li> <li>*.r2s</li> <li>*.r2s</li> <li>*.grib, *.grib2</li> <li>*.grib, *.grib2</li> <li>*.fst, etc.</li> </ul>
XYZ Point Set	<ul style="list-style-type: none"> <li>Append all XYZ files</li> </ul>	<ul style="list-style-type: none"> <li>*.xyz</li> </ul>

*Ticket #334 – Tools -> Map File(s).* Is a larger piece of new functionality now available in Blue Kenue. It will likely take years before all possibilities are completed and made available to the community. The main idea of this new feature was inspired by the already existing Map Object functionality within Blue Kenue, where one object is selected in the workspace and then one other object is mapped onto it. One drawback of this approach happens when we have a large number of mappings that we need to perform because we need to load the files into the workspace and then map one object at a time onto the object of interest. Thus was born the idea of Map File(s) where we start by selecting one object in the workspace but then we don't map one loaded object but we instead directly map one or more files containing data. As a matter of terminology, since there may be more than one file that is being selected and since we are mapping down to one selected object, we can call this operation a "reduction". There are currently 6 available reduction methods (see table above) within Blue Kenue.

The first reduction method, interestingly, was motivated by a need within another application called Green Kenue – a hydrology oriented software that relies on a shared underlying technology with Blue Kenue. In that first motivating example, the idea was to summarize the mean precipitation over an area of interest as collected from about a year's worth of precipitation data (about 1,200 files stored in grib format). In this case, a Rect 2D Scalar was created via Green Kenue's grid generation functionality to cover the area of interest (all "data" was initially set to 0mm). Then the empty grid was selected in the workspace and the "Average all grib files" reduction was performed in order to summarize the years' worth of data in the grid.

An example relevant to pre-processing of data for input to TELEMAC using Blue Kenue has since been implemented. In this case, a user was interested in developing a digital elevation model combining multiple tiles of high resolution Light Detection and Ranging (LiDAR) data over a region of



631 XYZ files appended onto an XYZ Point Set object using Map File(s)  
(In this case, each XYZ file is LiDAR topographic data [7])

interest in New Brunswick, on the east coast of Canada. The user collected 632 topographic files and converted each of them to XYZ format. Blue Kenue was used to load one of the XYZ files; which was then selected in the workspace and Map File(s) was used to append all of the other 631 files onto the selected XYZ Point Set object. The result was one XYZ Point Set object in the Blue Kenue workspace containing points from all 632 XYZ files. In addition, Blue Kenue did 2 more things; first it created a new table object containing a list of all files that were used during the reduction operation and added it as a child of the selected object in the workspace, and second, some new metadata was added onto the object in order to record which reduction operation was performed, approximately how long it took and how many files were selected by the user to map. This additional information may then be used in the future to help trace the origin of the processing and to support modelling quality assurance / control.

## VII. POTENTIAL FUTURE BLUE KENUE WORK

This section describes a few possible future activities related to Blue Kenue that may be of direct interest to the Blue Kenue community of users. Contributions, collaborations and/or contracts are very much welcome at any time.

### A. Additional Reductions for Map File(s)...

More reduction methods are certainly possible, either as additions to the current set of reductions for the 2 previously mentioned objects, or as reductions on new objects depending on the needs of the Blue Kenue users. For example, merging multiple \*.slf files (containing a single frame or multiple frames) may be of interest for some users. This may include preserving part of a model mesh and modifying another part and then merging them back together; or merging channel meshes with regular meshes, among other things. This would be a more direct methodology than the existing approach.

### B. Blue Kenue Reference Manual Migration and Update

The current manual [1] was last modified about 8 years ago and used software call FrameMaker [4] for its production. The last portion of 2019 will be used to migrate the existing information in this system to a new documentation preparation

system called LaTeX [5]. These new files will be managed through CHyMS [3]. Once the migration process has been completed then the LaTeX files will be updated to bring them closer to the current Blue Kenue features. Such placement under version control (in CHyMS) may help to more easily keep the information aligned in the future.

For example, Blue Kenue Community members interested in participating in keeping the user manual updated could request access to CHyMS (in 2020) and then request changes to the LaTeX files by submitting a patch file. The patch file would then be reviewed and considered to be applied. Examples of changes via patch files could be: (i) to fix small typos, (ii) to correct processes, or (iii) to add large paragraphs of helpful background and/or clarifying information. The idea is for the patches to be curated and for those that pass inspection to be applied to the reference manual. Proper acknowledgement would also be included in the subsequent Blue Kenue release.

### C. Micro-plastic particles in the Marine Environment

Modern numerical models can be effective in predicting the movement and fate of particles in oceans and waterways, and are routinely applied in other water quality contexts. Blue Kenue is proposed to aid research (where appropriate) in: (i) developing techniques for simulating the behaviour and transport of micro-plastics across a broad range of spatial and temporal scales of relevance; (ii) characterizing particle properties and degradation processes in diverse aquatic environments; (iii) helping to fill gaps in the availability of field observations for input to, and verification of numerical models; and (iv) suitability for other challenges in marine and freshwater environments such as debris transport and accumulation, ice jams and related flooding in rivers, oil spill simulation and emergency response, ecological or agent-based modelling

For example, Blue Kenue enhancements may include new components for: (i) analysis of remote sensing data to estimate micro-plastic concentrations in waterbodies; (ii) integration of numerical simulation results of hydrodynamics in lakes, rivers, estuaries and oceans, and (iii) prediction of micro-plastic transport, dispersion, degradation and accumulation.

### D. Tool(s) to Ease Preparation of Environmental Inputs

An ongoing new addition to TELEMAC2D is a river ice module named KHIONE. This module is to simulate main river ice processes including frazil ice formation and transport, border and dynamic ice and ice jam and its impact on river surface elevation and potential flooding. Main inputs to KHIONE in addition to usual inputs to open water version of TELEMAC2D are air and sky conditions as well as initial river temperature and frazil concentration. Blue Kenue can currently visualize outputs of the existing version of KHIONE. It is, however, worth exploring how and if Blue Kenue can be further developed to facilitate pre- and post-processing for TELEMAC2D river ice simulations.

For example, one possibility could be the development of tools to ease the preparation of format compatible environmental inputs. This includes automatic conversion of main data formats of climate models providing data such as



cloud coverage, wind, precipitation, air temperature and humidity.

#### CONCLUSIONS

CHyMS is important within the context of possible future Blue Kenue developments because it allows more than one developer to work on the code at a time and also helps transition (i.e. handing over) of code from one person to another during times of change. CHyMS is also very beneficial from the point of view of a communication mechanism between developers and users and/or to management and/or other sources of funding for new features and maintenance activities. CHyMS significantly helps to organize and stay on top of the most pressing issues facing Blue Kenue, Green Kenue, pyEnSim and ECDE along with continuing to keep historical applications such as AnemoScope, MarKE and others up-to-date with the latest improvements to the shared underlying technology.

#### ACKNOWLEDGEMENTS

All OpenTelemac forum users are thanked for taking their time to carefully explain any Blue Kenue issues they have encountered. They are also thanked for their patience. The NRC-OCRE is thanked for their sponsorship of this work over the past years. All NRC-OCRE past and present employees are thanked for their helpful feedback present in many CHyMS tickets. Martin Serrer is thanked for all of the work he has put into Blue Kenue over the years. I hope that he is now enjoying his well-earned retirement. Ivana Vouk is thanked for the need of new Green Kenue functionality that led to my design of the new Map File(s) functionality. Sean Ferguson is thanked for sharing 632 LiDAR datasets in XYZ format with me. Parishat Tanakoor is thanked for his excellent work migrating and helping to update the Blue and Green Kenue User Manuals that will make their way into future installers. Vahid Pilechi is thanked for this ideas in the section on possible Blue Kenue and micro-plastics related future directions and Hossein Babaei is thanked for his ideas in the section related to Blue Kenue and KHIONE. The anonymous reviewer is thanked for their time spent reading and commenting on the first submitted version of this paper. And lastly, Enda Murphy is thanked for his insightful internal review comments for both the initial and final submissions of this paper.

#### REFERENCES

- [1] Canadian Hydraulics Centre, National Research Council Canada (September 2011). “*Blue Kenue Reference Manual*”
- [2] TELEMAT-MASCARET consortium (August 2019). “*open TELEMAT-MASCARET – The mathematically superior suite of solvers – forum*”. Retrieved from <http://www.opentelemac.org>
- [3] Ocean, Coastal and River Engineering, National Research Council Canada (August 2019). “*Canadian Hydrological Model Stewardship Frequently Asked Questions*”. Retrieved from <https://chymn.nrc.gc.ca>
- [4] Wikipedia® (August 2019). “Adobe FrameMaker”. Retrieved from [https://en.wikipedia.org/wiki/Adobe\\_FrameMaker](https://en.wikipedia.org/wiki/Adobe_FrameMaker)
- [5] LaTeX3 Project (August 2019). “The LaTeX Project”. Retrieved from <https://www.latex-project.org/>
- [6] National Research Council Canada (August 2019), “*Blue Kenue: software tool for hydraulic modellers*”. Retrieved from <https://nrc.canada.ca>
- [7] Province of New Brunswick, Canada (October 2019), “*GeoNB Data Catalogue*”. From <http://www.snb.ca/geonb1/e/DC/catalogue-E.asp>



# Open channel model using a coupled MASCARET-MATLAB Model

Matthieu Breysse  
Hydraulic Engineering Center  
EDF  
La Motte Servolex, France  
[matthieu.breysse@edf.fr](mailto:matthieu.breysse@edf.fr)

**Abstract** — In studies performed by EDF's Hydro Engineering Centre, MASCARET software is widely used to model channels with associated dams and power plants.

This paper presents MASCARET simulations made to estimate the impact of a Programmable Logic Controller (PLC) dysfunction on the water level in the channels.

When the PLC that governs the level and flow regulation on the dam is not working, different scenarios are simulate with Mascaret to estimate where and when the water level will reach the top of the side embankments of the open-channels upstream of the dam.

This paper presents:

- MASCARET model used
- Power plants and dams characteristics
- MASCARET simulations with PLC dysfunction
- MASCARET MATLAB simulations with PLC dysfunction and additional safety PLC installed
- TELEMAC-2D simulation

## I. MASCARET MODEL

Fudaa-Mascaret version : 3.6

Code : Mascaret 8.1

Unsteady subcritical flow calculation

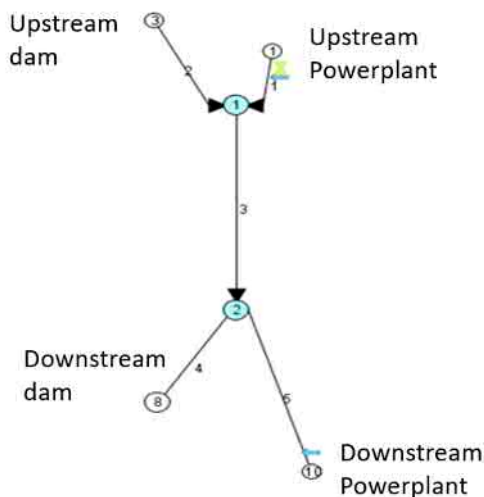


Fig. 1 Mascaret Model

Boundaries conditions used:

- 3 hygrograms for the 2 power plants and the upstream dam.
- Weir defined low  $Q = f(Z_{\text{upstream}})$  for the downstream dam [1]

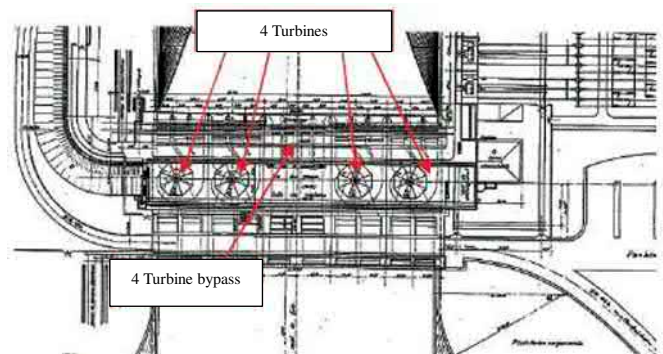
The time step is constant and is equal to 2 s.

The mesh is discretized with a size of 20 m along the 20 km of channels.

The blue arrows on the figure 1 represents the navigation locks.

## II. DOWNSTREAM POWER PLANT AND DAM

Downstream power plant has 4 turbines and a design flow of  $1680 \text{ m}^3/\text{s}$ . In case of turbines triggering, 4 turbine bypass can evacuate  $1280 \text{ m}^3/\text{s}$ .



Downstream dam is a 178 m long and 5 open gate-structure dam. Each of the 5 sluices is equipped with 2 fixed wheel gates:

- Overtopping superior gate
- Rising inferior gate

Each of the 5 sluices can spill up to  $1200 \text{ m}^3/\text{s}$

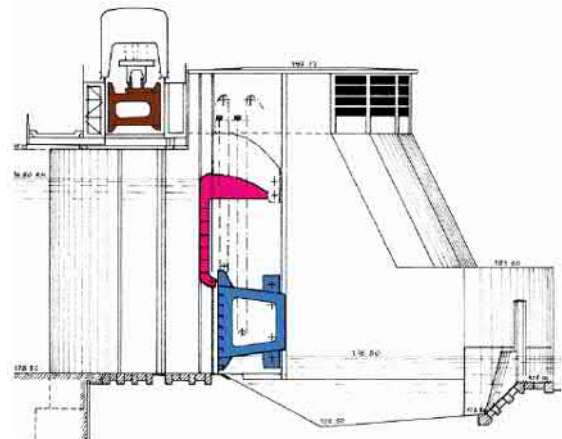


Fig. 2 Downstream dam cross section

The downstream dam have a new PLC and the MASCARET simulations will be used to estimate PLC dysfunction consequences.

### III. MASCARET SCENARIOS WITH DOWNSTREAM DAM PLC DYSFUNCTION

5 scenarios with PLC dysfunction are simulated:

- Scenario 1 : 2 cumulated disorders  
Constant flood gradient of the upstream dam  
Downstream dam's PLC out of order with all gates closed
- Scenario 2 : 3 cumulated disorders  
Downstream power plant flow from 1680 m<sup>3</sup>/s to 0 m<sup>3</sup>/s: 4 turbines triggered and turbines bypass out of order  
Downstream dam's PLC out of order with all gates closed
- Scenario 3 : 3 cumulated disorders  
Downstream power plant flow from 1280 m<sup>3</sup>/s to 960 m<sup>3</sup>/s: 4 turbines triggered and turbines bypass partially working  
Downstream dam's PLC out of order with all gates closed
- Scenario 4 : 3 cumulated disorders  
Downstream power plant flow from 1680 m<sup>3</sup>/s to 960 m<sup>3</sup>/s: 4 turbines triggered and turbines bypass partially working  
Downstream dam's PLC out of order with gates opened with 2640 m<sup>3</sup>/s outflow
- Scenario 5 : 2 cumulated disorders  
Inadvertent opening of the upstream dam  
Downstream dam's PLC out of order with all gates closed

For the 5 scenarios, water flow lines are computed on the 5 channels of the model.

The computation is ended when the water level reach the crest of the side embankment.

As a conservative approach, the calculated values are increased to incorporate uncertainties.

- Water raise compare to initial water flow lines are increased by 10%
- Duration before the water level reach the crest of the side embankment is reduced by 13%

As the scenario computed cannot be tested for real onsite, this method affords a greater level of protection.

Below is an example of result for the 4<sup>th</sup> scenario; the increased water flow line reach the crest of the side embankment in the headrace canal of the downstream power plant.

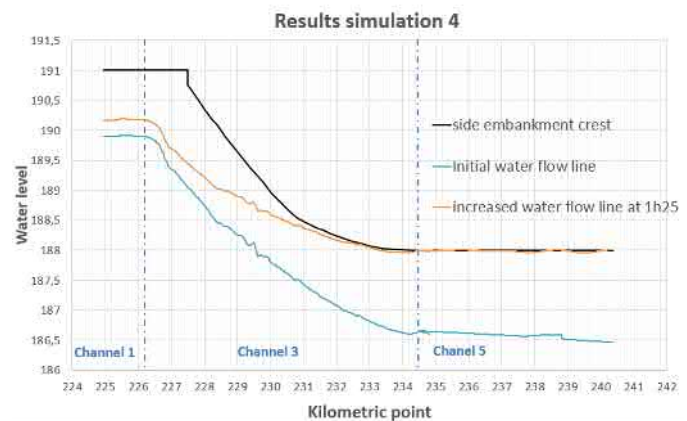


Fig. 3 Result for the 4<sup>th</sup> scenario  
Based on the increased flow line at 1h25m, the time evolution of the water level at the first location where the water will reach the crest is as following:

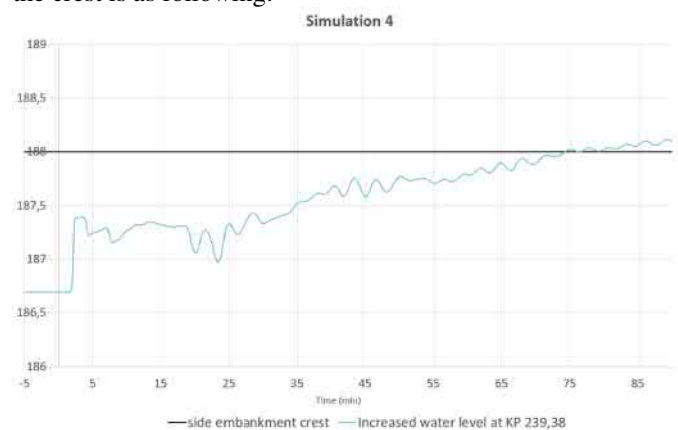


Fig. 4 Time evolution for the 4<sup>th</sup> scenario

The reduction of 13% of the duration suggest a potential reach of the side embankment crest after 1h15m.

The 5 scenarios allow to estimate the risk associated with the downstream dam PLC dysfunction (where and when the water level will reach the side embankment).

For scenarios associated with PLC error, FUDAA-MASCARET simulations showed a risk of spill along the side dams of the open-channel upstream of the dam.

Based on MASCARET results; to avoid spills and to strengthen the safety, EDF decided to install a safety PLC in association with the new regular PLC of the downstream dam.

The 5 scenarios are replayed with the simulation of the safety PLC.

### IV. MASCARET SCENARIOS WITH DOWNSTREAM DAM PLC DYSFUNCTION AND SAFETY PLC MODELED

The safety PLC is activated by floating switches when water level is higher than regular water level at the downstream dam. The safety PLC will maneuver the gates to stop the water level rising.

The safety PLC:

- Is activated when the float switch level sensor detect the rising level
- Commands the gates maneuvers
- Is deactivated when the float switch level sensor detect the lowering level

Safety PLC modelling in MASCARET need a complex boundary condition for the downstream dam. Indeed the downstream dam flow will vary with:

- Gates positions
- Upstream water level
- Downstream water level (downstream level can lower the theoretical gates flows)

3 options have been considered to model the scenarios with safety PLC operating the gates:

- A) MASCARET solution with the use of the boundary condition « Gate opening Z inf, Z sup = f(t) [2]
- B) Call MASCARET API with Python script
- C) Call MASCARET API with Leg'Eau

A) The boundary condition « Gate opening Z inf, Z sup = f(t) [2] is supposed to simulate a gate maneuvers. This condition has never been used in EDF Hydro studies and cannot model the complexity of the flow calculation.

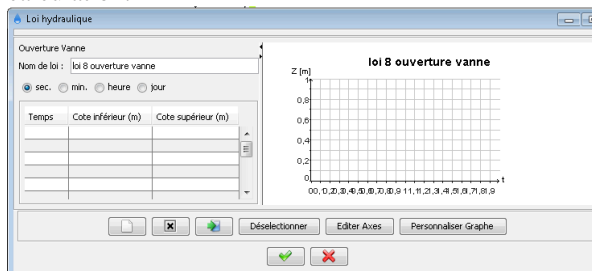


Fig. 5 Boundary condition Gate opening Z inf, Z sup

- B) Call MASCARET API with Python script that will calculate a new Weir defined low  $Q = f(Z_{\text{upstream}})$  at each time step.
- C) In association with EDF R&D, a MATLAB overlay called LEG'EAU has been built and used for several years by EDF Hydro engineers. This overlay, can do the pre and post-processing and can simulate the operation and the PLC of all boundaries of the model.

For this study, LEG'EAU was used to simulate a MASCARET model with variable boundary condition at the downstream dam ; when the safety PLC is activated, a new boundary condition is calculated with MATLAB for every time step.

This MATLAB MASCARET model was used to determine:

- Height of the switch level sensor that will active the safety PLC
- Safety PLC routine to command the gates maneuvers and to prevent any water level rising

## V. TELEMAC 2D MODEL TO DETERMINE THE POSITION OF SWITCH LEVEL SENSORS

Additionally to 1D simulation, a TELEMAC 2D model was used to determine the position of switch level sensors that will activate safety PLC of the downstream dam.

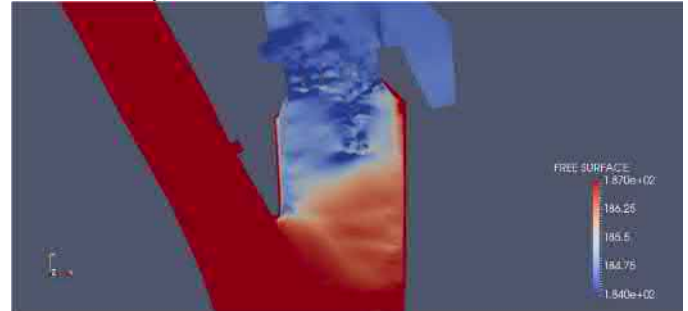


Fig. 6 Telemac 2D result

The figure 6 shows the free surface with a flow of 6000 m<sup>3</sup>/s through the 5 opened sluices of the dam.

As showed on the figure bellow, important level variation can appears between right and left bank of the dam:

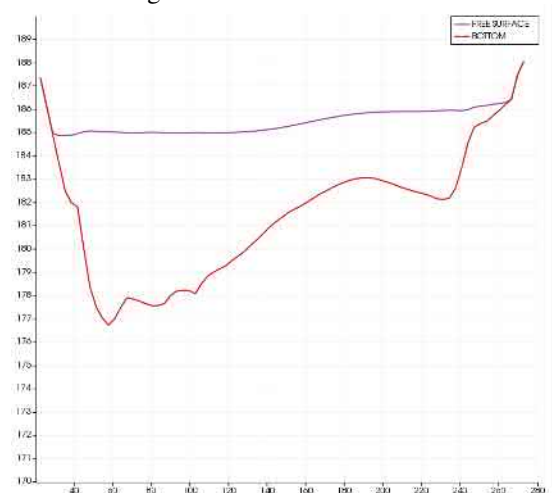


Fig. 7 TELEMAC 2D cross section result at the downstream dam

This figure shows that for high flow with the 5 sluices of the dam opened, the main flow is located on the left bank, where there is a strong lowering of the free surface.

To avoid being sensitive to the local drops of water, it was chosen to implant the switch level sensors on the beginning of the right bank at the headrace canal.

## VI. CONCLUSION

**MASCARET software allow to represent great lengths (20 km of channels) and simple boundaries conditions.**

**When a PLC needs to be model, MASCARET has no native solution to do so and a MATLAB MASCARET was used to simulate safety PLC.**

**To parameter the safety PLC using MATLAB MASCARET results, a fruitful collaboration between hydraulic and control-command engineers is needed.**

**To strengthen the methodology of the evaluation of a PLC dysfunction, it would be also important to evaluate the probability of the studied scenarios.**

REFERENCE

- [1] Mascaret v8.0 Application guide Copyright 2014 EDF – CEREMA
- [2] Guide de prise en main Fudaa Mascaret 3.0 – Notice GT 08.01 Avril 2008



# TatooineMesher: Anisotropic interpolation from 1D cross-sections and 2D channel mesher

Luc Duron, François-Xavier Cierco  
Hydraulic Engineering Department  
Compagnie Nationale du Rhône  
Lyon, France  
[l.duron@cnr.tm.fr](mailto:l.duron@cnr.tm.fr)

Khaled Saad  
Numerical modelling and high performance computing  
University of Bordeaux  
Bordeaux, France

**Abstract** — A set of scripts named TatooineMesher were developed at CNR to provide tools for the modeller to mesh rivers and interpolate bathymetry from discrete cross-section data for TELEMAC-2D calculations. The principles are also applied to the visualization of 1D model results (including MASCARET) as the surface reconstruction problem from discrete data is the same. The scripts made available for the community, are written in the Python programming language and rely on many standard scientific libraries.

The meshing and interpolation processes are described separately as they are implemented as such for the sake of versatility. The meshing part consist of a regular mesher (structured or not) following constraint lines and including many parameters to control density and positions of nodes. Different anisotropic interpolation methods (following the flow direction) to interpolate data between discrete cross-sections are available to the modeler.

## I. CONTEXT

### A. Aims of the developed scripts

The developed scripts can be applied to the following framework:

- pre-treatment for 1D models: interpolate intermediate cross-sections,
- post-treatment of 1D model: visualize results in 2D, especially in the framework of a coupling with TELEMAC-2D,
- pre-treatment for TELEMAC-2D river model: interpolate bathymetry and/or mesh river bed.

### B. Description of meshing issues

Hydraulic numeric modelling aims to estimate in every point of time and space the hydraulic variables such as: water discharge, water heights and velocities. The horizontal spatial discretization is done on a mesh (or grid) which consists of a set of triangular elements connected together. The mesh quality is crucial as the accuracy (including the diffusion terms) and the computation time are directly affected. Therefore, the definition of the mesh is adapted by the

modeller to its needs to have a satisfactory compromise between accuracy and computation cost.

The main issues to mesh a river are the integration of longitudinal constraint lines, lateral discretization of dykes and integration of structures (such as bridge piers and groynes). TatooineMesher generates a mesh (possibly not structured) with regular element sizes which are controlled by the user through some files (for polylines) and options (at least longitudinal and lateral target edge lengths).

### C. Description of interpolation issues

Hydraulic numerical simulation requires a large amount of topographic data to build an accurate digital elevation model. The bathymetry being often more complex to measure on permanently inundated river beds, long river reaches are usually only surveyed at some regular longitudinal position and discrete 1D cross-sections of the river channel are obtained.

With discrete cross-sections data, measurement points are not regularly spaced and the resolution of the cross-section profiles is generally much higher in the lateral than in the longitudinal direction of the river. That is why isotropic interpolation methods should not be applied and methods considering the anisotropy of the bathymetry were investigated.

The interpolation being crucial to estimate bathymetry between cross-sections, several 1D and 2D interpolation methods (linear, cubic...) were implemented within TatooineMesher and compared (see part IV.B).

### D. Overview of interpolator/mesher existing tools

In framework of 2D hydraulic modelling a large range of tools are available to mesh and/or interpolate a domain. In the TELEMAC community the commonly adopted software are: BlueKenue, Salome-Hydro (SMESH), SMS Mesh Module, Janet and GMSH [1].

Although they are often fast to compute and easy to use (they often include a GUI), they are often affected by some limitations such as:

- for those providing a channel mesher (e.g. BlueKenue, Salome-Hydro):

- mesh cannot be controlled by constraint lines,
- mesh is fully structured and not suited in case of longitudinal variation of the channel width,
- definition of constraint lines is restricted (number or proximity limitations, they must cross all cross-sections...),
- the interpolator is absent or is based on isotropic approaches.

In the context of surface reconstruction, a constraint line is a longitudinal polyline defining a change in the bathymetry. This notion is used in TatoonineMesher to constraint element edges to pass along these lines and to guide the interpolation.

TatoonineMesher aims to fill the lack of functionalities of the available software. Moreover, in the investigated tools, the channel interpolator is often too simple, and the mesh generation cannot be scripted (except for GMSH). For all these reasons, TatoonineMesher was developed as a standalone tool and cover different needs (see part I.A).

## II. MESH GENERATION

### A. General mesh specifications

The mesh generation process has to follow some rules in order to be optimized for further computations and to correspond to the modeller needs. Usual mesh specifications are listed below (not-exhaustive, for more details on mesh quality see [2]):

- nodes preferably located along cross-sections (to limit interpolation),
- nodes preferably located along constraint lines,
- elements edges do not cross constraint lines,
- element size and number of nodes controlled by the user (to optimize the computation time),
- elements are equilateral or possibly elongated along flow direction,
- the transition of element size is progressive.

### B. Steps of the channel mesh generator

The mesh generation is splitted into the 4 main following steps.

#### Step 1: Order cross-sections

- 1.1. Cross-sections are ordered from upstream to downstream. They are located with their curvilinear abscissa along the hydraulic axis,
- 1.2. Cross-sections which do not cross the hydraulic axis are ignored.

#### Step 2: Intersect cross-sections and constraint lines

The following steps describe how the domain delimited by two consecutive cross-sections and two constraint lines is meshed, in a so-called submesh (as see in Figure 1).

#### Step 3: Generate nodes for each submesh

- 3.1. A set of intermediate cross-sections are defined in accordance to the longitudinal space step (see Figure 1a),
- 3.2. Application of an affine transformation to ensure that  $X$  and  $Y$  coordinates of nodes follow constraint lines (see Figure 1b).

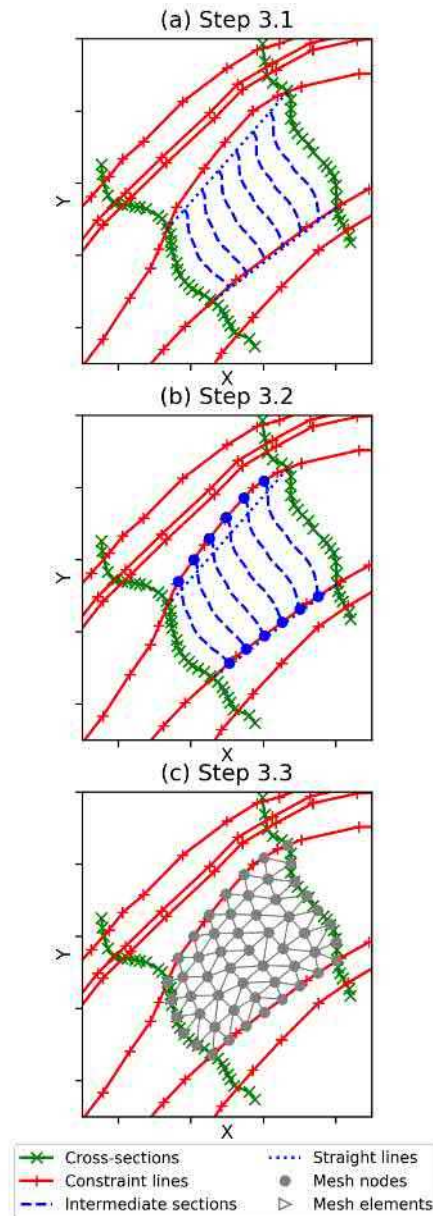


Figure 1 : Illustrations of the mesh generation steps for a single submodel

- 3.3. Lateral sampling of each intermediate cross-sections in accordance to mesh parameters (lateral space step or number of nodes), see Figure 1c.

#### Step 4: Triangulate over the whole domain

A constrained Delaunay triangulation is performed under the following constraints:

- coordinates of vertices/nodes are imposed (defined at step 3.1),

- segments along constraint lines and cross-sections are specified as hard lines.

The generated mesh operation leads to a “planar straight-line graph”.

### C. Overview of main features to control the mesh

#### C.1) Choice of the interpolation method of the coordinates of the constraint lines

If no constraint lines file is specified, TootoineMesher considers the banks of the river (right and left) as two constraint lines (Figure 2a). On the other hand, user defined constraint lines, which can intersect only a subset of cross-sections, are used to delimit the meshed domain (Figure 2b).

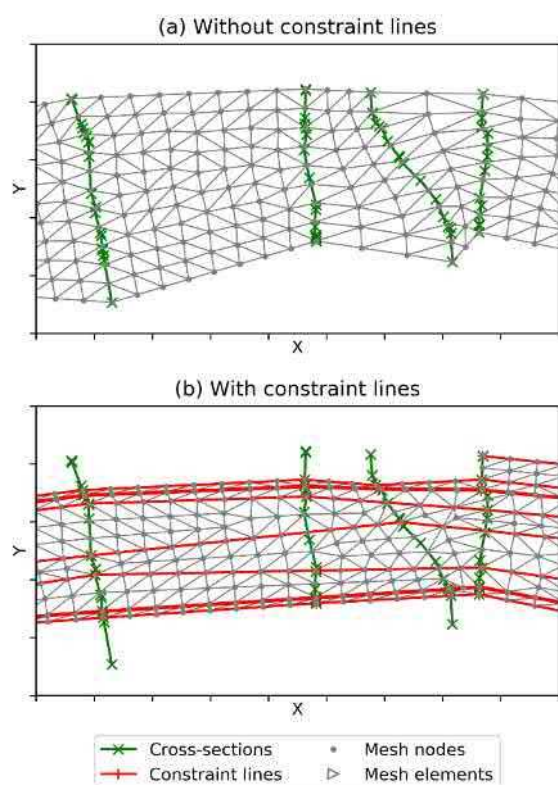


Figure 2 : Meshes generated without constraint lines (a) or with multiple constraint lines (b)

In addition to the vertices defining the constraint lines, the interpolation method between them can be computed with 2 different methods:

- linear interpolation (Figure 3a),
- Cubic Hermite Spline (CHS) interpolation (Figure 3b).

The CHS interpolation method is interesting to smooth constraint lines [3]. Moreover, if the modeller does not provide any constraint line, the river will certainly be less distorted with this interpolation (river width is more conservative).

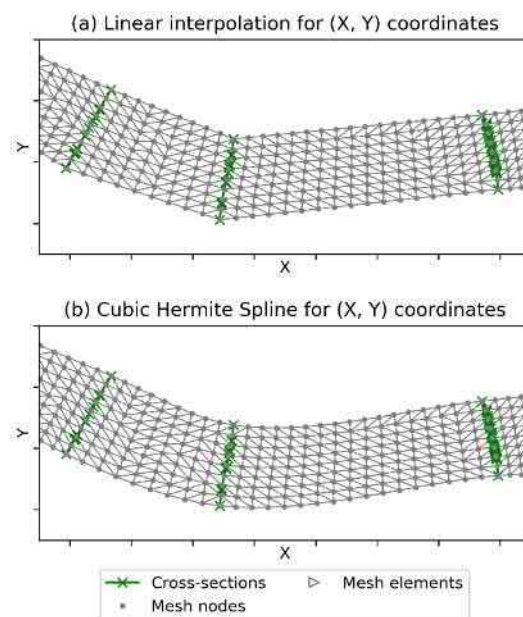


Figure 3 : Linear interpolation for X and Y coordinates of constraint lines (a) or cubic spline interpolation (b)

#### C.3) Option for planar projection of cross-sections

TootoineMesher has an option to make the squiggly cross-sections straight through a planar projection of cross-sections points on the line connecting left and right banks (see Figure 4).

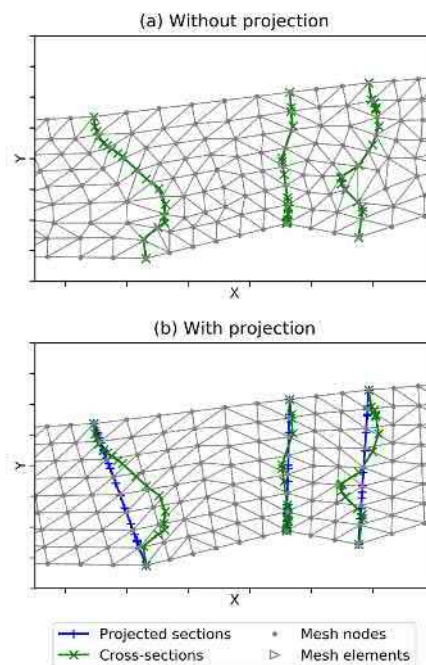


Figure 4 : Meshes generated without (a) or with (b) projection

This option makes the elements mesh adjacent to the cross-sections more organized. The initial bathymetry points are shifted but this can avoid elements to be oriented in the transversal direction.



### C.4) Lateral discretization

The lateral discretization of the mesh can be specified either through a constant space step (Figure 5a) or through a number of nodes along these cross-sections (Figure 5b). The first option is highly recommended if the river width varies, and this will generate an unstructured mesh in the lateral direction.

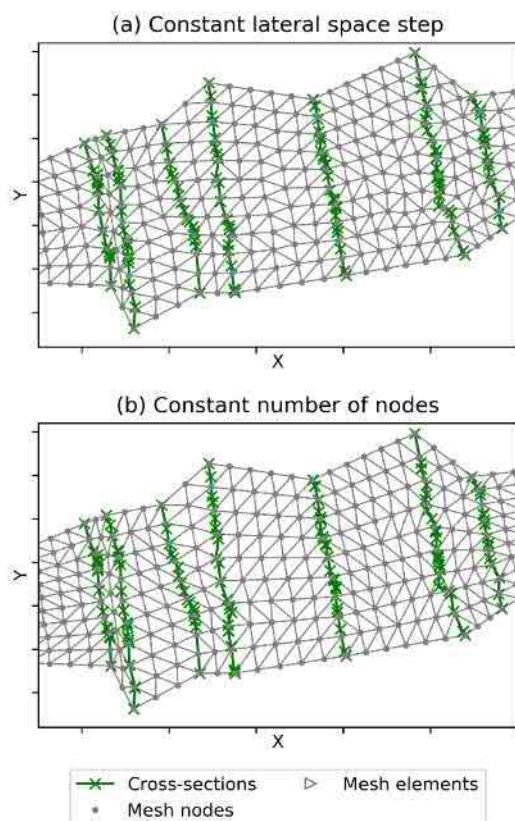


Figure 5 : Lateral discretization of the mesh with a constant lateral space step (a) or a constant number of nodes (b)

### C.5) Longitudinal discretization

The longitudinal discretization of the mesh is controlled by a space step which can be different from the lateral one (elements can be elongated if necessary).

An additional option is provided to the modeller to specify how intermediate points are defined. Two approaches are available:

- number of intermediate cross-sections is determined for each bed (or submesh) individually, leading to an unstructured mesh (Figure 6a),
- or is unique per profile (Figure 6b).

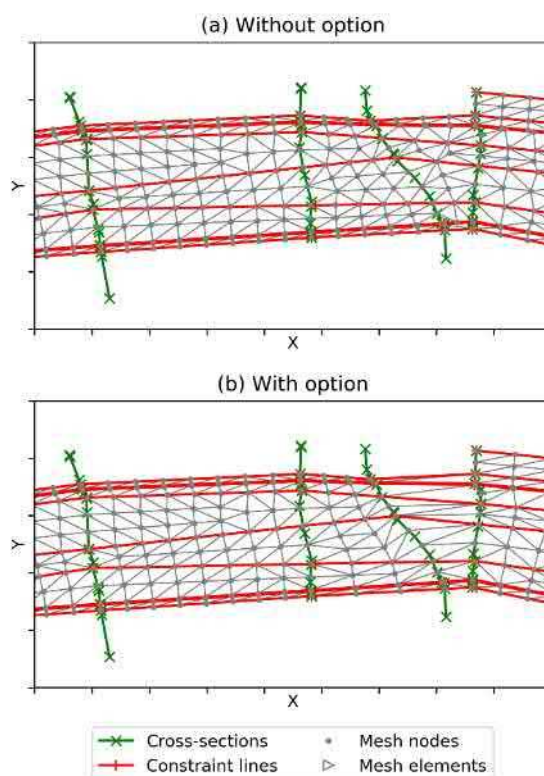


Figure 6 : Number of intermediate lines between two consecutive cross-sections different for each submesh (a) or identically laterally (b)

## III. INTERPOLATION

After having determined the nodes localization (during the mesh generation, see part II), the bathymetry elevation (or any variable defined along each cross-section) can be interpolated at their positions. This section presents the importance of the choice of spatial interpolation methods in interpolating river bathymetry.

### A. Isotropic interpolation methods not suitable

Some standard isotropic interpolation methods were tested to analyse their suitability to reconstruct surface from discrete cross-sections. Three interpolation methods already implemented in many GIS software are compared in Figure 7. The input data set consisting of cross-sections is represented in black and the reference (measured) surface corresponds to the left subplot.

This analysis shows that standard isotropic methods have major limitations/issues:

- interpolated bottom can be discontinuous,
- complex geometry might lead to inconsistencies, especially in curvatures or in case of non-straight cross-sections.



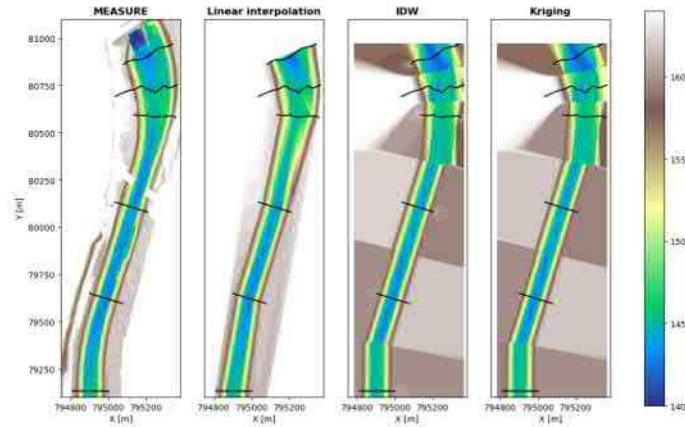


Figure 7 : Bathymetry measured (left) compared to interpolated bathymetry from elevation along cross-sections (3 interpolation methods: Linear; IDW (Inverse distance weighting) and Kriging)

### B. Flow-oriented coordinate system

The mesh built with TatooineMesher has a set of nodes regularly distributed in every submeshes. Each node can be identified with its  $X$  and  $Y$  coordinates in the Geographic coordinate system (e.g. Figure 1) or with the couple of coordinates  $(x_t, x_l)$  per submesh. These latter coordinates (ranging from 0 to 1) correspond respectively to the lateral and longitudinal dimensionless curvilinear distances (see Figure 8). The corresponding coordinate system is called “flow-oriented” and enables to take into account the anisotropy of the bathymetry (the 2 axes are orthogonal).

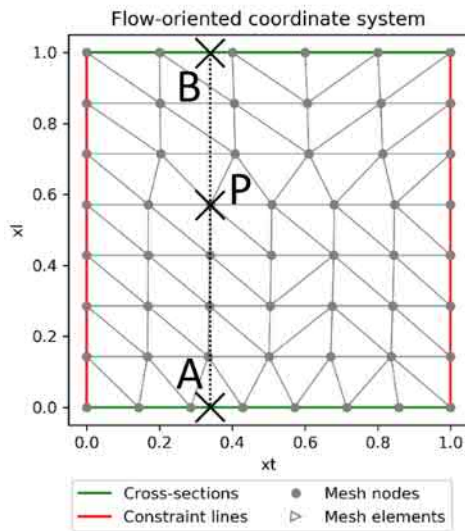


Figure 8 : Single submesh displayed in the flow-oriented coordinate system

### C. Consecutive 1D interpolators (lateral then longitudinal)

$P$  being a node between 2 consecutive cross-sections (with indices  $i$  and  $i + 1$ ). The bathymetry of  $P$  (denoted  $Z_P$ ) can be interpolated from its position  $(x_t, x_l)$  in the flow-oriented coordinate system. The bathymetry can be determined (for each bed individually) with 2 consecutive 1D interpolations as presented hereafter.

1. Two lateral interpolations to have  $Z_A$  and  $Z_B$ :  
 $Z_A = Z_i(x_t)$  and  $Z_B = Z_{i+1}(x_t)$
2. Longitudinal interpolation between these 2 values:  
 $Z_P = Z(x_t, x_l) = (1 - x_l) Z_A + x_l Z_B$

In the previous equations,  $Z_i(x_t)$  corresponds to the bottom elevation at  $x_t$  position along section  $i$ . The points  $A$  and  $B$  are respectively located along sections  $i$  and  $i + 1$  (thus their coordinates are  $(x_t, 0)$  and  $(x_t, 1)$  in the flow-oriented coordinate system).

The two distinct interpolations (lateral and longitudinal) can possibly be based on different methods. In the context of surface reconstruction from cross-sectional data, the linear interpolation is widely used (see [3] and [4]). In this section, only the choice of the lateral interpolation is analysed. A more complete comparison is presented in part IV.B.

The methods tested and implemented in TatooineMesher are:

1. Linear interpolation (polynomial of degree 1);
2. Spline interpolation (polynomial of degree 3) with different assumptions at boundaries:
  - a. Cubic spline,
  - b. Akima,
  - c. Piecewise Cubic Hermite Interpolating Polynomial (PCHIP).

A comparison of the interpolation methods on a simple cross-section is shown in the figure below. All the different methods ensure that the interpolated values pass through initial points.

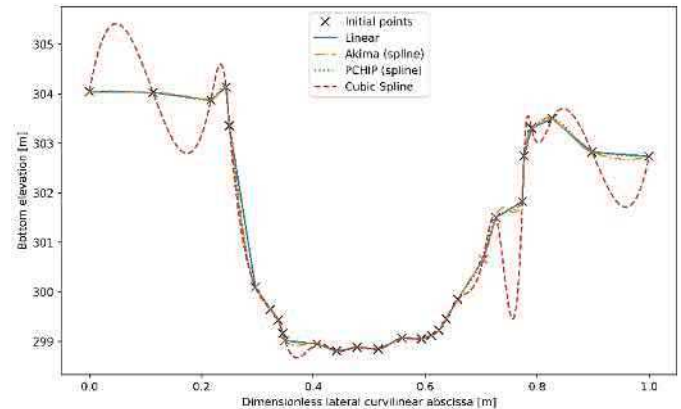


Figure 9 : Comparison of lateral interpolation methods for a cross-section

### D. Global 2D interpolators

A more complex approach is to perform a 2D interpolation for the whole domain in a global flow-oriented coordinates, which means that the y-axis corresponds to non-dimensionless values ( $x_l$  being interpreted a sequence ranging from 1 to the number of cross-sections). This method is not compatible if the number of constraint lines changes over the longitudinal direction ( $x_t$  would not be consistent). The bilinear and bicubic methods are implemented in TatooineMesher.

## IV. RESULTS AND DISCUSSIONS ON TEST CASES

## A. Mesh generation on “L’Étournel” site

A limited domain on the Upper Rhône River (upstream Génissiat dam) called L’Étournel is chosen to compare meshes generated with TutooineMesher with different space discretization options. This simple data set, presented in Figure 10, includes 25 cross-sections intersected by at most 5 constraint lines.

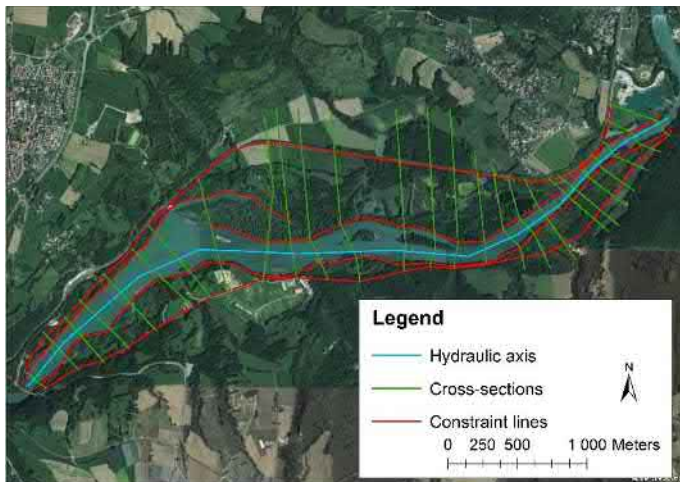


Figure 10 : Geometrical data used to mesh “L’Étournel” site

The different space discretization choices compared are presented in the Table 1.

Mesh ID	Lateral discretization	Option to have laterally the same number of nodes per submesh (see II.C.5)	Longitudinal discretization
1	$\Delta X_t=20\text{m}$	Without option	$\Delta X_l=20\text{m}$
2	$\Delta X_t=20\text{m}$	Without option	$\Delta X_l=30\text{m}$
3	$\Delta X_t=20\text{m}$	With option	$\Delta X_l=20\text{m}$
4	30 nodes	-	$\Delta X_l=20\text{m}$

Table 1 : Mesh generation parameters tested on L’Étournel site

The generated mesh characteristics are compared in Figure 11 with multiple probability density functions:

1. elements area
2. edge ratio per element
3. minimal angle per element.

The first barplot shows that the generated meshes have different number of nodes. The elongation of elements along the longitudinal direction (mesh 1 vs 2 which have a ratio of 1.5) is very efficient to minimize the number of elements (and indirectly the time step if CFL is fixed), and of course the minimal angles are getting slightly worse.

The quality of mesh n°4 is the worst, the element shape being highly heterogenous because the river reach width varies, while the number of nodes remain constant transversally. Consequently, the number of elements with an angle less than  $30^\circ$  is high.

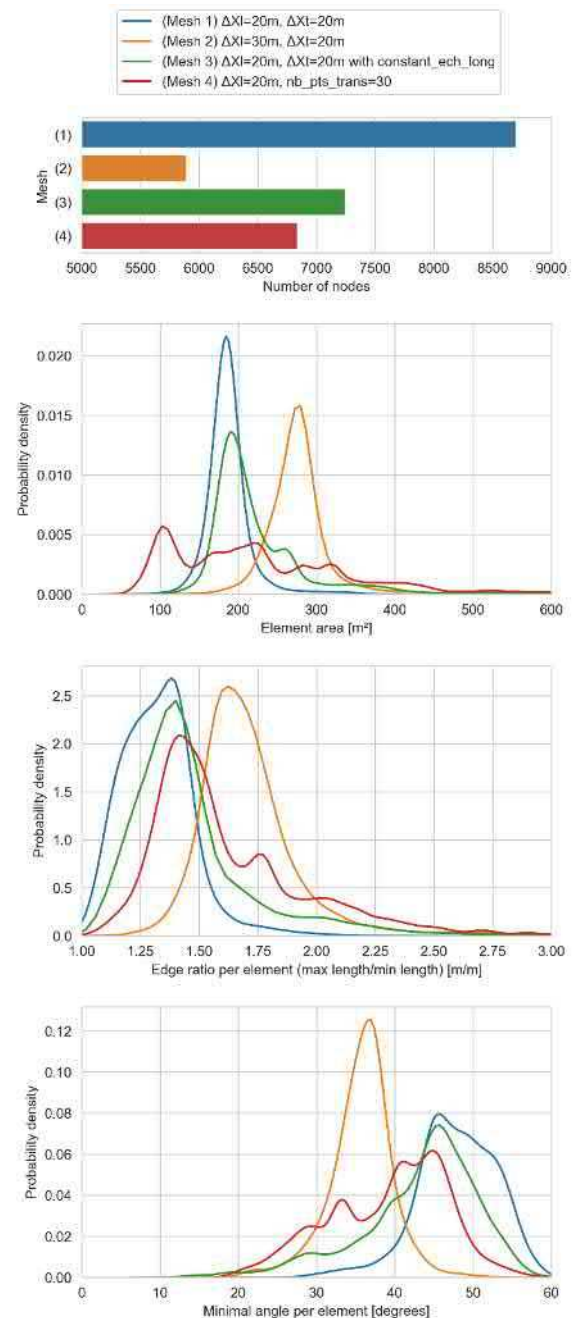


Figure 11 : Statistics on generated meshes

## B. Interpolation methods benchmark on a part of the Rhône river

A validation test case was used to compare a reference surface to the interpolated surfaces (with methods presented in parts III.C and III.D). The reference surface was measured by LIDAR and multi-beams to get a very fine dataset of 3D points.

The test case is in the region of Vaugris, which is located along the Rhône river. The river reach considered is 10km long and the river width is about 200m. A set of 27 cross-sections are positioned regularly at each 400m (see Figure

12). The cross-sections are straight and composed of 20 points. Two lateral constraint lines are used to define the river bed to be meshed.

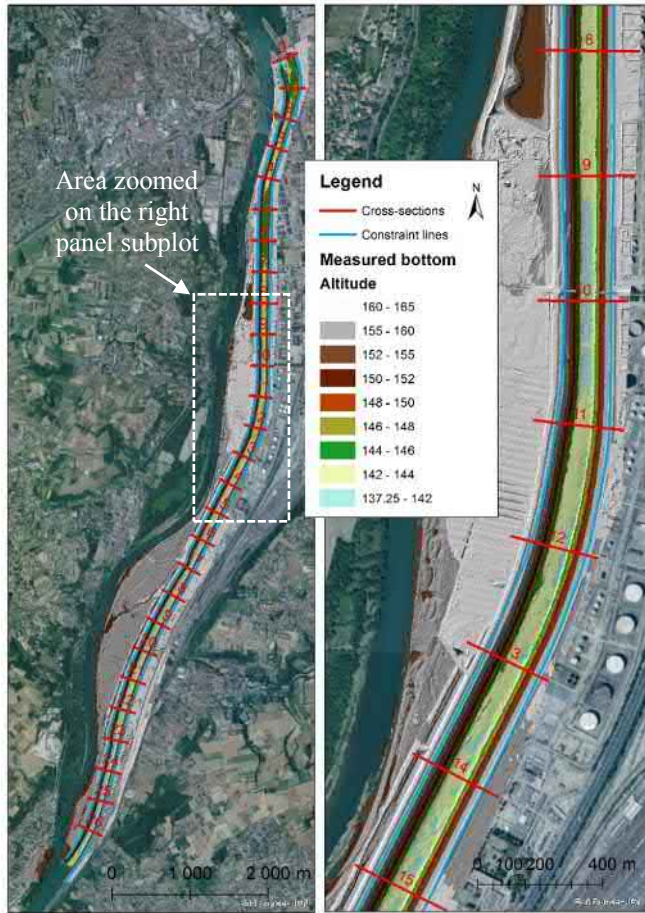


Figure 12 : Map of the “Vaugris” validation test case with the reference surface and input data (cross-sections and constraint lines)

This validation test case was used to compare the different interpolation methods with all other parameters and input data being equal. Six meshes were generated with strictly the same characteristics (space step are  $\Delta X=6.5\text{m}$  and  $\Delta X_L=10\text{m}$ , 50k elements) but with values at nodes depending on the interpolation method used. Two 2D global interpolation methods and four 1D lateral interpolation methods (in combination with a linear longitudinal interpolation) are compared.

As expected, differences between computed surfaces and the reference surface are spatially varying and are larger far from input data than in the vicinity of cross-sections data points. The performance of the different interpolation methods is assessed with the calculation of some statistical criteria:

- MSD = Mean Standard Deviation (closest to 0 is better),
- MAD = Mean Absolute Deviation (lowest is better),
- RMSD = Root-Mean Square Deviation (lowest is better).

These criteria are computed with PyTelTools [5] on the domain meshed by removing some specific local zones

(vicinity of bridges not represented by cross-sections) to compute reliable differences. Results are plotted in the Figure 13 for the 6 interpolation methods. The generated surfaces have almost a null bias (less than 3cm) and the absolute differences are on average around 48cm. The lateral 1D interpolation methods play a role in the interpolation because cross-section resolution is not very fine (with “only” 20 points) and the Akima spline interpolation performs well. Therefore, this latter lateral interpolation is recommended if cross-sections are not finely discretized, but if not, linear interpolation remains a very efficient and robust method.

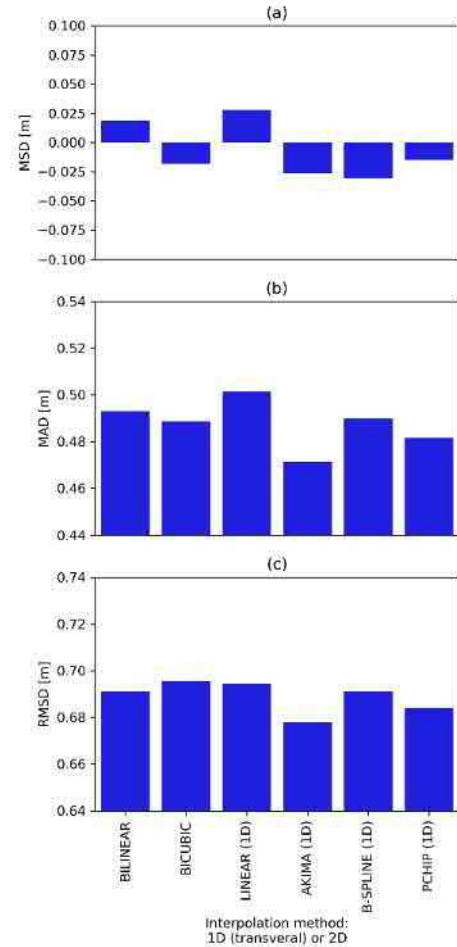


Figure 13 : Criteria computed to compare interpolation methods (a=MSD, b=MAD, c=RMSD)

## V. MAIN APPLICATIONS OF TATOOINEMESHER

The three main applications of TatooineMesher (see part I.A) correspond to different scripts which are described in this section.

### A. Densify profiles (*densify\_profiles.py*)

This tool is used to refine 1D cross-sections for a further 1D calculation, no mesh being generated.

### B. Interpolator and mesher (*interpolator\_and\_mesher.py*)

This script is dedicated to interpolation and/or channel meshing for 2D models.



### C. Visualize 1D model results (*mesh\_crue10\_run.py* and *mesh\_mascaret\_run.py*)

This last tool is based on the same principle of *interpolator* and *mesher.py* but input data correspond to a 1D model (composed of a set of branches with its associated cross-sections) and output file contains 2D temporal generated surfaces for every variable. The following data can be meshed and visualised:

- model geometry: bathymetry and friction coefficient spatialization,
- 1D hydraulic results: a set of steady states or a transient simulation. Variables might be 1D (do not change laterally, see Figure 14) or 2D as seen in Figure 15.



Figure 14 : Visualization of a 1D variable (Froude number) at a given time

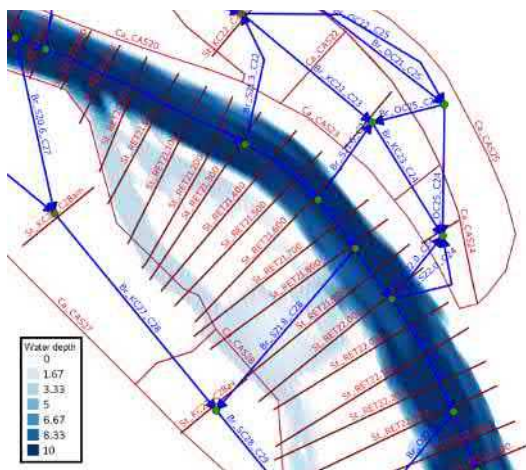


Figure 15 : Visualization of a 2D variable (water depth) at a given time

## VI. HOW TO USE THE SCRIPTS

### A. Installation and requirements

TatooineMesher is released under the GPLv3 license. The source code was developed in Python version 3 and relies on several Python scientific libraries:

- *NumPy*: numerical library for large multidimensional arrays, and high-level mathematical routines [6],
- *SciPy*: used for several interpolation methods [7],
- *triangle*: simple mesh generator proving a triangulation [8].

In addition to these standard packages, external packages (available on <https://github.com/CNR-Engineering>) are used to parse files:

- *PyTelTools*: to write mesh files from a given triangulation [5],
- *Crue10\_tools*: to read 1D geometry and results files from Crue and Mascaret (based on new *postel* module).

### B. Command line interface scripts

The developed scripts can be run through a command line with the relevant arguments. The help message can be displayed with *-h* argument. For more details, see online at <https://github.com/CNR-Engineering/TatooineMesher/wiki>.

### C. File formats used in TatooineMesher

Input data files can be provided in different formats and should fulfil some conditions. The Table 2 summarized them for the 3 types of input file.

File containing	Supported formats	Expected data
Cross-sections	shp, i3s	3D lines in arbitrary order but described longitudinal in the same direction (right to left bank, or the opposite)
Hydraulic axis	shp, i2s	A single 2D line oriented from upstream to downstream
Constraint lines (optional)	shp, i2s	At least 2 lines, not intersecting them and oriented in the same direction as the hydraulic axis
1D model	Crue10, Mascaret	Geometry and hydraulic results at sections
Output mesh	slf, t3s, LandXML	Mesh which can contain multiple temporal frame and variables

Table 2 : Characteristics of data input and output files of TatooineMesher

## VII. CONCLUSION AND PERSPECTIVES

TatooineMesher is a set of scripts released by CNR to provide efficient tools for 1D and 2D river modelling engineering with MASCARET and TELEMAC-2D. A channel mesher and an anisotropic interpolator were developed to reconstruct a 2D continuous surface from data at discrete cross-sections. A more complex mesher (e.g. GMSH) could be combined with TatooineMesher to mesh the floodplain or to provide an alternative mesher for river bed (to finely mesh obstacles and to adapt node density spatially). This will probably be investigated in the future.

## REFERENCES

- [1] C. Geuzaine and J.-F. Remacle, "Gmsh: a three-dimensional finite element mesh generator with built-in pre- and post-processing facilities". International Journal for Numerical Methods in Engineering 79(11), pp. 1309-1331, 2009
- [2] U. H. Merkel. "Generation and Quality of Unstructured Meshes", Telemac User Conference 2013, Karlsruhe (Germany)
- [3] D. Caviedes-Voullème et al., "Reconstruction of 2D river beds by appropriate interpolation of 1D cross-sectional information for flood simulation", Environmental Modelling & Software 61, 2014
- [4] B. Schäppi et al., "Integrating river cross section measurements with digital terrain models for improved flow modelling applications", Computers & Geosciences, 2009
- [5] L. Duron, Y. Wang, "PyTelTools: Python scripts and GUI to automate Telemac post-processing tasks", 2017, Graz (Austria)
- [6] T. E. Oliphant. A guide to NumPy, USA: Trelgol Publishing, 2006
- [7] E. Jones, T. Oliphant, P. Peterson, et al., SciPy: Open Source Scientific Tools for Python, 2001, <http://www.scipy.org/> [Online; accessed 2019-08-09].
- [8] J. R. Shewchuk, "Triangle: Engineering a 2D Quality Mesh Generator and Delaunay Triangulator", in Applied Computational Geometry: Towards Geometric Engineering, May 1996.



# Porting TELEMAT-MASCARET to OPENPOWER and experimenting GPU offloading to accelerate the TOMAWAC module

Judicaël GRASSET, Stephen M. LONGSHAW, Charles MOULINEC, David R. EMERSON  
STFC Daresbury Laboratory  
Warrington, United Kingdom  
judicael.grasset@stfc.ac.uk

Yoann AUDOUIN, Pablo TASSI  
EDF R&D  
Chatou, France

**Abstract**—In this paper the state of porting TELEMAT-MASCARET on the OPENPOWER architecture with different compilers is shown. A port to GPUs with OpenMP and OpenACC of a computationally intensive subroutine of TOMAWAC is also explained and the performance benefits shown, a comparison with an x86-64 machine is also presented. Finally ongoing work is presented and discussed: the port of a complete and more challenging test-case, a triple coupling case from EDF.

**Keywords:** OPENPOWER, POWER8, TOMAWAC, GPU, OpenACC, OpenMP

## I. INTRODUCTION

Currently TELEMAT-MASCARET is parallelised with MPI, although attempts at hybrid parallelism have been tried in the past [1]. Improving the parallelisation of TELEMAT-MASCARET is useful for users who frequently perform simulations that take a long time to calculate. Current computer trends favour the increase of the number of cores in a single processor and, as shown by Fig. 1, this is being combined with the addition of accelerators such as GPUs, and memory interconnects designed to reduce the latency that is introduced by transferring data between different memory locations. It is therefore now important that TELEMAT-MASCARET is modified to take advantage of this new kind of architecture.

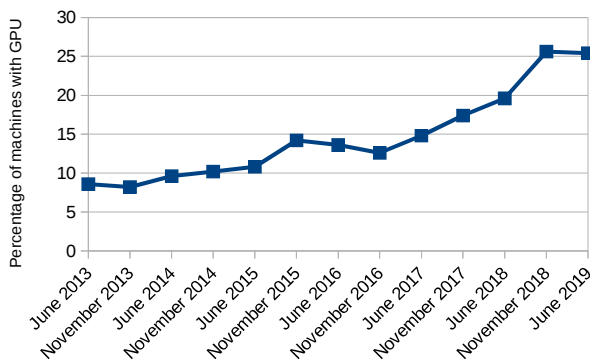


Figure 1. Evolution of the percentage of machines in the Top500 list that have GPUs in them.

There are two key options when choosing how best to run on GPUs, taking a low-level approach and programming directly with OpenCL or CUDA, or using pragma-based programming with OpenMP or OpenACC. The first option gives more control and usually more performance but it also means that a specific code has to be written and that two different versions of the same kernel have to be maintained. However, when using the pragma-based approach, changes to the code do not infer a re-write of the kernel, with the bulk of the changes needed being the addition of pragmas around the existing code. This approach reduces the burden on those that maintain the original codebase and means acceptance of changes is more likely. This work therefore concentrates on enabling GPU acceleration of portions of TELEMAT-MASCARET using a pragma-based approach.

This paper first presents a kernel of Tomawac ported to GPUs using OpenMP and OpenACC pragmas and tested on OPENPOWER and x86-64 architecture. The possibility of using GPUs acceleration on a more challenging test-case provided by EDF is then explored.

## II. RELATED WORK

An attempt to use GPUs with TELEMAT-MASCARET has already been made [1], however the method presented is different from the one described in this article. In [1], the authors replaced the original matrix-vector product of TELEMAT-MASCARET with the one from the MAGMA library [2], which is then able to be offloaded to GPU.

The primary problem they encountered was that the MAGMA library was not using the same matrix format as TELEMAT-MASCARET. Doing the conversion before and after every matrix-vector product prevented any real-world performance improvement. This work shows how directly accelerating the existing code without modifying the data structure used by TELEMAT-MASCARET is a better approach.

## III. MACHINES USED

### A. Paragon

The OPENPOWER foundation [3] is a consortium of entities working to provide an architecture revolving around the POWER processors and accelerators. In this work the

architecture used consists of IBM POWER8 processors and NVIDIA GPUs. The processors are interfaced to the GPUs with NVLink instead of PCI-Express. NVLink is a high-bandwidth proprietary interface developed by NVIDIA [4], it is also used here to enable GPU to GPU interconnection.

This work has almost entirely been done on the UK Research and Innovation Science and Technology Facilities Council's (UKRI-STFC) Paragon POWER8 cluster, maintained and run by the Hartree Centre [5] at Daresbury Laboratory in the UK. Each node of the cluster consists of 2 POWER8 CPUs, each with 8 physical cores (up to 8 hardware threads per core) and 4 NVIDIA P100 GPUs with NVLink 1.0 interconnects. Each P100 has 16GB of memory and the 2 POWER8 CPUs share 1TB of memory.

#### B. Wilkes-2

The Wilkes-2 cluster [6] is hosted at Cambridge University, in the UK. Each node of the cluster consists of one Xeon E5-2650 v4 2.2GHz CPU with twelve physical cores, and four NVIDIA P100 GPUs. Each P100 has 16GB of memory and the node has 96GB of memory.

The Wilkes-2 cluster has the same GPUs as the Paragon cluster, so little difference in computation time is expected between them. However, the Paragon cluster has NVLink to transfer data between the CPUs and GPUs, while Wilkes-2 has standard PCI-Express which means that in the case of high-volume data-transfer between CPUs and GPUs the Paragon cluster has an advantage.

### IV. PORTING TO THE OPENPOWER ARCHITECTURE

Before working on accelerating parts of TELEMAT-MASCARET using GPUs, it was first necessary to port and compile it using the OPENPOWER architecture. During testing, a significant bug with GCC for OPENPOWER was discovered, through this work this has been reported [7] and fixed in GCC 9.1. Similarly, a number of internal bugs within IBM's XL compiler have been found by this work, reported and fixed in the version 16.1.1.1. A single compilation issue when using the XL compiler remains in the current TELEMAT-MASCARET code-base but is easily rectified with a small patch. Finally, the PGI compiler tested is able to compile the latest stable version of TELEMAT-MASCARET (v8p0r2) but fails when compiling the trunk, this has been reported on the PGI bug tracker [8].

Further problems with compilation using all three compilers were found when using OpenACC and OpenMP, these have all been reported to the respective public bug trackers for GCC [9] and PGI [10] and internally to IBM.

Version	≥ PGI 18.10	≥GCC 9.1	≥XL 16.1.1.1
v8p0r2	Compile	Compile	Does not compile <sup>a</sup>
trunk	Does not compile <sup>a</sup>	Compile	Does not compile <sup>a</sup>

<sup>a</sup>. Compilation possible following application of patch to TELEMAT-MASCARET

Table 1. Summary of the current state of TELEMAT-MASCARET on OPENPOWER with different compilers.

### V. PORTING A KERNEL TO GPUS

#### A. Kernel Choice

In order to determine whether there would be any significant benefits to porting parts of TELEMAT-MASCARET to GPUs, a specific test-case was chosen. The case *fetch\_limited/tom\_test6.cas* of the wave propagation module TOMAWAC was a good candidate because it is computationally intensive and most of the computations are localised in a single subroutine. Even though it is a complete test case with initialisation, finalisation and calls of numerous subroutines, 95% of the computational time is spent in the *qnlin3* subroutine. Any benchmarks of this kernel shown will give the execution of the whole test case and not only the time of the *qnlin3* subroutine. The execution time is measured using the internal timers of TELEMAT-MASCARET.

The *qnlin3* subroutine is approximately 400 hundred lines long and mainly consists of a four-level nested loops and updates to two three-dimensional arrays. Each array can have its cells updated multiple times during a single call of the subroutine.

As the original test-case mesh is very small, it was refined twice in order to increase the computation time. This was achieved with Stbtel and the *python* scripts from the TELEMAT-MASCARET suite. The final mesh was made of 75 664 elements and 32 127 points. Some parameters in the *.cas* steering file have also been changed: "NUMBER OF TIME STEP" was increased to 400 and "TIME STEP" to 225.

#### B. ORIGINAL EXECUTION TIME

Each core of the POWER8 CPU is able to work at different levels of Simultaneous Multi-Threading, (SMT1, SMT2, SMT4 and SMT8). This means that each core can execute more than one thread at the same time, e.g. two threads with SMT2. This functionality is comparable with the Hyperthreading technology of Intel processors. While Intel's Hyperthreading can only currently be used to run a maximum of two threads in parallel, a POWER8 core is able to run up to eight. Benchmarks have shown that TELEMAT-MASCARET does not benefit from the use of SMT8 (maybe because the memory bandwidth is saturated, also SMT8 is not on par with SMT2 or SMT4 as it deactivates the CPU's instruction prefetcher [11]). As standard TELEMAT-MASCARET uses MPI parallelisation and is able to run on thousands of cores [12], early tests have showed that it is always beneficial to use SMT2 and in some cases SMT4 but never SMT8. This work therefore presents results using SMT1, SMT2 and SMT4.

Tables 2, 3 and 4 show that there is a significant difference in execution time for the same code, when compiled with different compilers but using the same basic optimisation parameters. The PGI compiler generates the fastest code, the IBM compiler produces code between 1.10 and 1.49 times slower than PGI and the GCC compiler generates code between 1.04 and 1.89 times slower than PGI. The biggest difference in execution time is noted when the

code is run on one or two nodes, while the smallest comes when the code is run on eight nodes.

Number of nodes	SMT1 execution time (s)	SMT2 execution time (s)	SMT4 execution time (s)
1	8442	6801	<b>6072</b>
2	4494	3376	<b>3172</b>
4	2240	1775	<b>1747</b>
8	1185	<b>980</b>	2489

Table 2. Execution time (s) comparison of the original code with different level of SMT when compiled with PGI.

Number of nodes	SMT1 execution time (s)	SMT2 execution time (s)	SMT4 execution time (s)
1	12 045	10 507	<b>8108</b>
2	6711	4274	<b>4186</b>
4	2697	<b>2254</b>	2276
8	1425	<b>1236</b>	2734

Table 3. Execution time (s) comparison of the original code with different level of SMT when compiled with IBM XL.

Number of nodes	SMT1 execution time (s)	SMT2 execution time (s)	SMT4 execution time (s)
1	15 973	9976	<b>7640</b>
2	6084	4338	<b>3899</b>
4	2865	2136	<b>2075</b>
8	1353	<b>1146</b>	2595

Table 4. Execution time (s) comparison of the original code with different level of SMT when compiled with GCC.

As shown in Tables 2,3 and 4, the performance difference between the compilers reduces as the number of MPI processes increases (and therefore the number of computations per MPI process decreases), therefore it can be hypothesised that the PGI compiler produces the fastest executable because of a better ability to vectorise the code. The vectorisation achieved by the PGI compiler appears efficient when there are a lot of computations per MPI process but when the processes have a small amount of work it does not make much difference.

### C. OPENACC

OpenACC is an open standard set of directives to offload computations on GPUs. Between the three compilers used for this work, only PGI and GCC provide an OpenACC implementation.

The modifications introduced to use OpenACC for GPUs with the TOMAWAC module required only small changes to the code. The key change is that, in order to get good performance, the four loops have been moved closer to each other and have been collapsed (as seen in code sample 1). However this revealed a problem when compiling with PGI. Collapsing the four loops meant the compiler replaced the four loops with a new one which iterates from 1 to the

multiplication of the four upper-bounds. In the original code the four max variables were 32 bit integers however, 32 bits is not enough to hold the multiplication of the four upper-bounds in the test-case used. The type has therefore been changed to a 64 bit integer. The problem has been mentioned in the PGI forum and they have proposed that the next version of the compiler will automatically use 64 bit integers when collapsing loops as an optimisation [10].

As the cells arrays can be updated several times during a single call to *qnl3*, it was necessary to protect each update in order to make sure that no cells were updated simultaneously. To do so, each update is put in an atomic operation. In a pure CPU implementation this would be considered a bad approach as atomic instructions are typically slow but here GPU performance implications appear minimal. On CPU, instead of using atomic it would have been possible to use a reduction on the arrays, at the cost of added memory usage.

Finally, in OpenACC there is no directive to distribute a loop across multiple GPUs. However, as TELEMAC-MASCARET is already parallelised with MPI we can easily take advantage of this. During the initialisation of TELEMAC-MASCARET each MPI rank is assigned to a GPU. When the process encounters a portion of code to offload, it sends it to the GPU it has been assigned to (assignment is maintained for the duration of the execution). E.g. when 4 MPI ranks are created, GPU 0 will be assigned to MPI rank 0 and GPU 1 to rank 1 and so on. When 8 MPI ranks are created, each GPU will have 2 MPI ranks assigned to it (since there are 4 GPUs on each node).

To validate that the modified code still gives the correct results, the result file is compared to the result file generated by the original code. In the benchmarks presented hereafter no differences between the two result files have been found.

Tables 3 and 4 show the results for the program compiled with the PGI and GCC compilers. It can be seen that the PGI implementation is the more efficient as it outperformed GCC by around three times. If these results are compared with the original execution time using MPI-only, then it shows that using GPU with OpenACC is highly beneficial. The program using GPU and compiled with the PGI compiler is between 4.4 and 5.5 times faster than the CPU MPI-only version and between 1.8 and 2.1 times faster for the program compiled with the GCC compiler.

<pre>do i=1,maxi !some operations do j=1, maxj !some operations do k=1, maxk !some operations do l=1, maxl arr(j,k,l) = arr(j,k,l) + 1</pre>	<pre>!\$acc parallel loop collapse(4) do i=1,maxi do j=1,maxj do k=1,maxk do l=1,maxl !some operations !\$acc atomic update arr(j,k,l) = arr(j,k,l) + x</pre>
--	---

Code sample 1. Comparison of of the original and after transformation of a simplified part of *qnl3*.

Number of nodes	Best original CPU execution time (s)	GPU (OpenACC) execution time (s)	Speedup (CPU / GPU)
1	6072	1367	4.4
2	3172	686	4.6
4	1747	342	5.1
8	980	179	5.5

Table 5. Comparison between CPU and CPU+GPU execution time with OpenACC when compiled with PGI.

Number of nodes	Best original CPU execution time (s)	GPU (OpenACC) execution time (s)	Speedup (CPU / GPU)
1	7640	4192	1.8
2	3899	2131	1.8
4	2075	1083	1.9
8	1146	554	2.1

Table 6. Comparison between CPU and CPU+GPU execution time with OpenACC when compiled with GCC.

#### D. OPENMP

Since version 4.0, OpenMP has offered its own GPU offloading capabilities similar to those provided by OpenACC, again these are pragma-based. Even though the pragmas are syntactically different from those in OpenACC, the ones used for offloading are functionally equivalent. The OpenMP offloaded version of *qnl3* is therefore very similar to the OpenACC one (see code sample 2).

As the PGI compiler used only supports OpenMP pragmas for CPU, the IBM compiler has been used to evaluate OpenMP GPU offloading performance. GCC also implements OpenMP GPU offloading but for unknown reasons the program always crashes when entering the GPU code, it has therefore been impossible to test it so far.

Table 7 shows the results for the OpenMP offloading compared to the original MPI version, the two being compiled with the IBM XL compiler. It can be seen that there is still a notable acceleration when using the GPUs. On two nodes, the version running on GPUs is three times faster than the original MPI version and it is four times faster on eight nodes. However the speedup achieved is smaller than the one achieved with OpenACC. In fact, the OpenMP version is about two times slower than the OpenACC version compiled with PGI. This difference in performance could be attributed to having to use the IBM compiler rather than the PGI compiler used for the OpenACC tests as the IBM compiler typically produces slower code (as can be seen in Tables 2 and 3).

Performance on 4 MPI ranks has been impossible to measure. The problem is the same as described in section IV.C. The difference is that using a 64 bit integer as an index loop does not solve the problem, the IBM XL compiler seems to still generate GPU code which uses 32 bit integer. This problem has been reported to IBM.

```
!$omp target teams distribute parallel do collapse(4)
do i=1,maxi
  do j=1,maxj
    do k=1,maxk
      do l=1,maxl
        !some operations
        !$omp atomic update
        arr(j,k,l) = arr(j,k,l) + x
```

Code sample 2. OpenMP offloaded version of a simplified *qnl3*.

#### E. MULTIPLE MPI PROCESSES PER GPU

Profiling using NVIDIA's nvprof utility shows that the PGI compiled OpenACC implementation uses about 25% of the total occupancy of each GPU. Furthermore, the kernel does not run continuously but only for about 60% of the total execution time of the whole program, so the GPU alternates between idle time (40%) and computing time (60%). In theory it should therefore be possible to run nearly 8 instances of the code on the GPU before hitting 100% usage for the test case shown. Also, as this case has a low memory consumption, there are no foreseeable problems running 4 instances of the code on one GPU from a memory consumption perspective. An added beneficial consequence of running four instances of the code on each of the GPUs means that every core of the POWER8 CPU is also used when SMT1 is assumed.

A profiling of the version compiled with GCC has been done and was notably different from the PGI one. With PGI the kernels were taking 25% of the GPU computational capability and running for 60% of the time, with GCC the kernels use only 12.5% of the GPU capacity and are running for 83% of the time. This shows that PGI, at least in this case generates kernels which are able to extract more parallelism and use more of the computational power of the GPU.

Tables 8 and 9 show the results for using multiple MPI processes per GPU (up to one MPI process per core of the CPU). These results demonstrate that it is beneficial to run multiple instance of the code on the GPU compiled with the PGI compiler, the code benefits from an acceleration between 1.25 and 1.49. However when the code is compiled with GCC, the acceleration (between 1.03) is almost non-existent when running multiple instances of the code on the same GPU.

The same test has also been tried with the OpenMP version of the offloading. Table 10 shows the results. As with the PGI+OpenACC version, the IBM+OpenMP version can also benefit from offloading multiple MPI processes on a GPU, the acceleration obtained is between 1.20 and 1.27.

Number of nodes	Best original CPU execution time (s)	GPU (OpenMP) execution time (s)	Speedup (CPU / GPU)
1	8108	Crash	–
2	4186	1401	3.0
4	2254	686	3.3
8	1236	336	3.7

Table 7. Comparison between CPU and CPU+GPU execution time with OpenMP when compiled with IBM XL.



Number of nodes	1 MPI per GPU execution time(s)	2 MPI per GPU execution time(s)	4 MPI per GPU execution time(s)
1	1367	1192	1090
2	686	612	532
4	342	303	253
8	179	146	120

Table 8. Comparison of execution time (s) when offloading multiple MPI processes on the same GPU with OpenACC when compiled with PGI.

Number of nodes	1 MPI per GPU execution time(s)	2 MPI per GPU execution time(s)	4 MPI per GPU execution time(s)
1	4213	4192	4086
2	2131	2115	2061
4	1083	1079	1051
8	554	553	539

Table 9. Comparison of execution time (s) when offloading multiple MPI processes on the same GPU with OpenACC when compiled with GCC.

Number of nodes	1 MPI per GPU execution time(s)	2 MPI per GPU execution time(s)	4 MPI per GPU execution time(s)
1	Crash	2533	2191
2	1401	1207	1098
4	686	603	542
8	336	302	280

Table 10. Comparison of execution time (s) when offloading multiple MPI processes on the same GPU with OpenMP when compiled with IBM XL.

#### F. COMPARISON WITH AN X86-64 MACHINE

This section provides results using a more typical x86-64 based cluster called Wilkes-2. It uses the same P100 GPUs as Paragon, but it does not have an NVlink interconnect between the CPUs and GPUs, this means that data transfers will be slower than on Paragon. As Table 11 shows, there is no significant differences in execution time between Wilkes-2 and Paragon when the code is offloaded to GPUs when using 1 to 4 nodes, this is most likely because data transfers in the presented case are small and infrequent. Currently it can be seen that when 8 nodes are used, execution time starts to rise again indicating a drop-off in scalability. However, given past experience and performance achieved using the Paragon Power8 system, this is unexpected behavior and may be attributed to a functional problem with the Wilkes-2 system. Further investigation of this problem will be undertaken.

#### VI. PORTING A CHALLENGING TEST-CASE TO GPUS

In the *fetch limited/tom test6.cas* test-case the performance bottleneck was the *qnl3* subroutine, taking about 95% of the execution time. So the offloading to GPU was relatively simple with only one subroutine to offload in order to get good performance. Our ongoing work now focuses on porting more subroutines to GPU to enable accelerated calculation of more complex cases.

Number of nodes	Original, 12 MPI per node, execution time (s) and speedup	4 MPI, 4GPU per node, execution time (s) and speedup (cpu/gpu)	12 MPI, 4 GPU per node, execution time (s) and speedup (cpu/gpu)
1	17 339	1319 (13.1x)	1199 (14.5x)
2	8088	652 (12.4x)	650 (12.4x)
4	3751	328 (11.4x)	320 (11.7x)
8	1900	564 (3.4x)	477 (4x)

Table 11. Comparison of execution time (s) between original code and offloading to GPUs with OpenACC on Wilkes-2 when compiled with PGI.

EDF have provided a test case named *Somme\_7days*. This is a triple coupling case using TELEMAC2D, SISYPHE and TOMAWAC. After profiling the code, it seems that most of the time is spent in Tomawac, but not in a single subroutine as with the presented test-case. In *Somme\_7days* there is no clear bottleneck to note. The profiling has been done with the Linux perf profiler [13], using one core of one POWER8 node and the code was compiled with the PGI compiler.

In Fig 2. it can be seen that the main time-consuming subroutines are *schar41\_per\_4d*, *log*, *qnl3* and *bief\_interp*. It should be noted that *log* is mostly called in *qwind1*, thus their execution times could be merged. The main difference with the previous work done on the *tom test6.cas* case is that this time it is not possible to offload one subroutine to GPU and get a significant acceleration, because no subroutine dominates. Another difference is that *qnl3* was computationally expensive, but in this case no subroutine is equally as expensive, for instance a single call to *qnl3* takes about 400 ms and a call to *bief\_interp*, which is the most time consuming subroutine, takes about 20 ms. The subroutine *bief\_interp* is the most expensive not because of the computational cost but because it is called very frequently during the execution of the program.

In order to get performance improvements with GPU offloading in this case, it will be necessary to offload multiple subroutines and since the subroutines are quick to execute and called thousands of times it is very important to minimise the data transfers between host machine and GPU. To achieve this it will be necessary to perform all transfers at the caller level and not within the offloaded subroutine. Doing so will introduce another complication, for instance it is easy to do the data transfers in *semimp* for all the offloaded subroutines that *semimp* will call. However if those subroutines are called outside of *semimp* then the data needed will not be available on the GPU, leading to a crash.

One solution would be to add a call to *acc\_is\_present* (or *omp\_target\_is\_present*) at the beginning of each offloaded subroutine, if the data is present the code will be executed on the GPUs and if not on the CPU. But doing so does not take into account that some subroutines might be modified to execute more efficiently on GPUs (like a collapse of the loops, as seen on code sample 1) and that these modifications are usually guarded with a compile-time *ifdef* in order to not duplicate the code and keep the two versions in the same file.

Since only one part of the code guarded by the *ifdef* will be compiled it will not be possible to select it arbitrarily at runtime. An elegant solution to this problem is still being considered.

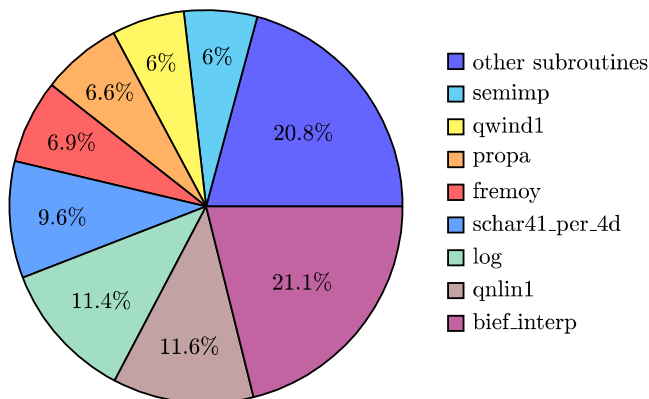


Figure 2. Profiling of the *Somme\_7days* test-case (1 MPI, 1 POWER8 core, PGI compiler, Linux perf profiler)

## VII. CONCLUSION

The last stable version of TELEMAT-MASCARET (v8p0r2) is now working on the OPENPOWER architecture with GCC, PGI and with IBM XL (when using a minor patch). An official certification has been granted by the OPENPOWER foundation for this stable version [14].

Progress has been made on porting parts of TOMAWAC to GPUs. This is working as expected and gives performance improvements on subroutines which are computationally intensive such as *qnlm3*, but more work needs to be done for subroutine which are less computationally intensive, such as *qnlm1*.

## ACKNOWLEDGEMENT

This work is supported by the Hartree Centre through the Innovation Return on Research (IROR) programme.

This work was partially performed using the Cambridge Wilkes service. Part of which is operated by the University of Cambridge Research Computing on behalf of the STFC DiRAC HPC Facility [15]. The DiRAC component of Wilkes was funded by BEIS capital funding via STFC capital grants ST/P002307/1 and ST/R002452/1 and STFC operations grant ST/R00689X/1. DiRAC is part of the National e-Infrastructure.

## REFERENCES

- [1] Hamza Belaoura, Intégration de la bibliothèque MAGMA dans le système TELEMAT-MASCARET, 2017, Université de Versailles, Saint Quentin en Yvelines, Internship report
- [2] <https://icl.utk.edu/magma/index.html> – Visited on the 2019-08-27
- [3] <https://openpowerfoundation.org/> – Visited on the 2019-08-27
- [4] <https://www.nvidia.com/en-gb/data-center/nvlink/> – Visited on the 2019-08-27
- [5] <https://www.hartree.stfc.ac.uk/Pages/home.aspx> – Visited on the 2019-08-27
- [6] <https://top500.org/system/179044> – Visited on the 2019-08-27
- [7] [https://gcc.gnu.org/bugzilla/show\\_bug.cgi?id=87689](https://gcc.gnu.org/bugzilla/show_bug.cgi?id=87689) – Visited on the 2019-08-27
- [8] <https://www.pgroup.com/userforum/viewtopic.php?f=4&t=6429> – Visited on the 2019-08-27
- [9] [https://gcc.gnu.org/bugzilla/show\\_bug.cgi?id=91410](https://gcc.gnu.org/bugzilla/show_bug.cgi?id=91410) – Visited on the 2019-08-27
- [10] <https://www.pgroup.com/userforum/viewtopic.php?f=12&t=6562> – Visited on the 2019-08-27
- [11] Sinharoy Balam, Van Norstrand J. A., Eickemeyer Richard J., et al. IBM POWER8 processor core microarchitecture. IBM Journal of Research and Development, 2015
- [12] Moulinec Charles, Denis Christophe, Pham C.-T., et al. TELEMAT: An efficient hydrodynamics suite for massively parallel architectures. Computers & Fluids, 2011, vol. 51, no 1, p. 30-34.
- [13] [https://perf.wiki.kernel.org/index.php/Main\\_Page](https://perf.wiki.kernel.org/index.php/Main_Page) – Visited on the 2019-10-02
- [14] [https://openpowerfoundation.org/?resource\\_lib=stfc-daresbury-laboratory-telemat-mascaret-v8](https://openpowerfoundation.org/?resource_lib=stfc-daresbury-laboratory-telemat-mascaret-v8) – Visited on the 2019-08-29
- [15] [www.dirac.ac.uk](http://www.dirac.ac.uk) – Visited on the 2019-09-29

# An Efficient Implementation of Parallelization in the Domain Decomposition of TELEMAC

Dzung Nguyen, T. Liepert, M. Reisenbüchler, K. Kaveh, M. D. Bui, P. Rutschmann  
Chair of Hydraulic and Water Resources Engineering  
Technical University of Munich  
Arcisstr.21. 80333 Munich

dzung.nguyen@tum.de

## Abstract:

In this study, we present an Open MPI-parallelized implementation of the domain decomposer PARTEL for TELEMAC. The domain decomposer PARTEL splits the computational domain into several partitions, which forms the basis of parallel simulations. In current TELEMAC releases, only serial mode has been implemented in PARTEL, which comes along with some limitations regarding the number of elements as well as the number of partitions to be decomposed. Depending on the hardware resources used for testing, the serial mode of PARTEL might take a significantly long computation time or eventually fail due to exceeding the memory limit of the computer. To overcome this bottleneck we fully parallelized the domain decomposition using Open MPI. This approach allows us to decompose a huge domain consisting of some ten million cells into hundreds of subdomains utilizing the available HPC resources at the Leibniz Supercomputing Center Munich, Germany (LRZ).

Our work focused on improving PARTEL code within the official release of TELEMAC version v7p2r3. Original PARTEL covers the decomposition of the boundary conditions, initial conditions and the parallel information data as well as the graph decomposition for the geometry file, which were developed in our MPI optimized PARTEL applying different techniques: e.g. the code was decoupled; the loops were unrolled; however global data information was maintained and algorithm consistency was kept. Applying a MPI parallelization scheme the memory usage by a single MPI process of PARTEL was reduced theoretically by a factor of  $O(NPARTS)$ , where  $NPARTS$  is the number of partitions. Our tests were performed on a HPC cluster called CoolMUC2 at the LRZ. For testing, a mesh of 20 million elements (case - I) and the other with 40 million elements (case - II) were used. The MPI-parallelized PARTEL was able to decompose the case-I-mesh into 1200 subdomains in approximately 25 minutes. In case - II, the program has completed the task with 600 subdomains generated in about 18 minutes. The tests were also done using the trunk version of TELEMAC, which is essentially equivalent to the major version 8. We observed that this version was not able to complete the tests in reasonable times (timed out after a few hours of running). Our concept can be extended to the later versions of TELEMAC in the future.

**Proposed session:** *Numerical methods, code coupling and high performance computing*

**Key words:** Domain decomposition, parallelization, Telemac, high performance computing,

**Speaker:** Dzung Nguyen

# Large-scale high-resolution urban flood modeling in the cloud using TELEMAC

Firas Saleh<sup>1</sup>, Victor Rodriguez, Corresponding author (Venkatsundar Ramaswamy),

<sup>1</sup>251 W 30th St, New York City, 10001, USA

vsundar@jupiterintel.com

## Abstract:

- Hyper-local flood simulations
- Large scale cloud computing
- Coastal-riverine interactions

Hyper-local flooding simulations over relatively large areas are increasingly being used to provide current and future flood risk projections. Additionally, cloud computing is emerging as a cost-effective, flexible, and lucrative alternative to the high-end computational resources currently used for local-scale flood risk estimation. We used a large variable resolution computational mesh in TELEMAC-2D to simulate flooding at metric scales from storm surge and rainfall over Houston and its surrounding areas. This study illustrates the opportunities and challenges associated with performing a large number of cloud-optimized simulations for flood risk estimation.

To increase computational accuracy and limit expenses, we selected a variable resolution mesh from multiple mesh configurations that captures local-scale urban features and various water bodies. The inundation depths and extents simulated with the different mesh configurations were compared to the maximum inundation extents, high water marks, gauge data, and crowdsourced data. The mesh configuration that provided an optimum tradeoff between cost and accuracy was then scaled to run large number of simulations to support long term flood risk assessments.

**Proposed session:** *from list of themes identified in the website*

**Key words:** Urban Flooding, Hazzard, Climate impacts, Houston

**Speaker:** Firas Saleh



# Introducing GAIA, the brand new sediment transport module of the TELEMAC-MASCARET system

*Contributors to GAIA in alphabetical order:* Yoann Audouin<sup>4</sup>, Thomas Benson<sup>5</sup>, Matthieu Delinares<sup>1</sup>, Jacques Fontaine<sup>4</sup>, Boris Glander<sup>2</sup>, Nicolas Huybrechts<sup>3</sup>, Rebekka Kopmann<sup>2</sup>, Agnès Leroy<sup>4,6</sup>, Sara Pavan<sup>4</sup>, Chi-Tuân Pham<sup>4</sup>, Florent Taccone<sup>4</sup>, Pablo Tassi<sup>4,6,\*</sup> & Regis Walther<sup>1</sup>

<sup>1</sup>Artelia; <sup>2</sup>BAW; <sup>3</sup>CEREMA; <sup>4</sup>EDF R&D; <sup>5</sup>HR-Wallingford; <sup>6</sup>Laboratoire d'Hydraulique Saint-Venant

\*Corresponding author: [pablo.tassi@edf.fr](mailto:pablo.tassi@edf.fr)

**Abstract**—GAIA is the brand new open-source, sediment transport and bed evolution module of the TELEMAC-MASCARET modelling system. GAIA is based on the historical sediment transport module SISYPHE, where a large number of improvements, corrections and optimizations have been implemented. Thanks to its unified framework, GAIA efficiently manages different sediment classes, sand-mud mixtures, etc. for both 2D and 3D spatial dimensions.

## I. INTRODUCTION

Over the last few decades, the access to more precise measurement data from both field and laboratory, the enormous increases in computer speed and power, and the requirement for more accurate predictions of sediment transport and bed evolution of river, coastal and estuarine zones, have motivated the scientific community to develop more rigorous and elaborate predictive tools for morphodynamics applications.

In light of this, the historical module SISYPHE of the TELEMAC-MASCARET modelling system (TMS) has been developed for more than 25 years [9], originally based on the same finite element structure as the two-dimensional code solving the shallow water equations\*.

Despite its robustness, flexibility and capability of dealing with a large number of river [4, 6, 11], coastal [3, 14, 20], and estuarine [15, 16, 7] sediment transport and morphodynamics problems [22], as well as the tremendous effort to deliver a module able to be used in both industrial and scientific contexts, a number of issues arose regarding the improvement of the treatment of graded and mixed (cohesive and non-cohesive) sediments, as well as the full compatibility between 2D and 3D processes.

From early discussions starting *circa* 2014 following the developments on mixed sediment implemented *ad hoc* by a consortium member for an estuarine model [5], going through strategic meetings, animated coffee debates and *hackathons* involving several members of the TELEMAC-MASCARET consortium, and more recently the participation of final users and an increasing number of threads with

suggestions and recommendations posted in the TMS's webpage forum, the brand new sediment transport and bed evolution module GAIA of the TMS is introduced.

GAIA, building upon the SISYPHE module, is able to model complex sediment and morphodynamic processes in coastal areas, rivers, lakes and estuaries, accounting for spatial and temporal variability of sediment size classes (uniform, graded or mixed), properties (cohesive and non-cohesive) and transport modes (suspended, bedload and both simultaneously). The generalized framework used for bed layering enables any combination of multiple size classes for both non-cohesive and cohesive sediment to be modelled simultaneously. Compatibility is ensured between an active layer model (an approach traditionally adopted for non-cohesive sediment) and the presence of different classes of fine sediment and consolidation. In contrast to SISYPHE, the quantity of each sediment class in the bed is evaluated using dry mass instead of volume, which minimizes roundoff errors.

Although invisible to the end user, suspended sediment transport processes are dealt with by the hydrodynamic modules (TELEMAC-2D or TELEMAC-3D), while near-bed, bedload and processes in the bottom layer are handled by GAIA. This allows a clearer treatment of sedimentary processes that happen in the water column, in the bed structure and at the water-bed interface, see Figure 1. GAIA can also be coupled with the modules for sediment dredging NESTOR, wave propagation TOMAWAC and water quality WAQTEL.

## II. SEDIMENT TRANSPORT PROCESSES IN THE WATER COLUMN

Suspended sediment particles being transported by the flow at a given time and maintained in temporary suspension above the bottom by the action of upward-moving turbulent eddies are commonly called *suspended load*. The equation describing mass conservation of suspended sediment is the advection-diffusion equation (ADE), that is valid only for dilute suspensions of particles that are not too coarse (i.e.,  $\leq 0.5$  mm). Within this new sediment transport framework, the solution of the ADE, com-

\*Interestingly, this shallow water code later evolved into a module that was baptized TELEMAC-2D.

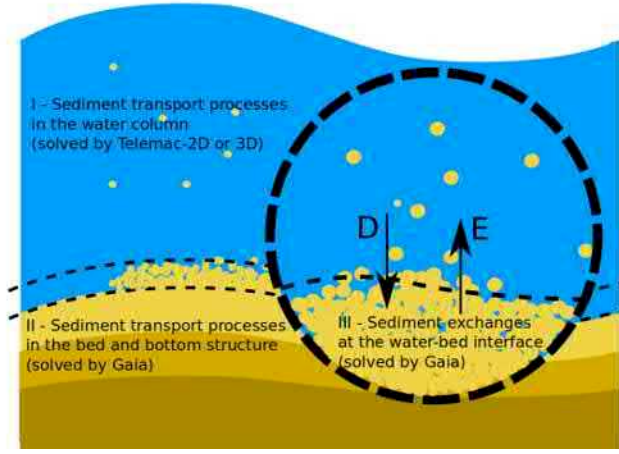


Fig. 1: Sketch summarizing the way in which the sediment transport mechanisms are dealt in GAIA. Above,  $D$  and  $E$  stand for deposition and entrainment fluxes.

pleted with appropriate boundary and initial conditions, is computed by TELEMAC-2D or TELEMAC-3D for 2D and 3D cases respectively. The solution procedure remains invisible to the user since the physical parameters are provided by the GAIA steering file. Two advantages of this procedure are evident: (i) to stay up-to-date with the numerical schemes and algorithm developments in the hydrodynamics modules for the solution of the advection terms and (ii) for a clearer distinction between sediment transport processes happening in the water column, in the near-bed, and in the bed structure (for example in cases where exchanges with the bottom are not required such as suspended sediment transport over a rigid bed).

### III. SEDIMENT TRANSPORT PROCESSES IN THE BED AND STRATIGRAPHY

#### A. Bedload transport

Sediment particles which are transported in direct contact with the bottom or next to the bed without being affected by the fluid turbulence are commonly called *bedload*. In contrast to SISYPHE, in GAIA bedload fluxes are computed in terms of (dry) mass transport rate per unit width, without pores:  $\mathbf{Q}_{mb} = \rho \mathbf{Q}_b$  in (kg/ms), with  $\mathbf{Q}_b$  the vector of volumetric transport rate per unit width without pores ( $\text{m}^2/\text{s}$ ), with components  $(Q_{bx}, Q_{by})$  along the  $x$  and  $y$  directions, respectively, and  $\rho$  the sediment density. Numerical computation of sediment fluxes in dry mass minimizes roundoff error, particularly for the mass transfer algorithms used for the bed layer model.

#### B. Bottom stratigraphy

For sand graded distributions, an algorithm based on the classical active layer formulation of Hirano is used [2]. The active layer supplies material that can be eroded or deposited as bedload or suspended load. Its thickness can be specified by the user or set by default to the value  $3 \times$

$d_{50}$ , with  $d_{50}$  the median diameter of sediment material contained in the active layer.

The bed model can be discretized by a constant number of layers along the vertical direction. Since layers are allowed to be emptied, the utilized number of layers at each mesh node can vary during a numerical simulation. When more than one sediment class is specified in the steering file, the following cases arise: (i) for a given initial bed stratification (i.e. through a given number of layers  $N_{lay}$ ), an active layer is added inside this stratification at the beginning of the simulation. In this case the total number of layers is  $= N_{lay} + 1$ ; (ii) if the initial bed stratification is not provided, the sediment bed is thus subdivided in two layers: the active layer and a substrate layer located directly below. In this case, the total number of layers is  $= 2$ .

To maintain a constant active layer thickness throughout the numerical simulation, at each time step the following procedures are performed:

- In the case of erosion, mass is taken from the active layer, therefore the sediment flux is transferred from the substratum (first non-empty layer below the active layer) to the active layer. Note that the rigid bed algorithm is applied to the active layer, i.e. only the sediment mass in the active layer is available at the given time step. This is important as bedload transport rate and/or the rate of entrainment for suspension are computed using the sediment composition available in the active layer.
- If the erosion during the time step exceeds the mass of sediment available in the top layer, this layer is fully eroded and a new erosion rate is computed using the composition of the layer underneath, that is now the surface layer.
- In the case of deposition, the increased thickness generates a sediment flux from the active layer to the first substratum layer.

#### C. Mixed sediments

The bed model algorithm introduced above has been modified to account for the presence of mud or sand-mud mixtures. Mixed sediment consists of a mixture of  $N_{nco} \geq 1$  classes of non-cohesive sediment (sand and/or gravel) with  $N_{co} \geq 1$  classes of fine, cohesive sediment. Non-cohesive sediments are assumed to be transported by bedload and/or suspension, while cohesive sediment is transported only by suspension.

In the algorithm for mixed sediments, the layer thickness results from the mass ratio of cohesive and non-cohesive sediment contained in each layer. If the cohesive sediment volume is  $\leq 40\%$  of the non-cohesive sediment volume, the layer thickness only depends on the mass of non-cohesive sediment volume. Conversely, if the cohesive sediment volume is  $\geq 40\%$  of the non-cohesive sediment volume, the layer thickness is computed from the non-cohesive sediment volume plus the cohesive sediment volume minus the

interstitial volume between non-cohesive sediment classes.

The presence of high concentrations of cohesive sediment in the bed are known to prevent bedload transport from occurring [21]. Therefore, in GAIA, bedload transport is only computed if the mass fraction of cohesive sediment in the active layer is  $\leq 30\%$ . In this case, the non-cohesive sediment can still be transported in suspension. In addition, erosion of non-cohesive sediment by bedload transport causes cohesive sediment present in the mixture to be entrained into suspension.

#### D. Consolidation processes

For the current version of GAIA, consolidation processes are based on the semi-empirical formulation originally developed by Villaret and Walther [23], which uses the isopycnal and first-order kinetics formulations. Consolidation of mud deposits is modeled using a layer discretization, where the first layer corresponds to the freshest deposit, while the lower layer is the most consolidated layer. Sediment deposition from the water column is added directly to the first layer. A rate (or *flux*) of consolidation is computed for each layer and for each class of cohesive sediment separately. The values of the computed fluxes depend on the availability of each class in the layer considered.

In the case of mixed sediment, the presence of non-cohesive sediment in the stratigraphy of the mixture is considered to not alter the cohesive sediment consolidation.

### IV. SEDIMENT EXCHANGES AT THE WATER-BED INTERFACE

The unified framework proposed for sediment transport processes in 2D and 3D eliminates unnecessary code duplication. Within this new code structure, the dimensionless entrainment rate of bed sediment into suspension per unit bed area per unit time  $E$  is computed by the same subroutine for both 2D and 3D dimensions. As in SISYPHE, for non-cohesive and cohesive sediments the dimensionless entrainment and deposition rates are computed for each sediment class following the formulae of [25] and [13, 8], respectively.

If different classes of cohesive sediment are present, deposition fluxes are computed for each sediment class according to its settling velocity. Conversely, as cohesive sediments have the same mechanical behaviour when they are in the bed, the same value of critical shear stress is used for all classes. Nevertheless, since the computation of erosion sediment fluxes accounts for the availability of each class, the computed values of erosion fluxes can be different for each sediment class.

In GAIA, the "simultaneous" paradigm allowing erosion and deposition to occur at the same time has been adopted [24]. This paradigm implies that sediment deposition takes place at all times regardless of the value of the bottom shear stress.

#### A. Erosion of mixed sediments

The composition of the sediment mixture in the surface (active) layer is taken into consideration when computing the critical shear stress for erosion and the erosion rate. This is achieved by combining the critical shear stresses for erosion for all the sediment classes (cohesive and non-cohesive), according to [10]:

- If the mass of cohesive sediment as a fraction of the mixture is  $\geq 50\%$ , then the erosion rate and critical shear stress for cohesive sediment alone is used.
- If the mass of cohesive sediment as a fraction of the mixture is  $\leq 30\%$ , then the erosion rate for non-cohesive sediment is used and the critical shear stress for non-cohesive sediment is used with a correction.
- If the mass of cohesive sediment as fraction of the mixture is  $\geq 30\%$  and  $\leq 50\%$ , then the values are interpolated between the previous values.

The total erosion rate is then distributed among the non-cohesive and cohesive sediment according to their respective fractions in the mixture.

#### B. Deposition processes

By default, the flux of non-cohesive sediment deposits from the water column is added to the first layer of the consolidation bed model. It can alternatively be considered to immediately settle through the fresh cohesive sediment and thus be added to a given layer (of a given concentration) chosen by the user.

### V. INFLUENCE OF WAVES ON SEDIMENT TRANSPORT PROCESSES

As in SISYPHE, the bottom shear stress due to the effect of waves and by the combined action of currents and waves are computed according to [19] and [17], respectively.

In GAIA, the computation of the maximum wave orbital velocity  $U_w$  can be performed according to the waves characteristics: (i) regular (monochromatic) or (ii) irregular (JONSWAP spectrum) [18] cases. The latter method calculates the r.m.s. orbital velocity  $U_{rms}$  and then converts it to a monochromatic orbital velocity  $U_w = \sqrt{2}U_{rms}$ , as required by many sediment transport formulae.

### VI. BED EVOLUTION

In GAIA, the bed evolution is computed by solving the mass conservation equation for sediment or *Exner equation*, expressed in terms of mass (see §III-A), where bedload, suspension or both sediment transport modes can be considered simultaneously. In its simplest form (only bedload, one sediment class) this equation reads:  $(1 - \lambda)\partial_t(\rho z_b) + \nabla \cdot \mathbf{Q}_{mb} = 0$ , with  $\lambda$  the sediment porosity and  $z_b$  the bed elevation above datum. In GAIA, two different morphological accelerators are proposed: (i) a morphological factor on the hydrodynamics, which distorts the evolution of the hydrodynamics with respect to the morphodynamics; and (ii) a morphological factor on the

bed, which distorts the evolution of the morphodynamics with respect to the hydrodynamics. The first option is suitable for river applications accounting for bedload transport whereas the second option is suitable for coastal and estuarine applications as it is compatible with suspended sediment transport processes.

Key physically-based processes that are retained in GAIA from SISYPHE include the influence of secondary currents to precisely capture the complex flow field induced by channel curvature in 2D simulations, the effect of bed slope associated with the influence of gravity, bed roughness predictors, the collapse of bed slope over a critical slope or angle of repose, and non-erodible bed areas.

## VII. EXAMPLES

Similarly to SISYPHE, the coupling between the hydrodynamics and sediment transport module is done by the keyword `COUPLING WITH = 'GAIA'` and the companion keyword `GAIA STEERING FILE`.

### A. Racetrack shape domain in 2D and 3D

A racetrack shape configuration has been adopted during the earlier developments of GAIA to assess its conservativeness properties, to test its ability at reproducing bed and layer thicknesses evolutions and to optimize the code implementation within the new module structure. To further simplify the involved physical processes, wind is considered as the only driving force of the flow and no liquid boundaries are included in the numerical simulations. The bump and the lateral banks in the initial bathymetry (see Figure 2) favor the bed evolution on both longitudinal and lateral slopes. Lateral banks allow the formation of dry areas in the computational domain. During the development process, the new implementations were tested using this model for a large number of cohesive and/or non-cohesive sediment combinations by coupling GAIA with either TELEMAC-2D or TELEMAC-3D. As an example, two of these configurations are presented below. This test is available in the example database of GAIA as it shows users how to set the model for different combinations of sediment classes. It can also be useful to advanced users who want to test their own developments on a simple configuration.

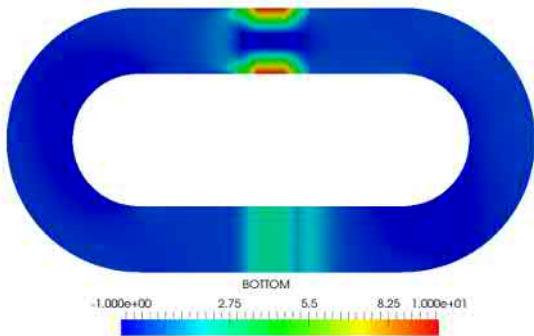


Fig. 2: Bathymetry for the racetrack shape case.

1) *Case 1:* The bottom structure consists of one layer with an initial thickness equal to 1 m. The sediment diameter  $D = 10 \mu\text{m}$ , the settling velocity  $w_s = 0.001 \text{ m/s}$ , mud concentration  $50 \text{ kg/m}^3$ , Partheniades constant  $M = 1 \times 10^{-4}$  and critical shear stress for erosion  $\tau_{ce} = 0.1 \text{ N/m}^2$ . The same steering file for GAIA has been used for both 2D and 3D cases.

As one sediment class of cohesive sediment is used, the corresponding keyword is `CLASSES TYPE OF SEDIMENT = CO`, where CO stands for cohesive sediments, see Appendix A. If consolidation is not considered in the numerical simulation, then `BED MODEL = 1`. For this test, the following keyword is required `SUSPENSION FOR ALL SANDS = YES`. If consolidation processes are accounted in the numerical simulation, the following keywords are provided, assuming a bottom discretization consisting of 4 layers:

```
BED MODEL = 2
/
NUMBER OF LAYERS FOR INITIAL STRATIFICATION = 4
LAYERS INITIAL THICKNESS = 0.25;0.25;0.25;0.25
CLASSES INITIAL FRACTION = 1.DO
/
LAYERS MUD CONCENTRATION = 50.DO;100.DO;200.DO;
300.DO
LAYERS CRITICAL EROSION SHEAR STRESS OF THE MUD =
0.1;0.2;0.3;0.4
LAYERS PARTHENIADES CONSTANT = 1.E-4; 1.E-4;
1.E-4; 1.E-4
LAYERS MASS TRANSFER = 0.01;0.005;0.001;0.000
```

2) *Case 2:* A mixed sediment bed material is considered, with 4 classes of non-cohesive sediments and 4 classes of cohesive sediments. For this case, the settling velocity values are provided for the cohesive sediments and computed by GAIA for the non-cohesive sediments. Assuming the bed model discretized with 4 layers and that accounts for consolidation processes, a sketch of the GAIA steering file is provided below:

```
CLASSES TYPE OF SEDIMENT =
NCO;NCO;NCO;NCO;CO;CO;CO;CO
CLASSES SEDIMENT DIAMETERS =
0.0002;0.0002;0.0002;0.0002;0.00001;
0.00001;0.00001;0.00001
CLASSES SETTLING VELOCITIES =
-9.;-9.;-9.;-9.;0.001;0.001;0.001;0.001
/-----
BED LOAD FOR ALL SANDS = YES
BED-LOAD TRANSPORT FORMULA FOR ALL SANDS = 5
/
SUSPENSION FOR ALL SANDS = YES
SUSPENSION TRANSPORT FORMULA FOR ALL SANDS = 1
/-----
BED MODEL = 2
/
NUMBER OF LAYERS FOR INITIAL STRATIFICATION = 4
LAYERS INITIAL THICKNESS =
0.25;0.25;0.25;0.25
CLASSES INITIAL FRACTION =
0.15D0;0.15D0;0.15D0;0.15D0;0.1D0;0.1D0;
0.1D0;0.1D0
/
LAYERS MUD CONCENTRATION =
50.DO;100.DO;200.DO;300.DO
LAYERS CRITICAL EROSION SHEAR STRESS OF THE MUD =
```



```

0.1;0.2;0.3;0.4
LAYERS PARTHENIADES CONSTANT =
1.E-4; 1.E-4; 1.E-4; 1.E-4
LAYERS NON COHESIVE BED POROSITY=
0.4D0;0.4D0;0.4D0;0.4D0
LAYERS MASS TRANSFER =
0.01D0;0.005D0;0.001D0;0.0D0

```

These examples can be found in the folders `examples/gaia/hippodrome-t2d` and `examples/gaia/hippodrome-t3d` of the TMS.

### B. Morphological evolution in a channel bend

The purpose of this test is to assess the ability of GAIA to reproduce the bed evolution in a channel bend under unsteady flow conditions. This test is based on the experimental setup (RUN 5) proposed by Yen and Lee [26]. In this case, the bed evolution of a 180° channel bend with an initial flat bottom is computed for a triangular-shaped inflow hydrograph. Numerical results are validated against measured contours of bed evolution at the end of the experiment and against measured bottom elevations at two different cross sections (90° and 180°). This case assumes non-cohesive graded sediment distribution with 5 sediment classes with diameters  $D=0.31, 0.64, 1.03, 1.69$  and  $3.36$  mm and initial distribution fraction = 20% for each class, being transported by bedload. In the GAIA steering file this is specified as follows:

```

BED LOAD FOR ALL SANDS = YES
SUSPENSION FOR ALL SANDS = NO
CLASSES TYPE OF SEDIMENT = NCO;NCO;NCO;NCO;NCO
CLASSES SEDIMENT DIAMETERS =
0.00031;0.00064;0.00103;0.00169;0.00336
CLASSES INITIAL FRACTION =
0.2;0.2;0.2;0.2;0.2

```

As an example, when the Meyer-Peter and Müller formula is used to calculate the solid discharge, the corresponding keyword is set up as follows:

```
BED-LOAD TRANSPORT FORMULA FOR ALL SANDS = 1
```

For all sediment classes, the sediment density is equal to  $\rho = 2650 \text{ kg/m}^3$ , the Shields parameter = 0.047 and the bed porosity  $\lambda = 0.375$ :

```

CLASSES SEDIMENT DENSITY =
2650.;2650.;2650.;2650.;2650.
CLASSES SHIELDS PARAMETERS =
0.047;0.047;0.047;0.047;0.047
LAYERS NON COHESIVE BED POROSITY = 0.37500

```

Two sediment layers with a total thickness equal to 20 cm are assumed. The bed structure is provided by the user's FORTRAN file `user_bedload_qb.f`.

The normalized bed evolution shown in Figure 3 evidences the asymmetrical section formed in the 180° bend under unsteady flow conditions, with the presence of a steady, forced bar located approximately between sections 30° and 90°. The model is therefore able to reproduce the expected sediment processes, with erosion along the outer bank and deposition along the inner bank. Figure 4 shows the comparison between laboratory observations and numerical results at the sections 90° and 180° of the channel bend using different bedload sediment transport

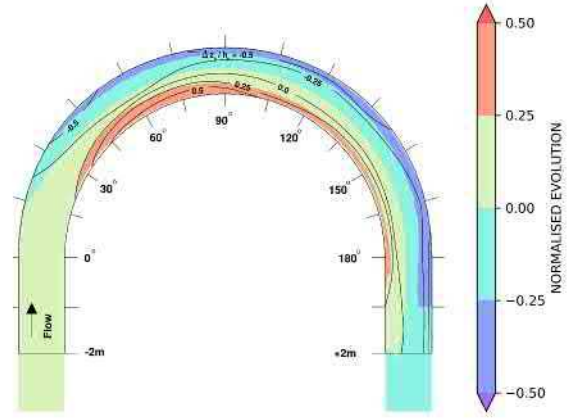
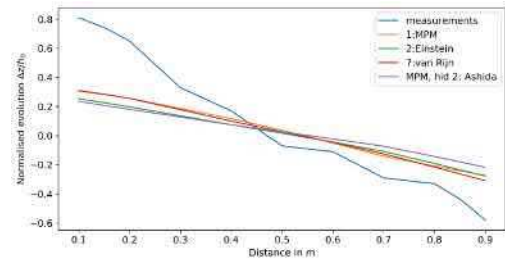
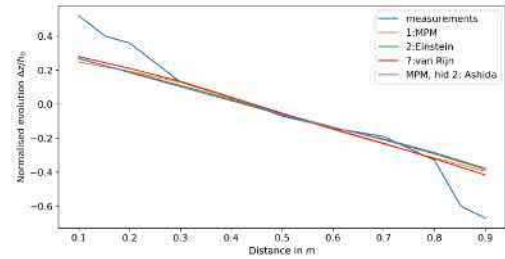


Fig. 3: Normalized bed evolution for the Yen & Lee's [26] channel bend.



(a) Section 90°



(b) Section 180°

Fig. 4: Comparison of observed vs. numerical normalized evolution.

formulae (Einstein, van Rijn, and Meyer-Peter and Müller with and without activating the Ashida's hiding factor). For this test case, numerical results were obtained without any calibration procedure. This example can be found in the folder `examples/gaia/yen-t2d` of the TMS.

### C. Rhine river application

An 11 km long stretch of the lower Rhine River near Düsseldorf (Germany) is used for comparison between the modules GAIA and SISYPHE. The morphodynamic calibration was adapted from an existing, longer reach model [1]. Figure 5 shows the model domain, boundaries and bathymetric information. For this river reach, the hydrodynamics is strongly influenced by the presence of large-amplitude bends. In the study area, field surveys

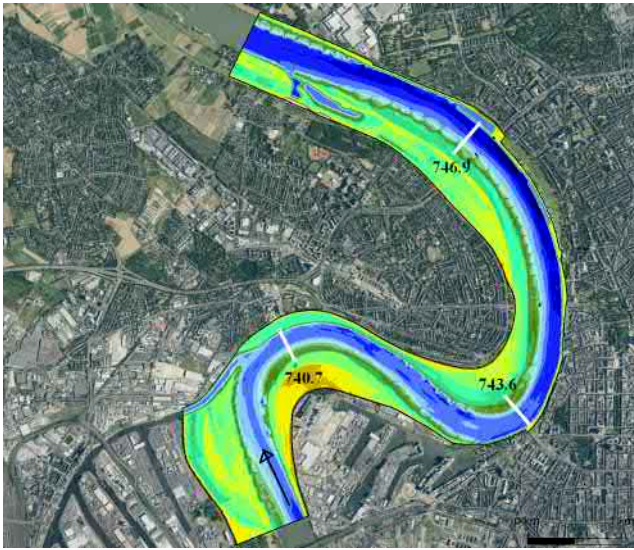


Fig. 5: Lower Rhine river topography and numerical model boundaries nearby Düsseldorf (Germany) (© Bundesamt für Kartographie und Geodäsie (2018)).

showed a tendency for the long term erosion, with periodic sediment management operations including artificial bed load supply as well as dredging and disposal activities. These operations were not accounted in the current version of the model. A total simulation time of 6.5 years of the natural hydrograph for the period January 1st 2000 to June 22nd 2006 was chosen. The model consists of 56,825 nodes and has a fine grid resolution in the range [5-50] m, that is able to capture the existing groyne geometries. The morphodynamic parameters for GAIA and SISYPHE were equivalent and are listed below:

- Hydrodynamic time step: 4 s, morphological factor 4.
- Nikuradse friction law, four different friction zones.
- Elder turbulence model.
- Multi-grain (10 sediment classes), Hirano-Ribberink multi-layer model (3 layers, constant active layer thickness: 0.1 m), bed load only.
- Meyer-Peter and Müller transport formula; Karim, Holly, Yang hiding exposure formulation.
- Soulsby and Talmon slope effect formulation.
- Secondary currents approach for morphodynamics, with the radius of curvature provided in an additional file.

For the total simulation time, the CPU time using GAIA ( $\approx 42$  h) was approximately 6% smaller compared with the CPU time using SISYPHE ( $\approx 45$  h) using 160 cores at a cluster (CPU Intel(R) Xeon(R) Gold 6138,  $2 \times 20$  cores per node) available at BAW. Table I presents mass balance results after the 6.5 year simulation time and summed-up for the 10 sediment classes for both SISYPHE and GAIA. The mass balance of both modules are satisfying and of a similar order of magnitude. Note that SISYPHE needed hardcoded checks and limitations in the `layer.f`

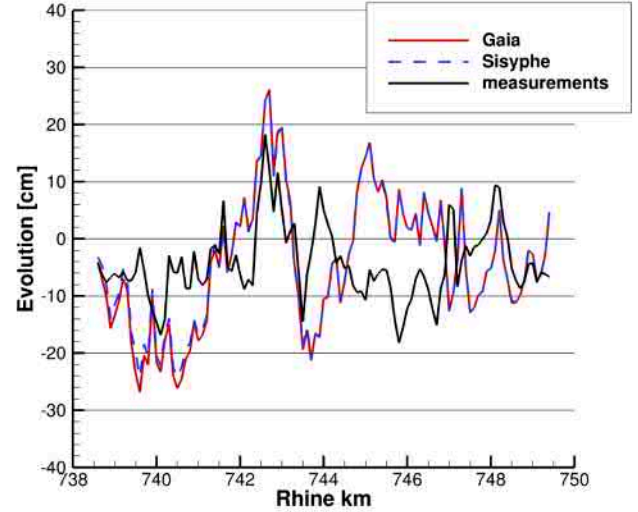


Fig. 6: Comparison of the mean bottom evolution after 6.5 years computed by GAIA and SISYPHE to measurements.

Mass balance	SISYPHE	GAIA
Mass lost ( $t$ )	493	655
Initial mass ( $Mt$ )	669	669
Relative error to initial mass	$0.7 \times 10^{-4}$	$1 \times 10^{-4}$

TABLE I: Comparison of final mass balance between SISYPHE and GAIA.

subroutine to ensure stability and mass balance, while GAIA worked straight out of the box.

One of the most important results of a morphodynamic simulation is the comparison of a simulated versus observed mean bed evolution over flow length. For this case, the mean bed evolution is computed each 100 m of the flow length in the area between the groynes. Figure 6 shows the comparison between simulated and measured mean bottom evolution for both modules SISYPHE and GAIA. Numerical simulations performed with GAIA and SISYPHE reasonably good fit the measurements and show similar results. In Figure 7 the difference between the bed evolution computed by GAIA and SISYPHE is presented. Most of the differences occur at the transition zone from rigid to movable bed. This effect is stronger near the model inlet which points to a different behaviour at the inlet boundary. Further investigations are necessary to clarify the causes. The bottom evolution and mean diameter distribution for the total simulation time are shown in Figures 8 and 9 for both GAIA and SISYPHE modules. In Figure 10, comparisons between SISYPHE and GAIA at cross sections Rhine-km 740.7, 743.6 and 746.9 (see Figure 5), show that the model is able to reproduce bed evolution levels at the meandering reach.

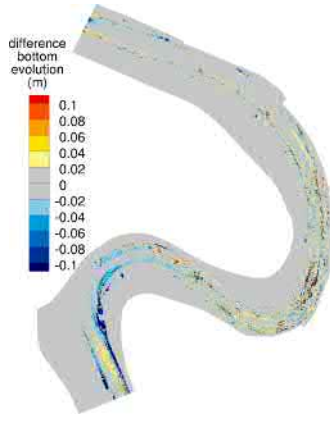


Fig. 7: Differences of the bottom evolution between GAIA and SISYPHE after 6.5 years.

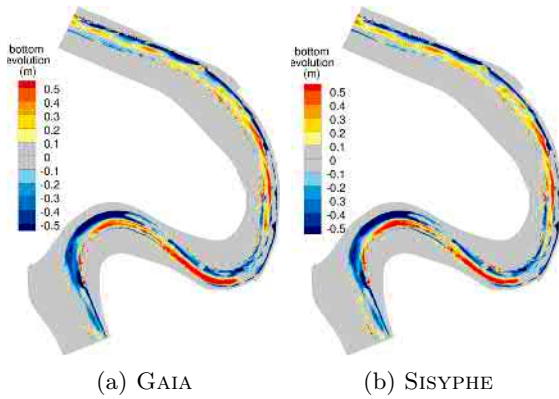


Fig. 8: Bottom evolution after 6.5 years

## VIII. OUTLOOK

Within this new code structure available in the TMS, a large number of complex physical processes commonly found in river, coastal and estuarine modelling applications benefit of an optimized framework.

GAIA can easily be expanded and customized to particular requirements by modifying user-friendly, easy-to-read, and well-documented FORTRAN files. Last but not least, theoretical aspects and validation test cases are documented and continually updated so that the quality of the source code remains assured.

For the current release of the TMS, the adaptation of the Continuous Vertical grain Sorting Model (CVSM) methodology [12] within the GAIA framework is underway.

Verification and validation cases presented in this work and being performed by the TMS's development team show that GAIA is on its way towards operational readiness.

## REFERENCES

- [1] B. Bleyel and R. Kopmann. "Influence of the layer model on a 2d sediment transport model: Hirano-Ribberink versus C-VSM". In *Proceedings of the XXVth TELEMAC-MASCARET User Conference, 9 to 11 October 2018, Norwich, UK*, pages 61–66, 2018.

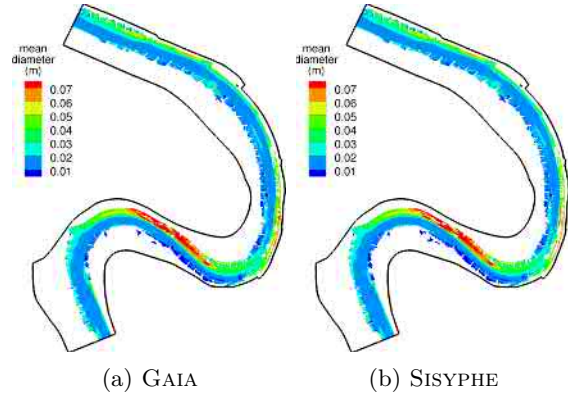


Fig. 9: Mean diameter distribution after 6.5 years

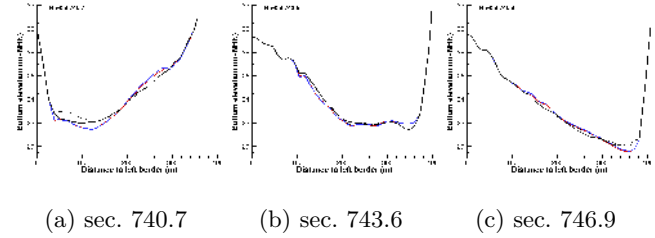


Fig. 10: Bottom elevation at different sections of the river reach, see Figure 5 for locations. Above, red line: GAIA, blue line: SISYPHE, black thick line: measured 2006 and black thin line: measured 2000.

- [2] A. Blom. "Different approaches to handling vertical and streamwise sorting in modeling river morphodynamics". *Water Resources Research*, 44(3), 2008.
- [3] J.M. Brown and A.G. Davies. "Methods for medium-term prediction of the net sediment transport by waves and currents in complex coastal regions". *Continental Shelf Research*, 29(11):1502–1514, 2009.
- [4] F. Cordier, P. Tassi, N. Claude, A. Crosato, S. Rodrigues, and D. Pham Van Bang. "Numerical study of alternate bars in alluvial channels with nonuniform sediment". *Water Resources Research*, 55(4):2976–3003, 2019.
- [5] M. de Linares, R. Walther, J. Schaguene, C. Cayrol, and L. Hamm. "Development of an hydro-sedimentary 3D model with sand-mud mixture - calibration and validation on 6 years evolution in the Seine estuary". In *Toorman, E.A. et al. (Ed.) INTERCOH2015: 13th International Conference on Cohesive Sediment Transport Processes, 7-11 September 2015, Leuven, Belgium*, pages 25–26, 2015.
- [6] S. Dutta, D. Wang, P. Tassi, and M.H. Garcia. "Three-dimensional numerical modeling of the bulle effect: the nonlinear distribution of near-bed sediment at fluvial diversions". *Earth Surface Processes and Landforms*, 42(14):2322–2337, 2017.
- [7] A. Giardino, E. Ibrahim, S. Adam, E.A. Toorman, and J. Monbaliu. "Hydrodynamics and cohesive sediment transport in the Ijzer estuary, Belgium: Case study". *Journal of Waterway, Port, Coastal, and Ocean Engineering*, 135(4):176–184, 2009.
- [8] R. B. Krone. "Flume Studies of the Transport of Sediment in Estuarial Shoaling Processes Final Report". University of California, 1962.
- [9] B. Latteux and J.M. Tanguy. "Système logiciel 'SISYPHE' de transport sédimentaire et d'évolution morphologique". Technical Report HE-42/89.39, Electricité de France – Direction des études et recherches, Département Laboratoire National d'Hydraulique Groupe Hydraulique Maritime, January 1990. Cahier de charges.

- [10] P. Le Hir, F. Cayocca, and B. Waeles. "Dynamics of sand and mud mixtures: A multiprocess-based modelling strategy". *Continental Shelf Research*, 31(10, Supplement):S135–S149, 2011.
- [11] A. Mendoza, J.D. Abad, E.J. Langendoen, D. Wang, P. Tassi, and K. El Kadi Abderrezzak. "Effect of sediment transport boundary conditions on the numerical modeling of bed morphodynamics". *Journal of Hydraulic Engineering*, 143(4):04016099, 2017.
- [12] U. Merkel. "C-VSM-II: Large scale and long time simulations with Sisyphe's continuous vertical grain sorting model". In *Proceedings of the XXIVth TELEMAC-MASCARET User Conference, 17 to 20 October 2017, Graz University of Technology, Austria*, pages 131–138, 2017.
- [13] E. Partheniades. "Erosion and deposition of cohesive soils". *Journal of the Hydraulics Division*, 91(1):105–139, 1965.
- [14] P.E. Robins, S.P. Neill, and M.J. Lewis. "Impact of tidal-stream arrays in relation to the natural variability of sedimentary processes". *Renewable Energy*, 72:311–321, 2014.
- [15] P. Santoro, M. Fossati, P. Tassi, N. Huybrechts, D. Pham Van Bang, and I. Piedra-Cueva. "Effect of self-weight consolidation on a hydro-sedimentological model for the Río de la Plata estuary". *International Journal of Sediment Research*, 34(5):444 – 454, 2019.
- [16] P. Santoro, M. Fossati, P. Tassi, N. Huybrechts, D. Pham Van Bang, and J.C.I. Piedra-Cueva. "A coupled wave-current-sediment transport model for an estuarine system: Application to the Río de la Plata and Montevideo Bay". *Applied Mathematical Modelling*, 52:107–130, 2017.
- [17] R. Soulsby. *"Dynamics of Marine Sands: A Manual for Practical Applications"*. Telford, 1997.
- [18] R.L. Soulsby and J.V. Smallman. "A direct method of calculating bottom orbital velocity under waves". *Hydraulics Research Wallingford*, 1986.
- [19] D. H. Swart. "Predictive equations regarding coastal transports". *Coastal Engineering* 1976, pages 1113–1132, 1976.
- [20] D. Van den Eynde, A. Giardino, J. Portilla, M. Fettweis, F. Francken, and J. Monbaliu. "Modelling the effects of sand extraction, on sediment transport due to tides, on the kwintebank". *Journal of Coastal Research*, pages 101–116, 2010.
- [21] M. van Ledden. "Modelling of sand-mud mixtures. Part II: A process-based sand-mud model". Technical report, Delft Hydraulics, 2001.
- [22] C. Villaret, J.-M. Hervouet, R. Kopmann, U. Merkel, and A.G. Davies. "Morphodynamic modeling using the Telemac finite-element system". *Computers and Geosciences*, 53:105–113, 2013. Modeling for Environmental Change.
- [23] C. Villaret and R. Walther. "Numerical modelling of the Gironde estuary". In *Physics of Estuaries and Coastal Sediments*, Liverpool, August 2008.
- [24] J. C. Winterwerp, W. G. M. van Kesteren, B. van Prooijen, and W. Jacobs. "A conceptual framework for shear flow-induced erosion of soft cohesive sediment beds". *Journal of Geophysical Research: Oceans*, 117(C10), 2012.
- [25] W. Wu. *"Computational River Dynamics"*. NetLibrary, Inc. CRC Press, 2007.
- [26] C.-L. Yen and K.T. Lee. "Bed topography and sediment sorting in channel bend with unsteady flow". *Journal of Hydraulic Engineering*, 121(8):591–599, 1995.

## APPENDIX

A summary of new keywords and printout variables is given below (variable values are provided as an example).

### A. New keywords

#### 1) General:

- **CLASSES TYPE OF SEDIMENT** = NCO;NCO;NCO;NCO;NCO, with NCO and CO for non-cohesive and cohesive sediments, respectively.
- **LAYERS NON COHESIVE BED POROSITY** = 0.37500 one value for each initial stratification layer (see below: A5 *Bed model*)

- **CLASSES SEDIMENT DENSITY** = 2650.;2650.;2650.;2650.;2650.
- **CLASSES SHIELDS PARAMETERS** = 0.047;0.047;0.047;0.047;0.047
- **CLASSES SEDIMENT DIAMETERS** = 0.00031;0.00064;0.00103;0.00169;0.00336
- **CLASSES INITIAL FRACTION** = 0.2;0.2;0.2;0.2;0.2

#### 2) Bedload:

- **BED LOAD FOR ALL SANDS** = YES
- **BED-LOAD TRANSPORT FORMULA FOR ALL SANDS** = 1. Use = 0 if the bed transport formula is provided by the user with the FORTRAN file `user_bedload_qb.f`.
- **CLASSES HIDING FACTOR** = 1.;1.;1.;1. default if HIDING FACTOR FORMULA = 0
- **MORPHOLOGICAL FACTOR ON TIME SCALE** = 1

#### 3) Suspended load:

- **SUSPENSION FOR ALL SANDS** = NO
- **CLASSES SETTLING VELOCITIES** = -9;-9;-9;-9;-9. Use = -9 if the settling velocity is computed by GAIA.
- **SUSPENSION TRANSPORT FORMULA FOR ALL SANDS** = 1
- **MORPHOLOGICAL FACTOR ON BED EVOLUTION** = 1

#### 4) Cohesive sediment:

- **LAYERS MUD CONCENTRATION** = 50.
- **LAYERS CRITICAL EROSION SHEAR STRESS OF THE MUD** = 0.1
- **LAYERS PARTHENIADES CONSTANT** = 1.E-4

#### 5) Bed model:

- **BED MODEL** = 1, options: = 1 multilayer case, GAIA sets automatically the active layer if several classes; = 2 multilayer with consolidation; and = 3 consolidation model based on Gibson's theory.
- **NUMBER OF LAYERS FOR INITIAL STRATIFICATION** = 1
- **LAYERS INITIAL THICKNESS** = 1

The subroutine `user_bed_init.f` allows the user to define the bed structure by a given (constant) number of layers.

#### 6) Consolidation:

- **NUMBER OF LAYERS OF THE CONSOLIDATION MODEL** = 1
- **LAYERS MASS TRANSFER** : 0.

#### 7) Numerics:

- **ADVECTION-DIFFUSION SCHEME WITH SETTLING VELOCITY** = 1

#### 8) Waves:

- **TYPE OF WAVES** = 2, the option by default is = 2 (irregular waves). Use = 1 for regular (monochromatic) waves.

### B. New printout variables

- **kRi**="fraction of cohesive sediment of class i, in k layer"
- **kXKV**="porosity of k layer"
- **kSi**="mass of non cohesive sediment of class i, in k layer"
- **kMi**="mass of cohesive sediment of class i, in k layer"

Above, **k** stands for the layer number (i.e. 1 is the first layer, 2 is the second layer, etc.).

### C. Converter SISYPHE to GAIA

The python script `converter.py` converts the steering files from SISYPHE to GAIA (to be used with caution): `converter.py sis2gaia sis_cas gaia_cas`, with `sis_cas` and `gaia_cas` the steering files for SISYPHE and GAIA, respectively.



# Method to integrate a simplified erosion channel during flood in reservoir simulation with Telemac

Eric Valette, Matthieu Sécher  
Centre d'Ingénierie Hydraulique EDF  
La Motte Servolex France  
[matthieu.secher@edf.fr](mailto:matthieu.secher@edf.fr)

Yoann Audouin, Jacques Fontaine, Cédric Goeury  
Laboratoire National d'Hydraulique et Environnement,  
EDF R&D, Chatou France

**A new tool which manage an automatic erosion channel generation in a TELEMAT 2D software is presented in this paper. This tool intended to solve the problem of overestimation of the water level that usually occurs when calculating a flood water line upstream a barrage without taking into account the erosion of the bottom.**

**The final result is a hypothetical equilibrium state corresponding to the lowest possible bottoms for the modeled flow, if the flood rise and the management of the reservoir level with barrage gates allowed enough time to reach this equilibrium state.**

## I. INTRODUCTION

Deposition of fine sediments could increase the bottom level of the reservoirs by several meters. If we don't take into account bottom evolution in numerical simulation of flood events, very high velocities (potentially supercritical flow) are obtained in front of the barrage. Consequently, simulated longitudinal water elevation could be higher than real water elevation. However, in reality, these high velocities cause the erosion of alluvial bottoms and the creation of a channel that will increase the flood capacity of the section in the reservoir. Generally, when the peak of the flood occurs on a barrage with all its gates opened, the longitudinal water elevation will be lower than that obtained with hard bottoms.

Hydro-sedimentary dynamics can be studied using Sisyphé. However, this kind of studies could be expensive in time and data.

A simplified approach is adopted here.

## II. OVERVIEW OF THE METHOD

A PYTHON script apply an automatic erosion channel in the TELEMAT 2D bottom model according to inflow rate and water elevation at the barrage. Starting with a simple description of the supposed outline of the future channel (using a GIS software), this module allows to:

- Dig a trapezoidal channel in the bathymetry, based on geometric parameters imposed by the user or derived from simple morphodynamic laws based on Ramette hypothesis [1].

- Start TELEMAT 2D calculation of a hydraulic steady state of the flood peak with the Application Program Interface (API) mode (TELAPY) to realize a digging of the channel.
- Automatically perform several post-processing (2D map of the velocities and the bathymetry obtained after channel application, water elevation, volume of sediments removed) allowing to analyze and control the steady state.

The final result is a hypothetical equilibrium state corresponding to the lowest possible bottoms for the modeled flow, if the flood rise and the management of the reservoir level with barrage gates allowed enough time to reach this equilibrium state.

## III. HOW TO DIG THE CHANNEL (THEORY)

### A. Channel set up

First of all the channel set up is realised using an SIG software to define:

- The hydraulic axis of the channel (polyline - shape file).
- The area in which the algorithm is able to enlarge the channel (polygon - shape file). This area is useful to exclude zone like dike, unerodable bottom, etc.

### B. Channel digging

Two options are implemented to dig the channel:

- The user define the depth of an initial channel upstream the dam, the slope and width of the channel.
- Depth, slope and width are calculated by the software based on morphodynamic laws based on Ramette hypothesis [1].

### C. Morphodynamic laws

Some hypothesis are realise to describe the theoretical channel dimension:

- Manning Strickler equation is available :

$$Q = K_t S R_h^{2/3} \sqrt{J_t} \quad (1)$$

With:

$K_t$ : Strickler coefficient ( $m^{1/3}s^{-1}$ ),

$S$ : Flow section ( $m^2$ ),

$R_h$ : Hydraulic radius (m),

$J_t$ : Slope of the energy grade line (m/m)

- The evolution of the bed to an equilibrium state is carried out spending the minimum of energy. As a result of this hypothesis, the Froude number is maximised and we have :

$$L = 18h \quad (2)$$

With:

$L$ : Width of the channel (m)

$H$ : Water depth (m)

- The shear stress is equal to the critical shear stress

$$\rho g R_h J_p = \tau_c \quad (3)$$

Where

$$J_p = J_t \left( \frac{K_t}{K_p} \right)^{3/2} \quad (4)$$

With:

$\rho$ : Water density ( $kg/m^3$ ),

$g$ : Gravity ( $m/s^2$ )

$\tau_c$ : Critical shear stress (Pa)

$K_p$  = Skin Strickler coefficient ( $m^{1/3}s^{-1}$ )

$J_p$ : Slope (due to skin Strickler coefficient) (m/m)

#### D. Analytic solution of Ramette criteria equations

The equations (1), (2), (3) and (4) have an analytic solution:

$$h = \left\{ \frac{\left( \frac{10}{9} \right)^{1/3} \cdot Q^2 \cdot \left( \frac{\rho g}{\tau_c} \right) \left( \frac{K_t}{K_p} \right)^{3/2}}{(18K_t)^2} \right\}^{3/13} \quad (5)$$

$$J_t = \left\{ \frac{18 \cdot \left( \frac{10}{9} \right)^2 \cdot K_t \cdot \left( \frac{\tau_c}{\rho g} \right)^{1/3} \cdot \left( \frac{K_p}{K_t} \right)^4}{Q} \right\}^{6/13} \quad (6)$$

$$L = 18h$$

If we consider a trapezoidal section, bottom width is given by:

$$B = L - 2 \cdot \frac{b}{2} = L - h/\alpha \quad (7)$$

With:

$B$ : bottom width of the channel (m),

$L$ : medium width of the channel (m),

$\alpha$ : stability angle of the sediment (elevation / base)

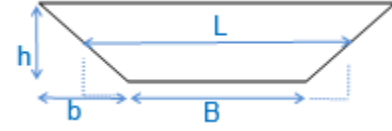


Figure 1: Trapezoidal geometrie.

This analytic system allow drawing curve of water depth as a simple function of critical shear stress and flow.

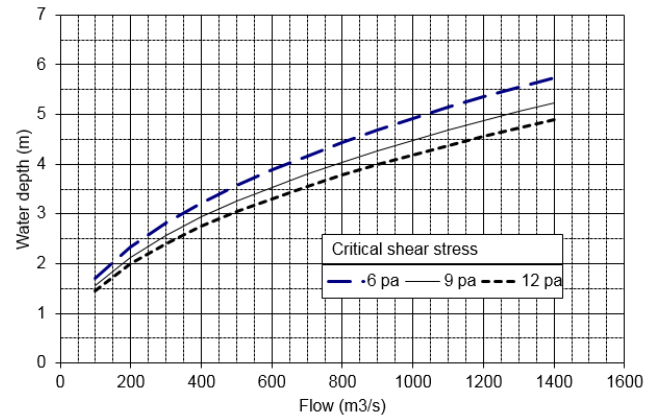


Figure 2: Water depth as a function of critical shear stress and flowrate.

#### IV. INTEGRATION AS A TELEMAR TOOL

Once the parameter of the channel choose by the user or compute with Ramette equation, the tool:

- Step 1: Apply the first erosion to shape the channel in the initial bathymetry with shapes file (polyline of the center of the canal, polygon limit of the channel) and geometrical parameters of the channel.
- Step 2: Create a StudyTelemac2D class used to prepare files and temporary folder of calculations and make a run with Telemac 2D API and the new bathymetry
- Step 3: If the depth is define by Ramette Law or Step 3 is converged the tool realized a final post-treatment to:
  - Calculate erosion volumes.
  - Create a text file with volume of erosion, the value of the criterion and the percentage of nodes where the target is not reached.
  - Generate map of several variables (Froude number, velocities, bathymetry, etc.)

Flowcharts of the tool are given figure 3 and figure 4

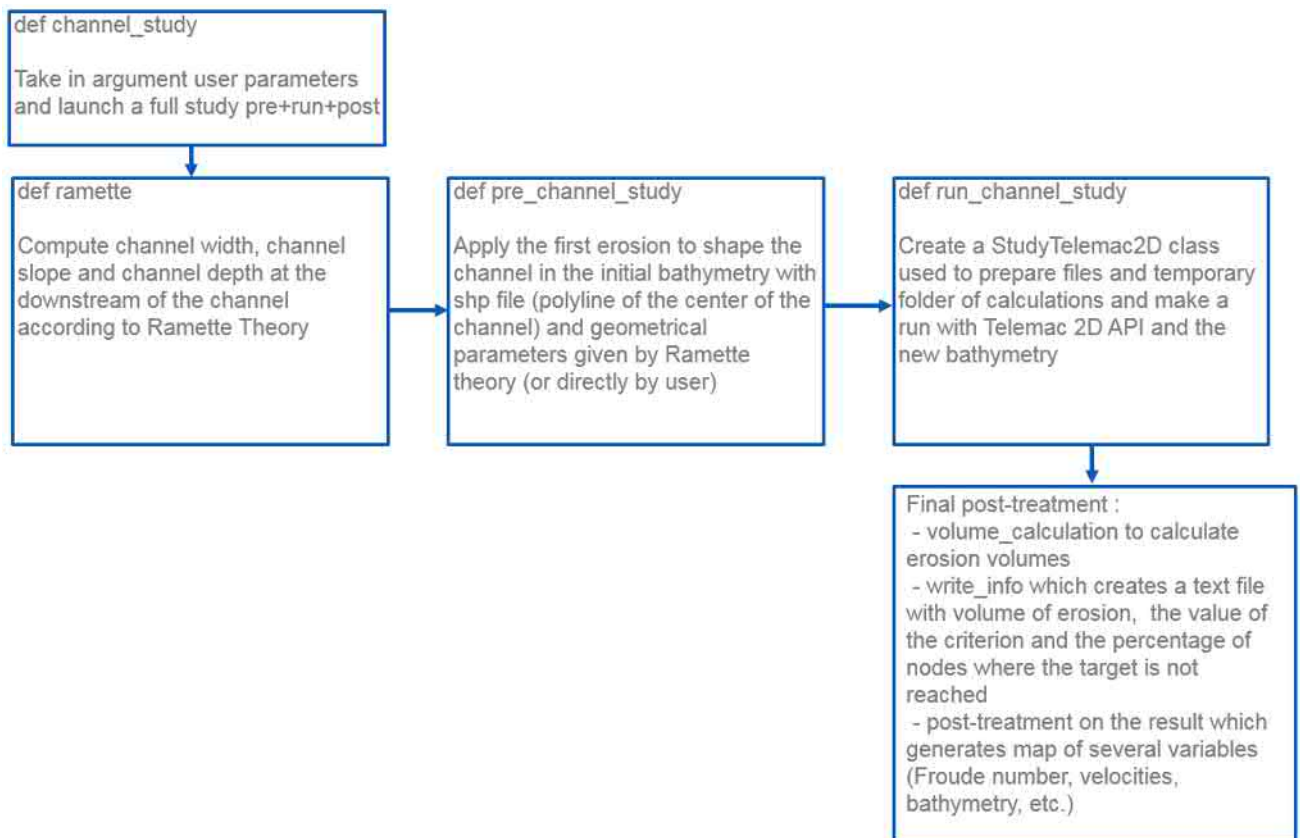


Figure 3: Flowchart with Ramette equations (figure 3)

## V. EXAMPLE

Figures 4, 5 and 6 illustrate the erosion channel created by the tool in a reservoir. The Flowrate was equal to 3 800 m<sup>3</sup>/s. the eroded volume is equal to 1.14 Million m<sup>3</sup> and the parameter calculated by Ramette equations with a critical shear stress of 12 Pa and a canal bank slope of 0.3 m/m are:

- Water depth : 7.90 m
- Slope :  $5 \times 10^{-4}$  m/m
- Width: 142 m.

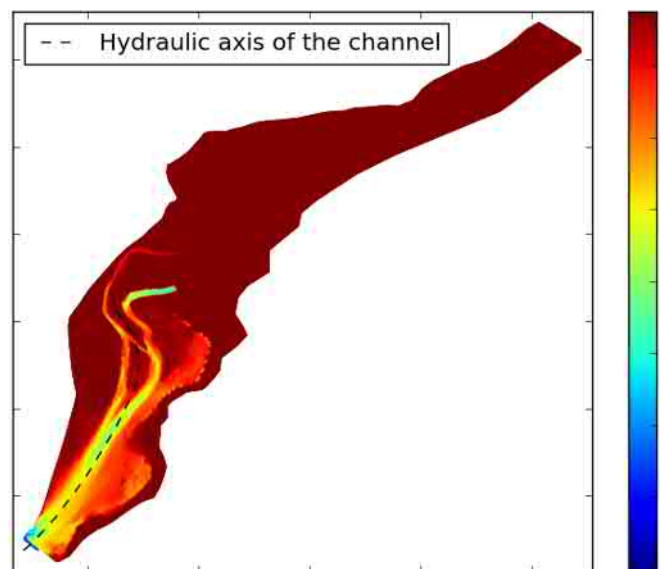


Figure 4: Initial bottom of the reservoir example with the line representing the hydraulic axis use to erode a channel

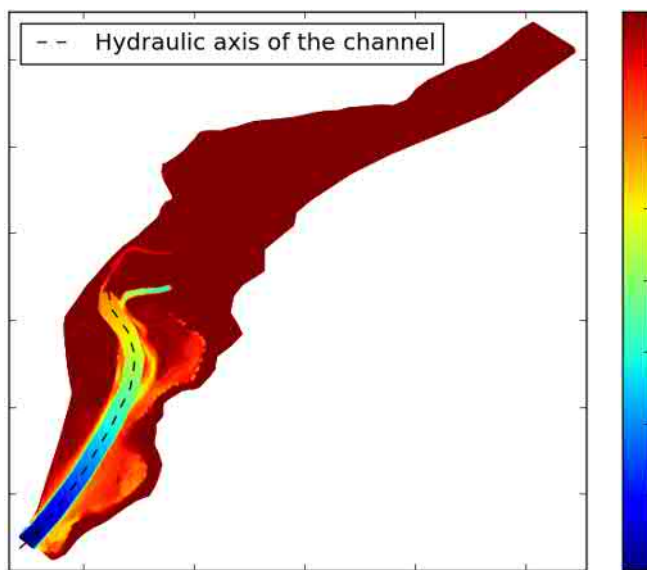


Figure 5: Final bottom of the reservoir example with the line representing the hydraulic axis use to erode a channel

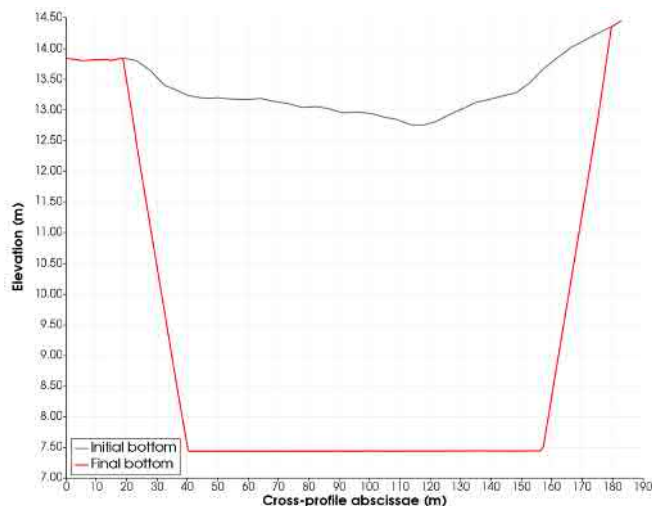


Figure 6: Cross profile of bottom before and after applying the erosion of the channel extracted at the middle of the channel

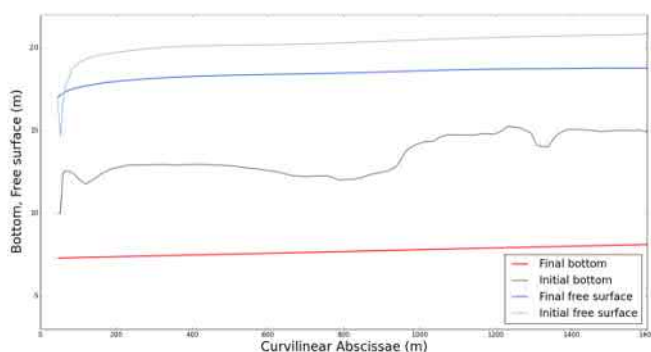


Figure 7: Longitudinal profile of bottom and free surface ( $3\,800\text{ m}^3/\text{s}$ ) before and after applying the erosion of the channel extracted along the hydraulic axis (see Fig. 4 and 5)

The figure 7 give the comparison of the initial and the final water level in the reservoir

## VI. TO CONCLUDE

This method should be considered as a tool decision support using to evaluate the potential margins between water elevations evaluated with fixed-bottom model and erodible bottom model. If margins are highlighted, a complete hydro-sedimentary calculation may be initiated; if not, civil work (increase levees elevation, increase of dam spillways capacity, etc.) can be directly considered.

Other applications can be considered with this method:

- first-order estimate of volumes eroded during flushing, or sluicing,
- first-order estimate of volumes eroded during reservoir drawdown.

This method was developed in PYTHON during a hackathon that was held over 3 days at the CIH with 3 members of EDF R&D and 2 members of EDF CIH.

## REFERENCES

- [1] M. Ramette, "Modélisation mathématique du processus morphologique des fleuves" AIRH, XIX congrès, New Delhi, India, 1981, pp 392-400
- [2] J-M. Hervouet, "Hydrodynamics of Free Surface Flows", Wiley, 2007, pp. 83–130.
- [3] Hunter, J. D. Matplotlib: A 2D graphics environment, IEEE COMPUTER SOC Volume 9 Number 3 Pages 90-95 (2007)
- [4] G. van Rossum, Python tutorial, Technical Report CS-R9526, Centrum voor Wiskunde en Informatica (CWI), Amsterdam, May 1995.



# Development of a hydro-morphodynamic Model for Sediment Management in the Rosenheim Reservoir

Diego Vladimir Aguirre Iñiguez, Minh Duc Bui, Stefan Giehl, Markus Reisenbüchler, Peter Rutschmann  
Chair of Hydraulic and Water Resources Engineering  
Technical University of Munich (TUM)  
Munich, Germany  
diego.aguirre@tum.de

**Abstract—** In this study, a hydromorphological model of the Rosenheim reservoir, one of the impoundments formed by a chain of run-of-river power plants along the Inn River (Germany), was developed by coupling TELEMAC-2D and SISYPHE. Available bathymetry surveys, conducted after the high magnitude flood events in 2005 and 2013, were used for calibration and validation respectively. The implementation of the subroutines modified by the Chair of Hydraulic and Water Resources Engineering of the Technical University of Munich together with the selection of a low angle of friction of the sediment for the secondary currents correction produced a good match between the measured and simulated cross-section profiles. The model's ability to predict the bed variation after the event was evaluated using the Brier Skill Score (BSS) and considering the initial bathymetry as the baseline prediction. Applying this technique, the three following parameters were considered: (i) phase error to assess the accuracy of the location of erosion and deposition processes, (ii) amplitude error to evaluate the bed evolution magnitude and (iii) mean map error to estimate the bias of the simulation against the measurements. The model was successfully calibrated and validated with BSS values being in the category of excellent and good together with a high number of cross-sections featuring low phase, amplitude and mean map errors. The calibrated model is presently applied to other flood events in the reservoir.

## I. INTRODUCTION

Human settlements along the floodplains of the Inn River have led to canalization, river training and construction of hydropower plants that have modified its natural hydromorphological and ecological characteristics [1, 2]. Throughout the operational years of the chain of hydropower plants (HPP) along the Inn River, a large amount of sediments have been trapped near the dams resulting in a strong alteration of the natural slope of the river [1]. The selection of a proper sediment management strategy for reservoirs is of great importance to avoid the loss of storage capacity, to manage floods safely, and to achieve a Good Ecological Status (GES). Calibrated hydro-morphological models can predict sediment transport processes realistically and thus be used as powerful tools in the decision-making process. Apart from the impact to the ecological environment and habitat connectivity, previous studies of the Inn River have concluded that the fine particles that form the bed have a highly dynamic response to the increasing of flow discharge during flood events [1] and therefore, a hydromorphological approach should be used in order to perform flood modelling. To this goal, the application

of the 2D numerical model, TELEMAC-2D (T2D), coupled with the sediment transport module, SISYPHE (SIS), from the TELEMAC-MASCARET System [3] is applied to the case study of the Rosenheim Reservoir as part of the Project of Development and Application of an Integrated Mathematical Model for Reservoir Sediment Management (NEREID). This project is part of the Programme for the Promotion of the Exchange and Scientific Cooperation between Greece and Germany IKYDA 2018.

## II. STUDY AREA

The study area is the Rosenheim Reservoir, one of the 16 impoundments formed by the dams of the chain of run-of-river HPP along the German side of the Inn River. The 11.2 km long river segment is bounded at the upstream by the Nußdorf HPP, at the Inn kilometer (rkm) 198.7, and at the downstream by the Rosenheim HPP at the rkm=187.5. The catchment area at this point of the Inn River is approximately 10,000 km<sup>2</sup> and the mean flow discharge 316 m<sup>3</sup>/s. Fig. 1 shows the location of the study site with respect to the city of Munich.

## III. MATERIALS AND METHODS

### A. Numerical model

The TELEMAC-MASCARET System has proven to be a powerful tool for the integrated river engineering projects. Specifically, the implementation of coupled numerical models between the 2D hydrodynamics module, TELEMAC-2D, and the sediment transport module, SISYPHE, have been successfully carried out for several case studies performed by

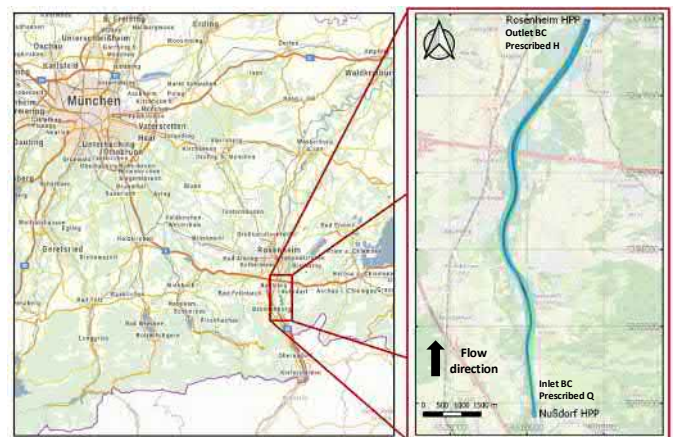


Figure 1. Location of the Rosenheim Reservoir (Adapted from [4,5])

the Chair of Hydraulic and Water Resources Engineering of the Technical University of Munich (TUM) [6–8]. The TELEMAC-2D module solves the depth-averaged free surface flow equations giving the user the possibility to select between different numerical schemes, solvers and physical parameters. On the other hand, the SISYPHE module solves the sediment balance equation to simulate the bed evolution and grain sorting. Depending on the application, the user can select between a range of sediment transport equations for bedload and suspended load. In addition, this module is capable of simulate non-uniform sediment transport, cohesive sediment and mixed sediment.

### B. Model set-up

We built an unstructured triangulated mesh using the software BlueKenue [9] paying special attention to the use of break lines to obtain a precise implementation of the river shape while maintaining a constant element size through the domain. The resulting mesh for this 11.2 km long reach had 26,034 elements with average edge lengths of approximately twelve meters.

The bed elevation at the grid points within the flood plains were interpolated using topography surveys obtained by airborne laser scans with resolution of one square meter. The implementation of different bathymetries depending of the event of interest was possible due to the existence of bathymetry surveys measured as cross-sectional profiles each 200 meters in different years.

### C. Hydrodynamic model

The model was configured to solve depth-averaged Saint-Venant Equations by using the fractional step method implemented in T2D, where the advection terms are solved using the method of the characteristics; and the propagation, diffusion and source terms by the finite element method [10]. Additionally, the  $k-\epsilon$  turbulence model with the default value for turbulent quantities was selected. To guarantee stability of the simulations and accuracy in the results, we chose a time step of one second. As in previous models [1] the bottom roughness was defined by the Strickler coefficient.

The information for the boundary conditions was obtained from the water stages and flow discharge measurements made by the HPP operator at the upstream and downstream of the weirs of the dams every 15 minutes. For the inlet boundary condition, we used the above-mentioned measurements at the downstream of the Nußdorf HPP as the prescribed flow discharge. In the same manner, for the outlet, we used the stage hydrographs at the upstream of the Rosenheim HPP weirs as a prescribed elevation boundary condition (see fig. 1). The flow discharge and stages hydrographs used for the simulations are depicted in figs. 2 to 4.

To determine the feasibility of using certain flood events as hydrodynamic calibration and validation periods, the availability of water level recordings at gauging stations located within the domain was analyzed.

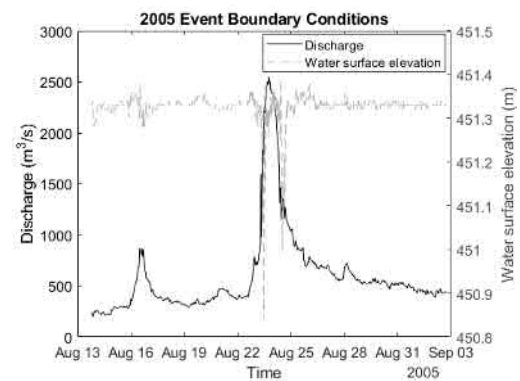


Figure 2. Boundary conditions for the 2005 event.

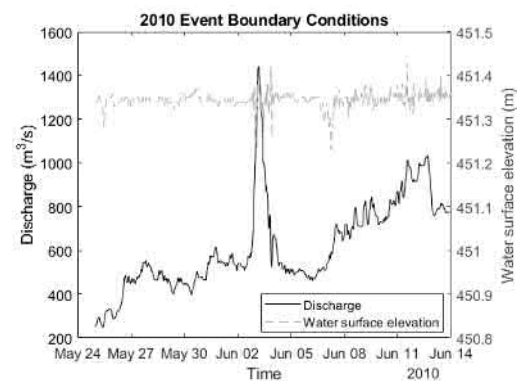


Figure 3. Boundary conditions for the 2010 event.

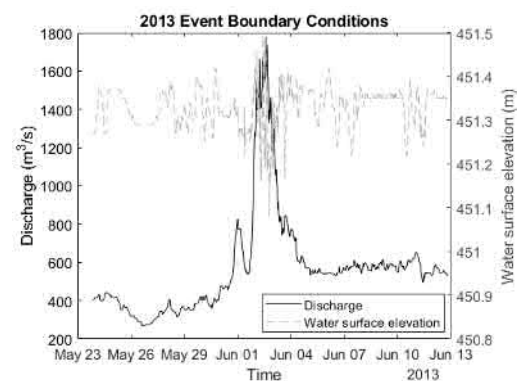


Figure 4. Boundary conditions for the 2013 event.

We concluded that the events of 2005 and 2013 would serve for the calibration period while the event of 2010 would be used for validation. The reason behind this decision is that only the upstream gauge was operating during the 2005 flood event. Fig. 5 presents the river stations where these data were recorded.

The bathymetry used for the calibration events was measured in 2003, which is considered the equilibrium bed elevation. In contrast, for the validation process, the implemented bathymetry was surveyed in 2009 since no high magnitude events were registered before the one of 2010.

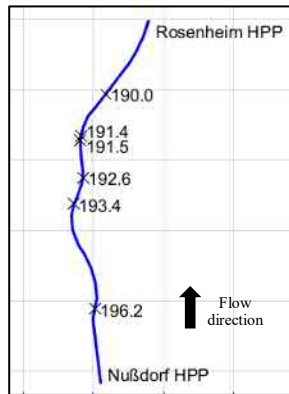


Figure 5. Location of the intermediate gauging stations used for the hydrodynamic calibration expressed as rkm.

#### D. Hydro-morphodynamic model

For the calibration and validation of the hydro-morphodynamic model, the boundary conditions for the fractional sediments were modified to allow a prescribed solid discharge at the inlet of the domain, as well as free open boundary for the sediments at the outlet. In order to generate the sediment discharge time series, concentration measurements taken in an upstream reservoir (rkm=211.0) were used to generate a sediment rating curve which is shown in fig. 6. Sieve analysis along the Inn River at the German side showed that there were two predominant sediment sizes: 0.16 and 0.40 mm in fractions of 0.4 and 0.6 respectively.

For calculating the sediment transport, formulas for total load were considered. The bed structure was discretized in two layers according to the modified subroutines for fractional sediment transport developed by the Chair of Hydraulic and Water Resources Engineering of the TUM [11], with a constant active layer thickness of 0.9 mm. Sediment slide, secondary currents, skin friction and slope effects were included in the sensitivity analysis. The elements outside of the riverbanks were set as non-erodible.

The availability of cross-sectional bathymetry surveys after the high magnitude flood events of 2005 and 2013 allowed choosing these as calibration and validation periods respectively. The summary of the calibration and validation periods used for the hydrodynamic clear water model and for the hydro-morphodynamic model is shown in table 1.

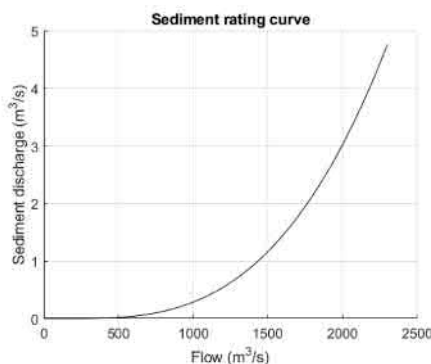


Figure 6. Sediment rating curve used for the inlet boundary condition.

TABLE 1: SUMMARY OF THE CALIBRATION AND VALIDATION PERIODS SELECTED FOR THE HYDRODYNAMIC AND HYDRO-MORPHODYNAMIC MODELS.

Period	Hydrodynamics		
	Event	Bathymetry	Modules
Calibration	2013 and 2005	2003	T2D
Validation	2010	2009	T2D
Period	Hydro-morphodynamics		
	Event	Bathymetry	Modules
Calibration	2005	2003	T2D+SIS
Validation	2013	2003	T2D+SIS

#### E. Model evaluation

The use of the goodness-of-fit parameters as recommended by [12] is well established in the calibration of hydrodynamic models and has been widely used for 1D parameters such as hydrographs or maximum water surface elevation along river profiles [6]. Therefore, the Nash-Sutcliffe Efficiency (NSE) was used for the assessment of the Hydrodynamic clear water model calibration. However, using a single parameter to determine the performance of a model to predict riverbed evolution processes might not be appropriate to perform a holistic evaluation. This makes the task of evaluating the results rather complicated. For this case study, we applied the Brier Skill Score (BSS) to evaluate the quality of the results as in the work of [13]. This method has been originally used in weather forecast models and uses a baseline prediction in order to quantify the skill of the new prediction of the model [14]. In hydromorphological models it is possible to use the initial river bed elevation as the baseline prediction [13]. Equation (1) shows the formula for the BSS, the set of observed values is  $X$ , the set of simulated values is represented by  $Y$  and the baseline predictions is  $B$ . Note that the angle brackets ( $\langle \rangle$ ) signify the mean value as indicated by (2) where  $n$  is the number of elements in  $X$ .

$$BSS = 1 - \langle (Y-X)^2 \rangle / \langle (B-X)^2 \rangle \quad (1)$$

$$\langle X \rangle = (X_1 + X_2 + \dots + X_n) / n \quad (2)$$

The use of the BSS allows the comparison of the skill of the model to simulate the sediment erosion and deposition processes along the whole domain depending on the availability of observed data. A perfect agreement between the simulation and observed values leads to a BSS equal to one, while any value of the BSS below zero stands for a simulation worse than the baseline prediction. Table 2 shows the recommended model performance classification ranges for the BSS by [13].

TABLE 2: RECOMMENDATION FOR MODEL PERFORMANCE CLASSIFICATION ACCORDING TO BSS (ADAPTED FROM [12])

Category	BSS Value
Excellent	1.0 – 0.5
Good	0.5 – 0.2
Reasonable/fair	0.2 – 0.1
Poor	0.1 – 0.0
Bad	< 0.0

The BSS can also be represented as a function of four parameters as shown in equation (3). Three of these parameters, namely  $\alpha$ ,  $\beta$  and  $\gamma$ , give further information of the skill of the model while measuring the phase error, amplitude error and map mean error respectively. The fourth parameter ( $\varepsilon$ ) is a normalization term [13]. Table 3 contains the ranges and the perfect agreement value of these parameters. Equations (4) to (7) show the formulas for calculated the parameters of the decomposition of the BSS. Note that these equations contain  $Y'$  and  $X'$ , which are the difference between the observations or simulations and the baseline prediction, see (8) and (9).

$$BSS = (\alpha - \beta - \gamma + \varepsilon) / (1 + \varepsilon) \quad (3)$$

$$\alpha = r^2_{Y'X'} = ((Y' - \langle Y \rangle) (X' - \langle X \rangle) / \sigma_{Y'} \sigma_{X'})^2 \quad (4)$$

$$\beta = (r_{Y'X'} - \sigma_{Y'} / \sigma_{X'})^2 \quad (5)$$

$$\gamma = (((Y' - \langle Y \rangle) - \langle X \rangle) / \sigma_{X'})^2 \quad (6)$$

$$\varepsilon = (\langle X \rangle / \sigma_{X'})^2 \quad (7)$$

$$X' = X - B \quad (8)$$

$$Y' = Y - B \quad (9)$$

We applied this methodology for the calibration and validation of the hydro-morphodynamic model comparing: (i) the mean bottom elevation profile to evaluate the skill of the model for simulating the erosion and deposition processes along the domain, and (ii) the cross-sectional profiles to measure the capabilities of this model to represent the morphological processes in the direction parallel to the main flow.

#### IV. RESULTS AND DISCUSSION

##### A. Hydrodynamic Calibration

The calibration process in TELEMAC-2D was carried out by modifying the Strickler coefficient, i.e. the bed roughness. We aimed to maintain physical values for this coefficient considering that lower velocities develop at the downstream of the reservoir, near the weirs of Rosenheim HPP, resulting in deposition of finer particles at the upstream. Fig. 9 shows the discretization of the calibrated Strickler coefficient along the domain.

As previously concluded by [1] it was not possible to find a set of roughness coefficients that could fulfill the water stages elevations for base flow and high flow conditions, this behavior can be observed in figs. 7 and 8. Therefore, we perform a calibration for base flow expecting that the hydromorphological model could simulate the highly dynamic riverbed evolution. Reaching NSE values falling within the categories of “satisfactory” and “very good” (according to [12]) for calibration and validation periods during base flow conditions, we considered that the clear water model was able

to adequately simulate flow velocities and water depths along the domain.

TABLE 3: DEFINITION OF THE DECOMPOSITION PARAMETERS OF THE BSS (ADAPTED FROM [12])

Parameter	Measure	Range	Perfect agreement
$\alpha$	Phase error	[0, 1]	1
$\beta$	Amplitude error	[0, + $\infty$ )	0
$\gamma$	Map mean error	[0, + $\infty$ )	0

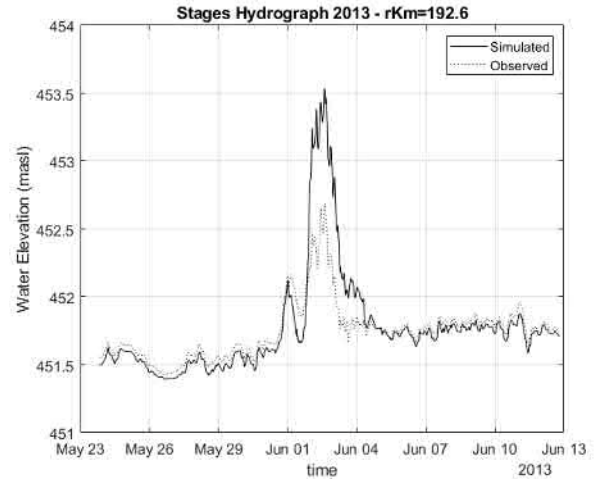


Figure 7. Stages hydrograph example for the calibration period reaching NSE=0.78 for base flow conditions

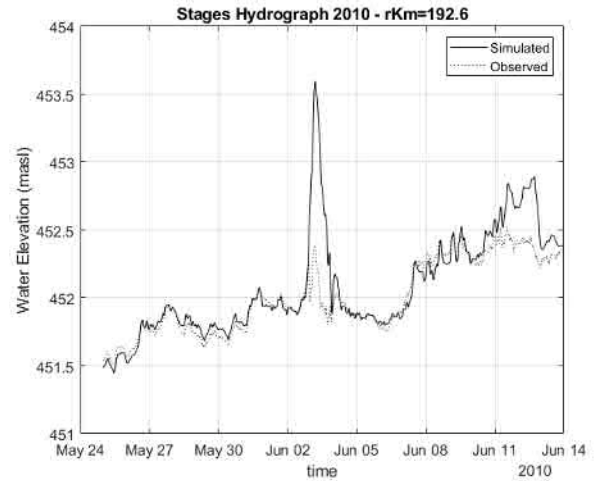


Figure 8. Stages hydrograph example for the validation period reaching NSE=0.90 for base flow conditions

##### B. Hydro-morphodynamic Calibration

After performing a sensitivity analysis with different sediment transport formulations it was considered that the Engelund-Hansen equation [15] for total load was adequate to represent the hydromorphological processes in the study area. Other total sediment transport formulations as the modified Engelund-Hansen Equation by [16] and the equation of Wu [17] were implemented leading to unsatisfactory results. For



the calibration process, the skin friction correction factor ( $\mu$ ) was implemented as a variable to be read from the Selafin file. In this manner, the value could be modified locally to alter the effective shear stress ( $\tau'_0$ ) and therefore the transport capacity of the domain as shown in (10).

$$\tau'_0 = \mu \tau_0 \quad (10)$$

During the calibration process, we intended to discretize the different values of the skin friction correction factor in the same segments as for the Strickler coefficients since in the boundary friction is associated to the skin friction [18]. However, some of these zones were further discretized in order to improve the results of the model. The discretization for this calibration factor is presented in fig. 9.

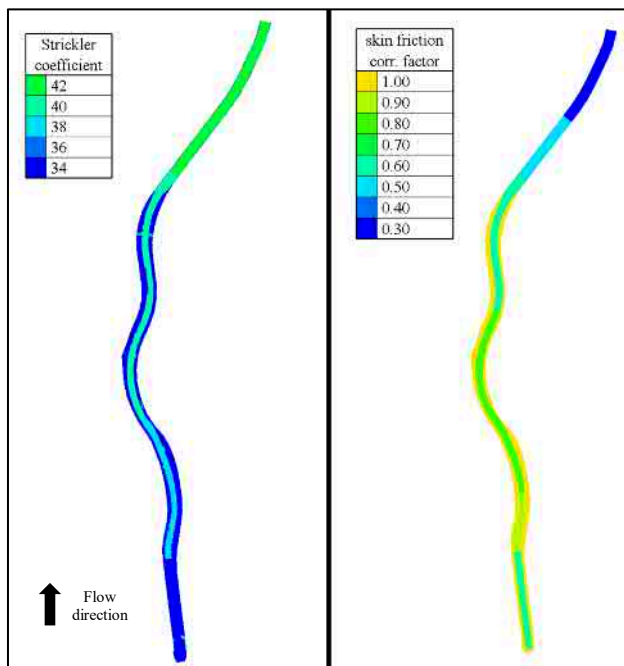


Figure 9. Calibrated Strickler coefficient (left), Calibrated skin friction factor (right).

Fig. 10 and fig. 11 are presented to assess the quality of the simulation along the domain by comparing the observed and the simulated mean bottom elevation profile (MBE) at the end of the event for the calibration and validation periods, this value was kept within a range of one meter for the majority of the surveyed cross-sections. For each figure, the gray indicates the MBE of the river before the event (i.e.: from the bathymetry of 2003 used as baseline prediction), while the red and the blue lines represent the observed and simulated MBE respectively. Furthermore, the absolute difference between the simulated and observed MBE is shown in figs. 10 and 11. Additionally, table 4 presents the BSS and the skill parameters for both the simulated periods.

An overall good performance of the developed numerical model is supported by the BSS values falling within the categories of “excellent” and “good” for calibration and validation respectively. However, the simulation of the event of 2005 led to lower phase, amplitude and map mean error results. By contrasting the  $\alpha$ ,  $\beta$  parameters for the calibration period with the graphical results showed in fig. 10, the model shows that it is capable of predicting erosion and deposition process at the correct location and by accurate volumes along the domain. This also leads to a low map mean error represented by a  $\gamma$  of 0.03.

The simulation of the event of 2013 showed a low model skill to estimate the right amount of sediment eroded and deposited along the domain even when these processes occurred in the correct locations except from some segments between  $rkm = 195.6$  and  $194.0$ . This behavior is reflected in a relatively high value of the phase error ( $\beta$ ). It is possible that 2003 bathymetry do not represent the real conditions of the morphology of the river before 2013 event.

TABLE 4: BSS FOR CALIBRATION AND VALIDATION OF THE HYDRO-MORPHODYNAMICS MODEL.

Event	BSS	$\alpha$	$\beta$	$\gamma$
2005 (calibration)	0.59	0.51	0.02	0.03
2013 (validation)	0.38	0.43	0.32	0.10

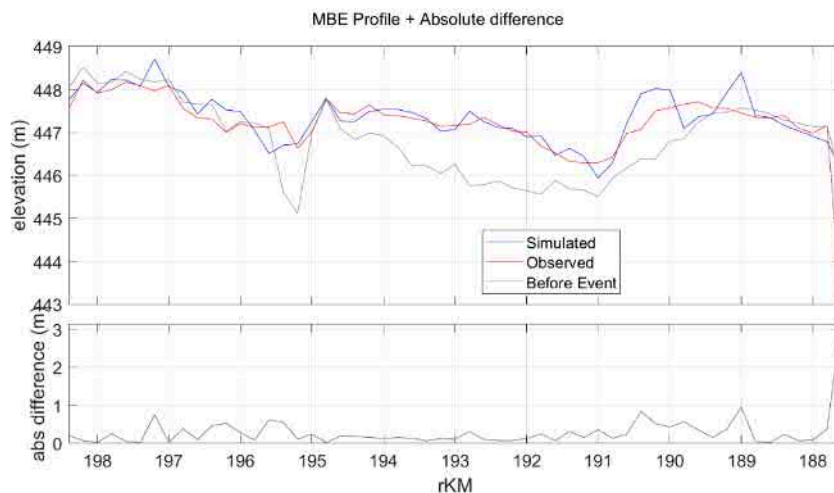


Figure 10. Comparison between observed and simulated MBE for the calibration period (top), Absolute difference (bottom).

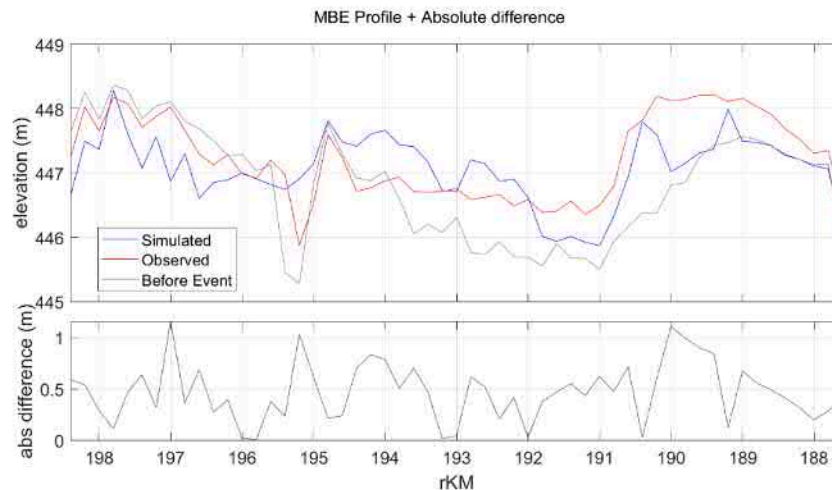


Figure 11. Comparison between observed and simulated MBE for the validation period (top), Absolute difference (bottom).

Along with the analysis of the MBE profiles, each cross-section was examined to evaluate the model capability to simulate sediment transport processes in the direction perpendicular to the main flow. Fig. 12 depicts some preliminary results at a cross section located at a river bend (rkm=192.6) for the simulation of the 2005 event. This result was not consistent with the observation, nor with the expected scour at the outer bank of the bend. This could be due to the hypothesis of the shallow water equations, which produce depth-averaged velocities that do not account for the decrease of the magnitude at the bottom caused by the slope effect and secondary currents.

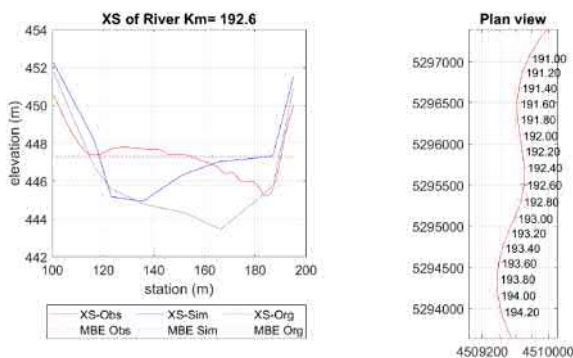


Figure 12. Results of a cross-sectional profile without considering the slope and secondary current effects.

To address the misrepresentation of the riverbed at the bends, we activated the consideration of the slope effect in the SISYPHE steering file using the Koch and Flokstra equation [19] and included the secondary currents effects to correct the intensity of the bed load transport rate. Additionally, we set a non-physical sediment friction angle of 3° to improve the results by limiting the element slope within the cross section. Therefore, since the banks were set non-erodible, the subroutine *maxslope.f* did not affect the shape of the channel. Fig. 13 shows the improvement of the cross-sectional profile simulation at the same cross-section (rkm=192.6) applying the corrections previously discussed.

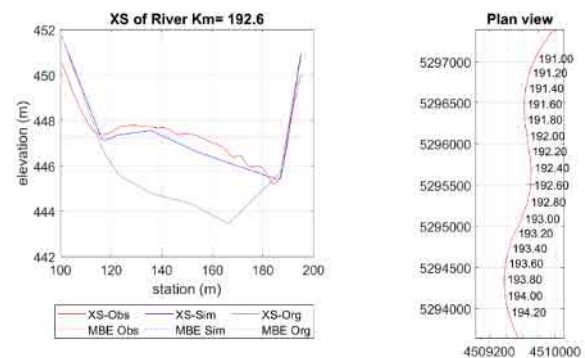


Figure 13. Results of a cross-sectional profile considering the slope and secondary current effects.

As in the MBE profile analysis, we applied the BSS skill criteria to all the 55 cross-section profiles of the reservoir. As expected, for the calibration period, the majority of the cross-sectional profiles were in the range of “reasonable” to “excellent” with a third of the total number of cross-sections in the highest category (18 out of 55). The river stations that resulted in high skill values were mostly found within the segment rkm=194.4 to 190.6, showing consistency with the plots presented in fig. 10. On the other hand, the majority of the cross-sectional profiles obtained from the simulation of the event of 2013 were considered worse than the baseline prediction. This is mainly due to the large amplitude error in most of the cross sections as it can be noted in fig. 14. Even if the erosion and deposition processes at the banks developed as expected along the cross-section, the model produced an overestimation of the total sediment accumulated in this section of the reservoir in the main direction of the flow. Table 5 summarizes the results of the skill of the model in the direction parallel to the main flow by indicating the quantity of cross-sections falling in each of the categories proposed by [13].

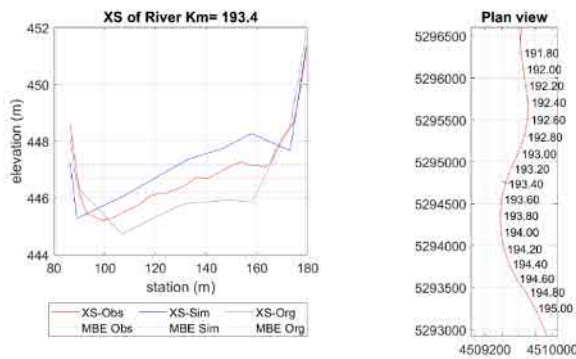


Figure 14. Poorly simulated cross-section profile due to excessive sedimentation.

TABLE 5 SUMMARY OF THE PERFORMANCE EVALUATION ALONG THE CROSS-SECTION PROFILES

Event	Number of cross-section profiles falling under:				
	<i>Excellent</i>	<i>Good</i>	<i>Reasonable/fair</i>	<i>Poor</i>	<i>Bad</i>
2005	18	9	3	1	24
2013	12	7	2	3	31

### C. River stages prediction by the hydro-morphodynamic model

At the stage of the developed model, the simulation of water levels at high flows was not improved. The overestimation attributed to highly dynamic particles at the bed was not confirmed by this case study. However, at some locations, the stage hydrograph for base flow conditions after the event presented better performance than the clear water model. This can be observed at the last third of the stage hydrograph depicted in fig. 15, where it is evident that the dashed red line maintains a constant offset with the observed values while the continuous black line, that shows the results of the hydro-morphodynamic model, fits almost perfectly to the observations. The river morphology after the simulation is closer to the observed one than the initial bathymetry (i.e.: 2003 survey) as demonstrated by the model performance evaluation based on the BSS parameters.

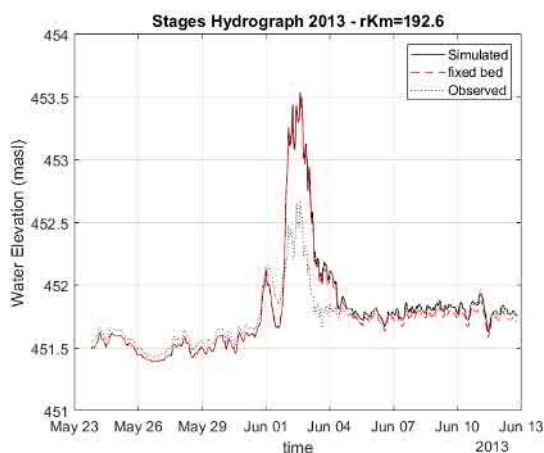


Figure 15. Poorly simulated cross-section profile due to excessive sedimentation.

## V. CONCLUSIONS

In this study, a hydro-morphodynamic numerical model using the TELEMAC-MASCARET system was developed and calibrated based on the information recorded during large magnitude flood events that occurred within the last 20 years. In general, the model provided a high performance for simulating hydromorphological processes within the domain by: (i) applying the total load sediment transport formula of Engelund-Hansen, (ii) implementing the improved fractional sediment transport subroutines by [11], and (iii) using a low friction angle of sediment for sediment transport in the main flow direction. Results from this model can be used for further studies to generate adequate sediment management strategies to improve the river ecological conditions.

A comprehensive analysis of the sediment balance of the upstream reservoir (Nußdorf Reservoir), where a turbidity gauging station is located, could lead to a definition of a better inlet boundary condition for this domain. Additionally, by replacing the total load sediment transport equation by an approach that considers bed and suspended load separately might reproduce the sediment transport processes more accurate. Finally, the improved model will be applied to study floods in this alpine catchment and give guidance for river management strategies.

## ACKNOWLEDGEMENT

The first author of this paper thanks the IKYDA project for the funding of this work and to the colleagues in the Chair of Hydraulic and Water Resources Engineering of the TUM for their knowledge and support through the development of the numerical model.

## REFERENCES

- [1] S. Giehl, M. B. Bui, and P. Rutschmann, "Effects of the dynamic bed on hydrodynamic modelling in the Inn River," in *New Challenges in Hydraulic Research and Engineering*, Trento, Italy, 2018.
- [2] K. Baumgartner, B. Gems, S. Walder, M. Federspiel, and M. Aufleger, "Influence of Bed-Load Transport on the Design of Flood Protection and Retention Measures in Gravel-Bed Rivers: Application of HYDRO\_FT-2D for the Tyrolean Inn River," in *Managing Water for Sustainable Development: Learning from the Past for the Future*, Kuala Lumpur, Malaysia, 2017, pp. 608–615.
- [3] EDF-R&D, *TELEMAC modelling system*, 2013.
- [4] OpenStreetMap contributors, *Planet dump retrieved from https://planet.osm.org*.
- [5] Bayerisches Staatsregierung, *Geoportal Bayern*. [Online] Available: <https://geoportal.bayern.de/bayernatlas/>. Accessed on: Apr. 14 2019.
- [6] M. Reisenbüchler, M. D. Bui, D. Skublics, and P. Rutschmann, "Enhancement of a numerical model system for reliably predicting morphological development in the Saalach River," *International Journal of River Basin Management*, vol. 10, no. 1, pp. 1–13, 2019.
- [7] S. Ateeq-Ur-Rehman, "Numerical Modeling of Sediment Transport in Dasu-Tarbela Reservoir using Neural Networks and TELEMAC Model System," Dissertation, Technische Universität München, München, 2018.
- [8] M. Reisenbüchler, M. D. Bui, D. Skublics, and P. Rutschmann, "An integrated approach for investigating the correlation between floods and river morphology: A case study of the Saalach River, Germany,"

- (eng), *The Science of the total environment*, vol. 647, pp. 814–826, 2019.
- [9] Canadian Hydraulics Centre (CHC), *Blue Kenue*. Ottawa, Canada, 2011.
- [10] J.-M. Hervouet, *Hydrodynamics of free surface flows: Modelling with the finite element method* / Jean-Michel Hervouet. Chichester: Wiley, 2007.
- [11] M. Reisenbüchler, M. B. Bui, and P. Rutschmann, “Implementation of a new Layer-Subroutine for fractional sediment transport in SISYPHE,” in *XXIIIrd TELEMAC-MASCARET User Conference*, 2016.
- [12] D. Moriasi *et al.*, “Model Evaluation Guidelines for Systematic Quantification of Accuracy in Watershed Simulations,” *Trans. ASABE*, vol. 50, no. 3, pp. 885–900, 2007.
- [13] J. Sutherland, A. H. Peet, and R. L. Soulsby, “Evaluating the performance of morphological models,” *Coastal Engineering*, vol. 51, no. 8-9, pp. 917–939, 2004.
- [14] A. H. Murphy and E. S. Epstein, “Skill Scores and Correlation Coefficients in Model Verification,” *Mon. Wea. Rev.*, vol. 117, no. 3, pp. 572–582, 1989.
- [15] F. Engelund and E. Hansen, “A monograph on sediment transport in alluvial streams,” Technical University of Denmark, Copenhagen, Denmark, Hydraulic Engineering Reports, 1967. [Online] Available: <http://resolver.tudelft.nl/uuid:81101b08-04b5-4082-9121-861949c336c9>. Accessed on: Jan. 16 2019.
- [16] J. P. Chollet and J. A. Cunge, “New interpretations of some head loss-flow velocity relationships for deformable movable beds,” *Journal of Hydraulic Research*, vol. 17, no. 1, pp. 1–13, <https://www.tandfonline.com/doi/pdf/10.1080/00221687909499596?needAccess=true&instName=Technical+University+of+Munich+%28TUM%29>, 1979.
- [17] W. Wu, *Computational river dynamics*. London: Taylor & Francis, 2008.
- [18] H. Chanson, *The hydraulics of open channel flow: An introduction ; basic principles, sediment motion, hydraulic modelling, design of hydraulic structures* / Hubert Chanson, 2nd ed. Amsterdam, Boston: Elsevier Butterworth Heinemann, 2004.
- [19] F. G. Koch and C. Flokstra, *Bed level computatios for curved alluvial channels*. [Online] Available: <http://publications.deltares.nl/Pub240.pdf>.



# Numerical Modelling of Local Scour Around Cylindrical Piers Including Secondary Flows Effects

Leandro Duran Santana  
Department Civil and Agricultural Engineering  
Universidad Nacional de Colombia  
Bogotá, Colombia  
ldurans@unal.edu.co

Jorge Alberto Escobar Vargas  
Department of Civil Engineering  
Pontificia Universidad Javeriana  
Bogotá, Colombia  
jorge-escobar@javeriana.edu.co

**Abstract**—The aim of the present study is to provide a computational low-cost numerical model be able calculating the local scour around bridge piers at a temporal and spatial scale of the river. A mathematical model based on the shallow waters equations including a parameterization of effects of secondary flows is presented. This mathematical model was implemented in Open Telemac software by modifying its source code in order to build the numerical model. In order to perform the parameterization of effects of secondary flows present in the phenomenon, a three-dimensional modeling of the flow field and local scour was performed using sedFoam computational tool implemented in OpenFoam. To carry out the calibration and / or validation of the proposed model, a measurement campaign was carried out in the Roncador Bridge piers located on the Magdalena River at the height of the town of Magangue, Bolivar. The measurements consisted in obtaining velocity data, depth of the water sheet, bathymetries and grain size of the bed. Measurements of velocity and depth of the water sheet were obtained with an Acoustic Doppler Current Profiler (ADCP). The bathymetries were performed with an echo sounder and a sonar type deeper. The bed shear stresses that are generated around the pile along with the scour holes in equilibrium and the velocity fields modified by the proposed model are presented.

## I. INTRODUCTION

Local scour in cylindrical piers is a highly complex phenomenon due to its three-dimensional behavior with highly turbulent processes acting in a bed that variable in time and space. The field of flow around a cylindrical pier is composed mainly of two vortex systems, the horseshoe-vortex and the wake-vortex, this vortex being generated at the moment in which the fluid comes into contact with the contour of the pier, of this very close to the contour, the velocity of the main flow should decrease drastically, which would produce a pressure gradient in the opposite direction to the flow (adverse pressure gradient), the boundary-layer adhered to the surface of the pier cannot withstand this adverse pressure gradient what produces an inversion of the flow and likewise a separation of the boundary-layer, this separation causes a rotational flow behind the pile, the so-called wake vortices.

The so-called horseshoe-vortex are produced by the approach flow to the pier, just at the moment when the flow hits upstream against the pile generates a gradient of pressures. Some researchers associate the formation of this gradient of pressures to the pressure of stagnation, which is a function of the density of

the fluid multiplied by the square of the velocity divided by 2 (Raudkivi A., 1986) [12]. If the pressure gradient that forms at the front of the pier is strong enough it generates a vertical downward flow, which in turn generates a three-dimensional detachment of the boundary layer, the downward flow along with this detachment ends up colliding with the bottom forming the horseshoe-vortex, which are transported downstream of the pile (Dargahi, 1990) [4].

Both the wake-vortex that acts as a vacuum and the horseshoe-vortex that directly strike the bed are the main mechanism of local scour.

Some researchers have proposed empirical or semi-empirical equations to calculate the maximum depth of scour as a function of average flow velocity, grain diameter, and depth of flow and diameter of the pile. These investigations are divided into two when there is a transport of bed sediments (Live-Bed) Neil, 1964 [10], Breusers HN, 1977 [2], Roulund et al, 2005 [15] and when there is no transport of bed sediments (Clear water) Laursen, 1960 [7], Jain & Fisher, 1979 [6], Raudkivi & Ettema, 1986 [13] and Vittal, 1994 [16]. These contributions have given glimpses of the behavior of the maximum depth that can occur in the pile, this behavior as a function of the approach velocity is shown in Fig 1.

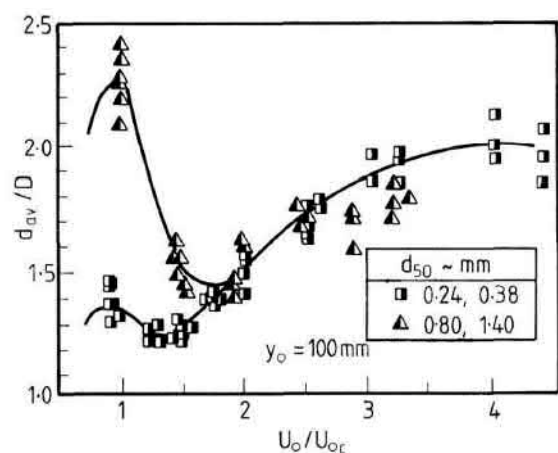


Figure 1. Maximum depth of scour as a function of the average flow velocity [8]

Fig. 1 shows two types of curves with similar behavior, the upper curve represents the average depth of scouring for coarse sediments ( $d_{50} \geq 0.8$  mm) and the lower curve the depth of scouring for fine sediments ( $d_{50} < 0.8$  mm), it is important to note

that for coarse sediments the maximum scour depth occurs just when the approach velocity is equal to the critical velocity, whereas for fine sediments the maximum scour occurs when the approach velocity is four times the critical velocity. It is also observed that for coarse sediments the scour is greater ( $2.5 \cdot D$ ) than for fine sediments ( $2.0 \cdot D$ ).

Due to the advance in computing that has been generated in recent years the phenomenon has been addressed using numerical or computational modeling, one of the first contributions to the subject was made by Olsen & Melaaen (1993) [11] who used the Navier-Stokes equations with the Reynolds average approach, this was the first three-dimensional model that was proposed in the literature that calculated the hydro-morphodynamics of the scour around bridge piers in a non-cohesive bed under clear water conditions. Other investigations such as these are those made by Richardson & Pancheng (1998) [14], Roulund et al (2005) [15], and Nagata et al (2005) [9]. On the other hand, Escarriaza & Sotiropoulos (2011) [5] were the first to model the undermining dynamics using the Large-Eddy Simulation (LES) and Detached-Eddy Simulation (DES) turbulence models to represent the flow around a circular bridge pier, in addition to coupling a Lagrangian bed transport model.

Finally, Chauchat et al (2017) [3] proposed a three-dimensional and two-phase solver for sediment transport applications, the mathematical model implemented is based on the volume of fluid (VOF) approach, therefore the sediment phase is modeled as a continuous, this tool allows to use several turbulence models (k- $\epsilon$ , k- $\omega$  and Mixing Length) and two different models of intergranular stress (Kinetic theory of granular flows and dense granular flow Rheology).

This solver (SedFoam) was used in the present investigation to establish the three-dimensional flows that occur around the pier over time, that is, as the scour hole develops, this with the intention of being able to parameterize the secondary flows (Vertical flows) that occur around the phenomenon.

## II. NUMERICAL MODEL

From the construction and analysis of three-dimensional numerical models, both hydrodynamic and morphodynamic, and from the detailed description of the phenomenon, a parameterization of the vertical flows (secondary flows) that occur around the bridge piers was determined.

The pisoFoam solver was used to determine the hydrodynamics of the phenomenon, pisoFoam is a transient solver for incompressible and turbulent flows that using the PISO algorithm, Fig. 2 shows the graphical results that show the velocity fields that are presented around a pile and that were calculated for fixed bed, in the figure the formation of the wake vortices is clearly seen (back side of the pile) and the horseshoe vortices (front face of the pile), in addition, the pressure gradient upstream of the pile was determined and calculated.

As previously mentioned, a modeling was performed with the SedFoam solver to determine the flow fields around the pile when a scour hole is generated, in Fig. 3 the shape of the scour hole generated for a 42 hours simulation is shown. With the analysis of these two models, the following mathematical model is presented based on the shallow water equations and

their results compared with data obtained in the Magdalena River.

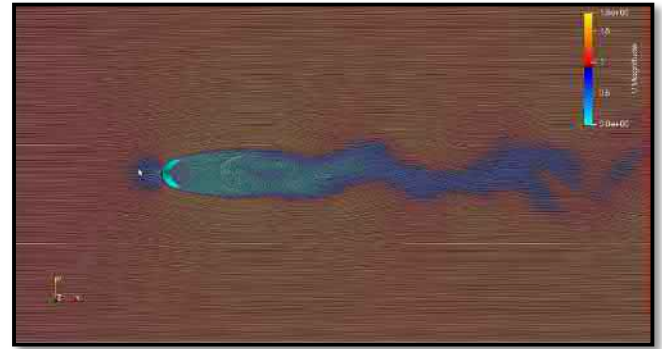


Figure 2. Three-dimensional flow field around bridge pier (Flow is from left to right).

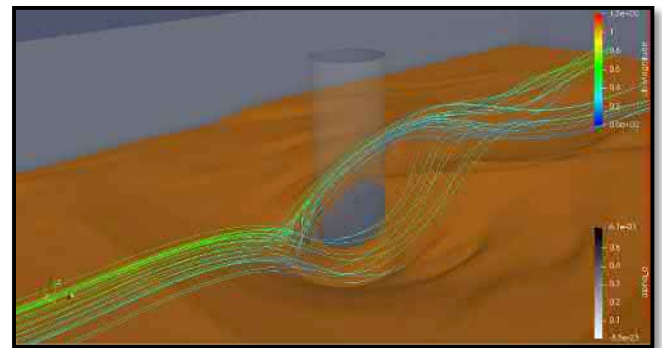


Figure 3. Three-dimensional and hydrosedimentological model of local scour around in bridge piers (Flow is from to right).

### A. Hydrodynamic Model

The governing equations for the flow are the depth-averaged shallow-water equations which are Saint Venant equations in two dimensions, this hydrodynamic model presents two momentum equations and an equation of continuity. These equations in Cartesian coordinates can be expressed as:

- Continuity Equation

$$\frac{\partial h}{\partial t} + \frac{\partial uh}{\partial x} + \frac{\partial vh}{\partial y} = 0 \quad (1)$$

- Momentum Equations

$$\frac{\partial u}{\partial t} + u \frac{\partial u}{\partial x} + v \frac{\partial u}{\partial y} = -g \frac{\partial H}{\partial x} + \frac{\eta}{h} \left( \frac{\partial^2 u}{\partial x^2} + \frac{\partial^2 u}{\partial y^2} + \frac{\partial^2 u}{\partial z^2} \right) + S_x \quad (2)$$

$$\frac{\partial v}{\partial t} + u \frac{\partial v}{\partial x} + v \frac{\partial v}{\partial y} = -g \frac{\partial H}{\partial y} + \frac{\eta}{h} \left( \frac{\partial^2 v}{\partial x^2} + \frac{\partial^2 v}{\partial y^2} + \frac{\partial^2 v}{\partial z^2} \right) + S_y \quad (3)$$

Where  $x$  and  $y$  are the Cartesian coordinates,  $u$  and  $v$  are the components of the velocity in the  $x$ -direction and  $y$ -direction, respectively,  $h$  is the depth of the water,  $H$  is the elevation of the water surface, that is, the depth of the water more the elevation of the bed ( $Z_b$ ) and  $S_x$  and  $S_y$  are source terms that in the present investigation refer to the friction produced in the bed, this is calculated from the shear stress in the bed  $\tau_x$  and  $\tau_y$  and these stresses can be expressed from of the Manning equation as:

$$S_x = -\frac{\tau_x}{h\rho} = -\frac{gn^2 u \sqrt{u^2 + v^2}}{h^{4/3}} \quad (4)$$

$$S_y = -\frac{\tau_y}{h\rho} = -\frac{gn^2 v \sqrt{u^2 + v^2}}{h^{4/3}} \quad (5)$$

Where  $\rho$  is the density of water,  $g$  is the acceleration due to gravity and  $n$  is the roughness coefficient of Manning.

### B. Morphodynamic Model

The prediction of bathymetric changes and sediment discharges are calculated from a morphodynamic model which is coupled to the hydrodynamic model so that sediment transport and flow occur simultaneously, this model contains a transport component of non-cohesive bed sediments and a component of the bed evolution from the conservation of the mass of sediments that can be expressed in Cartesian coordinates such as:

$$(1-\lambda) \frac{\partial Z_b}{\partial t} + \frac{\partial Q_{bx}}{\partial x} + \frac{\partial Q_{by}}{\partial y} = 0 \quad (6)$$

Where  $Q_{bx}$  and  $Q_{by}$  are the components of the solid transport vector ( $\vec{Q}_b$ ) in the  $x$  and  $y$  directions respectively,  $Z_b$  is the bed elevation as previously mentioned and  $\lambda$  is the porosity of the bed.  $Q_{bx}$  and  $Q_{by}$  is calculated from the background sediment transport rate as:

$$Q_{bx} = Q_b \cos \alpha \quad Q_{by} = Q_b \sin \alpha \quad (7)$$

Where  $\alpha$  is the angle between the solid transport vector and the downstream direction, i.e. with respect to the  $x$  coordinate axis, the bed sediment transport rate  $Q_b$  is calculated from empirical bed transport equations, in the present investigation the Meyer-Peter and Muller equations and the Einstein-Brown equation were used. These equations are defined according to the number of Shields that can be expressed as

$$\theta = \frac{\mu \tau_b}{(\rho_s - \rho) g d} \quad (8)$$

Where  $\tau_b$  is the shear stress at the bottom,  $\rho_s$  is the density of the sediment that is normally assumed to be 2.65 kg/m<sup>3</sup>,  $d$  is the characteristic diameter of the sediment, which for uniform sediments is equal to  $d_{50}$  and  $\mu$  is a factor of correction due to the background friction that is calculated from a relationship between coefficients of friction:

$$\mu = \frac{C'_f}{C_f} \quad C'_f = 2 \left( \frac{\kappa}{\log(12h/ks)} \right)^2 \quad (9)$$

Where  $\kappa$  is the von Karman coefficient which is equal to 0.4, the roughness height  $ks$  is a function of the sediment diameter  $ks = \xi_s d_{50}$  and the coefficient  $\xi_s$  is a parameter to be calibrated. Finally, the transport equations of bottom sediments that were used in the present investigation are presented:

- Meyer-Peter & Muller Equation

$$Q_b = \chi \sqrt{(g(s-1)d^3(\theta - \theta_{cr}))^{3/2}} \quad (10)$$

- Einstein-Brown Equation

$$Q_b = \sqrt{(g(s-1)d^3 \left( \frac{2}{3} + \frac{36}{d_d} \right)^{0.5} - \left( \frac{36}{d_d} \right)^{0.5}} * f(\theta) \quad (11)$$

$$f(\theta) = \begin{cases} 2.15 e^{-0.391/\theta} & \text{if } \theta \leq 0.2 \\ 40\theta^3 & \text{otherwise} \end{cases} \quad (12)$$

Where  $\theta_{cr}$  is the number of critical Shields that is equal to 0.047 for particle diameters between 0.2 and 2 mm,  $\chi$  is a coefficient or parameter for calibration and that by default is taken as equal to 8,  $s$  is the relative sediment density and is equal to  $s = \rho_s / \rho$ , it must be taken into account in the case of the Meyer-Peter & Muller equation if the number of Shields is less than the number of Shields critical the bottom sediment transport rate is equal to zero, On the other hand, the parameter  $d_d$  in the Einstein-Brown equation is equivalent to  $d_d = d[(s-1)g/\eta^2]^{1/3}$ , where  $\eta$  is the viscosity of the water.

Finally, the shear stress in the bottom is calculated, which depends on the velocity and a term associated with the pressure and the secondary flows around the pile, this effort is expressed as follows:

$$\tau_b = \frac{1}{2} \rho C_f (u^2 + v^2) + L \quad [13]$$

### III. DESCRIPTION OF FIELD DATA

In order to carry out a validation and / or calibration of the proposed model, a measurement campaign was carried out at different times of the year on the Magdalena River at the height of the town of Magangué, Bolívar, (See Figure 4). Over the river it extends the Roncador or Celeste bridge, which has a length of 2.3 km, a width of 15 m and a height of 32 m, in the bed of the river were built 4 piers with pile cap of 9 circular piles of 4 m in diameter, the campaign is composed of measurements of flow, bathymetries of the bed, granulometry and depth of sheet of water. The study section on the Magdalena River has a length of approximately 18 km, an average width of 600 m and an average depth of 15 m, to 7.6 km downstream of Magangué the river bifurcates generating an island (Isla Grande), the arm left to 1.2 km downstream again bifurcates generating a second island (See Fig. 4), finally the three arms are joined again at the height of Puerto Kennedy. Below are each of the equipment used in the measurements with their respective results.



Figure 4. Section of study on the Magdalena River.

#### A. Flow Data

The flow and velocity data were collected with an Acoustic Doppler Current Profiler (ADCP) of Teledyne RD Instruments brand, River Ray model which contains 3 transducers that work with a frequency of 600 kHz, in total 5 flow measurements were taken, the first at the height of Magangué in which velocities were obtained between 1.9 m / s and 0.5 m / s, a maximum depth of 17.22 m and a total flow of 4636 m<sup>3</sup> / s, in figure 5 the magnitude of the velocity at along the cross-section of the river, two more measurements were made just after the first fork where the left arm reported velocities between 1.6 m / s and 0.4 m / s, the maximum depth was 5.9 m and a total flow of 1465 m<sup>3</sup> / s, the right arm presented velocities between 0.2 m / s and 1.9 m / s, the maximum depth

was 10 m and a total flow of 3359 m<sup>3</sup> / s, then measurement was made just after the bridge piles on the right arm and were obtained velocities between 2.1 m / s and 0.6 m / s, a maximum depth of 14.2 m and a total flow of 3454 m<sup>3</sup> / s, finally a last measurement was taken downstream of the bifurcation, which showed velocities between 0.7 m / s and 2.2 m / s, a maximum depth of 16.6 m and a total flow of 4836 m<sup>3</sup> / s.

#### B. Bathymetry Data

The bathymetric data was collected with two echo sounders, the first of Valeport brand and MIDAS Surveyor GPS model, which contains 2 transducers one high frequency (210 kHz) and one low frequency (33 kHz), the working resolution is 0.01 m, the second Garmin echosounder model ECHOMAP Plus 64cv, which contains two working frequencies of 50 kHz and 200 kHz, the echo sounder has a resolution of 0.1m. Bathymetric data were obtained before construction of the bridge piers and two measurements were taken at different times of the year, in total approximately 20,000 points were obtained in the entire study section, these measurements yielded maximum depth data of 23 m. that generates levels below sea level, in figure 6 the bathymetric points raised before the construction of the bridge piers are observed, it can be seen that there is data between 12 m above sea level and -13 m above sea level, with this bathymetric information it was able to calculate the slope of the total river bed, that is, from end-to-end of the stretch and the maximum and minimum slopes between sections, which were 0.000522 m / m, 0.0302 m / m, 0.00147 m / m respectively.

The topography of the sector was obtained from the Light Detection and Ranging (LIDAR) technology with an airplane over flight having heights above sea level with resolutions of 5X5 m.

#### C. Granulometry Data

The granulometric data were taken with a steel drill reinforced with iron weights, which stabilize the sampling, 6 samples of bottom sediments were obtained, 3 in the right arm of the river and 3 in the other arm, in each arm was taken 2 relatively close to the edges and the last in the center of the cross-section. Then in the laboratory, specialized equipment Battersize was used to obtain the granulometric curve and have the mean diameter (d50) of the sediment.

#### D. Georeferenced Data

To make the georeferencing of the bathymetric points, the Hypack® Lite software was used, which allows bathymetric lifting with a coupling between a georeferencing instrument and an echo sounder, this results in points with planimetric information and also with elevation above sea level. In this measurement campaign, a Real Time Kinematic receiver (RTK) Sokkia brand model GRX2 was used as a georeferentation instrument.



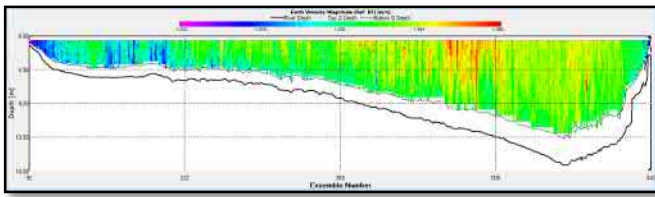


Figure 5. Magnitude of velocity along the cross section of the Magdalena River with ADCP.

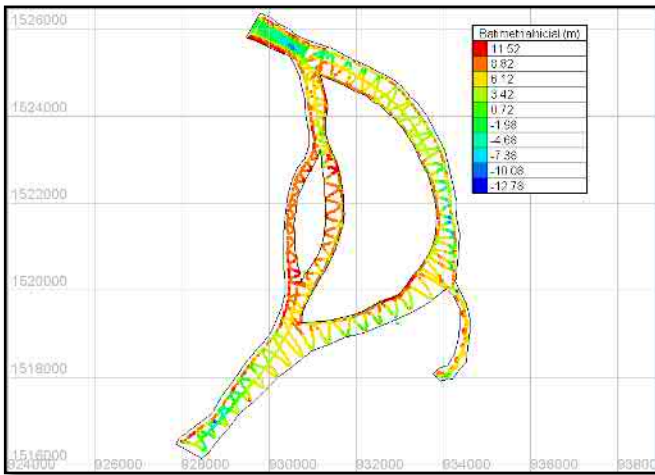


Figure 6. Bathymetric points before construction of bridge piers.

#### IV. RESULTS AND DISCUSSIONS

The numerical model was implemented on the OpenTelemac solvers suite whose code was modified according to the model proposed in the present investigation. In principle, the Telemac2D solver coupled with the Sysphe morphodynamic model was used, using two bed transport equations that were presented in numeral 2, in the present investigation the transport of sediments in suspension was not considered because the study carried out by Baker (1986) suggests that the effect of sediments in suspension are not radically significant in terms of the depth of scour in equilibrium, in this way two simulations were carried out with variable boundary conditions in time (Unsteady), starting with the data collected before the construction of the bridge piers, these simulated 7 days that had a computational cost of 8 hours each, the results of these simulations are presented below.

##### A. Velocity

The velocity field in the x-direction and y-direction is shown in Figure 7, in this image it is appreciated the 9 piles of the second Roncador Bridge pier, in the image on the left it can see the velocity in a color palette where red represents velocities above 1.26 m/s and the blue velocities below 0.14 m/s, in this image and in the following images the direction of the flow is from bottom to top, in the walls of the piles a no-slip boundary condition was applied, this is why low velocities are presented around them, this was done to simulate the velocity profile at the contact of a wall and with this the detachment of the boundary layer, in front of the piles the

stagnation point is observed where the velocity drops abruptly by an increase in pressure, this leads to an elevation of the water surface in front of each pile.

In the image on the right of Fig. 7, the vector velocity field is presented, where high velocities (greater than 1.53 m/s) are represented by the red color and long vectors and low velocities (less than 0.17 m/s) are represented by the color blue and short vectors, in these two images it can see behind each pile an area where the velocity is low and it increases as it moves away from the pile, in the simulations carried out no wake vortices were generated, This is because the distance between piles is very short and the wake behind each pile does not have enough space to move and collides with the next pile, in the last row of piles the strength and velocity of the flow is reduced and not the vortices are produced, besides it is observed that the flow that does not hit the piles is not altered too much by the accelerations or decelerations that take place inside the matrix of 9 piles. This wake that is observed behind the last row of piles extends several tens of meters affecting the flow field downstream of the piles.

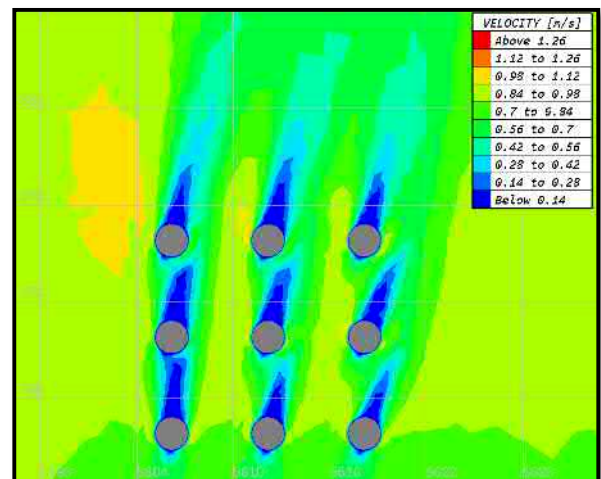


Figure 7. Velocity around the bridge group piers.

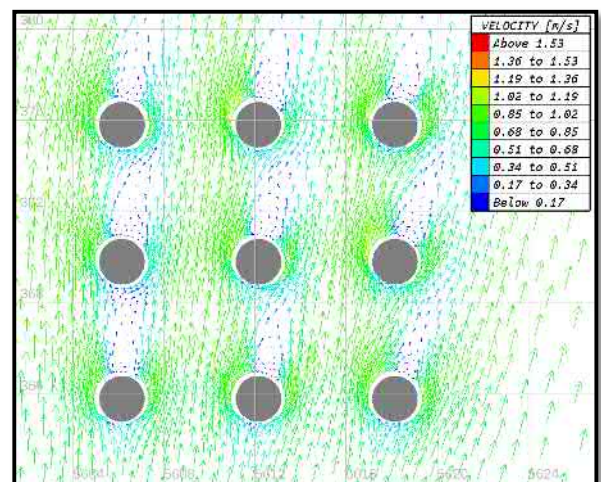


Figure 8. Velocity vector around the bridge group piers.

### B. Bed Shear Stress

The bed shear stress is shown in Figure 8 which was calculated from equation 13 which is a function of the velocity, in this figure the bed shear stress is plotted from isolines, from this way the red isolines represent efforts greater than 8.1 N/m<sup>2</sup> and the blue isolines represent efforts less than 0.9 N/m<sup>2</sup>, in the image it is appreciated that the shear stress follows a pattern similar to the velocity field, i.e., areas where at high velocities, high shear stress occur and vice-versa.

In figure 9 it is observed that the bed shear stress upstream of the pile is very low, almost zero, due to the low velocity that is generated in this area, on the lateral sides of the piles a fast change in the shear stress where it increases almost from zero to 7.2 N/m<sup>2</sup>.

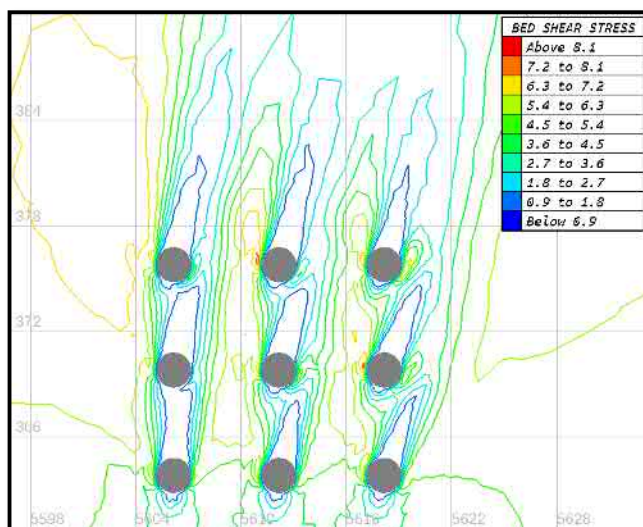


Figure 9. Bed shear stress around the bridge group piers.

### C. Scour

The depth of scour around the piles is shown in Figure 9, which was calculated from a bed transport equation that is a function of the shear stress in the bed and the number of Shields, finally from the spacial and temporal discretization of the Exner equation gives a change in the depth of the bed in each element of the computational domain.

In the image it is observed that the depth of the bed around the piles is plotted from isolines such as the shear stress, in this way, the light green to red isolines represent areas of granular material deposition and the isolines between the dark blue and dark green are areas that represent areas of scouring.

In the Fig. 10, it is clearly seen that the biggest scour occurs on the sides of the individual piles at approximately 45 ° of the axis parallel to the flow, this scour is joined with the scour of the pile next to it causing a damping effect of the scour, furthermore, it can be seen that on the back face of the piles, sedimentation zones have generated that join with the front face of the immediately following pile.

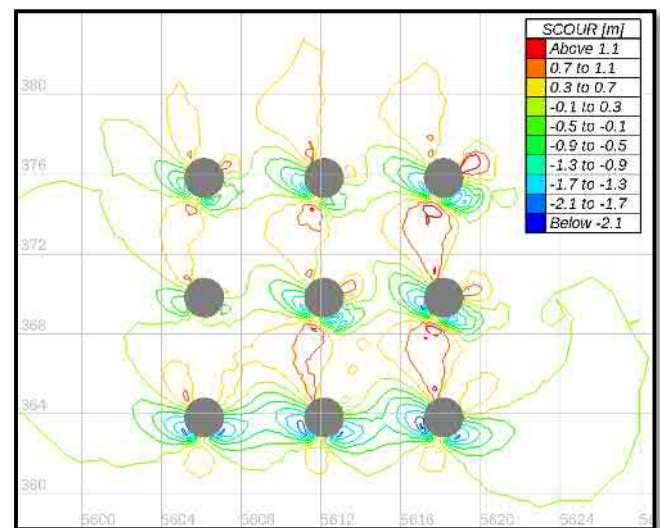


Figure 10. Local Scour around the bridge group piers.

## V. CONCLUSIONS

In the present investigation we present a two-dimensional numerical model that parameterizes the effects of secondary flows such as the vertical flows that appear in the front and back face of a circular and vertical pile, this model was validated and/or calibrated with data taken in the field on the Magdalena river at the height of the municipality of Magangué, to perform the parameterization, three-dimensional numerical models were used, both hydrodynamic and sedimentological, which were useful to determine the magnitude of the vertical flows and their incidence in the process of local scour.

The hydrodynamic model is based on the saint-venant equations and is coupled with a morphodynamic model that uses the Exner equation to calculate changes in bed depth, the numerical results showed that the present model is capable of capturing all the characteristics. The main undermining of the local scouring process, including those generated by the vertical flows showed that the maximum undercut in all the simulations did not exceed 2.5 m and that the depth of undermining in equilibrium was simulated quite well, finding small differences of maximum 10%.

The parameterization of the vertical flows is made from a modification of the shear stress equation in the bed, where a term that is in function of the pressure is added and allows to simulate the scour produced by these vertical flows, especially in the part at the front of the piles, the results show that the addition of this parameter is capable of generating the scour considerably, taking into account that the spatial and temporal scales are difficult to represent.

## ACKNOWLEDGEMENT

We want to grateful the Ponticia Universidad Javeriana for the support given in the loan of the measurement equipment and the Universidad Nacional de Colombia especially the

suggestions and contributions given by the engineer Jaime Ivan Ordoñez to the present investigation.

On the other hand, we would like to grateful the developers who participate in OpenFoam (SedFoam) and OpenTelemac (Sisyphé), which are the basis of the model presented in this document.

#### REFERENCES

- [1] Baker, C. J. (1986). Local scour at bridge piers in non-uniform sediment. *Thesis presented to the University of Auckland, New Zealand*, in partial fulfilment of the requirements for the degree of Master of Philosophy.
- [2] Breusers, H. N. (1977). Local Scour Around Cylindrical Piers. *Journal of Hydraulics Research*, 15, Pag. 211-250.
- [3] Chauchat, J., Cheng, Z., Nagel, T., Bonamy, C., Hsu, T. J. (2017). SedFoam-2.0: a 3-D two-phase flow numerical model sediment transport. *Journal Geosci. Model Dev.*, 10, Pag 4367-4392.
- [4] Dargahi, B. (1990). Controlling Mechanism of Local Scouring. *Journal of Hydraulics Engineering*, Pag. 1197-1214.
- [5] Escauriaza, C., & Sotiropoulos, F. (2011). Lagrangian model of bed-load transport in turbulent junction flow. *Journal Fluid Mechanics*, Pag. 36-76.
- [6] Jain, S. C., & Fisher, E. E. (1979). *Scour around circular bridge piers at high Froude numbers*. Springfield, Virginia: Report. Federal Highway Administration NTIS.
- [7] Laursen, E. M. (1960). Scour at bridge crossings. *Proceedings American Society Civil Engineers*, 86, Pag. 39-54.
- [8] Melville, B. (1984). Live-Bed Scour at Bridge Piers. *Journal of Hydraulics Engineering*, Pag. 1234-1247.
- [9] Nagata, N., Hosoda, T., Nakato, T., & Muramoto, Y. (2005). Three-dimensional numerical model for flow and bed deformation around river hydraulic structures. *Journal Hydraulics Engineering*, 131(12), Pag. 1074-87.
- [10] Neill, C. R. (1964a). *Local scour around bridge piers*. Alberta, Canada: Research Council of Alberta.
- [11] Olsen, N. R., & Melaaen, M. C. (1993). Three-dimensional calculation of scour around cylinders. *Journal Hydraulic Engineers*, 119(9), Pag. 1048-1054.
- [12] Raudkivi, A. (1986). Functional Trends of Scour at Bridge Piers. *Jorunal of Hydraulics Engineering*, Pag. 1-13.
- [13] Raudkivi, A., & Ettema, R. (1986). Clear water scour at cylindrical piers. *Journal of Hydraulics Engineering*, 109(3), Pag. 338-350.
- [14] Richardson, J. E., & Pancheng, V. G. (1998). Three-dimensional simulation of scour inducing flow at bridge piers. *Journal Hydraulics Engineering*, 124(5), (sf).
- [15] Roulund, A., Sumer, B., & Fredsoe, J. (2005). Numerical and experimental investigation of flow and scour around a circular pile. *Journal Fluid Mechanics*, 534, Pag. 351-401.
- [16] Vittal, N. K. (1994). Clear-Water Scour around bridge pier Group. *Journal of Hydraulics Engineering*, 120, Pag. 1309-1318.



# Sediment modelling for Poole and Christchurch Bays

Michiel A.F. Knaapen  
Coasts & Estuaries  
HR Wallingford  
Wallingford, United Kingdom  
m.knaapen@hrwallingford.com

Poole and Christchurch Bays (UK) have narrow beaches which attract many visitors to the area and are therefore essential for the local economy. However, the beaches suffer from ongoing erosion, making regular beach nourishments to maintain them necessary. Sea level rise may cause an increase in the required frequency of these nourishments. If one can determine where the sediment sinks are, i.e. the location where the eroded beach material ends up, it may be possible to recycle the material, by dredging in the area of the sediment sinks and returning this material to the area of the beach. For this purpose, a numerical model is developed that computes the waves, currents and sediment transport in the area between Swanage and the Isle of Wight. The model covers the English Channel with high resolution in the area of interest. To compute the yearly averaged transport, a 1 year simulation using the 2009 hydrodynamic and atmospheric conditions was run. This model will be the basis for future projects to determine the changes due to the proposed works, either in large scale engineering or beach nourishments.

## I. INTRODUCTION

Poole and Christchurch Bays (Fig. 1) have narrow beaches which attract many visitors to the area and are therefore essential for the local economy. However, the beaches suffer from ongoing erosion, making regular beach nourishments to maintain them necessary. In the 2013/2014 winter, the Bournemouth beaches lost 144,000 m<sup>3</sup> of sand, while the Sandbank peninsula in front of Poole Harbour lost a further 30,000 m<sup>3</sup> [1]. Sea level rise may cause an increase in the

required frequency of these nourishments. If one can determine

where the sediment sinks are, i.e. the location where the eroded beach material ends up, it may be possible to recycle the material, by dredging in the area of the sediment sinks and returning this material to the area of the beach.

There have been desk studies identifying the pathways [9]. These conclude that there is an eastward littoral drift, where the sand moves from Poole to Christchurch Ledge and then again along the beaches towards Hurst Spit. From there the sediment is then pushed out to sea past the Needles on the Isle of Wight. A westward transport is thought to exist north of the Dolphin Sands and Dolphin Banks, although this is contradicted by the work of Gallop et al [4], who find clockwise sediment transport around Dolphin Sands. Thus, there still is much uncertainty about the destination of the sediments that have been eroded from the beaches.

Therefore, a numerical model is developed that computes the sediment transport pathways in the English Channel, and focusses on the area between Swanage and the Isle of Wight. This model, with fully coupled TELEMAC, TOMOWAC and SISYPHE will be the basis in future projects to determine the changes due to the proposed works, either in large scale engineering or beach nourishments.

## II. THE MODEL

TELEMAC-2D was used to model an area covering the

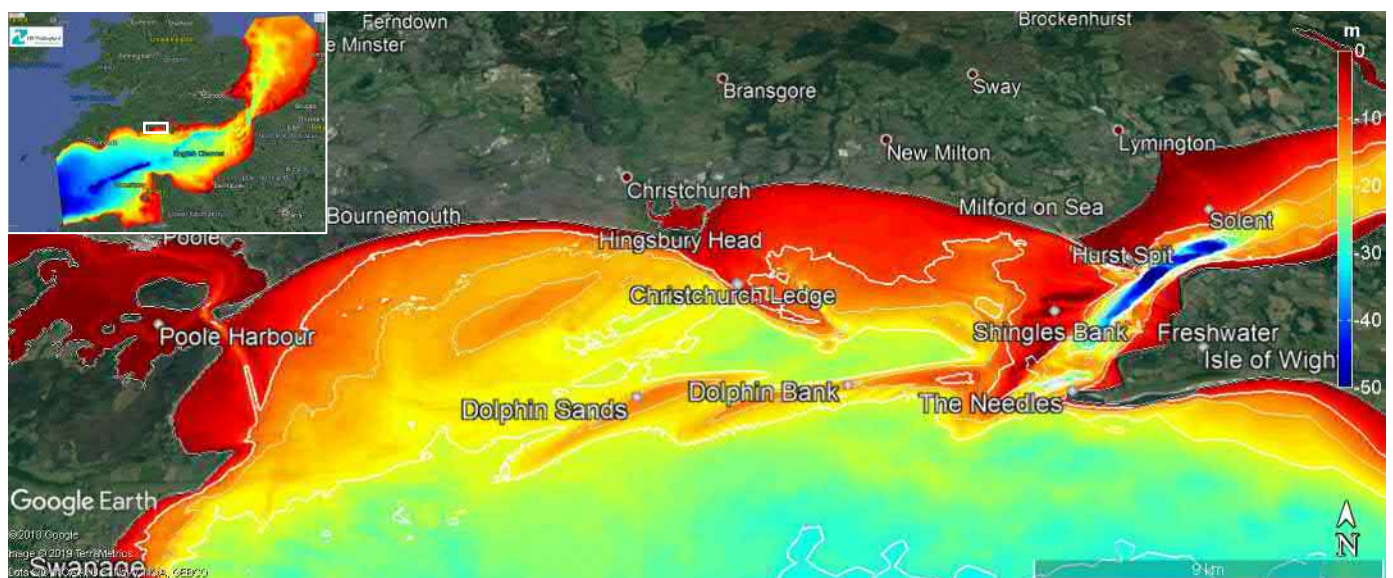


Figure 1 Model bathymetry for the area of interest, between Swanage and the Isle of Wight



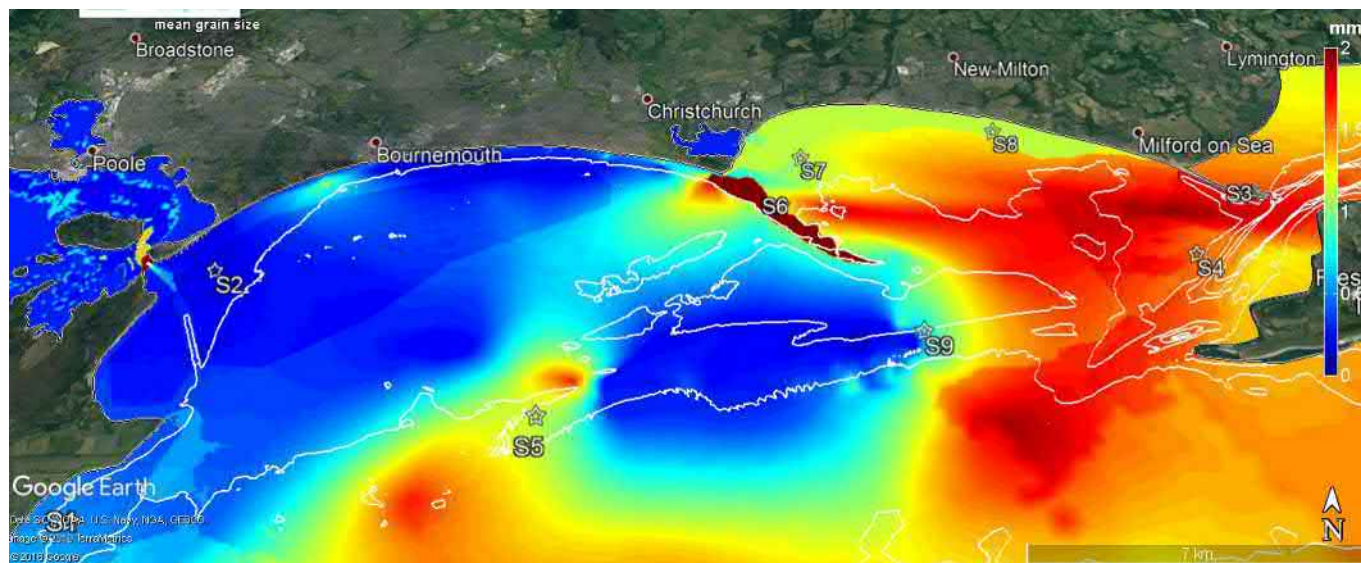


Figure 2 Mean grain size of the bed sediments

English Channel and the southern North Sea (Fig. 1 inset). The sediment transport near the coast is dominated by wave driven currents. To model these processes correctly, an accurate representation of the location of wave breaking is required. The original mesh has a resolution of 25 m, but to get an accurate representation of the longshore current and related sediment transport, the resolution is reduced to 5 to 10 m at the shoreline. At critical locations, such as Hurst Spit and Christchurch Ledge the resolution is approximately 5 m. At the more gentle sloping curved beaches the resolution is adjusted to 10 m. The resolution around the two offshore banks (Shingles Bank Dolphin Bank and Dolphin Sands) is about 50 m.

#### Bathymetry

Measured bathymetric data were collected from the UK Hydrographic Office (UKHO) and the Channel Coastal Observatory (CCO). The data sets are specified in Appendix **Erreur ! Source du renvoi introuvable.**, in **Erreur ! Source du renvoi introuvable.** and **Erreur ! Source du renvoi introuvable.**, respectively. The CCO data in the Solent, and Poole and Christchurch Bays were collected in a series of campaigns ranging from 2006 to the present, whereas the UKHO data were used in the wider model domain, surveyed since 2004. The resulting bathymetry in the area of interest is shown in Fig. 1.

#### Tidal conditions

The hydrodynamic conditions are dominated by tidal currents. These are included in the numerical model via water level variations at the offshore boundaries. The model has two open boundaries where water level boundary conditions are imposed, referred to as the western and eastern boundary, respectively. The offshore boundaries of the hydrodynamic model are driven by tidal levels extracted from the TPXO satellite altimetry dataset [10]. Tidal levels vary spatially and temporally along the offshore boundary. The TPXO global model of ocean tides is based on a best-fit of the Laplace Tidal

Equations and measured data collected along remote sensing tracks from satellites TOPEX/POSEIDON and Jason.

The TPXO model resolution of the European Shelf has a resolution of 1/30 degree (approximately 3.7 km). The tides are provided as complex amplitudes of earth-relative sea-surface elevation for eight primary (M2, S2, N2, K2, K1, O1, P1 and Q1) and 3 non-linear (M4, MS4 and MN4) harmonic constituents. Observations from more than 10,000 tidal gauges and other observed data have been used to validate the TPXO dataset.

#### Wave conditions

Wave boundary conditions for the model are taken from ERA5 ([5][6][11]). ERA5 (ECMWF ReAnalysis) gives an estimate of historical atmospheric activity based on numerical models combined with observations. ERA5 is the fifth major global reanalysis produced by ECMWF. Data processing for ERA5 is carried out by ECMWF, using ECMWF's Earth System model IFS, cycle 41r2. ERA5 provides high quality medium-high resolution estimates of atmospheric and surface wave parameters, with a horizontal resolution 31km, 137 vertical levels and data archived hourly. The first batch of ERA5, covering the period 2000 to 2018 is currently available, and will extend from 1950 to present when complete. ERA5 is being developed through, and ERA5 data are provided by, the Copernicus Climate Change Service. Time varying wave spectra from ERA5 are imposed at the boundaries of the TOMAWAC model.

#### Atmospheric conditions

Atmospheric pressure and wind speed and direction for the model are taken from ERA5 as well. ERA5 wind was calibrated against observations at Channel Light Vessel, leading to a correction, applied at high wind speeds. The derived wind speed correction factor increases linearly from 1 at 10m/s to 1.1 at 20m/s and above. Corrected wind speeds from ERA5 are interpolated spatially onto the model mesh and

applied to estimate wind stress in TELEMAC and wave generation in TOMAWAC.

#### *Bed composition*

In the model 6 sediment classes were defined ranging from silt to coarse gravel: 40  $\mu\text{m}$  (silt); 94  $\mu\text{m}$  (very fine sand); 188  $\mu\text{m}$  (fine sand); 375  $\mu\text{m}$  (medium sand); 1.0 mm (coarse sand); 20 mm (gravel). The fractions of these classes were determined based on a bed composition map using the work of Wilson [11], who combined publicly available data with relationships between shear stresses and grain sizes as well as water depth and distance to the shore to create a sediment map for the shelf seas around the United Kingdom and Ireland. This map has been supplemented by data provided by Poole and Bournemouth borough council and the bed composition of Dolphin Sands as published by Gallop et al. [4].

This bed composition data was corrected for known anomalies. Areas of hard seabed around Hengistbury Head, offshore of Studland were assumed to consist of gravels, which are (almost) immobile in the model. This means that minor erosion of the seabed may occur, but avoids potential model instabilities at the interface of non-erodible layers and the surrounding mobile bed. Silt was placed in areas inside the natural harbours, where the flow velocities are below 0.3m/s. Gravel is assumed in areas where the maximum velocities are above 1.5 m/s and sand/gravel mixtures in areas where the peak velocity exceeds 1 m/s. The resulting mean grains size in the model is shown in Fig. 2.

### III. MEASURED DATA

Poole Borough council commissioned a field campaign to validate the modelling. AWAC systems were placed in 9 locations (Fig. 2) in Poole and Christchurch Bays to measure water levels, currents and waves. Sediment concentrations were recorded using an OBS, which were calibrated using water samples. This calibration shows differences of up to 300%, in particular in cases of lower backscatter values. This indicates a significant uncertainty in the measured concentrations. To minimise the impact of the measurements errors, the measured concentration and velocity profiles were converted to estimates of the suspended transport load. These locations were identified as crucial locations to understand the sediment transport pathway: S1 Swanage; S2 Bournemouth beaches; S3 Hurst Spit; S4 Shingles Bank; S5 end of Dolphin Sands; S6 Christchurch Ledge; S7 Christchurch Harbour entrance; S8 Christchurch Bay beaches; S9 Dolphin Bank. The survey campaign by FUGRO [3] took place in December 2017 and January 2018. However, the AWAC system deployed at location S8 did not function properly. Therefore this Deployment 1 (D1) was followed by Deployment 2 (D2), wherein measurements were taken at locations S7 and S8 in February and March 2018.

### IV. CALIBRATION

The model was calibrated against short periods of the D1 survey campaign, each lasting several days. This calibration took place in phases. The flow model was calibrated against the measured data during a calm period (12/12/17 to 19/12/17)

and a period with more significant wave conditions (24/12/17 to 31/12/17). Two short periods (9/12/17 to 17/12/17 and 24/12/17 to 31/12/17) were used to calibrate the wave model. Finally, the period from 24/12/17 to 31/12/17 was used to calibrate the wave driven currents and sediment transport.

In the calibration the following parameters and processes have been varied:

- For the flows: Bed friction coefficient (Nikuradse, 0.05m); Turbulence model (constant); Viscosity (1.E-6); Wind (spatially varying from ERA5); Atmospheric pressure (spatially varying from ERA5); and advection scheme (1;5).
- For the waves: Wind generation (WAM cycle 3); Dissipation due to currents (Phillips) and spatially varying waves (ERA5);.
- For the sediment: Bed friction; spatially varying bed friction (no); Friction correction factor (flat bed); advection scheme (13); and Bed composition (spatially varying).

### V. VALIDATION

The validation of the model consisted of two parts. First, the model simulated the conditions during the survey deployment D1. This tests the capability of the model to simulate the temporal variability in the hydrodynamics and sediment transport of the area for locations S1 to S7 and S9. Table 1 shows the resulting error statistics, coefficient of determination (r-squared) and mean absolute error (mae). The water levels are predicted accurately in all locations, but S3 and S4. In the other locations, the R-squared value is above 0.9, indicating almost all temporal variations are accounted for, and absolute errors are in the order of 0.1m.

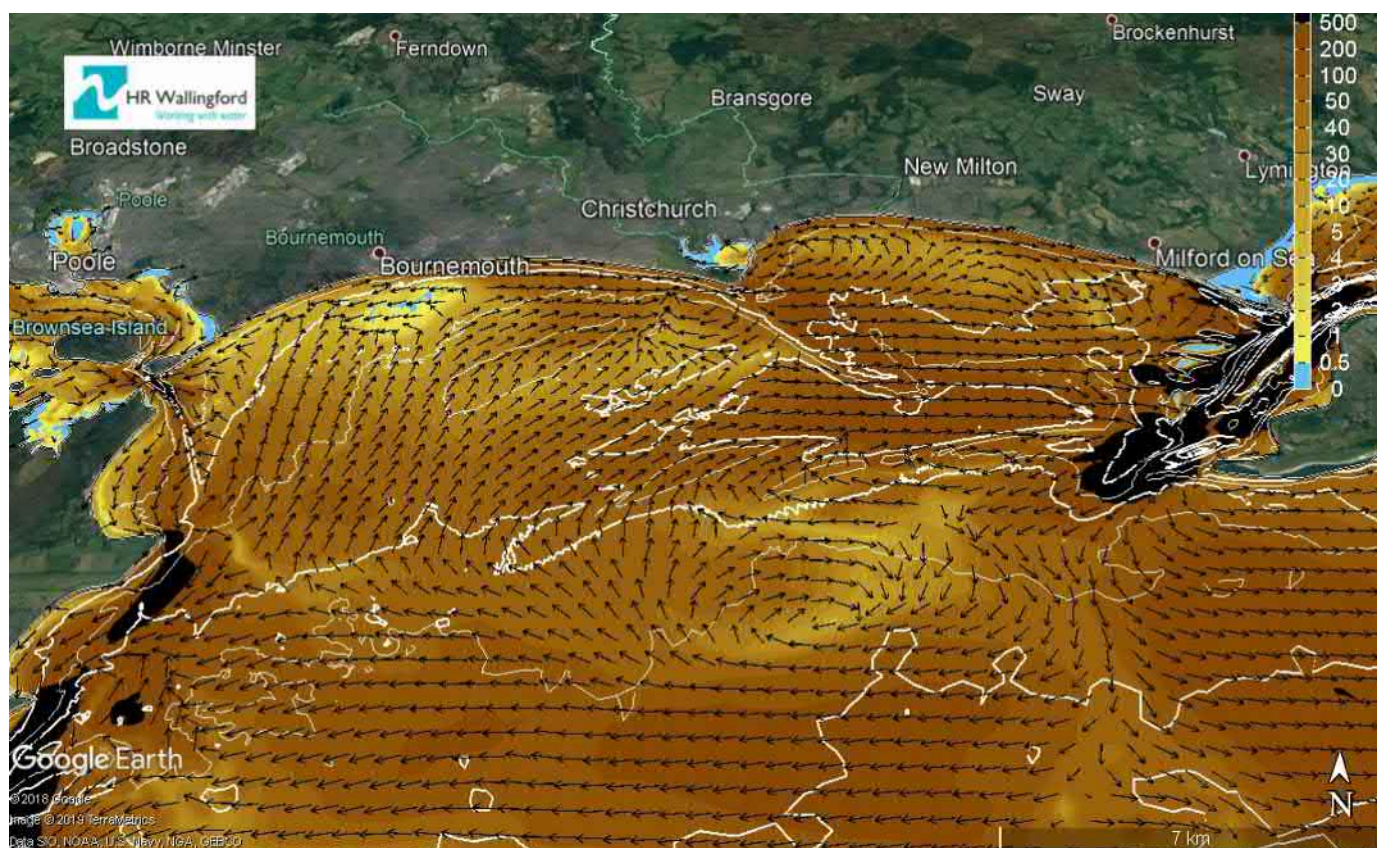
In locations S1, S2 and S7, the flow velocities are low, which means that small errors have strong impact on the R-squared (Table 5.2). However the mae is still small. In location S4, the mae is larger, despite a reasonable R-squared value.

The model quality for the significant wave height is positive as well. The R-squared values are between 0.7 and 0.9 indicating a good fit, while the mae's are below 0.3, with one exception. The only exception is location S4. The R-squared values are slightly lower in areas with lower wave heights (1 to 3), but there the mae's are smaller there.

The error statistics for the sediment transport are based on a derived measurement. The measured transport rate is taken as the product of the depth averaged concentration times the depth averaged velocity. This assumes that the gradients in the velocity profile and the concentration profile are minimal. In practice, sediment concentrations often drop on going up the water column, while velocities are lower closer to the bed. This makes it likely that the actual transport rate will be a bit lower than the value calculated from the measurements. In contrast, the modelled suspended sediment transport rate is a direct output of the model.



Figure 3 Residual sand transport rates (colour) and direction (arrows) in Poole and Christchurch Bays



The differences between the measured and modelled depth integrated suspended sediment transport rates are larger than those for wave of currents. For areas with sufficient hydrodynamic energy, the R-squared value is above 0.5, which is a good fit for sediment transport purposes. Where currents and waves are small (locations S1, S2 and S7), the R-squared value is very small, indicating no relationship between observed and measured values. The relative mae, the mean ratio between the prediction errors and the measured values, however, does not increase much in these locations.

In the next phase, the model was applied to the period of the D2 deployment. This tests how accurate the model is in location S8, which has not been used in the calibration, providing a measure for the spatial sensitivity of the model (Table 2). The accuracy in location S8 is better than the comparable location S7.

TABLE 1 VALIDATION ERRORS DEPLOYMENT 1

location	S1	S2	S3	S4	S5	S6	S7	S9
Water level								
r <sup>2</sup> (-)	0.90	0.91	0.41	0.94	0.91	0.90	0.92	0.93
mae(m)	0.10	0.11	0.55	0.79	0.10	0.18	0.12	0.12
Flow velocities								
r <sup>2</sup> (-)	0.25	0.60	0.89	0.83	0.90	0.83	0.54	0.73
mae(m)	0.11	0.05	0.19	0.24	0.05	0.08	0.06	0.08
Wave height								
r <sup>2</sup> (-)	0.75	0.78	0.74	0.75	0.86	0.85	0.83	0.88
mae(m)	0.17	0.14	0.11	0.28	0.26	0.21	0.26	0.25
Sediment transport rate								

r <sup>2</sup> (-)	0.16	0.14	0.67	0.56	0.80	0.43	0.15	0.54
mae <sup>a</sup> (-)	0.34	0.62	0.72	0.44	0.39	0.41	0.49	0.38

a. For the sediment a relative mae is used

TABLE 2 VALIDATION ERRORS DEPLOYMENT 2

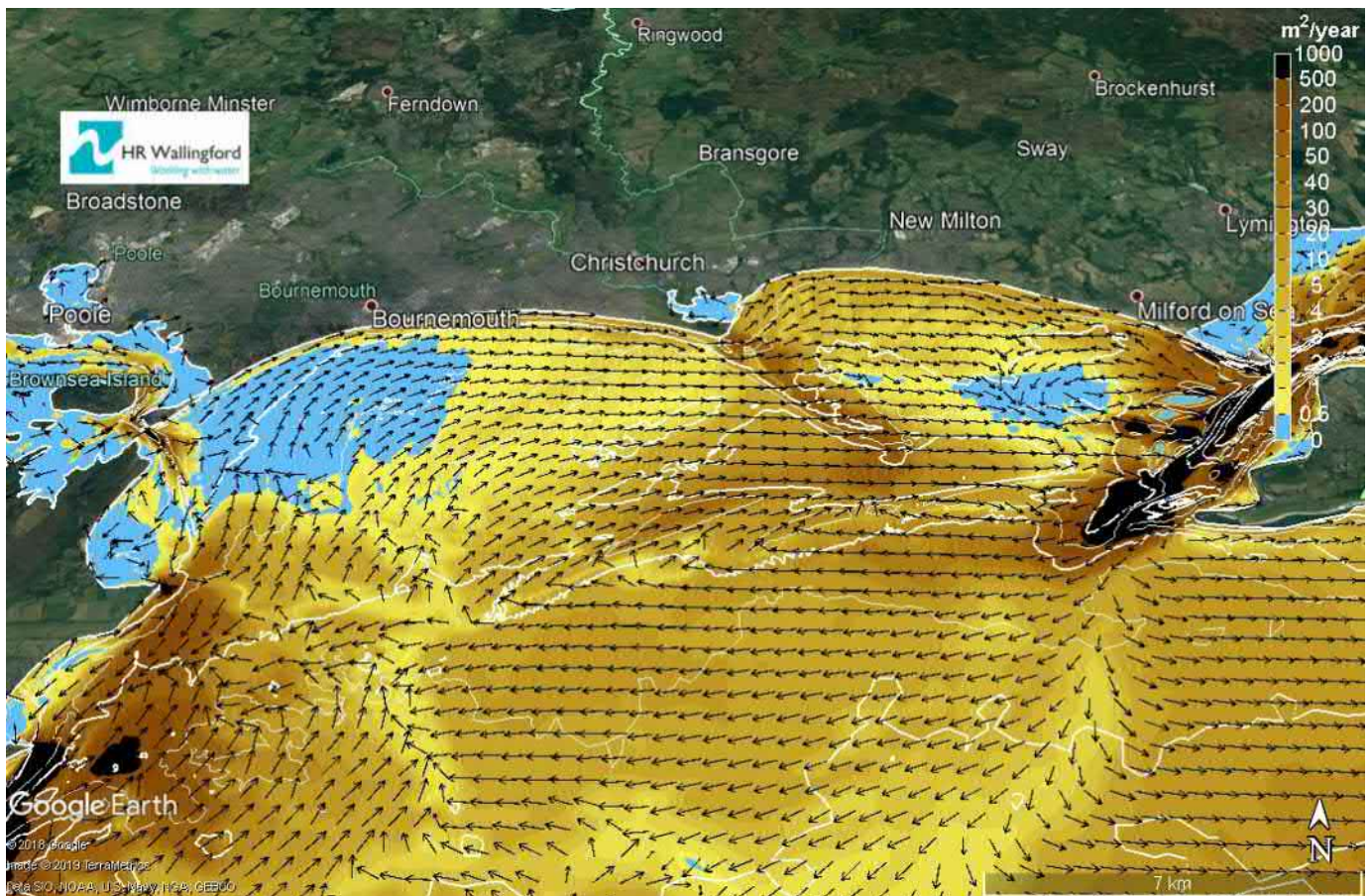
	Water level		Flow velocity		Wave height	
location	S7	S8	S7	S8	S7	S8
r <sup>2</sup> (-)	0.96	0.96	0.81	0.87	0.71	0.86
mae (m)	0.22	0.23	0.10	0.10	0.15	0.13

## VI. YEARLY AVERAGED SEDIMENT TRANSPORT

The averaged transport rates over the survey period are given in Table 3. The transport rates over the banks (location S5 and S9) are almost perfect, but with a small difference in the angle of the transport (below 30°). In location S3, near Hurst Spit, where the transport rates are high, the error in the transport rate is 60%, with a small error in the direction. In locations S1 the transport rates are smaller and the error in the rates drops to 20%, with a small 14° error in the direction. In locations S7 and S2, the errors in the transport are large with almost opposite directions, and the measured transport rate much higher than the modelled transport rate. In location S6, the direction is predicted well, but the modelled residual transport rate is much larger than measured.

The residual transport rates in Table 3 are generally of the same order as the mean absolute error in the instantaneous sediment transport rates given in Table 2.





interrupted by zones where the transport is west ward. The model indicates a nearshore sediment divide south of Bournemouth, which coincides with the small patch of coarse sediments visible in the seabed composition (Fig. 2); south of New Milton and north of Swanage Bay. Circulation cells are present on either side of Hengistbury Head.

When we isolate the transport rates of the sand fractions (Fig. 4), the pattern changes. There is a clear pathway of sand transport. The littoral drift takes the sand along the shorelines from west to east.

Within the bays the sand transport is consistently west to east, with the exception of the western part of Poole Bay and the eastern part of Christchurch Bay.

In the west of Poole Bay, the residual sand transport rates are very low, except near the shore, where wave breaking drives the littoral drift. Along the Bournemouth shoreline the sand transport rate is increasing indicating that it is eroding gradually. There are indications that there is a sand drift divide in front of breakwaters of Sandbanks (Fig. 5). However, the precise location strongly depends on the wave conditions and will vary from one year to the other. The monthly patterns indicate that there is a drift divide in most months somewhere along the Bournemouth shoreline, but the location varies over the months.

In Christchurch Bay, the sand arriving around Hengistbury Head is spread around the western side of the bay, rather than hugging the shoreline. The sand is then transported east by the littoral drift along Hurst Spit, but then (partly) brought back

TABLE 3 VALIDATION RESIDUAL SEDIMENT TRANSPORT

	rate			direction		
	AWAC	model	ratio	AWAC	model	error
	m³/m/s	m³/m/s	-	°N	°N	°
S1	5.6E-06	7.0E-06	0.80	203	215	-14
S2	1.5E-06	1.0E-06	1.50	291	46	-116
S3	1.0E-04	6.3E-05	1.59	100	107	-7
S4	7.6E-06	2.3E-05	0.33	172	96	77
S5	3.1E-06	2.8E-06	1.11	341	9	-23
S6	1.0E-05	5.1E-06	1.96	96	86	7
S7	2.1E-06	4.6E-06	0.46	227	65	162
S9	1.3E-05	1.2E-05	1.08	108	81	27

## VII. LONG TERM SEDIMENT TRANSPORT

To calculate the yearly residual transport pattern, the sediment transport was simulated for 2009. Based on total amount of energy in the wave conditions, the year 2009 was identified as representative for typical atmospheric conditions. The model was run for the whole year using TPXO water levels and ERA5 wind and wave conditions.

Fig. 3 shows the residual sediment transport for 2009. The total sediment transport shows a complicated pattern within the bays, with the typical transport direction from west to east



by the tidal currents from the Solent, to then go west again further south.

sediment samples suggest the presence of a lot of very fine sand and silt and an absence of coarser sediments. Most likely

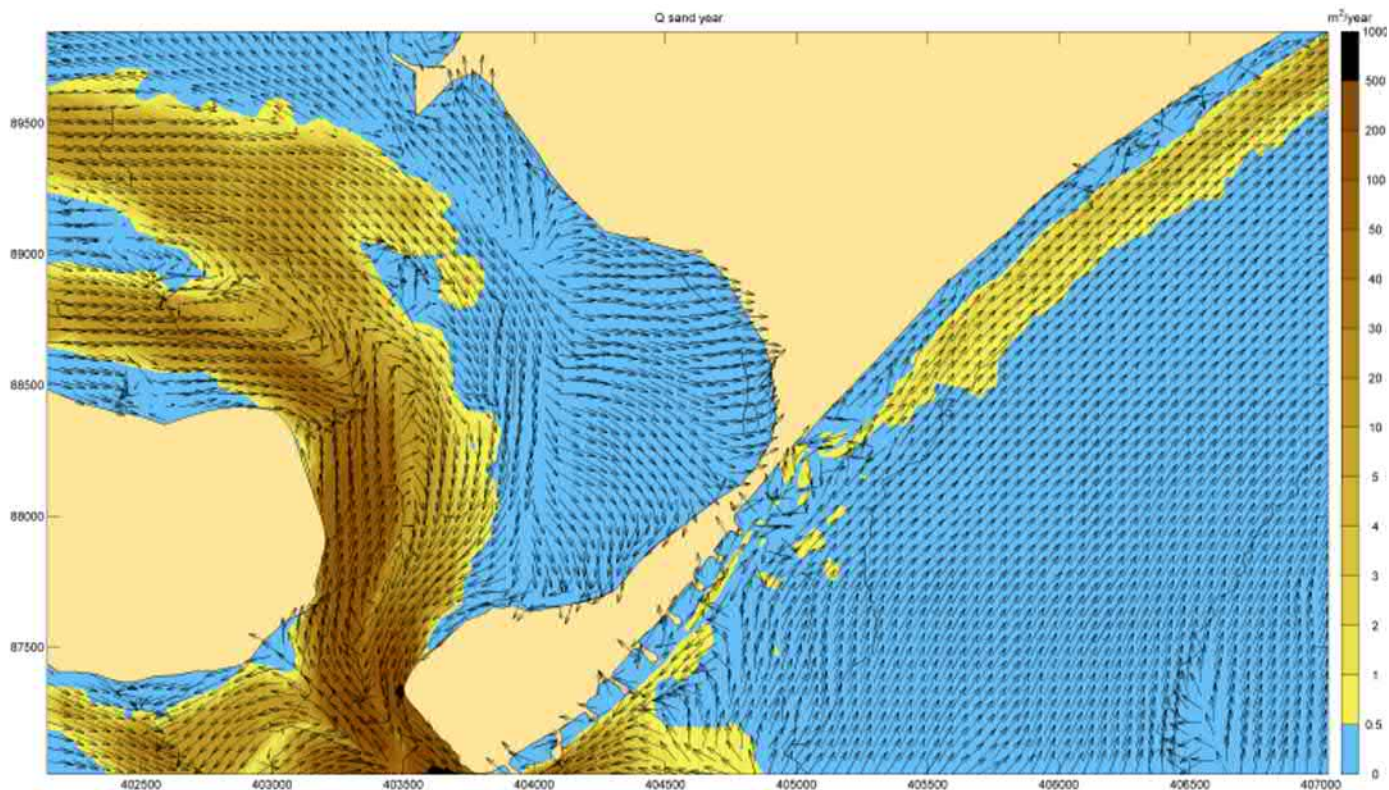


Figure 5 Drift divide in the sand transport along the Bournemouth beaches. The colours denote the residual sand transport rate (in  $\text{m}^2/\text{year}$ ), the vectors denote the transport direction

Eventually, the sand is transported into deeper water past the Needles by the tidal currents. From there a fraction of the sand (estimated to be about 20%) is moved further east past the Isle of Wight. The remainder of the sediment is moving west, along Dolphin Bank and Dolphin Sands. Reaching the wester end of Dolphin sands it turns north to be moved west along the sandbanks again. As a result this material will end up on the sandbanks or in the sandwaves moving around the banks.

#### VIII. EROSION DEPOSITION

Unfortunately, no validation data for morphological changes is available. Nevertheless, the resulting erosion deposition patterns (Fig. 6) look realistic. In general there is little change over the year as expected.

The navigation channel to Poole Harbour shows infill, which is in line with the knowledge that this channel requires maintenance dredging.

There is erosion of the seabed along the shoreline at the western half of Poole Bay, in line with the knowledge that the beaches have been nourished regularly

There are a few exceptions however, related to insufficient seabed data. There are significant bed level changes in the west of the Bays in front of Swanage. Here the bed composition map is inaccurate.

In between Dolphin Sands and Dolphin Bank, there is a circular erosion spot, which matches a location where

this is a clay outcrop; alternatively the sediment sample for this location is incorrect.

There are a lot of seabed changes in the area of Shingles Banks. This is no surprise, as shingles Bank is known to be a highly dynamic area. But on top of that, because of the active seabed and high energetic conditions, bathymetry and bed composition data is incomplete at that site.

#### IX. DISCUSSION

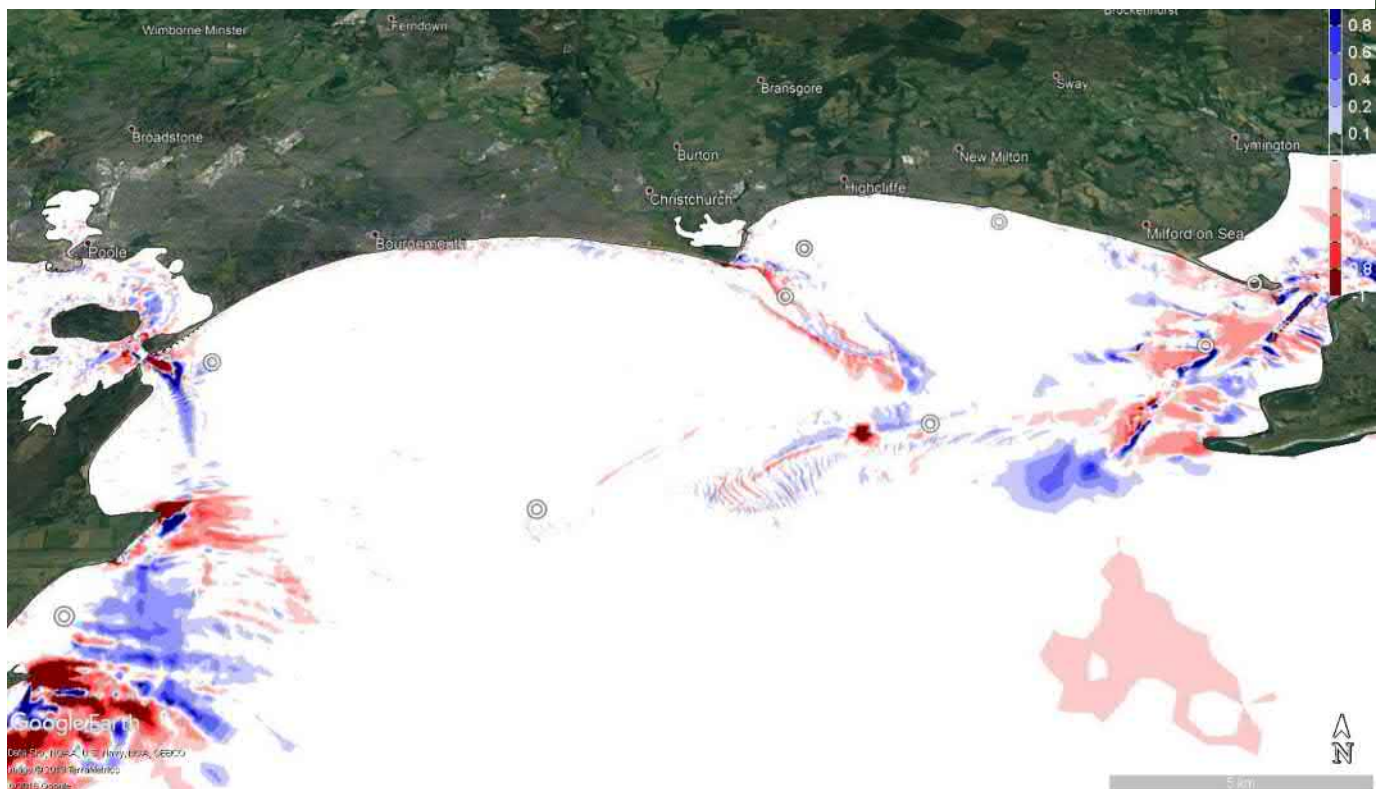
##### *Model quality*

The model reproduces the observed flows, waves and sediment transport well in most locations. In a few locations some issues remain. Most importantly, the lack of recent accurate bathymetry data for Shingles Bank causes disturbance of the flows and water levels in location S4 (Shingles Bank) and location S3 (Hurst Spit). This leads to an incorrect model representation of the sediment transport in this area as well.

In location S6, flows and waves are reproduced well. The predicted sediment transport, however, is still a bit high. The bed composition still allows more sediment to erode from Christchurch ledge than is happening in reality. This increases the transport in location S6 and S7. This additional transport could be the explanation for the incorrect transport direction in location S7.

The transport direction in location S2 is incorrect, but this location is in an area with inconsistent transport directions and

Figure 6 Erosion deposition pattern in metres



the transport rates are very small. So the results here are sensitive to small changes in the conditions. As the transport rates here are small and inconsistent, this error will have very little impact on the overall sediment transport pathways.

The sediment transport measurements are based on profile approximations of the flow velocities and concentrations in the water column higher than 0.5m above the bed. As most sediment transport occurs closer to the seabed, this is a large source of uncertainty in the measured transport rates. Still, the relatively good comparison between measured values and modelled values provides confidence in the model results as well as the measurements.

Currently, non-erodible layers such as rock and stiff clay are represented as gravel beds. This implies that during high energetic conditions they suffer from erosion. This makes the model less suitable for long-term erosion and deposition analysis.

#### Comparison with SCOPAC sediment pathways

The findings of the modelling in general supports the SCOPAC sediment transport [9]. However, there are a few differences:

- The modelled total sediment transport shows a sediment divide in front of Bournemouth for the total sediment transport, which is not present in the SCOPAC sediment pathways. This divide is not present for sand, but is driven by the transport patterns for the fine material. This divide is exactly in the location where the seabed composition is

sandier than other areas (Fig. 2) which would support the divide for fines in this location.

- SCOPAC [9] indicates a westward transport in the deeper part of the bay, north of Dolphin Sands. The model results presented here show this transport to occur further offshore, south of Dolphin Sands. North of Dolphin Sands, the transport is to the east, completing the clockwise sediment transport around the sandbank in agreement with the findings of Gallop et al [4].
- Similarly, the transport around the whole of Dolphin Bank is clockwise, more pronounced than New Forest District Council suggests.
- The sediment transport that passes Hengistbury Head spreads out over a fairly wide region into Christchurch Bay and does not stick to the shore as much as SCOPAC [9] is assuming.

## X. CONCLUSIONS

To analyse the sediment pathways of Poole and Christchurch Bay, a numerical model has been developed that models the waves, currents and sediment transport in the English Channel. The model has been calibrated and validated against measurements taken at 9 locations using AWAC systems. The model fits well with the wave and current observations and even reproduces most of the observed sediment transport.

The model works well as a tool to analyse the sediment transport pathways and to assess where material eroded from the beaches ends up. The model run of a whole year shows a clear pathway of sand along the beaches towards the east and back further offshore, south of Dolphin Bank and Dolphin Sands. Sediment is shown to circulate clockwise about Dolphin Bank and Dolphin Sands. Only a small part of the sand leaves the bay and is moved east along the Isle of Wight. However, lack of recent accurate bed level and sediment grain size information for Shingles Bank, leads to some inaccuracies at that location. In broad lines, the model results confirm the established views in literature on the sediment transport pathways. However, the model provides much more detail and adds some subtle nuances.

Although the model has not been developed to predict the future bed level changes, the resulting bed level changes are broadly in line with historic changes. Overall most changes are very subtle. There is some erosion of the beaches and the dredged navigation channel to Poole Harbour shows significant infill, a pattern confirmed by ongoing dredging requirements.

The results of this work suggest that, with the exception of the surf zone, the sediment transport modelling using the TELEMAC-TOMAWAC-SISYPHE coupling is accurate. It does however require high resolution bathymetry and bed composition data.

#### ACKNOWLEDGEMENT

The authors thank Fugro for making the AWAC data available to HR Wallingford, the Channel Coastal Conservatory, BCP Borough Council and NOC Southampton for the bathymetry and bed composition data for Poole and Christchurch Bays.

#### REFERENCES

- [1] A.P. Bradbury and T. E. Mason, "Review of south coast beach response to wave conditions in the winter of 2013-2014," Channel Coastal Observatory report, Reference SR0, 04 April 2014
- [2] J.R. Bidlot, S. Abdalla and H. Hersbach, "ERA5 wave data," in EGU General Assembly Conference, Vol. 19, p. 8707, April 2017.
- [3] Fugro "Poole Bay ADP and turbidity data, Data Report". Fugro report 173366-R-001(02), 2018.
- [4] S. Gallop, M.P. Wadey, C.E.L. Thompson, D. Harlow and J.K. Dix, "Offshore sediment transport pathways in Poole and Christchurch Bays," Technical Report, University of Southampton, 2016.
- [5] H. Hersbach, "The ERA5 Atmospheric Reanalysis. In AGU Fall Meeting Abstracts, February 2016.
- [6] H. Hersbach and D. Dee, "ERA5 reanalysis is in production," ECMWF Newsletter No. 147 – Spring 2016.
- [7] HR Wallingford, "Poole and Christchurch Bays Beach Management Support, Sediment Transport Modelling," HR Wallingford report DER5720-RT001-R01-00, 2017.
- [8] T. Mason, "Trialling a new approach to beach replenishment in Poole Bay," SC130035, Environment Agency. UK. ISBN: 978-1-84911-407-3, 2018.
- [9] New Forest District Council, "2012 Update of Carter, D., Bray, M., & Hooke, J., 2004 SCOPAC Sediment Transport Study," [www.scopac.org.uk/sts](http://www.scopac.org.uk/sts), 2017.
- [10] OSU, "OSU Tidal Data Inversion Software and Atlas," Oregon State University, 2008.
- [11] R.J. Wilson, D.C. Speirs, A. Sabatino and M.R. Heath, "A synthetic map of the north-west European Shelf sedimentary environment for

applications in marine science," Earth Systems Science Data, 10, 109-130, 2018.



# Ship-current interactions with TELEMAC

Juliette Parisi, Michael Turnbull, Alan Cooper, James Clarke

HR Wallingford  
Howbery Park, Wallingford, UK  
[j.parsi@hrwallingford.com](mailto:j.parsi@hrwallingford.com)  
[m.turnbull@hrwallingford.com](mailto:m.turnbull@hrwallingford.com)  
[a.cooper@hrwallingford.com](mailto:a.cooper@hrwallingford.com)  
[j.clarke@hrwallingford.com](mailto:j.clarke@hrwallingford.com)

**Abstract** — The Navigation Simulator is often used to train pilots and test harbour or channel designs. It combines hydraulic modelling with ship manoeuvring models and a team of experts (pilots, tug masters, naval architects and navigation specialists), all focused through a suite of real-time simulators.

Currently, the hydrodynamic modelling is an input of the ship simulator, i.e. it is carried out beforehand, the flow fields are then used by the ship simulator. This study presents how the effects of ships have been considered in the hydrodynamic modelling in order to improve ship navigation simulations. Several hydrodynamic scenarios were investigated:

- Representing the ships in the hydrodynamic model by imposing the ship hulls as a pressure field;
- Live communication between the hydrodynamic model and the ship simulator. The position and orientation of the ship is controlled by the ship simulator and passed on to the hydrodynamic model. The resulting flow fields and water elevation are calculated by the hydrodynamic model and fed back to the ship simulator;
- Including propeller wash.

The new developments were used in recent real-time navigation simulations. Feedback from pilots and tug masters is positive. Some instabilities in the hydrodynamic model remain and further developments are underway.

## I. INTRODUCTION

The TELEMAC system flow models, TELEMAC-2D and TELEMAC-3D, are free surface flow models which are not expected to apply to cases where the surface is not open to the atmosphere, including flows under ships and other floating objects. Nevertheless as engineers we frequently need to be able to take account of these things as the flow in a harbour, for example, may be significantly affected by the presence of a floating object and even more by a large moving ship.

Requests to investigate flows in such cases have motivated the following study. While it would seem that conventional CFD simulations are ideally suited to modelling free surface flows including stationary and moving ships because they can model non free surface flows, it would be necessary to set up a two way coupling of the CFD model and TELEMAC, and the CFD computations are likely to be computationally intensive and therefore take too much time in the context of a navigation simulation and would be prohibitive in the context of dynamic linking to a ship simulator.

## II. INFLUENCE OF LARGE SHIPS: CURRENT SHELTERING

TELEMAC-2D and TELEMAC-3D can be used to model ships by imposing a pressure field on the water surface, which represents the ship's hull. The pressure applied is proportional to the depth of the ship in the water. The pressure is given by the equation (1)

$$P = \rho g d \quad (1)$$

- $P$  is the pressure (Pa)
- $\rho$  is the water density ( $\text{kg/m}^3$ )
- $g$  is the acceleration due to gravity ( $\text{m/s}^2$ )
- $d$  is the depth of the ship in the water (m)

### A. Caisson test case

This method was first validated with the caisson test case, against preliminary CFD work carried out by HR Wallingford in 2013. The test case is a floating caisson, 75m wide, 500m long and a 10m draught. The total water depth is 250m and the uniform current is 1 knot (0.5144 m/s) following the AB section direction (section AB is shown in Fig. 3). The non-hydrostatic TELEMAC-3D model mesh size is 5m with 11 planes, and the 7<sup>th</sup> plane is fixed at 11m below the surface using sigma planes above and below. Having the 7<sup>th</sup> plane fixed at -11m guarantees having 6 planes capturing the flow underneath the floating body. Tests were also done for 21 planes and a longer duration of 12h. Fig. 1 shows the surface longitudinal velocity as a percentage of the ambient current from the TELEMAC-3D results and Fig. 2 from the OpenFOAM and CFX results. It shows TELEMAC-3D results are very similar between the different combinations and therefore 11 planes and 5h simulation is sufficient in this case. Fig. 3 shows a plan view of the TELEMAC-3D velocity and Fig. 4 shows a cross section of the TELEMAC-3D surface velocity along the section AB of the caisson.

The TELEMAC-3D speed downstream of the caisson agrees well with OpenFOAM and CFX results. These conventional CFD models can include non-free surface flows and also can model free surface flow using volume of fluid (VoF) techniques. However, the reduction in the speed upstream of the caisson is greater in TELEMAC than the other two models. The caisson test case confirms that TELEMAC-3D can reproduce flows around a floating caisson, which is very similar in shape to a large ship such as a Floating Liquified Natural Gas (FLNG) vessel.



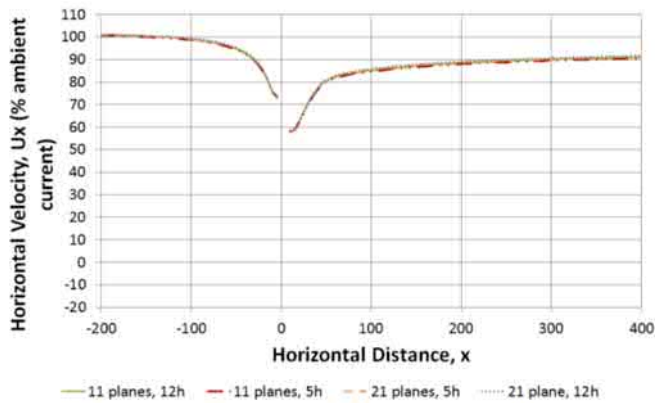


Figure 1: TELEMAC-3D longitudinal current velocity as a percentage of the ambient current at the free-surface along the section AB of the caisson for 90° current

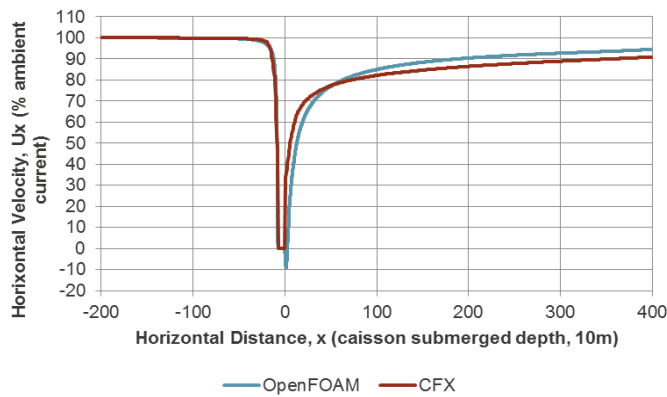


Figure 2: OpenFOAM and CFX longitudinal current velocity as a percentage of the ambient current at the free-surface along the section AB of the caisson for 90° current

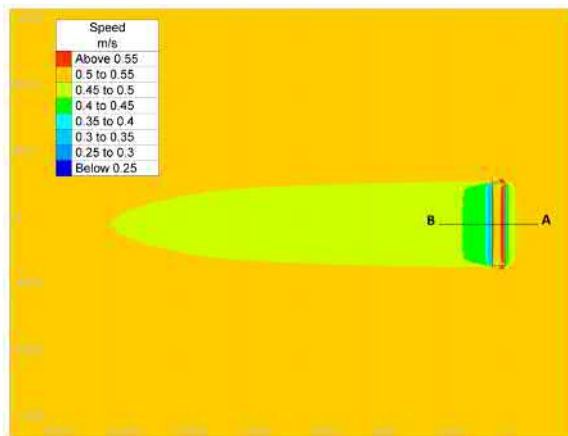


Figure 3: TELEMAC-3D velocity plan view

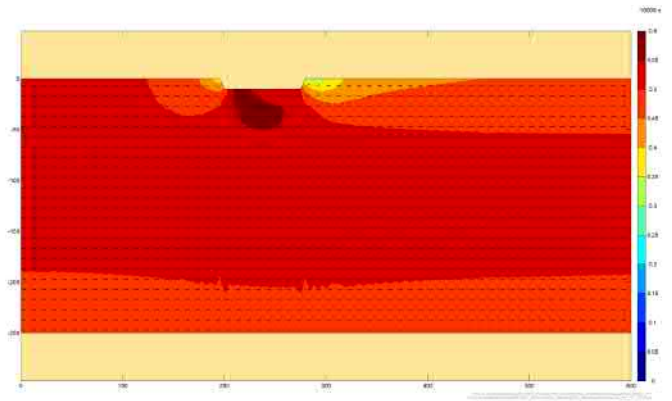


Figure 4: TELEMAC-3D velocity cross-section along the section AB of the caisson

### B. Live communication between TELEMAC and HR Wallingford ship simulator

HR Wallingford has two ship simulation centres, one in the United Kingdom and one in Western Australia. These simulators use time varying flow fields which are used to calculate the forces acting on simulated vessels. TELEMAC flow models are often used to provide these time varying flow fields and have been used for many years. Currently, these flow fields are an input to the ship simulator, i.e. the TELEMAC run is carried out beforehand.

As demonstrated for the caisson test case, large floating objects can have significant effects on the flow fields. In terms of navigation, this can have a significant impact on nearby vessels and is particularly important for vessel manoeuvring for side by side mooring such as LNG vessels approaching FLNG facilities.

In these situations the simulated flow field in the ship simulator must include the effect on the flow field of the FLNG and also respond to the movement (heading change) of the FLNG. For this reason, the TELEMAC-3D finite element flow model was developed to allow real time integration with the navigation ship simulator. The position and orientation of the ships is controlled by the ship simulator. This information is passed on to the TELEMAC-3D model, in which the position of the ship hull is imposed as a pressure field. The resulting current fields and water elevation are fed back from the TELEMAC model to the ship simulator in real time.

When first implemented, instabilities in the flow field occurred. They mostly depend on the size, shape and speed of the ship. Other factors are the water depth, the ambient flow and numerical parameters such as the time step, the number of planes and their distribution over the water column. In order to reduce instabilities, two approaches have been tried:

- The ship hull shape has been smoothed spatially to make the change in free surface less abrupt
- Time relaxation of the pressure fields: the pressure imposed depends on the requested value and the value at the previous time step. This prevents the free surface at a particular point changing too suddenly from one time to the next. This method is the same as that used

to compute culvert flows in TELEMAC while reducing unwanted oscillations.

- The mesh orientation and resolution was also optimised

Within the TELEMAC-3D model, these approaches combined significantly reduced model instabilities. However, when using the real time integration with the ship simulator, the ship hull cannot be excessively smoothed because it has an impact on the flow field used by the ship simulator. Overall, when setting a real case navigation simulation of a FLNG and vessels around it, the following parameters were used:

- The domain is a 4km wide and 6km long rectangle, with a uniform 240m water depth
- The TELEMAC-3D model mesh size is 6m near the FLNG growing to 100m on the boundaries (Fig. 5)
- 6 planes, spaced closer together near the surface than near the bed. More than 6 planes resulted in the TELEMAC-3D model running slower than real time
- Time step of 0.5s and time relaxation with a coefficient of 0.01. The corresponding formula (3) is given below, where  $P_t$  is the pressure at the time  $t$ ,  $P_{t-1}$  is the pressure at the previous time step and  $C_r$  is the relaxation coefficient

$$P_t = (1 - C_r)P_{t-1} + C_r P_t \quad (3)$$

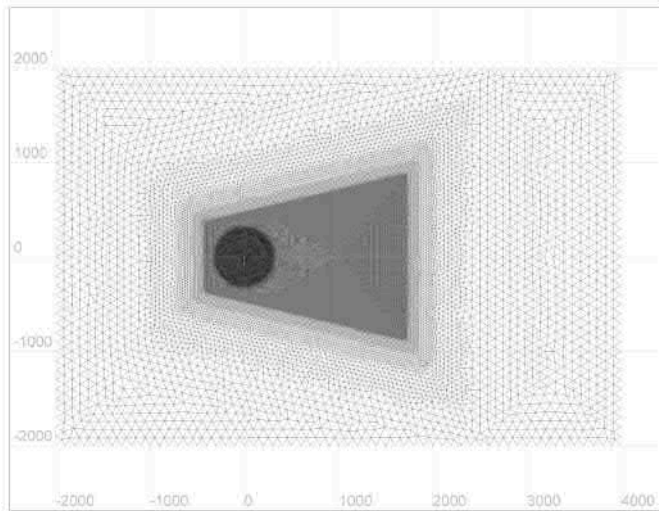


Figure 5: TELEMAC-3D mesh for a FLNG

The speed and velocity vectors, averaged over the top 20 m are plotted in Fig. 6, for an example with the FLNG stationary at 0°. The corresponding figure for the FLNG at 45° is shown in Fig. 7. Fig. 8 gives the vertical section through the middle of the FLNG, showing speed and velocity vectors for the 0° case.

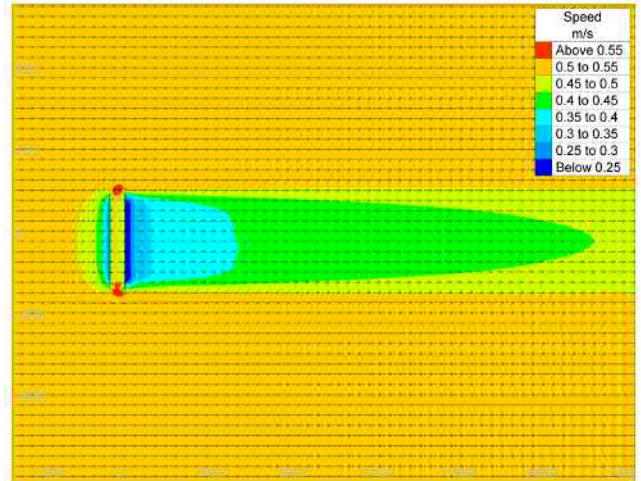


Figure 6: TELEMAC-3D Current sheltering – FLNG heading 0°

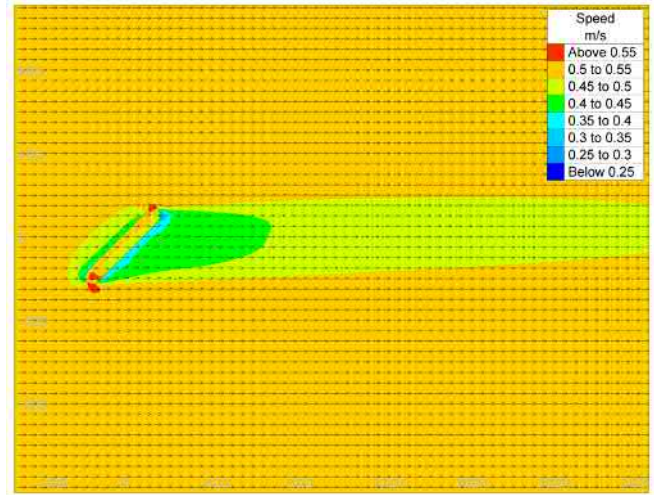


Figure 7: TELEMAC-3D Current sheltering – FLNG heading 45°

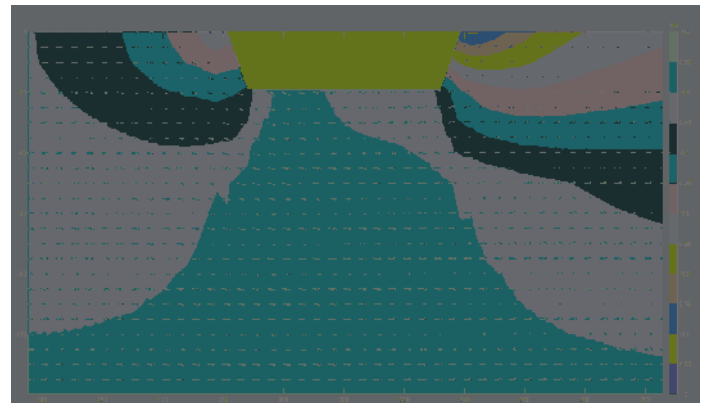


Figure 8: TELEMAC-3D midships vertical cross section – FLNG heading 0°

The real time integration of TELEMAC with the ship simulator was used to test manoeuvres as well as the familiarisation of tug masters and pilots for side by side FLNG operations (Fig. 9). Feedback was positive.



Figure 9: HR Wallingford navigation simulator snapshot – FLNG

### III. INFLUENCE OF TUG WASH

Some pilots have reported unusual flow when transiting through the channel of a harbour and passing another vessel near or at berth while being assisted by one or more tugs. These pilots believe that, under certain tide conditions, the thrust from the tugs builds up a localised flow condition across the navigation route with a potentially adverse effect on passing ships.

A tug wash model was developed and implemented in the existing harbour 3D flow model. The impact of the tug wash effects on the navigability of passing ships has been investigated using the HR Wallingford Ship Simulation System.

#### A. The tug wash model setup

The tug wash model was first setup and calibrated to estimate the likely tug thrust that may be present as computed by the TELMAC-3D flow model.

For this study a 27m ASD tug was used (Fig. 10). The corresponding characteristics are: 3,730kW 2x Schottel SRP1215; max rpm 314; diameter 2.4m; four blades; fixed pitch; two pods at 21.1m aft of bow fender, +/-2.3m from centreline, 3.7m below the waterline.



Figure 10: Tug Outboard Profile

In order to calculate the velocity in a thruster jet, the formulae (1) given by Blau and Van de Kaa [1] was used. The computed velocity for the tug, for 75% and 50% of its ballard pull is given in TABLE 1.

$$V_0 = C_3 \left( \frac{f_p P_d}{\rho_w D_p^2} \right)^{1/3} \quad (1)$$

- $P_d$  is the installed engine power (W)

- $f_p$  is the percentage of installed engine power
- $C_3$  is a coefficient equal to 1.17 for ducted propellers (determined by experiment)
- $\rho_w$  is the water density ( $\text{kg/m}^3$ )
- $D_p$  is the propeller diameter (m)

TABLE 1: THRUSTER JET VELOCITIES

$P_d$	$F_p$	$D_p$	$\rho_w$	$C_3$	$V_0$
$3730 \cdot 10^3$	75	2.4	1020	1.17	9.0
$3730 \cdot 10^3$	50	2.4	1020	1.17	7.8

The velocity computed is then implemented as a source of momentum within the 3D hydrodynamic model, at the appropriate location a few metres below the water surface. No water source is added, the TRISOU.f subroutine is modified to only add momentum.

#### B. The tug wash model validation

In order to validate the computed velocity for each tug thruster jet within the 3D hydrodynamic model, a schematic 3D model was used. The schematic model is a square 100m x 100m with a flat bathymetry at 2 metres below the still water level. A constant velocity in the tug thruster jets of 10 m/s for a period of 30 minutes was imposed, with a diameter of 1 m. Three vertical planes were used (one defining the surface, one the bed and the other in the middle, separating the water column in 2 layers, each 1 m thick) and the propeller was located at 1 m below the still water level. Horizontally, the mesh of the schematic model is based on a resolution of 1 m edges. Fig. 11 shows the current speeds at 45s for the full extent of the model. Fig. 12 and Fig. 13 show a close up view of the current speeds at 45s and 1800s, respectively.

Current speed time series were extracted at several distances from the propeller (white triangles in Fig. 12) and plotted in Fig. 14. All velocities shown in Fig. 11 to Fig. 14 were extracted from the middle plane, which is at the propeller level: 1 m below still water level.

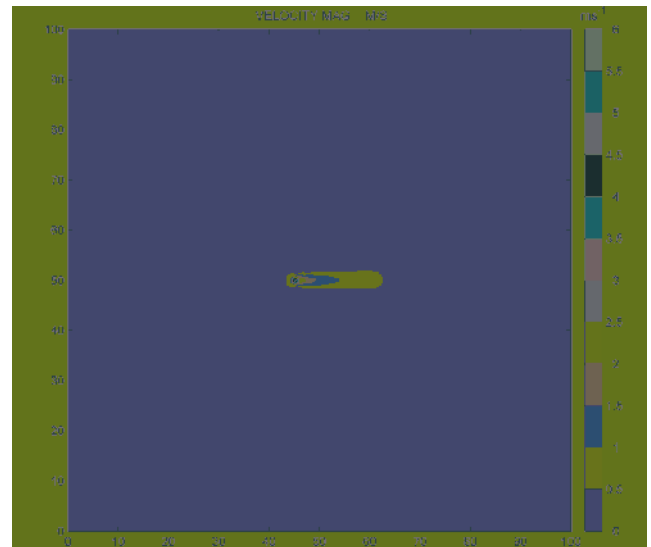


Figure 11: Schematic model full extent – Current speed at 45s



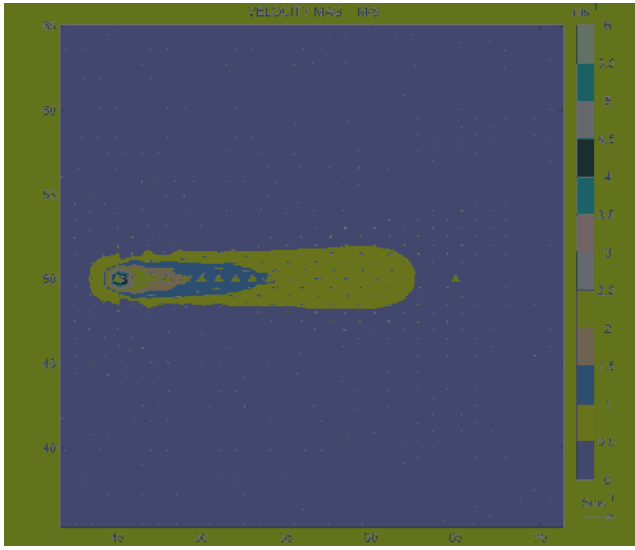


Figure 12: Schematic model – Current speed at 45s

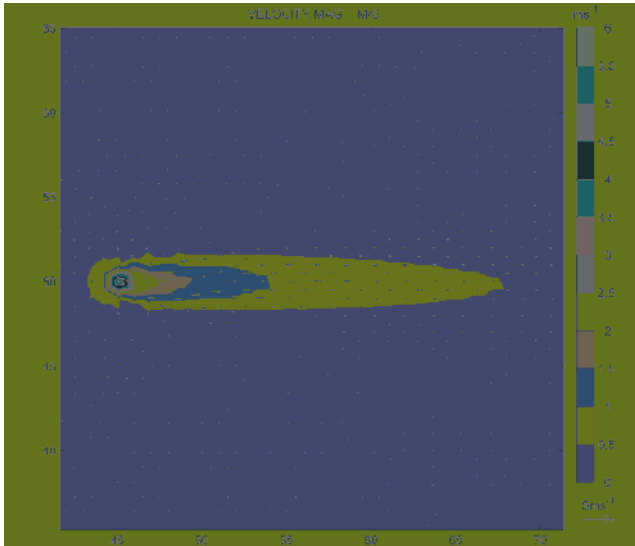


Figure 13: Schematic model – Current speed at 1800s

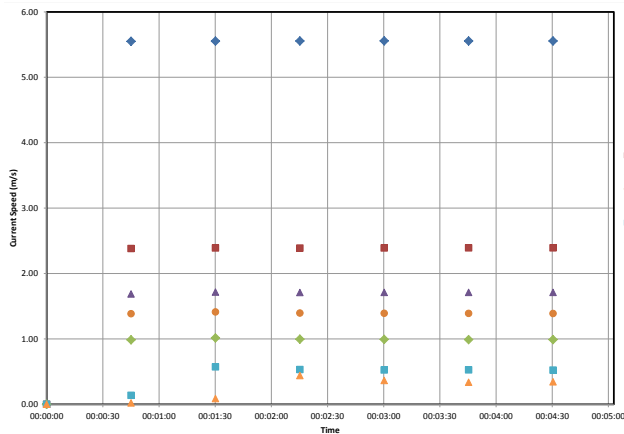


Figure 14: Current speed time series at several distances from the propeller, along the jet axis (White triangles in Figure 12)

In this schematic model, the current speed and its associated wake take about 3 minutes to achieve steady state,

as shown above in Fig. 14. The current speed also decreases quickly with the distance from the propeller along the jet axis. Fig. 15 gives a comparison between the model velocity decay and the formulation (2) of Albertson et al [2], also given in the PIANC guidelines ([3] Equation 8-1)

$$V_{axis} = \frac{1}{2C} V_0 \left( \frac{D}{x} \right). \quad (2)$$

- $V_{axis}$  is the flow velocity in the axis of the jet (m/s)
- $x$  is the horizontal distance from the propeller (m)
- $V_0$  is the efflux velocity (m/s)
- $C$  is a coefficient equal to 1.17 for ducted propellers (determined by experiment)
- $D$  is the diameter of the free jet (m)

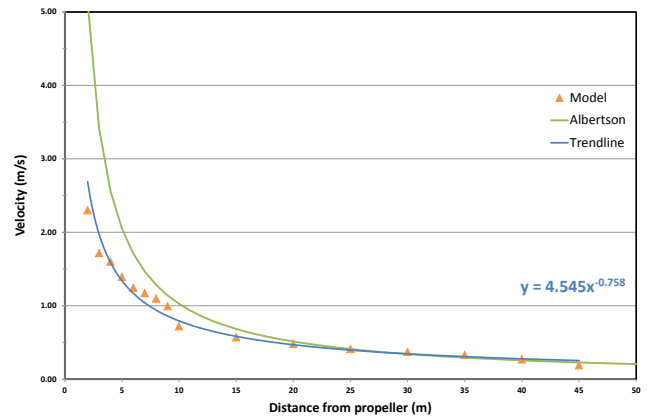


Figure 15: Velocity at 1800s from several distances from the propeller, along the jet axis

The trend line (the corresponding equation of which is shown in blue) and the formulation of Albertson are similar. The main differences appear to be within a 20 m distance from the propeller, that is, less than 10 propeller diameters downstream, where the jet has not yet reached its fully developed phase and therefore the estimation of velocities within the jet has a higher level of uncertainty. Note also that the formulation of Albertson assumes an infinite jet velocity at the propeller plane.

In the figures above (Fig. 11 to Fig. 15), the maximum velocity at the propeller is about 5.5 m/s. This is due to the fact that TELEMAC-3D applies the momentum within a volume, the size of which depends on the mesh resolution. Therefore, to be able to observe the propeller velocity 10 m/s applied in the model results, a finer mesh resolving the propeller dimensions would be needed. Separate validation tests were indeed carried out with finer meshes down to 0.5 m for the horizontal resolution and 0.25 m for the vertical resolution and an arbitrary propeller of 1 m in diameter, confirming the 10 m/s at the propeller location. This confirms that the effects of the propeller on the hydrodynamics are correctly represented. However, finer meshes also introduce numerical diffusion, resulting in lower velocities for distances greater than 20 m from the propeller (by about 0.1 m/s lower at 50 m). It is, therefore, not recommended to refine the mesh too much.



As the purpose of this study is to investigate flow patterns created a tens of metres away from the propellers, the comparison between the tug wash model and the Albertson formula is deemed acceptable and the 3D model is considered to be validated for this purpose.

### C. The tug wash model sensitivity

Sensitivity analyses specifically related to the tug jets were carried out, including the number of vertical layers representing the water column and the possible turbulence schemes. Also, in order to obtain a repeatable stable simulation so as to allow comparison between scenarios, sensitivity tests were performed to a number of numerical parameters such as model time step.

In the end, the parameters having the most influence on the results are summarised below.

- The horizontal and vertical turbulence scheme: Smagorinsky scheme (Smagorinsky 1963 [4]), used mainly for highly non-linear flows, with large scale eddy phenomena.
- The number of vertical planes: 12 was deemed to be the optimal number for computational efficiency.
- The time step: 2 seconds

### D. Passing ship results

A test case of a ship passing a recently moored vessel still under tug assistance was considered. The test case considered a scenario not long after slack water low tide (or the turning of the tide from ebb to flood) with three tugs in attendance holding a vessel at the berth which had been operating for 30 minutes at 75% power, then only two tugs operating at 75% for 30 minutes, which corresponds to a 9.0 m/s velocity. The aim of the test case was to determine if the tug wash had any influence on the passing ship.

The model bathymetry and the modelled water level time series around slack water low tide are presented in Fig. 16 and Fig. 17, respectively. The current speed and direction are plotted in Fig. 18. Time series were extracted at the location marked by a yellow triangle on Fig. 16. The current speed and direction contour plots are shown in Fig. 19 to Fig. 21 for snapshots. The colour scale only shows velocities up to 1m/s in order to see velocity patterns a couple of hundred metres away from the tugs. The velocity at the propeller is as described in Table 2 above, and diffuses quickly with the distance as shown in Fig. 15.

The results when integrated into real time ship simulation scenarios had a measurable effect on the passing ship with indications in the results of a recirculation eddy forming after sustained use of the tugs in this way.

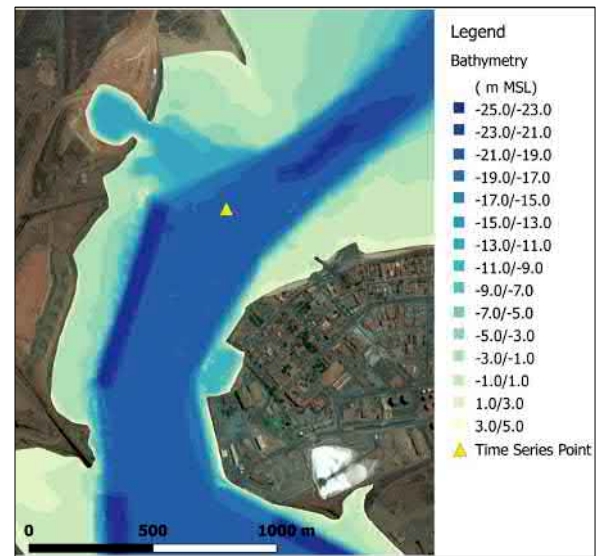


Figure 16: Bathymetry

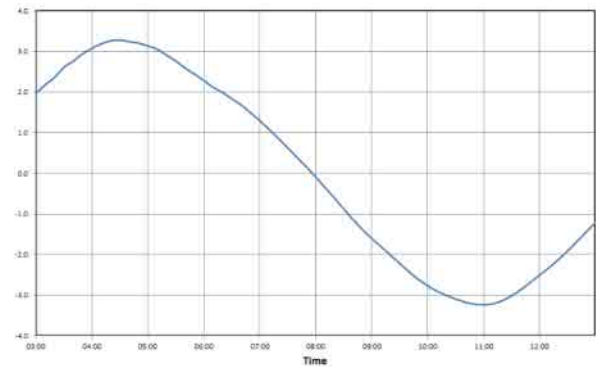


Figure 17: Free surface (m MSL) on the 30/01/2017

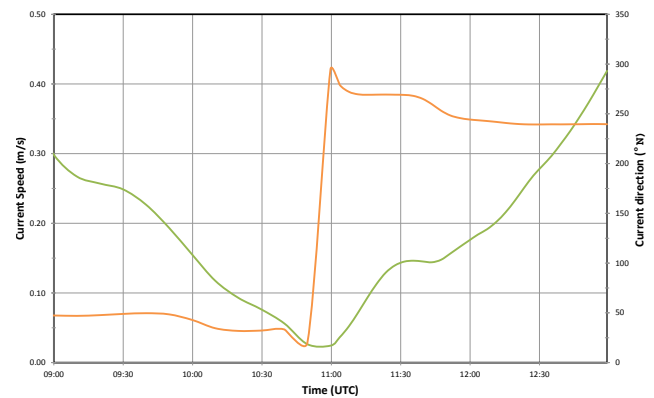


Figure 18: Current speed and direction on the 30/01/2017

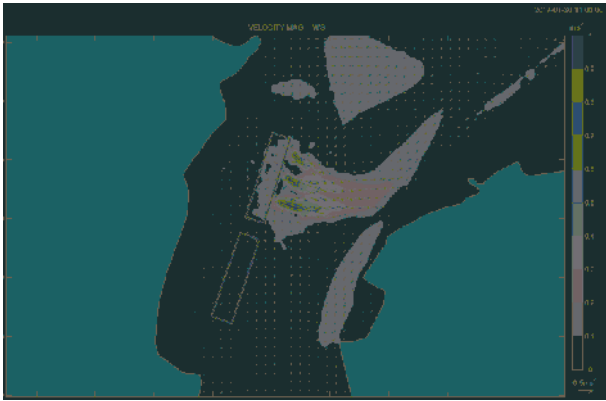


Figure 19: Current speeds and directions on 30/01/2017 at 11:00

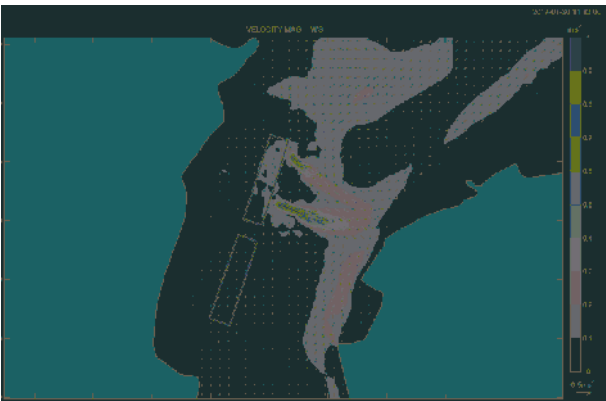


Figure 20: Current speeds and directions on 30/01/2017 at 11:12

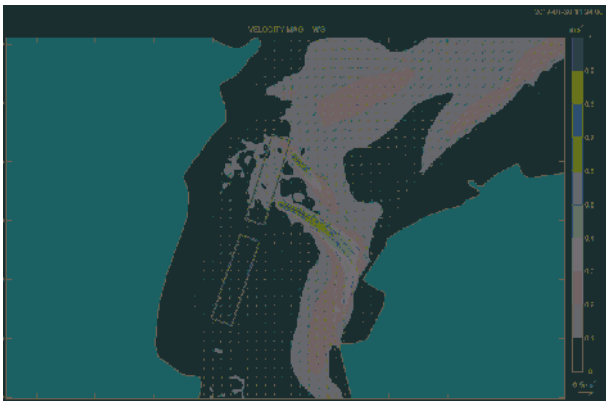


Figure 21: Current speeds and directions on 30/01/2017 at 11:20

#### IV. CONCLUSIONS

It has been found in practice that it is possible to use TELEMAC to make useful computations of the flow under and around floating objects. It is necessary, however, to treat such results with care for the following reasons:

- It is not clear whether the flow underneath the hull of the vessel is accurately modelled by imposing a pressure field. The shape of the hull is not guaranteed in this method to remain accurate as waves may travel across it. Also, the flow underneath the hull, especially if it is wide, is not a free surface flow in reality.
- The situation is more difficult if it is wanted to model a floating, moving vessel. The possibility of surface waves crossing the hull is now more likely resulting in the wrong hull shape. That is why a smooth representation of the hull shape was used. With a fine mesh in the horizontal it is possible to move the hull shape, as an air pressure variation, across the water surface. It is necessary to have several model cells to represent the transition from the deeper part of the hull to the water surface. The model time step needs then to be short enough to allow the vessel to cross each cell in several time steps. It is not expected that any rapidly moving vessel can be modelled without further refining the meshing processes. Another approach that may be useful for a moving vessel is to consider it instead to be stationary in a moving water flow.

It is clear that using a free surface flow model like TELEMAC to model a vessel's hull moving across the model mesh is an extension beyond normal use of such a flow model but once verified (e.g. against CFD) can by provide computationally efficient and representative flow fields resulting from the effect of floating structures.

It has been found that tug wash (propeller jet) can be usefully modelled in TELEMAC-3D for examples where the tug wash can have an influence on ships that are impacted by it.

#### REFERENCES

- [1] Blaauw, H.G. & E.J. van de Kaa (1978) *Erosion of bottom and sloping banks caused by the 2775 screw race of manoeuvring ships*. WLDelft Publication no. 202, Proc. 7th Intern. Harbour 2776 Congress, Antwerp, May 1978.
- [2] Albertson, M.L., Dai, Y.B., Jensen, R.A., Hunter Rouse (1950), *Diffusion of submerged jets*, 2765 ASCE Transactions Paper no. 2409, New York, 639-664.
- [3] PIANC (2012), Guidelines for berthing structures, related to thrusters.
- [4] SMAGORINSKY, 1963. General Circulation Experiments with the Primitive Equations, Monthly Weather Review, vol. 91, issue 3, p. 99.

# Computation of 3D coastal hydrodynamics through the vortex force formalism implemented by coupling TOMAWAC and TELEMAC-3D

Maria João Teles, Thierry Fouquet

LNHE, EDF R&D

Chatou, France

[maria.teles@edf.fr](mailto:maria.teles@edf.fr), [thierry.fouquet@edf.fr](mailto:thierry.fouquet@edf.fr)

Antonio Pires-Silva

IST, University of Lisbon

Lisbon, Portugal

Michel Benoit

Institut de Recherche sur les Phénomènes Hors-Equilibre

(Irphé - UMR 7342)

Aix Marseille Univ., CNRS, Centrale Marseille

Marseille, France

**Abstract** — The implementation of the new TELEMAC-3D-TOMAWAC coupled system [5] on the latest TELEMAC-MASCARET version (v8p1) is presented. The new coupled system, based on a vortex-force formalism [7] is applied on a barred beach test case. The improvement of three-dimensional wave-current interaction effects on the hydrodynamics description is evidenced.

## I. INTRODUCTION

The coastal domain is a complex hydrodynamic system where physical phenomena with different time and space scales interact. This is the case of waves and currents interaction.

The wave breaking process together with wave-induced currents can create a dangerous environment for swimmers and have a great impact on morphodynamics in the nearshore areas. Depending on the bottom morphology and on the incident wave field, currents can have different characteristics. If obliquely incident waves break on a alongshore uniform planar beach, a longshore current is generated. If the beach has, for example, sand bars or cusps, rip currents can be generated.

The wave-current environment is well described in a 2DH framework by the work of [1], through the radiation stress concept, already implemented by coupling the hydrodynamic model TELEMAC-2D [2] and spectral wave modelling TOMAWAC [3]. A couple of years ago, this approach was extended to TELEMAC-3D code assuming a uniform distribution of the radiation stresses over depth. Therefore the vertical structure of the flow was not properly assessed.

Nevertheless the three-dimensional (3D) structure of the flow can give relevant information about sediment transport, linked to the value of the velocities near the bottom, or to assess wave power availability at a certain location.

During the PhD thesis of Teles [4], [5] a new TELEMAC-3D - TOMAWAC coupling system was developed, based on a vortex force formalism.

The theoretical framework chosen was the glm2z-RANS [7] equations. To do so, the three-dimensional TELEMAC-3D equations were modified together with new boundary conditions and new parametrizations were included in TOMAWAC to calculate the wave forcing terms.

The purpose of this paper is to present the implementation of the developed TELEMAC-3D - TOMAWAC coupled system [4], [5] on the latest TELEMAC-MASCARET version (v8p1). The improvement of wave-current interaction effects on the 3D hydrodynamics description is evidenced.

In the following section a brief description of the new wave forcing terms included in TOMAWAC and the modified equations implemented on TELEMAC-3D is given together with the new key-words created in the steering file to activate this coupling mode.

In section III, a barred beach test case is used to analyse the vertical structure of the flow, followed by section IV, where some concluding remarks and perspectives are given.

## II. COUPLING SYSTEM

### A. Governing equations

To take into account the 3D effects of the combined environment the mathematical framework proposed by [7], the glm2z-RANS equations, was implemented. Following [8] the vertical current shear was neglected in the wave forcing terms.

The wave forcing terms are calculated in new fortran subroutines created in TOMAWAC model, namely:

- The momentum lost by waves from bottom induced wave breaking, through the variables FDX, FDY, calculated in fdiss3d.f;
- The momentum lost by waves due to bottom friction, through the variables FBX, FBY calculated in fbott3d.f;
- The wave enhanced mixing ( $v_{wz}$ ), with the variable FDK, calculated in fdissk.f;
- The bottom friction modified from the wave-current environment, with the variable CFW, calculated in fric3d.f;
- The Stokes drift ( $U_{\alpha s}$ ), through the variables UST, VST, calculated in uvstokes.f
- The wave induced pressure (J), with the variable WIP, calculated in wipj.f
- The momentum lost by waves due to white-capping together with the input momentum transferred from wind to the wave field, with variables FWX, FWY, calculated in moudiss.f and windiss.f.

These new terms are transferred to TELEMAC-3D model by means of source/sink terms on the mass (1) and momentum (2) conservation equations, and boundary conditions. Considering an incompressible fluid and the hydrostatic assumption, the new equations become:

$$\frac{\partial \hat{u}_\alpha}{\partial x_\alpha} + \frac{\partial \hat{w}}{\partial z} = 0 \quad (1)$$

$$\begin{aligned} & \frac{\partial \hat{u}_\alpha}{\partial t} + \hat{u}_\beta \frac{\partial \hat{u}_\alpha}{\partial x_\beta} + \hat{w} \frac{\partial \hat{u}_\alpha}{\partial z} = S_\alpha - g \frac{\partial \hat{\eta}}{\partial x_\alpha} + \frac{\partial}{\partial x_\beta} \left( v_H \frac{\partial \hat{u}_\alpha}{\partial x_\beta} \right) \\ & + \frac{\partial}{\partial z} \left( (v_z + v_{wz}) \frac{\partial \hat{u}_\alpha}{\partial z} \right) - \epsilon_{\alpha\beta\gamma} (f_3 + \omega_3) U_{\beta s} - W_s \frac{\partial \hat{u}_\alpha}{\partial z} - \frac{\partial J}{\partial x_\alpha} \end{aligned} \quad (2)$$

$(\hat{u}_\alpha, \hat{w})$  represent the quasi-Eulerian velocities ( $\alpha = 1, 2$  corresponding to horizontal coordinates), defined in a second order theory approach, by the difference between the Lagrangian mean velocities and the Stokes drift ( $U_{\alpha s}, W_s$ ).  $S_\alpha$  represents the hydrodynamic model horizontal source or sink terms of momentum, for instance, the Coriolis force. The acceleration due to gravity is given by  $g$ , and  $S_{x\alpha}$  represent the hydrodynamic model horizontal source terms, for instance, the Coriolis force.  $v_H$  and  $v_z$  are, respectively, the horizontal and vertical turbulence viscosities. The viscosity values can either be prescribed by the user or computed by a turbulence closure model. Furthermore, within the wave-current environment and due to wave breaking there is an enhancement of the vertical mixing. To take account of this effect, the approach proposed by [12] was followed by adding the wave-enhanced vertical mixing,  $v_{wz}$  to the vertical turbulence viscosity  $v_z$ :

$$v_{wz}(z) = c_b Q_{br} \frac{1}{3} \frac{H_s}{\sqrt{2}} D f^{wb}(z) \quad (3)$$

with :

$$f^{wb}(z) = \frac{1 - \tanh[k_b(\hat{\eta} - z)^2]}{\int_{-\hat{\eta}}^{\hat{\eta}} (1 - \tanh[k_b(\hat{\eta} - z)^2]) dz} \quad (4)$$

$Q_{br}$  represents the wave breaking sink term,  $D$  the total depth and  $k_b = \frac{\sqrt{2}}{a_b H_s}$ , with  $a_b = 1.2$  and  $c_b = 0.03$ .

The vortex force in  $x_\alpha$  direction, which is represented in  $\epsilon_{\alpha\beta\gamma} (f_3 + \omega_3) U_{\beta s}$ , is defined by the vectorial product between the mean flow vertical vorticity  $\omega_3$  and the horizontal Stokes drift  $U_{\beta s}$ . The Stokes-Coriolis force is represented by  $\epsilon_{\alpha\beta\gamma} f_3 U_{\beta s}$ .

Moreover, the bottom shear stress in the hydrodynamic model was modified in order to take into account the wave-current interaction effects on the bottom roughness (CFW), following [9]'s theoretical framework.

To guarantee mass conservation, the mass transport induced by the Stokes drift in the depth-integrated continuity equation (5) was included. The overbar symbol denotes a depth-integrated variable.

$$\frac{\partial \bar{h}}{\partial t} + \frac{\partial \bar{h} \hat{u}_\alpha}{\partial x_\alpha} = - \frac{\partial \bar{h} \bar{U}_{\alpha s}}{\partial x_\alpha} \quad (5)$$

At the offshore open boundary, in the case of no other external forcing terms (such as tidal forces), two conditions are imposed for the phase-averaged elevation (6) and the horizontal velocities (7) [11]:

$$\hat{\eta} = - \frac{J}{g} \quad (6)$$

$$\hat{u}_\alpha = - \bar{U}_{\alpha s} \quad (7)$$

The momentum lost by waves due to depth-induced wave breaking (FDX, FDY) and bottom friction (FBX, FBY) is imposed in the hydrodynamic model as free surface and bottom stresses, respectively. The momentum lost by waves due to white-capping together with the input momentum transferred from wind to the wave field (FWX, FWY) is also imposed as a surface stress in the hydrodynamic model.

### B. Implementation

In the following, we give a brief explanation on the way the coupled system works (Figure 1) [5]. Both TOMAWAC and TELEMAC-3D models run with the same horizontal mesh.

TELEMAC-3D starts the calculation. The Nikuradse roughness, the z-levels, and the computed depth-integrated velocities and mean surface elevation are communicated to TOMAWAC. In its turn, TOMAWAC computes, over a time step, the wave forcing terms: the Stokes drift components, the wave-induced pressure, the wave breaking and the bottom-induced dissipation momentum contributions. The last two terms are imposed as surface and bottom stresses,



respectively, in the hydrodynamic model. Furthermore, the wave model calculates the wave-enhanced vertical mixing coefficient  $\nu_{wz}$  that is added to the vertical turbulence viscosity in TELEMAC-3D. This process is repeated each time step or made within a coupling period defined by the user. The coupling period between TELEMAC-3D and TOMAWAC can be larger than the time step of the models. The time step of each of the models does not have to be the same, just a multiple of each other.

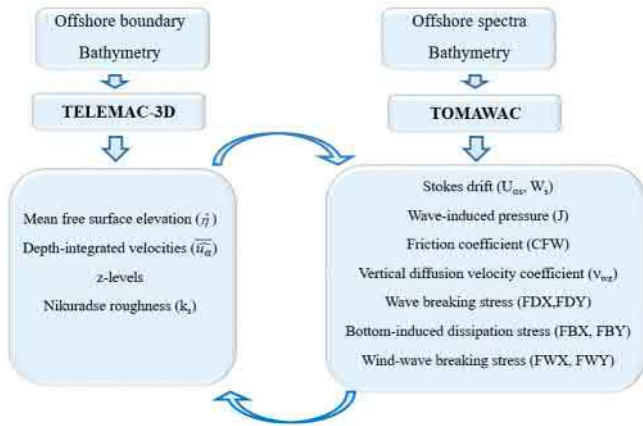


Figure 1 Scheme of the different terms computed and exchanged by TELEMAC-3D and TOMAWAC

### C. Steering file: new key words

In order to compute a wave– current environment in a 3D framework, with the coupling system based in the vortex force formalism described above, the user must include the key word *COUPLING WITH: TOMAWACT3D* in the steering file. The existing coupling, where the radiation stresses are distributed uniformly over the depth, is then distinguished from the new developments.

If the user wants to include the momentum lost by waves due to bottom friction the key word *BOTTOM FRICTION DUE TO WAVES* must be set to *TRUE* in the steering file. Please be aware that this term shall be included only when the vertical resolution near the bottom in TELEMAC-3D is sufficiently refined.

Moreover the wave enhanced vertical mixing formulation follows [12] approach with the same parameters used in that paper. A sensitivity analysis would be advised if the wave enhanced vertical mixing is expected to have a predominant role in the 3D flow dynamics.

## III. TEST CASE

In the present section the capability of the new coupled system to model rip currents is tested and the vertical structure of the flow is evidenced. The comparison of numerical results between the existing TELEMAC-3D – TOMAWAC coupling, based on the radiation stresses uniformly distributed over depth, and the new one, based on a vortex-force formalism is made.

### A. Rip current

The present test-case is based on laboratory wave-basin experiment [10]. The bathymetry is made of two bars which

induce wave breaking and the generation of a rip current system. The wave basin is 17.2 m in the cross-shore direction and 18.7 m in the longshore direction. The slope is 1:5 from offshore up to three meters from the wave maker and then 1:30 till the end of the beach. The generated waves are monochromatic and perpendicular to the beach.

The same wave basin configuration was defined on the numerical model. The computational domain was discretized equally for both models with 0.2 m in x- and y- directions (Figure 2). In TELEMAC-3D, 8 horizontal planes were distributed over depth.

The time step was set to  $\Delta t = 0.03$  s for both hydrodynamic and wave models. Conditions (4) and (5) were assigned at the offshore boundary and walls were defined at lateral and shoreward boundaries. The Nikuradse roughness was set to  $k_s = 0.01$  m. The k- $\epsilon$  model was the chosen turbulence model to compute the vertical turbulence viscosity. To take into account the wave-enhanced mixing in the hydrodynamic model due to wave breaking, the parameters  $c_b = 0.03$  and  $a_b = 1.2$  were used [12].

A value of  $\nu_H = 1.10^{-2} \text{ m}^2\text{s}^{-1}$  was set for the horizontal turbulence viscosity and  $\nu_z = 1.10^{-6} \text{ m}^2\text{s}^{-1}$ . The numerical simulations with TOMAWAC were performed with spectral parameters that match the monochromatic laboratory experiments. This way, a significant wave height was set to  $H_s = 0.067$  m. The minimum frequency was set to 0.187 Hz, the number of frequencies to 7 and the frequential ratio to 1.4. The directional discretization was made through 24 direction bins. For the depth-induced breaking the model proposed by [12] was chosen with  $\gamma_2 = 1.0$ .

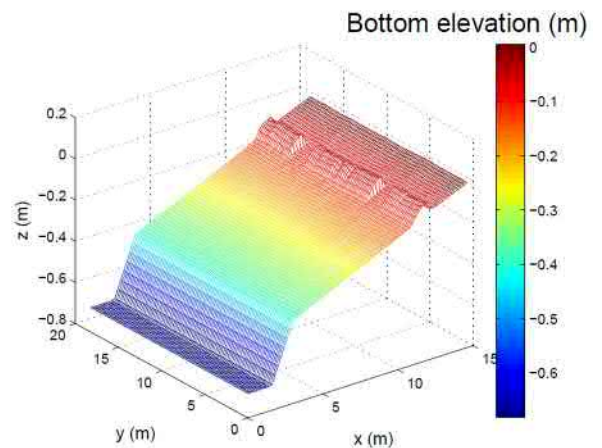


Figure 2 Wave basin bathymetry of the rip current test case

### B. Results

The wave height evolution over the domain is of major importance to correctly obtain the flow pattern of a rip current system. In its turn the current field is going to have a significant role on the wave height evolution [10]. Therefore a great influence is also noticed on the rip currents from the interaction with waves.

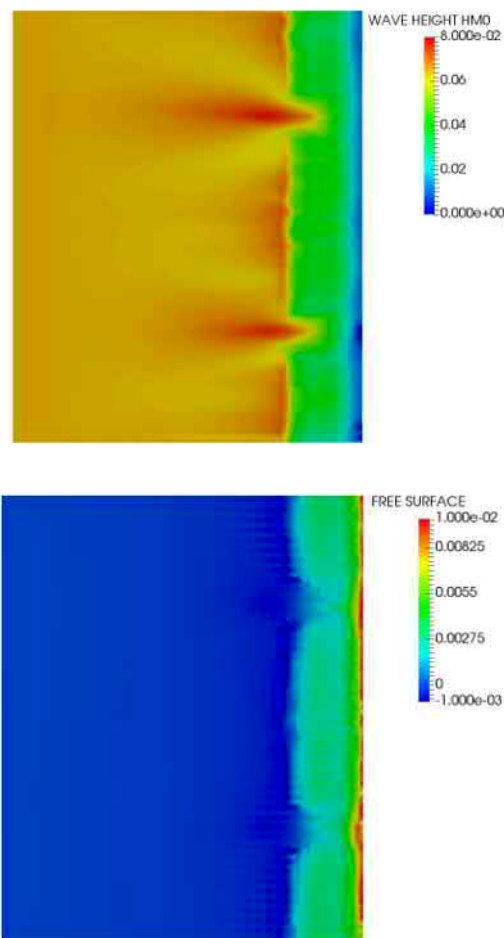


Figure 3 Wave height (m) and mean free surface elevation (m) patterns over the domain

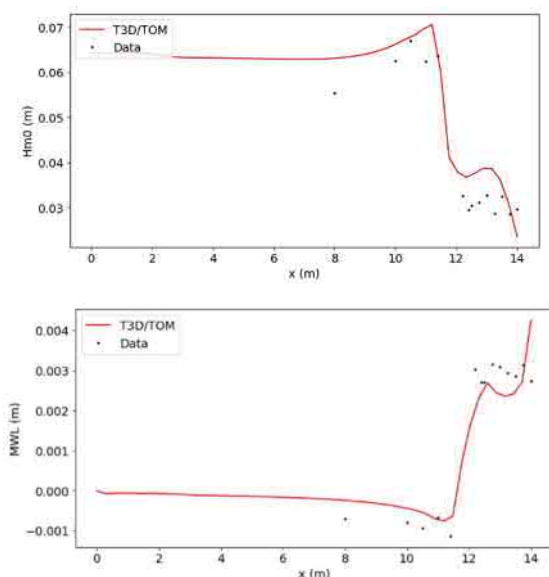


Figure 4 Cross-shore evolution of significant wave height (above) and mean water level (below) over the bar at  $y=9.2$  m. Comparison between numerical results (lines) and data (dots) from [14].

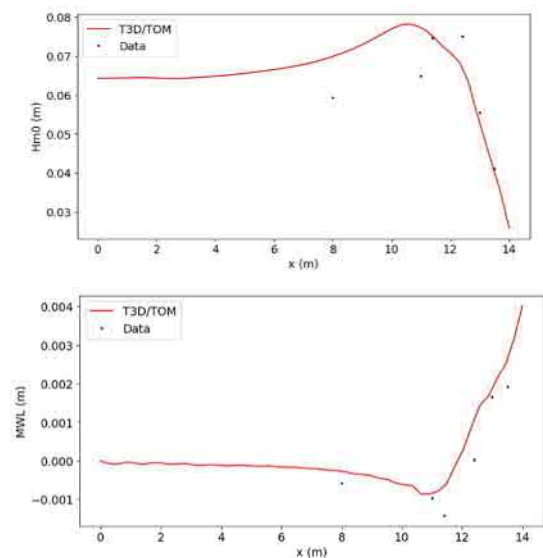


Figure 5 Cross-shore evolution of significant wave height (above) and mean water level (below) through the rip channel at  $y=13.6$  m. Comparison between numerical results (lines) and data (dots) from [14].

Due to bathymetry features, the wave pattern in the domain is quite different in the channel areas and over the bars (upper panel of Figure 3). The variation of the mean surface elevation (lower panel of Figure 3) alongshore induces longshore pressure gradients. The latter generate offshore oriented currents that converge into the rip channel and onshore oriented currents over the bar.

The breaking pattern reveals a quite distinct behaviour between the bar and the rip channel. While over the bars the waves break suddenly and then near the shoreline a second less intense breaking is observed, in the channel, due to the greater water depth, the waves break more progressively and penetrate further into the inshore zone of the channel, inducing a longshore current near the shoreline that flows away from the channel (Figure 6).

The comparison between numerical results and measurements of the significant wave height and mean water level over the bar (at  $y = 9.2$  m) and through the rip channel ( $y = 13.6$  m) are shown on Figure 4 and Figure 5 respectively. Over the bar the comparisons between the numerical simulations and data are similar. The waves break suddenly when encountering the bar and a sudden and significant rise of the water level occurs due to the strong wave breaking in this region. Through the rip channel, the coupled system reproduces quite well the progressive evolution of the wave set-up up to the shoreline but it shows some difficulties in reproducing the exact location where waves start to break through the rip channel. Possibly, the numerical opposing currents were too strong and induce the waves to break earlier than observed in the experiments.

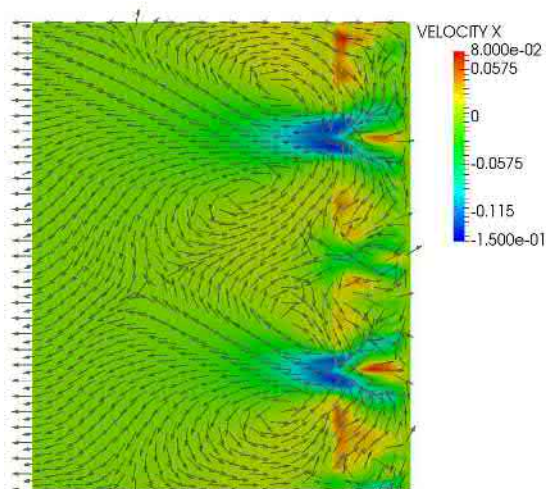


Figure 6 Depth integrated rip current (m/s) patterns over the domain

The vertical structure of the cross-shore and longshore currents is presented below in the longshore direction of the domain at  $x = 11.6$  m.

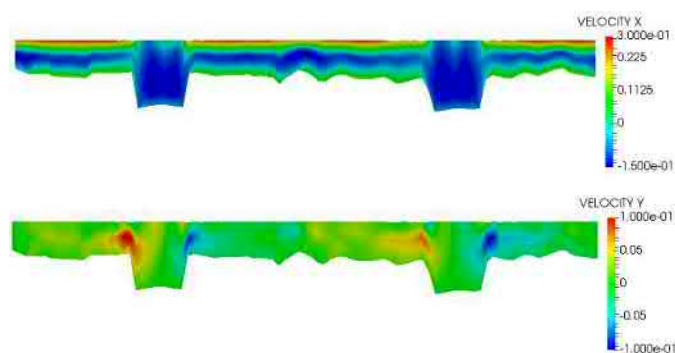


Figure 7 Alongshore variation of cross-shore and longshore current (m/s) components at  $x = 11.6$  m

It can be seen a strong vertical shear of the quasi-Eulerian cross-shore velocity component above the bar crest. It increases from bottom to the free surface, being oriented towards the shoreline. When encountering the bars, waves break, and a strong mass flux occurs. This can be confirmed by the vertical distribution of the cross-shore component of the Stokes drift (upper panel of Figure 8).

Within the rip channels, the vertical profile of the cross-shore velocities is not so sheared, but it shows relatively high negative velocities approximately in the middle of the water column. Then it starts to slightly decrease in magnitude towards the free surface and the bottom.

The longshore components of the quasi-Eulerian velocity are one order of magnitude lower than the quasi-Eulerian cross-shore velocities. This is caused by the weak longshore component of the Stokes drift (lower panel of Figure 8). Even so, they present high variability along the longshore bars and channels. At least three inflexion points for the velocities can be clearly identified: two in each channel and one over the bar. These inflexion points are generated by the variability of the mean surface elevation in the longshore direction which

in its turn exists due to the spatial variability of the dissipation rate of the incident wave field.

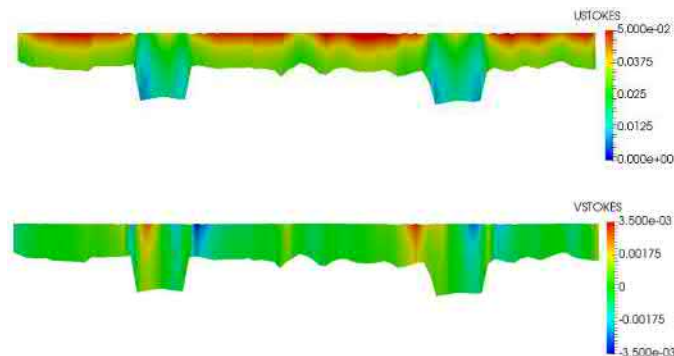


Figure 8 Alongshore variation of crossshore and longshore Stokes drift (m/s) components at  $x = 11.6$  m

In the figures below we plot the evolution of cross-shore and longshore current components along two cross-shore directions of the domain ( $y = 13.6$  m in the rip channel and  $y = 9.2$  m over the bar).

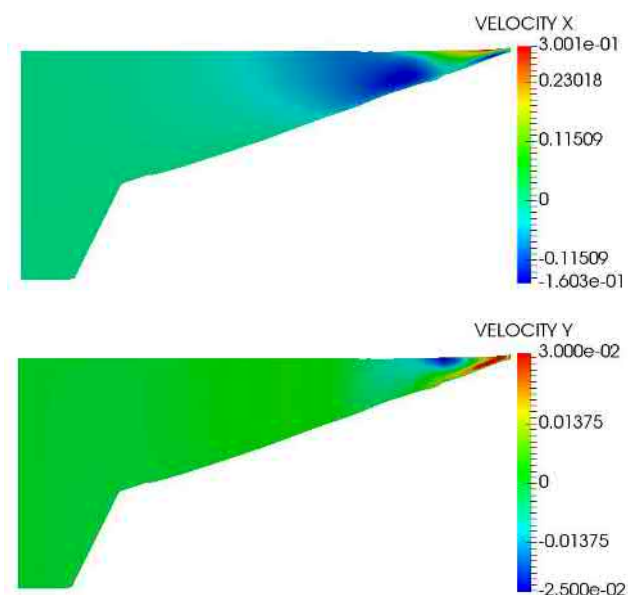
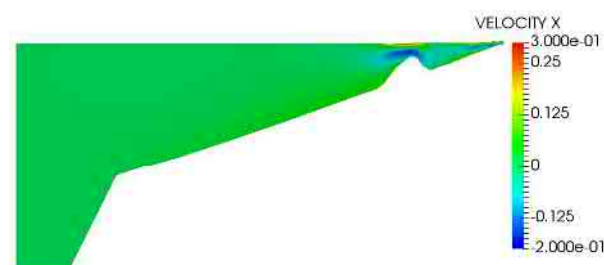


Figure 9 Crossshore variation of cross-shore and longshore current (m/s) components in the rip-channel at  $y = 13.6$  m.



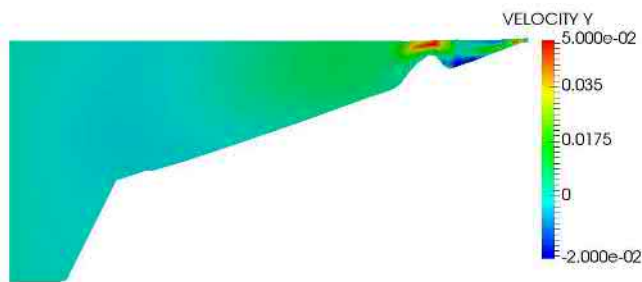


Figure 10 Crossshore variation of cross-shore and longshore current (m/s) components over the bar at  $y = 9.2$  m

It can be seen that in both wave breaking locations there is a strong vertical shear of the cross-shore quasi-Eulerian velocity: near the free surface it is directed onshore while near the bottom an undertow is verified. When analysing the rip current through the rip channel the velocities oriented offshore are stronger than the ones observed over the bar.

One of the great advantages of the vortex force formalism to describe waves and current interactions is that the vortex force is clearly distinguished. Therefore it is possible to study the circulations and water motions in the mean flow. Moreover, within this approach, it is possible to show the distribution of the vortex force over the domain that in its turn contributes to the vortices located between the bar and the channel and near the shoreline.

If the radiation stress is assumed to be uniformly distributed over the depth, the vertical structure of the flow cannot be assessed. As it is shown above, there is an important vertical shear of the velocity at certain locations of the domain, which can strongly impact the morphodynamics in similar beach configurations.

#### IV. CONCLUDING REMARKS

The implementation of the coupled system between the three-dimensional flow model TELEMAC-3D and the spectral wave model TOMAWAC [4], [5] in the next official TELEMAC-MASCARET v8p1 version is presented. The capability of the new coupled system, based on a vortex force formalism, to represent rip currents on a barred beach is assessed and the vertical structure of the flow is analysed.

Other parametrizations and vertical distributions of the non-conservative wave forcing terms should be the subject of further research.

Moreover in the present work, the vertical current shear is ignored within the wave forcing terms, and the horizontal diffusion velocity coefficient was set by using a simple approach (imposing a constant value along the domain). The former feature should be included and different and more complex turbulence modelling approaches should be tested.

#### ACKNOWLEDGEMENT

Maria João Teles would like to acknowledge the support of a PhD grant (SFRH/BD/61269/2009) from FCT (Fundação para a Ciência e Tecnologia), Portugal. The

authors would also like to acknowledge all the support given by the TELEMAC-MASCARET development team.

#### REFERENCES

- [1] Longuet-Higgins, M. S., Stewart, R. W., "Radiation stress and mass transport in gravity waves, with applications to surf beats. *Journal of Fluid Mechanics*", 1962, Vol. 13, pp 481-504.
- [2] Hervouet J.-M., "Hydrodynamics of free surface flows, modelling with the finite element method. Editions Wiley & Sons." ISBN 978-0-470-03558, 2007, 342 p.
- [3] Benoit M., Marcos F., Becq F., "Development of a third generation shallow water wave model with unstructured spatial meshing. *Proc. 25th Int. Conf. on Coastal Eng. (ICCE'1996)*", 2-6 September 1996, Orlando (Florida, USA), pp 465-478.
- [4] Teles M.J., "Wave-current modelling at local and regional scales", PhD thesis, University of Lisbon, Instituto Superior Tecnico, Lisbon, 2013.
- [5] Teles M.J., Pires-Silva A., Benoit M., "Computation of 3D coastal hydrodynamics through the vortex force formalism implemented by coupling. *Proc. 21<sup>st</sup> TELEMAC MASCARET User Conference*, 15<sup>th</sup> - 17<sup>th</sup> October, Grenoble", 2014, pp 11-17.
- [6] Andrews, D. G., McIntyre, M. E., "An exact theory of non linear waves on a Lagrangian mean flow." *Journal of Fluid Mechanics*, 1978a, Vol. 89, pp 609-646.
- [7] Ardhuin F., Rascle N., Belibassakis K.A., "Explicit wave-averaged primitive equations using a generalized Lagrangian mean." *Ocean Modelling*, Vol. 20(1), 2008, pp 35-60.
- [8] Bennis A.-C., Ardhuin F., Dumas F., "On the coupling of wave and three-dimensional circulation models: Choice of theoretical framework, practical implementation and adiabatic tests." *Ocean Modelling*, 2011, Vol. 40(3-4), pp 260-272.
- [9] Christoffersen, J. B., Jonsson, I. G., "Bed friction and dissipation in a combined current and wave motion." *Ocean Engineering*, 1985, Vol. 12, pp 387-949 423.
- [10] Haas, K. A., Svendsen, I. A., "Laboratory measurements of the vertical structure of rip currents". *Journal of Geophysical Research*, 2002, Vol. 107 (C5), 3047
- [11] Rascle, N. "Impact of waves on the ocean circulation." PhD thesis, Université de Bretagne Occidentale, France, 2007.
- [12] Battjes, J.A. and Janssen, J.P.F.M., "Energy loss and set-up due to breaking of random waves." In *Proc. 16th Int. Conf. Coastal Eng.*, pp 569-587, 1978.
- [13] Uchiyama, Y., McWilliams, J. C., Shchepetkin, A. F., "Wave-current interaction in an oceanic circulation model with a vortex-force formalism: Application to the surf zone". *Ocean Modelling*, 2010, Vol. 34, pp 16-35.
- [14] Haller, M. C., Dalrymple, R. A., Svendsen, I. A., "Experimental study of nearshore dynamics on a barred beach with rip channels". *Journal of Geophysical Research*, 2002 Vol.107 (C6), 3061.



# Impact of initial sediment conditions on numerical modelling of bedload transport

Martin Utz

Dept. of Hydraulic Engineering

Federal Waterways Engineering and Research Institute (BAW)

Karlsruhe, Germany

[martin.utz@baw.de](mailto:martin.utz@baw.de)

**Abstract—** The composition of river bed sediment is an important influencing factor of bedload transport. In numerical bedload transport models this composition is defined by the initial sediment condition, which specifies the grain size distribution at each calculation node. Probes, measurements taken from the field which yield sediment composition, are only available from limited locations within the calculation domain. From these point-based measurements assumptions must be made in regards to the spatial distribution of the sediment composition to define the initial sediment condition.

This study compares two different methods of generating a spatial distribution of the sediment composition, or in modelling terms the initial sediment condition. The first method uses pre-simulation and the second one uses spatial interpolation. The resulting differences of both methods are examined at two separate points during the modelling process: first at the generated initial conditions and second for the final results of the corresponding bedload transport simulations. The simulations are performed with TELEMAC-2D and SISYPHE.

The two methods lead to strong differences in the initial sediment conditions and also the bedload transport simulation results. Large differences are observed in bed level changes and bedload discharges. This study points out that a combination of both methods could be an appropriate way to generate an initial sediment condition.

## I. INTRODUCTION

The composition of river bed sediment is an important influencing factor of the bedload transport. This composition is described by grain size distribution, which is variable in the horizontal direction as well as in the vertical. In numerical bedload transport models the river bed composition is defined by the initial sediment condition, which specifies the grain size distribution at each calculation node for each defined layer. The layers divide the subsurface of each cell vertically into domains of homogeneous properties and approximate the continuous vertical variability of the sediment composition [1]. The uppermost layer of the

river bed determines the amount of sediment which is available for transport and therefore significantly influences the amount of transported sediment. Furthermore, the underlying layers become important players in case of erosion. So it is critical that the initial sediment condition provides accurate information about the sediment composition in terms of the grain size distribution at each computation node and also in vertical direction. Measured grain size distribution of bed material is only available at limited probed locations, single spots, within the calculation domain. Therefore it is necessary to generate a spatial distribution of the sediment composition based on the measurements. The measurements include, for example, surface grab samples of the bed material, which are sieved afterwards to get the grain size distribution. The generated spatial distribution is then used as the initial sediment condition for a bedload transport simulation.

This study presents two different methods to generate a spatial distribution of the sediment composition and thus the initial sediment condition. The first method is based on a pre-simulation. One of the disadvantages of this approach is that it requires a huge effort in terms of computation time, because an additional simulation is needed to generate the initial sediment condition. Also it is unclear how well the natural composition of the river bed is described by the pre-simulation results. Therefore within this study another method is developed, which is significantly less costly than the pre-simulation. This second method uses a spatial interpolation of the measured grain size. In addition the interpolation ensures that the initial sediment condition resembles the measured data as close as possible.

Within this study, first, the differences in the initial sediment conditions itself are examined. Second, the influence of the different initial conditions on the results of a bedload transport simulation is investigated using a numerical bedload transport model of the Lower Rhine nearby Düsseldorf, which is a segment of the model used in [2].

## II. GENERATION METHODS FOR THE INITIAL SEDIMENT CONDITION

### A. Pre-simulation

The first approach uses a pre-simulation to generate the initial sediment condition. Within this approach the averaged grain size distribution of the measurements is used as initial sediment condition for the pre-simulation. This yields a spatial homogeneous distribution of the sediment composition at the beginning of the pre-simulation. We assume that the measurements are representative for the river bed material. Thus the homogeneous spatial distribution represents the average natural river bed material without typical spatial variability. Due to sediment transport during the pre-simulation, the grain size distribution at each calculation node changes yielding a non-homogeneous spatial distribution. The non-homogeneous spatial distribution aims to resemble nature and is then used as the initial sediment condition for the main simulation. In the pre-simulation, different hydraulic boundary conditions can be selected. A convenient choice is a natural hydrograph covering several years. Another possibility is to use a constant discharge which is decisive for the forming of the river bed. When using a natural hydrograph it is reasonable to use a time-averaged grain size distribution and not the grain size distribution occurring at the last time step of the pre-simulation. Otherwise the sediment composition could be too heavily influenced by the discharge situation at the end of the pre-simulation.

An advantage of the pre-simulation is that it works with a sparse data base, due to only the mean of the measured grain size distributions being used. However, by averaging the field measurements the local information is neglected. Therefore all of the available information is not being used completely. Another problem is that the pre-simulation should be conducted with the same numerical parameters as the calibrated model, because these describe the natural behaviour of the model best. Though, these parameters are not available during the generation of the initial sediment condition, as the model is not calibrated at that time. Therefore an iterative procedure is necessary, which significantly increases required effort. Another disadvantage is that during the simulation only the sediment composition in the topmost layers changes due to the sediment transport. In the underlying layers the constant distribution, which was set as the initial sediment condition of the pre-simulation, remains.

### B. Spatial Interpolation

Spatial interpolation of measured grain size distribution is another approach for initial sediment condition generation. Usually measurement points are not close enough to perform an interpolation on a Cartesian coordinate system (Figure 1). Doing so would lead, especially in river bends, to unacceptable inaccuracies. Here the geometry of the river must be taken into account. A solution would be to perform the interpolation on a natural coordinate system somehow attached to the river. Unfortunately, the river geometry is not uniquely defined. In general a proper description of the river

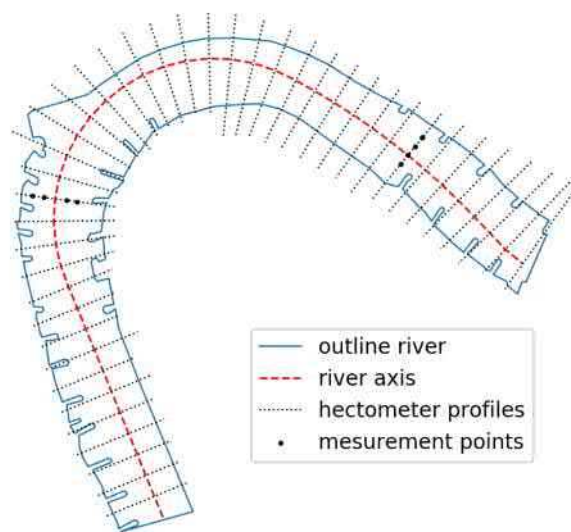


Figure 1: Schematic presentation of the river axis, the hectometer profiles and the location of measurement points.

geometry must cover the longitudinal direction as well as the perpendicular one. The interpolation used for this study is based on the river axis to describe the longitudinal direction and the hectometre profiles for the perpendicular one (Figure 1). Both are common location elements in the field of waterway engineering. On this defined natural coordinate system a linear interpolation is performed between the measurement points. Model domain on the outer perpendicular edge of the outermost measurements is consistently extrapolated from the outermost points, yielding the grain size distribution directly from the closest relevant outermost point. A more detailed explanation of the interpolation method can be found in [3].

The spatial interpolation takes into account the measurements location and optimally transfers the information content of each measurement into the initial sediment condition. A drawback of spatial interpolation is its vulnerability to incorrect measurements and outliers. Therefore it is important to check the measured data carefully before performing any interpolation.

## III. NUMERICAL MODEL AND INPUT DATA

### A. Model Settings

The numerical investigations use a bedload transport model based on TELEMAC-2D and SISYPHE version v7p2r0. The model domain covers an 11 kilometres long stretch of the lower Rhine River (Rhine-km 738.5 – 749.5) near Düsseldorf, Germany (Figure 2). The model uses five layers to discretize the vertical structure of the subsurface. The simulated time period is 6.5 years, starting on 01.01.2000 and ending on 22.06.2006. The upstream hydraulic boundary condition is obtained using the gauge at Düsseldorf (Rhine-km 744.2) and the downstream boundary is defined by the relation between water level and discharge.

The sediment boundary condition is set as an equilibrium boundary condition. The model distinguishes two areas, erodible and non-erodible. The erodible area (Figure 2) covers the river bed, including the groyne fields. Only the erodible area is generated in the initial sediment condition. In the non-erodible area, sediment deposition is possible. This deposition can be eroded later, but no erosion additional beneath the initial bottom elevation can occur.

For this study the bedload transport model of Meyer-Peter and Müller is used with a MPM coefficient of 5 and a morphological factor of 4. In addition the Hiding and Exposure approach of Karim, Holly and Jang is applied with the secondary currents correction provided by SISYPHE. The layer model of Hirano-Ribberink is used for modelling the subsurface. The porosity is assumed to be constant within the simulation and is set to 18 percent. Within the hydrodynamic simulation the Multidimensional Upwind Residual Distribution N-Scheme is used for discretizing the advection term. The bottom friction is calculated with the friction law after Nikuradse. Further information about the chosen approaches can be found in the manuals of TELEMAC-2D [4] and SYSYPHE [5]. The settings proved to be reasonable in preceding studies.

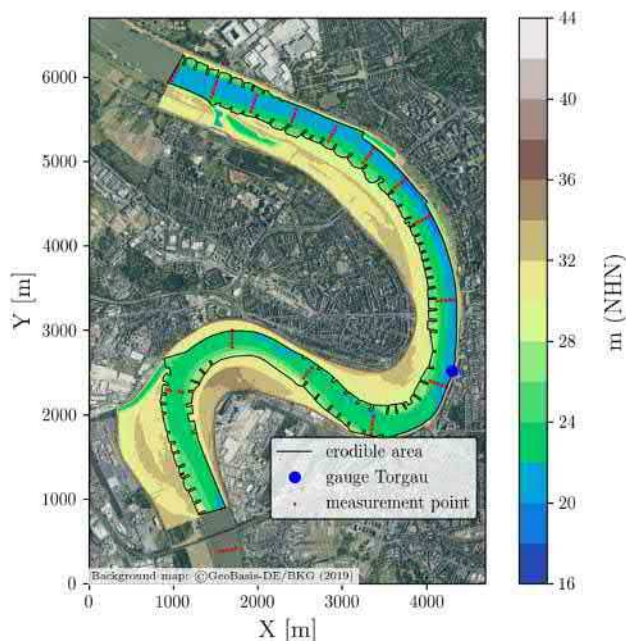


Figure 2: Model domain with topography, erodible area, the gauge location and measurement points of the cutting samples.

#### B. Input Data Initial Sediment Condition

Overall there are three measurement campaigns available within the model domain, which have recorded the grain size distribution of the river bed material. The first was

conducted in 1983, the second in 1995 and most recently in 2011/2012. Unfortunately none of these campaigns matches the simulated time period. With 73 measurement points the campaign from 2011/2012 is the most extensive and therefore is used as the basis data for the initial sediment conditions. Figure 2 shows the location of the measurement points. At each location two surface grab samples are taken, to cover the vertical variation of the sediment composition. The sieving of the samples yields their corresponding grain size distributions.

### IV. RESULTS AND DISCUSSION

#### A. Initial Sediment Condition

Based on the methods explained in Section II two different initial sediment conditions are generated. These initial sediment conditions provide a grain size distribution at each calculation node, for each layer. The pre-simulation changes the grain size distribution only in the two topmost layers. Therefore in layers three to five a homogeneous mean grain size distribution is defined. In case of spatial interpolation for layers three to five the same interpolated distribution is used as in the second layer, as there is only measured data from the two topmost layers available.

In Figure 3 and Figure 4 the spatial distribution of the mean grain diameter is displayed for the two initial sediment conditions. The mean grain diameter is a basic characteristic describing the sediment composition. Figure 3 and Figure 4 are cropped images of the first river bend within the domain in order to better show discussed phenomena. Nevertheless all observations made within this bend are also valid for the rest of the model domain.

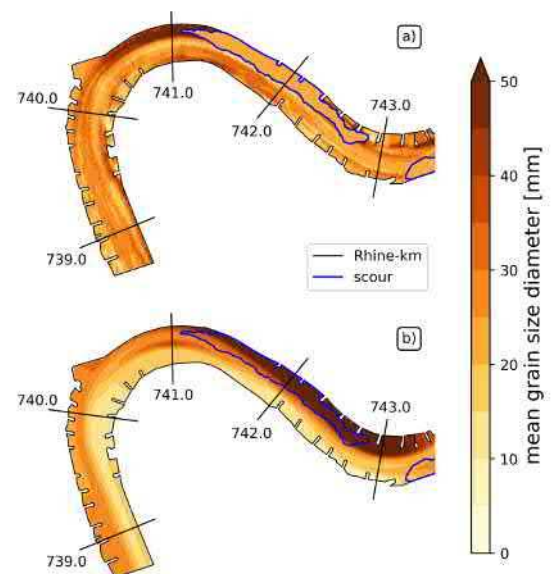


Figure 3: Initial sediment condition for the first layer, generated with a) the pre-simulation and b) the spatial interpolation

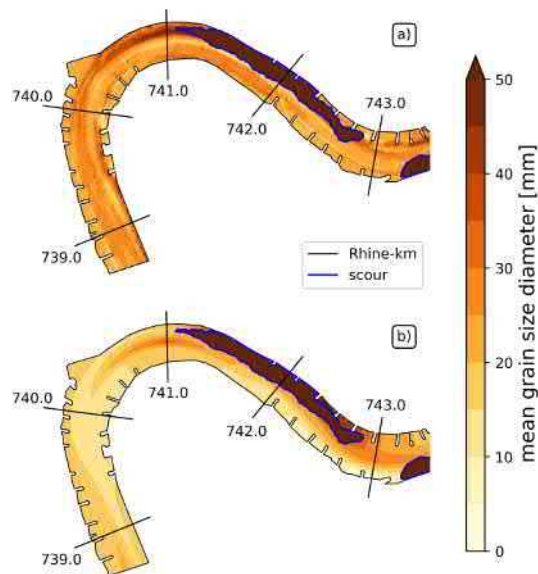


Figure 4: Initial sediment condition for the second layer, generated with a) the pre-simulation and b) the spatial interpolation

First consider Figure 3 which shows the initial sediment conditions for the first layer. Plot a) is generated by a pre-simulation and shows significant spatial variety. Only within the scour area is a constant mean grain size diameter noticeable. This shows one drawback of the pre-simulation. At the beginning of the pre-simulation this scour is covered by a layer of sediment with a thickness of a few decimetres. During the pre-simulation the covering is eroded, so that no information about the sediment composition in the scour area can be gained. Therefore the main grain size distribution in these areas is not only used as initial sediment condition for the pre-simulation, but also for the main simulation.

To prove if the spatial variety observed in plot a) corresponds with the measured data, we compare Figure 3 plot a) with plot b). This shows that the pre-simulation can't reproduce some basic phenomena, which are recognisable in the interpolated measured data, represented by plot b). For example the sorting of material within the bend, fine material in the inner side of the bend to the coarse material on the outer edge, is not properly reproduced by the pre-simulation. In addition the initial sediment condition generated by the pre-simulation shows a very strong coarsening at Rhine-km 741 in the outer edge. This coarsening is not visible in the interpolated data. During the pre-simulation a large amount of erosion takes place causing an overall coarsening of material at this location which cannot be backed by the measured data. So, one has to conclude, that the aim of the pre-simulation to resemble a

natural spatial distribution of the sediment composition is only reached to a limited degree. From this information one can conclude that the pre-simulation, where the goal is to generate a natural spatial distribution, has apparent limitations.

One major disadvantage to the second method, spatial interpolation, is the extrapolation of the most outer measurement points which leads, potentially, to unrealistic grain size distributions in the groyne fields. For example between Rhine-km 742 and 743 a larger mean grain size diameter leads to armouring, which is realistic in the main channel, but not within groyne fields. Thus, in absence of measurement points within groyne fields, the spatial interpolation leads to non-physical phenomena in the model, i.e. armouring in groyne fields. Additional measurement points in the relevant areas could solve this problem. An alternative is to make assumptions about the expected grain size distribution in the groyne fields and provide this information by fictitious measurement points to the interpolation.

Figure 4 shows the mean grain size diameters of the second layer. It is significant, that the mean grain size diameters of the interpolated initial sediment condition are much smaller than the mean grain size diameters of the initial sediment condition generated by the pre-simulation. This shows that the performed pre-simulation is not capable of properly reproducing the vertical distribution of the river bed material. The dark areas in Figure 4 represent the coarse material of the scours.

Table 1 emphasizes the primary problem of the pre-simulation method to reproduce the vertical structure of the river bed. Here the coarsening tendency is visible. This coarsening tendency is a general and well known problem, which can occur when using the bed layer model of Hirano-Ribberink and is not, in particular, a problem of the pre-simulation [1]. But it does point to the general problem. The pre-simulation amplifies issues and uncertainties from the numerical model by also embossing them to the initial sediment condition.

Table 1: Mean grain size diameter, averaged over the erodable area without the scours and the averaged grain size diameter of the measurements

Averaged mean grain size diameter	Initial sediment condition generated with		Measurements
	Pre-simulation	Spatial interpolation	
Layer 1	26.7 mm	22.8 mm	25.7 mm
Layer 2	25.0 mm	17.7 mm	21.1 mm



### B. Numerical Bedload Transport Model

The numerical bedload transport model is calibrated for the initial sediment condition generated by the pre-simulation. There is no de novo recalibration performed for the simulation with the initial sediment condition generated by the spatial interpolation. Thus it is ensured that the differences in the simulation results are solely caused by the differences in the initial sediment condition.

The differences between the initial sediment conditions discussed in the last section lead to significant differences in the bed level changes. That holds true for local bed level changes (Figure 5) as well as for the erosion rate (Figure 6). Comparing plot a) and b) of Figure 5 it shows, that the areas with sediment deposition correspond well, whereas the erosions differ significantly. The results of the numerical bedload transport simulations are highly sensitive in regard to the initial sediment condition. It appears that the initial sediment condition with finer bed material, generated by the spatial interpolation, increases the erosions significantly. The comparison of measured erosion rates to the simulated erosion rates (Figure 6) shows that the initial sediment condition based on the pre-simulation yields a good accordance. The variant based on spatial interpolation shows clear deviation from the measured erosion rate during the first four years. A de novo calibration could reduce this deviation, but between 2004 and 2006 the simulated erosion rate corresponds well to the measured one. Therefore it seems probable that the erosion at the beginning of the simulation is at least partially caused by initial effects of the model. These initial effects fail to appear for the variant with

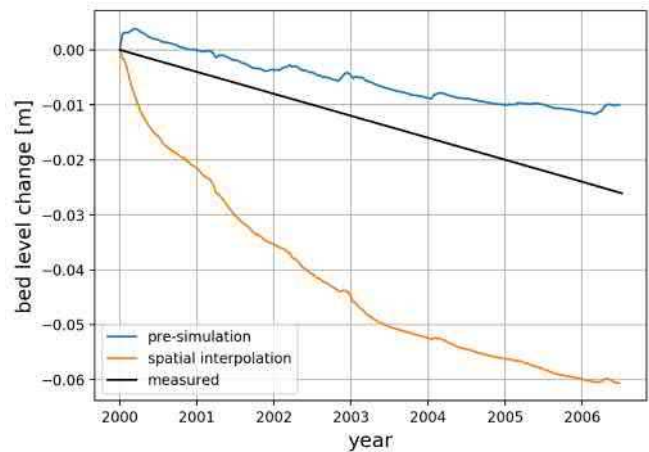


Figure 5: Erosion rates, calculated as bed level changes, averaged over the erodible area. The measured erosion rate is documented in [6]

pre-simulation, because they have already occurred during the pre-simulation.

The annual bedload discharges are not as sensitive to the initial sediment condition as the bed level changes (Figure 7). Both variants are able to reproduce the estimated annual bedload discharges in a proper way. It is noticeable, that the variant based on spatial interpolation, in this study, hits the estimation very well. The estimation is based on the relation of the discharge to the bedload discharge and the hydrographs for the considered period. The relation of the discharge to the bedload discharge is derived from the bed load transport measurements, which are taken regularly at Rhine-km 749.

### V. CONCLUSION

This study compares two different methods to generate the initial sediment condition for numerical bedload transport simulations. The first one is based on a pre-simulation and the second one on a spatial interpolation. Both methods use sediment composition measurements to generate a data set, which provides information about the grain size distribution at each calculation node of the model domain and defines therefore the initial sediment condition.

It appears that the two approaches lead to significant differences in the initial sediment conditions. Taking the measurements as a best guess of the natural sediment composition we have, it becomes clear that the pre-simulation can only roughly resemble the natural composition of the river bed. Some basic phenomena such as the sorting of bed material over the cross section within river bends cannot be reproduced properly by the pre-simulation. The interpolation method yields good results in areas with a sufficient number of measurement points. In areas with sparse measurement points the interpolation method is also limited to only a rough representation of the real conditions.

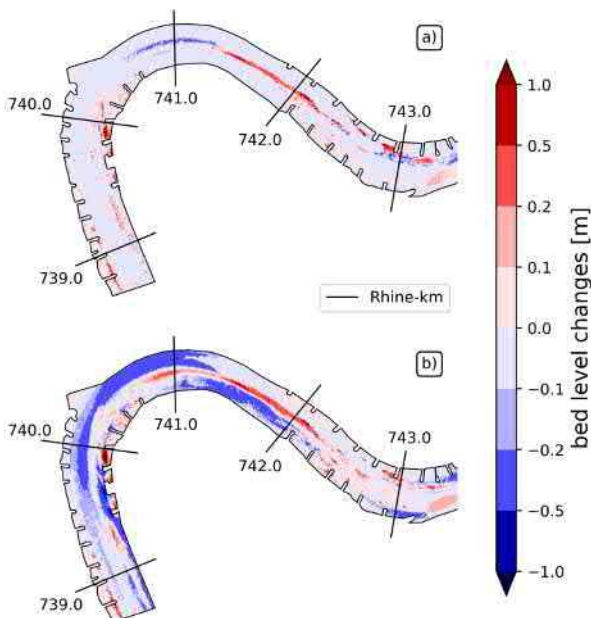


Figure 6: Bed level changes after 6.5 years.

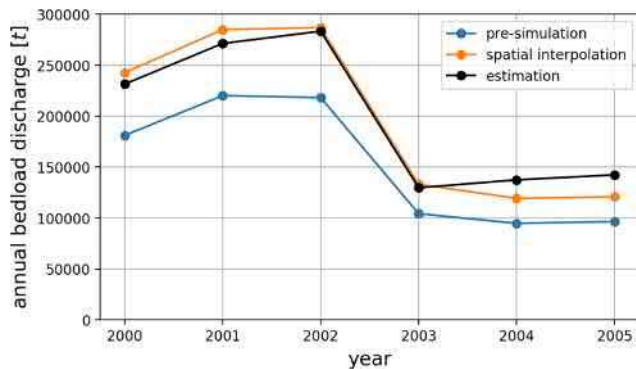


Figure 7: Annual bedload discharge. The estimation is based on [6]

The differences in the initial sediment condition cause significant differences in the results of the numerical simulations. That applies especially for bed level changes and to a lesser extent also for the bedload discharges. The resulting high sensitivity of the numerical model with regard to the initial sediment condition shows the importance of a conscientious generation of the initial sediment condition.

Another disadvantage of the pre-simulation is, that it intensifies the weaknesses of numerical model by embossing them into the initial sediment condition. Especially for a long term pre-simulation, as is used for this study, this becomes a serious problem. The simulation based on a spatially interpolated initial condition has overestimated the initial erosion clearly, probably due to initial effects. Therefore it seems reasonable to use a combination of both methods. First, an initial sediment condition should be generated by a spatial interpolation, which is ideally as close as possible to the measured data. Second, a short pre-simulation should be conducted using the interpolated initial sediment condition. This approach could decrease the initial effects, without getting the disadvantages of a long pre-simulation. Therefore it seems worth to test such a combined approach in a further reaching study. The effort of such a combined method, in terms of computation time, would be more than a pure interpolation, but still less than a long pre-simulation.

In addition, a more sophisticated interpolation algorithm could be applied e.g. Kriging [7] to improve spatial interpolation itself.

#### ACKNOWLEDGEMENT

This study results from the author's master thesis, which was supported by the Federal Waterways Engineering and Research Institute. The author's particular thanks go to his thesis supervisors for their support and advice.

#### REFERENCES

- [1] B. Bleyel, R. Kopmann, „Influence of the layer model on a 2D sediment transport model: Hirano-Ribberink versus C-VSM“, Proc.

of the 25th TELEMAC-MASCARET User Conference 2018, <https://hdl.handle.net/20.500.11970/105196>

- [2] L. Backhaus, T. Brudy-Zippelius and T. Wenka, “Comparison of morphological predictions in the Lower Rhine River by means of a 2-D and 3-D model and in situ measurements”, Proc. River Flow 2014, International Conference on Fluvial Hydraulics, Lausanne
- [3] M. Utz, “Einfluss der sedimentologischen Anfangsbedingung auf die numerische Modellierung des Feststofftransports” master thesis, 2018
- [4] TELEMAC-2D v7.0 User's Manual, 2014
- [5] SISYPHE v6.3 User's Manual, 2014
- [6] WSA Duisburg-Rhein, “Statusbericht Niederrhein – Erfolgskontrolle des Geschiebemanagements am Rheinstrom” Heft 1, 2008
- [7] J. P. Chiles, P. Delfiner: Geostatistics: Modeling Spatial Uncertainty. Wiley, New York 1999, ISBN 0-471-08315-1.

# Application of TELEMAC2D for water levels assessment in the Laita estuary, France

Nicolas Chini<sup>1</sup>, Pierre Timmerman<sup>2</sup>, Roger Delmas<sup>1</sup>

<sup>1</sup> ACRI-IN, Le Grand Large, Quai de la Douane, 29200 Brest, FR

<sup>2</sup> SMEIL, 1 rue Andreï Sakharov - CS 20245 - 29 394 Quimperlé cedex, FR

nicolas.chini@acri-in.fr

## Abstract:

Laita estuary is located along the Southern coast of Brittany, France. The estuary is 20km long, extending from the confluence of two tributaries, rivers Ellé and Isole, to its mouth where a complex sandbanks system lies. The watershed for the rivers covers about 885 km<sup>2</sup> (Berthou, 1964). The general morphology of Laita is common for a Breton estuary. It is characterised by a narrow and relatively shallow valley whose depth is underneath the high tide water level, allowing sea water to flow up to the confluence, where the lower part of the town Quimperlé sits.

The combination of spring tides, storm surge, and small flood event can lead to the inundation of the town. The events that happened during 2013-2014 winter led to several damages and the local community has decided to investigate a large range of options for estuary management to mitigate the effects of flooding. To help the decisional procedure, a numerical model, based on TELEMAC2D, was developed and used to assess the benefit of considered management procedures (dredging, floodplain levelling, riverbank management, ...) under several environmental conditions.

The constructed model was developed in order to take into account the complex geometry of the estuary mouth where the flow reversal is not concomitant with the tidal stage. The computational domain also includes the presence of large flood plains and bridge piers. And the model is built on an accurate topo-bathymetric dataset.

To reproduce accurately the water levels and currents along the maritime boundary, data from MARC database (formerly Previmer) are considered. The boundary conditions routine BORD.F is adapted to read the binary files, according to the procedure presented by Stansby et al (2013). The data are bilinearly interpolated in space for each boundary node and then linearly interpolated in time at each computational time step. That procedure is then compared to several tidal gauges and depth-averaged currents estimated by an ADCP. The overall comparison is acceptable and results obtained by TELEMAC2D are compared with results from previous studies. It appears that the model is not only able to simulate accurately the high water level but it improves low water levels estimations.

The model is then applied to estimate some indicators in order to assess the benefit of estuary management plans. The water level and flood duration are considered as the main metrics for the benefit estimation. The model is currently used by the local community for water quality issues and has currently been adapted to include urbanised areas in order to estimate the influence of an historical bridge on flooding probability.

**Proposed session:** *River, estuaries, maritime, coastal sediment processes*

**Key words:** Estuary, flooding, boundary conditions

**Speaker:** Nicolas Chini

# Three-dimensional hydrodynamic modelling in a bay of the Lake Mälaren to assess environmental impacts from a cooling and heating power plant production

Pierre-Louis Ligier, Non Okumura  
Power Generation and Dams Department  
Sweco Energy AB  
Stockholm, Sweden  
[pierre-louis.ligier@sweco.se](mailto:pierre-louis.ligier@sweco.se)

**Abstract**— The power production company Norrenergi owns a power plant in Solna, Stockholm county, Sweden, to produce heating or cooling energy by exploiting intake water's temperature. In its current configuration, the power plant is connected to the network of the Bromma sewage treatment plant, located in the northern part of Stockholm and uses this water for production. The planned commissioning of a new sewage treatment plant in Henriksdal in the southern part of the city, thought to replace the Bromma sewage treatment plant, will lead the current sewage network used by Norrenergi's power plant to be decommissioned. In order to maintain water supply for its power plant, Norrenergi is now seeking environmental permit to use water from the Bällstaviken bay in Solna where the old intake and outlet structures exist. This article presents the hydrodynamical modelling performed as part of the environmental permit application. The work has focused on describing the thermal dispersion conditions for an extreme energy demand in the summer (cooling production), where the released water temperature is increased between 5.5 and 10.0 °C during a daily cycle. Hydrodynamic modelling has been performed with the software TELEMAC-3D version 7.3. The first part of the modelling work has been to perform flow measurements in order to calibrate the model with respect to currents. Some preliminary dispersion tests showed that in their current configuration, the current intake and outlet structures, both located in the Bällstaviken bay, do not offer optimal production capacity due to a very high risk for a temperature shortcut. To mitigate this risk, a new location for the inlet has been investigated. A location in the adjacent Ulvsundasjön bay has been chosen which offers the possibility to take water from a greater depth with a cooler temperature especially during summer months, making it possible to reduce the relative temperature difference between the intake and outlet depths, hence lowering the environmental impacts. The thermal dispersion modelling has been performed for this intake configuration for several representative wind speeds and directions. The results show that the water temperature in the Bällstaviken bay is significantly increased due to its relatively small volume whereas impacts are, as expected, lower in the adjacent Ulvsundasjön bay which has a greater volume. The results also show a clear influence of wind direction on thermal dispersion conditions. The environmental risk assessment shows that the planned production is not expected to significantly alter

the flora and fauna in the study area mainly due its current low ecological status.

## I. INTRODUCTION

The power production company Norrenergi owns a power plant in Solna, Stockholm county, Sweden, to produce heating or cooling energy by exploiting intake water's temperature. To be able to continue its production, the power plant needs to use new source of water and is now seeking environmental permit to use water from the Bällstaviken bay in Solna where old intake and outlet structures exist. In the first section, an overview of the study area and of the power plant characteristics are presented. In the second section, the three-dimensional hydrodynamic model developed for the study is detailed. The article then focuses on the model calibration based on field measurements and the identification of key model parameters that have been used in all the simulations. Finally, a quick overview of the design thermal dispersion simulations is given with the related environmental impacts.

## II. PRESENTATION OF THE STUDY AREA

### A. Location and environment

The work presented in this paper concerns flow simulations in the bays of Bällstaviken and Ulvsundasjön located in the western part of the city of Stockholm, Sweden (see Fig. 1). Those two bays are part of the Lake Mälaren that flows into the Baltic Sea at several outlet points, the main one being around the Old Town island in the centre of Stockholm. The two bays receive water from a natural catchment drained by the Bällstaå River (38.9 km<sup>2</sup> with a mean annual discharge of approx. 0.3 m<sup>3</sup>/s) and from relatively small urban catchments. Bällstaviken is the smallest bay characterized by a water depth between 2 and 6 m whereas Ulvsundasjön covers a larger area and is significantly deeper (up to 15 m). Ulvsundasjön is connected to other bays in the eastern part of Lake Mälaren via two passages, the main one being located in the southern part of the study area. Environmental studies have characterized Bällstaviken and Ulvsundasjön bays' ecological status as low due to the presence of polluted sediments in harbours and the lack of important species (fauna and flora).





Figure 1: Location of the study area with a regional map (top) and the location of the Bällstaviken and Ulvsundasjön bays in the center of Stockholm (bottom). Bays are located inside the red polygons.

### B. Stratification

The bays of Bällstaviken and Ulvsundasjön present a stratification due to temperature gradients during the summer season (June to September). The stratification is more clearly marked in Ulvsundasjön (Fig. 2) than in Bällstaviken due to the limited water depth of the latter bay. During the rest of the year, the temperature gradients are minimal and therefore stratification is limited and is considered as negligible.

### C. Power plant

In its actual configuration, the power plant is taking water from the Bromma sewage treatment plant and releasing it into the Baltic Sea via a tunnel network. As the Bromma plant will be decommissioned, Norrenergi is willing to use water from the bays of Bällstaviken and Ulvsundasjön for energy production. This alternative is motivated by the existing old intake and outlet structures, located in the Bällstaviken bay, and could be reused without undertaking major refurbishment works.

Norrenergi is planning to increase energy production capacity for the plant with a maximal capacity of 105 MW. As

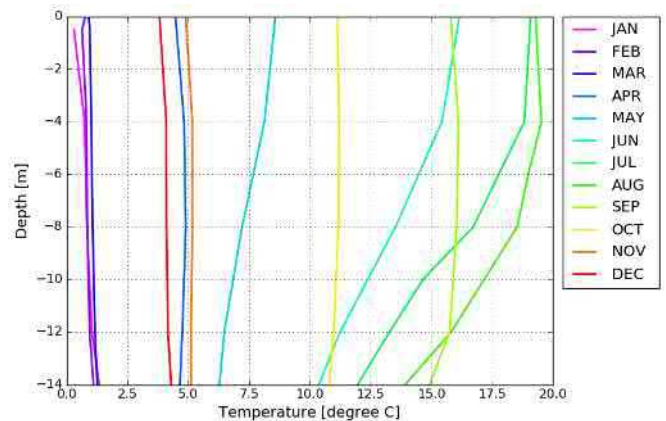


Figure 2: Monthly average of water temperature in Ulvsundasjön bay.

environmental impacts during the winter period (heating production, release of cooled water) are negligible, the project has been focused on assessing the expected thermal status of the bays during the summer period (cooling production, release of heated water) for a predefined design production sequence characterized by a constant water discharge (inflow and outflow) of  $2.5 \text{ m}^3/\text{s}$  and by a temperature increase in the outflow varying between  $+5.5$  and  $+10.0 \text{ }^\circ\text{C}$ , depending on the time of the day, compared to the reference water temperature at the intake. This design sequence has a duration of one week and is illustrated on Fig. 3.

The first dispersion simulations performed with the existing intake and outlet showed that the configuration of those structures was not appropriated for summer production as the intake is located too close to and higher than the outlet, pumping high amount of heated, less dense, water and hence dramatically reducing production capacity. It has then been decided to relocate the intake to a deeper part of the system. The point chosen is located approximately 1 km east of the outlet, in a region where the water depth is approximately 13 m, i.e. 9 m below the outlet level (see Fig. 4). This new location offers a natural advantage during the summer period when a strong temperature gradient is present between the

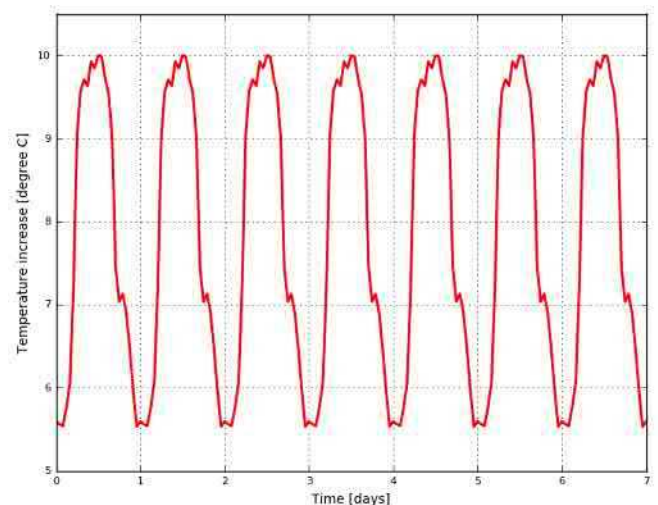


Figure 3: Design production sequence for outfall of heated water. Constant discharge of  $2.5 \text{ m}^3/\text{s}$ .

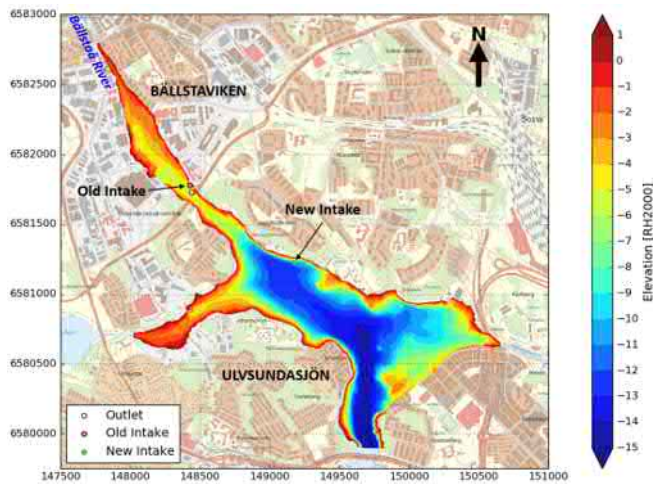


Figure 4: Model domain and bathymetry, location of the intakes and outlet structures. Coordinates for all maps are expressed in SWEREF 99 1800 (m).

water surface and the bottom, thus making it possible to reduce the environmental impacts with regards to the release of heated water and its dispersion near the water surface.

### III. PRESENTATION OF THE TELEMAC-3D MODEL

#### A. Model domain and bathymetry

The model domain covers the bays of Bällstaviken and Ulvsundsjön in their entirety over a surface of approx. 1.4 km<sup>2</sup>, see Fig. 4. A multibeam scanning from a recent bathymetrical survey was used to define bottom levels within the model.

#### B. Computational mesh

The computational domain is composed of a two-dimensional horizontal unstructured triangular mesh that has been duplicated 22 times along the vertical at fixed elevations to create a three-dimensional mesh. The lowest plane describes the bathymetry and the highest plane corresponds to the computed water surface. The two-dimensional horizontal mesh was created with BlueKenue and contains approx. 124,000 elements while the three-dimensional mesh contains approx. 2,600,000 elements. The mesh size in the horizontal plane is of approximately 5 m in the whole domain. The distance between the vertical planes is varying from 0.1 m at the free surface, 0.5 m down to 7 m deep, 1.0 m down to 10 m deep and 2.0 m below this level.

#### C. Initial and boundary conditions

A water temperature profile corresponding to the July month (see Fig. 2) has been defined as initial conditions. The water temperature at the free surface is 19.0 °C.

The hydrodynamic model has three open boundaries. In the Bällstaviken bay, an inflow boundary has been applied to model the inflows from the Bällstaå River. Prescribed discharges correspond to monthly average flow rates. In the Ulvsundsjön bay, two water level boundaries have been defined where the bay is connected to other parts of the Lake Mälaren. The prescribed water level at those boundaries corresponds to the mean (and regulated) water level for Lake Mälaren, +0.86 m in height reference system RH2000.

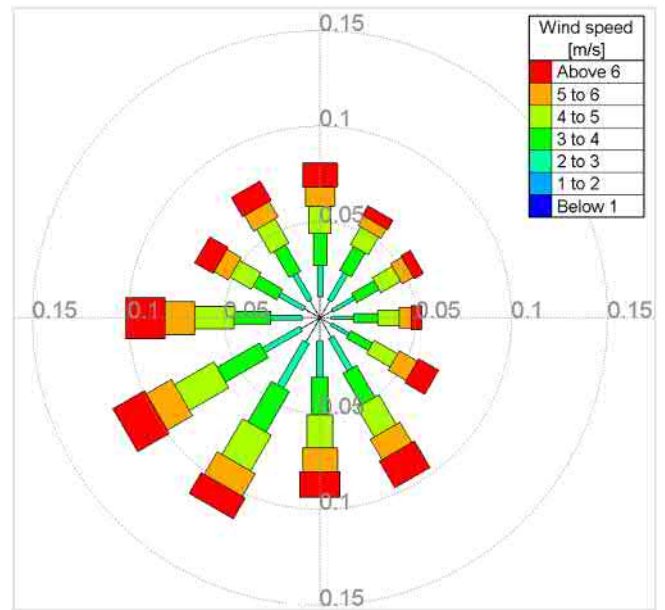


Figure 5: Wind rose from Bromma airport, period April to September.

Wind has been applied as a boundary condition at the water surface based on mean wind speeds for several representative wind directions. Mean wind speeds are of approximately 4 m/s according to the wind rose from the station of Bromma airport (time-series with 80 years of data) located less than one kilometre away from the model area, see Fig. 5.

Inflow and outflow to and from the power plant has been modelled with sink/source points using a constant flow rate of 2.5 m<sup>3</sup>/s. The intake has been conservatively placed at a depth of 7 m, to ensure that the reference intake temperature was not underestimated (important regarding environmental impacts). The outlet has been modelled with two source points as the structure ends with a box with two lateral openings in order to dissipate energy and increase mixing. Hence, the source points were defined without momentum. Water temperature at the outlet has been prescribed according to the design sequence presented in Fig. 3. The actual water temperature at outlet has been defined between 22.8 and 27.3 °C (i.e. between 5.5 and 10.0 °C warmer than the water temperature at intake depth, 17.3 °C, for an average July month).

#### D. Numerical settings

Water temperature has been defined as an active tracer to take buoyancy effects into account, and water density being computed as a function of water temperature using Eq. 1 [1,2].

$$\rho = \rho_{ref} \left[ 1 - 10^{-6} \cdot T(T - T_{ref})^2 \right] \quad (1)$$

Where  $\rho$  is the water density [kg/m<sup>3</sup>],  $\rho_{ref}$  is the reference water density at  $T_{ref} = 4$  °C (999.972 kg/m<sup>3</sup>) and  $T$  is the actual water temperature [°C].

Bottom friction was modelled using Nikuradse formulation with an equivalent sand roughness coefficient of  $k_s = 0.02$  m.

The hydrodynamic model has been run with TELEMAC-3D (version 7.3) in non-hydrostatic mode with a time-step of



5 seconds. Turbulence has been modelled with the  $k-\epsilon$  model in the horizontal plane and with Tsanis' mixing length model in the vertical direction (see section Calibration for more details). The advection scheme chosen for velocities,  $k-\epsilon$  and tracers is the explicit MURD scheme without tidal flats treatment. The model has been run on the Beskow computer at the PDC Center for High Performance Computing at the KTH Royal Institute of Technology, Stockholm.

#### E. Limitations

The hydrodynamic model has not been coupled with the atmospheric processes available in the WAQTEL module due to the lack of calibration data. One of the consequences is that the stratification profile could not be kept over long simulation periods, which would make the interpretation of the model results challenging with respect to the water temperature increase during the release period. It can be noted that tests were performed with the more computationally expensive MURD 2<sup>nd</sup> order and LIPS advection schemes. Although allowing a reduction of the numerical diffusion, the stratification was still altered during the simulation. To avoid having this issue, the model was run with a uniform initial water temperature equal to the surface temperature (19.0 °C). Tests showed that this simplification has minor incidence on the dispersion conditions as the water density difference between released water and ambient water at outlet depth is approximatively 10 times greater than the water density difference between intake and outlet depths.

Another consequence is that the energy exchanges between the water system and the atmosphere are not taken into account (solar radiation during day time, evapotranspiration and convection during night time). The energy gained through solar radiation is independent of the actual water temperature (i.e. identical during or outside release periods) whereas the energy loss through evapotranspiration and convection is function of the temperature difference between water and atmosphere (i.e. greater energy loss during periods with release of heated water). Hence, not taking into account those processes can be considered conservative regarding thermal dispersion as the temperature cooling occurring during night time is discarded.

### IV. CALIBRATION

#### A. Field measurements

Field measurements have been performed within the study area in order to acquire calibration data for the hydrodynamic model. Field measurements consisted of:

- Current velocity and direction as well as water temperature between bottom and water surface at one point.
- Wind velocity and direction as well as other meteorological parameters (air temperature, atmospheric pressure, precipitation) and water level variations at one point.

Measurements covered a period of one month and 10 days, between 2018-09-20 and 2018-10-31. Current measurements have been performed with an Acoustic Doppler Current

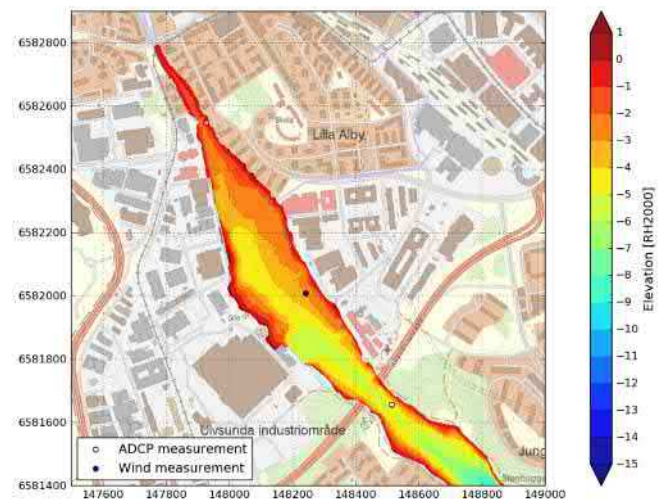


Figure 6: Location of field measurements.

Profiler (RDI/Teledyne Sentinel Workhorse 600 kHz ADCP). Due to budget constraints, only one ADCP has been used. It was then chosen to place the equipment at a relevant location regarding current circulation within the study area. As the volume of the Bällstaviken bay is small, water exchanges with the Ulvsundasjön bay should be modelled in a correct way in order to ensure a correct modelling of the water system and associated environmental impacts. The ADCP has then been located in the sound between the two bays in a location where the water depth was approximatively 5.5 m (see Fig. 6). The flow data consist of time-averaged values over a 15-minute period in eight 0.5 m-high measurement cells located between the bottom and the water surface. The standard deviation regarding this measurement set-up was of 0.0144 m/s. This value, quite large compared with the expected current velocities, was the result of a compromise between the number of cells and their size in the vertical direction due to the relatively small water depth at this location.

The weather station used for wind speed and direction and meteorological parameters was, for practical reasons, located on a pier owned by Norrenergi in Bällstaviken bay, approximatively 450 m northwest of the ADCP location (see Fig. 6). The measured wind speeds have been corrected from a height above ground in order to obtain values at a 10 m height reference using a classical logarithmic profile.

Water temperature measurements showed only small differences in the vertical direction, which was an expected result being given the period during which the measurements were performed (see Fig. 2). Consequently, no temperature stratification was defined in the hydrodynamic model for the calibration step. Water level measurements have been used as boundary conditions for the two southern open boundaries. Inflow rates from the Bällstaå River were not available. The model was run assuming an average monthly discharge for October of 0.256 m<sup>3</sup>/s.

#### B. Calibration case

The model calibration has been performed over a duration of seven days taken from the global measurement period. The period chosen, 2018-10-07 to 2018-10-14, shows mainly W-

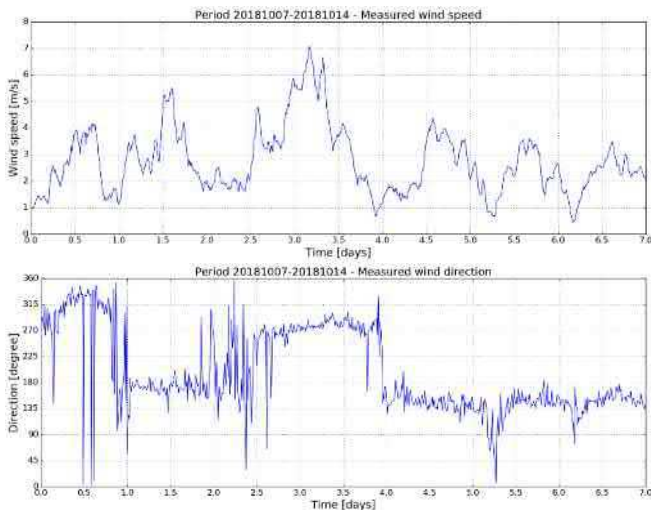


Figure 7: Measured wind speed (top) and direction (bottom) for the calibration period.

NW and SE-S winds with speeds ranging from 1 to 7 m/s. Wind directions correspond to those having the largest impact on dispersion conditions within the study area (see Fig. 7).

The initial model set-up consisted of the following features:

- Mesh size in horizontal direction: approx. 5 m.
- Vertical mesh spacing below water surface: 0.2 m.
- Turbulence model in horizontal and vertical directions: k-ε.
- Time-step: 5 s.
- Non-hydrostatic version.
- MURD scheme without tidal flats.

The mesh size in the horizontal direction and time-step were defined after preliminary tests through an iterative process in order to remove instabilities. These parameters as well as the MURD scheme and TELEMAC-3D's non-hydrostatic version have been used in all calibration runs.

The first results using the set-up described above showed very large differences with the flow measurements, with the highest simulated surface currents of about 0.05 m/s while 0.30 to 0.45 m/s was measured, as well as some discrepancy regarding current direction. The two main reasons to explain these differences are:

- Topographical effects acting on local wind speed and direction.
- Turbulence model in the vertical direction.

Experience on local wind climate indicates that NW and SE winds are concentrated below the bridge in the sound, creating a wind acceleration and a deviation of its direction. Unfortunately, this effect is not accounted for in the measurements as the weather station was placed at an undisturbed location. The large influence of this topographical effect could be estimated by comparing expected surface

currents for the maximal measured wind speeds based on Wu [3] cited in TELEMAC-3D's validation manual [4] in which surface current can be estimated with Eq. 2.

$$U_s = 0.55\sqrt{\tau_w/\rho_{air}} \quad (2)$$

Where  $U_s$  is the surface wind-generated current [m/s],  $\tau_w$  is the wind shear applied to the free surface [Pa] and  $\rho_{air}$  is the air density (typically 1.23 kg/m<sup>3</sup> at 15 °C). The wind shear  $\tau_w$  can be calculated according to the methods provided in [1]. Fig. 8 illustrates how the surface currents  $U_s$  varies with respect to wind speed. Surface currents in the range of 0.30 to 0.45 m/s are expected to be generated by wind speeds ranging between approximately 13 to 17 m/s, which are significantly larger than the measured undisturbed wind speeds during the calibration period (3-7 m/s).

In order to account for this topographical effect, a spatially varying correcting factor has been applied on both wind speed and direction by altering the subroutine `meteo.f`. The

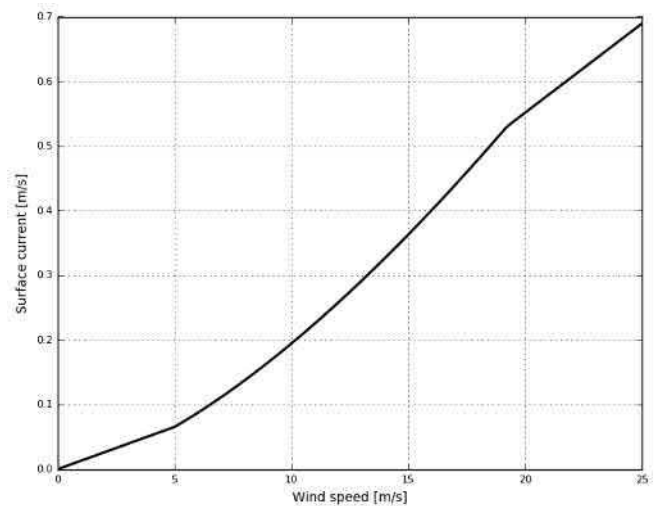


Figure 8: Estimated surface current as function of wind speed (Eq. 2).

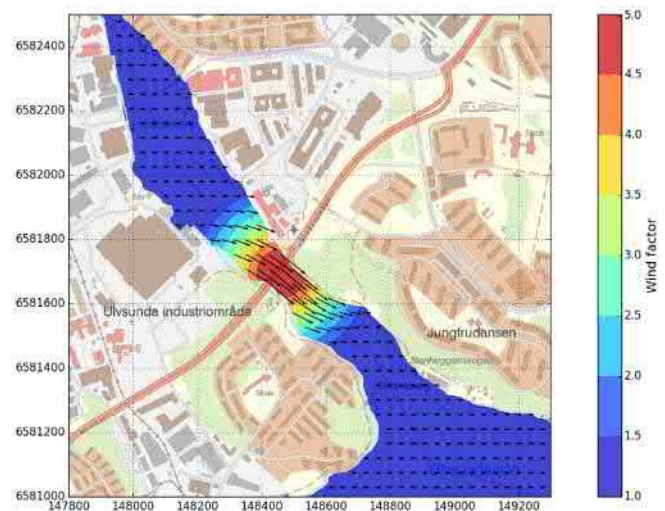


Figure 9: Wind correction factor on wind speed and wind direction. Example for a westerly (270°) wind.



correcting factor is applied to winds from sectors W-NW-N and E-SE-S, i.e. winds converging into the sound. The correction factor is applied linearly on wind speeds and directions from about 300 m downstream/upstream of the sound's center as depicted on Fig. 9. Several wind factor values have been tested, best results were obtained for a value of 5 which seems reasonable compared with the simple comparison detailed above.

Results from a simulation performed with the initial set-up and with the wind correction factor showed an improvement but still lower simulated values compared to surface current measurements, see Fig. 10.

Changing the turbulence model in the vertical direction from  $k-\epsilon$  to Tسانيس' mixing length model together with a refinement over the vertical just below free surface (0.1 m as recommended in [4]) yielded a good agreement between

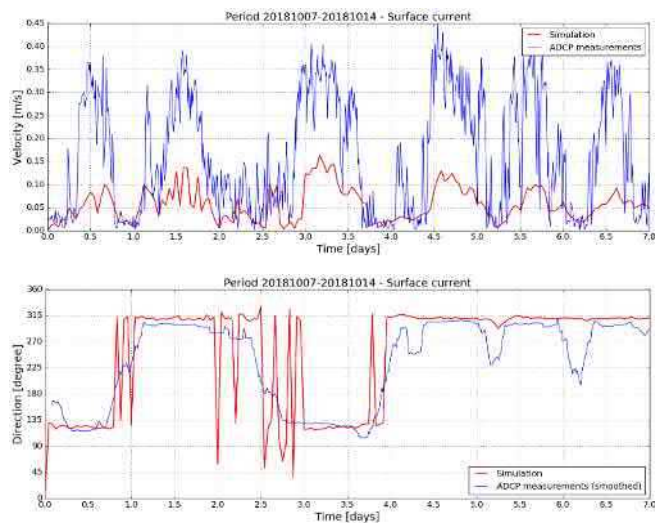


Figure 10: Calibration case, surface current velocity (top) and direction (bottom) with  $k-\epsilon$  turbulence model in all directions and with applied wind correction factor.

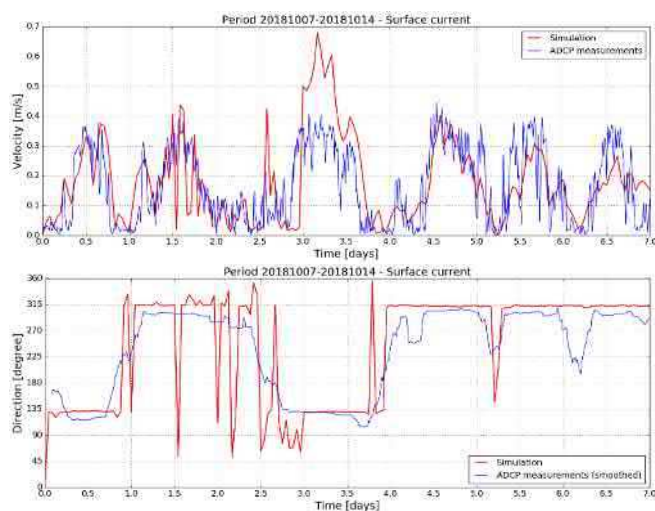


Figure 11: Calibration case, surface current velocity (top) and direction (bottom) with  $k-\epsilon$  turbulence model in horizontal direction, Tsanis' mixing length model in vertical direction, plane located 0.1 m below the water surface and with applied wind correction factor.

model results and field measurements, see Fig. 11. It can however be noted that the model overestimates the wind speed around day 3, where measured wind speeds were up to 7 m/s from SE. This difference can be due to the assumption of a linearly varying wind correction factor even for high wind speeds whereas the natural acceleration probably converges to a lower value above a given threshold speed. Surface current directions are also reproduced in a correct way. The rapid variations obtained from the model occur during periods when the wind directions are at the border of the considered range for the applied correction and should therefore be interpreted as artificial features without impact on the flow conditions for the design simulations. In Ulvsundsjön bay, i.e. outside of the sound where wind driven currents can develop over a sufficiently long fetch, the obtained surface currents are in good agreement with the estimated values based on Eq. 2.

The differences obtained on surface current velocities between  $k-\epsilon$  and Tsanis model are significant. With  $k-\epsilon$  and unlike classic mixing length models like Tsanis', the turbulent kinetic energy  $k$  at free surface, and indirectly the turbulent viscosity, is computed based on the local wind friction velocity [1]. Comparison between these two types of turbulence models on a simple channel test case with wind-driven currents shows very different viscosity patterns at the free surface, with higher viscosities and consequently lower velocities computed by  $k-\epsilon$  compared with Tsanis. The exact cause of these differences has not been investigated but the method used to compute  $k$ , together with the isotropy assumption and strong mesh distortion are likely to have an influence on those results.

Comparison between the model and the measurements between the bottom and free surface did not show a good agreement. Measured current velocities are ranging between approximately 0.01 and 0.04 m/s which means that the quality of the measurements is expected to be significantly affected by their precision (standard deviation of 0.0144 m/s). The results from the model are generally lower current

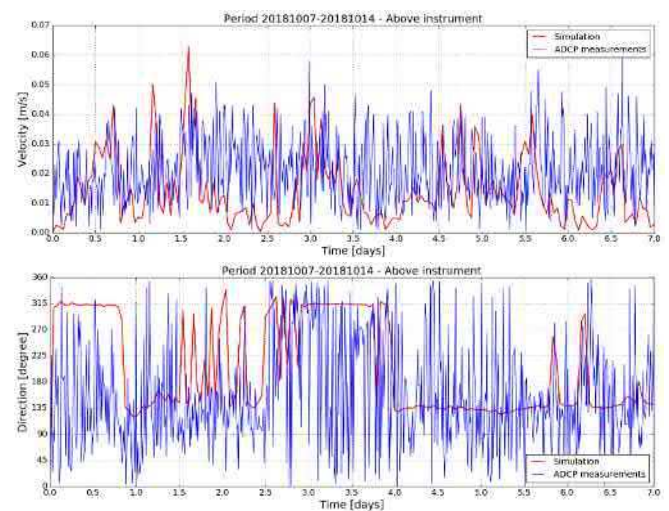


Figure 12: Calibration case, bottom current velocity (top) and direction (bottom) with  $k-\epsilon$  turbulence model in horizontal direction, Tsanis' mixing length model in vertical direction, plane located 0.1 m below the water surface and with applied wind correction factor.

velocities excepted during high wind speed periods and bottom current direction in opposite direction from the surface current, as expected, see Fig. 12.

Model calibration has however been considered satisfactory as it is essentially surface current conditions that are of relevance for the study of temperature dispersion. All design model runs have been performed with Tsanis' mixing length model in the vertical direction together with a plane located 0.1 m below the free surface.

### C. Validation case

The model validation has been performed over a duration of seven days between 2018-09-28 and 2018-10-05 taken from the global measurement period with mainly W-NW and SE-S winds with speeds ranging from 1 to 6 m/s, see Fig. 13. Due to the uncertainties on the current measurements between

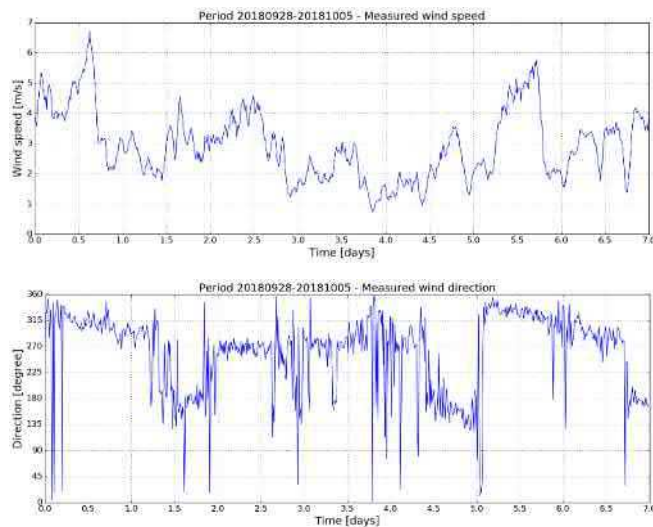


Figure 13: Measured wind speed (top) and direction (bottom) for the validation period.

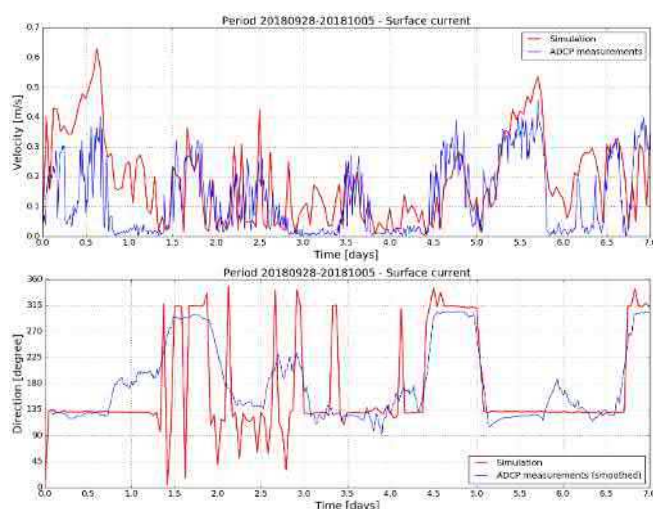


Figure 14: Validation case, surface current velocity (top) and direction (bottom) with  $k-\epsilon$  turbulence model in horizontal direction, Tsanis' mixing length model in vertical direction, plane located 0.1 m below the water surface and with applied wind correction factor.

bottom and free surface highlighted in the Calibration case section, only results regarding surface currents are considered.

The model has been run with similar set-up as for the calibration case. Comparison between the model results and the surface current measurements is presented in Fig. 14. Results from the model are in good agreement with the measurements and present similar features as the calibration case with an overestimation of surface current velocities when wind speed becomes larger than approximately 5 m/s and with abrupt current direction changes when undisturbed wind is oscillating around the limits of the direction range considered in the wind correction factor method. The hydrodynamic model is then considered to be validated with respect to surface currents and can be used safely for the range of wind speeds considered in the temperature dispersion study (average wind speeds of about 4 m/s).

## V. TEMPERATURE DISPERSION SIMULATIONS

### A. Overview of the simulated cases

Dispersion simulations have been performed for four scenarios with different wind directions. In three of these scenarios the wind direction and speed has been kept constant during the whole simulation period (seven days). The corresponding wind directions were the most frequent based on the wind rose from Bromma airport (NW, SE, SW), see Fig. 5, while the simulated wind speeds correspond to each sector's average value (3.5 to 4.1 m/s). The fourth scenario has been defined with a time-varying wind field decomposed into the four main directions (SW, NE, NW, SE) and applied during a similar seven-days period. The wind duration for each sector was based on its occurrence frequency according to the wind rose and using an average wind speed value of 3.8 m/s. The latter scenario features the most realistic dispersion conditions and therefore has been chosen to be described into detail in this article.

The results regarding surface temperature increase at the end of each period for a given wind direction are illustrated in Fig. 15. Temperature values are extracted at two points in the model, one which is representative for Ulvsundasjön bay and the other for Bällstaviken bay, and the results are shown as temperature increase relative to the initial temperature 19.0 °C, see Fig. 16.

As seen from the figures, Bällstaviken bay is affected by a clear increase in temperature of up to 2.5 °C during the first three days with wind from the SW and NE. During days 4 and 5, the temperature reduces by approximately 0.5 °C due to the wind from the NW which enhances the dispersion of the temperature plume towards Ulvsundasjön bay and the downstream boundary Lake Mälaren. Lastly, there is a significant increase in temperature of up to 2.8 °C in both Bällstaviken bay and the northern part of Ulvsundasjön bay with wind from the SW during days 5 to 7.

### B. Environmental impacts

In the Swedish environmental quality standards, it states that fish and mussels can be said to not be affected from a discharge of temperate water when the temperature increase is up to 3.0 °C or the water temperature does not exceed 28 °C.



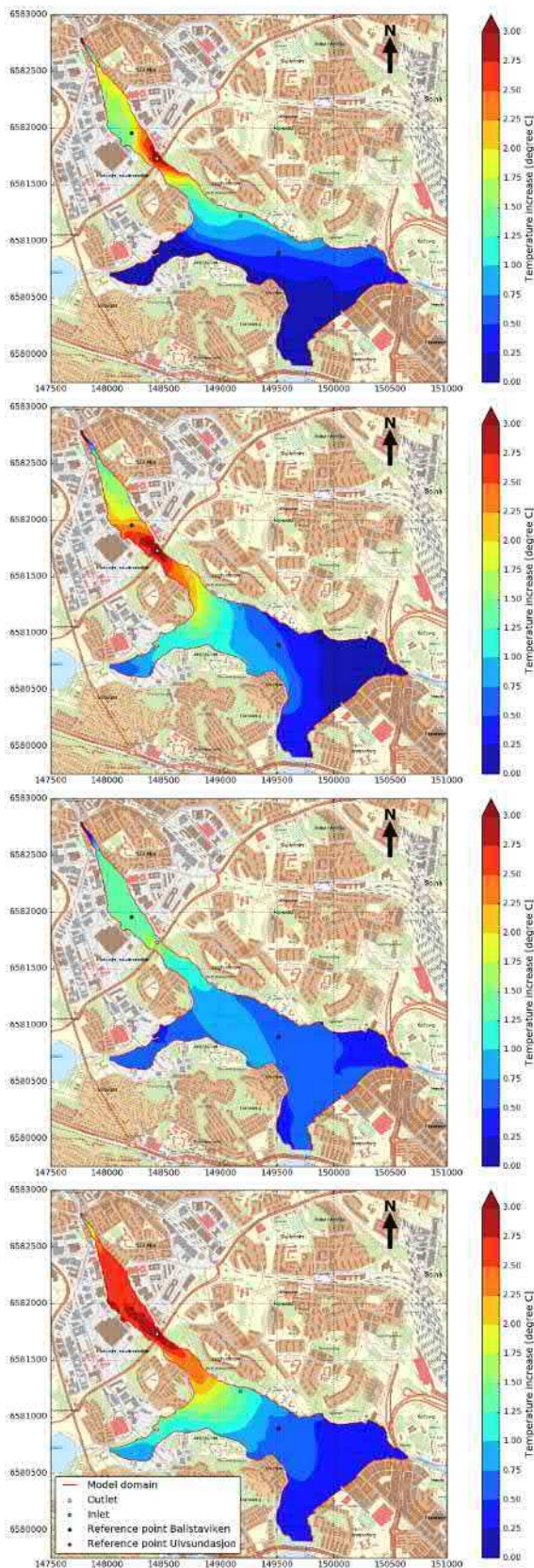


Figure 15: Temperature increase at water surface at the end of each given wind direction period (from top to bottom: SW, NE, NW, SE).

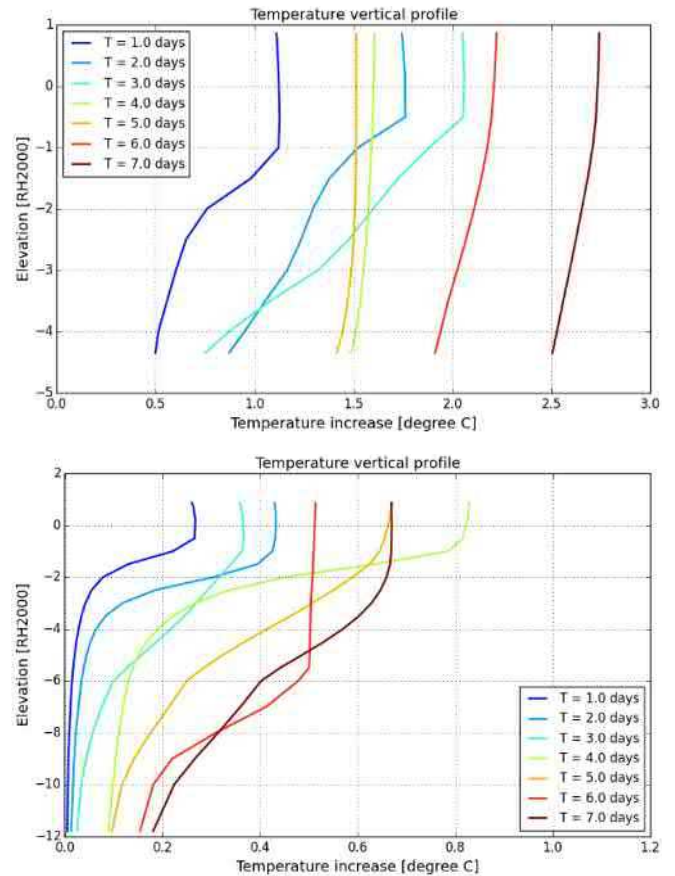


Figure 16: Vertical profiles of temperature increase for Ballstaviken (top) and Ulvsundsjön (bottom) bays. See locations on Fig. 15.

Both Ulvsundsjön and Ballstaviken bays meet this standard according to the results and thus assumed that the environmental impacts on fauna and flow are negligible. Furthermore, the heat pumps have open evaporators which increase the oxygen in the discharge water. This is expected to have a positive impact on the flora and fauna in Ballstaviken and Ulvsundsjön bays.

## VI. CONCLUSION

The main findings from the different steps involved in the presented work are as follows:

- The  $k-\epsilon$  turbulence model applied in the vertical direction tends to underestimate surface currents generated by wind.
- Tsanis' vertical mixing length model used with discretization of 0.1 m below the free surface provides results in good agreement with theory and field measurements.
- Topography can significantly influence the local wind speed and direction and is therefore an important factor to take into account in hydrodynamic modelling.

- It is necessary to use a coupling between TELEMAC-3D and WAQTEL in order to be able to model stable temperature stratification during long simulation periods and model temperature energy budget more precisely.
- The results from the hydrodynamic model could be used to conservatively estimate the environmental impacts related to the release of heated water in the Bällstaviken and Ulvsundsjön bays.

#### ACKNOWLEDGEMENT

The work presented in this article has been funded and

performed for Norrenergi as part of the environmental permit regarding the upgrade of the Solna heating and cooling power plant. Field measurements have been performed by the Finnish company Luode Consulting Oy.

#### REFERENCES

- [1] J-M. Hervouet, Hydrodynamics of free surface flows, John Wiley & Sons, Ltd, 2007.
- [2] EDF R&D, TELEMAC-3D User manual, Version 7.3, March 2018.
- [3] J. Wu., Prediction of Near-Surface Drift Currents from Wind Velocity. Journal of the Hydraulics Division, 1973, Vol. 99, Issue 9, pp. 1291-1302.
- [4] EDF R&D, TELEMAC-3D Validation manual, Version 7.3, March 2018.





The coastline is subject to a semi-diurnal tide with a range of about 2 m during neap tide, 4.1 m during spring tide and 5.5 m for the highest astronomical tides.

The characteristic flows of these rivers are given in the Table 1.

TABLE 1. CHARACTERISTIC FLOWS OF THE MAIN RIVERS

River	Surface	$Q_{min}$	$Q_{median}$	$Q_{10}$	$Q_{100}$
Ellé	603 km <sup>2</sup>	1 m <sup>3</sup> /s	9,5 m <sup>3</sup> /s	110 m <sup>3</sup> /s	330 m <sup>3</sup> /s
Isole	226 km <sup>2</sup>	0,5 m <sup>3</sup> /s	4,3 m <sup>3</sup> /s	51 m <sup>3</sup> /s	200 m <sup>3</sup> /s
Laita (down-stream Quimperlé)	832 km <sup>2</sup>	2 m <sup>3</sup> /s	13,9 m <sup>3</sup> /s	160 m <sup>3</sup> /s	> 500 m <sup>3</sup> /s

As the estuary is subject to an oceanic climate, there is a significant seasonal variation between winter and summer period.

The limit of the dynamic tide is at Quimperlé. However, the tide influences the water levels upstream only in the context of moderate flood flows. In high-flood conditions, the influence of astronomical tide on the upstream section is negligible.

The position of the salinity front varies during the tidal cycle, also depending on the coefficient and fluvial flow. Measurements and modelling results of this study show that the salinity front could reach 8 km upstream and during periods of high river discharge, the salt water mass is blocked at the river mouth.

### B. Main sources of contamination

For this study, only *Escherichia Coli* (*E. Coli*) is studied as a tracer of water quality. Within the Laita watershed, various sources of contamination are identified.

Firstly, the percentage of the population connected to a collective sanitation network was estimated at 65%. These networks are treated by 3 waste water treatment plants (WWTP) which have a direct outfall in the river. Two are located directly downstream Quimperlé and reject a significant concentration of bacteria. The third outfall is located at the mouth and is equipped of Membrane Bioreactor Module (BRM) treatment which allows a low concentration discharge (< 250 CFU/100ml).

Beside these installations, more than 1700 non-collective sanitation facilities were enumerated in the sub-watershed of the Laita.

Finally, 70 farms are listed on the study area, representing 3,785 ha of agricultural area in use. Diagnostics are currently realized to evaluate conformities of these different exploitations.

Other sources of contamination can be also listed, like sediments, recreational activities, avifauna...

### C. Water quality issues

On the Laita area, main issues on water quality concerns bathing waters, mussel farming and nautical activities like kayak.

Different threshold relative to French regulation exist and give a corresponding class of quality. Overtaking a critical threshold can conduct to use restriction or interdiction.

## II. BACTERIOLOGICAL MONITORING

To control the water quality in the Laita, many monitoring networks have been setup over the last 3 decades ([6], [9], and [2]). For this study, we used monitoring focused on main affluent which contains discharge measurements. We also have data on WWTP outlets (see Figure 2).

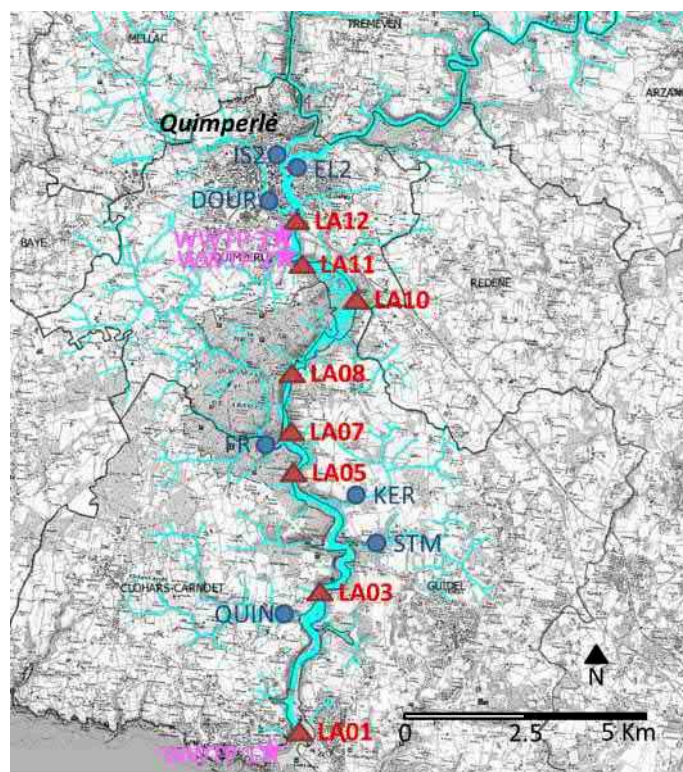


Figure 2. Location of monitoring points. Blue circles corresponds to measurements at affluent downstream, pink stars corresponds to WWTP outlets and red triangles corresponds to river surveys.

TABLE 2. CHARACTERISTIC FLOWS OF THE MAIN RIVERS

Bacteriological fluxes (CFU/s)	Mean			Percentile 95		
	Global	Wet	Dry	Global	Wet	Dry
Isole (IS2)	1.7E+07	7.6E+07	3.4E+06	1.9E+09	4.3E+09	8.1E+07
Ellé (EL2)	2.9E+07	1.2E+08	6.2E+06	2.6E+09	9.2E+09	8.0E+07
Dourdu (DOUR)	1.2E+07	2.1E+07	5.9E+06	5.8E+08	6.5E+08	5.5E+08
WWTP 3	1.1E+07	/	/	2.7E+08	/	/
WWTP 2	4.8E+06	/	/	5.7E+07	/	/
Frout (FR)	5.3E+05	6.7E+06	4.2E+04	7.4E+08	2.0E+09	6.9E+07
Keryhuél (KER)	4.9E+05	1.8E+06	4.5E+04	2.3E+07	2.4E+07	3.8E+05
St Michel (STM)	3.9E+05	7.4E+05	1.3E+05	2.4E+07	2.5E+07	5.0E+05
Quinquis (QUIN)	6.5E+05	1.6E+06	1.8E+05	5.9E+07	9.7E+07	5.0E+06
WWTP 1	2.8E+03	/	/	3.5E+04	/	/



The table 2 gives the bacteriological fluxes for the main sources of contamination of Laïta for wet period, dry period and global measurement period. The table gives mean and percentile results.

Measurements (E. Coli concentrations and discharge) are realized downstream of each affluent. We called a “dry period” when no rain was detected in the watershed during the 10 preceding days and “wet period” when there is a global river discharge increase due to rain in the last 24 hours.

Regarding the Figure 2, sources of contamination are surveyed but there are also measurement points along the river between the Laïta river mouth and Quimperlé (LA01 to LA12).

### III. MODEL SETUP

#### A. Computational grid

The computational grid extents from Quimperlé to ocean (figure below) in order to well represent mixing of ocean and river processes.

The grid is composed by 31 500 nodes and about 59 000 triangles. The mesh sizes range from 250 m offshore to 3 m around the Laïta bridge piers. It was built in order to obtain a reasonable computation time on a basic computer [1]. However, at the narrowest minor bed, the width of the bed is represented by 4 to 5 triangular meshes. However, this mesh resolution allows fulfilling the objective of the study that is to represent the plume behaviour at the estuary scale.

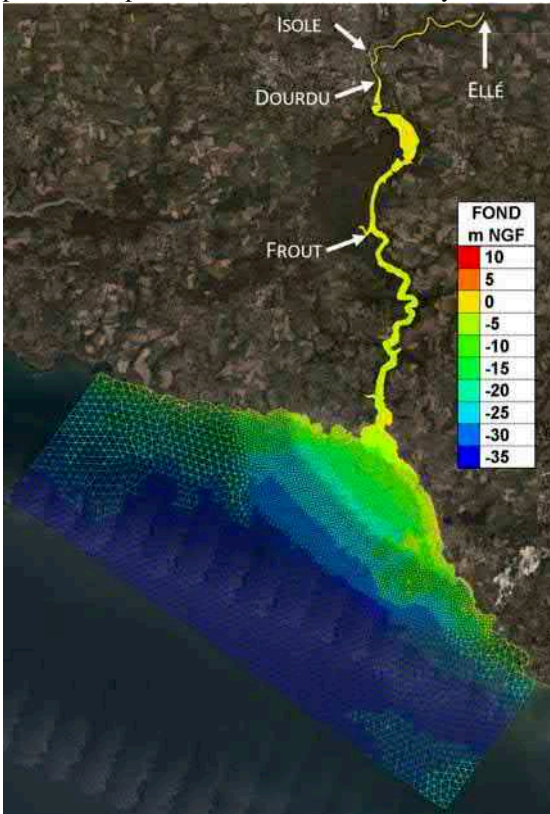


Figure 3. Representation of the computational grid

3D discretisation is made of 5 sigma plans. The distribution of the plans on the talweg is shown on the figure below.

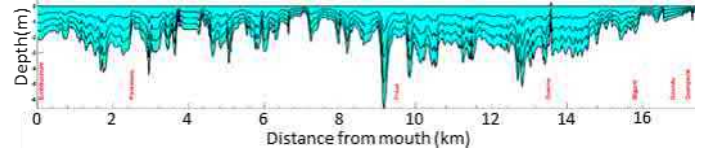


Figure 4. Vertical discretisation on river talweg.

#### B. Faecal decay law

The mathematical formulations of decay processes for E.coli, in this case, used as the indicator bacteria, are described below. Biodegradation is according to [8] defined as the biologically catalysed reduction in complexity of chemical compounds. Furthermore, it is described as the process by which organic substances are broken down from larger to smaller compounds by microbial organisms.[8]. The general degradation of faeces indicators such as E. Coli is assumed to follow a general exponential first-order model [3].

$$C(t) = C(t = 0) * e^{(-k*t)}$$

Where, C is the concentration of organism, t is the time and k is the decay rate coefficient at 20 °C.

The degradation rate coefficient can be described in several different ways.

The method for calculating k is based on information concerning water temperature, light intensity and salinity. In this case, an infinite oxygen supply is assumed [5].

The decay parameter k consists of decay contributions from light respectively dark conditions and is described in equation below.

$$k = K_m + K_L * I_z \quad (1)$$

Where,  $K_m$  is the decay contribution when dark conditions,  $K_L$  is the decay contribution when light conditions,  $I_z$  is the light intensity at depth z.

The decay contribution, when dark conditions, is calculated with equation below.

$$K_m = a_T * T - k_{m0} \quad (2)$$

Where,  $a_T$  is the temperature dependency constant for dark reaction, T is the actual water temperature and  $k_{m0}$  is the initial coliform decay rate constant for dark reaction. It is only valid between 4 and 24 °C.

$$K_L = S_m * \frac{(b_T * T + K_{L0})}{a * S_m - (\frac{1}{a}) * S} \quad (3)$$

Where, S is the actual salinity,  $S_m$  is the reference salinity constant, a is the correction for salinity constant,  $b_T$  is the temperature dependency constant for light reaction and  $K_{L0}$  is the initial coliform decay rate for light reaction. This equation is only valid between 12 and 34 °C [5].

The light intensity at depth z,  $I_z$  can be described by Lambert-Beer's law.

$$I_z = I_0 * e^{-\mu * z} \quad (4)$$

Where,  $I_0$  is the light intensity at the water surface,  $\mu$  is the extinction coefficient and z is the depth to the contamination. The extinction coefficient can be decided from the secchi depth, SD. For the determination of  $\mu$ , it is assumed that the secchi depth corresponds to the depth at which 15% of the

light radiation remains. This ratio may, however, range from about 10% up to 25% depending on the area.

$$\mu = -\ln\left(\frac{0.15}{SD}\right) \quad (5)$$

To sum up, the degradation of E.coli can be described in a single equation:

$$C_{E.coli} = C_{E.coli 0} * e^{\left(-\left((a_T * T - k_{m0}) + \left(S_m * \frac{(b_T * T + K_{L0})}{a * S_m - \left(\frac{1}{a}\right) * S}\right) * (I_0 * e^{-\left(-\ln\left(\frac{0.15}{SD}\right) * z\right)}\right) * t\right)} \quad (6)$$

This equation for degradation of E. coli is only subject to decay, and the decay processes describing the variations of the bacteria in time and space are dependent on external factors such as salinity, light influx and water temperature. Moreover, this formula has been already implemented in a Telemac 3D fortran file [9].

### C. Input

On the oceanic part, the model is first forced at its borders with a global tidal model TPXO [4] to take into account the variation of currents and water levels related to the astronomical tide.

The main affluents of the Laita are taken into account. A discharge and an E. Coli concentration can be applied. Effluent discharges from WWTP outfalls and any accidental pollution are also included in the modelling. They are represented by a concentration of micro-bacteria and a characteristic discharge.

A model is then launched with no bacterial concentration as initial condition. Contaminated water will mix with sea water within a few tidal cycles.

### D. Hydraulic model validation

Various hydraulic conditions were observed during February 2017 with an ADCP moored downstream of Quimperlé [1]. Cycles of spring and neap tides with a period of low flows (15 m<sup>3</sup>/s) and a period of flood (Q > 50 m<sup>3</sup>/s) could be recorded. This campaign was therefore very useful for calibrating the model for different hydraulic conditions. Comparisons between model and measurements show a good correlation with water level and velocities for all measured conditions.

Different monitoring has allowed also validating salinity dispersion model. Comparison shows that the distribution of salinity at the scale of sampling is well represented by the numerical model for the different campaigns studied. The model results are relatively close to the measurements.

### E. Bacteriological model calibration

Once it has been ensured that numerical model can represent all the hydraulic conditions measured, a calibration of the bacteriological dispersion model is carried out. Four surveys have been selected representing different hydraulic and tidal conditions (see Table 3) and for which main measurements upstream are available.

For each sources of contaminant, discharges (Q) and E. Coli concentrations have been settled according to measurements (see Table 4).

For WWTP 1 & 2, discharges and concentrations have been estimated with monthly mean due to a lack of measurements within these surveys. For WWTP 3, concentration values can be very high and then will show influence of this outfall in the estuary. For little affluents, there were no data available so it has been decided to not include them as they represent a minor part from contaminant sources.

TABLE 3. HYDRAULIC AND TIDAL CONDITIONS FOR THE 4 SURVEYS SELECTED FOR NUMERICAL MODEL CALIBRATION.

Survey #	date	Q Laita (m <sup>3</sup> /s)	Tidal coefficient
1	21/07/2011	2.95	64
2	09/04/2015	9.72	75
3	26/04/2012	63	65
4	15/12/2014	22.4	38

TABLE 4. DISCHARGES (M<sup>3</sup>/S) AND BACTERIAL CONCENTRATIONS (CFU / 100ML) FOR EACH SOURCES FOR MODEL CALIBRATION.

Survey #		1	2	3	4
Conditions		Summer - Dry	Winter - Dry	Winter - Rain	Winter - Rain
Ellé	Q	1.9	6.67	42	15.2
	[E. Coli]	78	38	2000	403
Isole	Q	1.05	3.05	21	7.2
	[E. Coli]	1000	1000	8900	500
Dourdu	Q	0.07	0.1	0.5	0.5
	[E. Coli]	14000	5840	2700	2990
Froust	Q	0.015	0.04	0.25	0.25
	[E. Coli]	510	1749	8300	457
WWTP 3	Q	0.04	0.04	0.04	0.04
	[E. Coli]	1 700 000	1 015 000	620 000	920
WWTP 2	Q	0.06	0.06	0.06	0.06
	[E. Coli]	32 000	32 000	32 000	32 000
WWTP 1	Q	0.02	0.02	0.02	0.02
	[E. Coli]	17	17	17	17

Figure 5 show E. Coli concentration model results of vertical Laita view from Quimperlé (right) to river mouth (left) for different moments of the tidal cycle (survey #1)

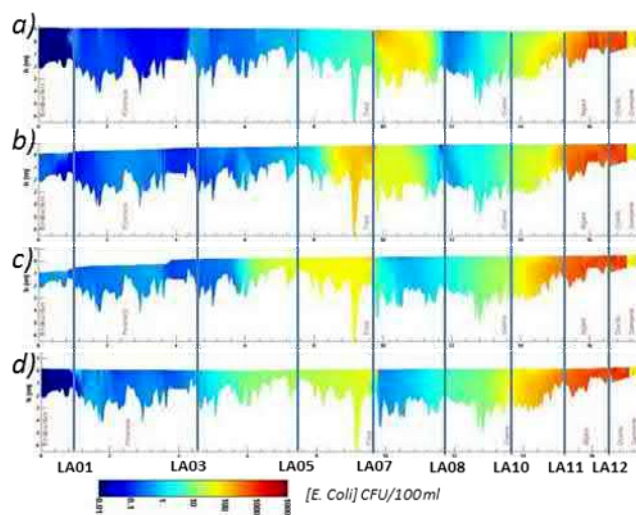


Figure 5. E Coli concentration model results of vertical Laita view from Quimperlé (right) to river mouth (left) for a) High tide (HT), b) HT-3h, c) Low tide (LT) and d) LT-3h.

Model results show the effluent dispersion according to tide with higher concentrations upstream decreasing until the



river mouth. The contribution of bacterial flow from the Frout River can be observed (LA07) with its plume going toward Quimperlé during flow inversion at high tide.

In all surveys investigated, a general decrease of bacterial concentration can be observed upstream to river mouth as the salinity of water column is higher.

As the journey of bacteria is relatively fast inside estuary (generally one tidal cycle depending on tide range and river discharge), effect of gradient salinity is very important on bacteria decay rate. Thus, model calibration was mainly focused on "a" parameter in equation 3. This parameter has firstly been set according to [10]. This value has a significant effect on bacterial mortality when mixing to sea water. Tuning this parameter with the four simulations based on surveys exposed above yield to a satisfying compromise (see Table 5).

TABLE 5. COMPARISON OF E. COLI CONCENTRATIONS (CFU/100ML) BETWEEN MODEL RESULTS AND OBSERVATIONS DURING MODEL CALIBRATION PHASE.

Survey #	LA12	LA11	LA10	LA08	LA07	LA05	LA03	LA01
1	obs.	8 300	6 600	6 100	1 400	510	460	46
	Model	2 000	11 000	2 760	75	200	120	3
2	obs.	728	1 494	1 104	2 779	1 749	858	94
	Model	789	3 400	2 350	1 450	1 130	650	81
3	obs.	8 300	11 000	6 100	7 700	8 300	11 000	8 900
	Model	3 880	4 180	3 900	3 610	4 830	3 430	2 910
4	obs.	465	480	434	563	457	633	919
	Model	650	670	590	470	410	350	210

Overall comparisons of model results with in-situ measurements are close. However, survey #3 and a few points of comparison give significant differences. Table 6 gives the differences between model and measurements.

TABLE 6. DIFFERENCES (CFU/100ML) BETWEEN MODEL RESULTS AND OBSERVATIONS DURING MODEL CALIBRATION PHASE.

Survey #	LA12	LA11	LA10	LA08	LA07	LA05	LA03	LA01
1	6E+03	-4E+03	3E+03	1E+03	3E+02	3E+02	4E+01	1E+01
2	-6E+01	-2E+03	-1E+03	1E+03	6E+02	2E+02	1E+01	-5E+00
3	4E+03	7E+03	2E+03	4E+03	3E+03	8E+03	6E+03	4E+03
4	-2E+02	-2E+02	-2E+02	9E+01	5E+01	3E+02	7E+02	3E+02

For survey #3, the model underestimates concentrations by  $10^3$  along the estuary. This campaign presents the highest discharge and probably, the measurement protocol for this high hydraulic condition is debatable.

Around LA12, LA11 and LA10, differences can also reach  $10^3$ . It can be caused by the estimation of bacterial flow of WWTP 1&2.

There are also uncertainties of contamination supply on a few minor affluents like in survey #4 around LA03 with St-Michel (STM) affluent.

Temperatures during surveys #2 and #3 are just below  $10^\circ\text{C}$  which is outside the range of validity for equation 5.

Otherwise, general differences between model and measurement are on range of  $10^1$  and  $10^2$  which is acceptable according to the several assumptions made in this model and to the bacterial measurements uncertainties.

Moreover, the model allows well representing the high decay rate in the mixing sea water transition as in survey #2 after LA05.

#### IV. MODEL APPLICATION

##### A. Mean conditions

In order to characterize the general behaviour of water quality in the estuary, eight scenarios were built depending on river discharge, contaminant flow, water temperature and tidal range. These scenarios are described in the table 7. They have been built according to measurements almost on 10 years of monitoring.

TABLE 7. DEFINITION OF 8 SCENARIOS TO CHARACTERIZE WATER QUALITY BEHAVIOUR IN THE LAITA ESTUARY.

Hydraulic condition	$Q_{\text{River}}$ Winter $T_{\text{water}} = 9^\circ\text{C}$		$Q_{\text{River}}$ Summer $T_{\text{water}} = 19^\circ\text{C}$	
Contaminant flow	Dry period	Wet period	Dry period	Wet period
Light intensity	$I_0 = 720\ 000$	$I_0 = 200\ 000$	$I_0 = 5\ 700\ 000$	$I_0 = 1\ 000\ 000$
Neap tide	Scénario 1	Scénario 3	Scénario 5	Scénario 7
Spring tide	Scénario 2	Scénario 4	Scénario 6	Scénario 8

Results are presented in the table 8 as the maximal concentration reached during simulation along the estuary for the 8 simulated scenarios.

TABLE 8. MAXIMAL E. COLI CONCENTRATION INSIDE LAITA ESTUARY FOR THE 8 CHARACTERISTIC SCENARIOS.

Scenario #	LA12	LA11	LA10	LA08	LA07	LA05	LA03	LA01
1	500	754	550	371	260	246	105	25
2	501	862	571	398	254	245	100	26
3	1 840	1 821	1 715	1 556	1 934	1 455	1 233	1 031
4	1 830	1 826	1 719	1 558	1 816	1 492	1 248	1 064
5	686	544	71	56	318	83	2	2
6	666	520	87	61	318	108	16	1
7	1 875	1 713	1 010	426	1 762	417	160	78
8	1 873	1 690	1 002	436	2 152	1 102	535	147

Highest E. Coli concentrations are mainly upstream.

Generally, concentrations change strongly during the tidal cycle and especially for "medium" or "low" flows. The bacterial decay rate is highly dependent on the salinity front behaviour.

For "high" flows (winter in wet period), E. Coli concentrations are relatively constant from upstream to river mouth. The estuary is composed of freshwater along the

estuary, regardless of tide. The bacterial decay rate is therefore lower.

Tide affects only downstream point (from LA08 to LA01). The tidal range is affectless on maximum E. Coli concentration.

For low discharges and mean E. Coli concentration, the area of influence of WWTP or minor affluents is limited.

### B. Peak or accidental effluent discharges

River discharge and E. Coli concentration presented in the 8 previous scenarios are based on the median of measurements. Other scenarios were also investigated with percentiles 95 as peak concentration or as accidental discharge.

An example is given below with the precedent scenarios 2 and 8 which are simulated with a WWTP concentration based on percentile 95 ( $7.10^6$  CFU/100ml for WWTP3 and  $8.10^5$  CFU/100ml for WWTP2). These 2 scenarios, called scenarios 9 and 10 simulate then a peak discharge for these installations. Results are given in Table 9 as maximal concentrations reached inside the estuary and are compared to scenarios 2 and 8.

TABLE 9. MAXIMAL E. COLI CONCENTRATION FOR SCENARIO 9 AND 10 COMPARED TO SCENARIO 2 AND 8 AND RATIO BETWEEN VALUES.

	LA12	LA11	LA10	LA08	LA07	LA05	LA03	LA01
<b>Scenario 2</b>	501	862	571	398	254	245	100	26
<b>Scenario 9</b>	501	9 263	4 942	2 925	1 720	1 739	633	122
<b>ratio 9/2</b>	1	11	9	7	7	7	6	5
<b>Scenario 8</b>	1 873	1 690	1 002	436	2 152	1 102	535	147
<b>Scenario 10</b>	1 873	8 499	4 079	1 543	2 182	1 125	552	151
<b>ratio 10/8</b>	1	5	4	4	1	1	1	1

These results show that during winter and dry weather (scenarios 2 and 9), the influence of WWTP with a 95 percentile is visible until LA01 while in summer and rainy weather (scenarios 8 and 10), it is visible only until LA07, at the confluence with the Froust river. Indeed, this river during rainy period is significantly contaminated due to most likely agriculture activities taken place up to the watershed. Thus, contamination from WWTP close to Quimperlé is mixed downstream with the supply of the Froust River at LA07.

These results allow affirming the role of WWTP on river mouth for specific conditions. This result is important as the river mouth area concentrates the entire mussel farming activities and water bathing quality issues

This exercise is done on each affluent or possible contaminant source in order to classify the stronger bacterial contributors regarding the river mouth issues (see Table 10)

Once this exercise has been done, different solutions has been proposed to decrease contamination for main sources. These solutions encompass for example a tertiary treatment for WWTP, investment on agriculture exploitation, action on non-collective sanitation or rehabilitation works on collective sanitation network.

All these solutions have been also tested with 3D numerical model in order to appreciate effects on the river mouth issues.

TABLE 10. PRIORITIZATION OF MAIN CONTAMINANT SOURCES

SOURCES	Mean flow order	Peak flow order
Isole (IS2)	2	2
Ellé (EL2)	1	1
Dourdu (DOUR)	3	4
WWTP 3	4	5
WWTP 2	5	7
Froust (FR)	7	3
Keryhuél (KER)	8	9
St Michel (STM)	9	8
Quinquis (QUIN)	6	6
WWTP 1	10	10

## V. CONCLUSION

To conclude, a numerical tool has been set up to represent bacterial dispersion in the Laïta River based on an equation calculating decay rate of E. coli dependent on external factors such as salinity, light influx and water temperature. The model has been calibrated with 4 in-situ campaigns and gives acceptable correlation. The calibration step showed importance to have a complete set of data and the necessity to take into account salinity effect in an estuary instead of constant decay rate as a T90 law.

Once the numerical tool has been validated, a complete analysis of the estuary and the main contaminant sources have been done to give prioritization and give solutions to improve the general water quality, above all close to the activities issues (mussel farming and bathing water).

## REFERENCES

- [1] Acri. Etude hydrologique, hydraulique et hydro-sédimentaire de la Laïta amont – Rapport technique provisoire 2018. réf.: A1523-1317-M-RE2-V1.1. Syndicat Mixte Ellé Isole Laïta.
- [2] Cellules Qualité des Eaux Littorales (CQEL) - Dreal Bretagne, Réseau des estuaires Bretons. Qualité des eaux: Présentation des résultats. Campagne 2012. Juillet 2013.
- [3] Chick H. & Martin C. J. 1908, The Principles Involved in the Standardisation of Disinfectants and the Influence of Organic Matter upon Germicidal Value, The Journal of Hygiene, vol.8:5, p.654-97.
- [4] Egbert, Gary D., and Svetlana Y. Erofeeva. "Efficient inverse modeling of barotropic ocean tides." Journal of Atmospheric and Oceanic Technology 19.2 (2002): 183-204.
- [5] Erichsen, A.C., Dannesø, J.G., Jørgensen, C., Mark, O. and Kaas, H. 2006, Implementation and description of different early warning systems for bathing water quality Original title: Etablering af badevandsprofiler og varslingsystemer i henhold til EU's nye badevandsdirektiv, Danish EPA, Miljøprojekt Nr 1101 (in Danish), <http://www2.mst.dk/udgiv/publikationer/2006/87-7052-126-3/html/helepubl.htm> [2017-08-30].
- [6] Ifremer (2019). Evaluation de la qualité des zones de production conchylicole. Département 29. Edition 2019. [rst.ode.littoral.ier/bo-19-001](http://rst.ode.littoral.ier/bo-19-001) 03/05/2019.
- [7] In Vivo (2013a). Diagnostic du fonctionnement hydro-sédimentaire de la Laïta. Rapport final. Syndicat Mixte Ellé Isole Laïta.
- [8] Joutey N. T., Bahafid W., Sayel H. & El Ghachtouli N. 2013, Biodegradation: involved Microorganisms and Genetically Engineered Microorganisms, Biodegradation-Life of Science, p.289
- [9] Labocca - SMEIL, Suivi de la qualité bactériologique des eaux du bassin versant Ellé-Isole-Laïta – Année 4 (2015-2016) March 2017.
- [10] Selmeus L. (2017). Dynamic modelling of bathing water quality with biodegradation of Escherichia coli in TELEMAR-3D. Master Thesis TVVR 18/5001.

# Telemac3D for aquatic ecological modelling: calibration of the coupled ecological library AED2

Francesco Piccioni<sup>1</sup>, Brigitte Vinçon-Leite<sup>1</sup>, Minh-Hoang Le<sup>3</sup>, Bruno J. Lemaire<sup>1</sup>, Celine Casenave<sup>2</sup>, Yi Hoang<sup>1</sup>, Magali Jodeau<sup>3,4</sup>, Chi-Tuan Pham<sup>4</sup>, Javier Vidal<sup>4</sup>, Nicole Goutal<sup>3,4</sup>

<sup>1</sup>LEESU, Ecole des Ponts ParisTech, AgroParisTech, UPEC, Champs-sur-Marne

<sup>2</sup>UMR MISTEA, Univ Montpellier, INRA, Montpellier SupAgro, Montpellier

<sup>3</sup>LHSV, Ecole des Ponts ParisTech, CEREMA, EDF R&D, Chatou, France

<sup>4</sup>LNHE, EDF R&D, Chatou, France

francesco.piccioni@enpc.fr

**Abstract:** The monitoring and preservation of water quality is one of the main challenges in modern society. Anthropogenic stressors originated from urbanization and industrialization can have a strong impact on water resources in terms of pollutant release and nutrient enrichment. Together with the on-going climate change, they can lead to the proliferation of primary producers and the eutrophication of the water bodies. Harmful algal blooms, and in particular cyanobacteria blooms, are an ever increasing concern worldwide as their occurrence strongly increases, expanding to higher latitudes due to warmer water temperature. Cyanobacteria are able to produce toxins that are dangerous to human health and represent a serious threat not only for the balances of an ecosystem but to human society as well. Aquatic ecological models are useful tools that can be used to simulate the biogeochemical cycle in a water body identifying the factors triggering events such as harmful algal blooms, in order to provide stakeholders with reliable projections for decision making. However, their calibration and validation often remains a challenging task: biological and chemical data deriving from field surveys are often sparse in space and time and, due to the complexity of the biogeochemical cycle, these models generally involve a high number of parameters to adjust. Aquatic ecological models need to rely on a robust hydrodynamic simulator, upon which the biogeochemical cycle is simulated. Telemac3D has recently been coupled by EDF R&D with the well-known ecological library Aquatic EcoDynamics (AED2).

In this context, we aim to test the performance of Telemac3D coupled with AED2 on a full scale experimental site by comparison with high-frequency in situ data. The study site is a small and shallow urban lake located in the east of Great Paris metropolitan area. The lake suffers from repeated and severe harmful algal blooms in summer and autumn. Aside from the traditional monitoring via field campaigns and water sampling, the study site is equipped with specific sensors recording data at high-frequency (every 10 minutes) for water temperature, pH, dissolved oxygen and for the concentration of specific pigments to monitor phytoplankton growth (chlorophyll-a and phycocyanin, considered as proxies for total biomass and cyanobacteria biomass, respectively). The use of high-frequency data allows on the first hand to test the capability of the model to reproduce daily cycles and rapid blooms events spanning only a few days, and on the other hand to gain in computational time while calibrating the model on a short time periods of two to three weeks.

Model results are compared with water temperature data at different depths to test the ability of the coupled hydrodynamic model to reproduce thermal stratification in the water column. The ecological module AED2 is set up to simulate two main algal groups present in the study site, green algae and cyanobacteria. High-frequency observations of chlorophyll-a and phycocyanin are used to calibrate the ecological model AED2 and to test its outcomes. Model results show that Telemac3D coupled with AED2 is able to correctly reproduce biomass growth in a water body over short bloom events spanning roughly three weeks. Even though a feedback originated from strong biomass growth can be detected in water temperature results, the model is also able to correctly reproduce thermal water column stratification. These possible feedbacks need to be taken into account when calibrating the heat-exchange budget at the water-air interface.

**Proposed session:** Water quality, biodiversity, ecology and environmental pollution

**Key words:** water quality, cyanobacteria blooms, thermal stratification

**Speaker:** Francesco Piccioni

# Thermal Stratification in Small Lakes with TELEMAC-3D: Showcase “Lake Monsterloch”

Dr. Uwe H. Merkel  
UHM River Engineering  
Karlsruhe  
[info@uwe-merkel.com](mailto:info@uwe-merkel.com)

**Abstract**—This paper shows ways to configure and optimize TELEMAC-3D, to get ready for the calibration of temperature stratigraphies in small lakes. Thermal stratifications are very sensitive to numerical instabilities and dispersion. Small lake models are additionally dominated by a high percentage of boundary nodes, a source of instabilities in numeric models.

The small “Lake Monsterloch” (english: “Monsters Hole”) is a good prototype study for the many central european lakes, that suffered the same problems in the exceptional hot summers of the last decade. The lack of rain and river discharge, plus the long heat periods from 2016 to 2019 and the rising agriculture based fertilisers in the water reduced the dissolved oxygen to nothing. Without vertical mixing effects, the consequence is the dying flora and fauna as well as the resulting rot odour nuisance.

Telemac proved to be the right tool to solve vertical heat exchange and simulate mixing solutions with low or no current, if one understands the definition ranges of the core routines well and if a couple of minor code fixes are added.



Fig 1: Impression of the boundary dominated lake with dead fish and firefighters trying to pump in fresh water. (Source: Rhein Neckar Zeitung, 22.09.2016)

## I. PROJECT & SITE “LAKE MONSTERLOCH”

The eastern neighbourhood is dominated by agricultural land, while the western river shore is one of Germany’s oldest cities, Speyer. The riparian corridor is only narrow at the project site, but it is a funnel in the vast riparian forests and water

networks of the Upper Rhine Valley, an important corridor on the North-South bird migration routes and an important breeding ground for fish, like the almost extinct German salmon. It is part of the “Blue Rippon” project, which focuses on the revitalization of riparian systems along the waterways. The River Rhine is Germany’s most important inland waterway, engineered for ship dimensions of 195 m x 22,8 m x 4 m. As the river itself is quite shallow and under permanent dredging maintenance, any kind of discharge diversion to the lake might lead to sediment disposals in the shipping corridor.

The project task is to prevent future lake ecosystem collapses due to overheating and oxygen loss without taking too much water from the main river.



Fig 2: Lake Monsterloch is located 1km east of the touristic UNESCO World Heritage site “Imperial Cathedral of Speyer” and only separated by a thin gravel dam from the River Rhine main channel. Dimensions: approx. Y: 1000 m \* X: 150 m \* Depth: 14 m (maps.google.de / 2.9.2019)

## II. KNOWN & UNKNOWN

### A. Temperature

Temperature measurements are available at two depth profiles close to the geometrical lake center over 2 years. Dissolved oxygen (most fish die below 3 mg/l) and conductivity (an indicator for salts) are available for some datasets. Missing is a gauging and monitoring system for the inflow and outflow. Discharge, temperature, oxygen and conductivity had to be approximated by values of the Rhine gauge in Speyer. The measurements show clearly the well



known 3 zones Epilimnion, Metalimnion and Hypolimnion. The model calibration is based on these two temperature depth profiles.

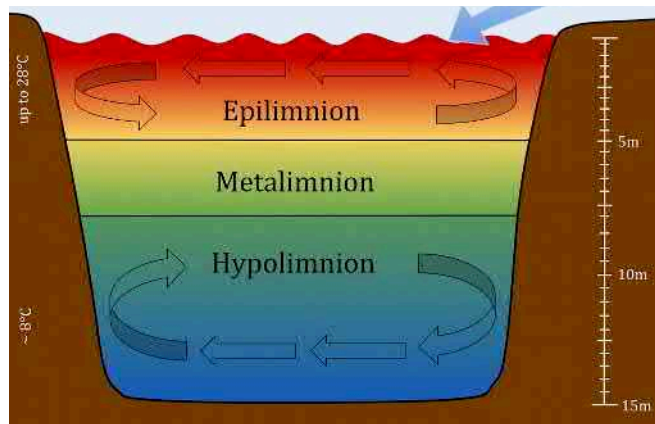


Fig 3: Typical temperature profile in summer (Source: Lake\_Stratification\_(11).svg / wikimedia.org / modified by author)

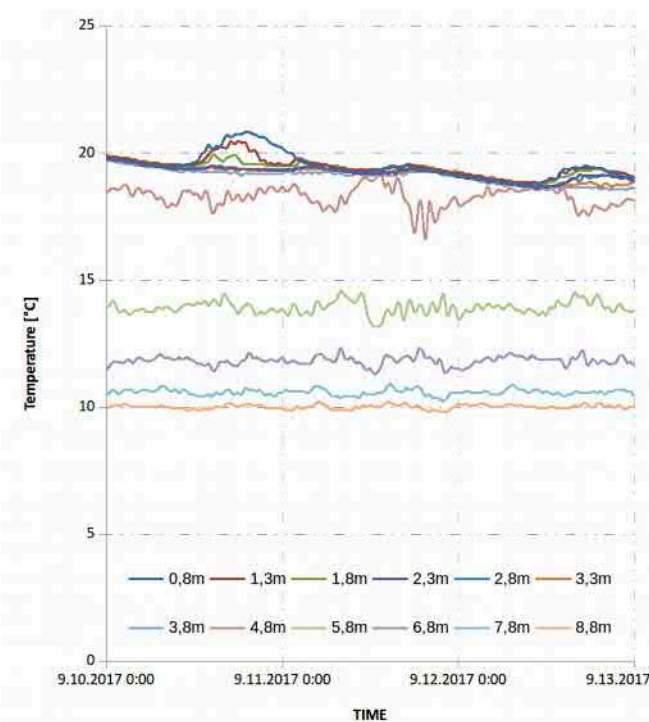


Fig 4: 3 days temperature recordings of 12 sensors on a rope: Some mixing processes only occur in the upper 2 m (day 1), others only in 4.8m depth, the thermocline (day 2).

### B. Groundwater

Additionally, three groundwater control points on the land site measure temperature, oxygen and conductivity, but do not show flow directions. Depending on the Rhine water levels, which might change one meter per day, the flow direction can change: towards and away from the river. The

groundwater temperature is approx. 10-11 °C, it is higher than the lake bottom temperature and it is normally free from dissolved oxygen. Depending on the Rhine, lake and groundwater levels, groundwater could enter or leave on the eastern site. The sources are normally spots, but not greater zones, due to the sediment's fluvial history. This type of sources, which might bring a few cubicmeters per second and hectare, are well known from neighbouring lakes, but were neither located nor monitored in the Monsterloch itself. There are some indications that cold oxygen free groundwater enters from east and exits to the west without reaching the warm surface, as well as warm and oxygen rich Rhine water could leak through the narrow dam the opposite way. As there are not enough fine resolution datasets, this potentially important component is not part of the calibration and stays the greatest unknown.

### C. Entry of sunlight and shade

Missing as well is the grade of coverage by water plants and turbidity, as well as the area percentage of shading by the surrounding trees. It is clearly visible in the calibration datasets, that in spring, when the water is clear and no water plants cover the surface, the irradiation is distributed over the upper 3-4 meters. By the end of summer, when the surface is covered and the turbidity rises, the energy input is only directly at the surface, this is the best time to calibrate the diffusion model.



Fig 5: Water plants like duckweed and water lilies plus floating dead organic material can occasionally cover the Rhine old arms to 100%.

## III. THE HYDRO-NUMERIC CRUX

Before the water quality tool WAQTEL can be used and mixing solutions can be studied, the model itself has to be

carefully tweaked to calculate the thermal stratigraphy right, with as few software features as possible.

The problem presented here and the solution approaches differ in many aspects from the usual recommendations for temperature mixing in *streaming* water.

The main parameter “temperature” is not only a tracer, but also a driver of movements, due to the temperature dependent density. Tracers are advected and diffused, separately from the movement of the water itself. If the resulting temperature values are only a little bit randomly biased locally, in one time step, a flow will be generated.

E.g. the tidal flat handling of tracers often ends up with infinity clippings or threshold handling. Even this minor residual temperature error noise at boundary points introduces a small current which mixes a lake model without inflow over weeks.

In difference to river flow models, which are dominated by horizontal eddies and velocities above 0.5 m/s, the lake model shows especially vertical movements with very low velocities. But, over weeks, even fake velocities of 0.01 m/s can mix up the whole lake. This small dispersion and computer algebra truncation based errors would be concealed if the main current is above 0.1 m/s, as for most cooling water mixing processes below power plants.

At a later model stage the use of WAQTTEL is planned. Currently the temperature is only imposed at the surface layer by a Fortran routine to keep the model as simple as possible.

Most of the developments and analysis were done on an academic, cubic tank model (T10) of only 10 m x 10 m, as it runs 14 days in 1 h. Severe disadvantages are listed in the following chapters.

Another academic, tank model (T125) was used to identify scale effects. Dimensions: 125 m x 1000 m x 14 m.

The final lake model runs 14 modeldays for ~1 000 000 cells with  $dt=1$  s in 6 h on 100 Xeon E5 v3 cores.

The kernel of the brute are the advection schemes. None is perfect, the ones which are good in tidal flat handling (LIPS, N) are not good enough in dispersion. The ones which are good in dispersion are weak with many industrial grade demands.

### A. Diffusion and Dispersion

Many subroutines and especially most advection schemes have an internal method imminent diffusion, called dispersion, which is not a physical process, but a byproduct of the linearisation mathematics and computer engineering. Only if this dispersion is minimised, the diffusion step is clearly calibratable and no density error based currents mix up the model.

The best example to learn about dispersion effects is the rotating “cone” example distributed with TELEMAT-3D. Initially a tracer is given in a rotating field of flow, its

concentration is 1. After 64 steps of advection without a diffusion calculation one would expect the tracer to remain unmixed. But the peak values in the table above show, that the “weak form of characteristics” advection scheme is the least dispersive option currently available, while others tend to mix the tracer to an unusable result.

Advection Scheme			Minimum Value	Peak Value
CHARACT.	WEAK		-0,0007	0,9579
SUPG			-0,0353	0,5653
LPO			0,0000	0,1754
NSC			0,0000	0,1754
N			0,0000	0,7235
N	PR-COR	OP2	0,0000	0,6631
N	PR-COR	OP3	0,0000	0,3136
PSI			0,0000	0,7241
PSI	PR-COR	OP2	0,0000	0,6618
PSI	PR-COR	OP3	0,0000	0,7910
LIPS			0,0000	0,3433
LPO_TF			0,0000	0,3433
NSC_TF			0,0000	0,3433

a. Results of the official Telemac-3D “Cone” test

The downside of the weak characteristics gets visual with the minimum value, which gets negative for the “cone” case, when mixing 0 with 1. The algorithm, which is superior when using averaged values, tends to overswing in single points, especially when the gradients are high. This problem reaches its maximum at tidal flat points, inflow cross sections, sources etc. If the weak characteristic advection is used for the flow field itself, than it is frequently showing pulsating boundaries. But on the other hand, inner eddies are not killed by strong dispersion of the velocity vectors. See [1,2,3] for advanced explanations on the principle of advection schemes and especially the weak form of characteristics.

As none of the other advection schemes comes close in terms of low dispersion, the weak characteristic scheme was used to test TELEMAT-3D against the measured thermocline over 14 days. As no external forces or flows were needed to test vertical temperature diffusion, the small tank of 10m x 10m with 1m edge length and 14 meters of depth seemed good enough and suitable fast for testing purposes. After some tweaking of thresholds, diffusion coefficients and other numerical parameters, the calculated results were less than 1°C in average from the measured values.

But the step to the real world model disappointed due to a surprising large number of overlapping problems which were hard to disassemble. Therefore a larger academic model was introduced: 125 m x 1000 m x 14 m with a plain or a V-shaped bottom, 55 vertical layers with no inflow or driving forces.

This 3rd model was used to search for scale effects and to accumulate the background velocity field noise which develops from truncation errors in various algorithms. This noise is amplified by the temperature-density algorithm and leads to physically not existing mixing processes. As this model should not develop any velocities at all, the parameter  $|U\_mean|$  is an identifier for this background noise based mixing.



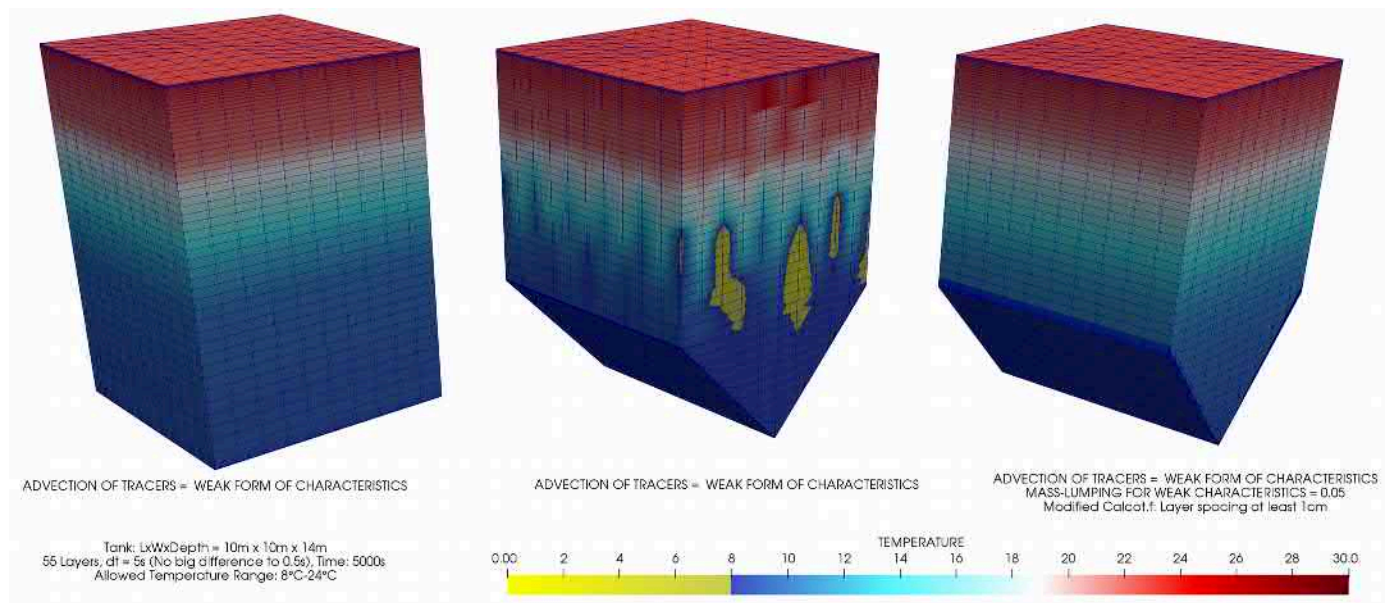


Fig 6: The least dispersive advection scheme does not work reliable with every mesh. It occasionally develops extreme temperatures which drive mixing flows.

Fig. 6 shows what happened when the tank only had an uneven bottom: Some layers are squeezed to zero strength, some bottom near cells get degenerated shapes.

The weak characteristics overswing here again especially for the temperature. The resulting error patterns generate local turbulences and finally, if the model doesn't crash, a 100% mix. The MASS-LUMPING stabilizes the problem, better than other parameters, but introduces dispersion again, what makes the whole model useless. See the following sections for more disadvantages and workarounds of the least dispersive advection scheme "weak form of characteristics".

Finally, despite all the later recommended improvements, the model was configured to the advection scheme "strong form of characteristics". Which is much more stable for practical projects, but had an up to 1°C higher rest error in the final calibration.

### B. Meshing & Inflow

The mesh brings in many parameters which generate dispersion or which force the use of helper subroutines, which bring in dispersion.

- Number of vertical layers

First tests showed that a good reflection of the thermocline can only be reached with at least 3 to 5 layers around the maximum curvature sections of the temperature depth profile. This results in up to 55 layers for the Monsterloch model on 14 m depth, where the first, second and last layer are 1 cm in thickness only.

- Less degenerated mesh elements

The "weak form of characteristic" instabilities could be reduced 100 times by a couple of changes in calcot.f. Mainly

the introduction of a minimum layer thickness of 0.1cm brought success. Truncation errors and instabilities are removed by a new mesh check section.

- Vertical layer spacing

A further significant source of dispersion is the mesh transformation handling. Neither sigma meshes nor the AMR technique were useful on longer time scales. Only hard coded elevations brought success, as they skip the reassignment of the z-coordinate at every time step with the following mass balancing. This is only possible, because the water level of the lake is close to constant and the topmost layer is the only one set dynamically.

- The Appendix

The boundary problems with the characteristic advection scheme got especially obvious when an additional tracer was introduced. "Fresh Water" with a concentration of 1 was pushed in at 2 m<sup>3</sup>/s over the inflow boundary or source points. But the balance showed only 1.6m<sup>3</sup>/s after 1 second, when there should be 2m<sup>3</sup>/s.

This problem does not occur with the other advection schemes. It is the result of the before mentioned tendency to overswing in zones of strong gradients and at boundary points. The problem can be tackled with a cheat: By adding a little inflow channel of only 5x5 mesh points where all tracers are surely 100% mixed.

This appendix (fig. 7) gets the tracer concentrations assigned in all inner and outer points, what overwrites the instabilities at the direct inflow boundaries. At the main model now enters the real concentrations (Share of fresh water, Share of groundwater, Temperature, Oxygen, Conductivity). This is for sure not a good universal solution, but a robust workaround.

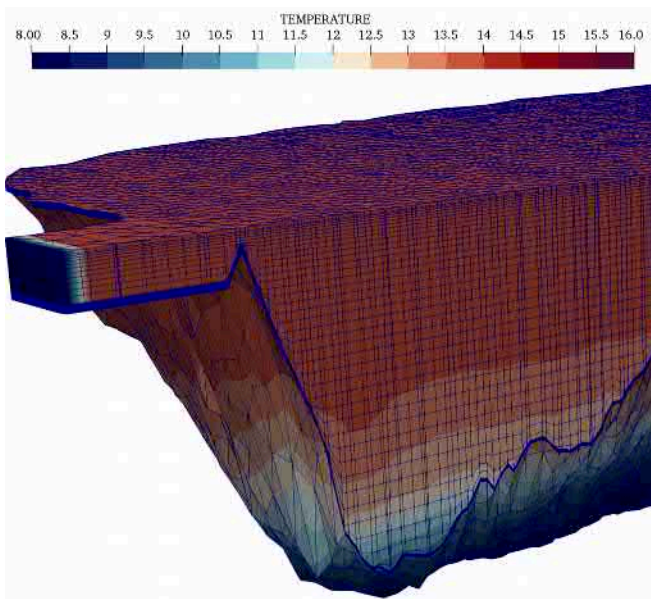


Fig 7: Every boundary and inner point of the short channel gets its tracer values assigned by Fortran code, not via the build in functions, to guarantee a noise free inflow temperature.

- Coordinate systems

The German standard coordinate system ist Gauss-Kruger, a Transverse Mercator variant with 7-digit coordinates.

X\_ORIGIN / Y\_ORIGIN: 0 m / 0 m

X\_MIN / Y\_MIN: 3460249.1860 m / 5464833.5055 m

The conversion of the geometry file to the coordinate system origin brought additional stability. Which subroutine produces the dispersion and truncation errors from the origin distance is still unknown.

X\_ORIGIN / Y\_ORIGIN: 3460249 m / 5464833 m

X\_MIN / Y\_MIN: 0.1860 m / 0.5055 m

Unfortunately, the values of X-Origin and Y-Origin, which are in the Selafin specs since two decades are still not fully supported by all pre- and post processing tools and occasionally even lost in the TELEMAC result file.

### C. Other submodels w. significant dispersion effects

- Tidal flats

The tidal flat algorithms have to deal with cells that run dry. Different options are possible for this case, but none of them works acceptable on temperature as tracer. The resulting residual temperature errors are not relevant as absolute values, but because they produce density variations which drive slowly, but always present velocity fields. The only way to get rid of them at present is to cut the very shallow parts from the model, to reduce it to at least 10cm depth under all conditions.

- Turbulence models

All T3D turbulence models were tested. Even though the “constant viscosity” produced the least velocity noise, and k-epsilon seems to produce the best mixing for the high inflow discharge tests, the combination of Smagorinsky (horizontal) and Mixing Length (vertical, NEZU & NAKAGAWA + Munk & Anderson) are recommended for the final productive runs, as they run more robust and reliable than K-Epsilon.

- Time steps

Shorter time steps with lower CFL numbers are commonly assumed to produce better velocity fields. But if more iterations are necessary, the amount of velocity noise accumulates to a visible niveau, once the model reaches a general low dispersion quality.

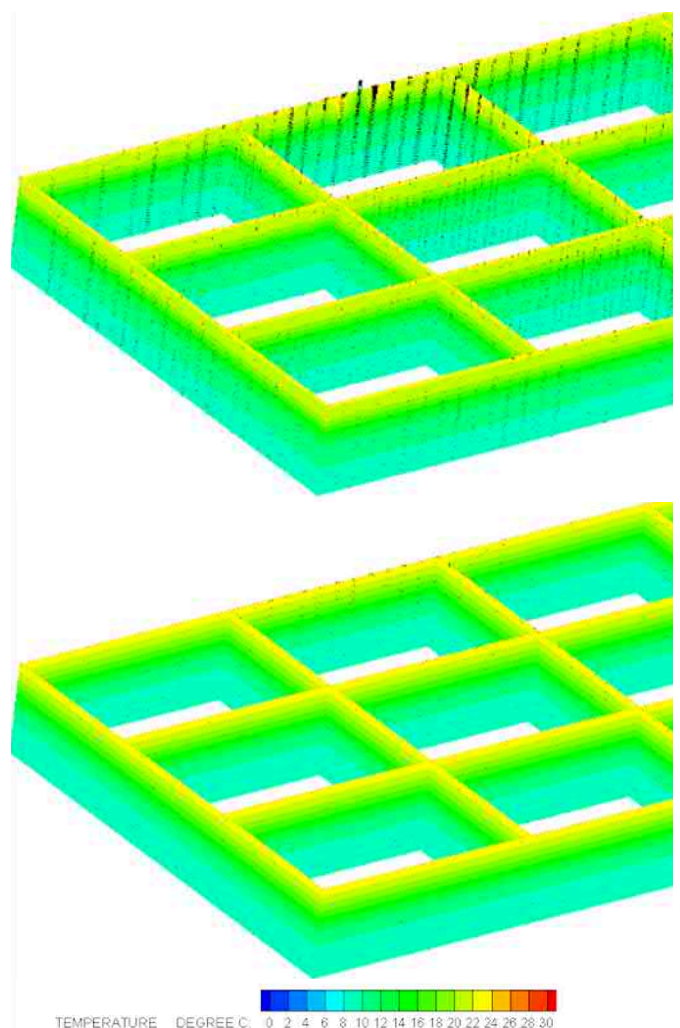


Fig. 8: Thermic stratification and velocity fields (arrows), that developed due to truncation and threshold errors in the temperature tracer after 4 hours. (Larger academic model T125, cross sectional view) Upper:  $dt=1s$ ,  $|U\_MEAN| = 0.0162$  m/s. Lower:  $dt=5s$ ,  $|U\_MEAN| = 0.002$  m/s.



Additionally advection schemes have an optimum point for the dispersion minimum, which correlates to the CFL number and is not necessarily at the shortest time step.

The conclusion is to harmonize the mesh edge length and time step length carefully to get the highest possible CFL number for the expected velocities. Tests with the “cone” model help to find suitable combinations.

#### IV. CALIBRATION RESULTS

The first calibration of the tank model, based on lake data, met the thermocline better than the final lake model displayed in figure 9. But, as some model parameters (exsp. the weak characteristics) were not transferable to a large scale model with irregular bottom and tracer inflow from outside, the concession to a practical model after use was the switch to the strong form of characteristics. The 16.5 °C warm epilimnion is 1 m too strong in the final timestep.

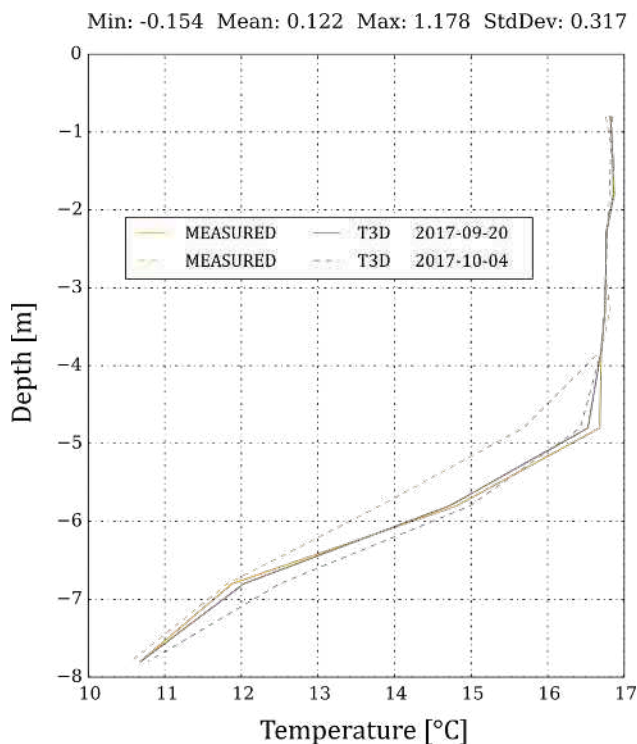


Fig. 9: Final model calibration: Temperature depth profile close to the lake center, without inflow.

Solid lines: Initial values.

Dashed lines: 14 days (~1 209 600 iterations) later.

One shall not forget: The calibration only tweaks parameters that are included in the model. The before mentioned missing groundwater, the unknown inflow temperature and the unknown shading percentage might shift the epilimnion up or down.

But as the final purpose of this model is the search for a mixing strategie, robustness is more important.

To get an impression how sensitive the model is to the (not measured!) inflow temperature and to show the mixing effects, see fig. 10 to 12.

Fig. 10 shows 14 °C warm water crossing the lake just on the surface without any significant impact on the deeper layers until it hits the opposite shore. (This happens at 2am, when the surface water is 1-2° colder than at 2pm) In most cases, the river water is constantly mixed, while the lake surface is even warmer (weather dependent) and the bottom stays colder (average annual temperature ~8.5 °C). Therefore the usual case would be fig. 12: Medium temperatures cross close to the thermocline at low velocities.

Tests with higher discharges of 10 m<sup>3</sup>/s showed first signs of vertical mixing by vertical eddies, driven by the inflow jet. But still, after 14 days, the water is not exchanged to 100 % in all zones.

At 100 m<sup>3</sup>/s (fig.11), the old water is exchanged to ~95% after 4 days.

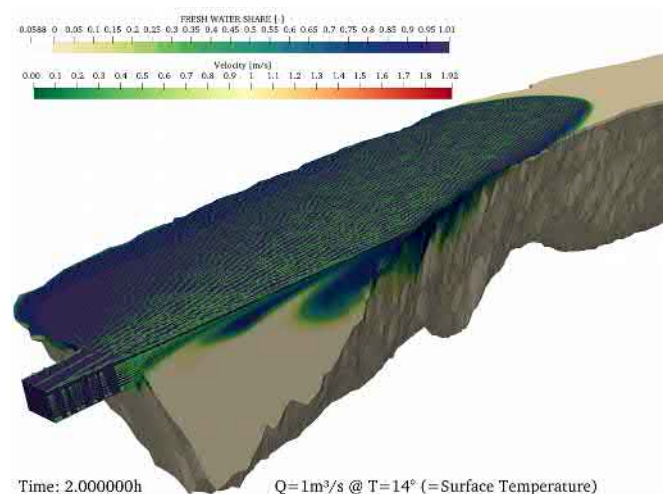


Fig. 10: 14°C fresh water crosses the lake without contact to deeper layers

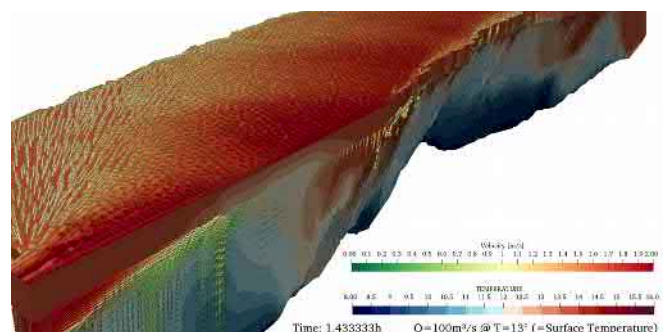
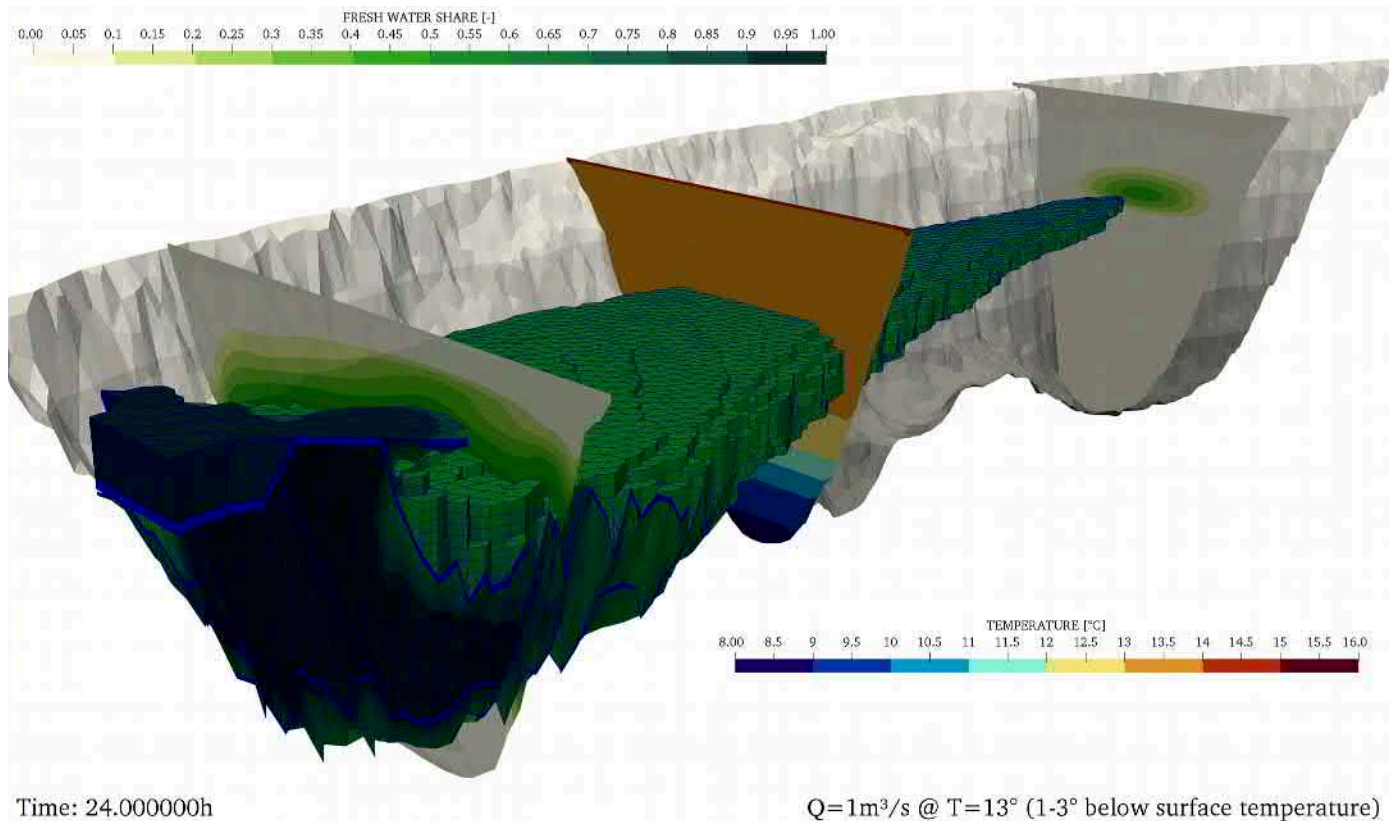


Fig. 11: Even a jet with 100 m<sup>3</sup>/s leaves zones with old water in the depth



*Fig. 12: Fresh water at  $13^\circ\text{C}$  immediately sinks and builds a bubble of fresh water in  $\sim 6$  meters depth. (the fresh water bubble is displayed here if the share  $> 50\%$ ). The second slice shows the temperature profile at midnight, but the surface temperature follows a measured daily cycle.*

## V. CONCLUSION & RECOMMENDATIONS

Temperature driven mixing processes without externally driven velocity fields reveal the accuracy and definition range of several TELEMAC-3D submodels and features. These models are not wrong from a mathematical point of view, but they have some limitations from the computer hardware architecture or just from the fact that one describes the real world with linearized and discretized models.

The verdict of this project is, that TELEMAC-3D is ready for vertical thermal stratification studies, if one cares for the here mentioned traps and if the dataset is good enough.

The recommendation for data collecting is to collect temperature, oxygen and other parameters not only in one depth profile, but also at inflow and outflow and in occasional measured cross sections. Shading by trees and water plants should be documented by a webcam or drones especially for small lakes.

For TELEMAC-3D it would be a big improvement if there would be further research and developments about the “weak form of characteristics”, e.g. a new tidal flat algorithm that conserves tracers and a new inflow algorithm that prevents the excessive mass loss of tracers.

The model is now usable to study mixing effects of geometry changes and to add WAQTEL features.

## ACKNOWLEDGEMENT

This project was a contract R&D work for the German Federal Waterways Engineering and Research Institute / Bundesanstalt f. Wasserbau (BAW). All datasets are owned and provided by the client. The client designs the new geometrical solutions for lake Monsterloch based on this model.

## REFERENCES

- [1] J.-M. Hervouet: Lecture 7: Advection schemes (2017). Available in different versions from different events. E.g. UHM Advanced User Training Course II – Telemac & Sisyphe in Full Depth, Karlsruhe
- [2] J.-M. Hervouet. Hydrodynamics of Free Surface Flows modeling with the finite element method. John Wiley & sons, LTD, 2007.
- [3] J.-M. Hervouet. The Weak Form of the Method of Characteristics, an Amazing Advection Scheme. Proceedings of the XXth TELEMACMASCARET User Conference; October 16-18, 2013.
- [4] S. Pavan; R. Ata; J.-M. Hervouet. Ongoing research on advection schemes. Proceedings of the 21st TELEMAC-MASCARET User Conference; October 15-17, 2014.

# Developing and validating a Telemac3D model for *E. coli* and norovirus dispersal through aquaculture systems

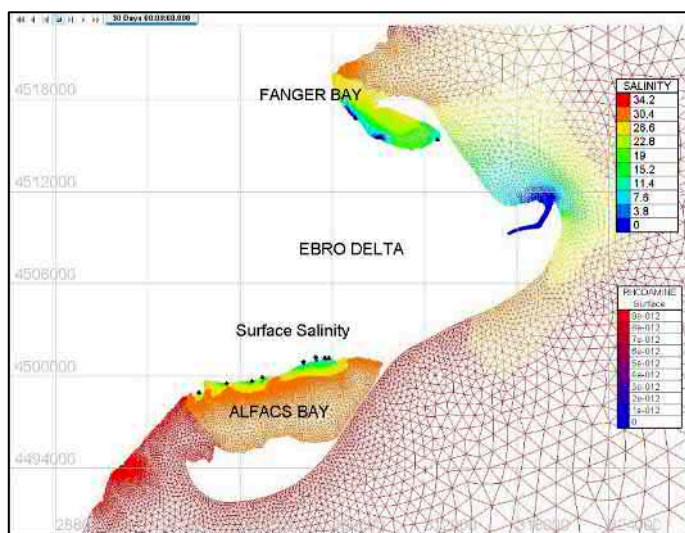
John Bacon, Simon Kershaw

Centre for Fisheries and Aquaculture Science, Pakefield Road, Lowestoft, NR33 0HT, UK

john.bacon@cefas.co.uk

The expansion and development of shellfish aquaculture has resulted in National regulatory bodies for water quality, turning to the use of numerical modelling to monitor the potential exceedance of thresholds of many pollutants or waterborne viruses. In shallow coastal or estuarine environments, locations of aquaculture developments near to wastewater discharges including storm overflows and other sources of contamination, are vulnerable to episodically high concentrations of substances with potentially harmful impacts on marine and human health.

Cefas has developed a series of Telemac3D models to monitor pollutant levels and effluent dispersion in several coastal locations in UK, France, Ireland and Spain. The example used in this paper, at Alfacs Bay in Eastern Spain, provides a microtidal environment and a temperate, shallow, seasonally stratified, coastal lagoon influenced by freshwater input of land drainage from the highly productive Ebro Delta region. Circulation and mixing in the bay are limited for much of the year giving the potential for nutrients and waste products related to the extensive bivalve farming systems located within a few hundred metres from the shoreline, to build up when conditions for the dispersal of these potential contaminants are poor.



The focus of the paper centres upon validating model simulations of the transmission of potentially harmful bacteria into areas of aquaculture production, comparing the modelled circulation of passive tracer release in Telemac3D, against a field experiment utilising a 12.4 h release of rhodamine dye tracer into the discharge at one of the coastal sewage treatment works (STW) outfalls. The validation of the model to simulate the dispersal of the rhodamine was used to calibrate the release of *E. coli* in the model. The Sant Carles de la Ràpita sewage treatment works discharges treated effluent into a drainage channel approximately 400 m north of the aquaculture sites. The *E. coli* released in

the model acts as a faecal indicator for the degree of contamination in the water and degrades as a function of temperature, salinity and insolation. Analysis of residence times for these parameters in the bivalve production areas is an important step to understanding how the transmission of bacteria and virus such as *Vibrio* spp. and Herpes OsHV-1 can be controlled. These potentially harmful microbes can present a human health risk in shellfish consumed raw or subject to insufficient treatment post harvesting or impact commercial production of Blue Mussel and Pacific Oyster.

Further work using particle techniques was carried out to investigate the transmission of another common waterborne human pathogen, norovirus (NoV). The behaviour of norovirus particles was matched as closely as possible to their physical parameters, the Lagrangian motion being more appropriate to their transmission than a diffuse tracer.

The results give confidence to regulators that the use of relatively inexpensive field experiments coupled with modelled simulations, microbiological transmission can be assessed and contaminant concentrations predicted under varying environmental conditions. These in turn can inform regulatory decisions for the management of aquaculture production.

**Proposed session:** Water quality, biodiversity, ecology and environmental pollution

**Key words:** Telemac3D, Pathogens, Particle Tracing, Water Quality, Virus, Rhodamine

**Speaker:** John Bacon



# Internal boundary conditions for Telemac

Clemens Dorfmann  
flussbüro OG – hydro engineering research  
Brockmanngasse 108, A-8010 Graz  
clemens.dorfmann@flussbuero.at

**Abstract:** Many of the rivers in Austria aren't natural flowing water courses anymore but are interrupted by hydro power plants for electricity generation. Typically, the weir at a run-of-river hydro power plant is equipped with gates which are used for controlling the water level in the impounding reservoir and the associated turbine outflow or, in case of floods, the weir overflow. The numerical modelling of a chain of hydro power plants in a river requires the use of internal boundary conditions in order to simulate the cascade effect.

In this contribution the implementation of internal boundary conditions in Telemac is presented. The numerical domain is composed of submodels where each represents a reservoir or a river section. The submodels are connected by internal boundary conditions at the virtual weirs which can be stage hydrographs or rating curves. At each internal boundary condition, the calculated outflow flux is simply transferred to the respective downstream submodel.

The implementation of the internal boundary conditions in Telemac has been validated by the 2D numerical simulation of an idealized river channel with three weirs and prescribed time dependent internal water level boundary conditions (Figure 1). The comparison of Telemac-2D with a 1D numerical model, which is equipped with state-of-the-art weir control routines, has shown almost perfect agreement in the calculated water levels and discharges.

With this rather simple approach more complex rules for the control of water levels and discharges at water constructions can be formulated. Furthermore, the method can be applied in the sediment transport module Sisyphe / Gaia for the accurate transfer of sediments at controlled water construction works.

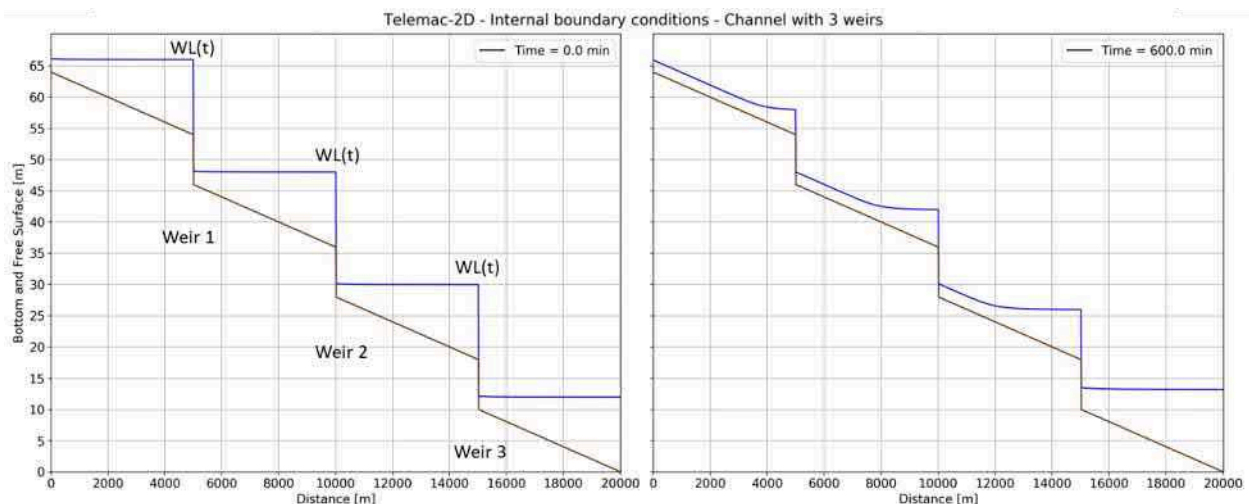


Figure 1 : Simulation of an idealized river channel with three weirs and time dependent water level boundary conditions

**Proposed session:** Waterworks, coastal structures design and sustainability

**Key words:** Internal boundary conditions

**Speaker:** Clemens Dorfmann



# Visualising uncertainties in coastal flooding

John H. Maskell

JM Coastal Ltd

Preston, United Kingdom

[john.maskell@jmcoastal.co.uk](mailto:john.maskell@jmcoastal.co.uk)

**Abstract—** Low-lying coastal and estuarine regions can be susceptible to flooding. Modelling coastal flooding is complex and is often the result of a combination of physical phenomena that need to be simulated to capture the extent of the inland inundation. Three case studies are considered in the UK, where uncertainty and drivers of coastal flood risk are explored through modelling and visualisations. At New Brighton, a town on the coast of the Eastern Irish Sea, an investigation of flood risk due to the combination of high-water levels and waves was carried out. A long-term Monte-Carlo simulation was used to simulate correlated samples of combined water levels and wave heights. Coastal flood simulations were then carried out for 8 samples of combined water levels and wave heights with a joint probability return period of 100 years. An offshore model system (TELEMAC-2D) was used in combination with a high-resolution nearshore modelling system (TELEMAC-2D coupled with TOMAWAC) to couple the tide and surge with the waves and simulate water levels and wave heights right up to the defence line. At the defence line overflow and wave overtopping rates were used as boundary conditions to an inundation model. The extent of coastal flooding in New Brighton varies significantly for wave-surge events with a joint probability of 100 years. Waves are an important flooding mechanism but are dependent on high water levels reducing the effective freeboard of the coastal defence. In a second case study uncertainty in coastal flooding was visualised at Hornsea due to the range of uncertainty in the 100-year return period coastal water elevation and the overtopping due to 3 m waves at the defences. In addition to the uncertainty, the wave overtopping is dependent on the water level that determines the freeboard at the defences. Considering the range of uncertainty at this location decreases or increases the simulated flood extent by 58% and 82% respectively. On December 5<sup>th</sup>-6<sup>th</sup> 2013, Cyclone Xaver generated storm surge levels along the coastal regions of the southern North Sea that were the highest on record at some tide gauge locations on the UK East Coast. Close to Boston dike failure led to the inundation of a recycling plant, a number of businesses and the surrounding crop fields. TELEMAC-2D was used to simulate the dike breach as it allows you to simulate dike breaching for a range of scenarios and growth mechanisms. Visualisations of the flooding due to the breach were created. Including dike breaching in coastal flood risk simulations is an important mechanism in determining the range of potential flood extents.

## INTRODUCTION

Coastal flooding in low-lying coastal regions can have devastating consequences as these regions can often be densely populated and have high concentrations of infrastructure. Coastal flooding is caused by meteorologically-driven events that cause high tidal levels and waves to flow inland beyond the expected high tidal extents, over natural topography and coastal defences. This can cause damage to buildings, roads and farmland as well as presenting a danger to life.

From a modelling perspective, coastal flooding is a complex task and is often the result of a combination of physical phenomena that needs to be simulated accurately to capture the true extent of the inland inundation. These include:

- Tide and storm surge modelling
- Wave modelling including wave overtopping and wave set-up
- High river and estuarine flows
- Defence breaching
- Inland propagation of the flood wave

Predicting coastal flooding at a particular return period has a degree of uncertainty associated with it. Some of the uncertainty may be safely ignored and will make little difference to the final simulated flood footprint. However, some of the uncertainty lies in such a range that it can make a significant difference to the predicted flood extent and cannot be ignored when considering the possible consequences for a given return period. Some sources of uncertainty in coastal flood modelling include the surge level and wave overtopping at the coast, the height and strength of the coastal defences and the Digital Terrain Model (DTM) and roughness for simulating inland inundation. At longer return periods the uncertainty increases and becomes harder to quantify, as does the consequence this uncertainty poses. Another challenge resides in relating this uncertainty in a meaningful way to decision or policy makers that may have implications for coastal planning. If the uncertainty in the 100-year return period surge level is  $\pm 0.4$  metres, what does that really mean or look like for a given location? In this paper we consider including these uncertainties and interactions of the main drivers of coastal flooding in flood simulations, and visualizing the differences made by their influence on the simulated flood extents for three case studies. We create visualisations as a way of looking at the impact of these uncertainties. This can be a good way of explaining potential flood risk to stakeholders in a way that is more intuitive.

Due to its location in the Eastern Irish Sea, New Brighton is affected by a large tidal range with potential storm surges and large waves. Although the town is protected by coastal defences such as the King's Parade Sea wall and breakwaters, the combination of high-water levels and waves has led to significant coastal flooding, most notably in December 2013 [1]. On 5<sup>th</sup> December 2013 flooding caused significant disruption and the council carried out a flood investigation report [2]. In this case study an investigation of flood risk due to the combination of high-water levels and waves was carried out using water level data from the tide gauge at Liverpool and the Liverpool bay WaveNet buoy [3]. Coastal flood simulations were then carried out for eight samples of combined water levels and wave heights with a joint probability return period of 100 years.

Hornsea on the UK East Coast has suffered from significant coastal erosion where sand transported by longshore drift, and subsequent cliff erosion, has led to a need to manage the region's natural defences to wave attack and flooding. Hornsea has also been flooded twice in recent times when storm surge and waves have overtopped the town's coastal defences. Significant flooding occurred in December 2013 and more recently on January 13<sup>th</sup> 2017, where predicted storm surge levels lead to an evacuation of part of the town as homes and businesses suffered flooding. Hornsea is susceptible to coastal flooding by surge and wave levels that exceed the coastal defence elevation as it has a region of low-lying land where flood warnings are issued by the Environment Agency (EA). The EA publish extreme sea levels in a coastal design sea levels database derived from extreme value analysis, joint probability and numerical modelling [4]. The database includes a range of uncertainty based on the methods used to derive each return period sea level. Potential flood footprints are simulated (using Flood Modeller [5]) at Hornsea due to the range of uncertainty in the 100-year return period coastal water elevation and the overtopping due to 3 m waves at the defences.

On December 5<sup>th</sup>-6<sup>th</sup> 2013, Cyclone Xaver generated storm surge levels along the coastal regions of the southern North Sea that were the highest on record at some tide gauge locations on the UK East Coast, exceeding those of the disastrous 1953 event. In Boston, Lincolnshire, the River Haven burst its banks as the storm surge propagated up the estuary flooding many homes, businesses and the historic church. Near Boston dike failure led to the inundation of a waste recycling plant, a number of warehouses, business units and the surrounding crop fields. In this case study TELEMAC-2D, including the breaching routine, is used to simulate this event and recreate the observed flooding.

## METHODS

### A. Case study 1

Observations of sea level at Liverpool Gladstone dock were downloaded from the British Oceanographic Data Centre (BODC) website for the period 1992 to 2017. The skew surges were calculated by subtracting the harmonic tidal high-water level prediction from the observed high-water level,

irrespective of phase difference in the same tidal cycle. Skew surge values that were greater than the 97.5 percentile value were retained. A probability density of function (PDF) of the tidal heights was generated using the harmonic predictions at Liverpool. It has been shown that there is no correlation between skew surge magnitude and tidal range [6]. Therefore, all skew surges have an equal probability of occurring with any tide where the probability of the total water level is simply the probability of the skew surge magnitude multiplied by probability of the tidal high-water magnitude from the tidal PDF. Return periods for extreme sea level were therefore determined using this Skew Surge Joint Probability Method [7]. Wave data was downloaded from the WaveNet buoy in Liverpool Bay. Maximum wave values at high water that were at least 24 hours apart were extracted from the data. A Weibull distribution was fitted to the wave heights and the 100-year return period wave height determined. Wave heights that were greater than or equal to the 100-year return period wave height were extracted from the data. Generalised Pareto Distributions (GPD) were fitted to the extreme observed waves and skew surges using a maximum likelihood estimator (MLE) to generate the shape ( $\alpha$ ) and scale ( $\beta$ ) parameters so that extreme tail distributions for both variables could be created. See (1) where  $\Pr(X > x)$  is the probability of a skew surge or wave height ( $X$ ) being greater than the value ( $x$ ),  $n$  is the number of values less than  $x$  and  $xl$  is the total number of values. A Monte-Carlo simulation was carried out to randomly sample the marginal distributions of skew surge and waves. Two thousand years of high-water levels and waves were generated taking into account the correlation between them [8]. See (2) where  $H_{sc}$  is the correlated wave height,  $\rho$  is the correlation coefficient,  $ss$  is the skew surge and  $H_s$  is the uncorrelated simulated wave height. The joint probability of every combination of water level and wave height could then be determined. These values were then gridded and contours of joint probability determined (Fig. 2).

$$P_r(X > x) = 1 - \left(\frac{n}{xl}\right) * (1 + \alpha * x/\beta)^{(-\frac{1}{\alpha})} \quad (1)$$

$$H_{sc} = (\rho * ss) + ((1 - \rho^2)^{0.5}) * H_s \quad (2)$$

Eight samples of combined wave and water level heights that make up the contour with a joint probability that relates to a return period of 100 years were selected to carry out detailed flood risk simulations. A regional Irish Sea model in TELEMAC-2D was used to determine the tidal distribution in the region. TPXO tidal boundary conditions [9] combined with the TELEMAC-2D option "COEFFICIENT TO CALIBRATE TIDAL RANGE" could be used to generate water levels at Liverpool that corresponded to water levels in the eight samples. A high-resolution nearshore model (Fig. 1) was created and time-series of water levels were extracted from the regional model as boundary conditions to the local model for each case. The high-resolution nearshore modelling system (TELEMAC-2D coupled with TOMAWAC) that couples the tide and surge with the waves was then used to simulate water levels and wave heights right up to the defence line. Only waves propagating from the west were simulated in this experiment which is the dominant wave direction in the

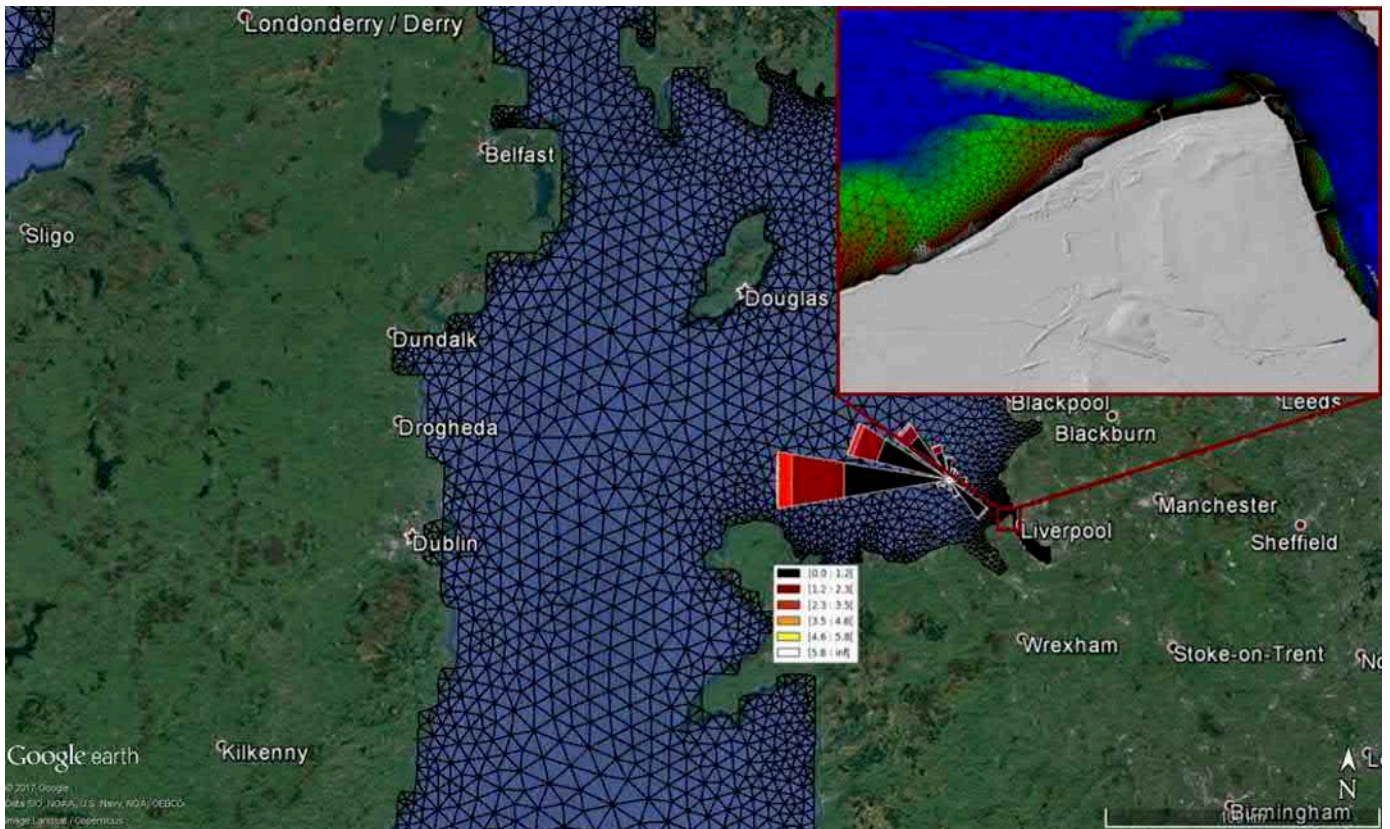


Fig 1. Low resolution Irish Sea mesh with nested high-resolution local mesh shown in close-up. High resolution mesh has 10 m elements at coast to accurately resolve coastal geometry and breakwaters. Wave rose with dominate wave directions and magnitudes also shown.

Eastern Irish Sea as shown by the wave rose (Fig. 1). At the defence line overflow and wave overtopping rates were calculated using equations detailed in the Eurotop manual [10]. The overtopping discharge due to the water level exceeding the defence height ( $Q \text{ m}^3/\text{s}$ ) was calculated using the weir equation (Equation 3) where  $C_d$  is the weir discharge coefficient (0.54),  $g$  is the acceleration due to gravity ( $9.81 \text{ m/s}^2$ ) and  $H$  is the water level that exceeds the height of the defence. This discharge was combined with the wave overtopping discharge calculated using EurOtop. There are uncertainties associated with the discharge calculated using the weir equation. However, they are not explored in this study. The combined wave and storm surge discharge was calculated from the nearest node in the nearshore model to each coastal boundary cell in an inundation model (Flood Modeller) and used as a one-way coupled boundary condition. The inundation model was developed using a 5 m resolution grid aggregated from 1 m lidar data from the EA open survey data. The maximum simulated flood footprint extent was output from Flood Modeller as an Esri Shapefile. This was added as a layer in Google Earth and used to produce images that visualise the extent of the simulated flooding in the town.

$$Q = C_d * (gH^3)^{0.5} \quad (3)$$

### B. Case study 2

Extreme sea levels around the UK coastline are published in the EA coastal design sea levels database and are derived from extreme values analysis, joint probability and numerical modelling. The database includes a range of uncertainty based on the methods used to derive each return period sea level [4]. Flood footprints at Hornsea were simulated (using Flood Modeller) due to the range of uncertainty in the 100-year return period coastal water elevation and the overtopping due to 3 m waves at the defences. No correlation between the wave height and the water level, or their joint probability, was determined. The wave overtopping is however dependent on the water level that determines the freeboard at the defences. The published range of uncertainty for the 100-year return period water level at Hornsea is  $\pm 0.4 \text{ m}$ . The range of uncertainty in the overtopping volume for the given wave condition can be examined by subtracting or adding one standard deviation to the coefficients in the equations that determine the mean overtopping discharge in the Eurotop manual [10]. The combined wave and storm surge discharge was calculated ( $Q \text{ m}^3/\text{s}$ ) and used as a boundary condition to force the inundation model (see methods Case study 1). The default footprint (Sim 0) was determined by the mean 100-year return period water level and the mean overtopping discharge. Six further flood footprints were generated using different combinations of the uncertainties in the water level



and the overtopping discharge for a given wave height (see Table 1). As in case study 1, Esri Shapefiles were generated and opened in Google Earth to create images to visualise the flood extent.

### C. Case study 3

To simulate the dike breach at the recycling plant near Boston in December 2013, a mesh was created in Blue Kenue using publicly available data. The mesh extends offshore from the study site to simulate the surge propagation into the region, resolving the River Haven and region of inundation at increased resolution. High-resolution LIDAR data (1 m) and a high density of mesh elements allowed the dike to be well-resolved. A North Sea TELEMAC-2D model was used to simulate storm surge in the region and provide boundary condition water levels to the higher resolution model. TELEMAC-2D allows you to simulate dike breaching for a range of scenarios and breach growth mechanisms. Based on knowledge of the breach location after site investigation, breach growth was simulated at this location as well as flow through the breach into the area behind during the event. The TELEMAC-2D breach routine was used to simulate the width of the breach (20 m), the breaching process, including the timing (HW – 1 hr), duration (3600 seconds), lateral growth and final elevation of the breach (0.0 m) and nodes on the meshed dike where the breach would develop. A three-dimensional visualisation of the dike breach and water levels was visualised using the TELEMAC-2D results file and a video create using the Blue Kenue software.

## RESULTS

### A. Case study 1

Combining water levels and wave heights with the same joint probability return period causes significant differences in the simulated flood extent with a range in flooded area of 0 m<sup>2</sup> to 10,300 m<sup>2</sup>. The largest simulated waves (5.9 m) cause no overtopping and inundation combined with a water level of 1.7 m. Joint probability wave heights decrease from 5.9 m to 2.3 m until the maximum inundation is reached (Fig. 2). The largest flooded area is caused by a water level of 6.6 m and a wave height of 1.2 m. A 100-year return period water level of 6.7 m with no waves causes a lower simulated inundation area of 10,140 m compared to the maximum of 10,300 m<sup>2</sup>. The largest flooded areas affect waterfront park areas along the mainly northerly orientated waterfront. However, flooding affects leisure and commercial properties such as a mini golf course and a retail and leisure park. Residential properties close to the waterfront within the estuary are more sheltered to waves from the west but are affected by flooding when the joint probability return period of 100 years is dominated by higher water levels.

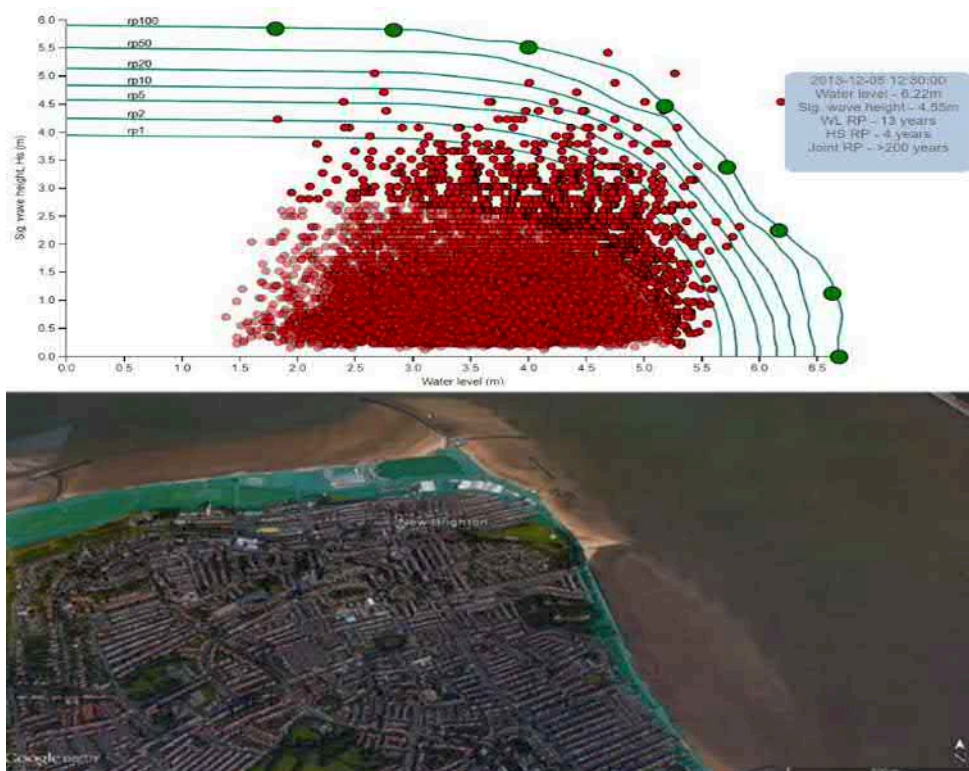


Fig 2. Observed combined surge and wave events (red points) and contours of equal joint probability. Visualisation of simulated coastal flooding due to surge (6.6 m) and waves (1.2 m) with a joint probability of 100 years.



### B. Case study 2

Including uncertainty in the 100-year return period water levels and in the overtopping equations for a given significant wave height at the coastal boundary at Hornsea leads to significant changes in the simulated inundation. The flood extents range from a minimum of 63,100 m<sup>2</sup> to a maximum of 271,875 m<sup>2</sup>, increasing the potential flood area by 4.3 times. The default experiment with a mean estimate of the 100-year return period water level and overtopping discharge for a 3 m wave height generates a simulated flooded area of 149,550 m<sup>2</sup>. Reducing the 100-year return period water level by the maximum estimated error range of 0.4 m or reducing the mean overtopping discharge by one standard deviation has similar effects on the change in simulated flood extent, reducing the simulated flood extent by 34% and 31% respectively. However, increasing 100-year return period water level by 0.4 m has a much bigger impact on the simulated flood extent than increasing the mean overtopping discharge by one standard deviation, increasing the simulated flood extent by 71% and 38% respectively. The worst-case scenario, whereby the maximum water levels and wave overtopping discharges are considered based on their uncertainty, increases the simulated flood extent by 82%.

Sim #	Table 1. Flood simulations			
	Surge (m)	Wave overtopping, $Q$ (m <sup>3</sup> /s)	Flooded area (m <sup>2</sup> )	% change
Sim 0	+/- 0	Mean	149,550	0
Sim 1	-0.4	-1 Std dev	63,100	-58
Sim 2	-0.4	Mean	98,550	-34
Sim 3	+/- 0	-1 Std dev	103,375	-31
Sim 4	+/- 0	+1 Std dev	206,450	+38
Sim 5	+0.4	Mean	254,325	+71
Sim 6	+0.4	+1 Std dev	271,875	+82



Fig 3. Range of simulated flood extents at Hornsea. Sim 0 (green), Sim 1 (blue) and Sim 6 (red) – see table 1.

### C. Case study 3

The TELEMAC-2D breaching routine meant that a breaching event could be simulated with prior knowledge of the breaching location and approximate width. The timing and

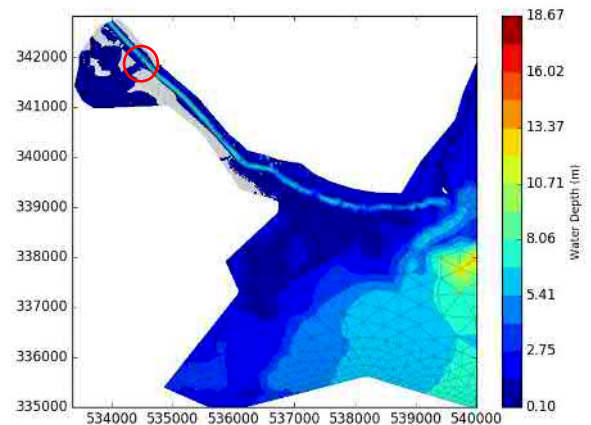


Fig 4. Simulated water depths in the River Haven including flow through a simulated dike breach (534500E,341800N). Breach location shown in red.

growth rate of the breach was based on assumptions in an attempt to reproduce the observed flooding behind the dike. Adding a breach development to the TELEMAC-2D simulation causes water to inundate the meshed region behind the breach. The observed inundated area was simulated including the flow of water through the dike breach, between two regions of raised land and into an area comprised of agricultural land and a recycling plant and industrial estate. The resultant simulated inundation could be visualised in 2D (Fig. 4) and 3D.

## DISCUSSION

### A. Case study 1

New Brighton is susceptible to flooding by both waves and storm surge. This includes both leisure, retail, residential and commercial properties. The extent of flooding is sensitive to the magnitude of the waves and water levels in combination. Combined water levels and wave heights with a joint probability relating to the same return period (e.g. 100 years) can produce significantly different flood extents. For the largest waves, the combined water level at the 100-year return period is relatively low. Therefore, there is little or no water at the toe of the coastal defences and, whilst the offshore waves are large, they break before reaching the defences and do not pose an overtopping risk. The decrease in wave height is initially gradual as the joint 100-year return period water level increases. Therefore, at a certain magnitude, although the water level is not high enough to overflow the defences, it is deep enough to allow offshore waves to reach the defences and cause overtopping, increasing the flood extent. The largest flood extent, as observed by other authors [11], occurs when the joint 100-year return period water level becomes high enough to overflow some of the defence crests. The largest flood extent occurs during the second highest water level sample. The decrease in water level from the highest is insignificant. Overflow of the defences still occurs whilst the presence of waves increases the flooding due to overtopping where the freeboard is negligible. Taken in isolation, the wave

heights and water levels are not associated with long return periods. However, in combination they become much rarer events. For example, the water level of 6.22 m and wave height of 4.55 m observed on 5<sup>th</sup> December 2013 have estimated return periods of 13 years and 4 years respectively (Fig. 2). However, taken together they have an estimated joint return period of 200 years or more, as observed in another study [1]. Therefore, it is important to consider the joint probability of the main drivers of coastal flooding to fully ascertain the bounds of the potential risk.

### B. Case study 2

Hornsea is susceptible to coastal flooding by surge and wave levels that exceed the coastal defence elevation as it has a region of low-lying land where flood warnings are issued by the Environment Agency. Therefore, uncertainties in the potential water levels at the coast and the total wave overtopping discharge due to waves can have a significant impact in this region. Uncertainty in the 100-year return period water level has the biggest impact on the extent of simulated flood extents. However, uncertainty in the overtopping discharge also creates significant changes for a given water level and should also be considered. As wave overtopping is dependent on the water level that determines the freeboard at the defences, uncertainties in both variables are not independent and should be considered in conjunction. It is evident that in regions such as Hornsea this uncertainty should be considered when planning coastal flood protection schemes as the difference in flood extents could really affect the efficacy of a particular scheme.

### C. Case study 3

Including breaching in TELEMAC-2D is a useful tool to simulate historic events and also potential flood risk scenarios. In this instance flooding would not have occurred if it were not for the dike breach, and only by including it in the simulation could the event be simulated. Therefore, when simulating flood risk scenarios for potential future events it is essential to include potential breach events, where appropriate, to fully understand the potential risk. However, this may be problematic due to the potential for multiple different breach scenarios both in terms of number of breach locations and breach extent and growth rate at a single breach location. Simulating multiple events and breach scenarios is computationally expensive due to the small time-step and element size needed to resolve dikes in the hydrodynamic simulation but could be partially resolved through the use of CPU clusters and parallel processing.

### CONCLUSION

This study has highlighted the need to include the interaction of the main drivers of flood risk, such as water level and wave height, as the magnitude of each component can have significant impacts on the extent of the potential flood risk. This includes other components not included in this study such as storm surge and high river flows in estuaries [12]. Uncertainties in the main drivers of coastal flood risk must also be included in simulations to fully understand the full extent of the potential risk at a given return period, or in the

magnitude of one the variables, such as wave height, leading to overtopping. The question for planners and stakeholders is whether to take the mean or a more conservative approach when considering the uncertainty. In terms of coastal flood risk protection schemes this will also depend on the budget available, the exposure at the coast (people and property) and what is determined to be an acceptable level of risk. Displaying the effect combinations of the main drivers of coastal risk, and uncertainty in their magnitudes, in visualisations of the simulated flood extent is a good way of conveying the impact in a way that is easy to understand to both experts and non-expert stakeholders.

### REFERENCES

- [1] Wadey M., Brown J., Haigh I. & Dolphin T. Assessment and comparison of extreme sea levels and waves during the 2013/2014 storm season in two UK coastal regions. *Nat. Hazards Earth Syst. Sci.* 15, 2209–2225 (2015).
- [2] Flood investigation report for December 5<sup>th</sup> 2013 – Wirral Council
- [3] <https://www.cefas.co.uk/cefas-data-hub/wavenet/data-policy/>
- [4] Environment Agency (2011) Coastal Flood Boundary Conditions for UK Mainland and Islands. Project: SC060064/TR2: Design Sea levels. <https://www.gov.uk/government/publications/coastal-flood-boundary-conditions-for-ukmainland-and-islands-design-sea-levels>.
- [5] <https://www.floodmodeller.com/>
- [6] Williams, J., K. J. Horsburgh, J. A. Williams, and R. N. F. Proctor (2016), Tide and skew surge independence: New insights for flood risk, *Geophys. Res. Lett.*, 43, 6410–6417, doi:10.1002/2016GL069522.
- [7] Batstone C. et al. A UK best-practice approach for extreme sea-level analysis along complex topographic coastlines. *Ocean Eng.* 71, 28–39 (2013).
- [8] Hawkes P.J. et al. The joint probability of waves and water levels in coastal engineering design. *Journal of Hydraulic Research.* 40, 241–251 (2002).
- [9] Egbert, Gary D., and Svetlana Y. Erofeeva. "Efficient inverse modeling of barotropic ocean tides." *Journal of Atmospheric and Oceanic Technology* 19.2 (2002): 183–204.
- [10] EurOtop - Manual on wave overtopping of sea defences and related structures (2018).
- [11] Prime, Thomas; Brown, Jennifer M.; Plater, Andrew J.. 2016 Flood inundation uncertainty: the case of a 0.5% annual probability flood event. *Environmental Science & Policy*, 59, 1–9.
- [12] Maskell, J.M., Horsburgh, K., Lewis, M.J. and Bates, P., 2013. Investigating river-surge interaction in idealised estuaries. *Journal of Coastal Research*. Volume 30, Issue 2: pp. 248 – 259.